



TECHNISCHE
UNIVERSITÄT
WIEN

DISSERTATION

Electronic correlation and transport phenomena in Mott and Kondo materials

zur Erlangung des akademischen Grades
Doktor der Naturwissenschaften (Dr. rer. nat.)

ausgeführt am Institut für Festkörperphysik
der Technischen Universität Wien

unter der Leitung von
Privatdoz. Dr. Jan M. Tomczak
Univ.Prof. Dr. Karsten Held

von
Dipl.Ing. Matthias Pickem, BSc
Matrikelnummer: 01125476

Wien, 2024

Deutsche Kurzfassung

Starke elektronische Korrelationseffekte stellen die Grundlage für eine Großzahl von physikalischen Phänomenen in Materialien dar, welche sich derzeit im Fokus der Festkörperforschung befinden. Das Verständnis korrelierter, elektronischer Zustände, deren Modifizierung durch externe Stimulation, und dadurch entstehende kollektive Anregungen, ist daher ein Leitthema der heutigen Forschung. Die vorliegende Dissertation beschäftigt sich in diesem Sinne mit zwei „Arten“ von Materialien: (i) Systeme, in denen starke elektronische Wechselwirkungen zu einer sogenannten Mott Lokalisierung führen können und (ii) Systeme, in denen die magnetische Kopplung lokaler Momente zu Signaturen des Kondo Effektes führt.

Da die Merkmale dieser Materialien über das Bild von unabhängigen Teilchen weit hinausgehen, ist es zuerst notwendig, eine passende quantenfeldtheoretische Beschreibung des Vielteilchenproblems einzuführen. Mit selbiger wird dann, im ersten Teil dieser Dissertation, das Übergangsmetalloxid SrVO_3 behandelt. Im Kontext jüngster Experimente, durchgeführt mit epitaxialen Kristallwachstumsmethoden, werden zuerst Varianten des für Mott Materialien charakteristischen Metall-Isolator Übergangs simuliert und diskutiert. Im Speziellen werden, mithilfe der dynamischen Molekularfeldtheorie, die entsprechenden Ein- und Zweiteilchen Propagatoren analysiert, welche die vorherrschenden Korrelationseffekte enkodieren. Diese Einsichten erlauben uns dann, die Spektraleigenschaften, vorherrschende Quantenfluktuationen und Transportkoeffizienten zu charakterisieren.

Der zweite Teil dieser Dissertation fokussiert sich auf die Korrelationsphänomene, die im, auf Cerium basierenden, Kondo Isolator $\text{Ce}_3\text{Bi}_4\text{Pt}_3$ auftreten. Mithilfe eines qualitativen Vergleichs mit dem periodischen Anderson Modells wird der atomare Aufbau und der daraus folgenden korrelierte Elektronenzustand diskutiert. Ausgehend davon wird, erstens, der Einfluss von simuliertem hydrostatischen Druck analysiert, um das beobachtete, nicht-kanonische Verhalten der Bandlücke im Experiment zu erklären. Daraufaufgehend wird, zweitens, ein Kandidaten Mechanismus identifiziert (Lebensdauer Effekte), welcher in der Lage ist, das bei tiefen Temperaturen beobachtete Phänomen der Saturierung des Widerstands in $\text{Ce}_3\text{Bi}_4\text{Pt}_3$ und ähnlichen Isolatoren mit Hybridisierungs Bandlücke zu beschreiben. Basierend auf demselben Mechanismus und darauf zugeschnittener Näherung werden anschließend alle höhergradigen Transportfunktionen abgeleitet, welche etwa die Grundlage für thermoelektrische und magnetoelektrische Transportkoeffizienten darstellen. Um die universelle Gültigkeit unserer entwickelnden Theorie zu bewerten, wird der Formalismus auf eine breite Palette von Modellen und realistischen Kristallstrukturen angewendet. Zudem stellen wir die entwickelten Methoden in Form eines Open-Source-Programmpaketes der wissenschaftlichen Gemeinschaft zur Verfügung.

Abstract

Strong electronic correlation effects are at the heart of a plethora of physical phenomena in materials at the forefront of condensed-matter research. Understanding the correlated electronic state and its modification by external stimuli, including the emergence of collective excitations, are among the leading topics of interest these days. The present thesis concerns itself with two distinct “types” of material classes: (i) systems where, through strong electron interactions, the effects of Mott localization are prevalent and (ii) systems where the magnetic coupling of local moments leads to signatures of the (lattice) Kondo effect.

As the emerging characteristics of these materials are, per definition, beyond a free-particle picture, it is necessary to first introduce an appropriate quantum-field theoretical description of the many-body problem. Then, the first part of this thesis will mainly focus on the transition-metal oxide SrVO_3 : Motivated by recent experiments that employ epitaxial growth methods, we scrutinize the, for Mott materials characteristic, observed metal-insulator transitions. With the help of dynamical mean-field theory (and beyond) the corresponding one- and two-particle propagators, encoding the prevalent correlations effects, are analyzed. These insights allow us to characterize spectral properties, quantum fluctuations and transport coefficients alike.

The second part of this thesis focuses on the emergent correlation phenomena in the cerium-based Kondo insulator $\text{Ce}_3\text{Bi}_4\text{Pt}_3$. By comparison with the prototypical periodic Anderson model, we scrutinize the crystal structure, its correlated electronic state, and the reason why hydrostatic pressure leads to a non-canonical behavior in experiment. From there, a candidate mechanism is developed that supports the phenomenon of resistivity saturation both in $\text{Ce}_3\text{Bi}_4\text{Pt}_3$ and other related hybridization-gap insulators. Based on the same underlying premise of lifetime effects, all higher order transport kernels, that build the foundation of thermoelectric and magnetoelectric transport coefficients, are derived and benchmarked. To assess the general validity of this formalism, it is applied on a wider range of models and realistic crystal structures. Furthermore we make the developed methodology available in the form of an open source program package.

Contents

	Page
List of publications	xi
Open source software	xii
1 Introduction	1
2 Mott materials and models thereof	5
2.1 The relevance of the Hubbard model	5
2.1.1 Kohn-Sham density functional theory	6
2.1.2 Towards strong interactions: Hubbard model	9
2.1.3 Localized multi-orbital basis and interaction matrix	13
2.2 The inconspicuous case of SrVO ₃	18
2.2.1 Crystal and band structure of bulk SrVO ₃	18
2.2.2 Interaction matrix parametrization	22
2.2.3 Many-body renormalizations: Dynamical mean-field theory	22
2.2.4 Experimental context	31
2.3 Triggering the Mott transition	35
2.3.1 A perspective on d ¹ perovskite Mott insulators	35
2.3.2 Distortion phenomena in substrate deposited SrVO ₃	38
2.3.3 Dimensionality reduction in thin films	63
2.4 Surface phenomena in SrVO ₃	77
2.4.1 Surface overoxidation of thick SrVO ₃ films	79
2.4.2 Evolution of apical oxygen coverage with film thickness	81
2.4.3 Effects of surface overoxidation	82
2.4.4 Structural intricacies of VO ₂ terminated films	92
2.4.5 Discussion	103

2.5	Non-local signatures in pristine SrVO ₃ monolayers	105
2.5.1	Band structure and density of states	106
2.5.2	Stoichiometric Mott insulator	108
2.5.3	Orbital reconfiguration under doping	110
2.5.4	DMFT susceptibilities	112
2.5.5	Phase diagrams	126
2.5.6	Orbital mapping	130
2.5.7	Non-local self-energy corrections	132
2.5.8	Binaural fluctuation diagnostics	143
2.5.9	Discussion and perspective	150
2.6	Self-consistent ladder dynamical vertex approximation	152
2.6.1	Synopsis	152
2.6.2	Optical conductivity	156
2.6.3	Two-dimensional Hubbard model	167
3	Kondo materials and models thereof	191
3.1	Local moments and the formation of Kondo insulators	191
3.1.1	Local impurity: Kondo effect	192
3.1.2	Periodicity: Lattice Kondo effect	198
3.1.3	The complication of magnetic ordering	212
3.2	Resistivity saturation in Ce ₃ Bi ₄ Pt ₃	219
3.2.1	Experimental evidence	220
3.2.2	Many-body corrections	221
3.2.3	Conductivity tensor	229
3.2.4	Discussion	238
3.3	Thermoelectric transport coefficients generated by intrinsic life times	240
3.3.1	Methodological context: Onsager coefficients	240
3.3.2	Kubo transport equations	246
3.3.3	Semiclassical Boltzmann limit	259
3.3.4	Transition-matrix elements	264
3.3.5	Discussion	265
3.4	Many-body transport phenomena in semiconductors	269
3.4.1	A new phenomenology of transport in semiconductors	271
3.4.2	Modeling materials	291
3.4.3	Summary	299

3.5	The Linear Response Transport Centre	301
3.5.1	Methodological context	302
3.5.2	Implementation	303
3.5.3	Technical details	304
3.5.4	Applications	313
3.5.5	Possible extensions	329
4	Conclusion	331
	Appendices	337
A.1	Many-body Green's functions	337
A.1.1	Matsubara Green's functions	337
A.1.2	Equation of motion	343
A.2	Matsubara summation technique	351
A.2.1	Spectral function	351
A.2.2	Occupation	353
A.2.3	Bare susceptibility	354
A.3	Two-particle correlation functions	356
A.3.1	Heat currents	356
A.3.2	Linear response in magnetic field	362
	Bibliography	371
	Acknowledgments	423
	Curriculum vitae	425

List of publications

- **2018-Jan-26** — Journal of the Physical Society of Japan **87**, 041004 [1]
 - A. Galler, J. Kaufmann, P. Gunacker, M. Pickem, P. Thunström, J.M. Tomczak, K. Held
 - “Towards ab initio calculations with the dynamical vertex approximation”
- **2019-Aug-7** — Computer Physics Communications **245**, 106847 [2]
 - A. Galler, P. Thunström, J. Kaufmann, M. Pickem, J.M. Tomczak, K. Held
 - “The AbinitioDFA Project v1.0: Non-local correlations beyond and susceptibilities within dynamical mean-field theory”
- **2020-Aug-12** — Physical Review B **102**, 085124 [3]
 - P. Kappl, M. Wallerberger, J. Kaufmann, M. Pickem, K. Held
 - “Statistical error estimates in dynamical mean-field theory and extensions thereof”
- **2021-Jan-15** — Physical Review B **103**, 035120 [4]
 - J. Kaufmann, C. Eckhardt, M. Pickem, M. Kitatani, A. Kauch, K. Held
 - “Self-consistent ladder dynamical vertex approximation”
- **2021-Jul-26** — Physical Review B **104**, 024307 [5]
 - M. Pickem, J. Kaufmann, K. Held, J.M. Tomczak
 - “Zoology of spin and orbital fluctuations in ultrathin oxide films”
- **2021-Sep-14** — Physical Review B **104**, 115153 [6]
 - P. Worm, C. Watzenböck, M. Pickem, A. Kauch, K. Held
 - “Broadening and sharpening of the Drude peak through antiferromagnetic fluctuations”
- **2021-Oct-11** — Communications Physics **4**, 226 [7]
 - M. Pickem, E. Maggio, J.M. Tomczak
 - “Resistivity saturation in Kondo insulators”
- **2021-Dec-29** — Advanced Electronic Materials, 2101006 [8]
 - J. Gabel, M. Pickem, P. Scheiderer, L. Dudy, B. Leikert, M. Fuchs, M. Stübinger, M. Schmitt, J. Küspert, G. Sangiovanni, J.M. Tomczak, K. Held, T.-L. Lee, R. Claessen, M. Sing
 - “Toward functionalized ultrathin oxide films: The impact of surface apical oxygen”
- **2022-Feb-22** — Physical Review B **105**, 085139 [9]
 - M. Pickem, E. Maggio, J.M. Tomczak
 - “Prototypical many-body signatures in transport properties of semiconductors”

- **2022-Sep-30** — Physical Review Research **4**, 033253 [10]
 - M. Pickem, J.M. Tomczak, K. Held
 - “Particle-hole asymmetric lifetimes promoted by nonlocal spin and orbital fluctuations in SrVO₃ monolayers”
- **2023-Jul-17** — SciPost Physics Codebases **16** [11, 12]
 - M. Pickem, E. Maggio, J.M. Tomczak
 - “LinReTraCe: The Linear Response Transport Centre”

Open source software

- **AbinitioDΓA** – <https://github.com/abinitiodga/adga>
 License: GNU General Public License v3.0
 Release year: 2017
- **HDF5 wrapper** – https://github.com/mpickem/hdf5_wrapper
 License: MIT
 Release year: 2018
- **LinReTraCe** – <https://github.com/linretrace/linretrace>
 License: GNU General Public License v3.0
 Release year: 2022

Chapter 1

Introduction

Solid state physics is the study of rigid, condensed matter whose macroscopic and microscopic physical properties arise from the electromagnetic forces between the ensemble of atomic nuclei and electrons. It provides the foundation for a wide range of material classes and is thus closely related with the adjacent fields of (quantum) chemistry, biophysics, electrical and mechanical engineering.

Due to the astronomic number of degrees of freedom, an exact treatment of the arising many-body problem is impossible. Through the late nineteenth and early twentieth century, accompanied by the development of quantum mechanics, huge strides were made in improving our understanding of both materials and the phenomena they exhibit. The vast number of accessible observables allowed a wide range of theories to emerge, many of which are nowadays taught in undergraduate classes: the Boltzmann transport equations, the Drude model, the Sommerfeld theory of metals, the models of Debye and Einstein to characterize lattice excitations, Bose-Einstein and Fermi-Dirac statistics within quantum theory, band theory and the concept of Brillouin zones, Bloch theorem, and of course various developments necessary in describing (macroscopic) magnetism in matter including the models of Ising, Heisenberg, and Stoner.

Scope

In this thesis we follow the footsteps of Hohenberg and Kohn. Our study will focus on the electronic state and the emergent phenomena thereof, whose modern-day foundation was created by density functional theory in 1964. Despite the strong Coulomb interaction between electrons the paradigm of effectively non-interacting electrons is frequently used to great success. In a lot of crystal environments, the large kinetic energy, and consequent delocalization, of the electrons allows for a description of (modified) plane waves throughout the periodic, ionic potential. The resulting electron density of the ground state and quantities derived thereof then oftentimes match experimental observables quite accurately. Theoretical treatment becomes more complicated, once (dynamic) correlation effects between the electrons can no longer be assumed to be negligible. This predominantly occurs in materials

in which atomic components contribute via highly localized, partially filled sub-shells (orbitals). The strongest localization can, in principle, be found in transition metals containing (3/4)d orbitals or lanthanides and actinides containing (4/5)f orbitals.

In transition metals, *the* manifestation of strong correlation effects beyond the formation of a Fermi liquid, is the Mott insulating state: The Coulomb repulsion impedes the flow of electrons to such a degree that they become locked to their respective atomic sites. In the vicinity of this state, electron renormalizations remain elevated and quantum fluctuations then may lead to a plethora of novel regimes such as the opening of a pseudogap, (unconventional) superconductivity, and correlation driven charge ordered or magnetic states. At this moment in time, the poster children of this class of materials are the copper based high-temperature superconductors. While intriguing in themselves, the focus of the first part of this thesis will instead be on perovskite structures: In recent times they gained increased interest as they represent an essential ingredient in the (applied) research of heterostructures, nanofilms, and superlattices. Recent developments include transparent conductors, Mott transistors, spintronic devices, absorber materials in solar cells, to name a few.

In rare-earth materials, the atomic-like 4f orbitals frequently lead to the formation of localized magnetic moments. This in turn, through the (direct or indirect) coupling to the conduction electrons of the other participating atoms/shells leads to the emergence of the Kondo effect. These so-called heavy-fermion systems display fluctuations that can magnify the effective electron masses by orders of magnitude. In extreme cases, even the formation of (Kondo) insulators becomes possible, which will be the focus of the second part of this thesis. Through the hybridization of the 4f elements, accompanied by the strong Coulomb repulsion, notably thermoelectric transport properties become significantly modified which can be exploited in, e.g., thermoelectrics. Similar to Mott materials, these types of compounds are oftentimes on the brink of ordered states and display a wide range of exotic phases under minute perturbations.

In order to capture these phenomena, an appropriate quantum-field theoretical framework builds the foundation of our approaches beyond density functional theory. As external perturbations/excitations are at the heart of all experimental observables, we will introduce and work with apt correlation functions that intrinsically encode the processes we are interested in. We will compute (i) many-body Green's functions to capture excitations generated by, e.g., photoemission spectroscopy, (ii) magnetic/charge susceptibilities to capture the intrinsic spin/density fluctuations, which, e.g., an external magnetic field couples to, and (iii) current-current susceptibilities to compute transport quantities that capture the effect of external electric fields and temperature gradients. In a less theoretically involved way, we will work with experimental methods that are capable of (in)directly probing the ionic environment of the underlying crystal structure of the employed samples. This includes electron diffraction, direct imaging based on the tunneling effect, or Fourier imaging via X-ray radiation.

Outline

In [Chapter 2](#) we introduce the many-body problem within the solid-state environment and the concept of the aforementioned density functional theory. After that we lay the ground work for the description of correlation effects within the dynamical mean-field theory. We present the necessary one-particle descriptors and interpretations thereof that are necessary to describe the renormalized Fermi liquid state found within the transition metal perovskite SrVO_3 . After that our focus remains on SrVO_3 , which we use as a launching pad towards the investigation of various metal-insulator transitions. When put in extreme conditions, e.g., the external deformation of thick film setups as well as geometric restrictions in thin films, metal-insulator transitions are oftentimes observed in experimental setups. From there, we move towards a true two-particle description, scrutinize possible correlation-driven ordered states and analyze the feedback of fluctuation onto the one-particle level in ultrathin SrVO_3 monolayers with the help of the dynamical vertex approximation approach employed in `AbinitioDΓA`. In this context, we also derive the necessary equations for a description of (multi-orbital) current-current susceptibilities in the presence of vertex corrections (necessary for optical conductivities) and benchmark the set of equations for a commonly employed testbed: the two-dimensional Hubbard model.

In [Chapter 3](#) we focus on Kondo physics in the context of strongly correlated Kondo insulators. We introduce the Kondo effect within a general quantum impurity and compare the resulting features to the lattice case present in the periodic Anderson model. The signatures of the latter are then used to analyze the non-canonical nature of $\text{Ce}_3\text{Bi}_4\text{Pt}_3$, for which we further compute the full conductivity tensors. From them, we seek to distill the main ingredients necessary for describing the peculiarity of the resistivity saturation phenomenon and develop an apt reductionist theory. Based on the approach of lifetime broadening, we (analytically) derive all higher order transport kernels necessary for a description of frequently employed thermoelectric and magnetoelectric transport coefficients. We (numerically) benchmark the derived equations and further apply them in the context of other correlated hybridization gap insulators to assess the validity of the approach. Finally we showcase our implementation of the derived transport kernels within `LINRETRACE` with a focus on the necessary technical details.

We conclude the thesis at hand by summarizing our results and providing an outlook on future avenues in [Chapter 4](#). The majority of technical details and derivations, which are not all original to this thesis, can be found in the [Appendices](#).

Software

Different software packages were used to analyze, as well as generate data and figures throughout this thesis: `NumPy` [13] and `SciPy` [14] as the main numerical toolkit, `Matplotlib` [15] for general data visualization, `Engauge digitizer` [16] for data digitization, `JaxoDraw` [17] for Feynman diagrams, `VESTA` [18] for crystal structure generation, `FermiSurfacer` [19] for Fermi surface visualization, `Mathematica` [20] for symbolic transformations and analytic checks, and `Keynote` for miscellaneous tasks like creating flowcharts, merging of figures and sketching of lattices.

The external software packages used throughout this thesis, which our results heavily rely on include the full-electron DFT implementation of `Wien2K` [21, 22], the pseudopotential DFT implementation of `VASP` [23, 24, 25, 26], the crystalline structure visualization of `XCrySDen` [27], the interface `Wien2Wannier` [28] to `Wannier90` [29] for maximally localized Wannier functions, the DMFT and two-particle sampling implementation of `w2dynamics` [30], the analytic continuation of `ana_cont` [31], and the charge self-consistent DFT+DMFT code by Haule [32].

The technical details of the implementation of `AbinitioDΓA` [2, 33], its extensions towards self-consistency [4] and optical conductivities, and `LINRETRACE` [11, 12], are described wherever necessary in the main text.

Chapter 2

Mott materials and models thereof

In this first of two primary results Chapters, we present those results that fall under the umbrella of “Mott physics”. Starting off, we begin by introducing the methodologies necessary to describe signatures that stem from strong electronic correlation effects. Simulating materials in a realistic fashion, one has to account for their structural, chemical, and orbital complexity. The most common basis for the modelling of solids is Kohn-Sham density functional theory, providing the necessary foundation to incorporate strong interactions within dynamical mean-field theory later on. Based on these techniques, the majority of this Chapter deals with the strongly correlated transition-metal oxide SrVO₃ (SVO) and its tendency to turn insulating when put under certain, extreme conditions. Starting from a simple bulk description we gradually move towards more complex thin-film setups. We consider various surface terminations including complications arising from surface oxidization found in “unprotected” films. At the end of this Chapter we revisit the initial gateway towards strong correlations, the one-band Hubbard model: Applying our newly developed self-consistent dynamical vertex approximation to the two-dimensional variant of the model, we are able to calculate optical spectra and provide insight into the importance of genuine two-particle corrections.

2.1 The relevance of the Hubbard model

The (non-relativistic) physics of an ensemble of atomic ions and electrons can be condensed into a single Hamiltonian of the form

$$\mathcal{H} = \underbrace{-\sum_{\alpha} \frac{\hbar^2 \Delta_{\alpha}}{2M_{\alpha}} + \frac{1}{2} \sum_{\alpha \neq \alpha'} \frac{Z_{\alpha} Z_{\alpha'} e^2}{|\mathbf{R}_{\alpha} - \mathbf{R}_{\alpha'}|}}_{\mathcal{H}_n} - \underbrace{\sum_{\alpha, \mu} \frac{Z_{\alpha} e^2}{|\mathbf{R}_{\alpha} - \mathbf{r}_{\mu}|}}_{\mathcal{H}_{ne}} - \underbrace{\sum_{\mu} \frac{\hbar^2 \Delta_{\mu}}{2m_e} + \frac{1}{2} \sum_{\mu \neq \mu'} \frac{e^2}{|\mathbf{r}_{\mu} - \mathbf{r}_{\mu'}|}}_{\mathcal{H}_e}. \quad (2.1)$$

M_{α} are the masses of the N_n positively charged nuclei with atomic number Z_{α} . $m_e \approx 9.10938 \cdot 10^{-31}$ kg is the mass of the N_e negatively charged electrons with the elementary charge given by

$e \approx 1.602176 \cdot 10^{-19} \text{C}$. The positions of the nuclei \mathbf{R}_α and electrons \mathbf{r}_μ are accounted for via their respective differences in the Coulomb potential.

In a periodic solid, within the Born-Oppenheimer approximation [34] the nuclei part \mathcal{H}_n decouples from the electronic part \mathcal{H}_e leaving the nuclei-electron interaction \mathcal{H}_{ne} as a static, attractive, external potential within a purely electronic picture. The large number of degrees of freedom (electron density of the order of $10^{23} / \text{cm}^3$ in common metals such as copper) makes explicit calculations impossible. Consequently one typically resorts to a density description based on the Hohenberg-Kohn theorems that read

- The ground-state energy of a system of N indistinguishable particles in an external potential is a unique functional of the particle density $\rho(r)$.

$$E_0 = \min_{\rho} \{E[\rho(\mathbf{r})]\} = E[\rho_0(\mathbf{r})] \quad (2.2)$$

- The minimum of the $E[\rho]$ functional can be determined from a variation of the particle density.

$$\left. \frac{\delta E[\rho(\mathbf{r})]}{\delta \rho(\mathbf{r})} \right|_{\rho_0(\mathbf{r})} = 0 \quad (2.3)$$

These theorems, proven in its original publication, Ref. [35], provide the theoretical pillars upon which most of modern solid state physics and quantum chemistry is based on. The Hohenberg and Kohn approach was then carried further by Kohn and Sham in Ref. [36] where they transformed the problem of determining the ground state density to solving a set of self-consistent *one-particle* Schrödinger equations. In the following we will detail this transition to the so-called Kohn-Sham density functional theory (DFT from here on) and the additions necessary to include strong correlation effects.

2.1.1 Kohn-Sham density functional theory

In Kohn-Sham density functional theory the energy functional is separated into distinct contributions

$$E[\rho] = \underbrace{T[\rho]}_{\text{kinetic energy}} + \underbrace{E_H[\rho]}_{\text{Hartree energy}} + \underbrace{E_{xc}[\rho]}_{\text{exchange-correlation energy}} + \underbrace{V_{\text{ext}}[\rho]}_{\text{external potential}}, \quad (2.4)$$

where the Hartree term results from the classic Coulomb repulsion of the involved electron density

$$E_H[\rho] = \frac{e^2}{2} \int d^3r \int d^3r' \frac{\rho(\mathbf{r})\rho(\mathbf{r}')}{|\mathbf{r} - \mathbf{r}'|} \quad (2.5)$$

and the external potential is provided by the nuclei background, see Eq. (2.1),

$$V_{\text{ext}}[\rho] = \int d^3r v_{\text{ext}}(\mathbf{r})\rho(\mathbf{r}). \quad (2.6)$$

Due to their complexity, the kinetic and exchange-correlation (XC) energy, which contains all other contributions, on the other hand cannot be simply expressed as a single analytic expression. As these terms are large, their errors must be controlled as best as possible. To this end, the core idea of Kohn and Sham was the introduction of a *non-interacting* reference-system whose ground-state density is identical to the real, interacting one. By transforming the many-body problem to a single-particle picture one is able to treat the kinetic part exactly, leaving only $E_{\text{xc}}[\rho]$ as an unknown. From the stationary requirement of Eq. (2.3) and the constraint to a fixed electron number

$$N_e = \int d^3r \rho(\mathbf{r}) \quad (2.7)$$

one obtains the condition

$$\frac{\delta T[\rho]}{\delta \rho(\mathbf{r})} + \int d^3r' \frac{\rho(r')}{|\mathbf{r} - \mathbf{r}'|} + \frac{\delta E_{\text{xc}}}{\delta \rho(\mathbf{r})} + v_{\text{ext}} = \mu, \quad (2.8)$$

where μ is the Lagrangian multiplier associated with the chemical potential [37]. It is now easily recognized that by gathering all non-kinetic terms into the so-called Kohn-Sham potential

$$v_{\text{KS}} = \int d^3r' \frac{\rho(r')}{|\mathbf{r} - \mathbf{r}'|} + \frac{\delta E_{\text{xc}}}{\delta \rho(\mathbf{r})} + v_{\text{ext}}, \quad (2.9)$$

we obtain an equation for a *non-interacting reference system*

$$\frac{\delta T[\rho]}{\delta \rho(\mathbf{r})} + v_{\text{KS}} = \mu \quad (2.10)$$

which can be satisfied by solving the corresponding one-particle Schrödinger equations for particles indexed by i [36]

$$\left[-\frac{\hbar^2}{2m} \Delta + v_{\text{KS}} \right] \Phi_i(\mathbf{r}) = \varepsilon_i \Phi_i(\mathbf{r}) \quad (2.11)$$

yielding

$$\rho(\mathbf{r}) = \sum_{i=1}^{N_e} \Phi_i^*(\mathbf{r}) \Phi_i(\mathbf{r}). \quad (2.12)$$

If the corresponding Kohn-Sham potential (or an adequate approximation thereof) is known, the ground state density is simply the result of a converged, self-consistent cycle. The various implementations often only differ in the way the wave functions are constructed (localized basis and/or plane waves) and the target systems (molecules, periodic solids) [21, 22, 24, 38, 39, 40].

It is important to emphasize that Kohn-Sham DFT, while imitating the real particle density via an artificial electron system, is per se free of approximations. The only real concern at this current point is the representability itself: Barring any discontinuities or singularities in the particle density,

absent in any realistic applications, the solution of the Kohn-Sham equations yields the correct ground state density, that ultimately can be connected to a single Slater determinant of the reference system. Of course this statement only holds true if the exact exchange-correlation potential $V_{xc} = \partial E_{xc}/\partial \rho$ was known.

Strictly speaking, the interpretation of the eigenenergies ε_i of the auxiliary reference system as excitation energies is not rigorously justified. In the most extreme case of a half-filled Mott insulator the Kohn-Sham equations, in principle, still allow an accurate description of the ground-state density and quantities derived from it. While its electronic compressibility for example would depict the underlying insulator, clearly however, the one-particle picture in itself breaks down. In particular, the system is no longer describable by a single Slater determinant. Consequently the auxiliary eigenvalues become meaningless, as any partially filled band will result in a gapless spectrum within Kohn-Sham DFT. For most weakly-correlated materials on the other hand, an empirical congruence to the energy spectrum cannot be denied however [37].

Naturally, the results of the aforementioned procedure are strongly dependent on the exchange-correlation potential which can only be approximated. As the separation of terms in Eq. (2.4) represents merely a shift of unknown variables into the exchange-correlation energy, it contains a plethora of higher-order correlation terms for which no exact expression is known in general. In order to justify possible approximations of the exchange-correlation potential, it is of great importance to get a better understanding through limiting cases. Here one typically considers (a) a slowly varying density and (b) a high density region. In a solid, the former is usually located in the interstitial volume between the atomic nuclei while the latter is found around the center of the nuclei themselves. In the slowly varying regime, one might expand the true kinetic and exchange-correlation energy in terms of densities and gradients thereof [36]

$$E_{xc}[\rho] = \int d^3r \varepsilon_{xc}(\rho) + \int d^3r \varepsilon_{xc}^{(2)}(\rho) |\nabla \rho|^2 + \dots \quad (2.13a)$$

$$T[\rho] = \int d^3r \frac{3}{10} (3\pi^2 \rho)^{\frac{2}{3}} \rho + \int d^3r t^{(2)}[\rho] |\nabla \rho|^2 + \dots \quad (2.13b)$$

The higher order correction terms whose errors scale with $|\nabla \rho|^2$ become vanishingly small, for an almost constant density ρ , allowing us to represent the exchange correlation potential as a local approximation

$$E_{xc}^{\text{LDA}} = \int d^3r \varepsilon_{xc}^{\text{LDA}}(\rho(\mathbf{r})). \quad (2.14)$$

In this so-called local density approximation (LDA) certain contributions, e.g., the exchange part, can be approximated by using the expression for a homogeneous electron gas. Correlation terms can be approximated and parameterized in a similar fashion. If the corresponding electron density is spin-polarized, one instead employs the local spin-density approximation (LSDA) whose parametrization

slightly differs. Beyond this purely local approximation, the natural next step is to take into account local gradients leading to the generalized gradient approximation (GGA) methods with

$$E_{\text{xc}}^{\text{GGA}} = \int d^3r \varepsilon_{\text{xc}}^{\text{GGA}}(\rho(\mathbf{r}), \nabla\rho(\mathbf{r})). \quad (2.15)$$

Here $\varepsilon_{\text{xc}}^{\text{GGA}}$ can be parameterized in various forms such as PW91 [41] or PBE [23]. For a more in-depth review about exchange-correlation potentials, please refer to the literature, e.g., Ref. [42]. Unless otherwise specified, DFT calculations in this thesis will be performed with PBE. For our purposes, i.e. strongly correlated systems, innovations in density functionals, while maybe providing quantitatively better input, cannot overcome the qualitative flaws discussed above.

In high density systems, the kinetic energy starts to dominate the energy total making the exchange-correlation energy less important in comparison [36]. As the kinetic part of the Kohn-Sham equation (2.11) is evaluated without approximation, this limit will become exact. Considering the different regions in a solid we can surmise that (a) near the atomic nuclei the high densities, screening the positive charge, are mapped correctly due to the dominance of the kinetic energy and (b) a slowly varying electronic density in the the interstitial region provides a wide volume where the local approximations hold. The overlap regions will be hence the main source of error, making different atomic compositions more prone to errors than others. Metals and alloys whose relevant bands are formed by spatially extended s- or p- orbitals will showcase smaller errors than compounds with more localized d- or f- orbitals, see Fig. 2.1. Owing to their nodeless radial wave functions, bands formed by 3d or 4f bands will produce significant ripples in the density. In a similar vein, problems arise in the computation of semiconductors whose band gaps are oftentimes not well reproduced [43, 44, 45]. Here it is argued that the systematic underestimation of the fundamental gap (defined by the difference between ionization potential and electron affinity) by Kohn-Sham DFT which employs “standard” LDA/GGA potentials is caused by their missing derivative discontinuity [43, 46, 47]. For this purposes more sophisticated exchange-correlation potentials, like meta-GGA, hybrid, or semilocal potentials have been developed, see, e.g., Refs. [48, 49, 50].

2.1.2 Towards strong interactions: Hubbard model

One of the most “basic” models that can rationalize the physics of strongly correlated materials, inherently difficult depictable in pure DFT, is the Hubbard model (HM). In its simplest one-band form with spin species $\sigma = \uparrow / \downarrow$, it reads

$$\mathcal{H}_{\text{HM}} = \sum_{\langle i,j \rangle, \sigma} t_{ij} \hat{c}_{i,\sigma}^\dagger \hat{c}_{j,\sigma} + U \sum_i \hat{n}_{i,\uparrow} \hat{n}_{i,\downarrow}, \quad (2.16)$$

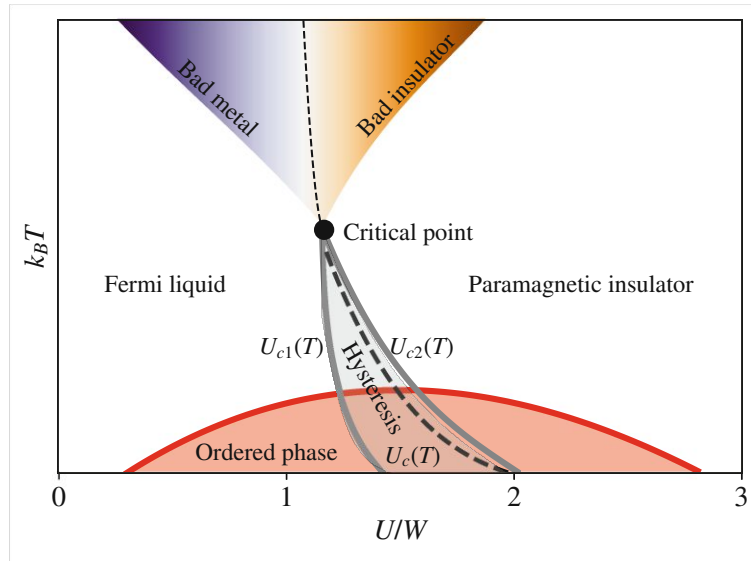


Figure 2.2: Schematic phase diagram of the half-filled Hubbard model within dynamical mean-field theory: Temperature $k_B T$ vs. interaction U normalized by the band-width W . The characteristics of the metal to insulator transition is strongly temperature dependent: Below a critical end point, the MIT is of first order. The resulting hysteresis is bounded by $U_{c1}(T)$ and $U_{c2}(T)$. Inside the hysteresis (gray), $U_c(T)$ marks the interaction strength at which the free energy of both obtainable solutions are identical [53]. Above the critical point, the phase diagram exhibits a gradual crossover between the metal and paramagnetic insulator. Please note that the schematically drawn (magnetically) ordered phase (red) oftentimes occurs at temperatures considerably higher than shown here [54].

One of the first attempts to quantitatively simulate the condition of Mott insulators in materials was done by Anisimov *et al.* [55], later on generalized to be basis-set independent in Ref. [56] by identifying the relevant atomic characters. The generalized functional builds on top of the local spin-density approximation (LSDA), i.e. LDA with spin dependence,

$$E^{\text{LDA}+U}[\rho] = E^{\text{LSDA}}[\rho] + E^U[\{n^\sigma\}] - E^{\text{DC}}[\{n^\sigma\}] \quad (2.17)$$

adding a correction terms depending on the density matrix $n^\sigma = \text{Tr}(n_{mm}^\sigma)$ of *localized orbitals* and a correction for the double-counting (DC). The necessity of the DC correction stems from terms that are already partially present within DFT and are added again through the local orbital potential. In principle there exist no exact expressions for DC, however phenomenological recipes have been developed among which the most widely used are the fully localized limit (FLL) and the around mean-field (AMF) solution, see Ref. [57] for a more detailed discussion. Please note that similar DC expressions are used within dynamical mean-field theory, see Section 2.2.3.

This atomic-like potential is capable of treating spin and orbital polarization on equal footing, providing an avenue towards correlation-induced insulators with long-range order. The interaction

parameter can be successfully tuned (or computed, see Section 2.1.3) to describe the ground state transition to an insulator in ordered phases. LDA+U however fails in reproducing the intricate phase diagrams of strongly correlated electron systems found, e.g., in transition metal oxides. While it encodes to most basic ingredients for the insulating state, LDA+U fails to address the finite temperature behavior of the Fermi liquid / Mott insulating state and their corresponding quasi-particle lifetimes, the formation of high frequency satellite features, etc. To this end we highlight the phase diagram of V_2O_3 sketched in Fig. 2.3.

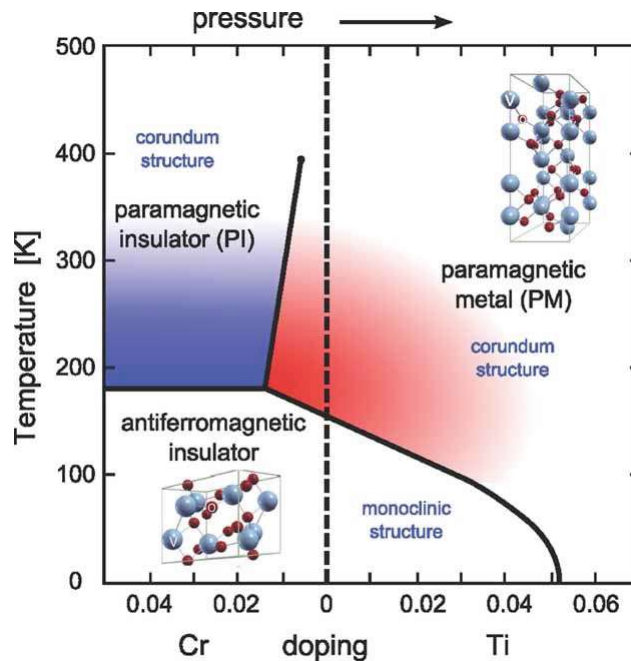


Figure 2.3: Schematic phase diagram of V_2O_3 showcasing a correlation induced metal-to-insulator transitions. Due to the complexity of multi-band systems all relevant energy scales (crystal-field splittings, orbital deformation, band width, interaction strength) must be considered to distil the full physical picture. [Reprinted with permission from Hansmann *et al.*, Phys. Status Solidi B **250**, 1251-1264 (2013). Copyright (2013) by John Wiley and Sons.] [58]

First, the undoped system (vertical, dashed line) showcases a temperature induced, abrupt metal to (antiferromagnetically ordered) insulator transition, in combination with a structural transition from corundum-like to monoclinic. Elementary doping to $(Cr_xV_{(1-x)})_2O_3$ or $(Ti_xV_{(1-x)})_2O_3$ induces chemical pressure, disrupting the initial metal to insulator transition. Titanium doping lowers the transition temperature whereas chromium doping triggers an insulator transition [59].¹

In order to capture these types of effects we need go beyond the approach of solving an effective

¹ For effects of chromium doping onto the electronic structure, please refer to Ref. [60].

non-interacting system in a self-consistently determined effective potential.² The current state-of-the-art method going beyond DFT is the dynamical mean-field theory (DMFT), see Section 2.2.2. At first sight the phase diagram of V_2O_3 mirrors that of the half-filled Hubbard model in Fig. 2.2: Chemical pressure increases the orbital overlaps, hopping amplitudes, and thus the bandwidth $W \propto t$ (note that this doping does not change the electron filling). However, as the underlying band structure is of multi-orbital character, a one-to-one comparison is inherently not valid [62]. Insulating and metallic driving forces strongly dependent on the detailed structural and crystal-field effects induced by doping through which orbital degeneracies are oftentimes lifted [58, 62].

2.1.3 Localized multi-orbital basis and interaction matrix

Modelling realistic setups requires a strong focus on crystal structure details. In this vein, the one-band Hubbard model can be generalized to its multi-orbital form in the typical paramagnetic formulation (equivalence of spins $\sigma = \uparrow / \downarrow$) via

$$\mathcal{H}_{\text{HM}} = \sum_{\mathbf{k}, \sigma} \sum_{lm} h_{lm}^{\mathbf{k}} \hat{c}_{\mathbf{k}l, \sigma}^{\dagger} \hat{c}_{\mathbf{k}m, \sigma} + \frac{1}{2} \sum_i \sum_{\substack{l'l'm'm'}} U_{lm'l'm'} \hat{c}_{im', \sigma}^{\dagger} \hat{c}_{il, \sigma'}^{\dagger} \hat{c}_{im, \sigma'} \hat{c}_{il', \sigma}. \quad (2.18)$$

The first term is a generalization of the hopping term of Eq. (2.16) whose creation/annihilation operators have been Fourier transformed to momentum space and whose hopping amplitudes and distances are encoded in the matrix elements $h_{lm}^{\mathbf{k}}$ of the one-particle Hamiltonian $H^{\mathbf{k}}$. It describes the one-particle kinetic energy for an arbitrary number of orbitals, including off-diagonal terms and can be modified to include the chemical potential via $h_{lm}^{\mathbf{k}} \rightarrow h_{lm}^{\mathbf{k}} - \mu \delta_{lm}$. The second term encodes all possible *local* two-particle interactions that conserve the total spin. In order to retrieve the H and U matrices for a given material, one first needs to introduce the concept of locality: We can connect the Hubbard model with the DFT energy spectrum via the field operator representation

$$\mathcal{H} = \sum_{\sigma} \int d^3r \hat{\psi}_{\sigma}^{\dagger}(\mathbf{r}) \left[-\frac{\hbar^2}{2m_e} \Delta + v_{\text{KS}} \right] \hat{\psi}_{\sigma}(\mathbf{r}) + \frac{1}{2} \sum_{\sigma, \sigma'} \int d^3r d^3r' \hat{\psi}_{\sigma}^{\dagger}(\mathbf{r}) \hat{\psi}_{\sigma'}^{\dagger}(\mathbf{r}') \frac{e^2}{|\mathbf{r} - \mathbf{r}'|} \hat{\psi}_{\sigma'}(\mathbf{r}') \hat{\psi}_{\sigma}(\mathbf{r}). \quad (2.19)$$

Here, $\hat{\psi}_{\sigma}^{(\dagger)}(\mathbf{r})$ annihilates (creates) an electron at position \mathbf{r} with spin σ . We construct these field operator from the corresponding Bloch wave functions

$$\psi_{\mathbf{k}, n}(\mathbf{r}) = e^{i\mathbf{k} \cdot \mathbf{r}} u_{\mathbf{k}, n}(\mathbf{r}) \quad (2.20)$$

² From this technical point of view, connections to mean-field theories are often made. In the traditional sense of the word (multiple interactions are replaced by an effective interaction), however, the Kohn Sham scheme is *not* a mean-field approach [61]. Through the self-consistency the Kohn Sham potential (different on every \mathbf{r} -point) is updated similarly to, e.g. the effective magnetic field of a spin of the Ising model. Conceptually, however, these two approaches have little in common.

via

$$\hat{\psi}_\sigma^{(\dagger)}(\mathbf{r}) = \frac{V}{(2\pi)^3} \int_{\text{BZ}} d^3k \sum_n \psi_{\mathbf{k},n}^{(*)}(\mathbf{r}) \hat{c}_{\mathbf{k},n,\sigma}^{(\dagger)}. \quad (2.21)$$

where $\hat{c}^{(\dagger)}$ annihilates (creates) an electron with crystal momentum \mathbf{k} , spin σ and orbital n . The Bloch functions represent modified plane waves, in which the periodicity of the lattice is encoded via $u(\mathbf{r}) \equiv u(\mathbf{r} + \mathbf{R})$. The integration is performed over the full Brillouin zone (BZ) and the summation is done over all possible bands n . Localized orbitals are then introduced via the Wannier basis, the solid state equivalent of atomic orbitals. Applying a specialized unitary basis transformation onto the initially delocalized Bloch functions one is able to obtain a maximally localized basis through

$$|\mathbf{R}n\rangle = \frac{V}{(2\pi)^3} \int_{\text{BZ}} d^3k e^{-i\mathbf{k}\cdot\mathbf{R}} \sum_{m=1}^J U_{mn}^{(\mathbf{k})} |\psi_{m\mathbf{k}}\rangle \quad (2.22a)$$

$$w_{n\mathbf{R}}(\mathbf{r}) = \langle \mathbf{r} | \mathbf{R}n \rangle \quad (2.22b)$$

whose momentum-dependent unitary transformation matrices $U_{mn}^{(\mathbf{k})}$, spanning the space given by J bands, are adjusted to minimize the real space spread

$$\Omega = \sum_n \left[\langle \mathbf{0}n | r^2 | \mathbf{0}n \rangle - \langle \mathbf{0}n | \mathbf{r} | \mathbf{0}n \rangle^2 \right]. \quad (2.23)$$

For a detailed mathematical and practical discussion on the topic of maximally localized Wannier functions, the relevant localization procedure and the problems arising for entangled bands, please refer to Ref. [63]. In the remainder of this thesis we will assume that the above procedure, wherever employed, generates exponentially localized Wannier functions which we then use to rewrite Eq. (2.19) into

$$\mathcal{H} = \sum_{\substack{\mathbf{R}_1, \mathbf{R}_2 \\ lm \\ \sigma}} h_{lm}(\mathbf{R}_1, \mathbf{R}_2) \hat{c}_{\mathbf{R}_1, \sigma}^\dagger \hat{c}_{\mathbf{R}_2, \sigma} + \frac{1}{2} \sum_{\substack{\mathbf{R}_1 \mathbf{R}_2 \mathbf{R}_3 \mathbf{R}_4 \\ l' m m' \\ \sigma \sigma'}} U_{lm' m l}^{\text{full}}(\mathbf{R}_1, \mathbf{R}_2, \mathbf{R}_3, \mathbf{R}_4) \hat{c}_{\mathbf{R}_3, \sigma'}^\dagger \hat{c}_{\mathbf{R}_1, \sigma}^\dagger \hat{c}_{\mathbf{R}_2, \sigma'} \hat{c}_{\mathbf{R}_4, \sigma} \quad (2.24)$$

with

$$h_{lm}(\mathbf{R}_1, \mathbf{R}_2) = \int d^3r w_{l\mathbf{R}_1}^*(\mathbf{r}) \left[-\frac{\hbar^2}{2m} \Delta + v_{\text{KS}} \right] w_{m\mathbf{R}_2}(\mathbf{r}), \quad (2.25a)$$

$$U_{lm' m l}^{\text{full}}(\mathbf{R}_1, \mathbf{R}_2, \mathbf{R}_3, \mathbf{R}_4) = \int d^3r d^3r' w_{m'\mathbf{R}_3}^*(\mathbf{r}) w_{l\mathbf{R}_1}^*(\mathbf{r}') \frac{e^2}{|\mathbf{r} - \mathbf{r}'|} w_{m\mathbf{R}_2}(\mathbf{r}') w_{l'\mathbf{R}_4}(\mathbf{r}). \quad (2.25b)$$

By applying the Wannierization procedure onto the correlated atomic orbitals we obtain *real-space* hopping elements and on-site energy levels. The former can be, via a Fourier transform and exploitation of translation symmetry, transformed into momentum space

$$h_{lm}^{\mathbf{k}} = \sum_{\mathbf{R}} e^{i\mathbf{k}\cdot\mathbf{R}} h_{lm}(\mathbf{R}, \mathbf{0}), \quad (2.26)$$

where the distances \mathbf{R} only include unit cell positions and do not include displacements inside the unit cell [64]. Let us note that this procedure is quite general (exceptions include topological materials where the minimization is neither rigorously defined, nor achievable) and one is able to project onto arbitrary, entangled energy windows. Including ligand orbitals in the Wannier basis (e.g., oxygen) is common practice.

Coulomb interactions, associated with these orbital can be obtained by evaluating the overlap integral Eq. (2.25b). As we essentially ignore a wide energy range outside our defined subspace, however, the unscreened Coulomb interaction is no longer a valid descriptor for the “low-energy” Wannier setup. Since we would indirectly neglect screening effects from other bands, we must first acquire a properly screened interaction for our chosen subspace. Commonly employed screening approaches include the constrained random phase approximation (cRPA) [65, 66, 67] and the constrained local density approximation (cLDA) [68, 69].

2.1.3.1 Constrained random phase approximation

The main idea behind the cRPA is the following: Polarization processes P are separated into two distinct contributions. Contributions P_d whose initial and final states are fully contained within our selected subspace and processes which connect to states outside the subspace $P_r = P - P_d$. A (downfolded) low-energy model necessarily cannot generate the latter processes, which is why a pre-screening of the bare Coulomb interaction

$$V(\mathbf{r}, \mathbf{r}') = \frac{e^2}{|\mathbf{r} - \mathbf{r}'|} \quad (2.27)$$

is required. These screening processes are inherently frequency and energy window-dependent and, if taken into consideration, generate a dynamical effective electron-electron interaction. *Symbolically*, the unscreened interaction V transforms into the screened interaction of the subspace W_d via a geometric series of polarization P_r insertions

$$W_d(\mathbf{r}, \mathbf{r}', \omega) = V + VP_rV + VP_rVP_rV + \dots = V + VP_rW_d = \frac{V}{1 - VP_r} \quad (2.28)$$

which is used as the new interaction in

$$U_{lm'm'l}^{\text{full}}(\mathbf{R}_1, \mathbf{R}_2, \mathbf{R}_3, \mathbf{R}_4, \omega) = \int d^3r d^3r' w_{m'\mathbf{R}_3}^*(\mathbf{r}) w_{l\mathbf{R}_1}^*(\mathbf{r}') W_d(\mathbf{r}, \mathbf{r}', \omega) w_{m\mathbf{R}_2}(\mathbf{r}') w_{l'\mathbf{R}_4}(\mathbf{r}). \quad (2.29)$$

Within cRPA the polarization is given by a single (virtual) particle-hole excitation. In the downfolded model, on the bosonic Matsubara axis, this process can be represented via (non-interacting) Green's

functions G_0 , see Appendix A.1,

$$\begin{aligned} P_{\text{cRPA}}(\mathbf{q}, i\omega_m) &= +\frac{1}{\beta} \sum_{\nu_n} \sum_{\mathbf{k}, a, b} G_0(\varepsilon_a^{\mathbf{k}}, i\nu_n) G_0(\varepsilon_b^{\mathbf{k}-\mathbf{q}}, i\nu_n - i\omega_m) \\ &= \sum_{\mathbf{k}, a, b} \frac{f_{FD}(\varepsilon_b^{\mathbf{k}-\mathbf{q}}) - f_{FD}(\varepsilon_a^{\mathbf{k}})}{\varepsilon_b^{\mathbf{k}-\mathbf{q}} - \varepsilon_a^{\mathbf{k}} + i\omega_m} \end{aligned} \quad (2.30)$$

where the sum over momenta \mathbf{k} and bands a, b are restricted according to the pre-defined window that generates P_r . The evaluation of the Matsubara sum $1/\beta \sum_{\nu_n}$, leading to the Lindhard expression consisting of Fermi functions f_{FD} and energies $\varepsilon_n^{\mathbf{k}}$ of the particle propagation is described in Appendix A.2. The analytic continuation to real frequencies can be done analytically, e.g., via $i\omega_m \rightarrow \omega + i0^+$ for the retarded response.

Eq. (2.30) can be evaluated via Bloch or Wannier functions, resulting in equivalent expressions [70]. The RPA concept can also be applied to the susceptibility instead of the polarization, leading to an enhanced (dampened) magnetic (density) response $\chi_{M/D}$, see Section 2.6.3.1 for a more detailed discussion. In order to extract the most relevant information, one typically restricts the number of dependencies

$$U_{lm'm'l'}^{\text{full}}(\mathbf{R}_1, \mathbf{R}_2, \mathbf{R}_3, \mathbf{R}_4, \omega) \rightarrow U_{lm'm'l'}^{\text{full}}(\mathbf{R}, \mathbf{R}, \mathbf{0}, \mathbf{0}, \omega) \quad (2.31)$$

allowing for a spatial (on-site versus off-site) and frequency analysis of the screened interaction. The latter is necessary if one wants to account for collective electron excitations, e.g., plasmons. Methodologies that intrinsically incorporate them are the GW approach [71] or the GW extension of dynamical mean-field theory GW +DMFT [72, 73, 74].

In order to connect this full interaction matrix into the initial *static* interaction problem of Eq. (2.18) we need to both truncate the spatial as well as the frequency information

$$U_{lm'm'l'} = U_{lm'm'l'}^{\text{full}}(\mathbf{0}, \mathbf{0}, \mathbf{0}, \mathbf{0}, \omega \rightarrow 0). \quad (2.32)$$

Due to the strong spatial screening the former is oftentimes well justified. The frequency dependence on the other hand is rarely insignificant since the difference of the static value (screening of a slowly moving particle) is commonly an order of magnitude smaller than the unscreened value ($\omega \rightarrow \infty$). For density-density interactions, it is actually possible to include a dynamical $U(\omega)$ in DMFT [75], which is however rarely done in practice.

2.1.3.2 Constrained local density approximation

A conceptually simpler approach is the constrained local density approximation. Here the on-site repulsion is defined as the energy cost that occurs when moving an electron between two sites,

initially occupied by n electrons (in this case 3d-electrons) [68]

$$2(3d^n) \rightarrow (3d^{n+1}) + (3d^{n-1}). \quad (2.33)$$

As U is an inherently renormalized quantity it contains screening effects from other electrons, i.e. the change in the number of localized electrons will be fully compensated by the “auxiliary” electrons, e.g. 4s. To account for this, Eq. (2.33) is usually rewritten into

$$U = \underbrace{\left[E(3d^{n+1}4s^0) - E(3d^n4s^1) \right]}_{\text{electron affinity}} + \underbrace{\left[E(3d^{n-1}4s^2) - E(3d^n4s^1) \right]}_{\text{ionisation energy}}. \quad (2.34)$$

With Janak’s theorem, relating the eigenvalues of the DFT to a derivative of the total energy E with respect to the occupation

$$\varepsilon_i = \frac{dE}{dn_i}, \quad (2.35)$$

one finds a direct connection to derivative of the relevant ε energies [76]

$$U = E(3d^{n+1}4s^0) - 2E(3d^n4s^1) + E(3d^{n-1}4s^2) = \frac{\partial^2 E}{\partial n_d^2} = \frac{\partial \varepsilon_d}{\partial n_d}. \quad (2.36)$$

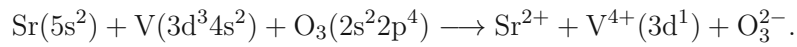
Supercell calculations imitating Eq. (2.36) (variation around the unconstrained occupation numbers) can then also be used to calculate the exchange interaction J [77]. U and J are then sufficient to parameterize the full interaction matrix, see Section 2.2.2.

These additions/removals of electrons naturally generate modifications to the Kohn Sham potential whose influence has to be eliminated to achieve a description of U that is as accurate as possible. There exist different approaches how to handle these corrections. Cococcioni *et al.* [69] for example removed this “rehybridization” by explicit subtraction of the curvature changes induced by the band structure of the non-interacting system. Anisimov *et al.* [68] instead employed a cut-off method where the hybridization of the 3d orbitals are explicitly “turned off”. For an application of cLDA in first principle calculations please refer to Refs. [76, 78, 79].

2.2 The inconspicuous case of SrVO₃

2.2.1 Crystal and band structure of bulk SrVO₃

Strontium vanadate plays an important role in the research of transition metal oxides: Owing to its perfect cubic crystal-structure and its “simple” electronic structure, it is often employed as test-bed material in both fundamental theoretical and experimental studies. SrVO₃ has also been proposed for use in technological applications as electrode material [80], transparent conductor [81, 82], sacrificial buffer layer [83], material in spintronic devices [84], and active material in a Mott transistor [85, 86]. Nominally, vanadium is in a d¹ configuration as a result of the (idealistic) valence electron transfer



In this ionic picture strontium and oxygen are in their noble gas configuration whereas vanadium remains in a chemically non-optimal 4+ valence. This has critical consequences when exposing the material to surface oxygen, a detailed discussion on this topic is presented in Section 2.4.

The octahedral array of the oxygen atoms in the perovskite structure, see Fig. 2.4, naturally lifts the five-fold degeneracy of the vanadium d-orbitals realised for isolated atoms. In SrVO₃, vanadium’s e_g = {d_{z²}, d_{x²-y²}} (t_{2g} = {d_{xy}, d_{xz}, d_{yz}}) orbitals point towards (away from) the surrounding oxygen ions and thus experience a large (small) Coulomb repulsion. In turn, a large separation of the two kinds of orbitals emerges. This allows us, for the given d¹ occupation, to perform a more reductionist t_{2g} modelling.

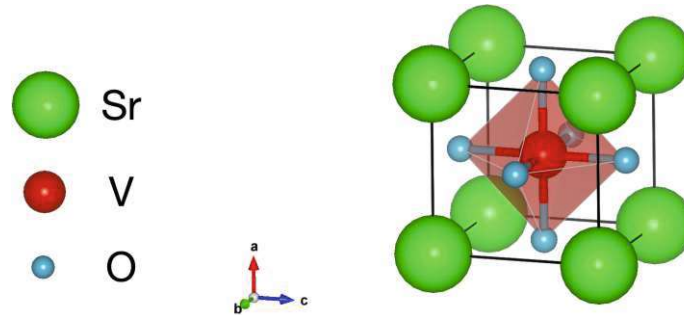


Figure 2.4: Perovskite crystal structure ABO₃. In SrVO₃ the transition metal vanadium (red) is surrounded by oxygen (blue), forming a corner shared VO₆ octahedron embedded in a cubic strontium (green) structure. The sphere radii are proportional to the atomic number. Due to the octahedral oxygen positioning the t_{2g} and e_g orbitals split. Figure generated with VESTA [18].

To provide context, we compare the realized octahedral coordination to the closely connected tetrahedral arrangement in Fig. 2.5 which yields a reversed crystal-field splitting (cfs). Supported by the

perfect ligand-crystal alignment, the octahedral setup experiences a local crystal-field splitting, Δ_{oct} , that is more than twice the size of the alternative tetrahedral splitting $\Delta_{\text{tet}} = 4/9\Delta_{\text{oct}}$ for identical ions, ligands and ion-ligand distances, also displayed in Fig. 2.5. Evidently the tetrahedral arrangement is not periodic (the shown cube cannot be a unit cell), making it only available as a purely local surrounding of the relevant atomic center.

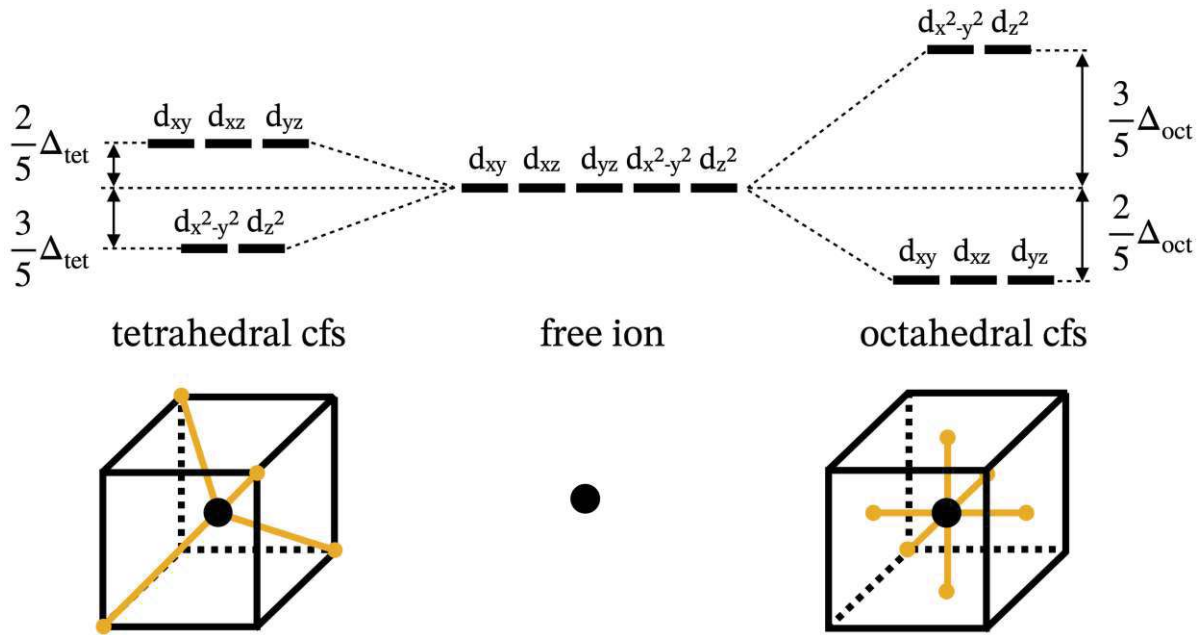
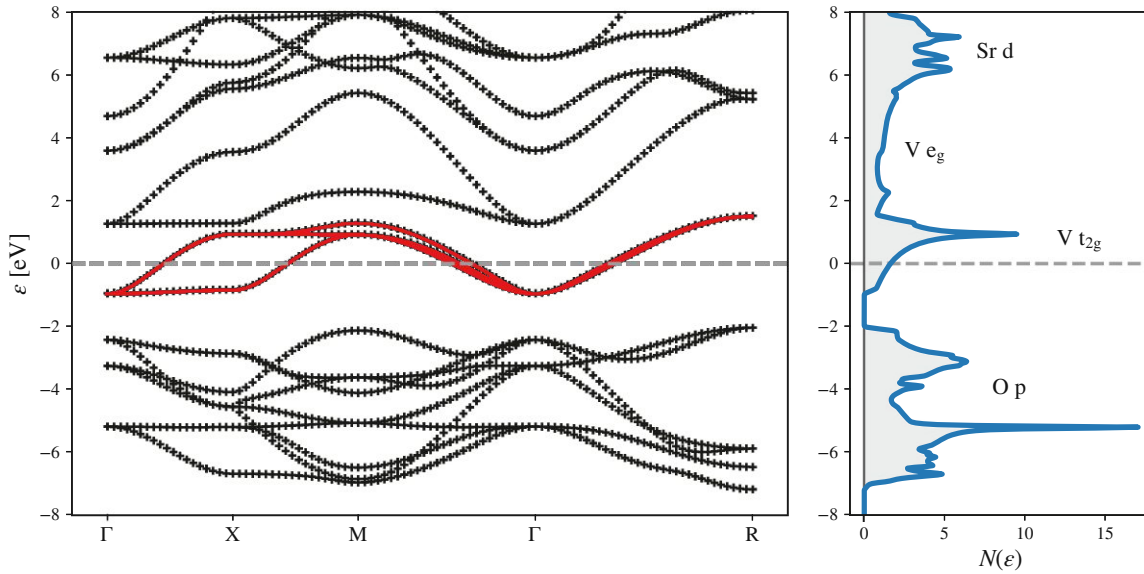


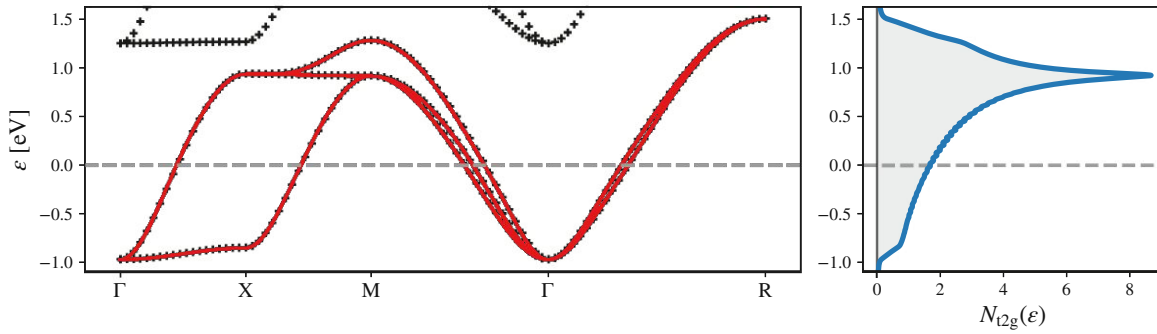
Figure 2.5: Schematic crystal-field splitting of idealistic d-orbitals in a tetrahedral and octahedral crystal environment. The e_g orbitals ($d_{x^2-y^2}$, d_{z^2}) are energetically favored in the tetragonal environment whereas the t_{2g} orbitals (d_{xy} , d_{xz} , d_{yz}) are favored in the octahedral environment. The overall crystal-field splitting between the two arrangements is connected via $\Delta_{\text{tet}} = 4/9\Delta_{\text{oct}}$ if one considers the same ions, ligands and ion-ligand distances. The illustrated d-levels are only meant to illustrate the splitting as, due to the additional overall electrostatic repulsion in a crystal, the absolute energy levels will naturally be elevated compared to the free ion case.

Within the PBE exchange correlation potential (used in all following SrVO₃ calculations) the energetically optimal lattice constant of SrVO₃ is determined as $a_{\text{SrVO}_3} = 3.85\text{\AA}$. The resulting band structure (and eigenvalues of the projected t_{2g} Wannier basis) is illustrated in Fig. 2.6 where the three aforementioned t_{2g} bands cross the Fermi level. The Fermi surface has the shape of three superposed cylinder-shaped tubes, as shown in Fig. 2.7.

The energetic separation of these t_{2g} orbitals to the six oxygen p-orbitals below, as well as to the e_g orbitals above, allows for a pristine projection with minimal orbital spatial spread $\Omega < 2\text{\AA}^2$. Strong orbital hybridization is mostly restricted to vanadium e_g with oxygen p. Due to the restricted energy



(a) Band structure and density of states in the energy range $-8\text{eV} < \varepsilon < 8\text{eV}$



(b) Band structure and density of states of the projected vanadium t_{2g} states

Figure 2.6: Density functional theory band structure of SrVO_3 along the high-symmetry momentum path Γ -X-M- Γ -R and the corresponding density of states (DOS) $N(\varepsilon) = \sum_{\mathbf{k}} \delta(\varepsilon_{\mathbf{k}} - \varepsilon)$. The Fermi level is located at $\varepsilon = 0$. (a) The projected t_{2g} Wannier basis is highlighted in red and is surrounded by six oxygen p bands ($\varepsilon < 0$) and the vanadium e_g states ($\varepsilon > 0$). (b) The zoom onto the (locally degenerate) t_{2g} states. The density of states is calculated from the projected Wannier basis, ignoring the (slightly) overlapping V e_g states. The DFT calculation was converged with $8 \times 8 \times 8$ k-points while the Wannier Hamiltonian was constructed on $20 \times 20 \times 20$ k-points instead. The DOS was calculated with $20 \times 20 \times 20$ (a) and $100 \times 100 \times 100$ (b), respectively.

window $\Delta E \approx \pm 1\text{eV}$, the resulting Wannier orbitals will be transformed from an atomic-like orbital to a molecular orbital expanding towards their adjacent oxygen atoms. This is a direct consequence

of the explicit exclusion of the oxygen ligands in the Wannier projection. Some of the oxygen orbital characteristic is therefore transferred onto the t_{2g} Wannier functions generating lobes on the adjacent oxygen centers, see, e.g., Ref. [87] for a Wannier function visualization in t_{2g} systems.

With respect to electronic structure calculations, this subspace selection is arbitrary: Any other energy window selection in combination with its corresponding screened interaction matrix should, at least in principle, generate the same physical result.³ The t_{2g} projection is popular, and especially important for our cases, due to the pre-defined *integer* filling. Introducing more orbitals changes the molecular orbitals: Nominal filling then does not necessarily result in the desired d^1 filling in the t_{2g} subspace. In, e.g., p-d calculations, that include all vanadium-d and all oxygen-p orbitals in the basis (total filling $N = 19$), the double-counting problem and the p-d Coulomb interaction become relevant [86, 88]. Without these corrective undertakings, the t_{2g} occupation lead to $n_{t_{2g}} > 1$, see Supplementary information of Ref. [86].⁴ There exist various strategies to properly shift the oxygen levels to their desired position, see the Supplementary information of Ref. [86], be it via a Hartree self-energy of the p-bands, a double-counting adjustment or a manual shift of orbital position. It is worth mentioning here, that these procedures are merely a vehicle to mimic a GW -like nonlocal exchange self-energy, missing in pure DMFT approaches. Since we are interested only in the low-energy physics and will rely quite heavily on perfect integer filling, we will avoid these problems altogether and restrict ourselves to the t_{2g} -only model.

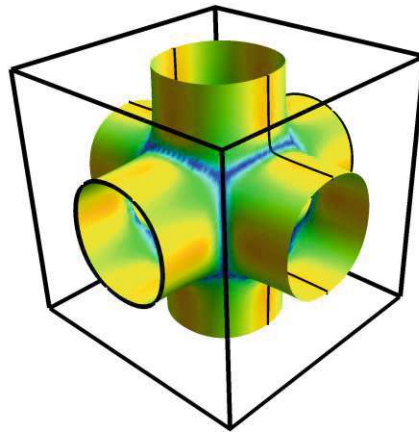


Figure 2.7: Three-dimensional Fermi surface of SrVO_3 . Each of the locally degenerate two-dimensional xy, xz, yz orbitals results in a cylindrical contribution, perpendicular to one another in momentum space. Figure created via FermiSurfacer [19].

³ In a broader context, this is however not general: for optical properties, e.g., one would need more orbitals to capture high frequency features.

⁴ Comparing photoemission spectroscopy data (Section 2.2.4) with p-d model dynamical mean-field calculations (Section 2.2.3) one finds a mismatch between the measured and calculated oxygen p position.

2.2.2 Interaction matrix parametrization

Having established the desired energetic subspace upon which will constitute the basis of our discussion, we now turn to the description of the interaction. We simplify the interaction matrix, introduced in Sec. 2.1.3, by resorting to a local, *static* Kanamori parametrization

$$\begin{aligned} \mathcal{U}_{\text{Kanamori}} = & \underbrace{U \sum_m \hat{n}_{m\uparrow} \hat{n}_{m\downarrow}}_{\text{intra-orbital density-density}} + \underbrace{\frac{1}{2} \sum_{\substack{m \neq m' \\ \sigma \sigma'}} [U' - \delta_{\sigma \sigma'} J] \hat{n}_{m\sigma} \hat{n}_{m'\sigma'}}_{\text{inter-orbital density-density}} \\ & + J \sum_{m \neq m'} \left[\underbrace{\hat{c}_{m\uparrow}^\dagger \hat{c}_{m'\downarrow}^\dagger \hat{c}_{m\downarrow} \hat{c}_{m'\uparrow}}_{\text{spin-flip}} + \underbrace{\hat{c}_{m\uparrow}^\dagger \hat{c}_{m\downarrow}^\dagger \hat{c}_{m'\downarrow} \hat{c}_{m'\uparrow}}_{\text{pair-hopping}} \right], \end{aligned} \quad (2.37)$$

valid for each site i with interaction parameters $U = 5\text{eV}$, $J = 0.75\text{eV}$ and $U' = U - 2J = 3.5\text{eV}$, based on cLDA calculations [79]. Let us note that in Ref. [79] the exchange parameter J was overestimated. For calculations of bulk SrVO₃ beyond static- U DMFT, see Refs. [78, 89, 90, 91, 92].

The Kanamori parametrization of Eq. (2.37) can be recovered from the generalized two-particle interaction term employed in our initial multi-orbital Hubbard model formulation in Eq. (2.18)

$$\mathcal{U} = \frac{1}{2} \sum_{\substack{l'm'm' \\ \sigma\sigma'}} U_{lm'm'l} \hat{c}_{m'\sigma}^\dagger \hat{c}_{l\sigma'}^\dagger \hat{c}_{m\sigma} \hat{c}_{l'\sigma} \quad (2.38)$$

via the mapping

$$U_{iiii} = U \quad (2.39a)$$

$$U_{ijij} = U' \quad (2.39b)$$

$$U_{ijji} = J \quad (2.39c)$$

$$U_{iijj} = J. \quad (2.39d)$$

The last term, U_{iijj} , can be explicitly ascribed to the pair-hopping contribution, whereas U_{ijji} is necessary to recover both the spin-flip contribution as well as the energy minimizing Hund's exchange term in the inter-orbital density-density contribution. This inseparability leads to the critical observation that any purely density-density interaction necessarily breaks $\text{SU}(2) \forall J > 0$.

2.2.3 Many-body renormalizations: Dynamical mean-field theory

Having introduced the t_{2g} Wannier projection accompanied by the $\text{SU}(2)$ symmetric Kanamori interaction parametrization, we have built an adequate framework upon which we can construct methods that capture (strong) local correlation effects beyond the capabilities of commonly employed exchange-correlation potentials. To this end we resort to the current state-of-the-art: dynamical mean-field

theory (DMFT). In this Section we will both introduce the physical motivation behind the theory and the corresponding quantum field theoretical description.

2.2.3.1 Concept

The core concept of dynamical mean-field theory can be described as an embedding of a single impurity Anderson model (SIAM) into an overarching, periodic lattice. This embedding process (typically accomplished in an iterative procedure) results in a characteristic hybridization function of the SIAM that accurately reflects the *local* lattice problem in which the Hubbard interaction naturally acts. Solving the underlying SIAM (numerically “exact” solutions exist) is therefore the gateway towards an accurate description of local correlations. As the DMFT algorithm is heavily relying on the quantum field theory formalism, please refer to Appendix A.1 for a brief introduction or refer to the relevant literature [93, 94]. In this formulation the propagation of a single electron/hole through the system is condensed into the (spin-dependent) one-particle Green’s function which on the imaginary time axis for the orbitals l, m reads

$$G_{lm}(\tau) \equiv G_{lm,\sigma}(\tau) = - \left\langle T_{\tau} \hat{c}_{l,\sigma}(\tau) \hat{c}_{m,\sigma}^{\dagger}(0) \right\rangle. \quad (2.40)$$

Here $\hat{c}^{(\dagger)}$ is the fermionic annihilation (creation) operator with T_{τ} as the time ordering operator. For lattice Hamiltonian with orbital indices, described in Eq. (2.18), this then translates to

$$G_{lm}^k = \left[(i\nu_n + \mu_{\text{lattice}}) \delta_{lm} - h_{lm}^{\mathbf{k}} - \Sigma_{lm}^k \right]^{-1} \quad (2.41)$$

on the (fermionic) Matsubara axis, see Appendix A.1.2. We employ a vector notation where $k = (\mathbf{k}, \nu_n)$ comprises both the momentum \mathbf{k} and the corresponding Matsubara frequency, $\nu_n = (2n + 1)\pi/\beta$. All interaction terms are encoded in the one-particle irreducible vertex, the self-energy, readily connected to the non-interacting Green’s function ($\Sigma \equiv 0$) via the Dyson equation

$$G = G_0 + G_0 \Sigma G, \quad (2.42)$$

describing all possible scattering processes, see Fig. 2.8 with possible, internal degrees of freedom.

$$G_{lm}^k = \overset{l}{\text{---}} \xrightarrow{\mathbf{k}, \nu_n} \overset{m}{\text{---}} = \overset{l}{\text{---}} \xrightarrow{\mathbf{k}, \nu_n} \overset{m}{\text{---}} + \overset{l}{\text{---}} \xrightarrow{\mathbf{k}, \nu_n} \textcircled{\Sigma_{ab}^k} \xrightarrow{\mathbf{k}, \nu_n} \overset{m}{\text{---}}$$

Figure 2.8: Dyson equation: The interacting (fat) and the non-interacting Green’s functions (thin) are connected via the self-energy: $G_{lm}^k = G_{0,lm}^k + \sum_{ab} G_{0,la}^k \Sigma_{ab}^k G_{bm}^k$. In our drawing convention, the arrow points from the annihilation operator to the creation operator, see Eq. (2.40).

The one-particle Green's function of the single impurity Anderson model

$$\begin{aligned}
\mathcal{H}_{\text{SIAM}} = & \underbrace{\sum_{lm,\sigma} \tilde{\varepsilon}_{lm} \hat{d}_{l,\sigma}^\dagger \hat{d}_{m,\sigma} + \frac{1}{2} \sum_{\substack{l'l'mm' \\ \sigma\sigma'}} U_{lm'm'l'} \hat{d}_{m',\sigma}^\dagger \hat{d}_{l,\sigma'}^\dagger \hat{d}_{m,\sigma'} \hat{d}_{l',\sigma}}_{\text{impurity}} \\
& + \underbrace{\sum_{\mathbf{k},\sigma} \sum_{lm} h_{lm}^{\mathbf{k}} \hat{c}_{kl,\sigma}^\dagger \hat{c}_{\mathbf{k}m,\sigma}}_{\text{bath}} + \underbrace{\sum_{\mathbf{k},\sigma} \sum_{lm} V_{lm}^{\mathbf{k}} \hat{c}_{kl,\sigma}^\dagger \hat{d}_{m,\sigma} + (V_{lm}^{\mathbf{k}})^* \hat{d}_{m,\sigma}^\dagger \hat{c}_{kl,\sigma}}_{\text{hybridization}},
\end{aligned} \tag{2.43}$$

on the other hand loses all the momentum information of the lattice and is instead described via

$$G_{lm}^{\nu_n} = [(i\nu_n + \mu_{\text{SIAM}}) \delta_{lm} - \tilde{\varepsilon}_{lm} - \Delta_{lm}^{\nu_n} - \Sigma_{lm}^{\nu_n}]^{-1} \tag{2.44}$$

where the hybridization function $\Delta(i\nu_n)$ is constructed as orbital matrix via

$$\Delta^{\nu_n} = \sum_{\mathbf{k}} \overline{(V^{\mathbf{k}})^T} \left[(i\nu_n + \mu_{\text{SIAM}}) \mathbb{1} - H^{\mathbf{k}} \right]^{-1} V^{\mathbf{k}}, \tag{2.45}$$

see Appendix A.1.2. Physically speaking, the hybridization function Δ^{ν_n} encodes all processes where an electron located on the impurity site enters the bath ($V^{\mathbf{k}}$), propagates through the bath (via the non-hybridizing, bath Green's function $[(i\nu_n + \mu_{\text{SIAM}}) \mathbb{1} - H^{\mathbf{k}}]^{-1}$), and finally re-enters the site ($\overline{(V^{\mathbf{k}})^T}$). Let us emphasize that we employ two distinct chemical potentials: μ_{lattice} for the lattice Green's function, and μ_{SIAM} for the impurity Green's function which will be adjusted independently from one another.

Returning to DMFT: The central point in the embedding scheme is that we require the local Green's functions of the lattice to coincide with the local Green's function of the SIAM

$$\sum_{\mathbf{k}} G_{\text{lattice}}^{\mathbf{k}} \stackrel{!}{=} G_{\text{SIAM}}^{\nu_n}. \tag{2.46}$$

Naturally, for any finite number of lattice dimensions DMFT remains an approximation. The resulting *local* self-energy, however, accurately reflects the projected impurity problem, containing all possible diagrams built from local propagators. As was shown in the earliest publications [95], when scaled properly, this locality becomes exact in the infinite dimension limit, i.e. the $d = \infty$ lattice fermions with local interaction are exactly described by the single-site model embedded by the dynamical mean-field. Surprisingly however, three dimensional systems, at least in the weak-coupling regime can be shown to be well approximated by it. Let us also note in the same vein that DMFT becomes exact in the strong coupling limit $U \gg t$.

2.2.3.2 Algorithm

In order to perform the embedding, one first defines the impurity model via the projection of the lattice. The energy levels $\tilde{\varepsilon}$ of the interacting fermions of Eq. (2.43) then correspond to the local Hamiltonian

$$\tilde{\varepsilon}_{lm} = h_{lm}(\mathbf{R} = 0) = \sum_{\mathbf{k}} h_{lm}^{\mathbf{k}}, \quad (2.47)$$

onto which the identical on-site interaction acts as employed in the lattice model. The DMFT embedding requirement is then achieved by a self-consistency scheme whose chosen starting point is usually the non-interacting solution, $\Sigma \equiv 0$ from which the initial hybridization function is constructed⁵

$$\Delta^{\nu_n} = (i\nu_n + \mu_{\text{SIAM}})\mathbb{1} - \tilde{\varepsilon} - \left[\sum_{\mathbf{k}} G_0^{\mathbf{k}} \right]^{-1}. \quad (2.48)$$

This defines the first iteration of the SIAM, allowing us to (numerically) compute the corresponding interacting impurity Green's function G_{SIAM}^{ν} via an impurity solver⁶

$$G_{0,\text{SIAM}} \rightarrow G_{\text{SIAM}} \quad (2.49)$$

and obtain the impurity self-energy via an inversion of the Dyson equation

$$\Sigma_{\text{SIAM}}^{\nu_n} = [G_0^{\nu_n}]^{-1} - [G_{\text{SIAM}}^{\nu_n}]^{-1}. \quad (2.50)$$

Identifying this self-energy, in the DMFT approximation, as the lattice self-energy

$$\Sigma_{\text{lattice}}^{\mathbf{k}} = \Sigma_{\text{SIAM}}^{\nu_n} \quad (2.51)$$

allows us to compute the local projection of the lattice Green's function

$$G_{\text{lattice,loc}}^{\nu_n} = \sum_{\mathbf{k}} \left[(i\nu_n + \mu_{\text{lattice}})\mathbb{1} - H^{\mathbf{k}} - \Sigma_{\text{SIAM}}^{\nu_n} \right]^{-1}. \quad (2.52)$$

Applying the DMFT self-consistency condition of Eq. (2.46), we can calculate a new non-interacting impurity propagator

$$\left[G_{0,\text{new}}^{\nu_n} \right]^{-1} = \left[G_{\text{lattice,loc}}^{\nu_n} \right]^{-1} + \Sigma_{\text{SIAM}}^{\nu_n} \quad (2.53)$$

⁵ Apart from parameter regimes where a hysteresis region exist, i.e. two solutions are possible for the same parameter set, there should in principle be no dependence on the starting point.

⁶ In this thesis we utilize the continuous-time quantum Monte Carlo (CTQMC) approach in the hybridization expansion (CTHYB) as implemented in w2dynamics [30]. The employed sampling algorithm will depend on the desired observables (segment, worm, etc.) which we will, for the sake of brevity, not discuss further in this thesis: Please refer to Ref. [96] for an introduction to worm sampling in higher order correlation functions. For an overview of CTQMC approaches in quantum impurity models, please refer to Ref. [97].

and extract a new hybridization function via

$$\Delta^{\nu_n} = (i\nu_n + \mu_{\text{SIAM}})\mathbb{1} - \tilde{\varepsilon} - \left[G_{0,\text{new}}^{\nu_n} \right]^{-1}, \quad (2.54)$$

circling us back to the beginning. This cycle is then iterated until the self-consistency condition is fulfilled and the local propagators of the lattice and the SIAM coincide. In a similar vein to density-functional theory (density ρ , eigenvalues ε_i), the local propagator G is accompanied by auxiliary quantities, the lattice propagators G^k . Contrary to DFT, however, these auxiliary descriptors arise from a controlled approximation of the self-energy where exact limits ($d \rightarrow \infty$, $U \rightarrow \infty$, $U = 0$) are obeyed. This makes these DMFT propagators physical in nature, oftentimes used to calculate renormalized band structures via its momentum-resolved spectral function and are an integral part of almost all diagrammatic extensions of dynamical mean-field theory [93].

Please note that in the so-called charge self-consistent DFT+DMFT approach [98, 99], the resulting self-energy can be interpreted as additional contribution to the Kohn-Sham potential, adjusting the total charge in the system. For *some* applications this outer feedback is vital to match experiment with theory. In this Chapter, however, we will restrict ourselves to the above algorithm, i.e. one-shot DMFT calculations.

2.2.3.3 Application

As a first example and for illustrative purposes, we apply DMFT to the t_{2g} model of bulk SrVO₃ which we argued above to contain the relevant low-energy physics. While nowadays, this is a simple exercise, the initial works [79, 100] were pioneering. The model consists of the three orthogonal t_{2g} orbitals (d_{xy} , d_{xz} , d_{yz}) spanning the relevant energy subspace around the Fermi level with band width $W \approx 2\text{eV}$. Using maximally localized Wannier functions we construct the Hamiltonian, discretized on a momentum grid of $20 \times 20 \times 20$ k-points in the Brillouin zone and supplement it with a static Kanamori interaction with the aforementioned parameters ($U = 5\text{eV}$, $J = 0.75\text{eV}$ and $U' = U - 2J = 3.5\text{eV}$). Due to the orthogonality of the orbitals we may introduce further simplifications in the DMFT algorithm. Instead of a full orbital matrix we simplify our Green's function sampling to a diagonal self-energy (hybridization function)

$$\Sigma_{\text{full orb}}^{\text{DMFT}} = \begin{bmatrix} \Sigma_{xy,xy} & \Sigma_{xy,xz} & \Sigma_{xy,yz} \\ \Sigma_{xz,xy} & \Sigma_{xz,xz} & \Sigma_{xz,yz} \\ \Sigma_{yz,xy} & \Sigma_{yz,xz} & \Sigma_{yz,yz} \end{bmatrix} \rightarrow \Sigma_{\text{orb diagonal}}^{\text{DMFT}} = \begin{bmatrix} \Sigma_{xy,xy} & 0 & 0 \\ 0 & \Sigma_{xz,xz} & 0 \\ 0 & 0 & \Sigma_{yz,yz} \end{bmatrix} \quad (2.55)$$

and discard all *local* inter-orbital contributions. Note however, that in the non-local DMFT lattice propagators G^k , inter-orbital signatures remain due to the Wannier Hamiltonian.

The DMFT self-consistent cycle is iterated at room temperature $\beta = 40\text{eV}^{-1} = 290\text{K}$ until convergence is reached, the resulting local Matsubara Green's function and self-energy is illustrated in Fig. 2.9. Please note that with this local viewpoint the t_{2g} orbitals are equivalent. While each of the three orbitals are considered fully in the DMFT cycle, their *local* contribution to the self-energy is identical. Bulk SrVO₃ is evidently a prime example of a correlated metal: The imaginary parts of

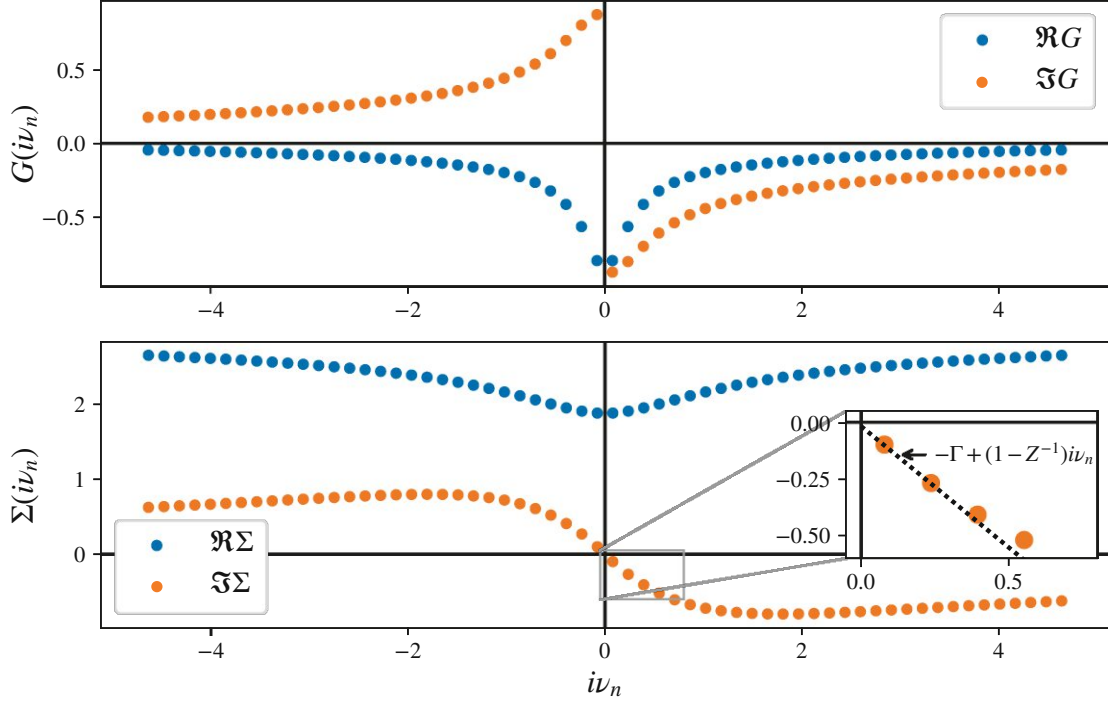


Figure 2.9: DMFT Green's function (top) and self-energy (bottom) of SrVO₃, calculated at room temperature $T = 290\text{K}$. Due to the local degeneracy of the t_{2g} bands in perfect cubic symmetry, all three orbitals are identical. The imaginary part of the Green's function around the first Matsubara frequency can be used as a proxy to gauge the metallicity of the system. The imaginary part of the self-energy allows for a validation of a Fermi-liquid. For the presented setup we find $\Gamma = 15\text{meV}$ and $Z = 0.5$.

the Green's function extrapolate to finite values for $\nu_n \rightarrow 0^+$, indicating a metallic spectral function $A(\omega = 0) > 0$, see Eq. (2.60). Similarly, the self-energy can be interpreted in the framework of Fermi-liquid theory: In this context the self-energy on the Matsubara axis can be Taylor expanded in the low-energy regime

$$\Sigma^{\text{FL}}(i\nu_n) \approx \Re\Sigma(i\nu_n \rightarrow 0^+) + i\Im\Sigma(i\nu_n \rightarrow 0^+) + i\frac{\partial\Im\Sigma(i\nu_n)}{\partial\nu_n}\Big|_{\nu_n \rightarrow 0^+}\nu_n + \mathcal{O}(\nu_n^2). \quad (2.56)$$

Inserting this expression into the initial Green's function allows for a different viewpoint on the

quasi-particle renormalization

$$\begin{aligned}
G &= \left[i\nu_n \left(1 - \frac{\partial \Im \Sigma(i\nu_n)}{\partial \nu_n} \Big|_{\nu_n \rightarrow 0} \right) + \mu - H^{\mathbf{k}} - \Re \Sigma(i\nu_n \rightarrow 0^+) - i \Im \Sigma(i\nu_n \rightarrow 0^+) + \dots \right]^{-1} \\
&= \left[i\nu_n Z^{-1} + \mu - H^{\mathbf{k}} - \Re \Sigma(i\nu_n \rightarrow 0^+) + i\Gamma + \dots \right]^{-1} \\
&= Z \underbrace{\left[i\nu_n - Z \left(H^{\mathbf{k}} - \mu + \Re \Sigma(i\nu_n \rightarrow 0^+) \right) + iZ\Gamma \right]^{-1}}_{G^{\text{FL}}} + \underbrace{\dots}_{G^{\text{incoherent}}} \tag{2.57}
\end{aligned}$$

where via

$$\Im \Sigma(i\nu_n \rightarrow 0^+) = -\Gamma \tag{2.58a}$$

$$\frac{\partial \Im \Sigma(i\nu_n)}{\partial i\nu_n} \Big|_{\nu_n \rightarrow 0^+} = 1 - Z^{-1} \tag{2.58b}$$

we defined the quasi-particle weight Z ($0 < Z \leq 1$) and the bare scattering rate Γ ($\Gamma \geq 0$). Through the self-energy the energy levels are shifted, compressed, and endowed with a finite life time (inverse scattering rate).⁷

The newly introduced Fermi liquid part of the Green's function G^{FL} describes now only the coherent quasi-particle excitations with weight Z . Within DMFT this prefactor Z can be regarded as the inverse of the mass enhancement

$$m_{\text{DMFT}}^* = \frac{m}{Z} \tag{2.59}$$

with respect to the band mass m from DFT. If the self-energy were to gain a momentum dependence, an additional momentum expansion around the corresponding Fermi momentum $\mathcal{O}(\mathbf{k} - \mathbf{k}_F)$ in Eq. (2.56) has to be taken into account.

The non-coherent part of the one-particle propagator $G^{\text{incoherent}}$ contains the remainder of the self-energy information, describing the non-Fermi liquid weight of $1 - Z$. In order to gain access to this information and to return to the real frequency axis we employ the analytic continuation technique. The information on the Matsubara axis and the real frequency axis are linked via a Hilbert transform⁸

$$G(i\nu_n) = -\frac{1}{\pi} \int_{-\infty}^{\infty} d\omega \frac{\Im G(\omega)}{i\nu_n - \omega} \equiv \int_{-\infty}^{\infty} d\omega \frac{A(\omega)}{i\nu_n - \omega}. \tag{2.60}$$

⁷ The fermionic Matsubara axis is inherently connected to the real frequency axis: Analytic functions X defined in the *upper complex half-plane* must coincide at the boundaries $X(i\nu_n \rightarrow 0^+) = X^{\text{ret}}(\omega = 0)$ and $X(i\nu_n \rightarrow \infty) = X^{\text{ret}}(\omega \rightarrow \infty)$. In turn, the (retarded) self-energy, defined on the real axis, results in equivalent definitions of $\Im \Sigma(\omega = 0) = -\Gamma$ and $\frac{\partial \Re \Sigma(\omega)}{\partial \omega} \Big|_{\omega=0} = 1 - Z^{-1}$. The real part of the latter is the result of the Cauchy-Riemann equations.

⁸ We define the Hilbert transform with a different sign compared to the definition in mathematics. The Green's function defined on the imaginary time axis via Eq. (2.40), requires an additional minus sign, such that the resulting spectral function is strictly positive, see Appendix A.2.

whose inversion, i.e. $G(i\nu_n) \rightarrow A(\omega)$ is an inherently ill-posed problem. For this purpose we resort to the so-called maximum entropy algorithm [101] as implemented in `ana_cont` [31]. Maximum entropy introduces the information entropy S as an additional regularization term with respect to a simple default model $D(\omega)$

$$S[A] = \int_{-\infty}^{\infty} d\omega \left(A(\omega) - D(\omega) - A(\omega) \log \frac{A(\omega)}{D(\omega)} \right) \quad (2.61)$$

which is used to find the *most probable* spectral function, commonly achieved by minimizing the functional

$$Q[A] = \frac{1}{2} \chi^2[A] - \alpha S[A] \quad (2.62)$$

with a scaling hyperparameter α and the merit function

$$\chi^2[A] = \sum_{n=1}^N \frac{\left[G(i\nu_n) - \int_{-\infty}^{\infty} d\omega \frac{A(\omega)}{i\nu_n - \omega} \right]^2}{\sigma_n^2} \quad (2.63)$$

evaluating the error-scaled (σ_n) deviation from the numerical data $G(i\nu_n)$ of a limited dataset on the fermionic Matsubara axis. In this thesis the hyperparameter α is determined via the `chi2kink` method [31], in order to fully benefit from the information fitting in Eq. (2.62). For a detailed mathematical discussion, please refer to the literature [101, 102].

The resulting *local* DMFT spectral function $A(\omega)$ and predicted (we neglect transition elements) photoemission spectroscopy (PES) signal $\propto A(\omega) f_{FD}(\omega)$ is illustrated in Fig. 2.10a. The spectral function displays the infamous three-peak structure where, as expected from the above consideration, we find renormalized, metallic features whose quasi-particle (QP) peak remains dominant around the Fermi level ($\omega = 0$). As the t_{2g} manifold only holds one electron (vanadium d^1) the center of the peak is located above the Fermi level. The lower Hubbard band (LHB) and upper Hubbard band (UHB) are beyond the Fermi liquid picture. Their weight is (asymmetrically) absorbed from the quasi-particle peak (weight $Z < 1$). At the considered temperature of $T = 290\text{K}$ we find a quasi-particle peak to lower Hubbard band ratio of 3.5.

Further, in Fig. 2.10b we also show the renormalized band structure $A(\mathbf{k}, \omega)$, DMFT's equivalent to the DFT band structure: quasi-particle excitations endowed with finite lifetimes and spectral renormalizations. Each vertical line in Fig. 2.10b represents a separate analytic continuation of G^k along the high-symmetry momentum path $\Gamma - X - M - \Gamma - R$. For comparison, we have overlain the resulting heat map with the DFT band structure of Fig. 2.6 (thin, white line). Here the second effect of the quasi-particle renormalization Z becomes apparent: a compression of the (DFT) band width. The linearization of the self-energy, see Eq. (2.56), valid around the Fermi level, leads to renormalized energy levels given by the eigenvalues of $Z \left(H^{\mathbf{k}} - \mu + \Re \Sigma(i\nu_n \rightarrow 0^+) \right)$ and through them, an accurate capturing of the correlation induced changes to the Fermi surface [64]. Away from the Fermi level,

the quasi-particle peaks may be shifted in a more nuanced fashion through the frequency dependence of the self-energy. Nonetheless, the renormalized bandwidth of SrVO_3 can be approximated well via $Z \cdot W \approx 1\text{eV}$.

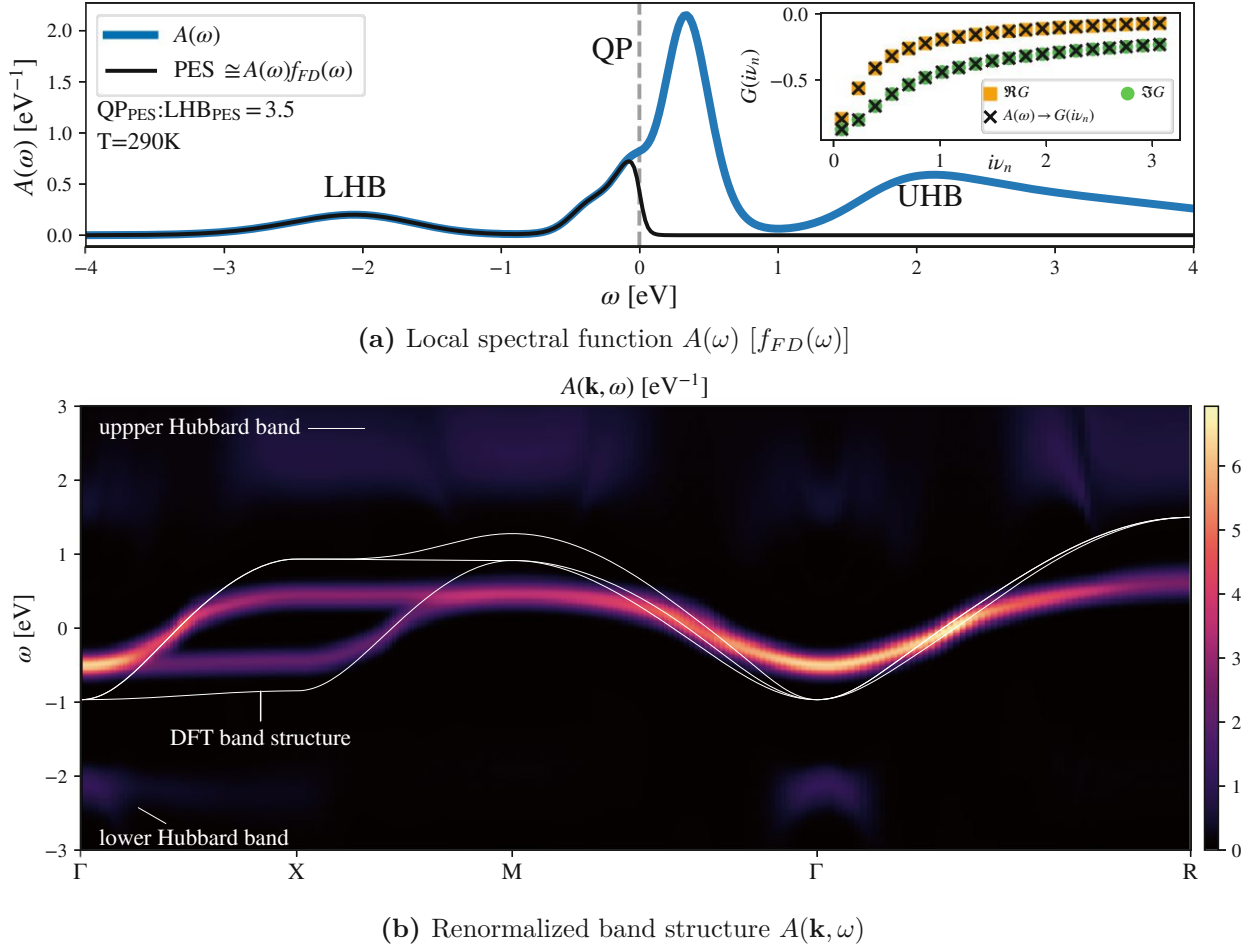


Figure 2.10: Spectral function(s) of SrVO_3 : (a) local $A(\omega)$, (b) $A(\mathbf{k}, \omega)$ as the renormalized DMFT band structure. The quasi-particle (QP) peak, slightly off-centered (Fermi level at $\omega = 0$), is encompassed by the lower and upper Hubbard band, representing the excitations of $N \rightarrow (N - 1)$ [$\omega < 0$] and $N \rightarrow (N + 1)$ [$\omega > 0$], respectively. In order to validate the analytic continuation we show the back transform $A(\omega) \rightarrow G(i\nu_n)$ via Eq. (2.60) in the inset of (a). Compared to the DFT band structure (thin, white line in b), DMFT endows the eigenstates of the Hamiltonian with a finite life time and shifts them accordingly. The result is a compressed band structure with a band width approximated well by $0.5 \cdot W_{\text{DFT}}$.

2.2.4 Experimental context

Having established the state-of-the-art DFT+DMFT treatment of strongly correlated materials, in order to confirm its validity, we must compare these results to experimental measurements. As the spectral function contains both information of electron ($\omega > 0$) and hole ($\omega < 0$) excitations we will, however, for a single measurement be restricted to either the negative (photoemission spectroscopy: PES) or positive part (inverse photoemission spectroscopy: IPES) of the spectrum. This becomes clear in the context of a *discrete* system with eigenstates $\mathcal{H}|n\rangle = E_n|n\rangle$ where the spectral function in its Lehmann representation reads

$$A(\mathbf{k}, \omega) \equiv \frac{1}{Z} \sum_{n,m} (e^{-\beta E_n} + e^{-\beta E_m}) |\langle n | \hat{c}_{\mathbf{k}}^\dagger | m \rangle|^2 \delta(\omega - (E_n - E_m)). \quad (2.64)$$

The (double) sum runs over all possible eigenstate permutations and Z is the partition function $Z = \sum_n \langle n | e^{-\beta E_n} | n \rangle$. In Eq. (2.64)

$$|\langle n | \hat{c}_{\mathbf{k}}^\dagger | m \rangle|^2 \equiv \langle n | \hat{c}_{\mathbf{k}}^\dagger | m \rangle \langle m | \hat{c}_{\mathbf{k}} | n \rangle \quad (2.65)$$

connects states from the N to the $N \pm 1$ particle sector. The resulting spectral function then differentiates between an energy gain or loss in this process, i.e. $A(\mathbf{k}, \omega > 0)$ corresponds to $E_n > E_m$ and consequently a probing of *unoccupied* states. $A(\mathbf{k}, \omega < 0)$ corresponds to $E_m > E_n$ and probes the *occupied* states instead.

As the underlying processes generating the photocurrent are identical as the ones described in Eq. (2.64), the PES signal can be readily connected to the spectral function. Ignoring the electromagnetic coupling details of the photon-induced excitations, a predictive PES spectrum can be obtained by multiplying the spectral function with the Fermi function $A(\omega) f_{FD}(\omega)$, see Fig. 2.10a. Due to the smearing effect of the temperature, the photoemission spectroscopy also gains access to energies slightly above the Fermi level, see, e.g., Ref. [103]. Similarly, a predictive IPES spectrum is obtained via $A(\omega)(1 - f_{FD}(\omega))$. For a more detailed derivation and the connection to the Green's function please refer to Appendix A.1. For a more detailed discussion on the technique of photoemission spectroscopy please see Ref. [104].

Qualitative validation

The existence of a lower Hubbard band can be determined by photoemission spectroscopy and its angle-resolved counterpart. Experimental detection, however, had first to overcome issues related to bulk sensitivity of the measurement. A second problem are the presence and potential influence of oxygen vacancies. Backes *et al.* [105] were able to disentangle the contribution stemming from oxygen vacancies, obtaining a clear LHB signal, see Fig. 2.11a. They grew pristine SrVO₃ in the

(001) direction via pulsed laser deposition with $\text{Sr}_2\text{V}_2\text{O}_7$ as target material in order to minimize oxygen vacancies. The samples were annealed at 550°C before being cooled down to 20K where the measurements, illustrated in Fig. 2.11, were performed with photon energies between $30 - 110\text{eV}$. By investigating the systematic effect of the dose-dependent effect of UV light radiation onto the clean sample, they were able to disentangle the contributions from the correlation effects (lower Hubbard band) and the impurity effects (oxygen vacancies). Please note that this radiation, confirmed by Fermi surface measurements, does not change the filling of the vanadium site.

The pristine sample (Fig. 2.11a, blue line and Fig. 2.11b) evidently showcases an LHB position around $E - E_F = -1.5\text{eV}$, consistent with the calculated spectral function in Fig. 2.10, albeit slightly higher positioned in the experiment ($\omega_{\text{DMFT}}^{\text{LHB}} \approx -2\text{eV}$). Comparing the ARPES spectrum (corresponding to only the xy band due to the employed light polarization) with the DMFT band structure, see Fig. 2.10b, we observe the same band width compression of the (occupied) states $\tilde{\varepsilon} = Z\varepsilon$ ($Z \approx 0.5$) and the identical quasi-particle peak position at $k_{\langle 100 \rangle} = 0$ (the Γ -point) around $E - E_F = -0.5\text{eV}$. Please note that the DMFT spectrum was calculated for $T = 290\text{K}$, whereas the PES measurements were performed at $T = 20\text{K}$. In this context, however, this comparison remains valid as the quasi-particle renormalization Z is typically only weakly temperature dependent (not shown).

Upon UV radiation, the QP:LHB ratio changes from 3:1 towards 1:2, allowing the LHB to dominate both the intensity of the PES and ARPES spectrum.

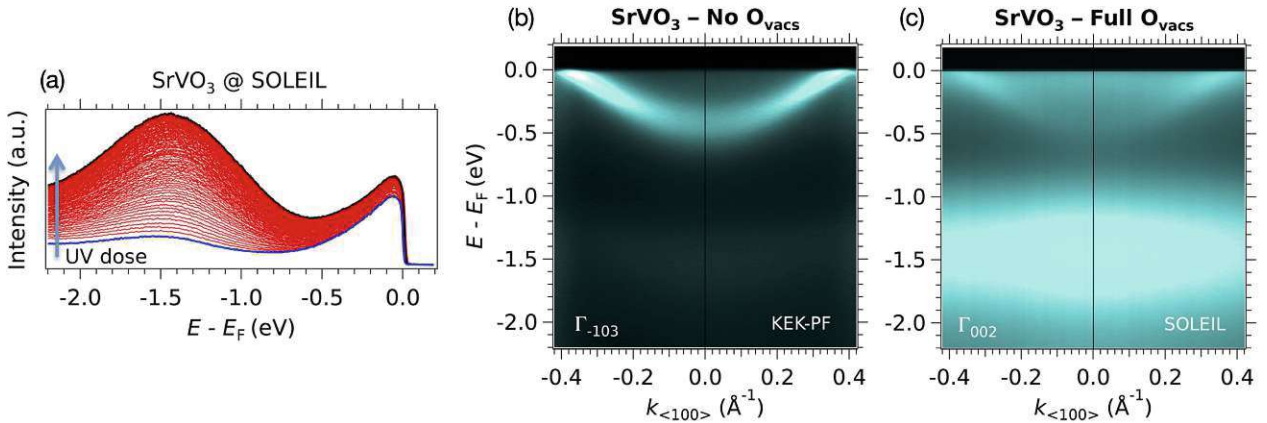


Figure 2.11: SrVO_3 photoemission measurements. (a) PES spectrum around the Fermi level for varying UV dose (blue line: in situ without radiation). (b-c) ARPES spectrum around the Γ point for (b) the pristine sample without oxygen vacancies and (c) with induced vacancies. The clear signature of a lower Hubbard band around $E - E_F = -1.5\text{eV}$ can be dominated by an extra oxygen signal. Note that due to the employed linearly polarized light, only the xy-band contributes to the ARPES signal. [Reprinted with permission from Backes *et al.*, Phys. Rev. B **94**, 241110 (2016). Copyright (2016) by the American Physical Society.] [105]

Photoemission spectroscopy is a surface technique, i.e. due to the inelastic mean-free path (IMFP) of the generated photoelectrons, the bulk of the signal stems from the layers close to the surface. As the penetration length depends strongly on the kinetic energy of the photoelectrons, tuning the incoming photon energy can be exploited to gain depth information of system. Eguchi *et al.* [106] used a photon energy range between 7eV and 21eV. In this energy regime, increased kinetic energies results in a smaller IMFP (cf. universal curve), i.e. *more* surface sensitivity. This reduced bulk contribution, surprisingly, results in a larger QP:LHB ratio. A similar observation will be made in Section 2.4 where a pristine (X-ray cleaned) surface results in a smaller QP peak compared to the native surface, decorated with apical oxygen (as created by pulsed laser deposition).

The Fermi liquid nature of the metal can be further validated via resistivity [107] and specific heat measurements [108]. Mass enhancement of the electronic quasi-particles drives an enhanced specific heat $c_v \propto 1/Z = m^*/m$. Electron-electron scattering processes on the other hand result in the typical Fermi liquid signature in the resistivity, showcasing a quadratic temperature behavior

$$\rho(T) = \rho_0 + AT^2 \quad (2.66)$$

up to temperatures comparably to the Fermi energy. Ref. [107] illustrated a perfect match up to $T = 200\text{K}$, above which the resistivity becomes linear.

Towards the quasi-particle breakdown

As evidenced above, pristine, bulk SrVO₃ is a moderately correlated metal. Recent experimental setups however showcased that there exist several ways to push SrVO₃ across the Mott transition and turn it insulating. With the advent of sophisticated deposition technique that allow for a layer-by-layer growth of samples, it has become possible to investigate effects of reduced dimensionalities (finite number of layers), geometric constraints (growth on substrates), quantum confinement, etc. Yoshimatsu *et al.* [85] were able to trigger an insulator transition by depositing SrVO₃ in a layer-by-layer fashion on a SrTiO₃ (STO) substrate. Fig. 2.12 illustrates the observed photoemission spectra, resolved for samples with various thickness $n = 1 \dots 100$ layers. Between $n = 6$ and $n = 100$ layers the valence spectrum around the Fermi level E_F experiences no significant changes. Below $n = 6$ a continuous suppression of the QP peak eventually transitions into the opening of a gap ($n = 2, n = 1$), rendering the samples insulating.

In this context, quantum well states, induced by the confinement in the (001) growth direction, have also been detected [109]. Based on this concept, Yukawa *et al.* [110] realized a wave-function engineering where a quantum well in a marginal Mott insulating state can be metallized by tuning the tunneling barrier to a second metallic quantum well. A different approach was taken by Wang *et al.* who considered SrVO₃ in its bulk form. By implanting helium ions into the sample they were

able to expand the out-of-plane lattice constant, eventually triggering a metal to insulator transition beyond a certain critical elongation [111].

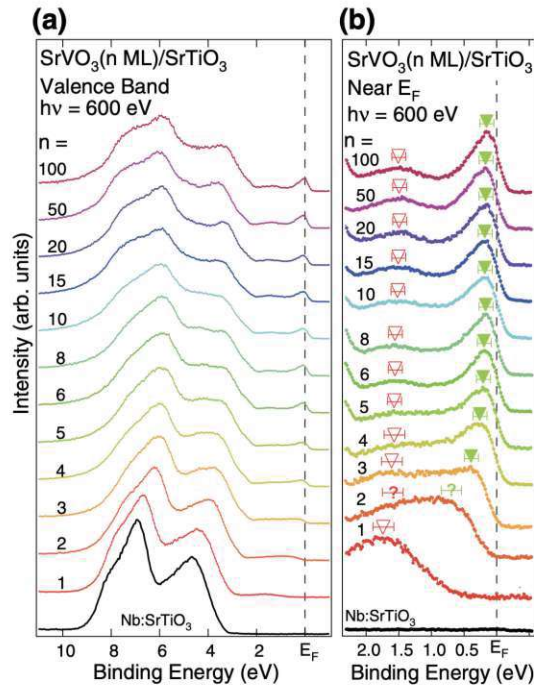


Figure 2.12: Photoemission spectra for SrVO₃ deposited on a SrTiO₃ substrate with a various number of layers $n = 1 \dots 100$. (a) PES for the valence band, (b) Zoom around the Fermi level E_F with focus on the quasi-particle peak and the lower Hubbard band. Below $n = 6$ the quasi-particle suppression eventually transitions the system into an insulating state. A gap is opened for $n = 2$ and $n = 1$. [Reprinted with permission from Yoshimatsu *et al.*, Phys. Rev. Letters **104**, 147601 (2010). Copyright (2010) by the American Physical Society.] [85].

All these varying conditions: dimensionality reduction, wave function manipulation, or strain induction, are therefore capable in triggering a Mott insulating state in the innocuous looking SrVO₃. Pinpointing the underlying mechanism for all these different concepts has been a hotly debated topic in recent times. At this moment in time, different viewpoints exist whether correlation effects [111], disorder [112], or other more intricate crystal structure effects are at the root of it. Uncertainties stemming from the growth process, including material-to-material interfaces, growth environment, and air exposure are especially cumbersome when trying to interpret the experimental results.

To this end, in this Chapter, we will try to tackle these various phenomena from the angle of pure electronic correlations. Analyzing the multi-orbital nature of the different setups, our goal is first to establish whether the observed Mott insulating states are achievable with a purely correlation driven mechanism and secondly, if possible, to find common denominators among the transitions to provide further avenues to advance the current understanding.

2.3 Triggering the Mott transition

Due to the $\text{Pm}\bar{3}\text{m}$ space group symmetry of the cubic SrVO_3 crystal, the vanadium t_{2g} (with O_h point group symmetry) orbitals spanning the low-energy subspace are locally degenerate, i.e. they can be transformed into each other via the application of crystal symmetries. This is the primary reason why the system remains in a metallic state even though the interaction strength, more than twice the size of the band width $U/W \approx 2$, would be sufficient to trigger an insulator transition in the one-band Hubbard model. Indeed in a one-orbital setting these kinds of interactions easily push the system deep into the insulating regime, see Fig. 2.2.

In orbitally degenerate systems with *integer* filling, the Mott insulating state can still be established [113], however larger interaction strengths are necessary to overcome the additional inter-orbital charge fluctuations. In recent years, experimental crystal-growth techniques have become more refined, through which different ways have been established to trigger a Mott transition in these types of perovskite transition metal oxides:

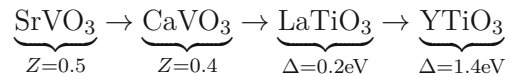
- Isovalent change in chemical composition
- Ultrathin films / heterostructures
- Strain engineering

In the following, we will briefly recapitulate these mechanisms before attempting to advance the understanding for the latter two.

2.3.1 A perspective on d^1 perovskite Mott insulators

2.3.1.1 Isovalent perovskite series

The most fundamental change to a material is the modification of its constituents. In this context one oftentimes considers the d^1 perovskite series



where from left to right the systems transitions from correlated metals (SrVO_3 and CaVO_3 : quasi-particle weight $Z < 1$) to correlation-induced insulators (LaTiO_3 and YTiO_3 : spectral gap $\Delta > 0$) [114, 115, 116]. Generally, this behavior cannot be purely attributed to a change in correlation strength, as the perovskite structures itself is modified when traversing the series, i.e. one needs to consider crystal distortions. Indeed, the cubic symmetry seen in SrVO_3 requires a particular balance of

the involved ionic radii which is commonly expressed in terms of the Goldschmidt tolerance factor [117]

$$t = \frac{r_A + r_O}{\sqrt{2}(r_B + r_O)} \quad (2.67)$$

with r_i being the ionic radius of the $i \in \{A, B, O\}$ ions of the ABO_3 structure. If t is far away from 1 the (ideal) perovskite structure will not be formed, resulting instead in a hexagonal or orthorhombic structure. This reduction in symmetry manifests itself in the above series as a tilting of the octahedra surrounding the B cation, distorting the crystal into a $GdFeO_3$ -type structure [87] in the process. While the V-O-V bond angle maintains the perfect 180° in $SrVO_3$ it is reduced to 160° in $CaVO_3$ [116], necessarily lifting the degeneracy of the t_{2g} states [118] and simultaneously decreasing the relevant band width, and thus the critical U_c of the Mott transition. This trend is further continued in $LaTiO_3$ and $YTiO_3$ where dynamical mean-field theory studies by Pavarini *et al.* [119] find that important orbital fluctuations become suppressed that initially stabilized the metallic behavior in the degenerate system. Their absence results in an insulating state, an orbitally polarized Mott insulator.

Suffice it to say, a one-to-one mapping to the one band Hubbard model, while oftentimes compelling in order to simplify the enormous complexities of the multi-orbital nature of these materials, is rarely an accurate representation of the full physical picture. Consequently, a thorough treatment of all relevant energy scales becomes a necessity.

2.3.1.2 Ultrathin films and heterostructures

Through recent experimental advances in epitaxy, it has become possible to effectively reduce the dimensionality of grown samples, providing a geometric approach to modify the electronic nature of materials. Growing crystalline layers in well-defined orientations on top of a pre-prepared substrate allows for the manufacture of an endless variety of thin films, heterostructures or super-lattices [120]. For insight into the experimental setups and techniques used in the state-of-the-art research please refer to Refs. [121, 122, 123]. The substrate material is commonly chosen to be electrically insulating and to be compatible with the epitaxial layers. This compatibility condition is imposed by differences of the crystal structures if a clean interface connection is supposed to be formed: lattice structures, lattice sizes, chemical compositions, to name a few. Combining two compounds with massively different lattice lengths, for example, is likely to introduce crystal defects in the growth process, preventing pristine samples.

Commonly used substrate materials include $SrTiO_3$, $LaAlO_3$, $BaTiO_3$, $KTaO_3$, $NdGaO_3$, $LiNbO_3$, LSAT, Al_2O_3 , Si, graphene, to name a few. Perovskite materials that have successfully been deposited in such ways include $SrVO_3$ [85], $SrRuO_3$ [124], $LaNiO_3$ [125], $La_{1-x}Sr_xMnO_3$ [126], $SrIrO_3$ [127], etc. Naturally this type of sample preparation is not only relevant for the study of Mott insulators, as we

do here, but is commonly used in different contexts, e.g., the study of emergent superconductivity in thin film pnictides such as FeSe [128]. A common occurrence among different heterostructures is the observation of a metal-to-insulator transition when the film thickness is reduced below a critical number of deposited unit cells, typically in the range of $\mathcal{O}(1) - \mathcal{O}(10)$: SrVO₃ | SrTiO₃ becomes insulating below 2-3 layers [85, 129], identical to SrVO₃ | LSAT [129, 130]. Introducing a capping layer, SrTiO₃ | SrVO₃ | SrTiO₃ increases the critical thickness to 6-7 layers [131]. LaNiO₃ | LaAlO₃ turns insulating below 2-4 layers, with a strong dependence on the final crystal layer termination (NiO₂ or LaO) [125]. Schwerwitzl instead found for the same system a critical thickness of 5 layers [132]. SrRuO₃ | SrTiO₃ turns insulating below 5nm (roughly 10 layers) while simultaneously experiencing a drop in the ferromagnetic phase transition temperature [133]. Metallization on the other hand is also feasible: The metal-to-insulator transition temperature of V₂O₃ can be systematically reduced if deposited on a silicon substrate [134, 135].

The variety of material combination and the plethora of emergent phenomena naturally makes finding a common denominator rather difficult, if not impossible. Simply attributing electronic changes to singular factors such as localization effects, disorder, or band width changes, is not sensible. As each of the above mentioned materials can be classified as strongly correlated, a detailed case-by-case study is necessary to understand the different behaviors. This includes, but is not limited to, systematic changes caused by the dimensional reduction, emergence of a modified interface region, induction of localization effects, as well as experimental complications such as defect formation caused by non-optimal growth conditions, and other environmental influences.

In this Chapter, we will discuss the most fundamental properties of vanadium's t_{2g} orbitals allowing us to extract a reductionist view of the underlying structure. Experimental complications that cause a deviation from these “simplistic” setups naturally complicate things and must be considered on equal footing. The effect of apical surface oxygen, e.g., will be discussed in Section 2.4.

2.3.1.3 Strain engineering

A complimentary, but linked way to manipulate the electronic structure with the potential to trigger a metal-insulator transition is strain manipulation. The main idea is simple: deforming the sample / unit cell necessarily modifies the electronic structure, as the “atomic orbitals” need to adapt to the new nuclei environment. Depending on the involved orbitals, their symmetry, and the type of strain applied, a change in band-widths, energetic positions, as well as interactions can be anticipated.

Strain inducing approaches include

- Change in substrate material (or a substrate material in general)
- Change in growth conditions
- Direct deformation (uniaxial or hydrostatic pressure)
- Atom implantation

A change in substrate material can make all the difference between tensile and compressive strain [136, 137, 138], while a change of growth conditions, more specifically growth temperature [139], can similarly result in a deformed lattice. While not the most common, another flexible method is atom implantation: applying ion irradiation onto a bulk material can effectively be used to continuously modify the lattice parameter, ideally without changing the nominal band filling / valency. Implanted Helium ions for example, were shown to not bond with the existing lattice, according to X-ray measurements [140]. Relevant for experimental reproduction, the effect is persistent, i.e. no perpetual external actuation is necessary, contrary to pressure-induced [141] or piezo-induced [142] strain changes. If the doping is performed in a successive fashion and the crystal structure is monitored via e.g. X-ray measurements, abrupt changes in the electronic signatures are then a direct reflection of strain-induced transitions. Besides possibly induced phase transitions this continuous tuning will naturally be accompanied by other “minor” effects like changes in the scattering potential, i.e. modified quasi-particle life times, especially noticeable in transport measurements.

2.3.2 Distortion phenomena in substrate deposited SrVO_3

2.3.2.1 Bulk metal-insulator transition

Wang *et al.* [111] successfully manipulated the out-of-plane lattice constant of epitaxially grown SrVO_3 on a single-crystal SrTiO_3 substrate by applying helium ion irradiation. This type of “strain doping” results in a purely uniaxial lattice expansion, circumventing the Poisson effect, without introducing local crystal defects as confirmed by a lack of evidence in X-ray diffraction (XRD) measurements. The process has been found to be invertible by vacuum annealing [140], suggesting that the implanted helium atoms populate interstitial sites of the lattice without the creation of atomic vacancies. This effectively provides a route in which the lattice strain can be independently and continuously controlled, providing a unique testing ground for probing electronic structures.

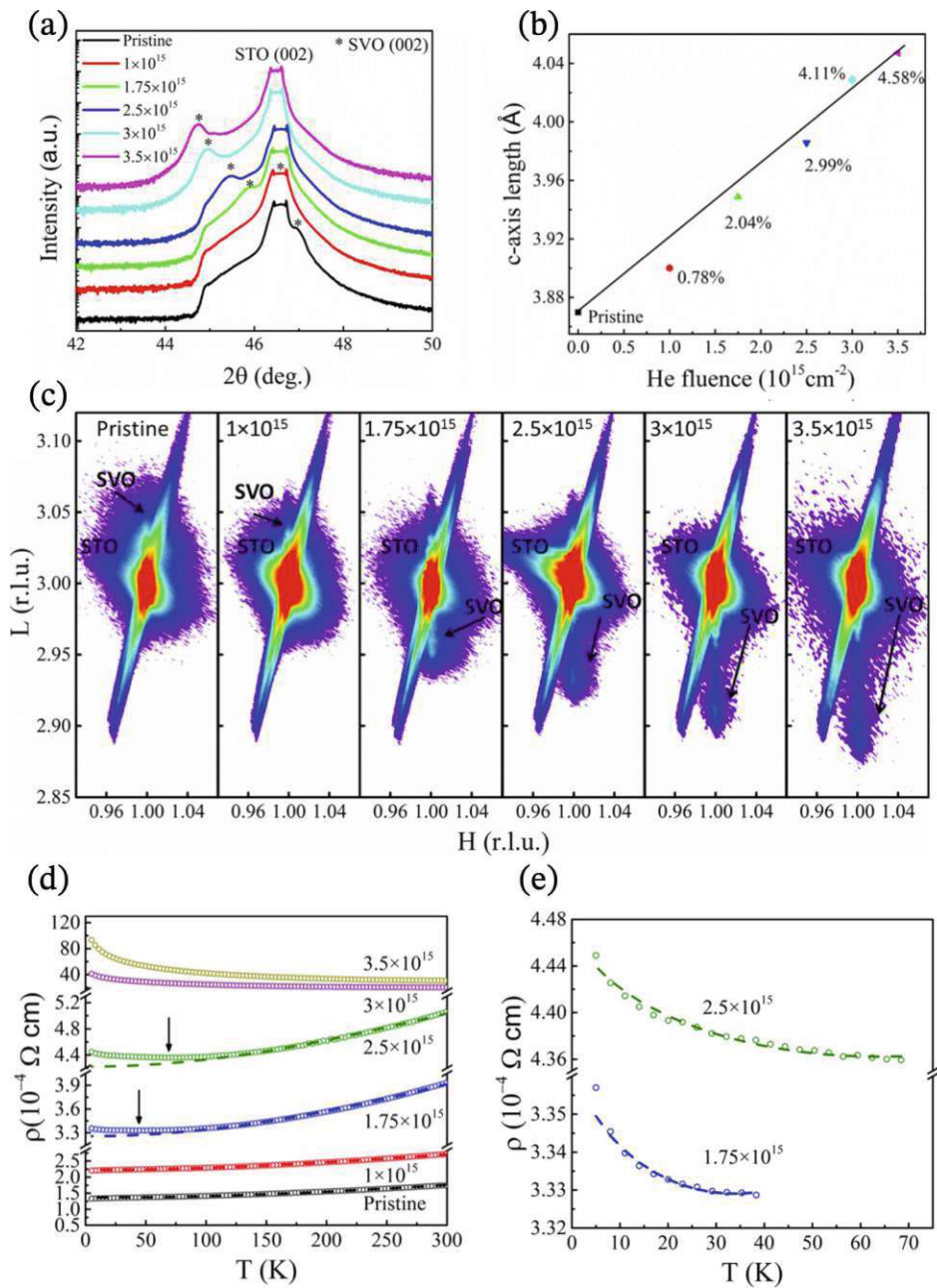


Figure 2.13: X-ray diffraction (XRD) and transport measurements of various helium irradiated samples of SrVO₃ on a SrTiO₃ substrate with 50nm thickness: (a) symmetric (002) XRD reflexes in the vicinity of the STO (002) signal, (b) corresponding c-axis elongation with increased helium fluence, (c) asymmetric (103) XRD that signals the proper in-plane locking between SVO and STO (d) temperature dependent resistivities (e) low temperature resistivity upturns observed in the 1.75 · 10¹⁵ and 2.5 · 10¹⁵ He / cm² samples fitted via Eq. (2.68). An increased helium fluence manipulates the c-axis while maintaining the in-plane lock to STO. This strain leads to a deviation from the Fermi liquid behavior (dashed lines are Fermi liquid extrapolations). [Reprinted with permission from Wang *et al.*, Phys. Rev. Materials **3**, 115001 (2019). Copyright (2019) by the American Physical Society.] [111]

The XRD patterns, lattice characterization and resistivity temperature profiles of the irradiated heterostructures are shown in Fig. 2.13 where the different helium fluences are color-coded. Panel (a) shows the XRD scan around the (002) reflection, comparing the pristine sample (black) with the irradiated ones. The “thin” films were prepared with a 50nm thickness ($\mathcal{O}(100)$ layers), initially reflecting the lattice mismatch between SrTiO_3 and SrVO_3 . With increasing fluence the position of the SVO (002) peak, marked by *, systematically shifts to smaller angles. This shift, translated to a c -axis length is illustrated in panel (b) where a continuous trend between fluence and expansion can be noted with the largest applied fluence of $3.5 \cdot 10^{15} \text{ He / cm}^2$ resulting in a c -axis expansion to $c = 4.04\text{\AA}$ (5% increase compared to bulk). The in-plane locking of SVO to the STO substrate for all considered samples can be confirmed by investigating the asymmetric (103) XRD reflection in panel (c). Slightly masked by the strong STO signal, the increased fluence shifts the SVO peak (marked by the arrow) to smaller L values while the H value, coinciding with STO, remains unchanged. Even for the largest induced strain, one can confidently conclude that the in-plane locking remains intact.

The electronic properties of the samples are then probed with transport measurements, see panels (d) and (e). The unperturbed, pristine sample exhibits the expected Fermi-liquid behavior with $\partial\rho/\partial T > 0$ for all temperatures. Increased helium fluence is accompanied by an overall increase in resistivity and the emergence of an upturn in the low temperature resistivity, marked by an arrow. This deviation from the Fermi-liquid state (dashed lines are extrapolations of the Fermi-liquid characteristics to lower temperatures) occurs at $T \approx 40\text{K}$ and $T \approx 70\text{K}$ in the $1.75 \cdot 10^{15}$ (blue) and $2.5 \cdot 10^{15} \text{ He / cm}^2$ samples (green), respectively. In this regime it can be argued (see fit in Fig. 2.13e) that the data can be interpreted via the equation for so-called quantum corrections to the conductivity (QCC) in three-dimensional systems [143]

$$\rho(T) = \frac{1}{\sigma_0 + a_1 T^{\frac{P}{2}} + a_2 T^{\frac{1}{2}}} + bT^2 \quad (2.68)$$

where in the residual term (accompanied by the standard Fermi-liquid T^2 behavior) σ_0 refers to the Drude conductivity, $a_1 T^{\frac{P}{2}}$ accounts for weak localization in three dimensions ($P = 2$: electron-electron scattering, $P = 3$: electron-phonon scattering) and $a_2 T^{\frac{1}{2}}$ accounts for the “renormalized electron-electron interaction” (REEI) representing the density of state correction at the Fermi energy. A similar analysis has previously been performed by Fouchet *et al.* [144] for SVO layers of varying thicknesses where it has been argued that mainly the REEI contribution is responsible for the mentioned low- T upturn. The metal-insulator transition was proposed to be driven by electron-electron interactions other than weak localization effects. Wang *et al.* [111] argue similarly with the assistance of a (not shown) positive magneto resistance to rule out the importance of the weak localization term. Please note that in this context, Mirjolet *et al.* [145] showcased that (parts of the) deviations from the perfect T^2 Fermi liquid behavior could also stem from strong electron-phonon coupling.

Irradiation induced weak localization (and thus a negative magneto resistance [146]), on the other hand, was for example found to be the insulator driving force in a similar setup where the rare-earth nickelates LaNiO_3 and PrNiO_3 were employed, see Ref. [147].

Going beyond this QCC regime, an additional fluence increase to $3.0 \cdot 10^{15}$ and $3.5 \cdot 10^{15}$ He / cm^2 (pink and yellow, respectively) triggers a qualitative change in the resistivity profile, now displaying an activated behavior with $\partial\rho/\partial T < 0$ throughout. Notably, the saturation value, $\rho(T \rightarrow 0)$, between $2.5 \cdot 10^{15}$ and $3.0 \cdot 10^{15}$ He / cm^2 increases tenfold, suggesting an abrupt metal-to-insulator transition. Similar transitions have been observed in related perovskite setups [125, 131] as well.

2.3.2.2 Tuning the crystal fields

While the authors of the study referenced above [111] performed DFT+DMFT calculations and attributed the samples' tendency to turn insulating to electronic correlations, they did not stabilize insulating solutions in their simulations. In this Section, we will provide a possible perspective for the hitherto elusive, correlation driven mechanism responsible for the observed trends in samples with $\mathcal{O}(100)$ layers. The interpretation of actual, thin films $\mathcal{O}(1 - 10)$ is a more complex endeavor, which we are going to embark on in Section 2.3.3.

The major simplification that arises when modelling ≥ 50 layers is that, to good approximation, the crystal can be considered in its (strained) bulk state [144]. Using the PBE [23] exchange-correlation potential, we find $a_{\text{SrVO}_3} = 3.85\text{\AA}$ and $a_{\text{SrTiO}_3} = 3.95\text{\AA}$ to be the energetically most optimal bulk values.⁹ Then, locking the in-plane lattice to the SrTiO_3 substrate $a = b = 3.95\text{\AA}$ we reduce the degrees of freedom of the system, assuming the tetrahedral symmetry is maintained and no bond distortions emerge (through, e.g., VO_6 octahedron rotations). This allows us, in principle, to perform a full parameter scan of the system by only having to vary the out-of-plane lattice length. The localized t_{2g} basis provides a first gauge for the underlying electronic structure. Besides the relevant (orbital-dependent) band widths W , we will mainly focus on the engineered crystal-field splitting (cfs)

$$\Delta_{\text{cfs}} = E_{xz/yz} - E_{xy} \quad (2.69)$$

as the difference of the *local* orbital $i \in \{xy, xz, yz\}$ energy levels, captured through the diagonal part of the Wannier Hamiltonian $H^{\mathbf{k}}$.¹⁰

$$E_i = \sum_{\mathbf{k}} h_{ii}^{\mathbf{k}} \quad (2.70)$$

The result of a c-axis scan is illustrated in Fig. 2.14. At $a = b = c$ (solid vertical line), cubic

⁹ We employ a setup identical to that in Sec. 2.2: The multi-orbital basis is constructed via maximally localized Wannier function projected on the three vanadium t_{2g} orbitals.

¹⁰ The local energy level can be also obtained directly through the density of states: $\varepsilon(\mathbf{R} = 0) = \sum_{\mathbf{k}} \varepsilon_{\mathbf{k}} = \sum_{\mathbf{k}} \int d\varepsilon \varepsilon \delta(\varepsilon - \varepsilon_{\mathbf{k}}) = \int d\varepsilon \varepsilon N(\varepsilon)$.

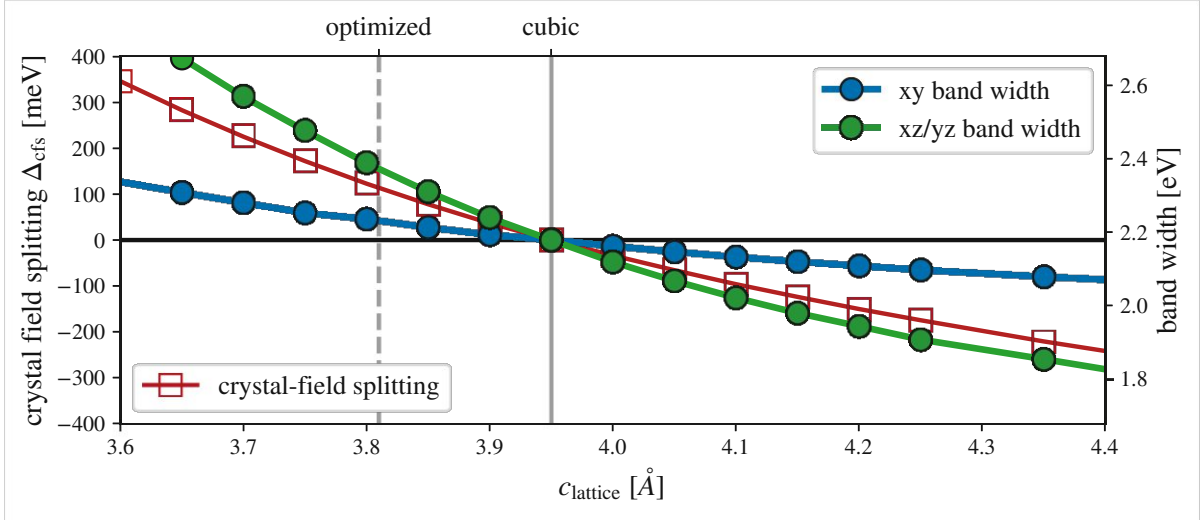


Figure 2.14: Crystal-field splitting (red line, left y-axis) and band widths of the xy and xz/yz orbitals (blue and green lines, right y-axis) of the deformed SrVO₃ unit cell. The in plane lattice constant is constrained to $a = b = 3.95\text{Å}$ of the substrate while the perpendicular c axis is varied. For $c < 3.95\text{Å}$ the xy-orbital is energetically favored ($\Delta_{\text{cfs}} > 0$), for $c > 3.95\text{Å}$ the xz/yz-orbitals are favored ($\Delta_{\text{cfs}} < 0$).

symmetry is retained, resulting in local orbital equivalence ($W_{\text{xz/yz}} = W_{\text{xy}}$) and a vanishing crystal field splitting $\Delta_{\text{cfs}} \equiv 0$. This artificial increase to the STO volume results, through decreased orbital overlap, in a decreased kinetic energy, $W_{a=3.95\text{Å}} = 2.17\text{eV}$, compared to the base case of bulk SrVO₃: $W_{a=3.85\text{Å}} = 2.42\text{eV}$ in Sec. 2.2. Energetically optimizing the volume naturally breaks this symmetry establishing a tetragonal lattice with a compressed out-of-plane lattice of $c = 3.81\text{Å}$ causing a finite cfs of $\Delta_{\text{cfs}} = +120\text{meV}$ to develop (see vertical, dashed line in Fig. 2.14). In this equilibrium, the in-plane tensile straining is compensated by an increased out-of-plane xz/yz orbital overlap, increasing their intra-band hopping amplitudes. This distortion then results in a joint band width increase of both the xy and xz/yz orbital to $W_{\text{xy}} = 2.22\text{eV}$ and $W_{\text{xz/yz}} = 2.36\text{eV}$, respectively. As expected, the xz/yz band width is more sensitive to c -axis manipulation than the xy band width. On the opposite end, the effects are reversed: Expanding the out-of-plane axis against its equilibrium tendency results in an positive crystal field splitting, now energetically favoring the xz/yz orbitals. Further elongating the vanadium-vanadium bonds away from equilibrium, both band widths decrease in value.

We summarize these changes in more detail in Fig. 2.15 where we plot the full band structure on a tetragonal high-symmetry path. For the selected examples, the $c = 3.65\text{Å}$, $c = 3.95\text{Å}$, and $c = 4.10\text{Å}$ structures, we find the in-plane range Γ -X-M- Γ to be virtually unaffected. Nonetheless, the Γ -degeneracy is lifted, and the Fermi surface pocket surrounding the Γ -point is slightly modified.

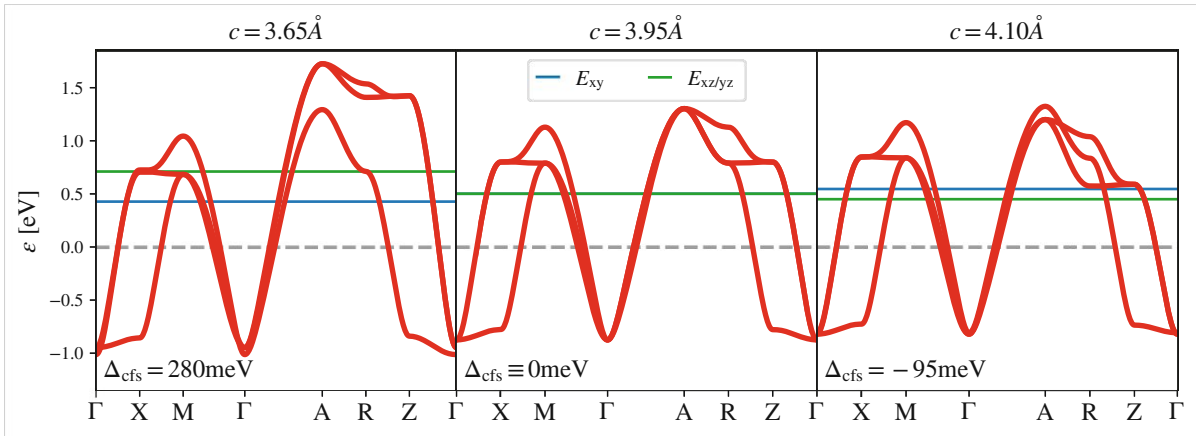


Figure 2.15: Band structure comparison of $c = 3.65\text{\AA}$ (left), $c = 3.95\text{\AA}$ (middle) and $c = 4.10\text{\AA}$ (right). Naturally, the majority of the changes occur in the k_z direction (k-path along Γ -A-R-Z- Γ) due to the changes to the out-of-plane orbital hybridization, affecting mostly *unoccupied* states. The local levels E_{xy} (blue) and $E_{xz/yz}$ (green) are marked accordingly and showcase the reversal of the crystal-field splitting.

Most of the structural changes are reflected in the unoccupied states for $k_z > 0$: the xz/yz orbital compression (elongation) widens (narrows) the dispersion by roughly 20% (10%) for the shown cases with respect to the cubic case $c = 3.95\text{\AA}$.

2.3.2.3 Stabilizing the Mott insulator

In the next step we transition to a dynamical mean-field theory treatment of these c -axis distorted structures. In order to stay consistent with Sec. 2.2, and for the sake of simplicity, we avoid any changes to the interaction parameters of the DMFT setup which remain in the Kanamori parametrization at $U = 5\text{eV}$, $J = 0.75\text{eV}$ and $U' = 3.5\text{eV}$, designed for SVO's bulk form. The uni-axial lattice deformation in principle modifies both the size of on-site and exchange terms [148], and the symmetry of the interaction parameters connected to the crystal symmetries, i.e. $U_{xy,xy,xy,xy} \neq U_{xz,xz,xz,xz} = U_{yz,yz,yz,yz}$, see, e.g., the supplementary material of Ref. [86]. In this Section we forgo an explicit analysis of these types of influences. If introduced, we expect only minor *quantitative* differences to occur in the DMFT phase diagram.

First, we perform a DMFT c -axis scan at fixed room temperature $T = 290\text{K}$ ($\beta = 40\text{eV}^{-1}$) and illustrate the resulting orbital occupations in Fig. 2.16. Crucially, we are able to stabilize a metallic solutions for all considered c -axis values, when initializing the simulations with a *metallic starting point* (here $\Sigma = 0$). Corresponding to the sign of the crystal-field splitting, the system naturally prefers occupying the lower-lying energy level(s) resulting in a orbital polarization mirroring the crystal-field.

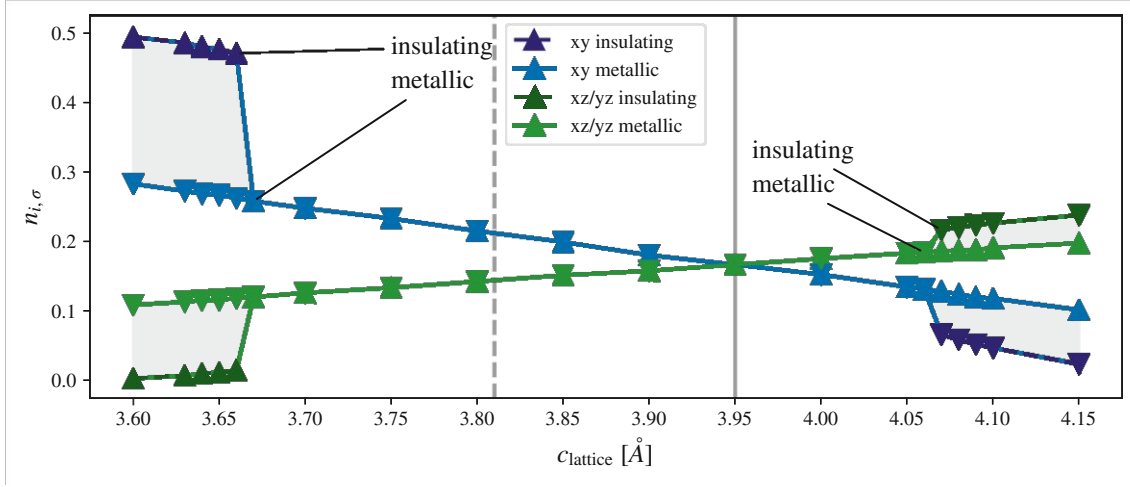


Figure 2.16: Orbital and spin resolved DMFT occupations at room temperature ($T = 290\text{K} - \beta = 40\text{eV}^{-1}$). The sudden jump in orbital polarization signals the transition to polarized, insulating solutions. In this parameter regime DMFT, starting from the non-interacting solution, always converges onto the metallic branch. The insulating branches have been obtained by “artificially” stabilizing the Mott insulator for an increased interaction $U = 6\text{eV}$ ($J = 0.75\text{eV}$, $U' = 4.5\text{eV}$). Once obtained we reduced the interaction, step-by-step to return to the standard bulk values $U = 5\text{eV}$ ($J = 0.75\text{eV}$, $U' = 3.5\text{eV}$). The dashed (solid) vertical line represents the energetically optimum (cubic) c_{lattice} value for the in-plane $a = b = 3.95\text{Å}$.

Moving away from the cubic $c = 3.95\text{Å}$ ($n_{i,\sigma} = 1/6$), we find an almost perfect linear variation of the occupations with c -axis strain. We theorize that this linear dependence results from the interplay of the crystal-field splitting and the band widths: The faster-than-linear increase (decrease) of Δ_{cfs} in the compressed (expanded) regime, is counterbalanced with a simultaneous increase (decrease) of orbital band widths, see Fig. 2.14.

Once metallicity is established in the system, we find that c -axis manipulation is unable to trigger a transition into an insulating solution, i.e. for the given temperature we are effectively locked onto the linear occupation branch. This observation might be the reason why the previously performed calculations [111] were only able to find this metallic branch. Critically, compressing or expanding the structure beyond specific thresholds, we find that the distorted crystal is capable of supporting an insulating solution, marked by lighter colors in Fig. 2.16. The regime where multiple solutions exist for the same input parameters defines a hysteresis, i.e. a first order phase transition occurs. In order to overpower the metallic solution we resorted to a technical “trick”, based on the inevitability of a Mott insulating state in integer filled systems above a finite critical interaction [113]. We find that, $U \geq 6\text{eV}$ ($U' = 4.5\text{eV}$) is sufficient to trigger the Mott insulator for $c \leq 3.85\text{Å}$ and $c \geq 4.00\text{Å}$, irrespective of the DMFT starting point. Once established, the interaction parameters of these auxiliary, insulating

solutions are then brought back to the values chosen for the bulk system by reducing U , step-by-step $U = 6.0\text{eV} \rightarrow 5.9\text{eV} \rightarrow \dots \rightarrow 5.0\text{eV}$ with each intermediate step representing a fully converged DMFT solution. The results of this procedure are orbitally polarized Mott insulators, marked by the separated branches in Fig. 2.16 that deviate from the linear behavior of n_i vs. c .

Within DMFT, these Mott insulating solutions represent the extreme case of a quasi-particle renormalization in the Fermi liquid picture: $Z = 0$, see Section 2.2.3: The quasi-particle peak of the three peak structure, see Fig. 2.10, breaks down, “distorting” the spectrum which now only consists of a lower and upper Hubbard band, separated by a (spectral) gap Δ . Without the presence of weight at the Fermi level, a finite energy ε is required to add or remove an electron, i.e. the (electron) system is insulating. From the view of the local impurity, this feat is only achievable by a suppression of the hybridization function Δ , connecting the local site to the (self-consistently determined) bath.¹¹ Simultaneously, the self-energy must push away the remaining (non-interacting) weight around the Fermi level for a gap to be opened: In a *half-filled, one-band* model this is achieved by a diverging, imaginary part of the self-energy, i.e. $\Im\Sigma(i\nu_n \rightarrow 0^+) \rightarrow -\infty$ [64]. In realistic multi-orbital systems, as is the case in this Section, the situation is more nuanced: through the interplay of the orbitals spectral weight may be shifted by the (real part of the) self-energy. In turn, the imaginary part may still behave Fermi-liquid-esque, see Eq. (2.56), even in the Mott insulating state. Naturally, here, extracted scattering rates Γ and quasi-particle weights Z via the low-energy Fermi-liquid expansion are no longer meaningful.

The (impurity) characteristics of the orbitally polarized Mott insulators at $c = 3.65\text{\AA}$ and $c = 4.10\text{\AA}$ are illustrated in Fig. 2.17a and Fig. 2.17b (right column), respectively, where we show a side-by-side comparison with the coexisting, metallic solutions (left column). In the metallic solutions the Green’s function G and self-energy Σ behaves similar to the cubic, bulk case, see Fig. 2.9. The finite hybridization at the Fermi level $\Im\Delta(i\nu_n \rightarrow 0^+) > 0$ leads to a metallic Green’s function $-\Im G(i\nu_n \rightarrow 0^+) > 0$ and a Fermi-liquid signature in the (imaginary part of the) self-energy. Contrary to the bulk case, the orbital degeneracy is lifted and a slight band shift via the real part of the self-energy occurs. In the insulator, on the other hand, the imaginary part of the Green’s function G and the hybridization function Δ clearly turn to 0 when extrapolated towards $i\nu_n \rightarrow 0^+$. Even though the Fermi liquid signature in $\Im\Sigma$ holds, the cfs-enforced orbital separation in $\Re\Sigma$ triggers the Mott insulator. Here a clear distinction occurs between the insulating solutions: The self-energy shift is restricted to the energetically lower lying orbital(s): xy-band in $c = 3.65\text{\AA}$ (blue) and the xz/yz-band in $c = 4.10\text{\AA}$ (green). Let us note that the commonly referenced “effective crystal-

¹¹ A single impurity Anderson model with finite hybridization will always lead to a metallic spectral function, irrespective of the interaction strength U . In this regard, the remaining quasi-particle weight $Z = 0^+$ of a (metallic) DMFT spectral function, at an interaction slightly below the Mott transition $U < U_c$, can be viewed as the Kondo resonance of the underlying impurity, see Section 3.1.

field splitting” $\Delta_{\text{eff}} = \Delta_{\text{cfs}} + \Re\Sigma_{xz/yz}(i\nu_n \rightarrow 0) - \Re\Sigma_{xy}(i\nu_n \rightarrow 0)$ [149] can only be used as a proxy for the Mott insulating phase. Here, the sign of Δ_{cfs} does not coincide with its correction $\Re\Sigma_{xz/yz}(i\nu_n \rightarrow 0) - \Re\Sigma_{xy}(i\nu_n \rightarrow 0)$ establishing the importance of the frequency dependence of $\Re\Sigma$.¹²

In the compressed structure ($c \leq 3.66\text{\AA}$) we find a state closely resembling the canonical half-filled one-orbital Mott insulator, hosted by the xy-orbital $n_{xy,\sigma} \lesssim 0.5$. In the expanded structure ($c \geq 4.07\text{\AA}$) we find the system to resemble an ideal two-orbital, quarter filled Mott insulator with $n_{xz,\sigma} = n_{yz,\sigma} \lesssim 0.25$. On these newly formed branches, see Fig. 2.16, the finite crystal field splitting is sufficiently large for the stabilization (via the above procedure) of an orbitally polarized DMFT self-energy. With this stabilized polarization the DMFT is capable of an almost complete occupation redistribution towards the lower lying orbital(s). The corresponding orbital-resolved spectral functions are illustrated in Fig. 2.18, where for the chosen c -axis values of $c = 3.65\text{\AA}$ and $c = 4.10\text{\AA}$ we find a spectral gap of $\Delta_{\text{DMFT}} = 350\text{meV}$ and $\Delta_{\text{DMFT}} = 250\text{meV}$, respectively. These are uncharacteristically small gaps for Mott insulator where one would typically expect $\Delta_{\text{DMFT}} \sim U$. Even in the heavily polarized solution, the underlying orbital fluctuations (whose energetic levels are only separated minimally in DFT) drive the system towards metallicity when compared to a strict one-band setup. Furthermore we find that once the coherent, insulating state has been established in either the compressed ($c < 3.95\text{\AA}$) or expanded structure ($c > 3.95\text{\AA}$), the DMFT gap Δ_{DMFT} is highly tunable as it scales linearly with the underlying cfs: $\Delta_{\text{DMFT}} \propto |\Delta_{\text{cfs}}|$ (not shown). Whereas the smallest, expanded structure ($c = 4.06\text{\AA}$) leads to an almost vanishingly small gap $\Delta_{\text{DMFT}} = \mathcal{O}(10)\text{meV}$, the largest, expanded structure ($c = 3.66\text{\AA}$) results in $\Delta_{\text{DMFT}} \approx 300\text{meV}$ (not shown). Due to the difficulties involving of stabilization of the compressed Mott insulator, we suspect that the insulating branch at $c < 3.95\text{\AA}$, see Fig. 2.16, could possibly extend to a larger c -threshold, beyond $c = 3.66\text{\AA}$ at presented $T = 290\text{K}$. Following the observed, linear dependence of $\Delta_{\text{DMFT}} \propto |\Delta_{\text{cfs}}|$, an insulating solution with a vanishingly small gap could *possibly* still exist beyond $c = 3.70\text{\AA}$.

Similar orbital effects occur in LaTiO_3 (Ti with nominal d^1 filling) where due to the inter-orbital fluctuations at the small crystal-field ($3 t_{2g} \rightarrow a_{1g}$, 2 degenerate e_g through a GdFeO_3 distortion), the observed band gap remains quite small: $\Delta = 0.2\text{eV}$ [150].

¹²The orbital polarization in the (real part of the) hybridization function Δ is less important. In the insulating solutions $\Re\Delta_{xz/yz}(i\nu_n \rightarrow 0) - \Re\Delta_{xy}(i\nu_n \rightarrow 0)$ is an order of magnitude smaller than its self-energy counterpart (not shown).

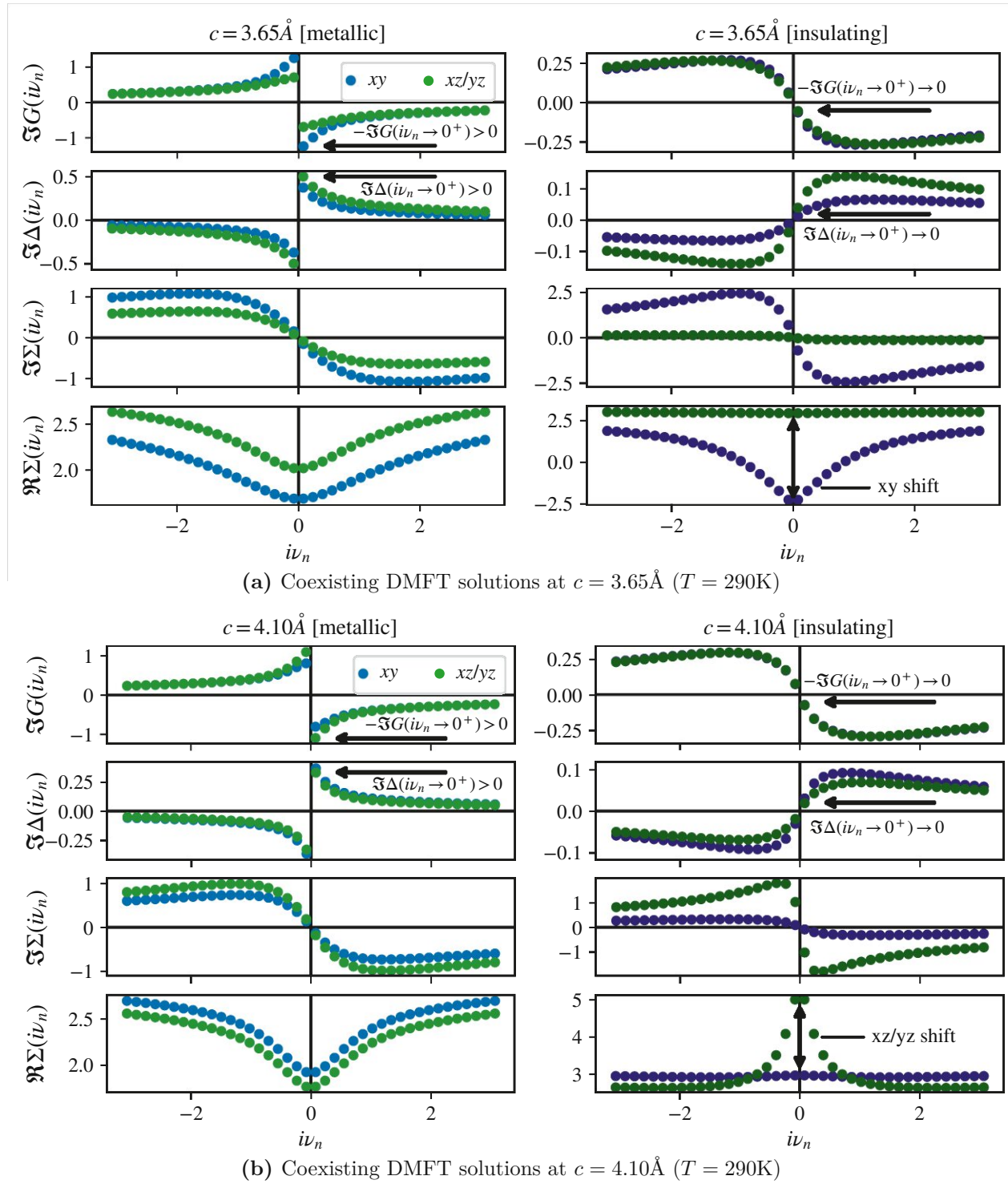


Figure 2.17: Orbital resolved imaginary parts of the (impurity) Green's function $\Im G$, imaginary parts of the hybridization function $\Im \Delta$ and self-energies Σ of the two coexisting DMFT solutions (left: metallic, right: insulating) for (a) $c = 3.65 \text{ \AA}$ and (b) $c = 4.10 \text{ \AA}$ at room temperature $T = 290 \text{ K}$. The insulating solutions ($-\Im G(i\nu_n \rightarrow 0^+) \rightarrow 0$) show the expected suppression of the hybridization function at the Fermi level ($\Im \Delta(i\nu_n \rightarrow 0^+) \rightarrow 0$) and a distinct enhancement of the cfs-induced orbital polarization in the real-part of the self-energy: $|\Re \Sigma_{xy} - \Re \Sigma_{xz/yz}|_{\text{insulating}} \gg |\Re \Sigma_{xy} - \Re \Sigma_{xz/yz}|_{\text{metallic}}$.

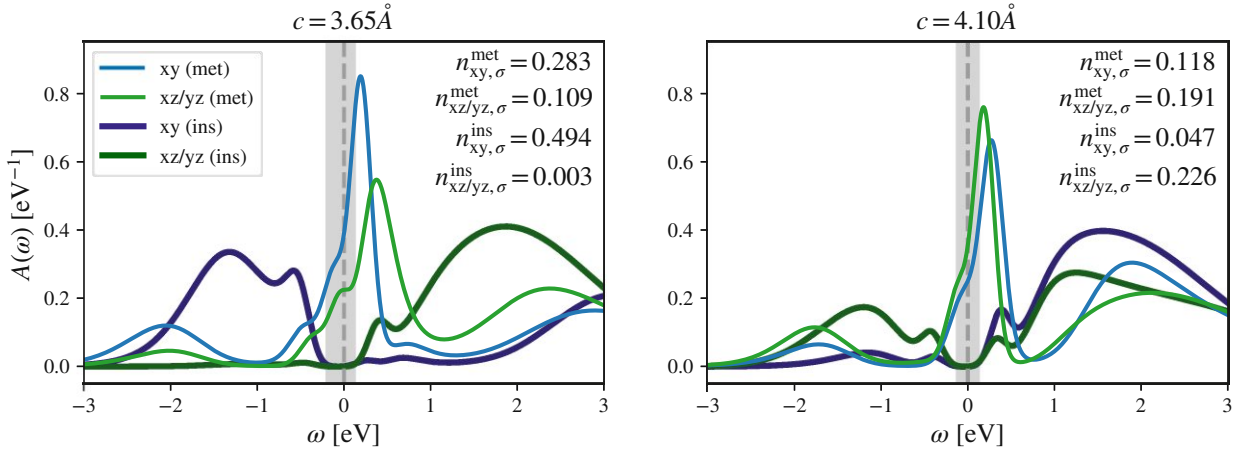


Figure 2.18: Orbital resolved DMFT spectral functions in the coexistence region of uniaxially distorted bulk SrVO_3 with an in-plane lock to $a = b = 3.95\text{\AA}$. We compare the metallic and insulating solutions in the compressed (left: $c = 3.65\text{\AA}$) and expanded (right: $c = 4.10\text{\AA}$) structure at room temperature $T = 290\text{K}$. The insulating solutions, with the spectral gap marked in gray, are characterized by a half-filled ($n_{xy,\sigma} \approx 0.5$) and quarter-filled ($n_{xz/yz,\sigma} \approx 0.25$) Mott insulator originating from the xy and xz/yz orbital(s), respectively.

2.3.2.4 Crystal-field dichotomy

To further analyze the DMFT solutions we now study the effect of temperature. This process is illustrated in Fig. 2.19 in the form of orbital occupations, where, starting from the insulating / metallic branch at room temperature $T = 290\text{K}$ we gradually increase the temperature. Each point represents a converged DMFT solution whose corresponding (total) spectral function is illustrated in Fig. 2.20 and Fig. 2.21, respectively.

Starting off with the compressed structure ($c = 3.65\text{\AA}$): The insulating solution is found to be stable up to $T = 390\text{K}$, above which the orbital polarization can no longer be maintained. Through increased thermal fluctuations, metallicity is introduced into the DMFT cycle, abruptly collapsing the insulating solution. Similarly to the previous c -axis scan, once this metallic solution is established, the system remains “locked” onto the metallic temperature branch. This is confirmed by starting from a high-temperature, metallic solution and cooling the system into the coexistence region (see arrows). Once the system is metallic, further temperature increase then only leads to a minor softening of the three-peak structure (loss of features in the quasi-particle peak), see Fig. 2.20, and a slight variation of the orbital occupation. Cooling on the metallic branch leads to a reduction in orbital polarization $n_{xy,\sigma} - n_{xz/yz,\sigma}$. This is in contrast to the insulating branch, where, once the polarized Mott insulator is established, further cooling pushes the system towards stronger orbital polarization, eventually

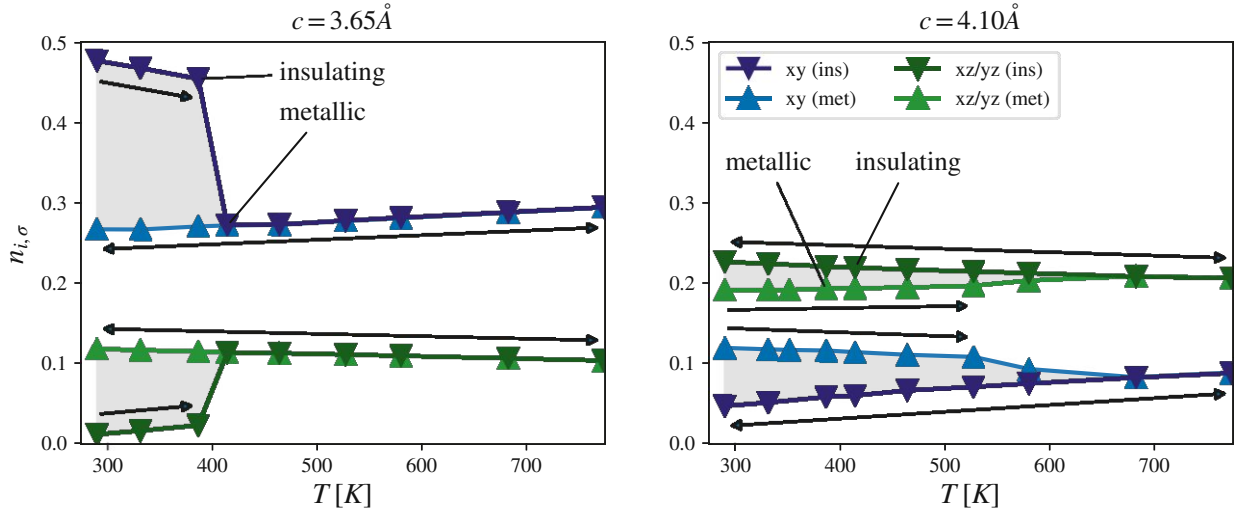


Figure 2.19: Orbital and temperature resolved DMFT occupations of the c-axis compressed structure (left: $c = 3.65 \text{ \AA}$) and expanded structure (right: $c = 4.10 \text{ \AA}$). The lines are the result of a step-by-step increase of the temperature starting from either the insulating or metallic solution (see arrows). The high-temperature slopes indicate that cooling stabilizes a low-temperature metallic solution for $c = 3.65 \text{ \AA}$ and an insulating solution for $c = 4.10 \text{ \AA}$. The abrupt drop of orbital polarization for $c = 3.65 \text{ \AA}$ highlights the difficult-to-stabilize insulating branch.

yielding a fully fledged, half-filled xy -orbital: $\lim_{T \rightarrow 0} n_{xy,\sigma}(T) = 0.5$.

The expanded structure ($c = 4.10 \text{ \AA}$) on the other hand exhibits the opposite temperature behavior to the compressed structure. Both metallic and insulating solutions remain intact up to $T = 570 \text{ K}$. Beyond $T = 700 \text{ K}$ the two branches recombine to a single *insulating* solution with residual weight around the Fermi level, a so-called bad insulator, see Fig. 2.21. The linear behavior in the orbital occupation, previously observed for the metal, now occurs for the insulating branch instead. We verified that cooling from this high temperature solution maintains the bad insulator, eventually stabilizing the spectral gap of the Mott insulator. Akin to the polarized insulator found at $c = 3.65 \text{ \AA}$, the orbital polarization eventually yields a complete depopulation of lower lying orbital for $T \rightarrow 0$. Here, the electron is now equally distributed in the quarter filled xz/yz orbitals with $\lim_{T \rightarrow 0} n_{xz/yz,\sigma}(T) = 0.25$, see the slope in Fig. 2.19. Contrary to the compressed system, here the metallic branch is the odd one out: heating the system beyond the critical threshold temperature ($T \approx 650 \text{ K}$), the quasi-particle peak suddenly collapses, its weight being distributed to the two satellite Hubbard bands.

From these high temperature characteristics we can now easily infer the behavior when varying the c-axis at elevated temperatures, comparable to those used in the epitaxial growth process. The hysteresis branches, appearing at lower temperatures in Fig. 2.16 disappear at higher temperatures,

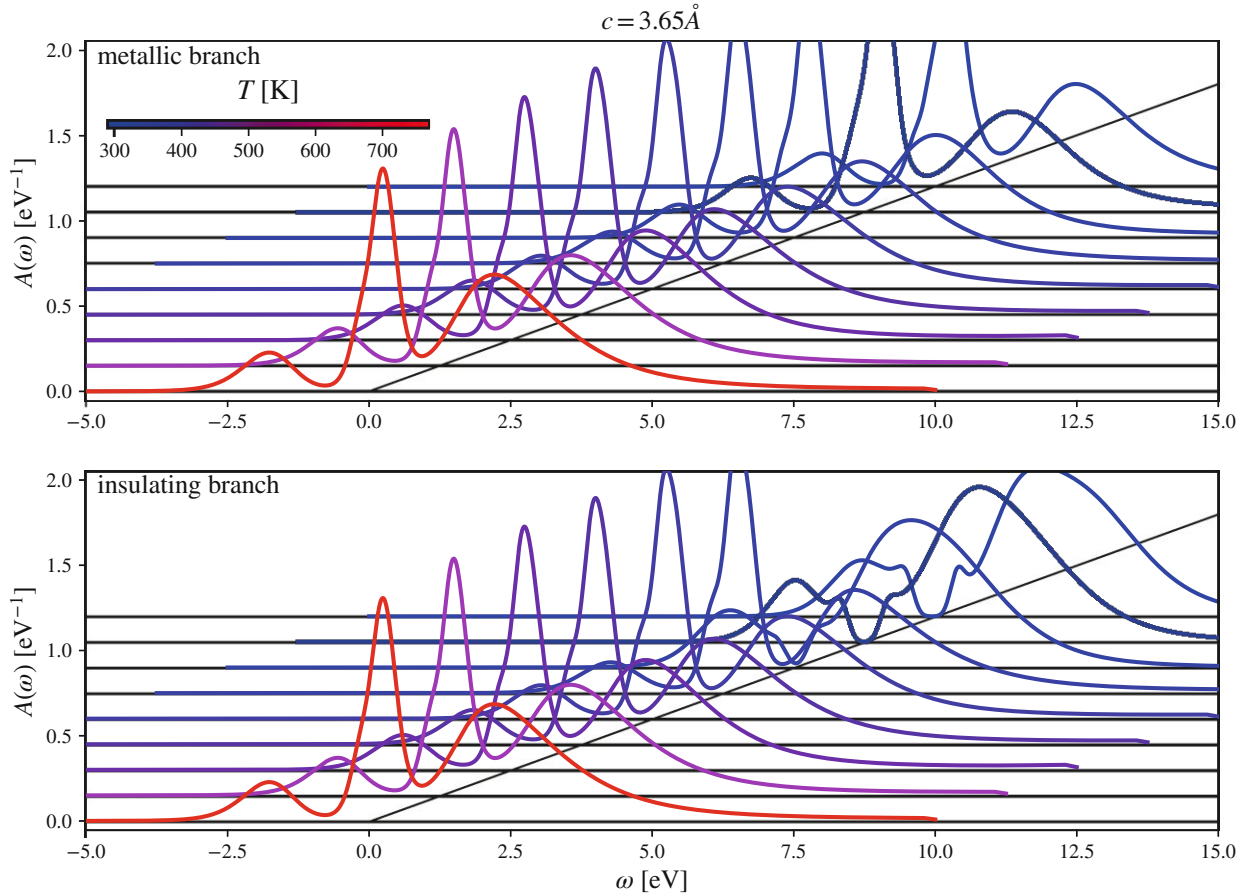


Figure 2.20: Spectral functions $A(\omega)$ for the two branches of the compressed structure $c = 3.65\text{\AA}$ above $T = 290\text{K}$, corresponding to the orbital occupations in the left panel of Fig. 2.19. Top: metallic branch. Bottom: insulating branch. The line color indicates the temperature (color map – red: hot, blue: cold). Cooling the system from the high-temperature solution (red) the system maintains the well-formed three-peak structure on the metallic branch (as in the top panel). The onset of the insulating solution corresponds to the temperature at which an orbital polarization can be (forcefully) generated within DMFT.

eventually resulting in a monotonous c -axis dependence. All *compressed* structures in the considered range ($3.60\text{\AA} < c < 3.95\text{\AA}$) should result in a coherent metallic Fermi liquid solution. The expanded structures on the other hand will at some critical c -axis threshold experience a *continuous* crossover from this metallic solution to the showcased bad insulator. This behavior is quantitatively reproduced in the intermediate temperature scan at $T = 770\text{K}$ ($\beta = 15\text{eV}^{-1}$) in Fig. 2.22a, where we showcase the orbital-resolved occupations $n_{i,\sigma}$, spectral functions $A(\omega)$, and the latter's value at the Fermi level $A(\omega = 0)$.

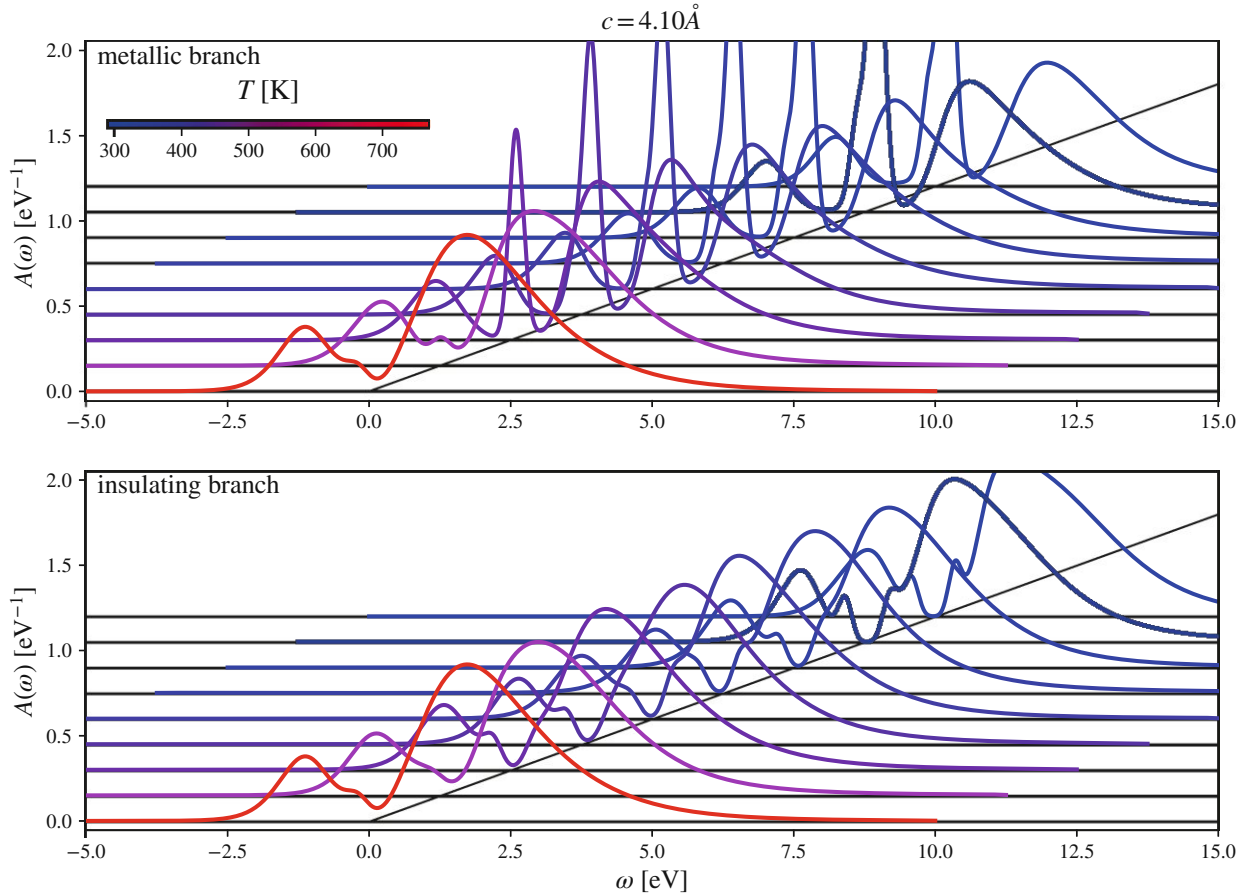


Figure 2.21: Spectral function $A(\omega)$ for the two branches of the expanded structure $c = 4.10\text{\AA}$ above $T = 290\text{K}$, corresponding to the orbital occupations in the right panel of Fig. 2.19. Top: metallic branch. Bottom: insulating branch. Same color coding as Fig. 2.20. Cooling the system from the high temperature “bad insulator” solution (red) leads to a coherent Mott insulator (insulating branch). Contrary to the compressed structure, the metallic solution is now the one that cannot be obtained via a temperature variation.

The cross-over to the high-temperature insulating solution is accompanied by a rather abrupt quasi-particle destruction. Assuming we are still above the critical end-point (the location of which will be estimated below), the transition in $A(\omega = 0)$ remains continuous. Despite the smooth orbital redistribution over the full c -axis variation, the quasi-particle peak is destroyed almost instantaneously above $c = 4.01\text{\AA}$, see inset of Fig. 2.22a. Surprisingly, at these elevated temperature the threshold for the lattice expansion is smaller than for the coexistence region at room temperature ($c = 4.06\text{\AA}$), see Fig. 2.16. Evidently, we find distinct differences when comparing to the metal-insulator transition of the half-filled one-band Hubbard model, see Fig. 2.2.

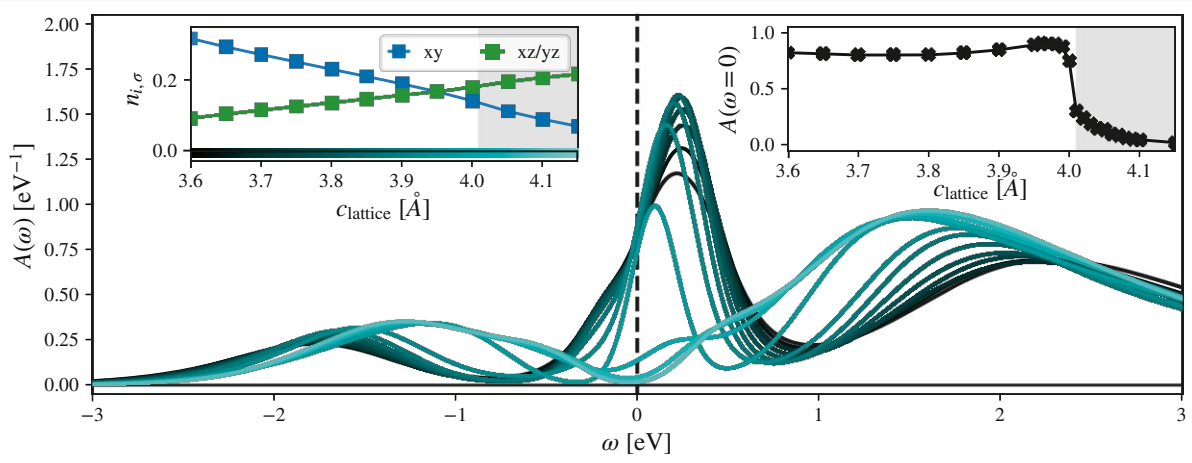
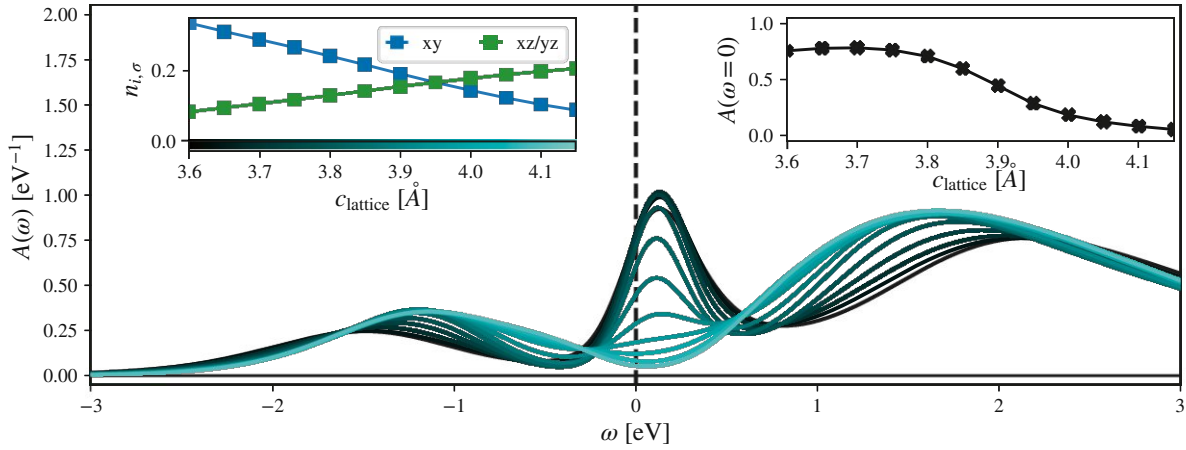
(a) Sharp transition at $T = 770\text{K}$ (b) Smooth transition at $T = 1160\text{K}$

Figure 2.22: (a) Intermediate temperature ($\beta = 15\text{eV}^{-1} - T = 770\text{K}$) and (b) high temperature ($\beta = 10\text{eV}^{-1} - T = 1160\text{K}$) spectral function scan including orbital occupations (left inset). The transition of the spectral function at the Fermi level $A(\omega = 0)$ is plotted in the right inset. At $T = 770\text{K}$, owing to the orbital redistribution, the system undergoes a minor quasi-particle peak evolution, but stays firmly metallic up to $c = 4.00\text{\AA}$. Beyond, an abrupt metal-insulator transition occurs, transforming the system into a thermally activated insulator (bad insulator). The drop in spectral weight occurs at crystal-field values between $\Delta_{\text{cfs}} = -33\text{meV}$ and $\Delta_{\text{cfs}} = -40\text{meV}$. A similar feature is missing in the compressed structure $c < 3.95\text{\AA}$. At $T = 1160\text{K}$, the system undergoes a similar, however much more gradual transition from metal ($c \leq 3.90\text{\AA}$) via bad metal ($3.90\text{\AA} \leq c \leq 4.0\text{\AA}$) to bad insulator $c \geq 4.0\text{\AA}$. Whereas the size of the quasi-particle peak is smaller at $T = 1160\text{K}$, the values at the Fermi level are comparable to $T = 770\text{K}$.

In the case of distorted SrVO_3 , the crystal-field splitting and the associated lifting of degeneracy plays the central role while changes in the band width are merely auxiliary side effects. Above the positive critical cfs, found at surprisingly small values $\Delta_{\text{cfs}} \approx -40\text{meV}$, the three orbitals destabilize into an effective two-orbital system. In this subsystem, the interaction now effectively acts on two bands, reducing the critical U_c necessary to trigger the insulator transition.¹³ Let us note that this type of mechanism has already been studied for symmetric two-band models in Ref. [151] where a similar, direct transition from metal to orbitally polarized insulator was observed for small cfs. Our setup hence generalizes these observation to the case of t_{2g} orbitals that are more commonly encountered in correlated materials. While a connection to the two-band model is not surprising, the way this connection is formed, however is.

Let us emphasize again, that the c-axis compressed structure lacks this high-temperature insulator phase, i.e. the metal-insulator coexistence region has a critical upper temperature. Furthermore the insulating solution in this coexistence region at room temperature requires a cfs that is roughly three times larger compared to its expanded counterpart: $\Delta_{\text{cfs}}(c = 3.65\text{\AA}) = +120\text{meV}$, $\Delta_{\text{cfs}}(c = 4.10\text{\AA}) = -40\text{meV}$. To some extent, the tendency to turn metallic is brought upon by the band width increase of the xz/yz orbitals, as they need to be depopulated in order to enforce the polarization. From this viewpoint, one could argue that the polarization process becomes easier the fewer bands have to be depopulated, i.e. $3 \rightarrow 1$ orbital (compressed) is more difficult to achieve than $3 \rightarrow 2$ orbitals (expanded). The resulting, strong polarization is, in this sense misleading, see Fig. 2.19. Despite an orbital polarization nearly doubling the size of the expanded structure ($c = 3.65\text{\AA}$: $n_{xy,\sigma} - n_{xz/yz,\sigma} \approx 0.5$, $c = 4.10\text{\AA}$: $n_{xz/yz,\sigma} - n_{xy,\sigma} \approx 0.25$), the insulating solution is quite fragile. In this context, an experimental validation may be adequate: Applying uniaxial pressure onto a simple SrVO_3 sample could potentially trigger this insulating solution. Assuming one is able reach the far end of the hysteresis, see Fig. 2.16, and assuming the DMFT solution thereafter is insulating, such a pressure experiment would provide direct access to the underlying crystal-field mechanism. Please note that, while it is clear that for $c > 4.15\text{\AA}$ the hysteresis will collapse onto an insulating solution, it is a priori not clear, whether $c \leq 3.6\text{\AA}$ will do the same. The increased xy band width of the latter may lead to a parameter regime where an insulating solution is not viable.

Finally, the first signs of the crystal field dichotomy can already be seen in the high temperature regime $T = 1160\text{K}$, see Fig. 2.22b. We find the identical, linear behavior of the orbital occupations (see inset), however, the transition from metal to insulator is now completely smooth. At this temperature the compressed structures $c < 3.95\text{\AA}$ still support a firmly metallic solution. Due to the increased thermal fluctuations, the quasi-particle peak is necessarily slightly suppressed and the Hubbard bands

¹³In a degenerate n orbital system with 1 electron per site the critical interaction strengths scales like $U_c(n) \propto \sqrt{n}U_c(n=1)$ [113].

are slightly more broadened. Upon changing the sign of the crystal-field splitting ($c \geq 3.95\text{\AA}$) the system quickly transitions into an incoherent (bad) insulator. Comparing the evolution of the spectral function at the Fermi level $A(\omega = 0)$ between Fig. 2.22a and Fig. 2.22b, we find an intriguing temperature dependence. Cooling the expanded structures ($c \geq 3.95\text{\AA}$) a sudden c -value threshold appears that clearly separates the two emerging regimes. As the band widths showcase only a minor variation around $c = 4.00\text{\AA}$ (and the on-site interaction U remains constant throughout), we can safely conclude that the cfs is the driving force of this behavior.

2.3.2.5 Orbital Widom line

In order to further scrutinize the cfs driving force, relevant for the experimental comparison, we first illustrate the detailed spectral function evolution along the transition at $T = 770\text{K}$ in Fig. 2.23.

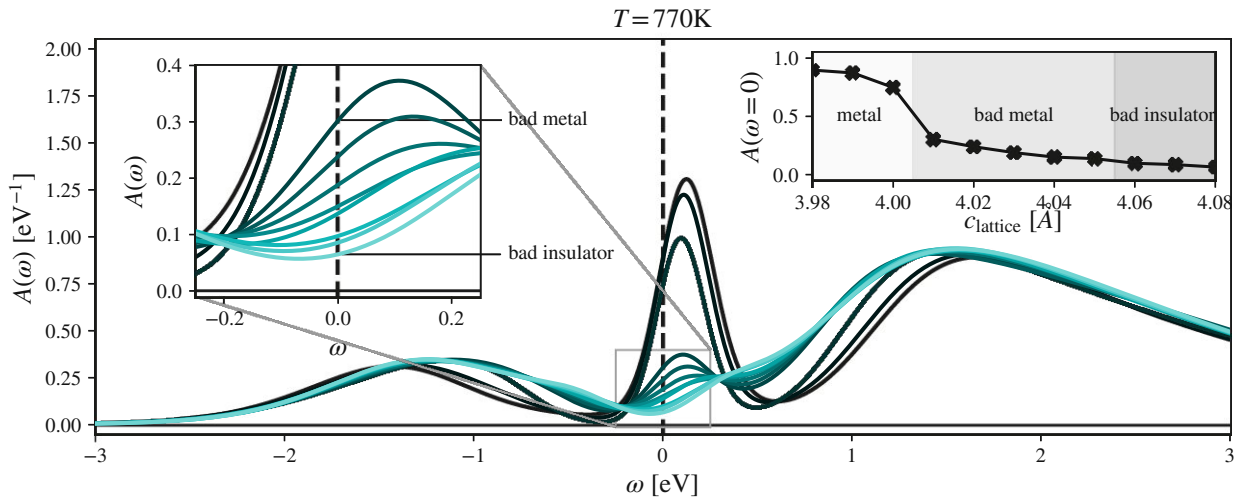


Figure 2.23: Detailed spectral function evolution across the metal-insulator transition at $T = 770\text{K}$ for a step size of $\Delta c = 0.01\text{\AA}$. Beyond a specific cfs threshold, the metallic solution abruptly collapses into a bad metal solution (minor quasi particle peak remains). In this regime, the spectral function slowly transforms where beyond $c \geq 4.06\text{\AA}$ it can be interpreted as bad insulator. The best characterization of this transition is done with either the curvature of the spectral function around the Fermi level $\omega = 0$ (see inset) or the absence of a local maximum near the Fermi level.

Each spectral function is now separated by a much smaller c -axis step size of $\Delta c = 0.01\text{\AA}$. We find that the abrupt drop of the spectral weight at the Fermi level (bad metal: $c = 4.01\text{\AA}$) is predated by a slight suppression of the quasi particle peak at $c = 4.00\text{\AA}$. The bad metal regime can be characterized by an intact, however strongly suppressed, quasi particle peak. Increasing the c -axis further, the local maximum of the quasi-particle peak is slowly transformed (see zoomed inset) into a local minimum beyond $c = 4.06\text{\AA}$ the spectral function, commonly referred to as bad insulator in the literature. The

quasi particle peak vanishes and is fully transformed into a thermally filled, insulating gap with a finite $A(\omega = 0) > 0$. Let us note that the marked transition between bad metal ($c = 4.05\text{\AA}$) and bad insulator ($c = 4.06\text{\AA}$) is only meant as a guide to the eye. A hard cut-off parameter is difficult to pinpoint for these non particle-hole symmetric spectral functions.

Cooling the sample, we find the cfs-driven transition to become even sharper, see Fig. 2.24 where besides the previous $T = 770\text{K}$ (black) we also showcase $T = 680\text{K}$ (red) and $T = 610\text{K}$ (blue).

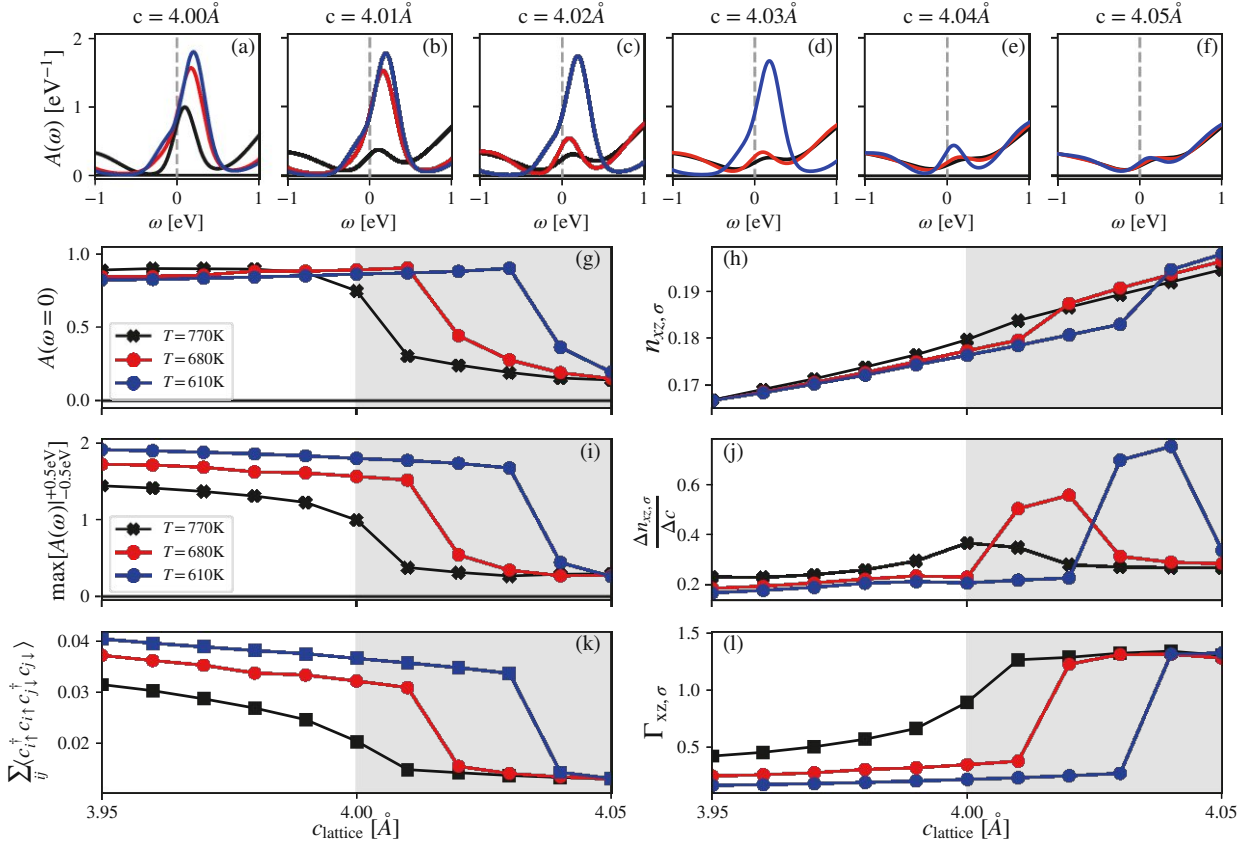


Figure 2.24: Evolution of the spectral function along the metal to bad metal / insulator transition $c = 4.00 \rightarrow 4.05\text{\AA}$ (a-f). We illustrate the transition for the temperatures $T = 770\text{K}$, $T = 680\text{K}$ and $T = 610\text{K}$. The corresponding values on the Fermi level $A(\omega = 0)$ and the size of the quasi particle peak $\max[A(\omega)]_{-0.5\text{eV}}^{+0.5\text{eV}}$ are plotted in panels (g) and (i), respectively. Cooling the system boosts the quasi-particle peak, for which a larger crystal-field splitting (larger c values) is necessary to turn the system insulating. The transition is characterized by a sudden change in orbital occupation $n_{xy,\sigma}$, see panel (h) and the resulting maximum of the (symmetric) numerical derivative thereof in panel (j). Further, the metal-insulator transition is accompanied by a drop-off of the total number of double occupancies (panel k) and an enhancement of the electronic scattering rate (panel l). For the necessary precision within DMFT, the total electron occupation is converged to $n = 1.000 \pm 0.001$.

Besides the spectral function evolution (panels a-f) we show the spectral function at the Fermi level (panel g), the size of the quasi-particle peak (panel i), the xz orbital occupation (panel h), its derivative with respect to the c -axis change (panel j), the total number of double occupancies $\sum_{ij} \langle \hat{c}_{i\uparrow}^\dagger \hat{c}_{i\uparrow} \hat{c}_{j\downarrow}^\dagger \hat{c}_{j\downarrow} \rangle$ ($i, j \in \{xy, xz, yz\}$) (panel k), as well as the extracted electronic scattering rate $\Gamma = -\Im \Sigma(i\nu_n \rightarrow 0^+)$, see Eq. (2.58a), in panel l.

Overall, cooling leads to an enhancement of the size of the quasi-particle peak with the value at the Fermi level being hardly affected. Through this stronger metallicity, the system is more resistant against the lattice deformation: a larger crystal-field splitting is necessary to trigger the insulating transition at lower temperatures. The drop of the quasi-particle is evidently accompanied by a modification of the orbital occupation, see panel (h). While at $T = 770\text{K}$ this is barely visible in the numerical derivative, see panel (j), the magnitude of the jump is quickly enhanced at slightly lower temperatures. Inspired by the “ordinary” Widom line in the doped Hubbard model ($\max_\mu 1/n^2 dn/d\mu$), see, e.g., Ref. [152], we are able to characterize the cfs-induced high temperature insulator transition via

$$c^{\text{oWL}}(T) : \max_c \left[\frac{dn_{xz/yz,\sigma}(T)}{dc} \right] \equiv \min_c \left[\frac{dn_{xy,\sigma}(T)}{dc} \right] \quad (2.71)$$

which we coin “orbital Widom line” (oWL). We theorize that this line originates from an anticipated critical end-point of the (coherent) metal-insulator transition, see Fig. 2.25 for a sketch. Moving towards this critical point via cooling, the size of the peak of $\frac{dn_{xz/yz,\sigma}(T)}{dc}$ will quickly grow in size until it eventually diverges exactly at the end-point. At and below the critical point the metal-insulator transition is then instead characterized by the emergence of a sharp orbital polarization, see Fig. 2.16, upholding a firm insulating solution.¹⁴ Across the oWL we, unsurprisingly, also find a drop-off in the total number of double occupancies $\sum_{ij} \langle \hat{c}_{i\uparrow}^\dagger \hat{c}_{i\uparrow} \hat{c}_{j\downarrow}^\dagger \hat{c}_{j\downarrow} \rangle$, as well as a strong enhancement of the electronic scattering rate $\Gamma = -i\Im \Sigma(i\nu_n \rightarrow 0^+)$ in the xz band. For the latter we employed a third order polynomial fit on the first 4 data points on the Matsubara axis and plotted the extrapolated value at $i\nu_n \rightarrow 0^+$ in Fig. 2.24l. Upon cooling, the drop in double occupancies becomes sharper and larger in size, where below the (anticipated) critical point the continuous transition must eventually transform into a kink, mirroring the sharp orbital polarization.

¹⁴An alternative connection to the “ordinary” Widom line is in the signature of the charge channel, see Section 2.5.4: The characteristic electronic compressibility $\kappa_e = 1/n^2 dn/d\mu$ can be connected to the charge response $\chi_D(\mathbf{Q} = \mathbf{0}, i\omega_m = 0)$, showing a maximum in the doped one-band Hubbard model [153]. In our setting, crossing the orbital Widom line, we find a maximum of the corresponding *eigenvalue* of the density channel $\lambda_D(\mathbf{Q} = \mathbf{0}, i\omega_m = 0)$ which is however, surprisingly, not reflected in any significant changes of the physical response $\chi_D(\mathbf{Q} = \mathbf{0}, i\omega_m = 0)$ (not shown).

2.3.2.6 Ordering instabilities

In the previously discussed DMFT solutions we viewed the systems from a purely local point of view with an enforced SU(2) symmetry. Through the captured local correlations, both the renormalization of the metallic solutions and the transition to Mott insulators can be captured adequately. Hitherto ignored, however, were possible ordering instabilities. A priori we would expect that if such instabilities were to exist in our presented data, they would emerge in regimes where anomalies exist. These are oftentimes divergences in the density of states near the Fermi surface, Fermi surface nesting and critical for our application: specific orbital configurations that are prone to ordering. In this Section we briefly surmise (and evidence) such orderings. For a proper technical introduction please refer to a later part of this thesis in Section 2.5.

In the compressed structure $c = 3.65\text{\AA}$ the insulating branch observed gives rise to conditions that are similar to the strong-coupling, one-band Hubbard model, see Fig. 2.2. Superimposed on the metal-insulator transition, the half-filled Hubbard model displays an antiferromagnetic (AF) phase transition. For large interaction strengths, Heisenberg superexchange J can lead to processes that lower the overall energy of the system by $\Delta E \propto J = -t^2/U$ if adjacent spins become anti-aligned. On the lattice points i , corresponding to the lattice position \mathbf{R}_i , instead of

$$(n_{\uparrow}, n_{\downarrow}) : (0.5, 0.5)_{i-1} \rightarrow (0.5, 0.5)_i \rightarrow (0.5, 0.5)_{i+1} \rightarrow \dots$$

the system will transition to

$$(n_{\uparrow}, n_{\downarrow}) : (1.0, 0.0)_{i-1} \rightarrow (0.0, 1.0)_i \rightarrow (1.0, 0.1)_{i+1} \rightarrow \dots$$

breaking spin symmetry and leading, e.g., to a checker-board spin order. As the hypercubic lattice provides the ideal conditions for such alignments, non-local fluctuations begin to proliferate and compete with thermal fluctuations, eventually leading to a second-order magnetic phase transition. Even away from these idealized conditions, order may emerge. This “non-optimality” is then reflected in a reduced transition temperature, i.e. a phase transition dome is formed as a function of a pertinent control-parameter, such as orbital filling. The xy -orbital in the multi-orbital $c = 3.65\text{\AA}$ structure represents such a case. The orbital polarization pushes this orbital into the vicinity of half-filling where we expect antiferromagnetic fluctuations to form. Having analyzed the corresponding two-particle susceptibilities (not shown) we can confirm these suspicions. Whereas the metallic solution remains firmly non-magnetic (the largest magnetic response found is $\chi_M(\mathbf{Q} = (\pi, \pi, 0)) = 10\text{eV}^{-1}$), the insulating solution appears to be below the critical ordering temperature: Indeed, at room temperature, $T = 290\text{K}$, the leading eigenvalues of the magnetic Bethe-Salpeter equation are found at $\mathbf{Q} = (\pi, \pi, 0)$ and $\mathbf{Q} = (\pi, \pi, \pi)$ with $\lambda_{(\pi, \pi, 0)}^M = 1.62$ and $\lambda_{(\pi, \pi, \pi)}^M = 1.68$, respectively (ordering sets in

for $\lambda > 1$). This effectively signals that the massive orbital polarization is necessarily accompanied by an AF phase transition. Please note that we cannot discern which spin arrangement is preferable as we cannot approach the phase transition from higher temperatures. Beyond $T = 390\text{K}$, the insulating solution breaks down and only the metallic solution (without any sign of ordering) remains, see Fig. 2.19.

In a similar vein the expanded structure ($c = 4.10\text{\AA}$) provides a setting that is prone to so-called orbital ordering, similarly promoted by superexchange. Here, the ordering stems, assuming only intra-orbital hopping, from virtual hopping processes where the energy gain of roughly $\Delta E \propto -t^2/U'$ is now proportional to the inter-orbital repulsion. Due to the c-axis elongation and the resulting crystal-field splitting the orbital occupation is transferred from the xy orbital to the the xz/yz orbitals. Due to the tetragonal symmetry they retain their local degeneracy, providing ideal conditions for order [154]. This ordering tendency can already be observed on the metallic branch: despite being relatively far away from the ideal condition, we find an eigenvalue of the density Bethe-Salpeter equation of $\lambda_{(\pi,\pi,\pi)}^D = 0.92$ at room temperature $T = 290\text{K}$. Pushing the system insulating redistributes the orbital occupation sufficiently to get close to $n_{xz/yz,\sigma} = 0.25$. There we can evidence commensurate ordering through the eigenvalue in the density channel $\lambda_{(\pi,\pi,\pi)}^D = 1.5$ which becomes larger than 1. That is, the system will favor an alternating occupation xz and yz orbitals throughout the lattice. Instead of

$$(n_{xz,\sigma}, n_{yz,\sigma}) : (0.25, 0.25)_{i-1} \rightarrow (0.25, 0.25)_i \rightarrow (0.25, 0.25) : i + 1 \rightarrow \dots$$

the system will transition to

$$(n_{xz,\sigma}, n_{yz,\sigma}) : (0.5, 0.0)_{i-1} \rightarrow (0.0, 0.5)_i \rightarrow (0.5, 0.0)_{i+1} \rightarrow \dots$$

where i , again, corresponds to the lattice position \mathbf{R}_i and the alternation is generated along all three directions, corresponding to $\mathbf{Q} = (\pi, \pi, \pi)$. Contrary to the manually suppressed AF order (via spin symmetrization after each DMFT iteration), signatures of the orbital structure can already be seen on the one-particle level of DMFT: For low enough temperatures and/or large enough (negative) cfs (e.g., $c = 4.45\text{\AA}$, $T = 290\text{K}$: not shown) the DMFT convergence fails. The orbital occupations (and self-energy) try to break the (local) symmetry of the Hamiltonian, split asymmetrically and alternate from iteration n to iteration $n + 1$, mimicking the order the system wants to, but cannot develop. Strictly speaking, for this reason we were not able to continue the c-axis scan of Fig. 2.16 to larger c-values and probe the other side of the indicated hysteresis. There, an explicit symmetry enforcement of the xz/yz orbitals or a supercell setup would be necessary to converge the DMFT calculation into its orbitally degenerate or orbitally ordered state, respectively.

2.3.2.7 Validation to experiment

For the purpose of comparing our result to the experiment of Wang *et al.* [111], see Fig. 2.13, we restrict ourselves to the analysis of the expanded structure. We combine the gained insight from DMFT into a temperature vs. c lattice constant phase diagram, sketched in Fig. 2.25, where we highlight the calculated parameter variations with gray lines and indicate the estimated phase boundaries. Please note that the exact positions of latter have not been calculated explicitly. Thus, phase boundaries are meant as guides to the eye.

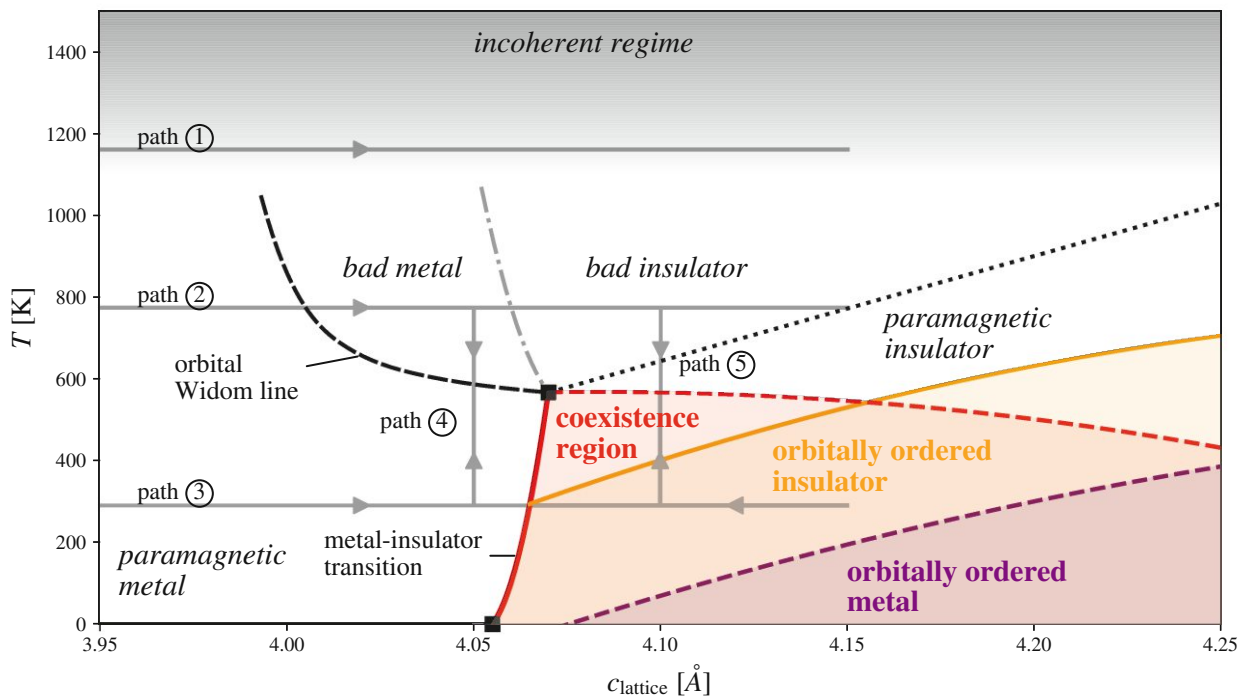


Figure 2.25: Phase diagram sketch of the expanded structure $c > a = b = 3.95\text{\AA}$. At elevated temperature, $T = 1160\text{K}$ coherence is partially lost (path ①: Fig. 2.22b) where a strong c -dependence remains and the system smoothly transitions into a bad insulator solution. Below these temperatures we find, at $T = 770\text{K}$ (path ②: Fig. 2.22a), a distinct transition from a paramagnetic metal to a paramagnetic insulating, akin to the one-band Hubbard model. Here, however, the transition of coherent to bad metal is enforced through the crystal-field splitting (cfs) and occurs rather abruptly. In the fully coherent regime, at $T = 290\text{K}$ (path ③: Fig. 2.16), we find a clear metal-insulator transition (red, solid), accompanied by a wide coexistence region (red). Depending on the size of the cfs we are able to enter the coherent metallic (path ④: Fig. 2.26) and the coherent insulating (path ⑤: Fig. 2.19 and Fig. 2.26) regime via cooling. In both the insulating and metallic regime, owing to the vicinity of ideal quarter-filling orbital order eventually emerges (orange and purple dome, respectively), i.e. a spontaneous breaking of the degeneracy of the xz/yz orbitals. Due to the enhanced orbital polarization, the ordering of the insulator necessarily occurs at higher temperatures.

At large temperatures, thermal fluctuations suppress the formation of quasi-particle peaks resulting in a partial loss of coherence for all lattice constants $c \geq 3.95\text{\AA}$. This phenomenon is shown at $T = 1160\text{K}$ in Fig. 2.22b: path ①. Note that this temperature is not yet sufficient enough to fully destabilize the metallic solution for $c < 3.95\text{\AA}$, where a modest quasi-particle peak remains. Cooling the system to intermediate temperatures $T = 770\text{K}$, see Fig. 2.22a, gives rise to the first detectable, distinctive regime caused by the crystal-field splitting: path ②. Below a critical $c = 4.00\text{\AA}$ a coherent, paramagnetic metal forms, displaying the characteristic three-peak structure. Beyond this threshold (the orbital Widom line; black dashed), a different phase emerges: the quasi-particle peak collapses giving way to, first, a bad metal, and, beyond, to a bad insulator solution. Within DMFT, this cross-over is accompanied by a jump in the orbital occupation, through which we can define a critical c -threshold, see Eq. (2.71).

Cooling further, we anticipate the orbital Widom line to end at a critical end-point (black square), below which we find the opening of a wide metal-insulator coexistence region. There, the metallic solution is valid up to surprisingly large c values: path ③. We find two distinct transitions from the established bad metal/insulator regions. Along path ④ ($c = 4.05\text{\AA}$, $T = 770\text{K} \rightarrow T = 290\text{K}$) the system changes from bad to coherent, paramagnetic metal whereas path ⑤ ($c = 4.10\text{\AA}$, $T = 770\text{K} \rightarrow T = 290\text{K}$) illustrates the entrance into the coherent, insulating regime, cf. Fig. 2.19 and Fig. 2.26. Once this coherent insulating solution has been established, further cooling naturally stabilizes the accompanied orbital polarization.¹⁵ In turn, the slope of the transition line (red) between the paramagnetic metal and the coexistence region must be positive. Eventually, in the insulating state, orbital ordering emerges, breaking the local degeneracy of the xz/yz orbitals. The shape of the orbitally ordered dome (orange, dashed) is also well founded: larger c -values result in larger Δ_{cfs} . The increased orbital polarization then pushes to the system closer to the “ideal” quarter-filling, thus increasing the transition temperature. Please note that we have also theorized that in the metallic regime of the coexistence region (bounded by the red, dashed line) we also expect orbital order to set in eventually ($\lambda_D = 0.92$ for $c = 4.10\text{\AA}$ and $T = 290\text{K}$). Due to the reduced orbital polarization in the metal, the transition temperature must necessarily be smaller compared to the insulator, see the purple, dashed boundary.

Due to the hysteresis, the metal-insulator transition at *zero temperature* is intriguing: crossing the coexistence region from small to large c , we theorize the persistence of a paramagnetic solution which we expect to be maintained beyond $c = 4.25\text{\AA}$. Due to the orbital order, a quantum critical point (black square) may emerge. Crossing the coexistence region from large to small c we expect to find

¹⁵In order to further characterize the stability of this behavior, a free energy comparison of the two coexisting solution, similar to Ref. [155], would be adequate. At this moment, we unfortunately do not yet have access to this expression within our employed impurity solver.

a sudden transition from an orbitally polarized insulator to the orbitally unpolarized paramagnetic metal. Please note that it is a priori not clear whether the orbital-ordering and the metal-insulator-transition boundaries overlap.

Comparing this extracted phase diagram to the experimental data of Wang *et al.* [111] we find overall reasonable agreement. The epitaxial growth process with helium irradiation, performed at $T > 900\text{K}$, would put the sample close to the incoherent regime in our phase diagram (shaded gray). According to our DMFT data, cooling the sample would then, depending on c , allow the stabilization of both the paramagnetic metal and insulator regimes. Quantitatively, the c -axis scan at room temperature (path ③) reveals a hysteresis onset which is compatible with the $3.0 \cdot 10^{15}$ ($c_{\text{exp}} = 4.03\text{\AA}$) and $3.5 \cdot 10^{15}$ He / cm^2 fluence samples ($c_{\text{exp}} = 4.05\text{\AA}$) of Ref. [111]. The minor quantitative difference is likely to stem from the DFT setup: Within PBE the lattice constant of SrTiO_3 is $a_{\text{STO}}^{\text{PBE}} = 3.95\text{\AA}$. This is a slight overestimation compared to the experimental value of $a_{\text{STO}}^{\text{EXP}} = 3.905\text{\AA}$. In order to generate the same critical crystal-field splitting in the real sample, the expanded sample would need a smaller crystal elongation compared to our calculations. This is evident in the smaller experimental c -values necessary for the onset of an activated behavior in the transport data.

In these two samples with the largest applied fluence, a negative slope $\frac{\partial \rho}{\partial T} < 0$ is observed in experiment for $T < 300\text{K}$ with a thermal activation behavior below $T \lesssim 20\text{K}$

$$\rho(T) \propto \exp\left(\frac{\Delta}{2k_B T}\right) \quad (2.72)$$

with an extracted gap of $\Delta = 6\text{meV}$ and $\Delta = 20\text{meV}$, respectively (fit not shown). Interestingly, this fit can not be extended to larger temperatures. This is, in principle, contradictory to our extracted DMFT phase diagram. Entering the insulating regime to the right side of the anticipated critical point, e.g., at $c = 4.10\text{\AA}$, the DMFT resistivity would certainly display a thermally activated behavior up to temperatures where $k_B T \approx \Delta$ (full coherent temperature range for $c = 4.10\text{\AA}$). This disparity, however, could be explained via the effects of the implanted helium atoms and the vicinity to the metal-insulator transition. The increased scattering, in combination with the almost vanishingly small gap, could theoretically lead to a lifetime smearing of the spectral gap, that will dominate the transport characteristic at elevated temperature $T > 100\text{K}$. In this scenario, the true activated behavior (with potential resistivity saturation, see Section 3.4) would then only emerge at low temperatures where the opened gap is smeared only by the broadening effects of the temperature. Additionally, we cannot exclude that the cfs-driven DMFT gap has an inherent temperature dependence due to the decreased inter-orbital fluctuations upon cooling. Please note that weak localization (WL) effects may also influence the conductivity. Despite having modelled the system as three dimensional, in experiment there exist only a limited number of unit cells $\mathcal{O}(100)$. The ‘‘effective reduction to two dimension’’, combined with the orthogonal t_{2g} orbitals, may promote WL effects, enhancing the

resistivity and modifying its temperature profile.

The (small) size of the extracted gap $\Delta = \mathcal{O}(10)\text{meV}$ is in line with our expectations: Beyond the cfs-threshold (metal-insulator transition or the orbital Widom line) arbitrarily small gaps may be stabilized within DMFT as the DMFT spectral gap scales linearly with the underlying crystal-field splitting $\Delta_{\text{DMFT}} \propto |\Delta_{\text{cfs}}|$ (not shown). The evidenced gaps via the activated behavior of the resistivity, see Fig. 2.13d, are then likely caused by the vicinity of the metal-insulator transition, see Fig. 2.25 (red, solid line).

Samples with less than $3 \cdot 10^{15} \text{ He / cm}^2$ fluence ($c_{\text{exp}} \leq 4.00\text{\AA}$), instead exhibit Fermi liquid behavior, $\rho(T) \propto T^2$, which is only interrupted at very low temperatures, interpreted as an enhanced renormalized electron-electron interaction contribution [111]. Indeed, this transport data is congruent with our DMFT phase diagram: Owing to the lattice-deformation induced crystal-field splitting, the insulating solution exists only above a critical c-axis value. Too little fluence provides no access to these cfs values, providing only a gateway into the metallic regime, i.e. Fermi liquid behavior emerges. In this regime the variation of the fluence then mainly affects the static disorder in the system, and thus the overall size of the resistivity, not its qualitative features.

To finalize this Section, we showcase the evolution of the spectral functions of the two characteristic solutions, best describing the metallic and insulating samples, in Fig. 2.26. For both cases, the high temperature solution at $T = 770\text{K}$ stabilizes a thermally activated insulator which, upon cooling, transforms into either a firm, paramagnetic metal ($c = 4.05\text{\AA}$) or a coherent insulator ($c = 4.10\text{\AA}$). Adjusting for the SrTiO_3 lattice mismatch between PBE and experiment provides us an almost perfect, quantitative match of the relevant insulating gaps compared to Wang *et al.* [111].

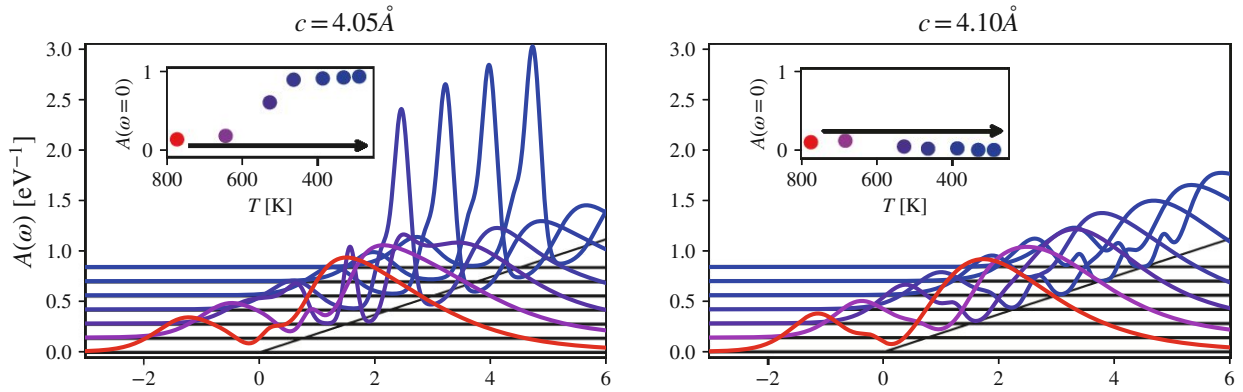


Figure 2.26: Spectral function evolution for $c = 4.05\text{\AA}$ (left) and $c = 4.10\text{\AA}$ (right) upon cooling. Separated by the critical point, the former enters the coherent metallic regime while the latter enters the insulating regime. These two paths correspond to path ④ and path ⑤, respectively in Fig. 2.25 and illustrate the cfs-induced metal-insulator transition observed by Wang *et al.* [111].

2.3.3 Dimensionality reduction in thin films

2.3.3.1 Surface protection and metal-insulator transition

In this Section we transition from thick films, that we were able to effectively simulate with a (distorted) bulk-like setup, to thin films consisting of only a few unit cells (uc). We consider the same material combination as in the previous Section, i.e. SrVO₃ and SrTiO₃. Here, SrTiO₃ is used both as substrate as well as capping material to achieve a protection against the environment. This protection is necessary once samples have to be moved out of the vacuum environment that is initially necessary for controlled, high quality crystal growth. Without these protecting layers, the surface tends to oxidize, apparent in the qualitative change of the core level spectroscopy signal of vanadium 2p shown in Fig. 2.27, reproduced from Ref. [131]. If terminated with a VO₂ layer, excess oxygen bonds with the surface vanadium atoms, modifying their valence from 4+ to an inert 5+ noble gas configuration. This in turn modifies the oxygen 2p states and therefore the photoemission core spectra. A considerable number of capping layers, $\mathcal{O}(10)$, is necessary to achieve full protection, as demonstrated by the comparison of in situ and ex situ spectra in Fig. 2.27. For a detailed theoretical and experimental discussion of the explicit effects of surface oxidization, please refer to Section 2.4.

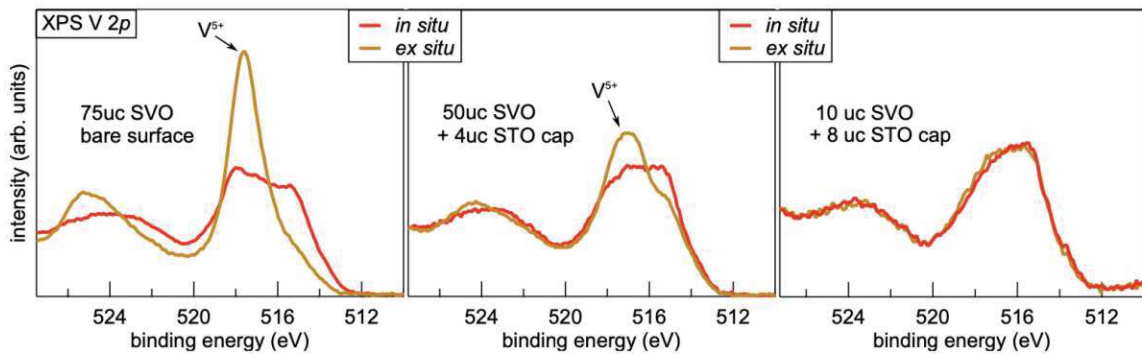


Figure 2.27: Film protection via capping is necessary if the sample is transferred outside the vacuum chamber. Given enough protection layers (left: none, middle: 4uc STO, right: 8uc STO) the core level spectroscopy of the vanadium atom (V 2p) remains unchanged in and ex situ. [Reprinted with permission from Philipp Scheiderer, PhD thesis: “Spectroscopy of Prototypical Thin Film Mott Materials”, Universität Würzburg (2019)] [131]

Moving on to transport measurements, the sheet resistivity reveals an interesting thickness dependence in Fig. 2.28: the 75uc sample exhibits Fermi liquid behavior, identical to the pristine films from Section 2.3.2, see Fig. 2.13. Lowering the number of layers down to 12uc and 10uc, a low-temperature upturn can be observed, akin to the radiation damaged samples, close to the insulator

transition from the previous Section. Consequently, a minimum emerges at a characteristic temperature that separates the Fermi liquid from the “quantum regime”, possibly characterizable by Eq. (2.68). Here, the crossover temperature correlates with the number of layers instead of the irradiation fluence. At 6uc and below, the resistivity profile qualitatively changes to a thermally activated behavior $\rho \propto \exp(\frac{\Delta}{2k_B T})$, from which a gap size can be extracted. 6uc, 4uc, and 3uc correspond to $\Delta = 140\text{meV}$, $\Delta = 32\text{meV}$, and $\Delta = 1\text{meV}$, respectively, see the Arrhenius fit in Fig. 2.28b. Given that the irradiated bulk-like films exhibit a comparable behavior to these (protected) films

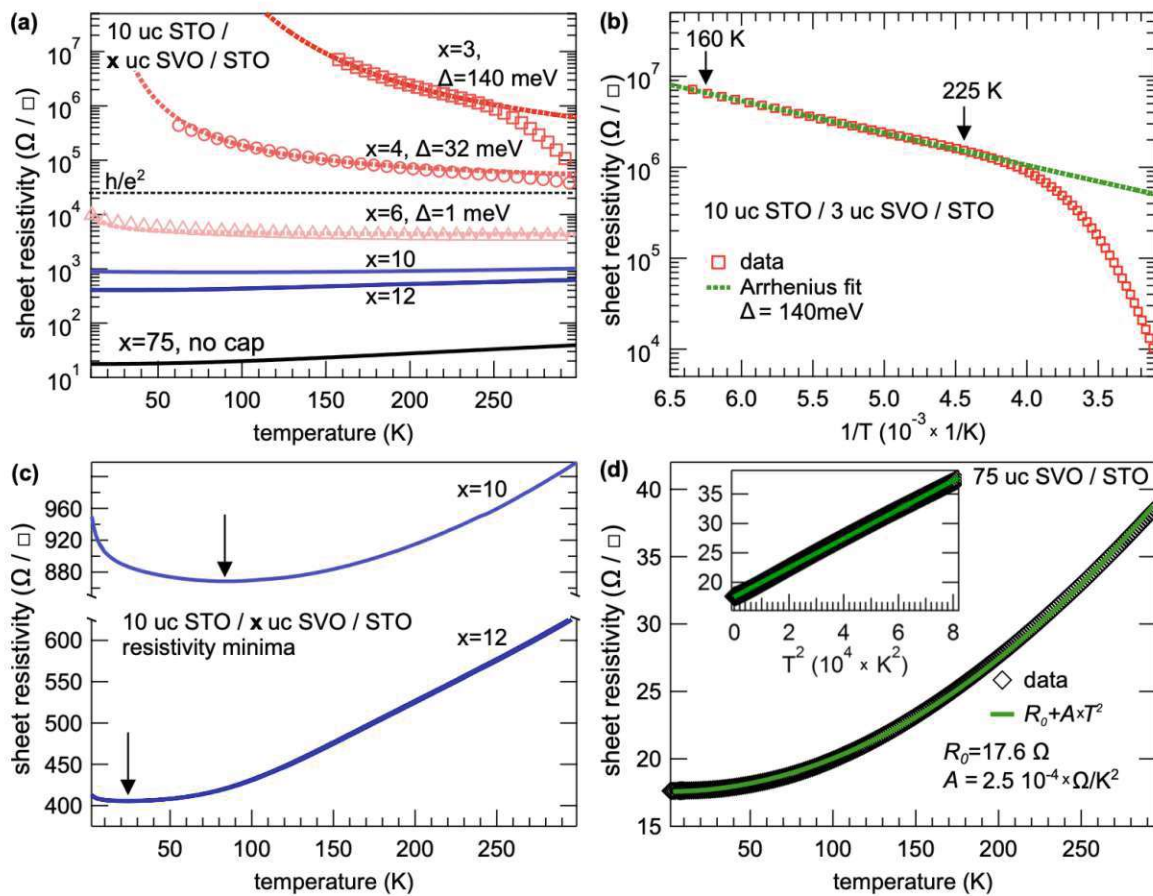


Figure 2.28: Sheet resistance measurements of various x uc thick SrVO_3 samples on SrTiO_3 substrate *with* surface capping. (a) Formation of the activated activated behavior below 6 unit cells. (b) Arrhenius fit for the 3 uc sample. (c) Resistivity upturn below a global resistivity minimum for the 10 and 12 uc samples. (d) Fermi liquid behavior of the pristine 75 uc sample. [Reprinted with permission from Philipp Scheiderer, PhD thesis: “Spectroscopy of Prototypical Thin Film Mott Materials”, Universität Würzburg (2019)] [131]

with reduced thickness, it is natural to inquire whether the pertinent driver of the observed insulator transition is identical. In this Section we will therefore analyze the effect of the dimensionality reduction qualitatively. As the critical thickness of insulating films is in the single digit range, a bulk description is no longer valid, requiring us to model the full heterostructure explicitly.

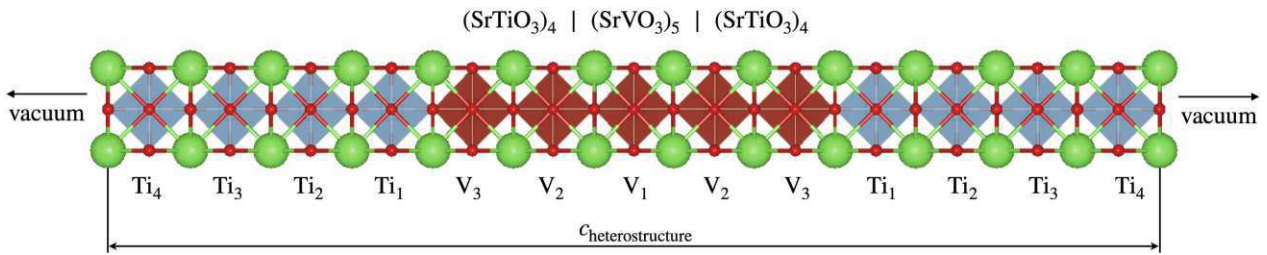
2.3.3.2 Heterostructure optimization

As starting point of the heterostructure modelling, we choose an inversion symmetric setup: x unit cells of SrVO_3 are wedged between m unit cells of SrTiO_3 on both ends: $(\text{SrTiO}_3)_m | (\text{SrVO}_3)_x | (\text{SrTiO}_3)_m$. This structure is padded with sufficient vacuum ($\approx 10\text{\AA}$) in the z -direction to avoid any periodicity-induced end-to-end hybridization within DFT. A single k -point in the non-periodic z -direction is therefore sufficient to safely capture the two dimensional Brillouin zone. In order to simulate the interfaces to the substrate and capping layers, we constrain the atoms of the outer most SrTiO_3 unit cells to their bulk positions.¹⁶ Given enough SrTiO_3 layers, this adequately mimics the transition to bulk. All other internal atomic positions are then fully force relaxed in order to determine the energetically most optimal structure. As the outer unit cells, including their absolute positions in the setup, are constrained, this merely corresponds to a *local* energy minimum. Indeed, a scan through the total length $c_{\text{heterostructure}}$ in z -direction of the entire heterostructure is required to find the *global* minimum.

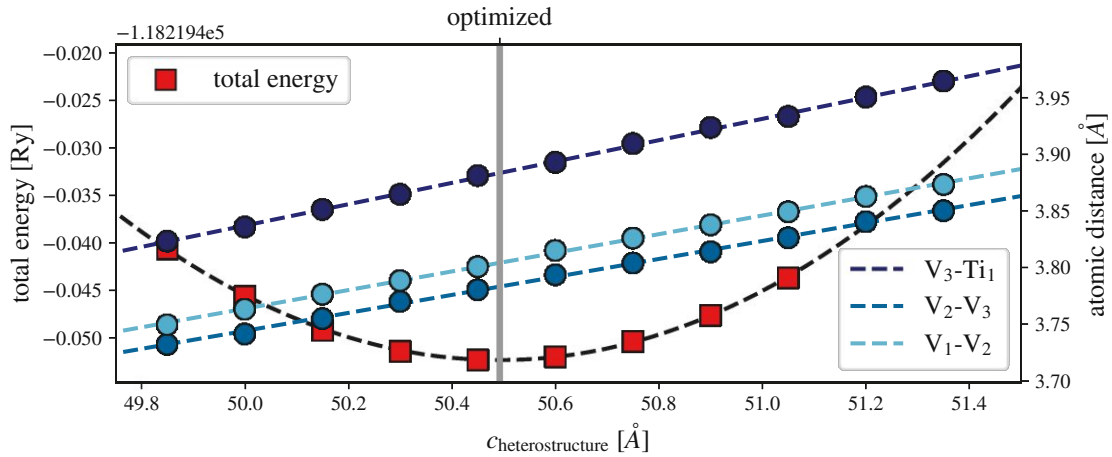
An exemplary result of this optimization approach for the 5uc structure is illustrated in Fig. 2.29. We find the typical quadratic energy vs. elongation dependence¹⁷ accompanied by a linear dependence of the internal $V_i-V_{i\pm 1}$ distances and the V-Ti interface spacing. The internal V-V distances at optimal energy roughly correspond to the equilibrium value of bulk SrVO_3 $c_{\text{V-V}} = 3.81\text{\AA}$, see Section 2.3.2, whereas the V-Ti distance is close to the average of the SrTiO_3 and the SrVO_3 lattice constants $c_{\text{V-Ti}} = 3.90\text{\AA}$. Consequently, the resulting crystal-field splitting is in line with in-plane constrained bulk, i.e., around 130meV. The interface vanadium atom V_3 represents the only outlier which, due to its less restricted positioning, experiences an orbital splitting only half the size of its neighbor. Once an “internal bulk” can be established, changing the number of layers hardly affects the splitting, see Table 2.2 where we compare the $x = 1, 3, 5, 7$ structures. In this context, $x = 1$ can be considered as a special case where despite the large degeneracy splitting at the Gamma point, see Fig. 2.30, the overall (k-integrated) crystal-field is quite small. From this point of view, it is apparent that, here, the band-width effect must play a more dominant role.

¹⁶This most outer SrTiO_3 unit cell is terminated with SrO, see Fig. 2.29c. We checked in similar structures that the switch to the TiO_2 termination does not influence the band structure.

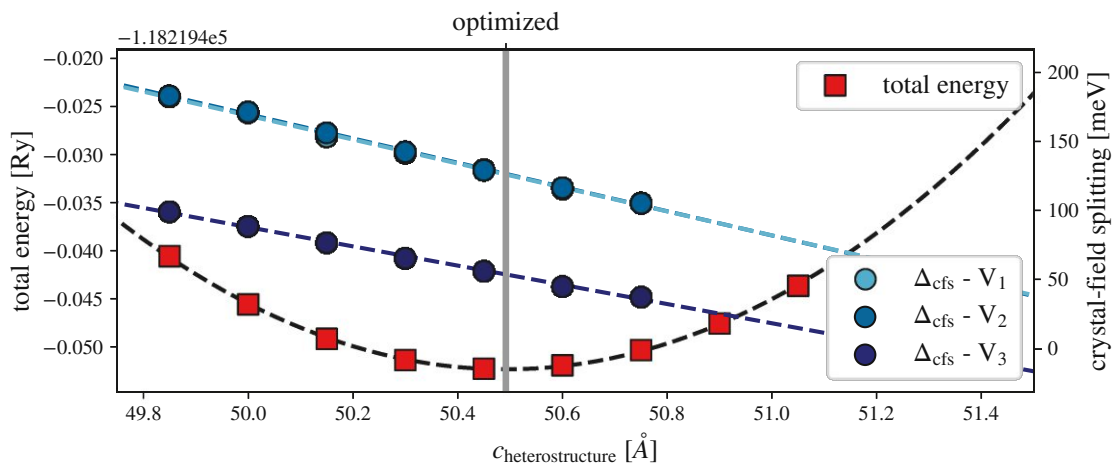
¹⁷Let us note that in order to recover this dependence in WIEN2k, the atomic muffin-tin radii must be identical in the different structures. In the default setup this is not the case, as they are adjusted to fill up the maximal available space.



(a) crystal structure



(b) atomic positions



(c) crystal field splitting

Figure 2.29: Exemplary behavior of the global optimization of the capped 5uc SrVO₃ structure: (a) crystal structure, (b) internal atomic distances, (c) crystal-field splitting as a function of the overall c-axis length of the heterostructure. The total energy (also plotted in (b) and (c)) showcases the typical quadratic dependence (dashed line: fit via $E \propto E_0 + (c - \bar{c})^2$) on the heterostructure length. The crystal-field splitting and the internal atomic distances showcase perfect linear behavior (colored, dashed lines). At the global energy minimum (vertical, gray line), the internal vanadium atoms mirror the bulk case, see Sec. 2.3.2. Due to the less restrictive crystal environment, the interface vanadium experiences a reduced crystal-field splitting.

The Wannier-projected vanadium t_{2g} band structures for these selected layer thicknesses are illustrated in Fig. 2.30: lacking out-of-plane hopping, the $x = 1$ structure experiences the largest band width effect, resulting in $W_{xz/yz} = 1.2\text{eV}$, half of the xy orbital. Adding additional layers then provides an increasing number of xz/yz hopping in the z-direction, until eventually, the system approaches the bulk regime. Please note that only in the infinite limit do we obtain momenta in z-direction. For any finite number of layers the Brillouin zone remains restricted on the (k_y, k_z) plane and showcases overlapping quantum well states. For the out-of-plane xz/yz orbitals, we find the band widths W tabulated in Table 2.1, compared to $W_{xz/yz}^{\text{bulk}} = 2.35\text{eV}$ for the case of bulk constrained to the in-plane SrTiO₃ lattice parameters. The xy orbital on the other hand experiences only limited dimensionality effects, maintaining $W = 2.2\text{eV}$ for all $x > 1$.

sample thickness	1	3	5	7	bulk
W_{xy} [eV]	2.05	2.2	2.2	2.2	2.22
$W_{xz/yz}$ [eV]	1.2	2.0	2.2	2.25	2.35

Table 2.1: Dimensionality induced band width effects of capped SrVO₃ wedged between a SrTiO₃ substrate and capping. The dimensionality reduction is naturally most prominent in the xz/yz orbital whose band widths slowly approaches the corresponding bulk value for $x \rightarrow \infty$. Bulk in this case refers to the constrained equilibrium found at $a = b = 3.95\text{\AA}$ and $c = 3.81\text{\AA}$.

sample thickness	1	3	5	7	atom	
Δ_{cfs} [meV]			⋮	53	V ₄	
			⋮	56	121	V ₃
		⋮	79	129	121	V ₂
		20	129	129	118	V ₁
		⋮	79	129	121	V ₂
			⋮	56	121	V ₃
				⋮	53	V ₄

Table 2.2: Crystal field splitting Δ_{cfs} [meV] of the vanadium atoms V_i , cf. Fig. 2.29, in the considered samples with $x = 1, 3, 5, 7$ thickness. Compared to the crystal field splitting at the energy optimized (constrained) bulk ($c=3.81\text{\AA}$, $\Delta_{\text{cfs}} = 120\text{meV}$), we see virtually no difference except at the interface layers. (Note that for the $x = 1$ case, the singular SrVO₃ in itself is the interface layer) There, due to the less restricted positioning, the crystal field effects are less pronounced.

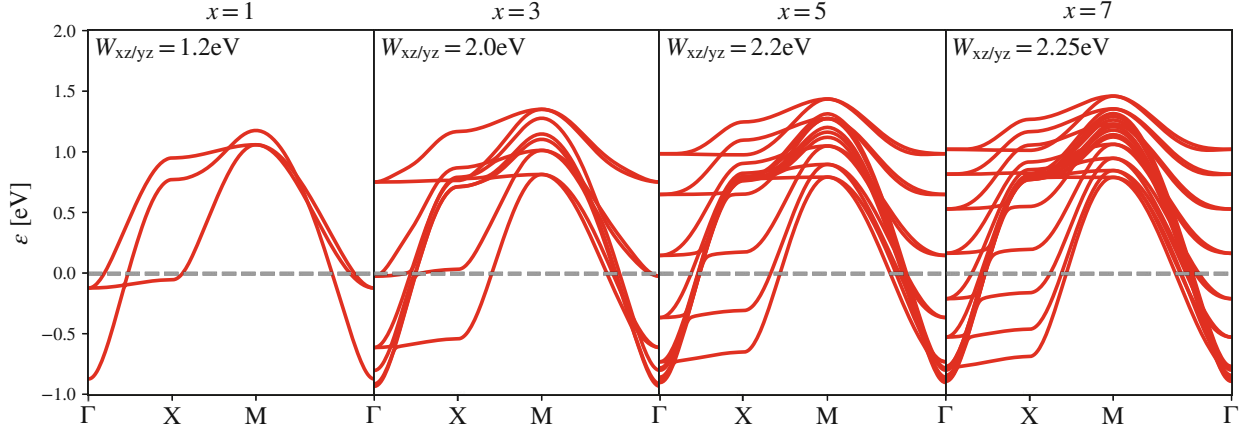


Figure 2.30: Projected vanadium t_{2g} band structure and its evolution for an increasing number of SrVO_3 layers. A direct band structure comparison to bulk is not helpful, as the (periodic) k_z information of bulk does not translate well to the thin film layer information purely on the k_{xy} plane. This effective “backfolding” results in the formation of quantum well states (x distinct energy levels at Γ with an additional dispersion in k_x/k_y direction).

2.3.3.3 Multi impurity dynamical mean-field theory

Given these heterostructure low-energy models, our first goal is to determine whether the metal-insulator transition, observed around $6\mu\text{eV}$, can be simulated in a realistic manner. For this purpose the DMFT setup looks as follows: the projected, local Wannier basis will in principle contain all possible orbital and site combinations. If ordered correctly, one can introduce an overarching structure of the (periodically continued) supercell visualized in Fig. 2.29a, highlighted in Eq. (2.73) in color. Due to the t_{2g} orbital structure, intra-layer hopping will be mostly restricted to nearest neighbor, intra-orbital (in-plane: $xy \leftrightarrow xy$, $xz \leftrightarrow xz$, $yz \leftrightarrow yz$) whereas inter-layer hopping will inherit the out-of-plane hopping that was lost by the missing z -periodicity. Most notably, π -bonds will form between $xz/yz(V_i) \leftrightarrow xz/yz(V_{i\pm 1})$ and to some degree, miniscule δ -bonds between $xy(V_i) \leftrightarrow xy(V_{i\pm 1})$.

$$H_{\text{wannier}}^{\mathbf{k}} = \begin{bmatrix} h_{xy,xy}^{V_1,V_1} & h_{xy,xz}^{V_1,V_1} & h_{xy,yz}^{V_1,V_1} & h_{xy,xy}^{V_1,V_2} & h_{xy,xz}^{V_1,V_2} & h_{xz,yz}^{V_1,V_2} & \dots \\ h_{xz,xy}^{V_1,V_1} & h_{xz,xz}^{V_1,V_1} & h_{xz,yz}^{V_1,V_1} & h_{xz,xy}^{V_1,V_2} & h_{xz,xz}^{V_1,V_2} & h_{xz,yz}^{V_1,V_2} & \dots \\ h_{yz,xy}^{V_1,V_1} & h_{yz,xz}^{V_1,V_1} & h_{yz,yz}^{V_1,V_1} & h_{yz,xy}^{V_1,V_2} & h_{yz,xz}^{V_1,V_2} & h_{yz,yz}^{V_1,V_2} & \dots \\ h_{xy,xy}^{V_2,V_1} & h_{xy,xz}^{V_2,V_1} & h_{xy,yz}^{V_2,V_1} & h_{xy,xy}^{V_2,V_2} & h_{xy,xz}^{V_2,V_2} & h_{xy,yz}^{V_2,V_2} & \dots \\ h_{xz,xy}^{V_2,V_1} & h_{xz,xz}^{V_2,V_1} & h_{xz,yz}^{V_2,V_1} & h_{xz,xy}^{V_2,V_2} & h_{xz,xz}^{V_2,V_2} & h_{xz,yz}^{V_2,V_2} & \dots \\ h_{yz,xy}^{V_2,V_1} & h_{yz,xz}^{V_2,V_1} & h_{yz,yz}^{V_2,V_1} & h_{yz,xy}^{V_2,V_2} & h_{yz,xz}^{V_2,V_2} & h_{yz,yz}^{V_2,V_2} & \dots \\ \vdots & \vdots & \vdots & \vdots & \vdots & \vdots & \ddots \end{bmatrix} (\mathbf{k}) \quad (2.73)$$

Within DMFT, we will retain the purely on-site Coulomb repulsion, i.e. we apply the same Kanamori parametrization for each considered vanadium site V_i of the supercell. This effectively means, that we can simplify the multi impurity problem by sampling each impurity separately. Local correlations are thus only generated within the intra-layer block, reflected in the self-energy structure given in Eq. (2.74). Please note that the full structure of the Wannier Hamiltonian still enters into the DMFT problem via the Dyson equation which integrates over k_x and k_y .

$$\Sigma_{\text{imp diagonal}}^{\text{DMFT}}(i\nu_n) = \begin{bmatrix} \Sigma_{xy,xy}^{V_1,V_1} & \Sigma_{xy,xz}^{V_1,V_1} & \Sigma_{xy,yz}^{V_1,V_1} & 0 & 0 & 0 & \dots \\ \Sigma_{xz,xy}^{V_1,V_1} & \Sigma_{xz,xz}^{V_1,V_1} & \Sigma_{xz,yz}^{V_1,V_1} & 0 & 0 & 0 & \dots \\ \Sigma_{yz,xy}^{V_1,V_1} & \Sigma_{yz,xz}^{V_1,V_1} & \Sigma_{yz,yz}^{V_1,V_1} & 0 & 0 & 0 & \dots \\ 0 & 0 & 0 & \Sigma_{xy,xy}^{V_2,V_2} & \Sigma_{xy,xz}^{V_2,V_2} & \Sigma_{xy,yz}^{V_2,V_2} & \dots \\ 0 & 0 & 0 & \Sigma_{xz,xy}^{V_2,V_2} & \Sigma_{xz,xz}^{V_2,V_2} & \Sigma_{xz,yz}^{V_2,V_2} & \dots \\ 0 & 0 & 0 & \Sigma_{yz,xy}^{V_2,V_2} & \Sigma_{yz,xz}^{V_2,V_2} & \Sigma_{yz,yz}^{V_2,V_2} & \dots \\ \vdots & \vdots & \vdots & \vdots & \vdots & \vdots & \ddots \end{bmatrix} (i\nu_n) \quad (2.74)$$

Due to the orthogonality of the orbitals we can again, identical as in the bulk crystal, reduce the CTQMC complexity further by assuming an orbital diagonal hybridization function.

$$\Sigma_{\text{orb diagonal}}^{\text{DMFT}}(i\nu_n) = \begin{bmatrix} \Sigma_{xy,xy}^{V_i,V_i} & \Sigma_{xy,xz}^{V_i,V_i} & \Sigma_{xy,yz}^{V_i,V_i} \\ \Sigma_{xz,xy}^{V_i,V_i} & \Sigma_{xz,xz}^{V_i,V_i} & \Sigma_{xz,yz}^{V_i,V_i} \\ \Sigma_{yz,xy}^{V_i,V_i} & \Sigma_{yz,xz}^{V_i,V_i} & \Sigma_{yz,yz}^{V_i,V_i} \end{bmatrix} (i\nu_n) \rightarrow \begin{bmatrix} \Sigma_{xy,xy}^{V_i,V_i} & 0 & 0 \\ 0 & \Sigma_{xz,xz}^{V_i,V_i} & 0 \\ 0 & 0 & \Sigma_{yz,yz}^{V_i,V_i} \end{bmatrix} (i\nu_n) \quad (2.75)$$

Starting off with the monolayer case $x = 1$ and using the previously employed interaction parameters ($U = 5\text{eV}$), DMFT unequivocally stabilizes an insulating solution, see Fig. 2.31a. Indeed, we find that, here, any initial starting point suffices to drive the system into becoming a Mott insulator. As the out-of-plane hopping of the xz/yz orbitals are restricted by the SrTiO_3 layers, they become fully one-dimensional and their band width is reduced to $W_{xz/yz} = 1.2\text{eV}$. With the cfs playing no crucial part in the setup ($\Delta_{\text{cfs}} = 20\text{meV}$) we find a purely band width driven Mott insulating state. This is confirmed by similar, out-of-equilibrium setups with larger or smaller total heterostructure lengths. While the change in crystal-field splitting necessarily affects the resulting DMFT orbital occupation, it has no defining influence on the insulating solution. Owing to the full dimensionality reduction, 2D orbital \rightarrow 1D orbital, this behavior is exclusive to the monolayer case.

Larger heterostructures ($x > 1$) can be, by and large, compared to the *compressed* bulk structures from Section 2.3.2. Therefore, contrary to the expanded structures, we will inherit the same type of “hidden” metal-insulator transition. This insulating dome was neither accessible via a modification of the c-axis, nor the temperature in the bulk. The heterostructure behaves similarly: Once a (structurally optimized) $x > 1$ heterostructure is in a metallic state, it remains there unless artificially

forced out of it. Naturally, to be able to analyze this possible insulating state, we are forced to apply the previously employed “technical trick”: first, we stabilize insulating solutions via an enhanced interaction strength where for all considered structures we found $U = 6\text{eV}$ ($J = 0.75\text{eV}$, $U' = 4.5\text{eV}$) to be sufficiently large. After this, we reduce the interaction parameters in a step-by-step fashion to re-approach the bulk starting point ($U = 5\text{eV}$). The results of this process are listed in Table 2.3. We find none of the larger heterostructures $x > 1$ to be able to support a stable Mott insulator for the bulk interaction parameters. Instead, we find critical interactions U_c , below which the insulating solution breaks down. This critical U_c gradually increases with the number of layers x .

sample thickness	1	3	5	7	bulk
U_c [eV]	< 5.0	5.15	5.25	> 5.5	$5.25 < U_c < 5.5$

Table 2.3: Dimensionality induced critical interaction parameters, above which the orbitally polarized, insulating solution of the $(\text{STO})_m | (\text{SVO})_x | (\text{STO})_m$ heterostructure can be stabilized within DMFT.

In this setup, an increasing number of layers x leads to larger *average* crystal-field splitting as the inner most $(x - 2)$ layers contribute with a bulk-like $\Delta_{\text{cfs}} \approx 120\text{meV}$, see Table 2.2. Consequently, the increased critical interaction evidences the importance of band width changes in the dimensionality reduction. Please note however, that these band width changes are still secondary to the main driving force of the insulator, the crystal-field splitting. The critical interaction value is particularly sensitive beyond 5uc where we find a jump from $U_c = 5.25\text{eV}$ to $U_c > 5.5\text{eV}$. Interestingly, the critical interaction for 7uc is larger than in the bulk ($a = b = 3.95\text{\AA}$, $c = 3.81\text{\AA}$). Due to the lack of interface consideration, the bulk crystal is from a cfs as well as a general numerical point of view, much more stable with respect to its insulating solution.

As pointed out earlier, in this type of fragile Mott solution, any introduction of metallicity will immediately lead to a break down of the insulator and the convergence toward a Fermi liquid state for all U values considered. DMFT calculations with multiple impurities in this respect are thus rather difficult to maneuver, especially when tiny deviations in the setup or the DMFT cycle could collapse the desired state. Furthermore, when moving to a multiple impurity basis, the double counting correction becomes important¹⁸, adding an additional source of uncertainty.

Attempting to match the experimental data we now *empirically* choose $U = 5.25\text{eV}$ and apply it to all considered structures $x = 1, 3, 5, 7$. Through this interaction value we ensure that all structure $x \leq 5$ remain insulating. One can argue in favor of a slight increase in on-sight repulsion, as dimensionality reduction is known to slightly enhance interaction values, as shown by cRPA calculations, see, e.g.,

¹⁸For a single impurity t_{2g} basis the double counting correction acts on all three orbitals identically, allowing us to absorb it into the chemical potential.

the supplementary information of Ref. [86]. The simulated spectral functions (fat lines: multiplied with Fermi functions to mimic the photoemission signal, dashed lines: full spectral function) are illustrated in Fig. 2.31a. The DMFT spectral gaps are surprisingly consistent with the extracted gaps from the activated behavior of the resistivity measurements of Fig. 2.28. We find DMFT gaps of $\Delta_{x=1} = 400\text{meV}$, $\Delta_{x=3} = 200\text{meV}$, and $\Delta_{x=5} = 60\text{meV}$.

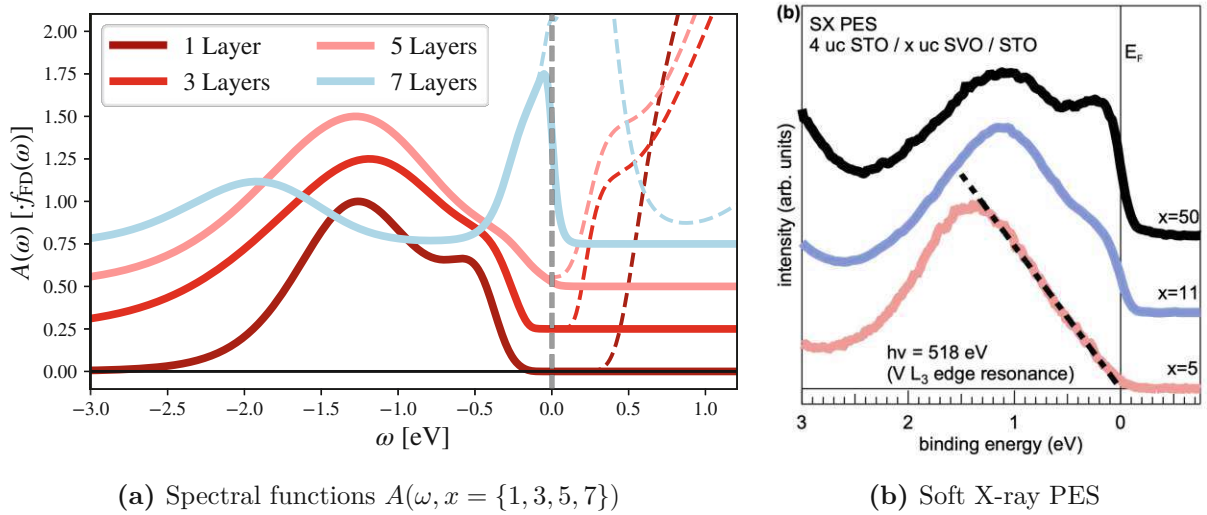


Figure 2.31: (a) Spectral functions $A(\omega)$ (dashed) and the corresponding theoretical PES signal ($A(\omega) \cdot f_{\text{FD}}(\omega)$) of the considered heterostructures with thickness $x = 1, 3, 5, 7$. In these *compressed* samples, the polarized, insulating solution can no longer be maintained in the 7uc sample for the employed $U = 5.25\text{eV}$. There the system stabilizes strong Fermi-liquid features. (b) Soft X-ray photoemission (PES) measurements for samples with thickness $x = 5, 11, 50$. In experiment, the dimensionality induced metal-insulator transition is more gradual where the large lower Hubbard band peak (around binding energy 1eV) might be influenced by oxygen vacancies. [Reprinted with permission from Philipp Scheiderer, PhD thesis: “Spectroscopy of Prototypical Thin Film Mott Materials”, Universität Würzburg (2019)] [131]

As these spectral functions are a summation of $x \times 3$ analytic continuation, the lower Hubbard band has only minimal features. Increasing the number of bands thus softens the spectrum. For $x = 5$, due to the size of the gap $\Delta \approx 2k_B T$, we find a thermally filled gap at $T = 290\text{K}$. The transition to the metallic solution at $x = 7$ is abrupt: Here, the insulating solution fully gives way to a firmly developed three-peak spectrum, similar to bulk. In the experimental setup, see Fig. 2.31b, this transition is found to be more gradual, where $x \gg 10$ layers are necessary to form a quasi-particle peak that rivals the size of the LHB.¹⁹ As the epitaxy process is sensitive to the given oxygen environment,

¹⁹In order to penetrate the capping, soft X-ray must be used. Here, only four protecting STO layers were used. In order to avoid over oxidization, see Fig. 2.27, the SXPES measurements were performed in situ.

at this moment we cannot discern the purely electronic signal from the oxygen background, that has been suggested to be positioned roughly at the LHB position [105].

As discussed in Section 2.3.2, this type of orbital polarization induced Mott insulator found in the compressed structure remains incredibly fragile and it is a priori not clear whether such a state can realistically develop in the prepared sample. At least in the bulk form, neither *c*-axis nor temperature variation is capable of stabilizing the Mott insulator. As we have evidenced, even the compressed bulk state is found to be close to this envisaged scenario $5.25\text{eV} < U_c < 5.50\text{eV}$ compared to the employed $U = 5\text{eV}$. Transport measurements however reveal a low resistivity with Fermi liquid behavior, see Fig. 2.28d, with a gradual transition from $x = 75$ to $x = 3$. If this “hidden” (antiferromagnetic) insulator were to emerge, we would instead expect a jump of the resistivity in the orders of magnitude, as is the case in resistivity profile of the temperature induced insulating state of V_2O_3 [156]. Nonetheless, we are able to establish a realistic connection between the thick film (bulk) insulator mechanism and the dimensionality reduction found in thin films. The cfs mechanism, supported by band width narrowing in thin films, is evidently able to generate a metal-insulator cutoff at a surprisingly large number of layers ($x = 6$) The resistivity measurements of Fig. 2.28 however suggests that our modelled heterostructures do not paint the full picture of the MIT and additional experimental information is required.

2.3.3.4 Interface quantification

Indeed, this information comes from X-ray standing wave (XSW) spectroscopy experiments, performed by Judith Gabel, that are capable of directly measuring the atomic positioning, which is at the heart of our proposed mechanism. The reflex positions, and the derived atomic deviations from bulk, are illustrated in Fig. 2.32 (full circles).

Not only does the XSW data quantitatively contradict our previous structure assumption (compression of V-V bonds due to the in-plane constraint), it actually suggests that the opposite occurs: a V-V, V-Ti, and Ti-Ti bond elongation along the *z*-direction (full circles, in comparison the uncapped positions are marked with a “+”). This behavior defies naive expectations and, in particular, implies a negative Poisson ratio. High-angle annular dark field scanning transmission electron microscope (HAADF-STEM) measurements across the interface of 50uc SrVO_3 on top of SrTiO_3 [112] find a similar behavior, where the first three interface layers exhibit elongated bonds, before returning to the compressed bulk values. (a similar effect has been observed in LaNiO_3 | LaAlO_3 thin films [125]) Simultaneously, the contrast of the obtained images reveal a considerable strontium deficiency in the affected layers ($\approx 10\%$). Additionally, an elemental concentration mapping concludes that an interface-diffusion mixing between the V and Ti atoms occurs. The latter was already suggested previously by Li *et al.* [157] who argued that this process, potentially accelerated by an enhanced

growth temperatures, generates confined defects that might cause convoluted changes to the heterointerface. However, Ti $L_{2,3}$ and V $L_{2,3}$ electron energy loss spectra (EELS) scans, performed on the interface, suggest a four peak splitting where the valence state of the diffused Ti remains close to 4+, maintaining overall charge neutrality.

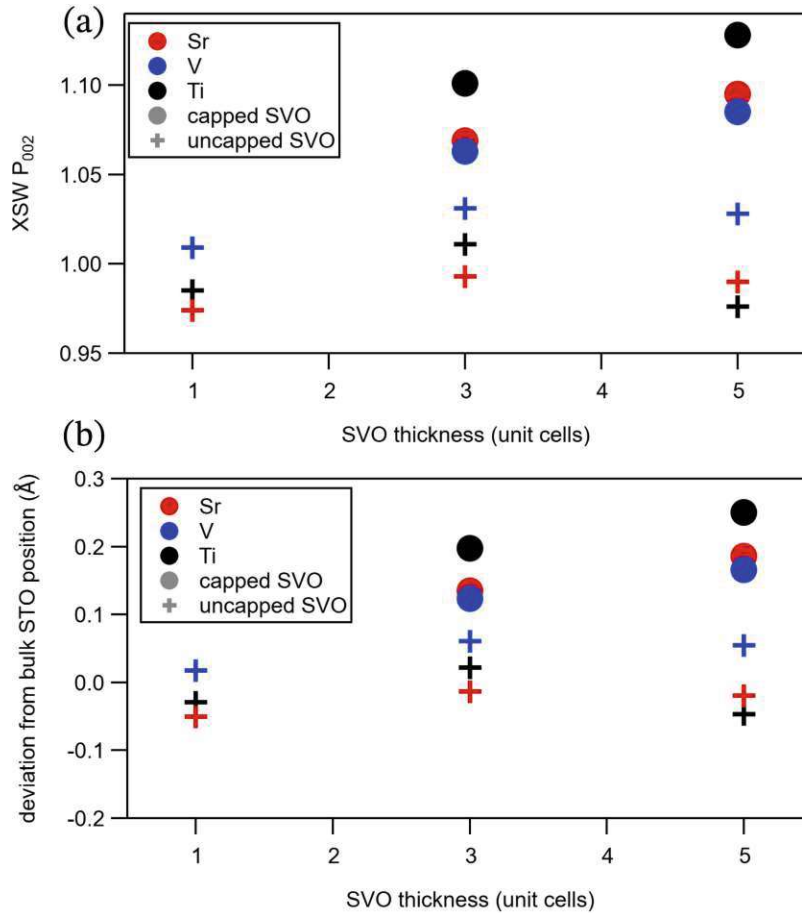


Figure 2.32: X-ray standing wave (XSW) measurements. (a) The coherent XSW P_{002} reflex shows an expansion of the V-V and V-Ti position in the capped samples (full circles). Uncapped samples (crosses) show virtually no difference to the bulk STO distances. (b) Deviation of the atomic positions compared to bulk SrTiO_3 : the V-V bonds are elongated in the range of 0.1 – 0.3 Å compared to SrTiO_3 positions. This is in stark contrast to the simulated heterostructure optimization in Section 2.3.3.2. [Printed with permission from Judith Gabel and Michael Sing. Private communication, not published.]

In this context the strontium deficiency might be a result of the high temperature growth process in combination with oxygen vacancy diffusion from the substrate itself. Possibly, due to this extreme local environment, fewer Sr atoms might bond onto the surface, explaining the drop in concentration

in the first three interface layers. Please note that these deficiencies are not solely based on a specific material mismatch, but are also observed in homoepitaxial growth of SrTiO₃ on itself (SrTiO₃ | SrTiO₃) [158]. Lattice expansion, in general, is also a commonly reported effect in bulk and thin films, resulting from an oxygen deficiency [157, 159, 160, 161].

As expected, for $x = \mathcal{O}(1 - 10)$ layers, interface effects play a dominant role in the underlying structure. For all the thin film calculations so far, none of these extrinsic or local non-stoichiometric effects were included in our consideration. Super-cell calculations including impurities would be necessary to treat these effects ab initio, this is however beyond the scope of this thesis. In order to qualitatively assess this type of interface effect (localized lattice expansion caused by diffusion or by the strontium / oxygen vacancies causing only lattice irregularities while maintaining the Ti and V valency) we simply resort to a remodelling that takes into account these on-average structural consequences and adjust the atomic positions to those which were observed within XSW in Fig. 2.32.

We have to stress here, that deviations from integer filling of the vanadium d -shell are critical in the context of the many-body theory: doping impairs the stabilization of a Mott insulating solution. If this type of doping were to exist in the sample (or in the DMFT setup), it would result in an intermediate valence state, making thin films more likely to be metallic than insulating. Yet, the exact opposite is observed, implying a localization of defect charges. Within DFT, this has been discussed for SrVO₃ in Ref. [162] where vacancies have been shown to induce only localized changes to the surrounding vanadium and strontium ions.

Expanded films

Setting up structures with the measured positions of Fig. 2.32 result in the band structure changes illustrated in Fig. 2.33. Through the bond elongations, the overall band width becomes reduced, which we previously determined to be a critical auxiliary effect next to crystal-field splitting. The values cfs of the different vanadium sites are listed in Table 2.4.

sample thickness	3	5	atom index
Δ_{cfs} [meV]	⋮	-120	V ₃
	-96	-104	V ₂
	-78	-97	V ₁
	-96	-104	V ₂
	⋮	-120	V ₃

Table 2.4: Crystal field splitting of the expanded capped structures. As the elongation of the internal atomic distances is largest at the interface, it experiences the largest (negative) cfs. Atomic indices refer to a structure as illustrated in Fig. 2.29.

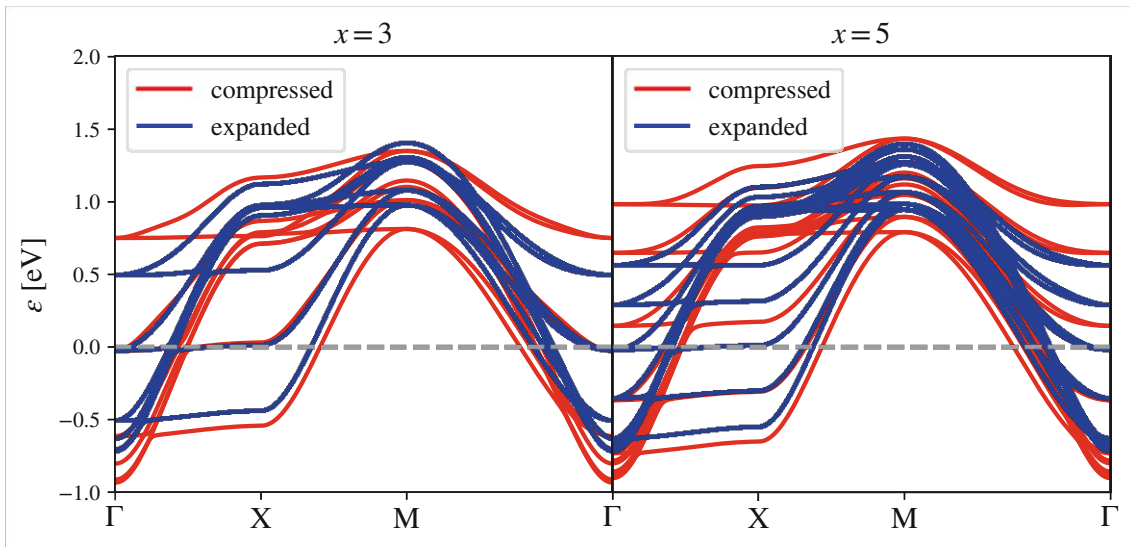


Figure 2.33: Comparison of projected V t_{2g} band structures between the compressed structures at the global energy minimum and the “artificially expanded” structures whose atomic distances are modelled after the X-ray standing wave data from Fig. 2.32. Left panel: $x = 3$ layers, right panel $x = 5$ layers. The lattice expansion leads to a compression of the quantum well states around the Γ -point where the energy of the lowest occupied state is increased and the energy of the highest unoccupied state is decreased.

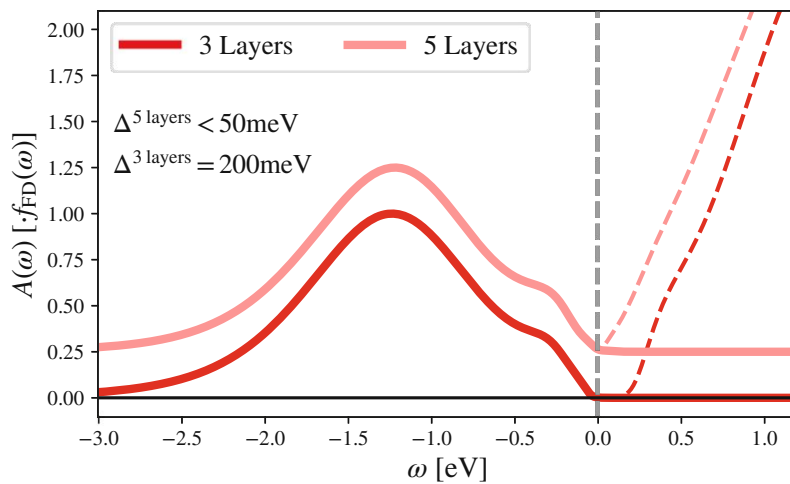


Figure 2.34: Spectral functions $A(\omega)$ (dashed) and the corresponding theoretical PES signal ($A(\omega) \cdot f_{\text{FD}}(\omega)$) of the heterostructures with thickness $x = 3, 5$ modelled after the X-ray standing wave data in Fig. 2.32. Contrary to the compressed heterostructures, this insulating solution can be acquired via cooling and, for the given atomic distances, does not require an increased Coulomb interaction, i.e. both heterostructures were simulated with $U = 5\text{eV}$ ($J = 0.75\text{eV}$, $U' = 3.5\text{eV}$).

As the interface V-Ti distance is elongated the furthest also its interface crystal field splitting is the largest. Comparing these values to the previously considered constrained bulk, we find optimal requirements: $\Delta_{\text{cfs}} = -100\text{meV}$ corresponds to roughly $c = 4.10\text{\AA}$, see Fig. 2.25, providing a direct entrance into the insulating regime via cooling.

Indeed, the heterostructure shows identical behavior: the insulating solution is easily attained at high temperature and bulk interaction values $U = 5\text{eV}$ ($J = 0.75\text{eV}$, $U' = 3.5\text{eV}$). At room temperature the insulating solution is inaccessible from a metallic starting point and must be, again, forcefully stabilized. This behavior, however, is not at odds with the resistivity profile of Fig. 2.28 as we can access this solution, via cooling. Given these modifications, we obtain an akin spectral gap of the $x = 3$ and $x = 5$ heterostructure of $\Delta_{x=3} = 200\text{meV}$ and $\Delta_{x=5} < 50\text{meV}$, see Fig. 2.34.

General applicability

Insulating behavior which at its heart is caused by a lattice expansion stemming from defects constitutes a much more general mechanism. Crystal-field splitting induced only via substrate strain requires a significant lattice mismatch which could lead to incompatibility between substrate and deposition material. Here we have to stress that within our theoretical considerations a mismatch of $\Delta a_{\text{PBE}} = 0.1\text{\AA}$, consistent in the PBE exchange correlation functional [23], was employed. Realistic bulk SrTiO_3 and SrVO_3 crystals, however mismatch by only $\Delta a_{\text{EXP}} = 0.05\text{\AA}$, half of the simulated PBE value. Being one of the most critical input parameter in the simulation of the compression mechanism of thin films, further reduction of the cfs would lead to an even more fragile, or even unstable, Mott insulating solution.

From this point of view, a valence maintaining, substrate induced, lattice expansion provides a much more general avenue towards generalized thin film Mott insulators. Being in principle applicable to every possible material combination, as well as more generalized super lattices, emphasizes the importance the crystal-field splitting as (one of) the main driving force(s). Especially in protected layers a much broader study of distortion and orbital effects of the various insulating thin film states is appropriate. As the cfs can easily be manipulated by pressure and its effect identified via (linearly polarized) spectroscopy, this would provide a promising avenue towards a wide range of not-yet-understood Mott physics.

2.4 Surface phenomena in SrVO₃

- This Section is based on “Toward Functionalized Ultrathin Oxide Films: The Impact of Surface Apical Oxygen” by Judith Gabel, [Matthias Pickem](#), Philipp Scheiderer, Lenart Dudy, Berengar Leikert, Marius Fuchs, Martin Stübinger, Matthias Schmitt, Julia Küspert, Giorgio Sangiovanni, Jan M. Tomczak, Karsten Held, Tien-Lin Lee, Ralph Claessen and Michael Sing [8] and its Supplementary Information. Adopted text passages have been marked accordingly.
- Sample preparations, measurements and validations were performed by our collaborators Judith Gabel, Philipp Scheiderer, Lenart Dudy, Ralph Claessen, and Michael Sing. For an overview of the employed experimental techniques and methods, please refer to the Supplementary Information of Ref. [8].
- Density functional theory simulations and interpretation of theoretical results were done in close collaboration with Marius Fuchs and Giorgio Sangiovanni.

In the preceding Section, the surface of the SrVO₃ films was assumed to be sufficiently protected from external influences. Indeed, in Section 2.3.2 we employed a bulk description of thick films, $\mathcal{O}(50)\text{nm}$, whereas the explicit consideration of capping layers in the modelling of thinner films, $\mathcal{O}(1 - 5)\text{nm}$, in Section 2.3.3 was necessary to treat the substrate and capping interface on equal footing. The empirical modelling of the observed critical thickness (6 – 7 unit cells) in stoichiometric (nominal d^1 filling) and pristine setups was shown to derive from a crystal-field driven insulating state, akin to the distortion driven insulator in the bulk crystal. Within this modelling, the limited number of unit cells in the out-of-plane direction decreases the itinerancy of the electrons, mainly modifying the band width of the xz/yz orbitals. These band structure effects, accompanied by the relatively strong on-site repulsion found in vanadium compounds, allow a formation of an insulating ground state with an unexpectedly large critical thickness. Through the unintuitive interface effects (negative Poisson’s ratio) observed in X-ray standing wave measurements, questions however remain about the structural, surface, and electronic modifications in the vicinity of perovskite interfaces.

The observation of 5+ deposited unit cell displaying insulating behavior came initially as a surprise as the first metal-insulator transitions in ultrathin SrVO₃ were found to occur at around 2uc in *unprotected* structures, see Ref. [85]. The first realistic attempt at understanding this observation was made in Ref. [86] where an idealized heterostructure was modeled: two layers of SrVO₃ on top of a SrTiO₃ substrate (with identical in-plane lattice constants as used in the previous Section 2.3).

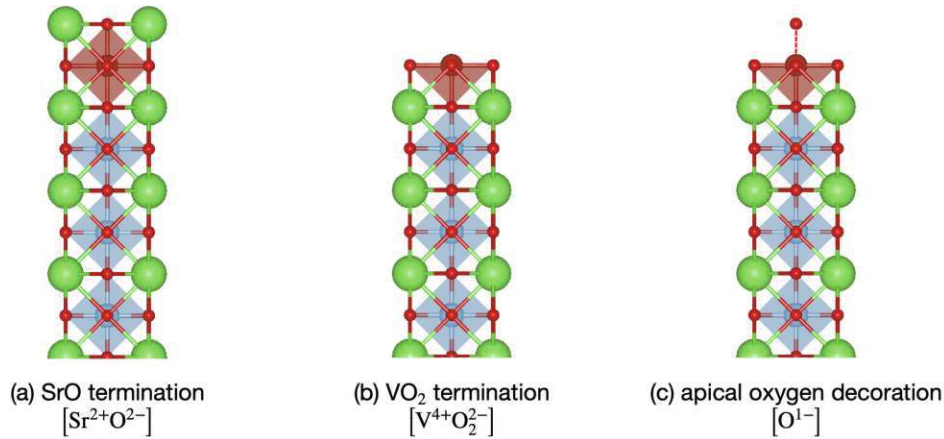


Figure 2.35: SrVO₃ | SrTiO₃ thin film heterostructure: different SrVO₃ surface terminations resulting from the stacking of SrO and VO₂ planes. The SrO termination (a) leads in theory to a chemically inert surface. The VO₂ termination (b) halves the surface adjacent VO₆ octahedron and exposes the inner vanadium atom. Surplus oxygen then is allowed to close this octahedron, oxidizing the surface (c).

Critically, the epitaxially deposited SrVO₃ was modelled with a strontium oxide (SrO) vacuum termination, see Fig. 2.35a. Similar modelling has been done for other perovskite oxides as well [163]. While not found in pulsed laser deposition (PLD) setups, from a surface protection point of view this SrO termination would be preferable: The electron transfer (Sr²⁺O²⁻) in the ionic picture results in a chemically inert surface with strontium and oxygen in their noble gas configuration. The resulting structure, barring surface induced crystal distortions, then closely resembles the previously considered, protected thin film structures. There, the SrO-VO₂-SrO-VO₂-... layer stacking in the (001) direction of SrVO₃ can be uninterruptedly continued into the SrTiO₃ substrate/protection via SrO-VO₂-SrO-TiO₂-SrO. Dynamical mean-field calculations reveal that the two-layer system with the SrO termination is on the verge of the Mott transition, being highly susceptible to external perturbations such as strain, electric field or temperature [86].

Following experimental guidance from samples produced via PLD (the same technique that was used in Ref. [85] and Ref. [164]) we will show that this modelling is inherently flawed. Indeed, direct and indirect surface analysis show that heterostructures instead form the chemically less inert VO₂ surface termination instead, see Fig. 2.35b. In this Section we characterize the effects of this termination by analyzing various sample thicknesses. Through surface diffraction, core-level, as well as angle-resolved photoelectron spectroscopy we highlight the drastic effects occurring without surface protection, even if the samples are kept *in situ*. Inspired by these insights we will perform realistic DFT+DMFT calculations to gain a better understanding of the effects onto the electronic structure

and the resulting formation of a Mott insulating state whose description naturally becomes more nuanced.

2.4.1 Surface overoxidation of thick SrVO₃ films

The nominal $3d^1$ occupancy of V in SrV⁴⁺O₃ poses a challenge for the sample preparation, because the most stable vanadium valence, which corresponds to a noble gas configuration, is not V⁴⁺ but V⁵⁺ making SVO films prone to overoxidation. This becomes apparent in Figure 2.36a, where X-ray photoelectron spectroscopy (XPS) was employed to record the V $2p_{3/2}$ core level spectra of an epitaxial 75 nm thick SVO film grown by pulsed laser deposition (PLD) with a nominal VO₂ surface termination. For the sample exposed to air prior to the XPS measurement the spectrum (labelled *ex situ*) is dominated by a strong peak around a binding energy of 518 eV that is assigned to V⁵⁺ ions by comparison to reference data of different vanadium oxide compounds [165]. However, even for films analyzed immediately after the PLD growth without an exposure to air, pentavalent vanadium is detected [166], as is seen from the *in situ* spectra in Figure 2.36a. The spectra were recorded at different electron emission angles ϑ to check whether this V⁵⁺ signal originates from the SVO film surface. The V⁵⁺ component is stronger at higher ϑ , i.e. in more surface sensitive measurement geometries, which suggests that the over-oxidation occurs near the SVO surface. For a quantitative account, the angle-dependence of the relative V⁵⁺ content $I(\text{V}^{5+})/[I(\text{V}^{4+})+I(\text{V}^{5+})]$ was fitted (see Figure 2.36b) within a microscopic model taking into account the relative V⁵⁺ content in each VO₂ layer of the film and the depth-dependent damping of the photoelectrons (see Supporting Information in Ref. [8]). We found that the V⁵⁺ component stems almost exclusively from the topmost layer while the subsurface layers only contribute to the V⁴⁺ component.

Complementary structural information is provided by low-energy electron diffraction (LEED). The *in situ* observed diffraction pattern of a thick film in Figure 2.36c exhibits a $\sqrt{2} \times \sqrt{2}$ R(45°) reconstruction. The associated reciprocal and direct space surface unit cells are marked in the pattern and in the structural model of the surface by dashed green and black squares for the cubic perovskite and the reconstruction, respectively. The same surface reconstruction was reported in the literature for similarly grown SVO films [109, 166, 164], and a recent scanning tunneling microscopy (STM) study by Okada *et al.* [164] identifies adsorbed oxygen ions as its microscopic origin. They find that additional oxygen ions occupy half of the apical sites above the surface vanadium ions, thereby closing every other VO₆ octahedron, see Fig. 2.35c. The oxygen presumably adsorbs during the growth of the samples which is performed in an oxygen background atmosphere. This microscopic picture is consistent

with the over-oxidation of the topmost VO_2 layer inferred from the modelling in Figure 2.36b since every excess oxygen ion drains two electrons from the V $3d$ band and thereby (nominally) generates two V^{5+} ions, as sketched in the structural model in Figure 2.36d [164]. Therefore, we conclude that a complete electronically dead (d^0) surface layer forms on a thick SVO film terminated with an apical oxygen induced superstructure while the rest of the film remains virtually unaffected. This happens even when the SVO film is only handled in an ultrahigh vacuum environment. Note that the apical oxygen is chemisorbed and can only be removed by prolonged annealing at high temperatures.

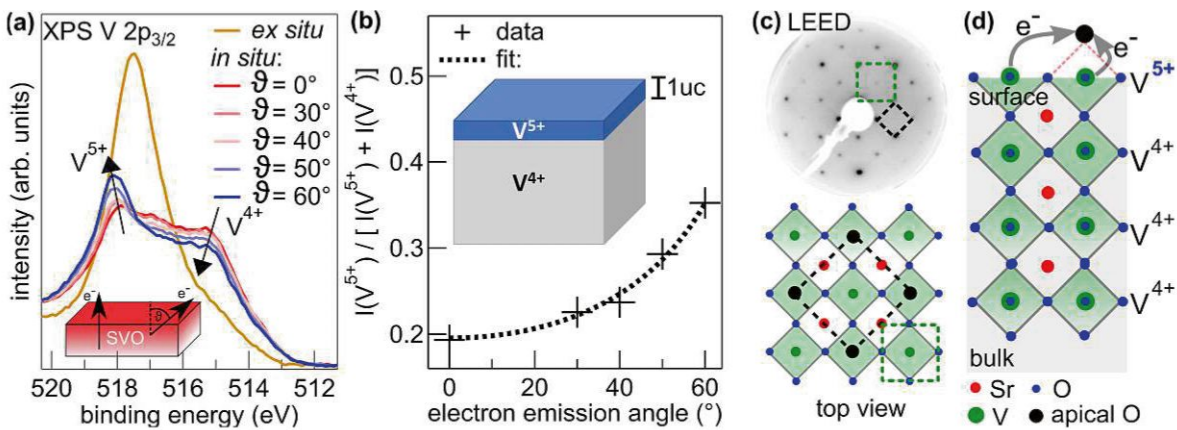


Figure 2.36: a) V $2p_{3/2}$ spectra of a 75 uc thick SVO film exposed to air (*ex situ*) are dominated by a strong V^{5+} signal evidencing the oxidation of the SVO film. XPS on *in vacuo* (*in situ*) handled SVO films at different electron emission angles ϑ detects a V^{5+} signal that emanates from the surface, even without exposure to air. b) Model fit of the angle-dependent relative V^{5+} content $I(\text{V}^{5+})/[I(\text{V}^{4+})+I(\text{V}^{5+})]$. The best match is achieved with a d^1 occupancy throughout the film except for a single dead layer at the very surface with d^0 occupancy. c) Top: The LEED pattern of a thick SVO film exhibits a $\sqrt{2} \times \sqrt{2}$ R(45°) surface reconstruction consistent with the ordered adsorption of oxygen ions at apical sites as detected in an STM study [164]. Bottom: Structural model of the SVO film surface decorated with apical oxygen. d) Structural model of the SVO film showing the additional oxygen ions draining electrons from the film surface.

The observed dead-layer phenomenon in the epitaxially grown (001) direction can only be supported by a final VO_2 termination to vacuum. This is at odds with *some* of hitherto performed theoretical studies [86]. Of course, more sophisticated growth setups have been used to manipulate the final termination of these types of perovskite structures, e.g., alternating deposition of La_2O_3 and NiO targets to obtain LaNiO_3 films [125] or an explicit selection of the termination using hydroxylation [167]. It would be an interesting avenue applying the same technique for SVO layers.

2.4.2 Evolution of apical oxygen coverage with film thickness

With the surface overoxidation essentially only affecting the valence of the topmost SVO layer, it can be mostly neglected for the physical properties of thick SVO film. When the SVO film thickness is reduced to only a few unit cells, the adsorbed oxygen ions may, however, have a strong bearing on the electronic properties of the films. In the next step, we thus investigate ultrathin SVO films of 2 to 6 uc thicknesses *in situ* immediately after their growth. Figure 2.37a depicts the corresponding XPS V 2p_{3/2} spectra together with that of the 75 uc thick film, normalized to the integral V 2p spectral weight. The spectra exhibit a systematic trend: The intensity of the V⁵⁺ component increases with the film thickness and saturates above 6 uc SVO. To back up the observation in the V 2p spectra, we present the corresponding LEED patterns in Figure 2.37b, where the $\sqrt{2} \times \sqrt{2}$ R(45°) reconstruction ascribed to apical oxygen adsorption is present on all samples. However, compared to the 1 × 1 spots, the fractional order reflections (marked by the arrows) lose their intensity with decreasing film thickness. This becomes apparent in Figure 2.37c in which the intensity of the LEED pattern is analyzed along the dotted line in 2.37b. With the line profile normalized to the peak intensity of the 1 × 1 reflection, the $\sqrt{2} \times \sqrt{2}$ R(45°) spots clearly weaken with decreasing SVO thickness, indicating a declining (ordered) surface coverage with adsorbed oxygen, consistent with the trend revealed by XPS for the V⁵⁺ component in Figure 2.36a. Note that the intensity changes in the diffraction pattern do not permit a quantitative estimate of the total amount of adsorbed oxygen, as LEED detects only the ordered apical atoms incorporated in the superstructure and is not sensitive to oxygen adatoms randomly occupying the remaining apical sites. Nonetheless, since the apparent trend detected in the LEED patterns mirrors that observed in the V 2p_{3/2} spectra, we arrive at the conclusion that the coverage of adsorbed apical oxygen and hence the fraction of V⁵⁺ ions gradually reduce with decreasing SVO film thickness.

We speculate that the dependence of the surface apical oxygen coverage on the film thickness is related to the impact which the additional oxygen has on the average number of V 3d electrons in the ultrathin films. A full coverage with surface apical oxygen in an ordered $\sqrt{2} \times \sqrt{2}$ R(45°) arrangement induces one V⁵⁺ ion per surface unit cell. A thick film provides a large reservoir of 3d electrons and therefore the average change of the vanadium valence is negligible. When the film thickness decreases at constant coverage, the relative share of the V⁵⁺ ions generated by the surface apical oxygen increases. For instance, at 2 uc film thickness half of the vanadium ions would be rendered from tetra- to pentavalent at full coverage with surface apical oxygen in an ordered $\sqrt{2} \times \sqrt{2}$ R(45°) arrangement. This may not be energetically favorable, as a result a lower coverage might develop.

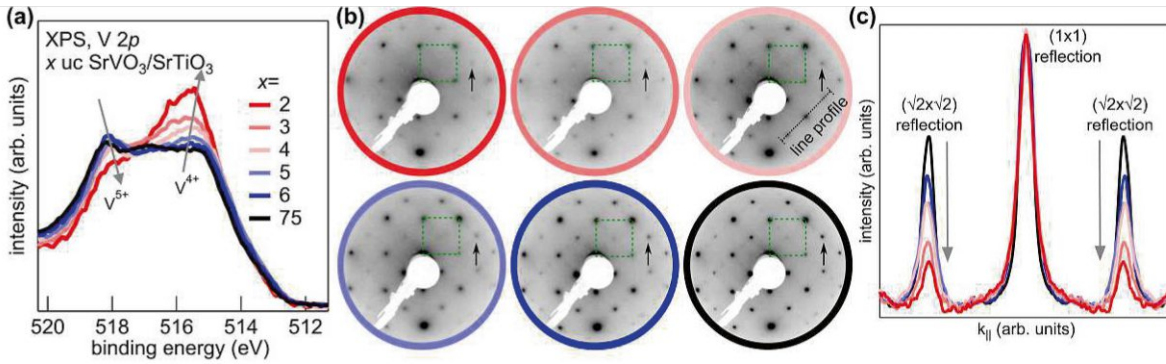


Figure 2.37: a) $V 2p_{3/2}$ spectra of SVO films with thicknesses across the dimensional crossover show the V^{5+} signal decreasing for thinner films. b) Corresponding LEED patterns where the diffraction pattern of the cubic perovskite unit cell is marked by dashed squares. The $\sqrt{2} \times \sqrt{2} R(45^\circ)$ surface reconstruction (see spot highlighted by arrows) is present on every sample. c) Intensity of LEED spots along the line profile indicated in b). The line profiles are symmetrized with respect to the (1×1) reflection. At smaller SVO thicknesses the reflections assigned to the surface reconstruction lose intensity with respect to the diffraction pattern of the cubic perovskite.

2.4.3 Effects of surface overoxidation

To investigate experimentally the effect of the apical oxygen on the electronic structure, a 6 uc SVO/STO film was probed by soft X-ray photoelectron spectroscopy with the degree of surface overoxidation being varied in a controlled manner. These measurements were performed with synchrotron radiation for two reasons. First, due to the tunability of the synchrotron light, core levels and valence band can be probed at the same photoelectron kinetic energy and thus the same probing depth. We chose low photoelectron kinetic energies around 105 eV, at which the inelastic mean free path of the photoelectrons amounts to only 3.5 Å (see Supplementary of Ref. [8]), ensuring a high sensitivity to the topmost SVO layers. Second, with the intense hard X-ray beam available at a third generation synchrotron the apical oxygen can be effectively removed through photon-induced desorption [168], thereby restoring a clean surface. Using these tactics, we have investigated the sample in two states: (i) the state immediately after the PLD growth, which is characterized by additional apical oxygen adsorbing on the VO_2 -terminated surface during the growth in an oxygen background pressure and which remains intact through an ultrahigh vacuum transfer to the synchrotron, and (ii) the state after removal of the apical oxygen by irradiation of hard X-rays. The corresponding $V 2p$ spectra of the two states are presented in Figure 2.38a, where the presence and removal of apical oxygen for the states before (blue) and after (red) the hard X-ray exposure is confirmed by the pronounced and nearly quenched V^{5+} components, respectively, at 518 eV binding energy.

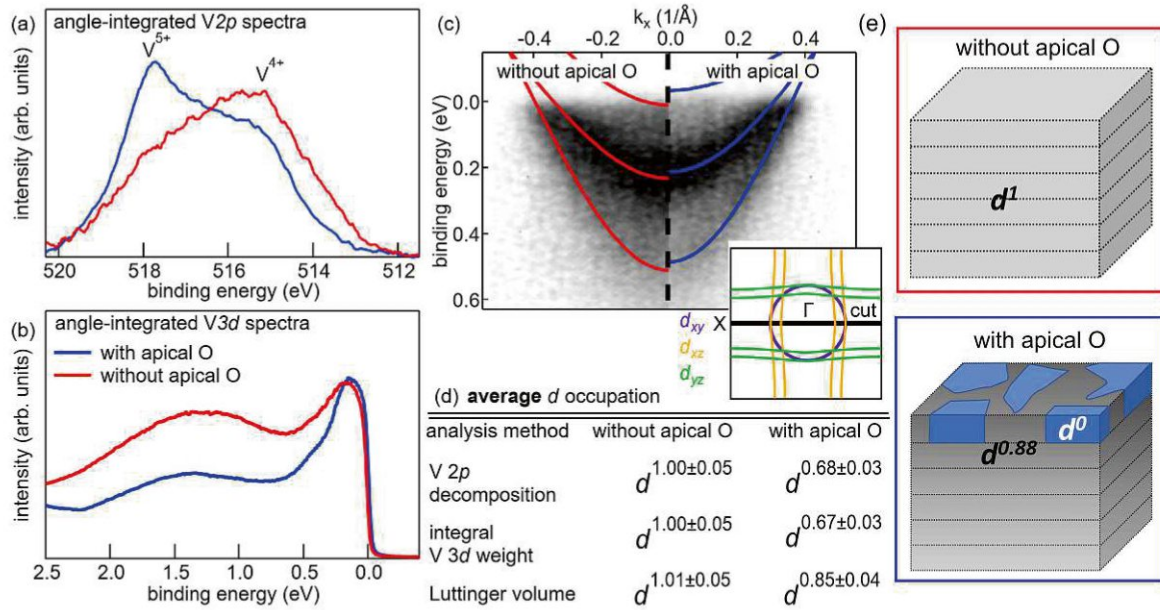


Figure 2.38: Effect of the surface overoxidation on the electronic structure of a 6 uc SVO film. The angle-integrated V 2p a) and 3d b) spectra, normalized to integration time, change notably between the states with and without apical oxygen coverage which signals a pronounced shift in the average V valence/V 3d occupation. c) The angle-resolved V 3d spectra for a film without (left) and with (right) apical oxygen hardly differ indicating a barely changing band filling in the metallic domains. d) The d occupations estimated by different methods indicate that the d occupation is homogeneous for the clean surface while domains with different d occupation form when apical oxygen adsorbs as sketched in e).

2.4.3.1 Change in vanadium occupation

To quantify the effect of the apical oxygen on the electronic structure, we determine the V 3d occupations in both states using three different methods. First, from a decomposition of the V 2p_{3/2} spectral weight into the V⁴⁺ and V⁵⁺ contributions we obtain and indicate in Figure 2.38d what we call the average d occupation in the probed volume, *i.e.*, the equivalent d occupation of a homogeneous SVO film. With the V 2p spectrum of the film without apical oxygen not displaying a V⁵⁺ feature, we assume that the film is stoichiometric in this state and is characterized by a d^1 occupation. The V 2p spectrum of the film with apical oxygen is decomposed into a V⁴⁺ and a V⁵⁺ contribution by a fit. The V⁵⁺ signal is modeled by a single Voigt peak. Due to the V⁴⁺ spectrum being dominated by final state effects, the V⁴⁺ reference has a complicated peak shape [169, 170] and has to be determined

experimentally under identical conditions as the spectrum to be fitted. We thus use the spectrum of the film without apical oxygen as the V^{4+} reference. The relative V^{4+} weight yields the d occupation subsequently where we find that the average d occupation is lowered to $d^{0.68}$.

V 2p decomposition : without apical O $\rightarrow d^1$

V 2p decomposition : with apical O $\rightarrow d^{0.68}$

An independent estimate of the average d occupation can be obtained from the total (angle-integrated) V 3d weights for the two states, normalized to integration time. The corresponding spectra are depicted in Figure 2.38b. The V 3d valence states span the first 2 eV below the Fermi level and display the characteristic line shape of a strongly correlated metal, featuring an incoherent lower Hubbard band (LHB) at about 1.5 eV and a metallic quasiparticle (QP) state at the Fermi level [114]. To this end, the near Fermi edge spectra are normalized to the X-ray intensity and integrated in angle over the range of one Brillouin zone. The integral V 3d weight is then estimated by integration over the QP and LHB energy range. We find that the overall V 3d weight drops by 33% when the clean surface is compared to that with apical oxygen, in line with the 32% decrease in the average d occupation inferred from the V 2p spectra (see Supporting Information in Ref. [8]). Note that the presence or absence of apical oxygen not only affects the total intensity but also the line shape of the angle-integrated V 3d spectrum.

V 3d integral weight : without apical O $\rightarrow d^1$

V 3d integral weight : with apical O $\rightarrow d^{0.67}$

Yet another way of probing the V 3d band filling utilizes the determination of the Luttinger k -space volume enclosed by the Fermi surface. For this purpose, we evaluate the momentum-dependent band structure recorded by angle-resolved photoemission spectroscopy (ARPES). Figure 2.38c shows band maps measured along the Brillouin zone cut sketched in the inset for the states with and without apical oxygen. From them, band dispersion was fitted to the peak positions based on the SVO tight binding model [109]. To determine the Luttinger volume, the total area enclosed by the Fermi surface has to be estimated. Furthermore, only d_{xz} -like bands could be observed in our measurement geometry. Based on the Fermi surface of bulk SVO from band-theory [109], we infer the Fermi surface map for all orbitals over the entire Brillouin zone under the assumption that the FS areas are layer-independent. Note that three quantum well states form for the d_{xz} - and d_{yz} -like bands while each SVO layer is assumed to contribute a d_{xy} -like band.

Assuming a 6 uc homogeneous SVO film, we derive the average d band fillings from the observed Fermi wavevectors and the known symmetry and shape of the Fermi surface to be $d^{1.01}$ and $d^{0.85}$ for the states without and with apical oxygen, respectively, the values of which are also included in the table in Figure 2.38d for comparison (see Supporting Information in Ref. [8]).

Luttinger volume : without apical O $\rightarrow d^1$

Luttinger volume : with apical O $\rightarrow d^{0.85}$

For the sample state of a *clean* surface, the table in Figure 2.38d shows that all three methods yield the same result, namely, essentially a d^1 occupation as expected from the nominal electron configuration of vanadium in stoichiometric SrVO₃ (see top sketch in Figure 2.38e). In contrast, the resulting d occupations differ noticeably for the state with apical oxygen: while we observe larger than 30% reductions in the d occupations inferred from the angle-integrated V 3*d* and V 2*p* spectra, the Luttinger volume derived from the angle-resolved V 3*d* measurements decreases by a much smaller amount of only 16% upon the addition of surface apical oxygen. In general, such a discrepancy is indicative of an electronic phase separation into metallic and insulating regions on mesoscopic or microscopic length scales, as also observed for SrTiO₃ [171]. This is because the band filling extracted from ARPES mapping is only susceptible to the metallic domains (as insulating regions do not contribute to the Fermi surface), whereas the angle-integrated V 3*d* and V 2*p* spectra average the band filling over both insulating *and* metallic domains and are insensitive to the spatial distribution of the d electrons.

2.4.3.2 Electronic phase separation

In light of this phase separation scenario, we consider the coexistence of insulating d^0 and metallic d^{1-x} domains for the sample state with apical oxygen in line with the experimental results summarized in Figure 2.36. We model the SVO film by an inhomogeneous phase separation where laterally scattered d^0 domains are confined to the topmost layer and embedded in a homogeneous metallic matrix of band filling d^{1-x} that extends 6 uc in depth, as shown in the bottom sketch of Figure 2.38e. We vary x and the surface coverage of the d^0 domains to yield the V⁵⁺/V⁴⁺ ratio and Luttinger volume that are consistent with the corresponding measured V 2*p* spectrum and ARPES band map. Note that, while modelling the V 2*p* core level intensity, we take into account the exponential damping of the photoelectrons from sub-surface layers.

The contributions of these sub-surface layers to the measured valency d_{PES} is the result of a weighted sum ranging over all unit cells

$$d_{\text{PES}} = \frac{\sum_{i=1}^6 d_i e^{-\frac{c_i}{\lambda \cdot \cos \theta}}}{\sum_{i=1}^6 e^{-\frac{c_i}{\lambda \cdot \cos \theta}}}, \quad (2.76)$$

where each layer provides a position dependent signal. c_i refers to the depth of the vanadium atom in the i^{th} layer from the top, i.e., $c_i = (i - 1) \times c_{\text{lattice}}$, d_i refers to the (average) occupation of the i^{th} layer, $\lambda = 3.5 \text{ \AA}$ is the inelastic mean free path for the “activated” photoelectrons and θ is the detector angle. Throughout the modelling the experimentally employed detector angle of $\theta = 5^\circ$ will be used. The denominator is necessary to properly normalize the signal. For the considered horizontal phase separation, as indicated in Fig. 2.38e, the two phases contribute separately, i.e.

$$d_{\text{PES}}^{\text{separation}} = \alpha \underbrace{\frac{\sum_{i=1}^6 d_i^{\text{dead}} e^{-\frac{c_i}{\lambda \cdot \cos \theta}}}{\sum_{i=1}^6 e^{-\frac{c_i}{\lambda \cdot \cos \theta}}}}_{\text{“dead” domains}} + (1 - \alpha) \underbrace{\frac{\sum_{i=1}^6 d_i^{\text{metal}} e^{-\frac{c_i}{\lambda \cdot \cos \theta}}}{\sum_{i=1}^6 e^{-\frac{c_i}{\lambda \cdot \cos \theta}}}}_{\text{metallic domains}} \quad (2.77)$$

where α is the proportion of the dead layer domains. Evidently, $d_1 = 0$ in the “dead” domain.

We reproduce the experimental results for the 6 uc SrVO₃ film in the state with apical oxygen with a $d^{0.88 \pm 0.05}$ band filling for its metallic regions and $\alpha = (35 \pm 7)\%$ of its surface turned into a d^0 dead layer, i.e. $d_{i=1}^{\text{dead}} = 0$ and $d_{i>1}^{\text{dead}} = d_i^{\text{metal}} = 0.88 \pm 0.05$. It should be noted that the probing depth of our photoemission experiments amounts to about 10.5 Å (3-times the photoelectron inelastic mean free path), and sets a limit on the depth sensitivity of the angle-integrated measurements, and hence the above estimates are most relevant to the three topmost SrVO₃ layers.

The average d -occupation, as measured via the Luttinger volume, then should coincide with the d -occupation modelling of Eq. (2.77),

$$d_{\text{Luttinger}} = \alpha \cdot d \cdot \frac{5}{6} + (1 - \alpha) \cdot d = d(1 - \frac{\alpha}{6}) = 0.83. \quad (2.78)$$

The homogeneous d -electron distribution, i.e. all metallic vanadium site being equally occupied, is the simplest model which is able to conform to all acquired occupation measurements in Section 2.4.3.1. Whereas further simplifications fail to reproduce the required trends, additional vertical phase separation cannot be excluded: These additional scenarios are collected and assessed in Table 2.5.

model	assumed layer occupation	α	d_{PES}	$d_{\text{Luttinger}}$	LEED V ⁵⁺
(1) homogeneous hole doping [8]	$d_{\text{dead}} = [0, d^x, d^x, d^x, d^x, d^x]$ $d_{\text{metal}} = [d^x, d^x, d^x, d^x, d^x, d^x]$ $x = 0.88$	0.35	0.67	0.83	partial
(2) fully ordered coverage	$d = [0, 1, 1, 1, 1, 1]$	1	0.34	0.83	full
(3) partially ordered coverage	$d_{\text{dead}} = [0, 1, 1, 1, 1, 1]$ $d_{\text{metal}} = [1, 1, 1, 1, 1, 1]$	0.5	0.67	0.92	partial
(4) interface induced separation (3 layers)	$d_{\text{dead}} = [0, 1, 1, d^x, d^x, d^x]$ $d_{\text{metal}} = [1, 1, 1, d^x, d^x, d^x]$ $x = 0.87$	0.49	0.67	0.85	partial
(5) interface induced separation (1 layer)	$d_{\text{dead}} = [0, 1, 1, 1, 1, d^x]$ $d_{\text{metal}} = [1, 1, 1, 1, 1, d^x]$ $x = 0.60$	0.49	0.67	0.85	partial
(6) surface induced separation (3 layers)	$d_{\text{dead}} = [0, d^x, d^x, 1, 1, 1]$ $d_{\text{metal}} = [d^x, d^x, d^x, 1, 1, 1]$ $x = 0.89$	0.37	0.67	0.85	partial
(7) surface induced separation (1 layer)	$d_{\text{dead}} = [0, 1, 1, 1, 1, 1]$ $d_{\text{metal}} = [d^x, 1, 1, 1, 1, 1]$ $x = 0.60$	0.17	0.67	0.85	partial

Table 2.5: Different phase separation scenarios. Based on the assumed layer occupation (second column) the average d occupation (d^x) and domain proportion (α) can be fitted to achieve matching (within error bars) occupation with the PES measurements (d_{PES}) and Fermi surface measurements ($d_{\text{Luttinger}}$). The LEED columns refers to the size of the $\sqrt{2} \times \sqrt{2}$ reflex in Fig. 2.37. The 6uc reflex must be partially suppressed (“partial”) compared to the thick (75uc) sample where the LEED signal is maximized (“full”). A green cell background color indicates matching data, a red indicates a data mismatch with experiment. Scenario (1) describes the model described in the main text, whose predicted observables can be also attained via scenarios (4-7) which include a vertical phase separation. Scenarios (2-3) are listed to showcase the apparent problems.

For instance, scenario (2), a fully ordered coverage results in a (vertically) d -distribution of $d = [0, 1, 1, 1, 1, 1]$ and necessarily fulfills the required Luttinger occupation of 5/6. However, this scenario is incapable of reproducing the dampened vanadium 2p signal, $d_{\text{PES}} = 0.34$, as well as the suppressed $\sqrt{2} \times \sqrt{2}$ -R45° LEED signal. Scenario (3), a partially ordered coverage ($\alpha = 0.5$) with nominal d^1 occupation on all vanadium sites, except the one that is decorated with additional, apical oxygen reproduces the correct PES signal. However, the resulting Luttinger volume is largely overestimated with $d_{\text{Luttinger}} = 0.92$. Additional vertical separation may be introduced in the most sensible way via an interface-driven or a surface-driven doping: For both scenarios, we consider a one-layer and a three-layer transition where the brute-force parameter fitting of α and x results in scenarios (4-7)

listed in Table 2.5. For the case of the one layer surfaced-induced separation, scenario (7), an alternate interpretation is possible: 17% (α) dead domain (ordered apical oxygen) is accompanied by 50% of pristine VO_2 termination, with the remaining 33% consisting of disordered apical oxygen, causing the drop of surface d occupation.

One unresolved question remains the observed V^{5+} signal strength of the 6uc structure, however: As Fig. 2.37 shows, the (normalized) V 2p spectra of the 6uc sample almost coincides with the 75 uc sample, indicating the proximity to saturation. In this context we consider the top layer of the 75 uc sample to be fully depleted, hence we assume the majority of this observed V^{5+} signal to stem from it. Photoelectrons originating from the surface vanadium sites, experience only minimal dampening, as they don't have to traverse through other layers before arriving at the detector. In principle none of the considered thin film scenarios would lead to the evidenced saturation, suggesting additional (hitherto unknown) difference between the thin and thick film samples. Oka *et al.* [172], e.g., revealed through scanning tunneling spectroscopy further structural differences: They observed a $\sqrt{5} \times \sqrt{5}$ -R26.6° reconstruction for films with fewer than 10uc. Instead of apical oxygen in the $\sqrt{2} \times \sqrt{2}$ -R45° reconstruction, the $\sqrt{5} \times \sqrt{5}$ reconstruction is formed by additional *strontium* adatoms providing additional surface electrons and modifying the local electronic structure. It is argued that this formation is caused by oxygen deficiencies in the bulk and the resulting nonstoichiometry of strontium and titanium atoms near the surface [173], affecting the growth of the overlying SrVO_3 film. Beyond a certain number of layers this effect is minimized and the surface properties are determined purely by the deposition material SrVO_3 and the surrounding atmosphere during the growth process. The measured differential conductance dI/dV spectrum further showed a large difference between the $\sqrt{5} \times \sqrt{5}$ terraces and the $\sqrt{2} \times \sqrt{2}$ terraces at zero bias voltage $V = 0$. The former shows an almost gap-like signature around $V = 0$, indicative of a suppression of the local density of states, while the latter is firmly metallic. While our LEED pattern, presented in Fig. 2.37 shows no indication of any longer range order, except for the $\sqrt{2} \times \sqrt{2}$ reconstruction, we cannot exclude further surface modification.

In all scenarios, open questions about the surface reconstructions remain. Especially intriguing are the possible effects onto the observed metal-insulator transition of the unprotected samples. To gain a better understanding, more thorough surface analysis is necessary.

2.4.3.3 Change in photoemission line shape

Our findings of apical oxygen altering the electronic structure are at variance with the interpretation put forward by Backes *et al.* [105] of their synchrotron-based ARPES results on SVO films, see

also Section 2.2.4. They observe strong changes in the spectral line shape as a function of UV irradiation and attribute them to beam-induced oxygen *vacancies* forming in the SVO lattice. This interpretation is incompatible with our data, where the X-ray induced nearly 50% increase of V 3d spectral weight (Figure 2.38b) is accompanied by a massive V 2p spectral weight transfer from the V⁵⁺ to the V⁴⁺ component (Figure 2.38a), rather than any noticeable further reduction of V (from V⁴⁺ to V³⁺) expected for oxygen vacancy formation. Note that their samples showing the large changes in spectral weight were transferred in air and then annealed in vacuum to recover a clean surface. We suspect that the annealing process did not remove all the excess surface oxygen, which then desorbed under the intense UV light, as reported in this work. Despite the different interpretations we observe essentially the same dependence of the V 3d spectral function on radiation dose.

The V 3d spectral shape clearly begins to evolve upon the desorption of apical oxygen. With the V 3d weight exclusively originating from the metallic domains, this indicates a variation in their electronic properties. In particular, the apparent increase in the ratio of the LHB and QP weights may signal increased correlations in the absence of apical oxygen, which might be partly explained by the *d* occupation being driven closer to an integer filling. Furthermore, the topmost layer of the SVO film can exhibit enhanced correlations due to reduced coordination numbers [79, 174] and thus a different QP to LHB ratio from the bulk. The presence of *d*⁰ domains in the topmost layers of the film with adsorbed oxygen will suppress this surface contribution and alter the V 3d spectral function. Alternatively, defects in the topmost layer may lead to enhanced scattering and hence broadening of the QP feature. When *d*⁰ domains develop with the adsorption of apical oxygen, surface defects are shielded by the dead layer, scattering becomes less important, and the V 3d line shape will feature a sharper QP peak.

To illustrate this point further, we characterize the quasi-particle peaks of the sample with apical oxygen (as deposited) and the sample that was treated with UV light (without apical oxygen) in Fig. 2.39. For this purpose, we fit the PES spectrum of the untreated sample (panels a-b) with two distinct Lorentzian peaks

$$L(\omega; \omega_0, \Gamma) \propto \frac{\Gamma}{(\omega - \omega_0)^2 + \Gamma^2} \quad (2.79)$$

to mimic the lower Hubbard band (LHB) and the quasi-particle peak (QP). Here, ω_0 and Γ represent the center position and the broadening of the Lorentzian, respectively. The total spectrum was then multiplied with a Fermi function at the measurement temperature $T = 50\text{K}$ and additionally broadened by a convolution with a Gaussian to accurately reflect the measurement process. The characteristic Gaussian broadening $\sigma = 45\text{meV}$ (FWHM = $2\sqrt{2\ln 2}\sigma = 105\text{meV}$) was chosen such that the slope around the Fermi level, $\omega = 0$, matches the experiment, see panel (b): solid, blue line vs. dotted, green line. The fit results in $(\omega_0, \Gamma)_{\text{LHB}} = (-1.48\text{eV}, 0.91\text{eV})$ and $(\omega_0, \Gamma)_{\text{QP}} = (0.10\text{eV}, 0.3\text{eV})$.

Notably, the quasi-particle peak is centered at $\omega > 0$, in accordance with the DMFT spectral function of bulk SrVO₃, cf. Fig. 2.10.

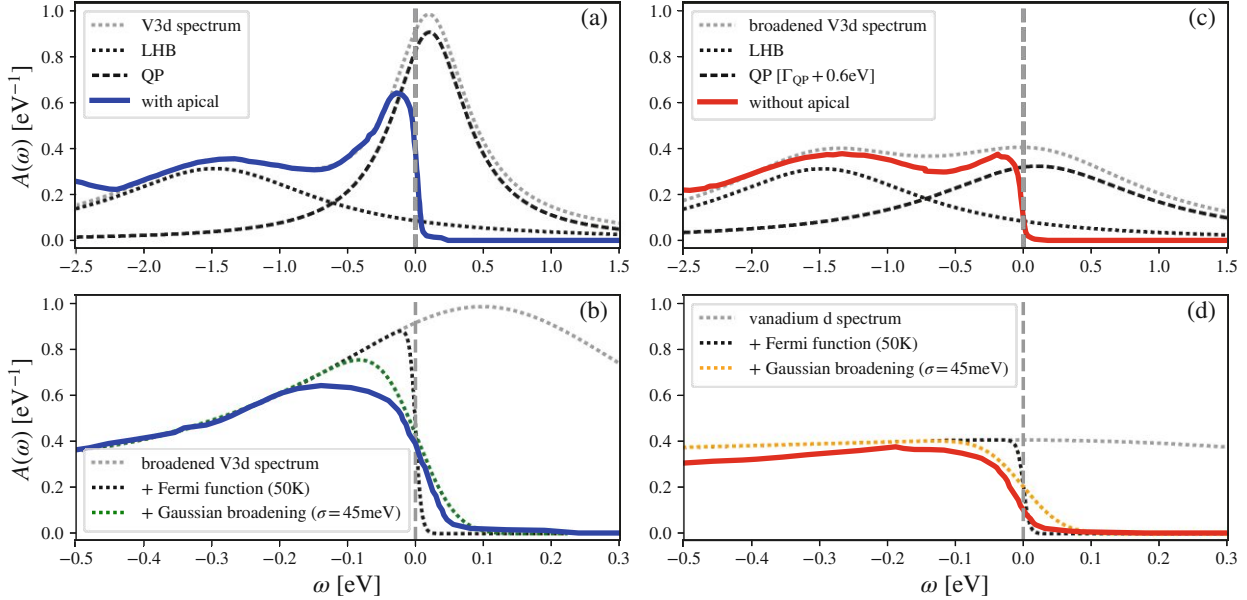


Figure 2.39: Photoemission spectrum (PES) of the sample with apical oxygen (a,b) and without apical oxygen (c,d). The PES signal *with* apical oxygen (blue) was fitted with two distinct Lorentzian peaks, mimicking the lower Hubbard band (LHB) and the quasi-particle peak (QP). The combined spectrum was then multiplied with a Fermi function ($T = 50\text{K}$) and broadened with a Gaussian ($\sigma = 45\text{meV}$) to take the intrinsic and extrinsic broadening of the measurement into consideration. The broadening is chosen such that the slope around the Fermi level of the experiment is captured accurately. The PES signal of the sample *without* apical oxygen can then be recreated by reusing the Lorentzians of the sample with apical oxygen and simply broadening the QP peak by an additional $\Gamma = 0.6\text{eV}$.

The *shape* of the PES spectrum of the “cleaned” surface (panels c-d) can then be recovered by increasing the “scattering rate” of the quasi-particle peak: $\Gamma_{\text{QP}} = 0.33\text{eV} \rightarrow \Gamma_{\text{QP}} = 0.93\text{eV}$. With the application of the identical Fermi function and Gaussian convolution we find almost perfect agreement when comparing to the measured PES signal (solid red line). Note that we do not compare directly to the vanadium 3d spectrum given in Fig. 2.38 that was normalized to integration time. We instead adjusted the spectral weight of the sample without apical oxygen to match the sample with apical oxygen which itself was normalized to 1. The disparity is caused by the evidence p-doping in the samples with apical oxygen, see Fig. 2.38. All other parameters (prefactors, etc.), however, were unchanged in this procedure.

This line shape characterization thus suggests that the removal of surface oxygen recovers the

vanadium d^1 occupation and simultaneously alters the coherence of the quasi-particle peak, suppressing the QP:LHB ratio, without affecting the rest of the occupied vanadium d spectrum $\omega > -2\text{eV}$.

2.4.3.4 Persistence of the insulator transition

Despite the phase separation complications, ultraviolet photoemission measurements on a set of SrVO₃ samples with different thicknesses confirm the presence of the thickness-induced Mott transition in our samples. Our valence band spectra measured with unmonochromatized He I _{α} ($h\nu \approx 21\text{ eV}$) radiation are depicted in Figure 2.40a and are compared to the results of Yoshimatsu *et al.* [85] shown in Figure 2.40b. The main characteristics of the transitions are found to be identical in both experiments. The thick SrVO₃ films exhibit the well-known two peak structure of lower Hubbard band and quasi-particle peak with a clear Fermi cutoff signaling the correlated metal phase. Upon decreasing the SrVO₃ thickness, spectral weight is transferred from the QP to the LHB and eventually at a SrVO₃ thickness of 2 uc the QP is completely suppressed with only the LHB remaining.

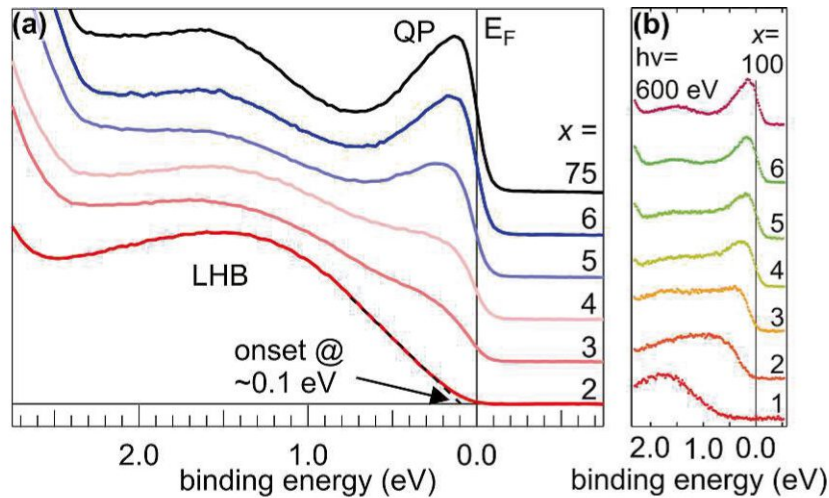


Figure 2.40: a) Photoemission valence band spectra of our SVO films with various thicknesses x measured with He I _{α} radiation compared to b) a similar measurement series from Yoshimatsu *et al.* [85] collected at a photon energy of 600 eV. In both data sets thick SVO films exhibit a Fermi cutoff and the typical two peak structure for a correlated metal consisting of QP and LHB while the QP spectral weight at the Fermi level gradually vanishes for smaller film thicknesses and a crossover into the Mott insulating phase is observed at a film thickness of 2 uc.

2.4.4 Structural intricacies of VO₂ terminated films

From the theoretical point of view, the complications introduced by apical oxygen makes the task of pinpointing the exact mechanism of the metal-insulator transition of unprotected, “dirty” samples quite challenging: Even in the detailed analysis of the 6 uc sample, deep in the metallic regime, questions about the horizontal and vertical phase separation remain. It is unclear which changes might occur if one continues to reduce the dimensionality towards the vicinity of the critical insulating thickness. We are currently not aware of a detailed surface (and interface) analysis for films below 4 unit cells. In order to model these heterostructures to closely resemble realistic samples one would first need to survey the possible surface rearrangements, tendency towards (self-)doping, the effects of possible crystal defects, etc. Unfortunately this represents a herculean task outside the scope of this thesis. To advance the current understanding of the Mott transition in these systems, we will restrict ourselves to domains where we expect that a *pristine* model can be upheld, i.e. a clean surface (or perfect surface reconstruction), nominal filling, and no defects. Systems will be considered with either a completely flat, VO₂ terminated surface or with a fully reconstructed, perfectly ordered apical surface configuration.

The hetero-structures used here were prepared akin to Sec. 2.3.3: In the (001)-direction n layers of SrVO₃ are layered on top of 5 layers SrTiO₃ where the final termination of the surface SrVO₃ layer is VO₂. The in-plane lattice constants of the structures without apical oxygen are identically constrained to the bulk value of SrTiO₃ ($a = b = a_{SrTiO_3}$). The structures with apical oxygen on the other hand are represented via a $\sqrt{2} \times \sqrt{2}$ super cell ($a = b = \sqrt{2}a_{SrTiO_3}$) where every other surface vanadium is connected with an additional oxygen atom. In z-direction the structures are surrounded by a sufficiently large vacuum layer (roughly 20Å) in the z-direction.

The atomic force relaxation is adjusted for the vacuum termination: With the exception of the SrTiO₃ layer furthest away from the surface SrVO₃, whose atomic positions are kept fixed to imitate the transition to bulk, all atomic positions are completely relaxed using the pseudo-potential code VASP [23, 24, 25, 26]. The full-electron DFT calculation of these structures are then performed with WIEN2k [21], where we verified the consistency of the internal forces between the two codes. The down-folding to a localized vanadium t_{2g} Hamiltonian is done with the Wien2Wannier [28] interface to Wannier90 [29]. Important to note is that the applied SU(2)-symmetric Kanamori interaction is chosen to be consistent with the compressed, protected films, i.e. $U = U_{intra} = 5.25\text{eV}$, $J = 0.75\text{eV}$, $U' = U_{inter} = U - 2J = 3.75\text{eV}$, which slightly deviates from the more commonly used bulk values in literature [119] and the ones used for the bulk description in Section 2.3.2.

2.4.4.1 Surface induced crystal distortions

Both considered surface terminations are illustrated in Fig. 2.41 for the exemplary case of $x = 3$ layers. There, the atomic dislocations are directly taken from the atomic force relaxation. For our intents and purposes our analysis focuses on the resulting (vertical) V-V inter-layer and V-Ti interface distances and their effect on the residual crystal-field splitting. For all considered structures $x = 1 \dots 6$ this data is illustrated in Fig. 2.42 and Fig. 2.43.

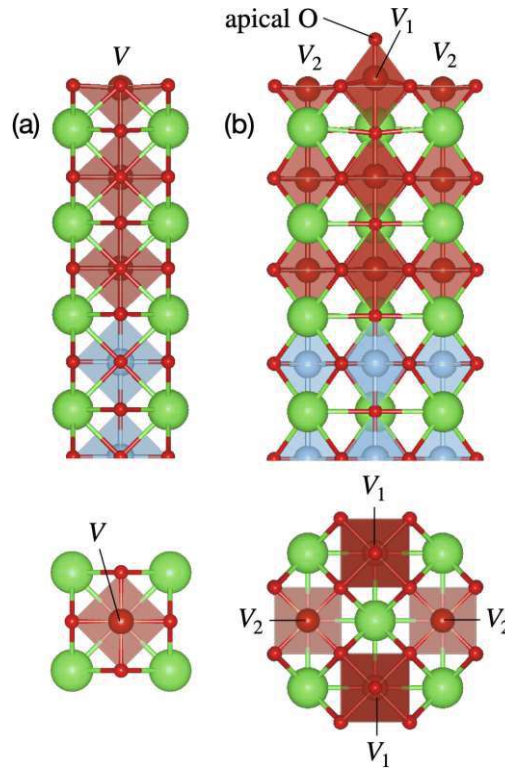


Figure 2.41: Considered (force relaxed) surface termination of unprotected thin films: $(\text{SrVO}_3)_3 | (\text{SrTiO}_3)$. Green: Sr, Small Red: O, Large Red: V, Blue: Ti. Front and top view of the (a) flat VO_2 termination and (b) the $\sqrt{2} \times \sqrt{2}$ supercell where every other surface vanadium atom V_1 is connected with an additional apical oxygen atom.

Pristine VO_2 termination

Starting off with the pristine VO_2 termination: The surface layer (layer 1) relaxes into a concave shape, i.e. the vanadium site sits slightly below the adjacent oxygen ligands leading to a localized compression of the V-V[Ti] spacing, irrespective of the number of total SVO layers.²⁰ This results in

²⁰This is opposite to the force relaxation of the SrO terminated structures. There, the surface layer relaxes into a convex shape, i.e. the vanadium site is above the adjacent oxygen ligands, elongating the V-V[Ti] spacing instead.

a surface vanadium vanadium spacing ($x \geq 2$) of $c_{V-V} \approx 3.7\text{\AA}$ and a comparable vanadium titanium spacing for the monolayer ($x = 1$) of $c_{V-Ti} \approx 3.8\text{\AA}$. The offset of 0.1\AA between $x = 1$ and $x > 1$ at $n = 1$, see Fig. 2.42a and Fig. 2.43d stems from the lattice constant mismatch between SVO and STO when simulated/relaxed with DFT using the PBE exchange-correlation potential.

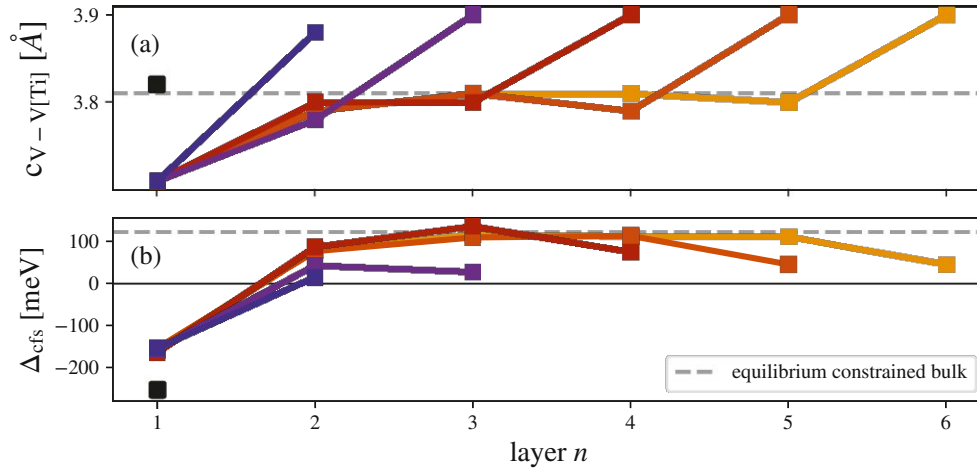


Figure 2.42: Structure analysis of $x = 1 \dots 6$ layers (shades from black to yellow) of pristine SrVO_3 on a SrTiO_3 substrate with a VO_2 termination to vacuum. The layers n are numbered in order: surface ($n = 1$) \rightarrow substrate $n = x$. (a) Internal atomic distances $c_{V-V[Ti]}$. (b) Resulting crystal-field splitting (cfs). Due to the VO_2 termination, the out-of-plane apical oxygen of the VO_6 octahedron is severed, resulting in a strong, negative crystal-field splitting. In the inner structure we find an expected, 'bulk-like' behavior with a positive cfs, resulting from the in-plane expansion/compression. Both the surface and interface effects are localized only to the first two layers.

Due to the severing of the apical oxygen in the VO_2 termination, the cfs becomes inverted, compared to the “strained bulk” case in Section 2.3.2. The missing overlap with the p_x/p_y orbitals of the now lacking oxygen atom, results in less electrostatic repulsion and therefore a lowering of the xz/yz orbital energies [5]. The monolayer displays $\Delta_{cfs}^{\text{surface}} = -250\text{meV}$ (black square in Fig. 2.42b) while the multi-layer structures display a slightly reduced $\Delta_{cfs}^{\text{surface}} = -150\text{meV}$ caused by the change of the local layer environment. The latter is more than 5 times the splitting necessary to push the equivalent bulk state insulating. As more layers are added, we see that the effect of the SrTiO_3 interface remains localized to only the adjacent SrVO_3 layer. This is manifested in an equidistant out-of-plane spacing $c_{V-V} \approx 3.8\text{\AA}$ for the “inner” layers, recovering the expected bulk value, accompanied by a modified interface c_{V-Ti} . Similarly, the effect of the vacuum termination is localized to the two top surface layers. Combining the effects in the vicinity of surface and the substrate, structures with $x \geq 4$ reach a bulk-like inner structure. There, the aforementioned surface, and interface distortions

lead to a sign switch of the crystal-field splitting: For $x = 6$, see Fig. 2.42b (orange line) the surface induced, negative cfs is already reversed in the adjacent layer ($n = 2$), after which the bulk-like $\Delta_{\text{cfs}}^{\text{bulk}} = 120\text{meV}$ is established ($n = 3 \dots 5$). Only at the interface ($n = 6$), akin to the capped layers (see Section 2.3.3) the crystal distortion is relaxed and a slight reduction in cfs occurs, approaching $\Delta_{\text{cfs}}^{\text{interface}} \approx 50\text{meV}$ for thick films. We expect this interface effect to be upheld in the $x \rightarrow \infty$ limit due to the lattice mismatch.

Apical oxygen decoration

Decorating the VO₂ surface termination with (ordered) oxygen requires the consideration of two inequivalent vanadium atoms. In order to achieve a perfectly ordered pattern, every other vanadium site is covered with an additional apical oxygen atom, resulting in a $\sqrt{2} \times \sqrt{2}$ reconstruction as described in Section 2.4.1: The vanadium below the added oxygen ($V_1 \equiv V_{\text{apical}}$) and the vanadium next to it ($V_2 \equiv V_{\text{clean}}$), see Fig. 2.36.

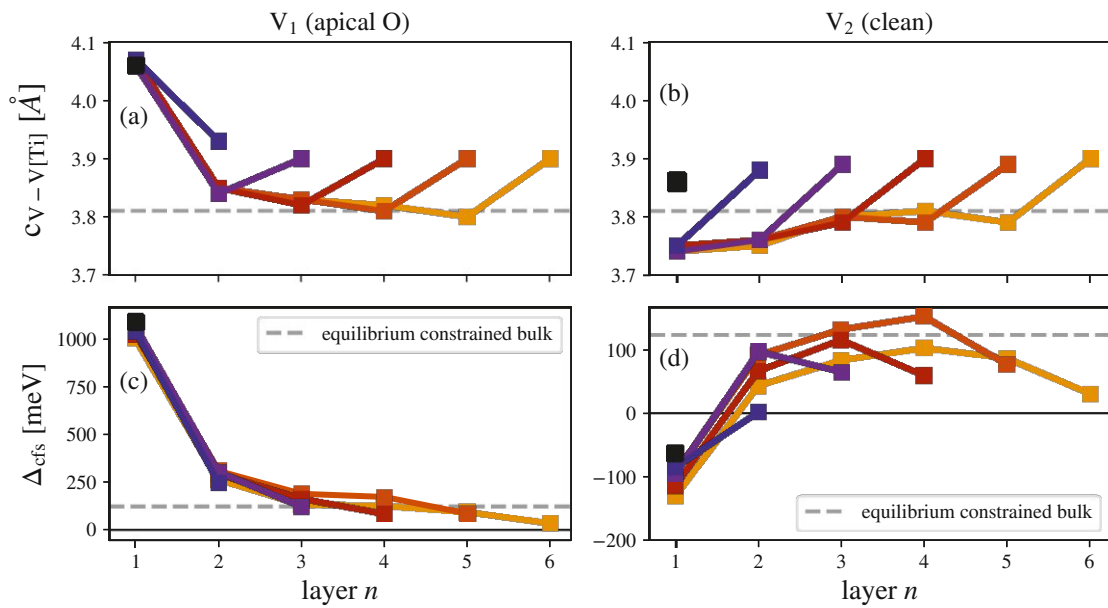


Figure 2.43: Structure analysis of $x = 1 \dots 6$ layers (shades of black to yellow) of $\sqrt{2} \times \sqrt{2}$ SrVO₃ with apical oxygen coverage. The layers n are numbered in order: surface ($n = 1$) \rightarrow substrate $n = x$. The internal atomic distances $c_{V-V[\text{Ti}]}$ (panels a-b) result in the crystal-field splitting (cfs) shown in panels c-d. The left column (a,c) describes the vanadium atom below the additional, apical oxygen (V_1) while the right column (b,d) describes the adjacent vanadium site (V_2).

The qualitative trends of the pristine sample, panels b,d in Fig. 2.43, are maintained for V_{clean} where the aforementioned cfs reversal between surface and inner structure occurs. Minor, quantitative

differences mainly stem from the adjacency to the oxygen decorated vanadium sites which experiences surprisingly large distortions in comparison. The apical oxygen “pulls” the vanadium towards the vacuum, see Fig. 2.41, resulting in a competition between the neighboring convex distortion of the “clean” vanadium. Akin to the VO_2 terminated samples, the structural effects of this bond elongation is strongly localized, having only a minor effect on the lower SVO layer. The cfs of all vanadium atoms beneath the apical oxygen is now positive throughout the structure, reaching a massive $\Delta_{\text{cfs}} \approx 1000\text{meV}$ at the surface. With the apical oxygen present, the hybridization of the surface vanadium’s xz/yz orbitals is no longer severed, increasing their local energies. The enormous orbital separation is caused by the large disparity of the Coulomb environment between the t_{2g} orbitals: The xz/yz orbitals now experience a Coulomb repulsion from p_x/p_y orbitals of the apical oxygen without the balancing effect of the (missing) strontium (Coulomb attraction via the Sr^{2+} ions), that would form the complete SrO layer. Combined, the surface vanadium site polarizes fully into a purely xy -character. In the layers below, on the other hand, the normal bulk-like environment is quickly established. Below the third layer ($n = 3$) we find no longer any significant difference between the adjacent “apical” and “clean” vanadium sites.

2.4.4.2 DMFT validation via the 6uc structure

Having established the crystal distortions and crystal-field characteristics in the *unprotected*, SrVO_3 layers, deposited on a SrTiO_3 substrate, we now investigate how the electronic structure is affected by many-body effects, using DMFT. As a starting point, we analyze the structures that *approximate* the experimental samples considered in Section 2.4.3: $x = 6$ layers of SrVO_3 with either a “clean” surface or a fully reconstructed surface with ordered oxygen, i.e. 50% coverage.

The (multi-impurity) DMFT setup for the various layer thickness x is similar to Section 2.3.3: We employ a slightly enhanced Kanamori interaction with $U = 5.25\text{eV}$ ($J = 0.75\text{eV}$, $U' = U - 2J = 3.75\text{eV}$) and no inter-impurity interaction, resulting in the self-energy orbital structure, as shown in Eq. (2.74). The interaction strength is larger than the bulk value, see Section 2.3.2, in order to compensate for the uncertainty in the Wannierization procedure²¹ and the difficulties involving converging insulating DMFT solutions ($x < 3$, see next Section) with several impurities whose local levels differ strongly. The results of the DMFT treatment at room temperature $T = 290\text{K}$ is shown in Fig. 2.44.

²¹ We find strong band entanglement of the unoccupied vanadium d, titanium d and strontium d states. Projecting onto a purely vanadium t_{2g} basis, the minimization procedure of Wannier90 is highly sensible with respect to the initial energy window and the number of bands used.

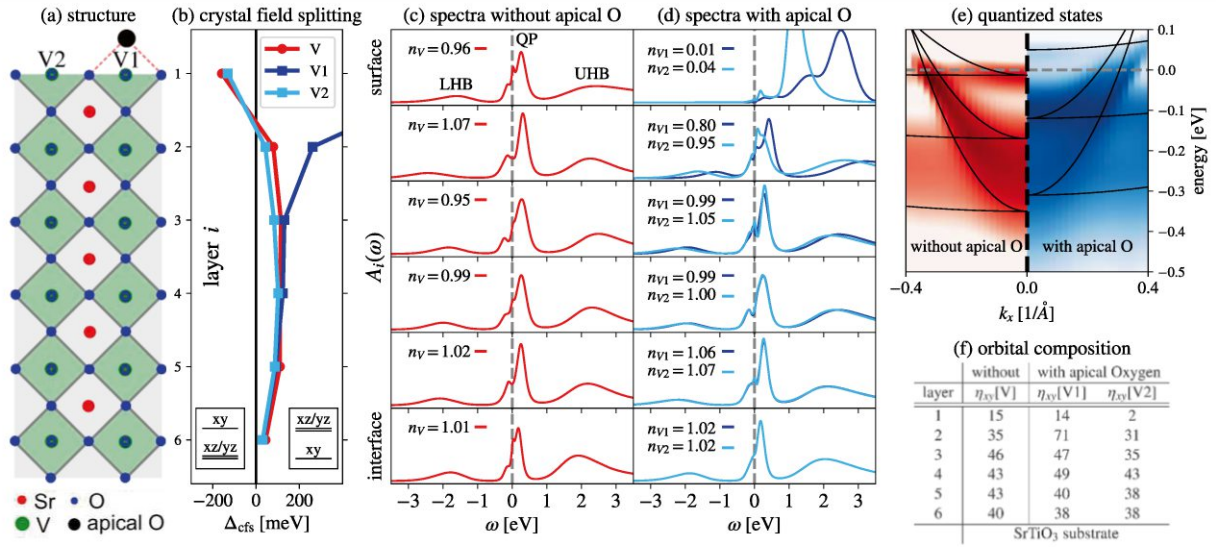


Figure 2.44: a) Sketch of the calculated 6 uc heterostructure. b) Crystal field splitting Δ_{cfs} of the vanadium t_{2g} orbitals from DFT. With an apical oxygen (black dot) there are two inequivalent vanadium sites “V1” and “V2” per layer, without they are equivalent and denoted by “V”. The corresponding local orbital energy levels are illustrated in the two insets. The crystal field splitting of “V1” in the two topmost layers is a direct result of the apical oxygen. At the surface layer the crystal field splitting for “V1” is 1 eV which is outside the drawn energy range. c,d) Layer(i)-resolved DMFT spectral functions $A_i(\omega)$ for 6 uc SVO (c) without and (d) with apical oxygen. e) Quantized states along the k_x direction ($k_y = 0$) in the structures with and without apical oxygen (lines are obtained from parabolic fits to the second derivative of the shown intensity map). f) Orbital composition of the different vanadium sites as the percentage of the xy occupation $\eta_{xy} = \frac{n_{xy}}{n_{xy} + n_{xz} + n_{yz}}$ for the layers from top to bottom. The proportion of the xz/yz orbital can be obtained *via* $\eta_{xz/yz} = (1 - \eta_{xy})/2$.

The spectral functions in Figure 2.44c are metallic for all layers with the usual three-peak structure. All vanadium sites can be roughly described with a nominal d^1 configuration (i.e., V^{4+}). However, because of the layer-dependent crystal field splitting Δ_{cfs} the orbital compositions differ vastly, see Fig. 2.44f. With apical oxygen, the crystal field splitting for “V2” is quantitatively similar to the case without oxygen in Fig. 2.44b. The splitting for vanadium ions “V1”, however, is dramatically changed, even inverted, near the surface. In all, apical oxygen-induced changes in the crystal and electronic structure are confined to the uppermost two layers, see the DMFT spectral functions in Figure 2.44d (cf. also Section 5 in the Supporting Information for calculations on films of different thicknesses). Whereas the third to sixth layer are practically identical to the case without apical oxygen in

Figure 2.44c, the top layer shows dramatic qualitative changes: it is insulating and contains only pentavalent vanadium with a d occupation $n_{V_{1,2}} \approx 0$, *i.e.*, no occupied states below the Fermi level at 0 eV (see Fig. 2.44d, top row). The apical oxygen drains one electron from each of the two vanadium sites in the top layer, whereas the subsurface layers are again close to a V^{4+} configuration except for the V1 site of the second layer which has $n_{V_1} = 0.8$. With the apical oxygen draining all electrons from the surface layer, it becomes a dead (insulating) layer. The other layers then essentially behave as the film without apical oxygen but with one layer –the dead one– less. Because of the confinement to five layers (six without apical oxygen), quantum well states as shown in Fig. 2.44e develop [109] which closely mirror the ARPES spectrum shown in Fig. 2.38c.

Let us note, that the observed changes in the photoemission line shape, see Section 2.4.3.3, is beyond the considered DMFT setup. As a firm, metallic state is recovered for all vanadium sites in the structure without apical oxygen and all vanadium site below the dead-layer in the structure with apical oxygen, we find no evidence of a quasi-particle suppression between the two scenarios.

2.4.4.3 Metal-insulator transition and dead-layer phenomenon

As DMFT provides a reasonable good description when including strong correlations we now re-analyze [86] the critical thickness of the metal-insulator transition: We focus on $x = 2, 3, 4$ layers of $SrVO_3$, see Figure 2.45, as a critical thickness of $x = 2$ has been observed. As alluded to in Section 2.3.3, in the monolayer the xz/yz orbital experience a complete restriction of the out-of-plane hopping, significantly decreasing their band width to roughly $W_{xz/yz} \approx 1\text{eV}$. Irrespective of surface termination (capping, SrO to vacuum, VO_2 to vacuum), the Mott transition in the monolayer is purely band-width driven. In a similar vein, a complete surface reconstruction, *i.e.* apical oxygen decoration on every other vanadium site, on top of the monolayer leads to a complete depopulation of the vanadium 3d states. A DMFT treatment then becomes redundant as the system develops a band gap already within density functional ($\Delta_{\text{DMFT}} \approx 0.3\text{eV}$, data not shown). The results of the DMFT treatment at room temperature $T = 290\text{K}$ are shown in Fig. 2.45, where we illustrate the layer-dependent spectral function including their respective vanadium occupation n_V . The structures $x = 2, 3, 4$ are plotted as the columns whose layers are ordered from surface (top) to interface (bottom).

Pristine VO_2 termination

The structures *without* apical oxygen, see Figure 2.45a, experience a metal-to-insulator transition between $x = 2$ and $x = 3$. The insulating state at $x = 2$ is characterized by a gap of around $\Delta = 0.2\text{eV}$ and essentially a d^1 occupation in both layers. This insulating state breaks down for

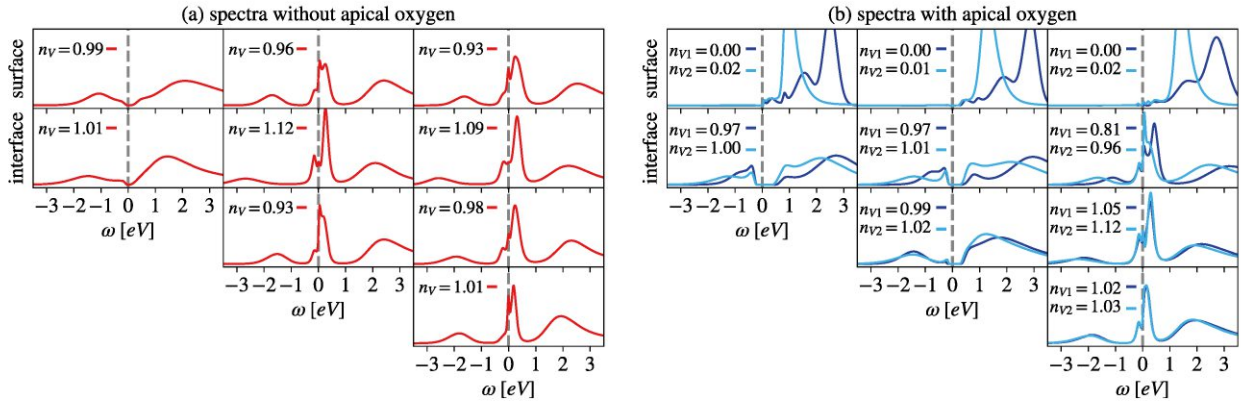


Figure 2.45: a) Layer-dependent DMFT valence spectra for the structures without apical oxygen for $x = 2, 3, 4$ layers of SVO. b) Layer- and site-dependent DMFT valence spectra for the structures with apical oxygen for $x = 2, 3, 4$. Each structure is represented by a vertically ordered array of x spectral functions, where the top row always represents the surface layer which is also an interface to the vacuum. The metal-to-insulator transition occurs between 2 and 3 layers for the structures without apical oxygen and between 3 and 4 for the structures with apical oxygen. Independent of the overall electronic state we find an electronically dead surface layer for the structures with apical oxygen.

the $x = 3$ and $x = 4$ structures where deviation from the the nominal d^1 occupancy occur in the individual layers.

Adding additional layers causes first and foremost a xz/yz inter-layer hopping induced band width widening, quantitatively almost identical to capped films. Contrary to the homogeneous crystal-field splitting observed there ($\Delta_{\text{cfs}}(n) > 0 \forall n \in \{1 \dots x\}$, x : number of layers), instead a competition emerges through the cfs inversion along the z -direction: The negative cfs on the surface effectively reduces the vanadium's three-orbital state to a two-orbital one which, in combination with the large on-site interaction, provides the fundamental mechanism that tries to drive the system towards a Mott insulator. Irrespective of the overall electronic state, the surface layer becomes heavily orbitally polarized, with $n_{xz/yz,\sigma}$ close to quarter filling, see Table 2.6.

This surface polarization then “competes” with the lower lying layers as the electronic states of the different layers heavily influence each other via layer-to-layer hybridization. For $x = 2$, the interface layer experiences little to no degeneracy lifting through the cfs, see Fig. 2.42b, establishing a competition between the fully polarized surface and an, effectively, orbitally degenerate interface. As Fig. 2.45 illustrates, the metallicity inducing hybridization is overcome and a Mott insulating state is established. Please note that, similar to Section 2.3.2 at room temperature, the insulating solution is difficult to stabilize: From a metallic seed ($\Sigma = 0$), DMFT always converges into a metallic

$x =$	1 [Mott]	2 [Mott]	3 [Metal]	4 [Metal]
surface	[0.000 0.250]	[0.001 0.246]	[0.077 0.200]	[0.068 0.198]
⋮		[0.205 0.150]	[0.180 0.190]	[0.197 0.174]
⋮			[0.192 0.137]	[0.233 0.129]
interface				[0.218 0.143]

Table 2.6: Site-resolved DMFT orbital occupations $[n_{xy,\sigma}|n_{xz/yz,\sigma}]$ in the structures *without* apical oxygen, calculated with $U = 5.25\text{eV}$ ($J = 0.75\text{eV}$, $U' = 3.75\text{eV}$) at room temperature $T = 290\text{K}$. Structures with $x = 1$ and $x = 2$ stabilize a fully polarized, quarter-filled surface vanadium site $n_{xz/yz,\sigma} \approx 0.25$, pushing the whole system Mott insulating. Metallicity emerges at $x = 3$ and beyond, accompanied by a drop of this surface polarization.

solution. In order to overcome this tendency, we stabilized the Mott insulator with an enhanced $U = 6$ ($J = 0.75\text{eV}$, $U' = 4.5\text{eV}$), after which we, step-by-step, reduce the interaction strength in order to maintain the insulating state. Fig. 2.45a, $x = 2$ then represents the solution for the aforementioned $U = 5.25\text{eV}$. Note however, that this is not the upper boundary for the $x = 2$ heterostructure: we find $U_c \leq 5.15\text{eV}$ (not shown). For the sake of consistency we have chosen to apply $U = 5.25\text{eV}$ for all considered heterostructures in this Section.

The resulting spectral function with its DMFT spectral gap $\Delta_{\text{DMFT}} = 200\text{meV}$, resembles the photoemission spectra ($\propto A(\omega)f_{FD}(\omega;T)$, $f_{FD}(\omega;T)$: Fermi function at temperature T) from Fig. 2.40 surprisingly well. Adding a third layer, the additional out-of-plane hybridization becomes too “overbearing” and the surface polarization can no longer overcome the pull towards metallicity: The spectral functions of all layers turn metallic simultaneously and the strong orbital polarization is slightly lifted, see Table 2.6. Please note that even for $U = 6\text{eV}$ the $x = 3$ heterostructure without apical oxygen (and all larger ones $x \geq 4$) remains firmly metallic when initializing the DMFT with a metallic seed (not shown).

Apical oxygen decoration

The heterostructures with apical oxygen, see Figure 2.45b, on the other hand exhibit a metal-to-insulator transition between $x = 3$ and $x = 4$. All considered cases with apical oxygen exhibit an electronically dead surface layer, independent of the electronic behavior of the SrVO_3 layers beneath it. Please note that this dead layer is *not present* in DFT, where the surface layer vanadium exhibits an average filling of $n \approx 0.3$. Only through the added interaction is the system able to repel the rest of this filling and distribute it amongst the lower lying layers. We argue that this dead surface layer causes an effective reduction of the structure’s thickness, thus increasing the numbers of layers

necessary to stabilize the metallic solution. Again, the insulating structures ($x = 2$ and $x = 3$) display essentially the ideally expected d^1 configuration for all vanadium sites except for the 'dead' surface. Similar to the $x = 3$ structure without apical oxygen, the metallic state for the $x = 4$ structure is accompanied by a larger variation of the d -occupation among the layers.

In these structures *with* apical oxygen, a similar cfs mechanism emerges. For both inequivalent vanadium sites the surface becomes the primary driver of the insulating state. The orbital polarization differs between the inequivalent sites: the negative cfs of the clean vanadium is identical to the VO₂ terminated structure, whereas the apical oxygen induces a strong, positive cfs. The electronic surrounding of the latter is akin to a SrO termination [5, 86, 175]. The insulating driving forces are hence more nuanced: Having reduced the effective thickness by depopulating the surface layer, the layer adjacent to the surface now tries to drive the system into an insulating state. The vanadium sites below the apical oxygen (V_1) *all* polarize strongly towards a one-band state (half-filled xy band: $n_{xz,\sigma} \geq 0.47$), in accordance with the sign of the crystal-field splitting, see Table 2.7. The "clean" vanadium sites, on the other hand, prefer the occupation of the xz/yz orbitals, despite the *positive* cfs below the surface. We theorize that this is a result of the strong crystal distortions below the apical oxygen and the electronic interplay between the adjacent vanadium sites in the Mott insulating state.

Once the system is too large $x \geq 4$, the strong orbital polarization breaks down at all vanadium sites and metallicity emerges, see Fig. 2.45b. The layer-dependent spectral functions turn metallic simultaneously, except for the surface layer whose vanadium sites remain depleted and the dead-layer persists. Orbital occupations emerging from this electronic state now more closely reflect the crystal-field splittings in Fig. 2.43c and Fig. 2.43d, i.e. $n_{xy,\sigma} > n_{xz/yz,\sigma}$ at all vanadium sites below the surface, see Table 2.7.

$x =$	2 [Mott]	3 [Mott]	4 [Metal]
surface	[0.001 0.000]—[0.001 0.004]	[0.000 0.000]—[0.001 0.004]	[0.000 0.001]—[0.000 0.006]
⋮	[0.483 0.003]—[0.022 0.240]	[0.480 0.002]—[0.084 0.209]	[0.305 0.049]—[0.168 0.155]
⋮		[0.481 0.008]—[0.131 0.188]	[0.259 0.133]—[0.201 0.179]
interface			[0.257 0.125]—[0.210 0.154]

Table 2.7: Site-resolved DMFT orbital occupations $[n_{xy,\sigma}|n_{xz/yz,\sigma}]_{V_{apical}} - [n_{xy,\sigma}|n_{xz/yz,\sigma}]_{V_{clean}}$ in the structures *with* apical oxygen, calculated with $U = 5.25\text{eV}$ ($J = 0.75\text{eV}$, $U' = 3.75\text{eV}$) at room temperature $T = 290\text{K}$. Irrespective of the electronic state, a "dead" surface layer develops with $n_{i,\sigma} \approx 0$. In the Mott insulating state ($x = 2$, $x = 3$), both inequivalent vanadium sites orbitally polarize: vanadium below the apical oxygen forms a half-filled state in the xy-band $n_{xy,\sigma} \approx 0.5$, the (lateral) adjacent vanadium is close to quarter-filling $n_{xz/yz,\sigma} \approx 0.25$. Beyond $x = 4$ metallicity emerges and the orbital polarization drops at all vanadium sites in the structure. $x = 1$ is not shown as the structure is already insulating within DFT.

2.4.4.4 Metal-insulator transition validity against experiment

Viewed together, the two extreme cases of either a clean surface (VO_2 termination) or an ordered surface with additional apical oxygen in the $\sqrt{2} \times \sqrt{2}$ formation, theoretically, support a metal-insulator transition with critical thickness 2 – 3. Contrary to the homogeneous crystal-field splitting (in combination with a slight band width reduction) observed in *protected* thin films, see 2.3.3, here the surface dominates the electronic structure, inducing strong differences between the various vanadium sites. Evidently, the metal-insulator transition is triggered by a strong polarization stemming purely from the surface which turns the whole system insulating, at least within DMFT.

As we have established in Section 2.4.3, however, thin films deposited via PLD are more nuanced and display a wide range of electronic phenomena that we have not taken into consideration. Despite this, the insulating mechanism evidenced above can be viewed as a reasonable starting point towards more realistic modelling of unprotected SrVO_3 heterostructures: The thin films experience at a minimum, a lateral phase separation, see Section 2.4.3, that is strongly dependent on the thickness of the sample. Revisiting Fig. 2.40, the experimental metal-insulator transition is further accompanied by a continuous suppression of the ratio QP : LHB when moving from $x = 75$ to $x = 2$. This is possibly a side-effect of the evolution of the reduction of apical oxygen coverage upon reducing the number of layers, see Section 2.4.2. That is, fewer layers lead to less oxygen absorption which leads to a more broadened valence spectrum. Indeed, the same analysis performed for $x = 3$ (comparing the surface with and without apical oxygen) leads to a similar change of the extracted d -occupation via the V2p composition or the integral V3d weight (private communication with Judith Gabel; not shown). However, the change of the shape of the quasi-particle contribution in the PES spectrum is less severe than in the $x = 6$ sample. At this $x = 3$ structure, assuming a coexistence between areas with and without apical oxygen, it is therefore doubtful that parts of the sample are already turned insulating as the quasi-particle peak of the UV cleaned sample is less coherent compared to the sample measured with surface oxidization.

Once both the “clean” and ordered surface turn Mott insulating below $x = 2$ any potential doping from the remaining, non-ordered oxygen adatoms *may* be fully localized, maintaining the d^1 occupation on the vanadium sites, vital for the Mott scenario in DMFT. In turn, it is possible for the system to become insulating on the full macroscopic scale, resulting in a spectral gap determined by the “clean” surface, see Fig. 2.45, as $\Delta_{\text{DMFT}}(x = 2, \text{clean}) < \Delta_{\text{DMFT}}(x = 2, \text{apical})$.

This scenario is, however, speculation on our end: Open questions/scenarios that need to be answered/investigated include

- (i) the effect of possible unordered apical oxygen onto the electronic state,
- (ii) the influence of the SrTiO_3 substrate that include vacancies or (as of yet) unaccounted distur-

tions as seen in Section 2.3.3,

- (iii) the possibility of additional surface reconstructions as seen in Ref. [172], and
- (iv) a p-doping analysis for samples with fewer than $x = 6$ layers, especially in the insulating regime below $x = 3$.

2.4.5 Discussion

Viewed together, our theoretical and experimental results provide a detailed picture of the adsorption of oxygen at the apical sites of SVO films and its impact on their electronic properties. The DMFT calculations consider the limiting case where every second vanadium in the film surface is decorated with an apical oxygen. They show that at this coverage the $3d$ shell of the V atoms in the topmost layer is completely depleted while the d^1 occupation of all layers beneath remains virtually unaffected. For the 75 uc thick SVO film, whose apical oxygen coverage matches the supposition of the DMFT calculations, the formation of a complete d^0 layer at the surface is indeed observed experimentally in our depth-dependent XPS measurements.

We also find a d^0 phase forming in the surface layer of the 6 uc SVO film when decorated with apical oxygen. However, it does not cover the entire surface. We observe additionally a slight electron depopulation of the metallic regions driven by the presence of apical oxygen. The latter observation is elusive to our calculations which assume a full coverage of apical oxygen in an ordered $\sqrt{2} \times \sqrt{2}$ R(45°) arrangement. Here it is interesting to note that the fractional order LEED reflections in Figure 2.37c are weaker for the 6 uc SVO film than for the 75 uc one, suggesting that, unlike the much thicker film where the coverage of the $\sqrt{2} \times \sqrt{2}$ R(45°) reconstruction is more complete, the surface of the 6 uc SVO film should have regions covered by apical oxygen ions that do not follow the same long range order as well as regions covered by less apical oxygen. There, the local lattice distortion and thus the crystal field splitting may be reduced and favor light p doping of the film instead of complete depletion of the d band of the surface layer.

Beside the change in the d occupation, we also observe that the V $3d$ spectral shape begins to evolve upon the desorption of apical oxygen. With the V $3d$ weight exclusively originating from the metallic domains, this indicates a variation in their electronic properties. In particular, the apparent increase in the ratio of the LHB and QP weights may signal increased correlations in the absence of apical oxygen, which might be partly explained by the d occupation being driven closer to an integer filling.

Furthermore, the topmost layer of the SVO film can exhibit enhanced correlations due to reduced coordination numbers [79, 174] and thus a different QP to LHB ratio from the bulk. The presence of d^0 domains in the topmost layers of the film with adsorbed oxygen will suppress this surface contribution and alter the $V 3d$ spectral function. Alternatively, defects in the topmost layer may lead to enhanced scattering and hence broadening of the QP feature. When d^0 domains develop with the adsorption of apical oxygen, surface defects are shielded by the dead layer, scattering becomes less important, and the $V 3d$ line shape will feature a sharper QP peak.

We have demonstrated that the presence of apical oxygen has a strong bearing on the electronic properties of ultrathin SVO films in terms of the layer-dependent crystal-field splitting, d occupation, number of quantum well states, and orbital composition. In addition, we observe electronic phase separation, in both lateral and vertical directions, into metallic and insulating domains.

Since the apical oxygen is present also on SVO films only handled in ultrahigh vacuum and changes the electronic structure in the same thickness range in which also the transition from a correlated metal into a Mott insulating phase occurs (see Ref. [85]), it is a natural step to link these two phenomena. While we can safely assert that the metal-insulator transition is influenced in many ways by surface chemical effects and that a description within a simple Mott type scenario falls short, a full understanding of the complex interplay between the thickness-dependent electronic transition and the adsorption of apical oxygen requires further studies and is beyond the scope of the present work.

2.5 Non-local signatures in pristine SrVO₃ monolayers

- This Section combines the results of “Zoology of spin and orbital fluctuations in ultrathin oxide films” by [Matthias Pickem](#), Josef Kaufmann, Karsten Held, and Jan M. Tomczak [5] and “Particle-hole asymmetric lifetimes promoted by non-local spin and orbital fluctuations in SrVO₃ monolayers” by [Matthias Pickem](#), Jan M. Tomczak, and Karsten Held [10]. The adopted text passages are marked accordingly.
- The diagrammatic introduction to the (Abinitio) dynamical vertex approximation was initially published in Ref. [33]. This introduction has been compiled based on an equivalent, more detailed derivation from my master thesis [176].
- Two-particle results beyond DMFT were obtained with the `AbinitioDFA` package published as “The `AbinitioDFA` Project v1.0: Non-local correlations beyond and susceptibilities within dynamical mean-field theory” by Anna Galler, Patrik Thunström, Josef Kaufmann, [Matthias Pickem](#), Jan M. Tomczak, and Karsten Held [2].

In this Section we are going to study the quasi two-dimensional SrVO₃ monolayer. In the bulk crystal, the t_{2g} orbitals overlap in 2 spatial directions resulting in a 2D like density of states with its corresponding van Hove singularity above the Fermi level, see Fig. 2.6b. Truncating these orbitals by a double-sided termination to vacuum and the SrTiO₃ interface leads to qualitative changes to the density of states of the out-of-plane, xz/yz orbitals. The xz/yz orbitals become one-dimensional as one hopping direction is fully suppressed, fully transforming the shape of the density of states. In turn, different van Hove singularities are generated, proximity towards which are known to promote non-local signatures in the self-energy [177].

As we already alluded to above, this geometry-induced quenching of kinetic energy is the primary driving factor for the insulating state in the SrVO₃ monolayer. Here, we are first going to detail the stability of this bandwidth mechanism, after which we consider the possible emergence of long-range ordered phases, so far ignored by our DMFT calculations. To this end we transition from the one-particle to a two-particle description, necessary to study spin and charge responses and, ultimately, also non-local correlations via the dynamical vertex approximation (DFA). Indeed, the latter builds upon DMFT and introduces non-local corrections to the self-energy via momentum dependent two-particle vertex functions.

For the monolayer system we consider both the VO₂ and the SrO surface termination: the former being the result of the commonly employed SrVO₃ epitaxy deposition. The latter has to our knowledge

hitherto not been achieved experimentally, however would be the preferable configuration due to being less prone to surface overoxidation.

Both terminations are modelled on top of a substrate of six unit cells of SrTiO₃ surrounded by sufficient vacuum of around 10Å in z-direction. Whereas the SrO termination is modelled with one unit cell of SrVO₃, the VO₂ termination is modelled with one half of a unit cell, see insets in Fig. 2.55). In both setups the transition between SrTiO₃ and SrVO₃ consists of a TiO₂ - SrO - VO₂ interface, consistent with experiment [112, 157], while the other end of the SrTiO₃ substrate is terminated via SrO to vacuum. Identical to all previous SrVO₃ | SrTiO₃ heterostructures, we initialize the in-plane lattice constant with the PBE-optimized value for bulk SrTiO₃ $a_{\text{SrTiO}_3} = 3.95\text{\AA}$. To treat the surface properly the two unit cells of SrTiO₃ furthest away from SrVO₃ are then constrained to a_{SrTiO_3} , simulating the transition to the SrTiO₃ bulk, while all other internal atomic positions are fully relaxed, purely within density functional theory.

The DMFT setup is consistent with all previous simulations, i.e. we project onto maximally localized V- t_{2g} orbitals, using the WIEN2Wannier [28] interface to Wannier90 [29], see Fig. 2.46. These Wannier Hamiltonians are supplemented with an effective SU(2)-symmetric Kanamori interaction of $U = 5\text{eV}$, $J = 0.75\text{eV}$, $U' = 3.5\text{eV}$. In the following, deviations from the nominal d^1 filling are generated purely by a shift of the chemical potential. The Hamiltonians themselves are kept constant under doping.

2.5.1 Band structure and density of states

Both, SrO and VO₂-terminated films result in similarly looking DFT band structures whose relevant orbitals around the Fermi level are of vanadium t_{2g} character, see Fig. 2.46. The densities of states (DOS) of these orbitals showcase the abrupt surface termination of the sample: While the xy -projection (blue line) keeps its two-dimensional character (as in bulk SrVO₃) the (locally degenerate) xz - and yz -projections (green lines) now become one-dimensional and, concomitantly, display a strongly reduced bandwidth. Consequently a van-Hove singularity emerges, which, at zero doping, is in close proximity to the Fermi level. Indeed, in the VO₂ (SrO) terminated system this singularity is situated slightly below (above) the Fermi level. On top of this dimensionality reduction we find the crystal-field splitting (cfs)

$$\Delta_{\text{cfs}} = E_{xz/yz} - E_{xy}, \quad (2.80)$$

to have opposite signs for the two different setups: The *positive* cfs of the SrO terminated monolayer, $\Delta_{\text{cfs}} = +0.13\text{eV}$, is a direct result of the tensile strain caused by the (in-plane) lattice mismatch between SrVO₃ and SrTiO₃ ($a_{\text{SrVO}_3} < a_{\text{SrTiO}_3}$). The in-plane expansion triggers a structural com-

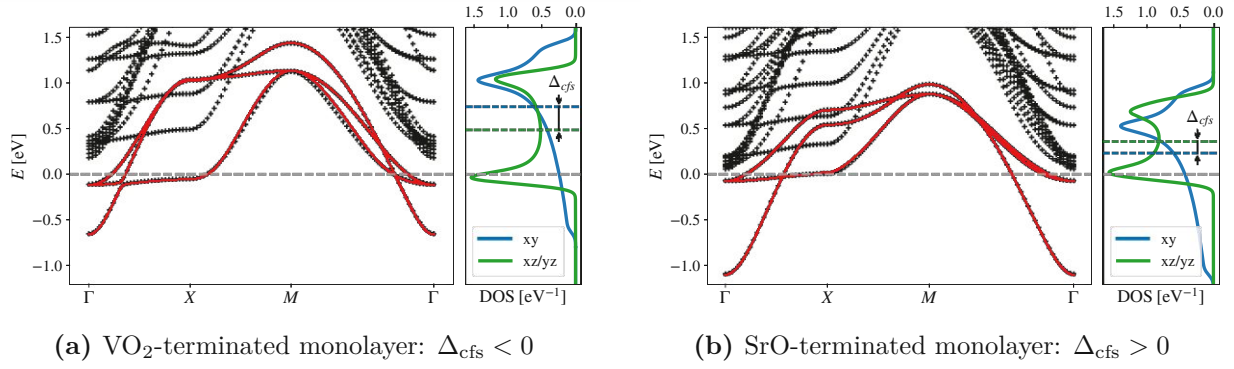


Figure 2.46: Band structures and density of states. (a) VO₂ and (b) SrO terminated monolayer. Left: DFT band structure along a momentum path through the Brillouin zone (black dots) overlain with the t_{2g} -orbital projected Wannier dispersion (red lines). Right: the resulting density of states (DOS) clearly shows the (quasi-) 2D character of the xy -orbital (blue) and the 1D character of the locally degenerate xz/yz -orbitals (green). The local orbital energy levels are marked as dashed horizontal lines in the DOS. We find a crystal field splitting of $\Delta_{\text{cfs}} = -0.252\text{eV}$ for the VO₂ terminated layer and $\Delta_{\text{cfs}} = +0.126\text{eV}$ for the SrO terminated monolayer.

pression in the perpendicular direction, so as to keep the volume approximately constant.

This structural anisotropy translates into an electronic anisotropy [178]: The evident breaking of the cubic symmetry of SrVO₃ lifts the three-fold t_{2g} degeneracy, making the xy -orbital energetically favorable. The same effects take place in the VO₂ terminated monolayer as well. There, however, the geometric distortion gets overcompensated by the missing SrO layer: severing the apical oxygen of the transition metal coordination octahedron results in a reversed, *negative* $\Delta_{\text{cfs}} = -0.25\text{eV}$. The xz/yz orbitals have their lobes pointing in the z -direction, towards the lobes of the oxygen p_x/p_y orbitals. The missing overlap to the absent apical oxygen leads to less electrostatic repulsion, thus lowering the energy required to occupy these states. Another contributing factor is the abrupt termination to vacuum, removing any restriction in the positive z -direction for the structural relaxation: The VO₂ (SrO) terminated system results in a concave (convex) final termination, i.e., the last VO₂ (SrO) layer bends inwards (outwards). For both systems we find almost identical xy orbitals with a nearest-neighbor hopping $t_{xy} \sim -230\text{meV}$, next-nearest-neighbor hopping $t'_{xy} \sim -70\text{meV}$ and bandwidth $W_{xy} \sim 2.1\text{eV}$. The xz and yz orbitals of both systems, on the other hand, can be described purely by nearest-neighbor hopping along the x or y direction, respectively: The VO₂-terminated monolayer allows for a large hopping amplitude ($t_{xz/yz} \sim -300\text{meV}$), resulting in a slightly larger bandwidth $W_{xz/yz} = 1.2\text{eV}$ in Fig. 2.46a, compared to only $W_{xz/yz} = 0.95\text{eV}$ ($t_{xz/yz} \sim -200\text{meV}$) for the SrO-terminated monolayer in Fig. 2.46b.

2.5.2 Stoichiometric Mott insulator

Next, we analyze the electronic structure for the stoichiometric samples ($n = 1$) on the many-body level, using DMFT at room temperature $T = 290\text{K}$: While in the VO_2 -terminated monolayer (Fig. 2.47a) the out-of-plane xz/yz -orbitals realize a *quarter-filled* Mott insulator with a gap of 0.5eV , in the SrO terminated monolayer (Fig. 2.47c) the in-plane xy -orbital hosts an essentially *half-filled* canonical Mott insulator with a gap of 1.2eV . This difference can be traced back to the bare crystal-fields. Indeed, DMFT amplifies the effect of the DFT cfs for both terminations, leading to the depletion of the energetically higher lying orbital(s), i.e., the xy and the xz/yz orbital(s) for the VO_2 and SrO termination, respectively. This correlation-enhanced orbital polarization [62] leads to an effectively reduced orbital-degeneracy. As a consequence, charge (inter-orbital) fluctuations are suppressed and the critical interaction for reaching the Mott state diminishes [119, 149, 179]: The Coulomb interaction is large enough to open a Mott gap in the SrO (VO_2) terminated monolayer with a single (two-fold) degenerate lowest orbital, while three-fold orbitally degenerate bulk SrVO_3 is a stable metal. Let us note that the evidenced orbital polarization persists when including charge self-consistency, which only yields minor corrections because charge is only redistributed between orbitals, not between sites [99].

However, for both terminations the insulating behavior is actually driven by a *combination* of the crystal-field splitting [86] and the reduced band-widths [85]. Whereas the crystal-field splitting is essential for the bilayer system [86], we find that the bandwidth reduction alone is sufficient to drive the monolayers insulating. We illustrate this in Fig. 2.47b and Fig. 2.47d where we take the original Hamiltonians and set the cfs artificially to zero by shifting the local orbital energies. Both systems remain insulating in DMFT. Unswayed by the cfs, however, the Mott gaps turn out smaller and orbital occupations (in both cases: $n_{xy,\sigma} > n_{xz/yz,\sigma}$) only reflect the asymmetry of the orbitals' DOS. Let us note here that if we instead keep the cfs unchanged and adjust the xz/yz -bandwidths such that $W_{xz/yz} = W_{xy}$ both systems remain firmly metallic.

To investigate the stability of the insulating state further, we perform DMFT calculations for various intra-orbital interaction strengths U . While keeping the Hund's coupling J fixed to 0.75eV , we adjust the inter-orbital interaction strength U' according to spherical symmetry ($U' = U - 2J$) [180]. Note that, in contrast to U , J is hardly screened so that there is much less uncertainty and ambiguity than for U . Fig. 2.48 shows the orbital occupations depending on the interaction U : Starting from our standard value $U = 5\text{eV}$ (vertical dashed line), going to larger interaction strengths simply stabilizes the insulating solution further, while also increasing the orbital polarization slightly. Smaller interaction strengths on the other hand, reduce the orbital polarization until, eventually, the insulating

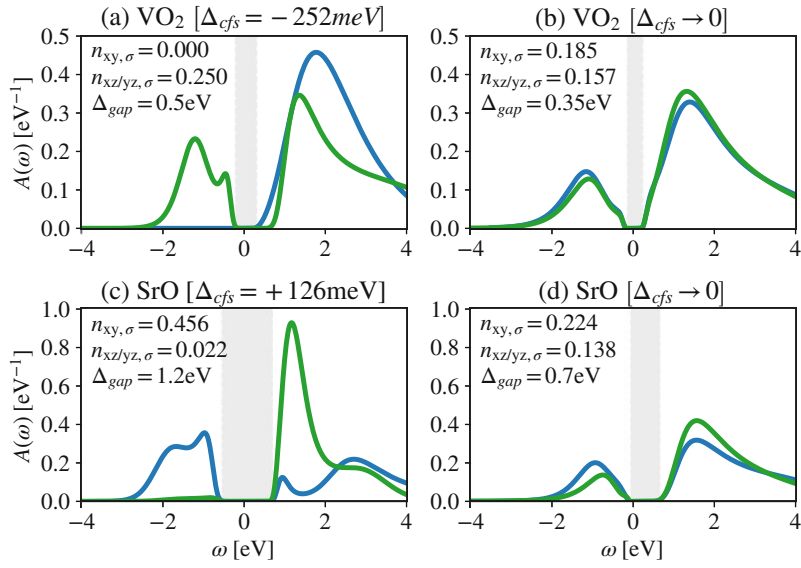


Figure 2.47: Mott insulating ground state. DMFT spectral functions $A(\omega)$ for (a) the VO₂ terminated and (c) the SrO terminated structure at $U = 5\text{eV}$ and room temperature ($T = 290\text{K}$). In both cases a wide Mott gap forms which is accompanied by a strong orbital polarization. Removing the crystal-field splitting, the reduced bandwidth alone results in a Mott insulator (b,d) with a slightly smaller band gap.

solution can no longer be stabilized. This metal-to-insulator transition is, as expected within DMFT, of first order (hysteresis or coexistence regime marked in gray in Fig. 2.48) and manifests itself by a sudden drop of the orbital polarization. The Mott insulating state is stable down to $U = 4.5\text{eV}$ ($U = 4.1\text{eV}$) for the VO₂ (SrO) terminated monolayer.

The stability of the stoichiometric Mott insulating solution is in particular important when doping away from it, see Sec. 2.5.3. As long as the stoichiometric sample is insulating, we expect that any variation of the interaction will have no qualitative impact on the DMFT phase diagram. A smaller on-site repulsion will merely lead to weaker orbital polarizations and shifted boundaries in the phase diagrams, Fig. 2.55a,b.

On top of the Mott physics discussed here, weak localization through disorder may play an additional role in the insulating behavior of transport properties [112]. However, the suppression of the one-particle spectra for thin films [85], magneto-transport results for SrVO₃ thin films on an LSAT substrate [181] as well as SrVO₃/SrTiO₃ superlattices [182] argue against a dominant weak localization scenario for the insulator. Similar observations have been made for CaVO₃ thin films on SrTiO₃ substrate [183].

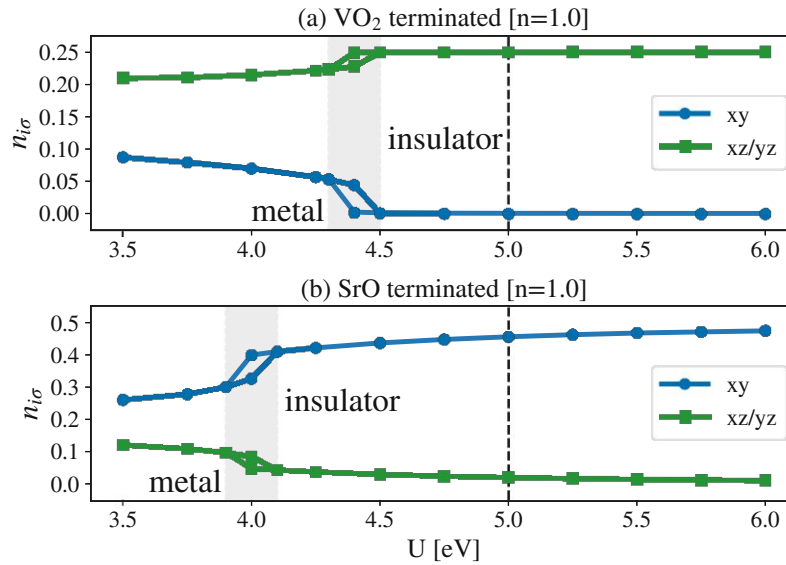


Figure 2.48: Stability of Mott insulating state. Spin-dependent orbital occupation $n_{i\sigma}$ vs. intra-band interaction strength U at room temperature $T = 290\text{K}$; Hund's coupling $J = 0.75\text{eV}$; inter-band interaction $U' = U - 2J$. (a) The VO₂ terminated monolayer is effectively a two-orbital quarter-filled system ($n_{xz/yz,\sigma} \sim 0.25$) while (b) the SrO terminated monolayer becomes effectively a half-filled one-orbital system ($n_{xy,\sigma} \sim 0.5$) at large enough interaction strengths. Both lead to a Mott localization of carriers which can be upheld even if we reduce the interaction. The transition to the metallic solution is accompanied by a tight hysteresis after which the orbital polarization drops rapidly. The calculations under doping in the next figure are performed for $U = 5\text{eV}$ (vertical, dashed black line).

2.5.3 Orbital reconfiguration under doping

We will now discuss the electronic structure of the doped monolayers in their non-symmetry broken phases: From the information of orbital occupations and degeneracies, we motivate possible ordering instabilities (that will then be quantitatively assessed in Sec. 2.5.4).

First, the stoichiometric insulating state in Fig. 2.47 and the various orbital occupations in Fig. 2.49, indicate that our systems are asymmetrical with respect to doping with electrons ($n > 1$) or holes ($n < 1$). The VO₂ terminated monolayer (Fig. 2.49a) somewhat upholds its orbital polarization when holes are introduced to the system. Such orbital occupations of the bipartite lattice system make the system prone to a staggered, checkerboard orbital ordering (cOO) [184, 185], as two orbitals may now be occupied alternately on neighboring lattice sites. This is energetically favorable, since

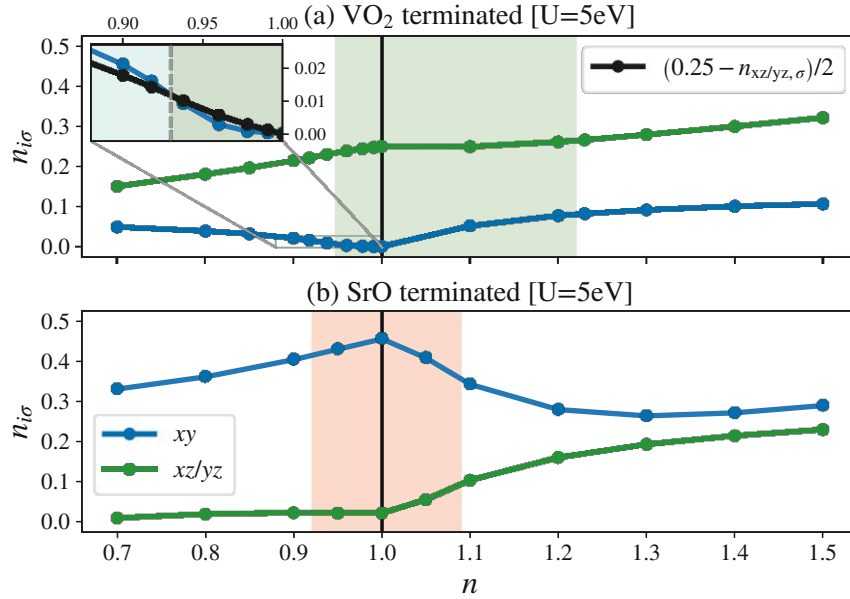


Figure 2.49: System trends with doping. Spin-dependent orbital occupation at $T = 290\text{K}$, resolved for the $i = xy$ and xz/yz -orbitals. (a) The VO₂ terminated system around nominal filling ($n = 1$) can be effectively described by two quarter-filled (xz/yz) orbitals. (b) The SrO terminated system at and below nominal filling can effectively be described by a single half-filled (xy) orbital. The former explains the tendency for checkerboard orbital ordering, while the latter promotes antiferromagnetism in Fig. 2.55. The shaded areas around undoped SrVO₃ represent the doping levels at which we find these checkerboard and antiferromagnetic orderings in DMFT at this temperature. Inset: Semi-empirical condition where stripe orbital ordering emerges: If we frustrate the local site enough, we find a transition from checkerboard to stripe orbital-order (indicated by a change in background color)

a nearest-neighbor hopping then results in a state where different orbitals are occupied so that a (virtual) hopping process costs only $U' = U - 2J$ instead of U .

Doping with more holes, see Fig. 2.49a, the VO₂-terminated monolayer quickly moves away from quarter-filling by redistributing electrons from the xz/yz -orbitals into the xy -orbital, disfavoring orbital ordering (OO). As we shall see in Sec. 2.5.4, before OO is fully suppressed upon hole doping the ordering vector changes to stripe orbital ordering (sOO) above a particular filling of the so far auxiliary xy -orbital. Electron doping on the other hand maintains the quarter-filled state for longer, where for fillings up to $n \sim 1.2$ the additional electrons solely occupy the xy -orbital. Only above $n \sim 1.3$ we see a coincidental increase of all orbital occupations, again disfavoring orbital order.

The SrO-terminated monolayer (Fig. 2.49b) is even more asymmetrical: Introducing holes does not affect the effective one-band description of the system and the sparsely filled xz/yz orbitals remain almost depleted. More interesting is the electron-doped side, where the multi-orbital character is promoted. In this electron-doped regime, the Hund's coupling J will promote a parallel spin alignment of the electrons in the three orbitals. It is natural to expect that the hopping transfers this local spin alignment into an FM order on the lattice, but other orders such as OO may emerge here as well [186]. For strong Coulomb interactions and in an insulating state, these competing phases can be understood by superexchange as in the classical Kugel-Khomskii spin-orbital models [187]. These phases have also been found in early DMFT calculations for a two-band model [184] and an oversimplified Stoner criterion predicts FM order of the m -fold degenerate Hubbard model for $A(0) (U + (m - 1)J) \geq 1$ [188]. At extremely large dopings around $n \sim 1.5$, the physics changes once again: The system now consists of three quite equally filled orbitals where the xz/yz orbitals approach quarter-filling. Similarly to stoichiometric filling in the VO_2 terminated monolayer, such degenerate quarter-filled orbitals may lead again to orbital ordering.

2.5.4 DMFT susceptibilities

2.5.4.1 Linear response theory

We now put the above analysis of potentially ordered phases on firm footing: The susceptibility χ describes the response of a system to an external perturbation. In the vicinity to a continuous (second order) phase transition the system becomes increasingly sensitive to these perturbations and promotes the corresponding fluctuations²² The phase transition itself is then characterized by a diverging susceptibility on an infinite correlation length ξ , the system orders. Please note that no external field is necessary to trigger the order of the system (spontaneous divergence). Commonly, the resulting ground state does not exhibit the same (continuous) symmetries determined by the Hamiltonian \mathcal{H}_0 , a so-called spontaneous symmetry breaking occurs. In a ferromagnet, e.g., the underlying system is invariant under $\text{SU}(2)$ transformation. By the commencement of a finite magnetization, the spins are no longer rotationally invariant, i.e. the ordered ground state exhibits less symmetry than the system itself.

From a practical point of view, our goal will be to investigate the tendency towards order via a numerical evaluation of susceptibilities, including their temperature dependence. Close to the divergence, the system will display several characteristic critical exponents, e.g. $\chi \propto (T - T_c)^{-\gamma}$, $\xi \propto (T - T_c)^{-\nu}$ (T_c : critical temperature) that are connected via scaling relations [190].

²²The uniform magnetic susceptibility $\chi_M(\mathbf{q} = \mathbf{0}, i\omega_m = 0)$ can, e.g., be connected to the fluctuations of the magnetization M via $\chi_M(\mathbf{q} = \mathbf{0}, i\omega_m = 0) = \frac{1}{k_B T} \langle (M - \langle M \rangle)^2 \rangle$ [189].

Given a system consisting of a Hamiltonian \mathcal{H}_0 with one-particle and possibly two-particle terms, a perturbation $a(t)$, quite generally, couples to a quantum mechanical operator \hat{A}

$$\mathcal{H}(t) = \mathcal{H}_0 - a(t) \cdot \hat{A} \quad (2.81)$$

resulting in a time-dependent Hamiltonian. In this context we are then interested in the out-of-equilibrium changes of some measurable (bosonic) observables $\langle B \rangle$

$$\langle \hat{B} \rangle_a(t) - \langle \hat{B} \rangle_{a=0} = \int_{-\infty}^t dt' \chi_{BA}(t-t') a(t') + \mathcal{O}(a^2(t)) \quad (2.82)$$

Within linear response theory the infinite series of Eq. (2.82) is truncated after the first order. Please note that time dependent observable must now be evaluated with respect to the corresponding time-dependent density matrix $\rho(t)$

$$\langle \hat{B} \rangle_a(t) = \frac{\text{Tr}(\rho(t)\hat{B})}{\text{Tr}(\rho(t))} \quad (2.83)$$

governed by Eq. (2.81). In order to simplify this problem one commonly employs the Kubo formalism [191, 192]. Assuming a slow relaxation of the system (eigenstates of the system do not change) and slowly varying density matrix, one can derive the Kubo-Nakano expression

$$\chi_{BA}(t-t') = -\frac{1}{i\hbar} \Theta(t-t') \langle [\hat{B}(t), \hat{A}(t')] \rangle_{a=0} \quad (2.84)$$

evaluated with respect to the *unperturbed* system, \mathcal{H}_0 . As our calculations are performed on the imaginary time τ or (bosonic) frequency $i\omega_m$ axis, we usually define the associated Matsubara susceptibility

$$\chi_{BA}(\tau) = \langle T_\tau \hat{B}(\tau) \hat{A}(0) \rangle_{a=0} \quad (2.85a)$$

$$\chi_{BA}(i\omega_m) = \int_0^\beta d\tau e^{i\omega_m \tau} \chi_{BA}(\tau) \quad (2.85b)$$

where T_τ orders the bosonic operators from left to right according to their time arguments $\tau > 0$: $\langle \hat{B}(\tau) \hat{A}(0) \rangle$; $\tau < 0$: $\langle \hat{A}(0) \hat{B}(\tau) \rangle$. If necessary, the return to real time and frequency is performed via analytic continuation $\chi(\omega) = \chi(i\omega_m \rightarrow \omega + i0^+)$. In the analysis of *static* responses (pivotal for ordering) this is not necessary as the full information is encoded in the zeroth frequency $i\omega_m = 0$.

In this Section, we are first and foremost interested in the responses to an external magnetic field and the more abstract response to a change of the chemical potential. Electromagnetic fields coupling to the current operator resulting in an optical response (optical conductivity $\sigma(\omega)$), will be discussed in Section 2.6.

A *static*, external magnetic field (\mathbf{B}) couples to the system via the electronic spins S_i arranged on the lattice

$$\mathcal{H} = \mathcal{H}_0 - \mu_B g \sum_i \hat{\mathbf{S}}_i \cdot \mathbf{B} \quad (2.86)$$

with the Bohr magneton $\mu_B = e\hbar/(2m_e)$ and the gyromagnetic ratio ($g \approx 2$ for electrons without spin-orbit coupling) as coupling constants. The chemical potential μ on the other hand is commonly already included in the Hamiltonian and couples to the electron numbers, n_i , of the lattice sites i

$$\mathcal{H} = \mathcal{H}_0 - \mu \sum_i \hat{n}_i \quad (2.87)$$

In spin-1/2 systems the density and spin operators in this type of coupling can be represented via

$$\hat{n} = [\hat{c}_\uparrow^\dagger, \hat{c}_\downarrow^\dagger] \mathbb{1} \begin{bmatrix} \hat{c}_\uparrow \\ \hat{c}_\downarrow \end{bmatrix} = \hat{c}_\uparrow^\dagger \hat{c}_\uparrow + \hat{c}_\downarrow^\dagger \hat{c}_\downarrow \quad (2.88a)$$

$$\vec{\hat{S}} = [\hat{c}_\uparrow^\dagger, \hat{c}_\downarrow^\dagger] \frac{\hbar}{2} \vec{\sigma} \begin{bmatrix} \hat{c}_\uparrow \\ \hat{c}_\downarrow \end{bmatrix} = \frac{\hbar}{2} \begin{bmatrix} \hat{c}_\uparrow^\dagger \hat{c}_\downarrow + \hat{c}_\downarrow^\dagger \hat{c}_\uparrow \\ -i\hat{c}_\uparrow^\dagger \hat{c}_\downarrow + i\hat{c}_\downarrow^\dagger \hat{c}_\uparrow \\ \hat{c}_\uparrow^\dagger \hat{c}_\uparrow - \hat{c}_\downarrow^\dagger \hat{c}_\downarrow \end{bmatrix} \quad (2.88b)$$

where $\vec{\sigma}$ are the Pauli matrices in vector form ($\sigma_x, \sigma_y, \sigma_z$). Magnetic and density responses, corresponding to the perturbations of Eq. (2.86) and Eq. (2.87), then correspond to

$$\chi_M(\tau) \equiv \chi_{S^z S^z}(\tau) = g^2 \langle T_\tau \hat{S}^z(\tau) \hat{S}^z(0) \rangle - g^2 \beta \langle \hat{S}^z \rangle \langle \hat{S}^z \rangle \quad (2.89a)$$

$$\chi_D(\tau) \equiv \chi_{nn}(\tau) = \langle T_\tau \hat{n}(\tau) \hat{n}(0) \rangle - \beta \langle \hat{n} \rangle \langle \hat{n} \rangle, \quad (2.89b)$$

respectively. Let us emphasize here that the magnetic response must be identical in all three spin directions $\chi_M = \chi_{S^x S^x} = \chi_{S^y S^y} = \chi_{S^z S^z}$ [193]. In both correlation functions the disconnected expectation values are not taken into consideration: These terms stem from “non-physical” Feynman diagrams stemming from the disconnected Wick contractions, see Appendix A.1, and do not contribute to the physical processes we want to capture. Whereas in Eq. (2.89b) the density density correlation function is corrected by a density offset, the correction of Eq. (2.89a) is in principle redundant as we operate under the assumption of an unordered phase, i.e. $\langle \hat{S}^z \rangle \equiv 0$.

Employing the Kubo formalism, expectation values occurring in correlation functions such as Eqs. (2.89b-2.89a) are implicitly always taken from now on with respect to the unperturbed system. The gyromagnetic prefactor g^2 in χ_M takes into consideration the coupling of the magnetic field onto the Hamiltonian. Please note that we ignore the μ_B^2 scaling, which needs to be taking into consideration when transforming the magnetic susceptibilities into SI units.

Eqs. (2.89a) and (2.89b) encode the purely spin and charge fluctuations as the coupling (\mathcal{A}) and measurement (\mathcal{B}) operators are identical. In the following we will restrict the spin considerations

to the commonly chosen z -axis. This restriction allows for a major simplification of the corresponding diagrammatic considerations as density and magnetic susceptibilities can now be based on the generalized, spin-dependent density-density correlation function

$$\chi_{nn}^{\sigma\sigma'}(\tau) = \langle T_\tau \hat{n}_\sigma(\tau) \hat{n}_{\sigma'}(0) \rangle - \beta \langle \hat{n}_\sigma \rangle \langle \hat{n}_{\sigma'} \rangle \quad (2.90)$$

via

$$\chi_D = \chi_{nn}^{\uparrow\uparrow} + \chi_{nn}^{\downarrow\downarrow} + \chi_{nn}^{\uparrow\downarrow} + \chi_{nn}^{\downarrow\uparrow}, \quad (2.91a)$$

$$\chi_M = \chi_{nn}^{\uparrow\uparrow} + \chi_{nn}^{\downarrow\downarrow} - \chi_{nn}^{\uparrow\downarrow} - \chi_{nn}^{\downarrow\uparrow}. \quad (2.91b)$$

For our intents and purposes it is customary to Fourier transform the imaginary time axis to (bosonic) Matsubara frequencies. In the context of DMFT, the *impurity* responses, allowing for multiple orbitals, can be then condensed into

$$\chi_M^{\text{imp}}(i\omega_m) = g^2 \sum_{l'} \int_0^\beta d\tau e^{i\omega_m \tau} \langle T_\tau \hat{S}_l^z(\tau) \hat{S}_{l'}^z(0) \rangle - g^2 \sum_{l'} \beta \delta_{\omega_m, 0} \langle \hat{S}_l^z \rangle \langle \hat{S}_{l'}^z \rangle, \quad (2.92a)$$

$$\chi_D^{\text{imp}}(i\omega_m) = \sum_{l'} \int_0^\beta d\tau e^{i\omega_m \tau} \langle T_\tau \hat{n}_l(\tau) \hat{n}_{l'}(0) \rangle - \sum_{l'} \beta \delta_{\omega_m, 0} \langle \hat{n}_l \rangle \langle \hat{n}_{l'} \rangle. \quad (2.92b)$$

2.5.4.2 Two-particle diagrammatic content

Inserting the occupation operator into Eq. (2.90) reveals the intrinsic two-particle nature of the aforementioned correlation functions

$$\chi_{nn}^{\sigma\sigma'}(\tau) = \lim_{\tau_1 \rightarrow \tau^-; \tau_2 = \tau} \lim_{\tau_3 \rightarrow 0^-} \underbrace{\langle T_\tau \hat{c}_\sigma(\tau_1) \hat{c}_\sigma^\dagger(\tau_2) \hat{c}_{\sigma'}(\tau_3) \hat{c}_{\sigma'}^\dagger(0) \rangle}_{G_{\sigma\sigma\sigma'\sigma'}^{(2)}(\tau_1, \tau_2, \tau_3, 0)} - \beta \langle \hat{n}_\sigma \rangle \langle \hat{n}_{\sigma'} \rangle \quad (2.93)$$

which are evidently connected to specific spin-combination of the two-particle Green's function $G^{(2)}$ on the imaginary time axis. Let us emphasize that the two-particle Green's function is defined with a different operator ordering compared to the density density correlation function of Eq. (2.90). The mismatch can be circumvented by a correct limit of the τ arguments $\tau_1 \rightarrow \tau^- < \tau$, $\tau_3 \rightarrow 0^- < 0$. As this introduction to two-particle diagrammatic is kept (relatively) brief, please refer to Appendix A.1 for a more detailed discussion on the topic.

In order to handle the diagrammatic content of the two-particle Green's function itself it is common to first transform $G^{(2)}$ into the frequency space. The resulting frequencies of this Fourier transform are in principle three arbitrary *fermionic* Matsubara frequencies which are restricted by the underlying energy conservation. By introducing specific (frequency) notations, see Appendix A.1.1.5, one is

able to get a transparent view of the relevant scattering processes. In the context of this thesis we exclusively employ the so-called particle-hole (ph) notation

$$G_{\sigma\sigma\sigma'\sigma'}^{\omega\nu\nu'} = \int_0^\beta d\tau_1 \int_0^\beta d\tau_2 \int_0^\beta d\tau_3 \underbrace{e^{i\nu_n\tau_1} e^{-i(\nu_n-\omega_m)\tau_2} e^{i(\nu'_n-\omega_m)\tau_3}}_{\text{ph notation}} \left\langle T_\tau \hat{c}_\sigma(\tau_1) \hat{c}_\sigma^\dagger(\tau_2) \hat{c}_{\sigma'}(\tau_3) \hat{c}_{\sigma'}^\dagger(0) \right\rangle, \quad (2.94)$$

describing processes where a bosonic frequency $i\omega_m$ of a particle-hole excitation is transferred. Naturally, this notation has no influence on the underlying diagrammatic content. The other two commonly employed notations include the transversal particle-hole ($\overline{\text{ph}}$) notation and the particle-particle notation (pp), see Appendix A.1.1.5.

Performing the Dyson expansion for the interacting system and applying Wick contractions we are able to separate three distinct terms

$$G_{\sigma\sigma\sigma'\sigma'}^{\omega\nu\nu'} = \underbrace{\beta G_\sigma^\nu G_{\sigma'}^{\nu'} \delta_{\omega_m,0}}_{\text{disconnected}} - \underbrace{\beta G_\sigma^\nu G_{\sigma'}^{\nu-\omega} \delta_{\sigma\sigma'} \delta_{\nu\nu'}}_{\text{connected}} + \underbrace{G_\sigma^\nu G_{\sigma'}^{\nu-\omega} F_{\sigma\sigma\sigma'\sigma'}^{\omega\nu\nu'} G_{\sigma'}^{\nu'-\omega} G_{\sigma'}^{\nu'}}_{\text{connected}}, \quad (2.95)$$

see Fig. 2.50. The first two terms stem from a separation of the four-point correlation into two two-point correlation functions, i.e. *interacting* one-particle Green's functions, and describe the independent (renormalized) propagation of a particle-hole pair, the so-called *disconnected* contribution.

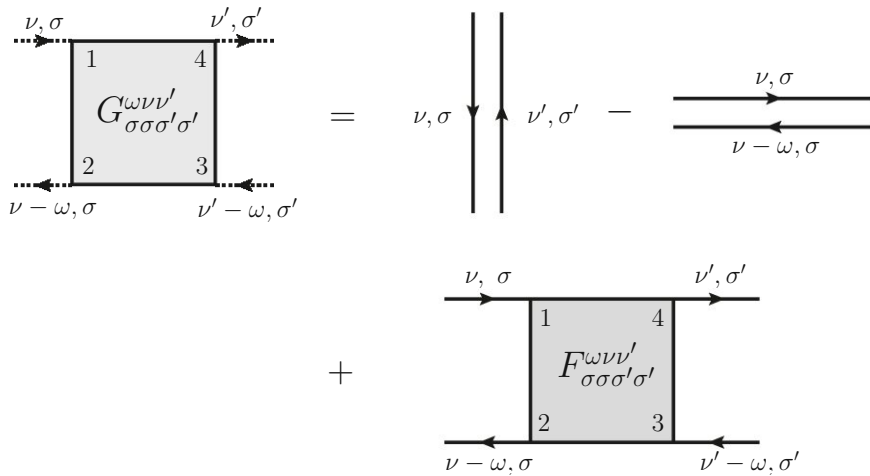


Figure 2.50: Diagrammatic content of the two-particle Green's function, encoding the propagation of two (renormalized) Green's function with and without interaction with one another. All possible particle-hole interactions can be summarized in the full vertex F . Note that while in the two-particle Green's function the outer legs are only indicated for their external dependencies, the full vertex is actually attached with four Green's functions. The internal enumeration of the vertex F is done anti-clockwise starting from the upper left corner.

In the last term all possible diagrams are gathered which are inherently linked, the so-called *connected* contribution. These connections are summarized in the full vertex F , which in most circumstances can be thought of as a generalized scattering matrix, akin to the self-energy Σ on the one-particle level.

The *generalized* susceptibility then simply follows by subtracting the “vertical” disconnected contribution

$$\begin{aligned}\chi_{\sigma\sigma\sigma'\sigma'}^{\omega\nu\nu'} &= G_{\sigma\sigma\sigma'\sigma'}^{\omega\nu\nu'} - \beta G_{\sigma}^{\nu} G_{\sigma'}^{\nu'} \delta_{\omega m, 0} \\ &= \underbrace{-\beta G_{\sigma}^{\nu} G_{\sigma'}^{\nu-\omega} \delta_{\sigma\sigma'} \delta_{\nu\nu'}}_{\chi_0^{\omega\nu\nu'}} + G_{\sigma}^{\nu} G_{\sigma}^{\nu-\omega} F_{\sigma\sigma\sigma'\sigma'}^{\omega\nu\nu'} G_{\sigma'}^{\nu'-\omega} G_{\sigma'}^{\nu'},\end{aligned}\quad (2.96)$$

which corresponds to the removal of the offset terms appearing in Eq. (2.93).²³ The *physical* susceptibility is obtained by summing over all external *fermionic* frequencies

$$\begin{aligned}\chi_{nn}^{\sigma\sigma'}(i\omega_m) &= \frac{1}{\beta^2} \sum_{\nu_n, \nu'_n} \chi_{\sigma\sigma\sigma'\sigma'}^{\omega\nu\nu'} \\ &= \underbrace{-\frac{1}{\beta} \sum_{\nu_n} G_{\sigma}^{\nu} G_{\sigma'}^{\nu-\omega} \delta_{\sigma\sigma'}}_{\chi_0^{\omega}} + \frac{1}{\beta^2} \sum_{\nu_n, \nu'_n} G_{\sigma}^{\nu} G_{\sigma}^{\nu-\omega} F_{\sigma\sigma\sigma'\sigma'}^{\omega\nu\nu'} G_{\sigma'}^{\nu'-\omega} G_{\sigma'}^{\nu'},\end{aligned}\quad (2.97)$$

corresponding to a connection of the in- and out-going particle-hole pair, see Fig. 2.51.

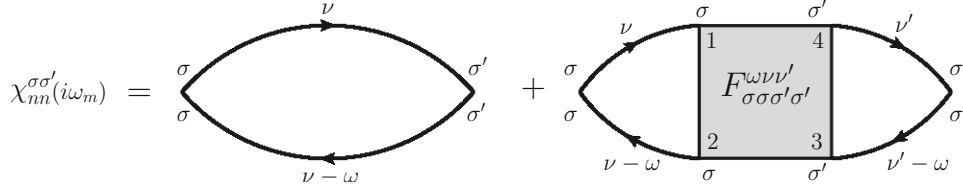


Figure 2.51: Diagrammatic representation of Eq. (2.97). The bubble diagram (left) contributes only for identical spins $\sigma = \sigma'$. The internal enumeration of the vertex F is done anti-clockwise starting from the upper left corner.

From a mathematical point of view, this is identical to setting the imaginary times of the particle-hole pairs to the same value $\tau_1 = \tau_2 = \tau$ and $\tau_3 = 0$.²⁴

²³The fermionic frequency summation over the disconnected Green’s functions $1/\beta \sum_{\nu_n} G^{\nu}$ (with correct Fourier transform prefactor) results in the Green’s functions evaluated at $\tau = 0^-$, mirroring Eq. (2.93). These summations then reproduce the occupations, see Appendix A.2, cancelling the correction term exactly.

²⁴This can easily be recognized in the ph notation: The Matsubara sums over the complex exponential functions in δ -functions that eliminate one integral each $\frac{1}{\beta^2} \sum_{\nu_n, \nu'_n} G^{\omega\nu\nu'} = \frac{1}{\beta^2} \sum_{\nu_n, \nu'_n} \int \int \int d\tau_1 d\tau_2 d\tau_3 e^{i\nu_n \tau_1} e^{-i(\nu_n - \omega_m) \tau_2} e^{i(\nu'_n - \omega_m) \tau_3} G^{(2)}(\tau_1, \tau_2, \tau_3, 0) = \int d\tau_1 e^{i\omega_m \tau_1} G^{(2)}(\tau_1, \tau_1, 0, 0)$.

In summary, the spin-resolved density-density susceptibility describes the excitation of a particle-hole pair. The corresponding particle and hole propagators can then either travel independently (only being renormalized by their own respective self-energies) or experience scattering events between them via the vertex F . We now turn our focus onto exactly this full vertex F and its numerical treatment.

2.5.4.3 Vertex topology

As the main driver of diverging susceptibilities is the full two-particle vertex F , an adequate treatment is necessary to capture the associated phase transitions. Topologically, the diagrams of the full vertex can be classified into four different categories via the parquet equation (2.98), illustrated in Fig. 2.52,

$$F = \Lambda + \Phi_{pp} + \Phi_{ph} + \Phi_{\overline{ph}}. \quad (2.98)$$

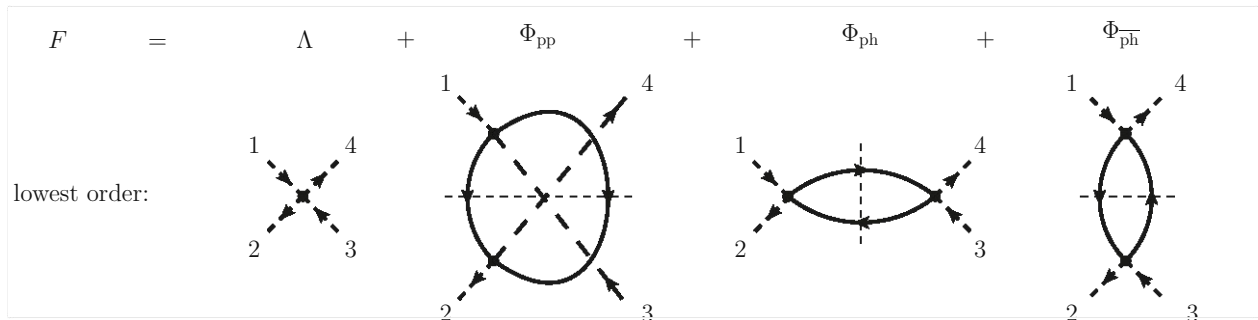


Figure 2.52: Diagram classification according to their topology. Two-particle reducibility separates all possible diagrams in four distinct groups: Λ : fully irreducible, Φ_i : reducible in channel $i \in \{pp, ph, \overline{ph}\}$. The exemplary diagrams show the lowest order in terms of the interaction U (represented as dot). The dashed propagators imply that they do not contribute to the diagram.

Diagrams that *cannot* be separated by cutting two internal Green's function lines (two-particle fully irreducible vertex Λ) and diagrams that *can* be separated (two-particle reducible vertices Φ). Depending on which pair of line this internal separability refers to, one distinguishes between the so-called:

- particle-particle (pp) channel – reducible between the pairs 13 – 24,
- particle-hole (ph) channel – reducible between the pairs 12 – 34,
- particle-hole transverse (\overline{ph}) channel – reducible between the pairs 14 – 23.

Importantly, if a diagram can be separated in one of the three channels, it cannot be separated in any other channels [93]. This allows for three equivalent reformulations of Eq. (2.98)

$$F = \Gamma_{\text{ph}} + \Phi_{\text{ph}} \quad (2.99a)$$

$$F = \Gamma_{\overline{\text{ph}}} + \Phi_{\overline{\text{ph}}} \quad (2.99b)$$

$$F = \Gamma_{\text{pp}} + \Phi_{\text{pp}}, \quad (2.99c)$$

the so-called Bethe-Salpeter equations (BSE). The susceptibilities utilized in this thesis can all be inherently connected to particle-hole excitations ($\propto \hat{c}^\dagger \hat{c}$). In this context, the DMFT susceptibilities are based on an approximation to the full vertex F constructed via the *particle-hole* Bethe-Salpeter equation (2.99a).

2.5.4.4 Spins: Channel parametrization

Symbolically within the ph channel, the reducible property of the Φ_{ph} vertex can be generated if irreducible vertices Γ_{ph} are connected with one another by $(GG)_{\text{ph}}$ propagators. All possible, sequentially joined reducible contributions lead to the geometric series

$$\begin{aligned} \Phi_{\text{ph}} &= \int \Gamma_{\text{ph}}(GG)_{\text{ph}}\Gamma_{\text{ph}} + \int \Gamma_{\text{ph}}(GG)_{\text{ph}}\Gamma_{\text{ph}}(GG)_{\text{ph}}\Gamma_{\text{ph}} + \dots \\ &= \int \Gamma_{\text{ph}}(GG)_{\text{ph}}F, \end{aligned} \quad (2.100)$$

connecting Γ , Φ and F . The integral denotes a summation over all possible internal degrees of freedom. As these quantities represent true two-particle interaction matrices, their spin dependence requires some consideration. Calculations are performed in the non-symmetry-broken (paramagnetic phase, SU(2) symmetry maintained), i.e. in- and outgoing spins must conserve the total spin. This restriction reduces the number of spin permutations from $2^4 = 16$ to 6, encoded in

$$F_{\sigma\sigma} = \Gamma_{\sigma\sigma} + \int \sum_{\sigma''} \Gamma_{\sigma\sigma''} G_{\sigma''} G_{\sigma''} F_{\sigma''\sigma} \quad (2.101a)$$

$$F_{\sigma\sigma'} = \Gamma_{\sigma\sigma'} + \int \sum_{\sigma''} \Gamma_{\sigma\sigma''} G_{\sigma''} G_{\sigma''} F_{\sigma''\sigma'} \quad (2.101b)$$

$$F_{\overline{\sigma\sigma'}} = \Gamma_{\overline{\sigma\sigma'}} + \int \Gamma_{\overline{\sigma\sigma'}} G_{\sigma} G_{\sigma'} F_{\overline{\sigma\sigma'}} \quad (2.101c)$$

with the commonly used spin abbreviation, see Fig. 2.53.

$$\sigma\sigma \leftrightarrow \sigma\sigma\sigma\sigma$$

$$\sigma\sigma' \leftrightarrow \sigma\sigma\sigma'\sigma'$$

$$\overline{\sigma\sigma'} \leftrightarrow \sigma\sigma'\sigma'\sigma.$$

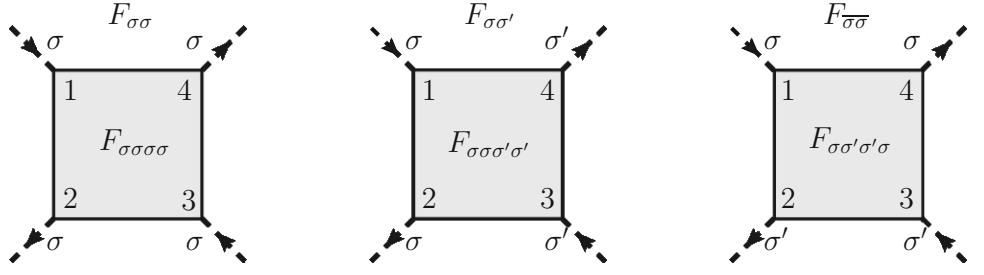


Figure 2.53: Spin abbreviation for the six possible spin permutations $\uparrow\uparrow, \downarrow\downarrow$ (left) — $\uparrow\downarrow, \downarrow\uparrow$ (middle) — $\overline{\uparrow\downarrow}, \overline{\downarrow\uparrow}$ (right).

Through the internal spin summation Eqs. (2.101a) and (2.101b) become intrinsically coupled

$$\begin{bmatrix} F_{\uparrow\uparrow} & F_{\uparrow\downarrow} \\ F_{\downarrow\uparrow} & F_{\downarrow\downarrow} \end{bmatrix} = \begin{bmatrix} \Gamma_{\uparrow\uparrow} & \Gamma_{\uparrow\downarrow} \\ \Gamma_{\downarrow\uparrow} & \Gamma_{\downarrow\downarrow} \end{bmatrix} + \int \begin{bmatrix} \Gamma_{\uparrow\uparrow} & \Gamma_{\uparrow\downarrow} \\ \Gamma_{\downarrow\uparrow} & \Gamma_{\downarrow\downarrow} \end{bmatrix} \begin{bmatrix} G_{\uparrow}G_{\uparrow} & 0 \\ 0 & G_{\downarrow}G_{\downarrow} \end{bmatrix} \begin{bmatrix} F_{\uparrow\uparrow} & F_{\uparrow\downarrow} \\ F_{\downarrow\uparrow} & F_{\downarrow\downarrow} \end{bmatrix} \quad (2.102)$$

whereas the internal spins (via spin conservation) in Eq. (2.101c) become restricted

$$\begin{bmatrix} F_{\uparrow\downarrow} \\ F_{\downarrow\uparrow} \end{bmatrix} = \begin{bmatrix} \Gamma_{\uparrow\downarrow} \\ \Gamma_{\downarrow\uparrow} \end{bmatrix} + \int \begin{bmatrix} \Gamma_{\uparrow\downarrow}G_{\uparrow}G_{\downarrow}F_{\uparrow\downarrow} \\ \Gamma_{\downarrow\uparrow}G_{\downarrow}G_{\uparrow}F_{\downarrow\uparrow} \end{bmatrix}. \quad (2.103)$$

For the preserved $SU(2)$ symmetry, we are allowed to uncouple the matrix equation (2.102) by “symmetrizing” the spin-combinations via

$$D \equiv \uparrow\uparrow + \uparrow\downarrow \quad (2.104a)$$

$$M \equiv \uparrow\uparrow - \uparrow\downarrow \quad (2.104b)$$

resulting in

$$\begin{bmatrix} F_D \\ F_M \end{bmatrix} = \begin{bmatrix} \Gamma_D \\ \Gamma_M \end{bmatrix} + \int \begin{bmatrix} \Gamma_D G G F_D \\ \Gamma_M G G F_M \end{bmatrix} \quad (2.105)$$

with $G_{\uparrow} = G_{\downarrow} = G$. We recover expressions that are diagonal in the new (D)ensity and (M)agnetic “channels”, naturally connected to Eqs. (2.88a) and (2.88b). The symmetrization exactly mirrors the definition of the density and the (z-component of the) spin operator allowing for an easy translation between the two-particle vertex description and physical observables. Please note that the magnetic channel can be further connected to

$$M \equiv \uparrow\uparrow - \uparrow\downarrow \stackrel{SU(2)}{\equiv} \overline{\uparrow\downarrow} \quad (2.106)$$

via a spin rotation (angle $\phi = \pi/2$) about the y-axis, identifying Eq. (2.103) as the magnetic channel [193]. Within this reformulation of the particle-hole channel we are thus able to rid ourselves completely from spin-descriptors with the full information of the ph channel compressed into the two newly constructed density and magnetic channels.

As the transverse particle-hole channel is deeply connected to the particle-hole channel via the crossing symmetry the D/M channel not only provides the full information of the ph-channel, but also of the $\overline{\text{ph}}$ -channel [193]. An explicit treatment is therefore not necessary. This argument no longer holds, however, when constructing corrections to the self-energy (see Section 2.5.7) as the involved vertices have to obey crossing symmetry (Pauli principle). There, the ph and the $\overline{\text{ph}}$ channels have to be treated on equal footing.

Let us note that throughout this thesis we are going to neglect the momentum dependence of the pp channel, i.e. Φ_{pp} is assumed to be local. The particle particle channel encodes observables such as pair excitations, present, e.g., in the vicinity of superconducting instabilities. Inside the symmetry broken superconducting phase, the corresponding expectation value $\langle \hat{c}_{\mathbf{k},\uparrow}^\dagger \hat{c}_{-\mathbf{k},\downarrow}^\dagger \rangle$ then becomes finite. Furthermore, diagrammatic feedback ($\Gamma_{\text{pp}} = \Lambda + \Phi_{\text{ph}} + \Phi_{\overline{\text{ph}}}$) between the channels can however not be excluded which one has to be mindful about when evaluating pre-selected channels.

2.5.4.5 Frequency: Matrix representation

Before being able to extract information from the aforementioned Bethe-Salpeter equations (2.105), they need to be implemented in matrix form to do so in an efficient manner. First, the particle-hole reducible propagators are rewritten into the bare susceptibility

$$\chi_0^{\omega\nu\nu'} = -G_\sigma^\nu G_\sigma^{\nu'-\omega} \beta \delta_{\nu\nu'}, \quad (2.107a)$$

$$\chi_0^{\omega\nu\nu} = -G_\sigma^\nu G_\sigma^{\nu-\omega}, \quad (2.107b)$$

where the former appears in the two-particle Green's function, see Eq. (2.95), with corresponding units [eV⁻³]. The latter expression (note the change in the superscript) has units of [eV⁻²] and is employed in the Bethe-Salpeter equation

$$\begin{aligned} F_r^{\omega\nu\nu'} &= \Gamma_r^{\omega\nu\nu'} + \frac{1}{\beta^2} \sum_{\nu''\nu'''} \Gamma_r^{\omega\nu\nu''} (-G_\sigma^{\nu''} G_\sigma^{\nu''-\omega} \beta \delta_{\nu''\nu'''}) F_r^{\omega\nu'''\nu'} \\ &= \Gamma_r^{\omega\nu\nu'} + \frac{1}{\beta} \sum_{\nu''} \Gamma_r^{\omega\nu\nu''} \chi_0^{\omega\nu''\nu''} F_r^{\omega\nu''\nu'}. \end{aligned} \quad (2.108)$$

ensuring the correct dimensionality of the full vertex F (Γ [eV], $\chi_0^{\omega\nu\nu}$ [eV⁻²], F [eV]). The prefactor $1/\beta$ [eV] accompanies most Matsubara summations and the minus sign takes the additional fermionic loop of “GG” into consideration. The internal (fermionic) Matsubara summation $\sum_{\nu''}$ can then

be translated into a simple matrix multiplication by constructing the two-particle vertices $X^{\omega\nu\nu'}$ ($X = F, \Gamma, \chi_0$, etc.) in the following numerical form

$$X^{\omega\nu\nu'} = \begin{bmatrix} X^{\nu-2\nu'-2} & X^{\nu-2\nu'-1} & X^{\nu-2\nu'_0} & X^{\nu-2\nu'_1} \\ X^{\nu-1\nu'-2} & X^{\nu-1\nu'-1} & X^{\nu-1\nu'_0} & X^{\nu-1\nu'_1} \\ X^{\nu_0\nu'-2} & X^{\nu_0\nu'-1} & X^{\nu_0\nu'_0} & X^{\nu_0\nu'_1} \\ X^{\nu_1\nu'-2} & X^{\nu_1\nu'-1} & X^{\nu_1\nu'_0} & X^{\nu_1\nu'_1} \end{bmatrix} (i\omega_m). \quad (2.109)$$

That is, every transfer frequency is represented by a separate matrix whose first fermionic frequency spans the rows and whose second fermionic frequency spans the columns. Naturally, one has to implement a (symmetrical) cutoff frequency $\nu_{-n} \dots \nu_{n-1}$ ($\nu_n = (2n + 1)\pi/\beta$). It is then easy to see that multiplying two such matrices

$$Z^{\omega\nu\nu'} = \frac{1}{\beta} \sum_{\nu''} X^{\omega\nu\nu''} Y^{\omega\nu''\nu'}, \quad (2.110)$$

resolves the internal frequency summation. Extending this concept to multiple orbitals, one needs to adopt a so-called frequency-orbital compound index: $\nu \rightarrow (\nu, lm)$, $\nu' \rightarrow (\nu, m'l')$ where $lmm'l'$ is the corresponding orbital permutation. The multi-orbital representation of $X^{\omega\nu\nu'}$ then reads for a two-orbital system

$$X^{\omega\nu\nu'}_{lmm'l'} = \begin{bmatrix} X^{\nu-1\nu'-1}_{1111} & X^{\nu-1\nu'-1}_{1121} & X^{\nu-1\nu'-1}_{1112} & X^{\nu-1\nu'-1}_{1122} & X^{\nu-1\nu'_0}_{1111} & X^{\nu-1\nu'_0}_{1121} & X^{\nu-1\nu'_0}_{1112} & X^{\nu-1\nu'_0}_{1122} \\ X^{\nu-1\nu'-1}_{1211} & X^{\nu-1\nu'-1}_{1221} & X^{\nu-1\nu'-1}_{1212} & X^{\nu-1\nu'-1}_{1222} & X^{\nu-1\nu'_0}_{1211} & X^{\nu-1\nu'_0}_{1221} & X^{\nu-1\nu'_0}_{1212} & X^{\nu-1\nu'_0}_{1222} \\ X^{\nu-1\nu'-1}_{2111} & X^{\nu-1\nu'-1}_{2121} & X^{\nu-1\nu'-1}_{2112} & X^{\nu-1\nu'-1}_{2122} & X^{\nu-1\nu'_0}_{2111} & X^{\nu-1\nu'_0}_{2121} & X^{\nu-1\nu'_0}_{2112} & X^{\nu-1\nu'_0}_{2122} \\ X^{\nu-1\nu'-1}_{2211} & X^{\nu-1\nu'-1}_{2221} & X^{\nu-1\nu'-1}_{2212} & X^{\nu-1\nu'-1}_{2222} & X^{\nu-1\nu'_0}_{2211} & X^{\nu-1\nu'_0}_{2221} & X^{\nu-1\nu'_0}_{2212} & X^{\nu-1\nu'_0}_{2222} \\ X^{\nu_0\nu'_0}_{1111} & X^{\nu_0\nu'_0}_{1121} & X^{\nu_0\nu'_0}_{1112} & X^{\nu_0\nu'_0}_{1122} & X^{\nu_0\nu'_0}_{1111} & X^{\nu_0\nu'_0}_{1121} & X^{\nu_0\nu'_0}_{1112} & X^{\nu_0\nu'_0}_{1122} \\ X^{\nu_0\nu'_0}_{1211} & X^{\nu_0\nu'_0}_{1221} & X^{\nu_0\nu'_0}_{1212} & X^{\nu_0\nu'_0}_{1222} & X^{\nu_0\nu'_0}_{1211} & X^{\nu_0\nu'_0}_{1221} & X^{\nu_0\nu'_0}_{1212} & X^{\nu_0\nu'_0}_{1222} \\ X^{\nu_0\nu'_0}_{2111} & X^{\nu_0\nu'_0}_{2121} & X^{\nu_0\nu'_0}_{2112} & X^{\nu_0\nu'_0}_{2122} & X^{\nu_0\nu'_0}_{2111} & X^{\nu_0\nu'_0}_{2121} & X^{\nu_0\nu'_0}_{2112} & X^{\nu_0\nu'_0}_{2122} \\ X^{\nu_0\nu'_0}_{2211} & X^{\nu_0\nu'_0}_{2221} & X^{\nu_0\nu'_0}_{2212} & X^{\nu_0\nu'_0}_{2222} & X^{\nu_0\nu'_0}_{2211} & X^{\nu_0\nu'_0}_{2221} & X^{\nu_0\nu'_0}_{2212} & X^{\nu_0\nu'_0}_{2222} \end{bmatrix} (i\omega_m). \quad (2.111)$$

Importantly, the orbital enumeration is different along the rows and columns

along column : 11 \rightarrow 12 \rightarrow 21 \rightarrow 22

along row : 11 \rightarrow 21 \rightarrow 12 \rightarrow 22

in order to correctly capture the order of the orbital summation

$$Z^{\omega\nu\nu'}_{lmm'l'} = \frac{1}{\beta} \sum_{\nu'', ab} X^{\omega\nu\nu''}_{lmab} Y^{\omega\nu''\nu'}_{bam'l'}. \quad (2.112)$$

As seen in Eq. (2.108), when handling propagator insertions the necessary prefactors are not necessarily intuitive. The most “fool-proof” way of determining them is by the aforementioned dimensionality analysis. For a detailed description of the numerical implementation employed in `AbinitioDMT`, used throughout this thesis, please refer to Ref. [2].

2.5.4.6 Lattice susceptibilities

Having established a framework for the description of genuine two-particle quantities, we now turn our focus onto an approximation thereof. Within DMFT the above two-particle vertex F is only accessible via the underlying quantum impurity problem, i.e. we are at first restricted to local susceptibilities and local vertices. In order to insert lattice information into these local quantities, the Bethe-Salpeter equations have to be inverted. The momentum-dependence then is generated purely through the one-particle propagators G^k .

This procedure can be symbolically summarized as:

- (i) Calculate the *local* two-particle full vertex F_r^ω
 - Sample impurity two-particle Green’s function $G^{(2)}$
 - Subtract disconnected terms
 - Amputate external legs
 - Symmetrize vertex F_r^ω , $r \in \{D, M\}$
- (ii) Extract the *local* two-particle irreducible vertex Γ_r^ω
 - Inversion via $\Gamma_r^\omega = F_r^\omega (1 + \chi_0^\omega F_r^\omega)^{-1}$
- (iii) Reconstruct the momentum dependent vertex F_r^q :
 - Inversion via $F_r^q = (1 - \Gamma_r \chi_0^q)^{-1} \Gamma_r^\omega$

In the first inversion we employ the local Green’s function

$$\chi_0^\omega = -\frac{1}{\beta} \sum_{\nu_n} G_\sigma^\nu G_\sigma^{\nu-\omega}, \quad (2.113)$$

whereas in the second inversion the non-local lattice Green’s functions are used instead

$$\chi_0^q = -\frac{1}{\beta} \sum_{\nu_n} \sum_{\mathbf{k}} G_\sigma^k G_\sigma^{k-q}. \quad (2.114)$$

Due to the way the “lattice” vertex is constructed in the ph-channel, only a single transfer momentum \mathbf{q} is generated. The internal and external Green’s function momenta are “lost” as we are forced to sum

over the remaining internal and external momenta to close the diagram. As these irreducible vertices are known to diverge in certain parameter regimes [194, 195], we try to avoid any numerical representation of them. Combining the deconstruction and construction of the BSE, allows us to circumvent this problem while simultaneously speeding up the computation. The algebraic reformulation looks as follows

$$\begin{aligned}
F_r^q &= (1 - \Gamma_r^\omega \chi_0^q)^{-1} \Gamma_r^\omega & (2.115) \\
&= \left[(\Gamma_r^\omega)^{-1} - \chi_0^q \right]^{-1} \\
&= \left[\left(F_r^\omega (1 + \chi_0^\omega F_r^\omega)^{-1} \right)^{-1} - \chi_0^q \right]^{-1} \\
&= \left[(1 + \chi_0^\omega F_r^\omega) (F_r^\omega)^{-1} - \chi_0^q \right]^{-1} \\
&= \left[(F_r^\omega)^{-1} + \chi_0^\omega - \chi_0^q \right]^{-1} \\
&= \left[(F_r^\omega)^{-1} - \chi_0^{q,\text{nl}} \right]^{-1} \\
&= \left[\left(1 - \chi_0^{q,\text{nl}} F_r^\omega \right) (F_r^\omega)^{-1} \right]^{-1} \\
&= F_r^\omega \left[1 - \chi_0^{q,\text{nl}} F_r^\omega \right]^{-1}
\end{aligned}$$

with $r \in (D, M)$ and $\chi_0^{q,\text{nl}} = \chi_0^q - \chi_0^\omega$. This newly constructed, momentum dependent vertex $F_r^q = F_r^{(\mathbf{q}, \omega)}$ then needs to be inserted back into the form of a generalized susceptibility

$$\chi_r^q \equiv \chi_r(\mathbf{q}, i\omega_m) = -\frac{1}{\beta} \sum_{\nu_n} \sum_{\mathbf{k}} G_\sigma^k G_\sigma^{k-q} + \frac{1}{\beta^2} \sum_{\nu_n, \nu'_n} \sum_{\mathbf{k}, \mathbf{k}'} G_\sigma^k G_\sigma^{k-q} F_r^{q\nu\nu'} G_\sigma^{k'-q} G_\sigma^{k'}, \quad (2.116)$$

see Fig. 2.54, for which now an internal momentum summation is required. By introducing the lattice via the non-local propagators, the resulting *physical* magnetic and density responses now correspond to

$$\chi_M^{\text{lattice}}(\mathbf{q}, i\omega_m) = g^2 \sum_{ij, ll'} e^{i\mathbf{q} \cdot (\mathbf{R}_i - \mathbf{R}_j)} \int_0^\beta d\tau e^{i\omega_m \tau} \left[\langle T_\tau \hat{S}_{il}^z(\tau) \hat{S}_{jl'}^z(0) \rangle - \beta \langle \hat{S}_{il}^z \rangle \langle \hat{S}_{jl'}^z \rangle \right] \quad (2.117a)$$

$$\chi_D^{\text{lattice}}(\mathbf{q}, i\omega_m) = \sum_{ij, ll'} e^{i\mathbf{q} \cdot (\mathbf{R}_i - \mathbf{R}_j)} \int_0^\beta d\tau e^{i\omega_m \tau} \left[\langle T_\tau \hat{n}_{il}(\tau) \hat{n}_{jl'}(0) \rangle - \beta \langle \hat{n}_{il} \rangle \langle \hat{n}_{jl'} \rangle \right] \quad (2.117b)$$

where i, j are indices for the lattice sites $\mathbf{R}_{i(j)}$ and l, l' are orbital indices.

Eigenvalue decomposition

In order to gain more information about the proximity and the characteristic of the nearby phase transition, we also decompose the matrix $\chi_0^{q,\text{nl}} F_r^\omega$. Due to the time reversal symmetry (TR), $\chi_0^{q,\text{nl}} F_r^\omega$

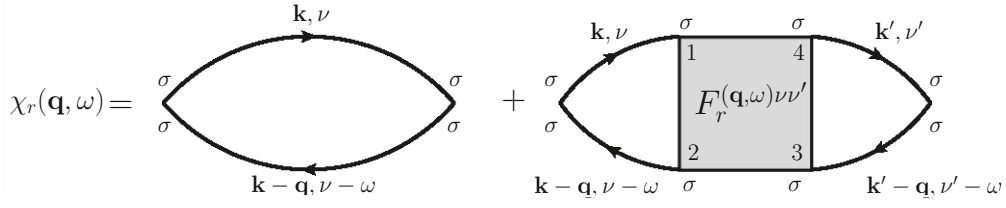


Figure 2.54: Lattice susceptibility in the symmetrized channels $r \in \{D, M\}$, see Eq. (2.116). Through the symmetrization, the spin dependencies are absorbed into the vertex $F_r^{q\nu\nu'}$. All other employed one-particle propagators are spin-independent, i.e. $G = G_\uparrow = G_\downarrow$.

is a symmetric matrix in the employed frequency-band compound index, see Section 2.5.4.5, as the two-particle object (Green's function $X = G$, vertex $X = F$, generalized susceptibility $X = \chi_0$, etc.) obeys

$$X_{lmm'l'}^{qkk'} \stackrel{\text{TR}}{=} X_{l'm'\sigma'}^{\bar{q}\bar{k}'\bar{k}}, \quad (2.118)$$

with the connection between $q = (\mathbf{q}, i\omega_m)$ and $\bar{q} = (-\mathbf{q}, i\omega_m)$ and similarly for k and k' [33]. The inversion of $(1 - \chi_0^{q, \text{nl}} F_r^\omega)$ is no longer possible if the leading, purely real valued, eigenvalue is equal or larger to 1. This is easily shown by the eigenvalue decomposition

$$[1 - \chi_0^{q, \text{nl}} F_r^\omega]^{-1} = [1 - Q\Lambda Q^{-1}]^{-1} = Q^{-1} [1 - \Lambda]^{-1} Q \quad (2.119)$$

and the inversion of the $n \times n$ diagonal matrix Λ resulting in

$$[1 - \Lambda]^{-1} = \begin{bmatrix} (1 - \lambda_1)^{-1} & & & \\ & (1 - \lambda_2)^{-1} & & \\ & & \ddots & \\ & & & \ddots \end{bmatrix} \quad (2.120)$$

where we assume $\lambda_1 > \lambda_2 > \dots > \lambda_n$. In this context the rank of the matrix is $n = 2n_f \cdot n_{\text{bands}}^2$ where n_f is the number of employed positive, fermionic frequencies and n_{bands} the total number of considered bands. Please note, that the leading eigenvalue crossing $\lambda_1 = 1$ does not necessarily lead to a “physical divergence”, as the eigenvector matrices Q may fully suppress its contribution. This is however, very rarely the case.

Simplifications via diagonal hybridization functions

Throughout this thesis we have simplified the local problem, underlying the DMFT cycle, by assuming a diagonal hybridization function resulting in a diagonal self-energy, see Section 2.2.3. This reduction in complexity of the sampling of the one-particle Green's function also leads to a massive simplification of the sampling of the two-particle Green's function. As the local one-particle propagators are

diagonal in the orbital space, i.e. $G_{l,\nu} \propto \delta_{l,\nu}$, the two-particle Green's function “inherits” the orbital composition of the employed interaction matrix, see Section 2.2.2. For the case of the Kanamori parametrization, this reduces the number of possible spin-orbital combinations from $N = (2n)^4$ to $N = 6(3n^2 - 2n)$, reducing the scaling from $\mathcal{O}(n^4)$ to $\mathcal{O}(n^2)$, where n are the number of *correlated* bands, that we sample in the impurity problem.²⁵

Consistency

Since the transfer momentum is an arbitrary input parameter when evaluating the non-local vertex, we are able to perform a full momentum scan and are not restricted to singular \mathbf{q} -vectors. Note that the uniform response ($\mathbf{q} = \mathbf{0}$) can also be determined in DMFT via calculations including an explicit magnetic field. The susceptibility is then determined by the derivative at 0 magnetic field

$$\chi_M(\mathbf{q} = \mathbf{0}) = \left. \frac{\partial M}{\partial B} \right|_{B \rightarrow 0} \quad (2.121)$$

As DMFT is a conserving theory and therefore respects the Ward identities, both methods necessarily agree with each other [196]. Note that these susceptibilities still are only approximations within DMFT. Only in the infinite dimension limit does the irreducible vertex Γ of the impurity become exact, from which the lattice susceptibilities follow.

In the following, the sampling of the two-particle Green's function is done by continuous-time quantum Monte Carlo simulations in the hybridization expansion [197, 97] using w2dynamics [30] with worm sampling [96]. Momentum-dependent DMFT susceptibilities are calculated from the local vertex, following the aforementioned procedure, using the `AbinitioDΓA` [2, 33] program package.

2.5.5 Phase diagrams

For the prevailing magnetic and orbital orders, Fig. 2.56a and Fig. 2.56b displays the relevant DMFT susceptibilities at temperatures above the respective instabilities. Maxima in the shown susceptibilities indicate type and \mathbf{Q} -vector of the dominant fluctuations. Fig. 2.56c illustrates, for selected examples, the critical behavior of the (inverse) susceptibilities and (inverse) correlation lengths emerging when said maxima turn into instabilities. Magnetic instabilities occur where the static susceptibility in the magnetic channel $\chi_M(\mathbf{Q}, i\omega_m = 0)$ diverges at a critical temperature, indicated by the intercept of $\chi^{-1}(\mathbf{Q})$ with the temperature axis in Fig. 2.56c. Ferromagnetism (FM) and antiferromagnetism (AF) correspond to the usual ordering vectors $\mathbf{Q} = (0, 0)$ and $\mathbf{Q} = (\pi, \pi)$, respectively. The incom-

²⁵ 6 spin combinations ($\sigma\sigma, \sigma\sigma', \overline{\sigma\sigma'}$) and $n + 3n(n - 1)$ orbital combinations: n intra-orbital contributions ($iiii$) and $3n(n-1)$ inter-orbital contributions ($ijjj, ijji, ijij$). For the t_{2g} case, $n = 3$, this leads to a reduction from 1296 to 126 spin-orbit combinations.

mensurate magnetism (iM), that we find for the VO₂-termination, corresponds to an ordering vector \mathbf{Q} with fixed length $|\mathbf{Q}| = \delta \geq 0$, see Fig. 2.56a and Fig. 2.57.

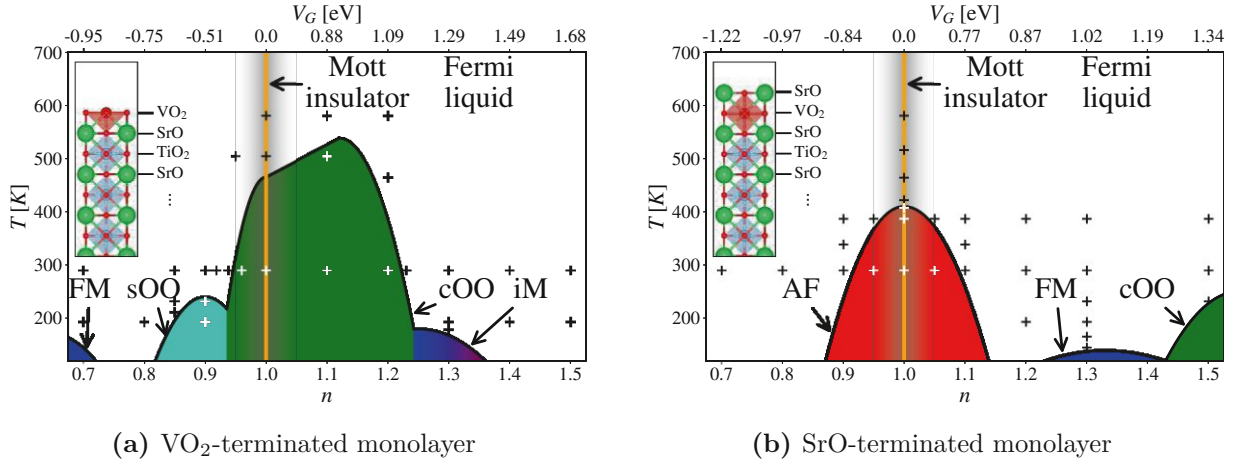


Figure 2.55: Phase diagrams. (a) VO₂ and (b) SrO terminated monolayers of SrVO₃ on a SrTiO₃ substrate (see insets) realize various phases as a function of the number of electrons per site in the low-energy t_{2g} (n ; lower x -axis) or gate voltage (V_G ; upper x -axis): antiferromagnetism (AF: red), ferromagnetism (FM: blue), incommensurate magnetism (iM: blueish), checkerboard orbital order (cOO: green), stripe orbital order (sOO: turquoise). The thus colored domes indicate the formation of long-range order within dynamical mean-field theory (DMFT). The $+$ -signs indicate points for which many-body calculations were performed (black signs represent non-divergent, white signs divergent DMFT susceptibilities). Based on the dominant susceptibilities, the color domes have been drawn as a guide to the eye.

We now assess the instabilities resulting in the phase diagrams, Fig. 2.55a,b. *Antiferromagnetic* (AF) order from super-exchange is facilitated by effectively half-filled orbitals. For the d^1 configuration of SrVO₃, only the SrO-terminated monolayer provides this favorable condition. Indeed, there, the positive crystal-field realizes a half-filled, Mott insulating xy -orbital that then hosts AF order, see the diverging susceptibility in Fig. 2.56c. Note that AF order was also predicted for a SrRuO₃ monolayer on SrTiO₃ around nominal stoichiometry [198]. There, the d^4 configuration results in an essentially fully occupied xy -orbital, and the staggered moment is instead carried by half-filled xz/xz orbitals. In both cases, doping with either electrons or holes suppresses the AF state.

Doping the SrVO₃ monolayer with either termination towards their respective van-Hove singularities, i.e., hole (electron) doping for the VO₂ (SrO) terminated sample (see Fig. 2.46) results in a strongly increased spectral density around the Fermi level within DMFT. Concomitantly doping generates

an orbital configuration where all involved orbitals are close to equally filled, promoting energy minimization through Hund's exchange J and therefore a parallel alignment of the involved spins. This situation, leading to *ferromagnetism* (FM), is found around $n = 0.7$ in the VO₂-terminated and near $n = 1.3$ in the SrO-terminated sample. In both cases, ferromagnetism is hosted by the degenerate xz and yz -orbitals. Subleading non-local AF fluctuations are, however, still present in the xy -orbital of the SrO-terminated system. Indeed, an antiferromagnetic stripe pattern, $\mathbf{Q} = (0, \pi)$, and symmetrically related at $\mathbf{Q} = (\pi, 0)$, appears, indicated by additional local maxima in the susceptibility, see Fig. 2.56b. Quite notably, in the absence of Hund's rule coupling FM fluctuations are strongly suppressed and said frustrated AF spin-fluctuations would be on par with them (additional data, not shown). Moreover, we also find incommensurate magnetic order in the VO₂-terminated system around $n = 1.3$ in the xz/yz -orbitals (iM at $n = 1.3$ in Fig. 2.56a). There, instead of a specific ordering vector \mathbf{Q} the magnetic susceptibility is maximal for all vectors \mathbf{Q} with origin $(0, 0)$ and a length of $\delta = |\mathbf{Q}| \geq 0$, i.e., roughly a circle in the \mathbf{q} -plane. Upon lowering temperature, δ increases and in close vicinity to the ordered phase anisotropy develops; the maximum susceptibility within the circle is found at $\mathbf{Q} = (\pm\delta, \pm\delta)$, see Fig. 2.57. These clear maxima suggest that a kind of frustrated ferromagnetism develops where the xy -orbital disturbs the alignment of the xz/yz -orbitals. Doping beyond $n = 1.3$ further increases δ (data not shown). Let us note here that throughout the phase diagram we did not find any magnetic instabilities supported by Fermi surface nesting.

The other prevalent type of instabilities we find are of *orbital-ordering* type between the degenerate xz/yz orbitals and can be monitored in the density channel

$$\begin{aligned} \chi_{oo}^{xz/yz}(\mathbf{Q}, i\omega_m = 0) &= \sum_{ij\sigma\sigma'} e^{i\mathbf{Q}\cdot(\mathbf{R}_i - \mathbf{R}_j)} \int d\tau \langle T_\tau (n_{i,xz,\sigma} - n_{i,yz,\sigma})(\tau) (n_{j,xz,\sigma'} - n_{j,yz,\sigma'})(0) \rangle \\ &\equiv 2\chi_D^{xz,xz} + 2\chi_D^{yz,yz} - 2\chi_D^{xz,yz} - 2\chi_D^{yz,xz} \end{aligned} \quad (2.122)$$

Towards quarter-filling ($n_{i,\sigma} = 0.25$) of the xz/yz -orbitals, i.e., at and around stoichiometric filling in the VO₂-terminated monolayer and around $n \sim 1.5$ in the SrO-terminated setup, the wave-vector of critical fluctuations is firmly $\mathbf{Q} = (\pi, \pi)$. As previously alluded to, this leads to a *checker-board orbital-order* (cOO), consistent with model expectations [184, 185]. We note that the xy -orbital does not participate in the ordering, as signaled by susceptibility enhancements being confined to components of the other two orbitals. The xy orbital can also be passive at larger fillings or valencies: With one electron more, a t_{2g}^2 OO—with xy -orbitals near half-filling and one electron alternating in the xz and the yz -orbital—can occur in YVO₃ (LaVO₃) if Y (La) ions are partially replaced by Ca (Sr) [199], cf. Refs. [200, 201]. An OO with all three t_{2g} -orbitals participating on the other hand is

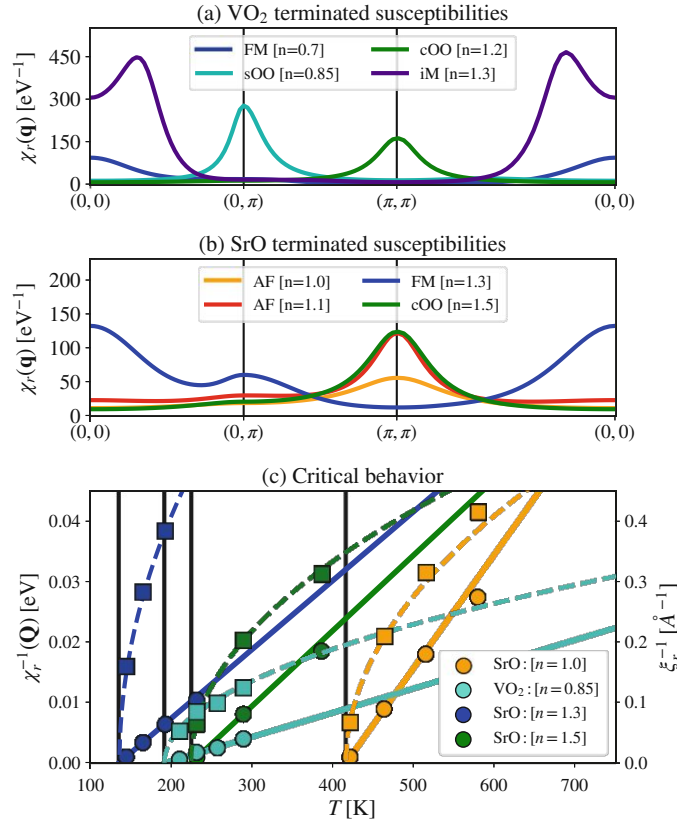


Figure 2.56: DMFT susceptibilities and criticality. Momentum-dependence of the susceptibility $\chi_r(\mathbf{q})$ for (a) the VO₂ terminated and (b) the SrO terminated SrVO₃ monolayer in the vicinity of the respective phase transitions. The dominating component can be either found directly in the magnetic channel (r ="M", Eq.(2.117a)) or be obtained via a linear orbital combination of the density channel (r ="D"). (c) Temperature-dependence of the inverse DMFT susceptibility $\chi_r^{-1}(\mathbf{Q})$ (first diverging r , \mathbf{Q} at selected dopings; circles, left axis) for selected points from (a) and (b); lines are linear fits. Intersections with the T -axis denote the transition temperature for the respective order. On the secondary (right) axis the corresponding inverse correlation lengths ξ_r^{-1} are shown (squares, right axis); dashed lines are fits to mean-field behavior.

highly frustrated for a cubic lattice [202]. Due to the strong asymmetry around nominal filling in our monolayers, we also find a strong asymmetry of the corresponding cOO-dome in Fig. 2.55a, where the cOO transition temperature even increases upon electron-doping. If we move too far away from ideal quarter-filling, the ordering temperature is suppressed rapidly. Despite this suppression of cOO we find an additional emerging ordering for $n \sim 0.9$ in Fig. 2.55a. The corresponding ordering can again be described via Eq. (2.122) with, however, a characteristic vector $\mathbf{Q} = (0, \pi)$ (and $\mathbf{Q} = (\pi, 0)$

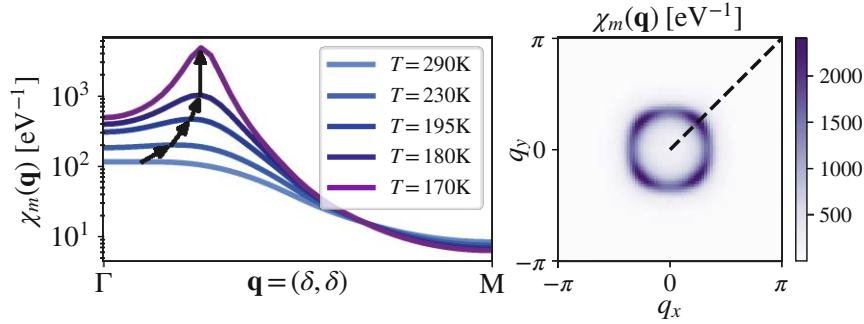


Figure 2.57: Incommensurate magnetism (iM). Left: magnetic susceptibility $\chi_m(q)$ along the high-symmetry path $\Gamma \rightarrow M$ for the VO_2 -terminated monolayer at $n = 1.3$ at various temperatures. Right: magnetic susceptibility $\chi_m(q)$ for $T = 170\text{K}$ in the planar Brillouin zone. The susceptibility is maximal roughly on a circle centered around $\mathbf{q} = (0, 0)$. Upon lowering temperature the maximum of the susceptibility moves to larger \mathbf{q} -vectors. Close to the transition temperature we find anisotropy on this circle where the susceptibility is clearly maximal (purple) for $\mathbf{q} = (\pm\delta, \pm\delta)$.

related via symmetry), describing *stripe orbital-ordering* (sOO). The cOO-to-sOO transition under hole-doping is not realized by a continuous move of the ordering vector from $\mathbf{Q} = (\pi, \pi)$ to $\mathbf{Q} = (0, \pi)$. Instead, increased hole-doping suppresses cOO while simultaneously promoting sOO. We conjecture that this transition can be ascribed to the “auxiliary” xy -orbital, that does not contribute to the susceptibility enhancements of either fluctuations. Illustrated in the inset of Fig. 2.49 we find a semi-empirical condition that links the preference for stripe over checkerboard orbital order to the filling of the xy -orbital: $n_{xy,\sigma} = (0.25 - n_{xz/yz,\sigma})/2$ below which checkerboard ordering and above which stripe ordering is preferred by the system. Effectively, enough d_{xy} occupation frustrates the local site enough for stripe ordering to be energetically favorable. As for the electron-doped side, the orbital-ordering domes in both systems disappear when doping too far away from quarter-filling.

2.5.6 Orbital mapping

Depending on the surface termination, SrO or VO_2 , the monolayer is an effectively half-filled one-orbital or a quarter-filled two-orbital Mott insulator. This orbital polarization is derived from the crystal-field splitting having opposite signs for the two terminations and to be significantly enhanced by electronic correlations. Electron or hole-doping reveals multi-orbital effects: For the SrO-termination, AF-fluctuation are dominant around nominal filling. Doping with electrons populates the xz/yz -orbitals; they order ferromagnetically ($n \sim 1.3$) or realize checkerboard orbital order ($n \sim 1.5$). For the VO_2 termination checkerboard xz/yz orbital-order already dominates around

nominal filling. Doping then instead promotes the xy -orbital which acts as a mediator for ferromagnetism and stripe orbital-order on the hole-doped side and incommensurate magnetism on the electron-doped side. While the change in magnetic fluctuations and orders could be observed in neutron experiments, experimentally evidencing the orbital fluctuations is only possible indirectly: the staggered pattern of xz and yz -orbitals will result in a dynamic (potentially static) alternation of the bond-length in the x and y direction, possibly detectable in future X-ray measurements.

In all, the orbital polarization is the essential driver of the phase diagram of the SrVO₃ monolayer on SrTiO₃. We therefore summarize the DMFT results in Fig. 2.58 in form of an orbital occupation map. The considered surface terminations each realize, under doping, a characteristic trajectory in the n_{xy} vs. $n_{xz} + n_{yz}$ space. As an outlook, we include a third possibility—a SrVO₃ monolayer with SrTiO₃ on both sides: At nominal filling this sandwich is, again, a Mott insulator. However, owing to the symmetric embedding, the crystal-field is minute (but positive). The computation of ordering instabilities of capped ultra-thin films, in which quantum confinement effects could be studied in a more controlled fashion, is left for future work.

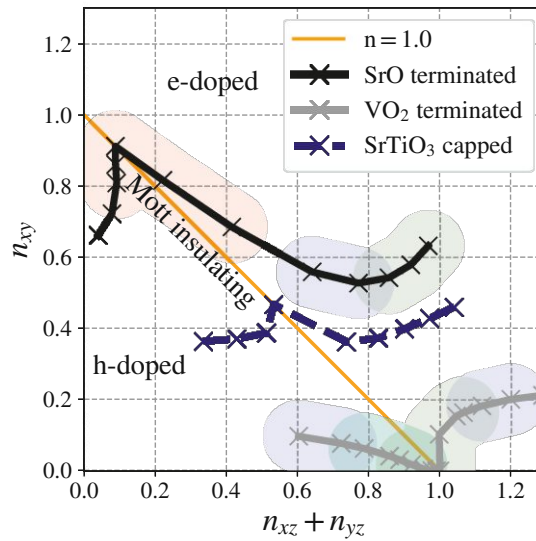


Figure 2.58: Global phase diagram of SrVO₃ monolayers on SrTiO₃. DMFT orbital occupations of each setup are mapped into a n_{xy} vs. $n_{xz} + n_{yz}$ graph. Due to the reduced bandwidth in the monolayer on a SrTiO₃ substrate, any orbital occupation repartitioning of the nominal $n = 1$ filling (orange line) realizes a Mott insulator. Besides the here discussed SrO (black) and VO₂ (gray) termination, as an outlook we showcase the effect of embedding a SrVO₃ monolayer in a SrTiO₃ sandwich (navy blue, dashed).

2.5.7 Non-local self-energy corrections

On the dynamical mean-field level, many-body renormalizations are assumed to be isotropic (i.e., independent of momentum). In 3D this is mostly a good approximation (see, however, Ref. [203]). Yet, when the effective dimensionality is reduced, as in our ultrathin film, renormalizations become increasingly non-local [178]. The major question we will answer next is: *To what extent do the non-local critical fluctuations—in the vicinity of the associated ordered states—lead to momentum-selective renormalizations?* To elucidate this question, we use the **AbinitioDfA** [33, 1, 2] methodology and scrutinize the electron self-energy $\Sigma(\mathbf{k}, i\nu)$ in the vicinity of the DMFT ordering instabilities. The considered points in the phase diagrams are illustrated in Fig. 2.59.

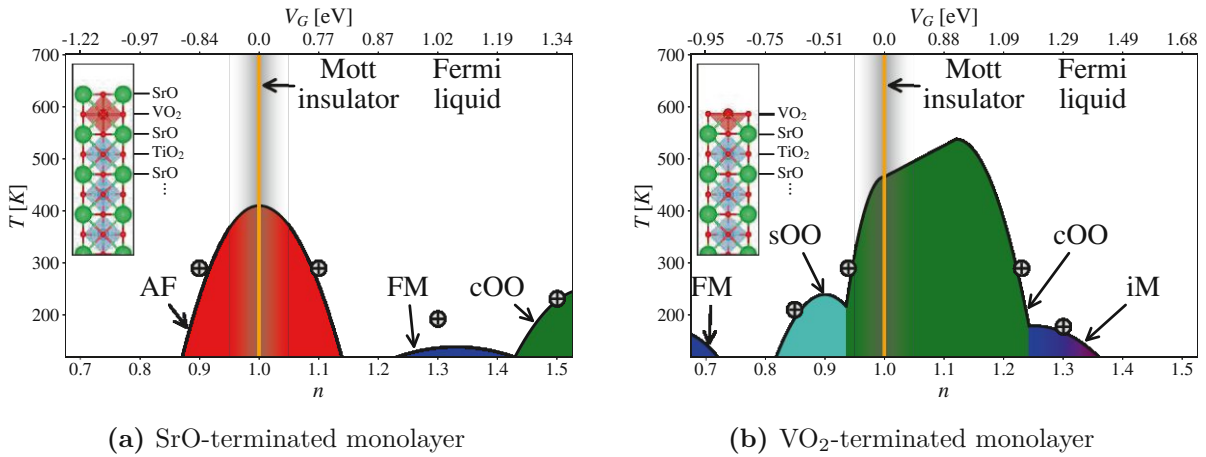


Figure 2.59: Phase diagrams. (a) SrO- and (b) VO₂-terminated SrVO₃-monolayer on top of a SrTiO₃ substrate (see insets for crystal structures) exhibit numerous phases as a function of electrons per site (n ; lower x -axis) in the low-energy vanadium t_{2g} orbitals or gate voltage (V_G ; upper x -axis): antiferromagnetism (AF: red), ferromagnetism (FM: blue), incommensurate magnetism (iM: blueish), checkerboard orbital order (cOO: green), stripe orbital order (sOO: turquoise). The colored domes mark the occurrence of long-range order within dynamical mean-field theory (DMFT); adapted from Ref. [5]. The “+”-marks indicate points for which we present DfA (and DMFT) data in the present paper.

As a starting point, Fig. 2.60 shows the DMFT Fermi surface for the SrO-terminated SrVO₃ monolayer at the four selected dopings (left to right). They are obtained from the Green’s function at imaginary time $\tau = \beta/2$ ($\beta = 1/k_B T$). This procedure corresponds to a spectral function $\overline{A}(\mathbf{k}, \omega = 0)$ that is averaged over a frequency-interval $\sim k_B T$ around the Fermi level.

The upper panels display the contribution of the xy orbital and the lower panels the xz orbital

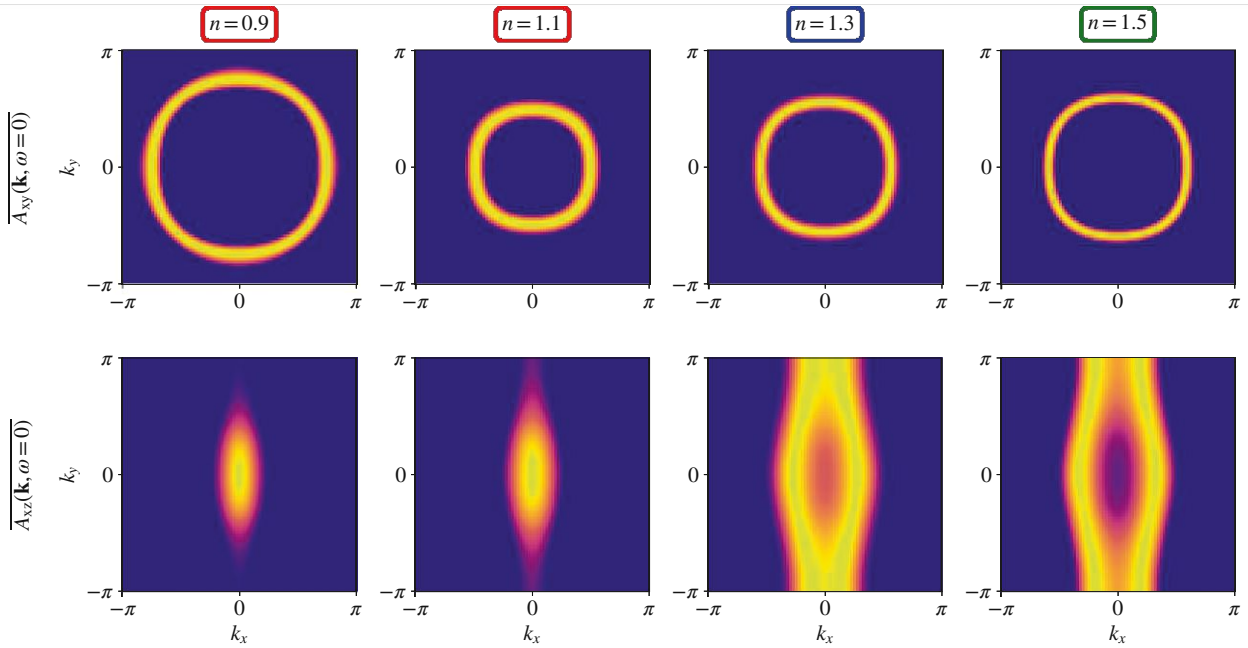


Figure 2.60: SrO-terminated monolayer – DMFT Fermi surface for the points highlighted in Fig. 2.55a: $n = 0.9$ ($T = 290\text{K}$) and $n = 1.1$ ($T = 290\text{K}$) order AF at low T (red box indicating the color code of Fig. 2.55), FM at $n = 1.3$ ($T = 190\text{K}$; blue box), and cOO at $n = 1.5$ ($T = 230\text{K}$; green box).

(the yz orbital is equivalent to the latter if rotated by 90°). Doping with 10% electrons or holes, the system transitions from an orbitally polarized Mott insulator to a metal, where the xz and yz orbitals are now slightly filled, pushing the AF phase transition to lower T . The aforementioned orbital reconfiguration and its asymmetry with respect to $n = 1$ is especially noticeable in the sizes of the xy Fermi surface, cf. Fig. 2.49. Larger electron doping “activates” the multi-orbital nature of the system where the increased occupation causes the energetically higher-lying xz and yz orbitals to be filled at a more rapid pace compared to the xy orbital. The Fermi surface of the xz orbital therefore transitions from a thin strip ($n = 0.9$; $n = 1.1$) to the more usual cylinder-shaped form ($n = 1.3$; $n = 1.5$).

The Fermi surfaces of the selected points of the VO₂-terminated SrVO₃ monolayer are illustrated in Fig. 2.61. Inverting the role of the xz/yz and the xy orbitals compared to the SrO-termination, we now observe a small hole pocket for the xy orbital in Fig. 2.61. Reducing the filling from $n = 0.94$ to $n = 0.85$, this xy Fermi-surface pocket becomes slightly enhanced, albeit it remains small.

Identical to the SrO-terminated monolayer, increasing the beyond $n = 1.2$ activates the xz/yz .

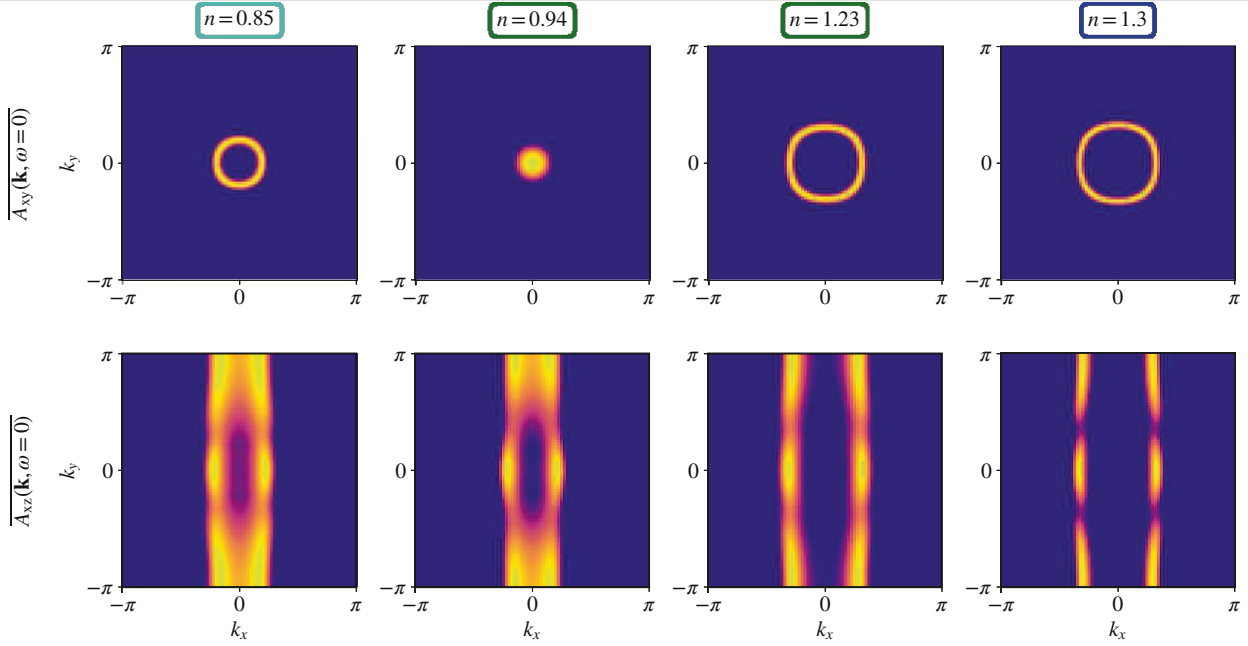


Figure 2.61: VO₂-terminated monolayer – DMFT Fermi surface for the points highlighted in Fig. 2.55b: $n = 0.94$ ($T = 290\text{K}$) and $n = 1.23$ ($T = 290\text{K}$) order cOO at low T (green box indicating the color code of Fig. 2.55), $n = 0.85$ sOO ($T = 210\text{K}$; turquoise box), and $n = 1.3$ iM ($T = 190\text{K}$; blue box).

While for $n = 1.23$ the cOO still dominates, further doping from $n = 1.23$ to $n = 1.3$ instead changes the DMFT ordered state from cOO to incommensurate magnetism (iM) with a small \mathbf{q} -vector in Fig. 2.55. It has, however, little effect on the the spectral signatures. The sharper Fermi surface for $n = 1.3$ can be explained by the slight decrease in the temperature and the fact that *local* DMFT correlations get reduced the farther we are away from half-filling.

Note that the “empty” spots in the xz Fermi surface of the VO₂-terminated monolayer are not present in the SrO-terminated monolayer. This behavior stems from the increased band hybridization of the underlying t_{2g} projection, see Fig. 2.46.

2.5.7.1 Dynamical vertex approximation

In this Section we are going to give a concise (technical) introduction to the ladder variant of the dynamical vertex approximation employed in `AbinitioDGA`. A more detailed discussion of the method can be found in Refs. [33, 176]. A broader discussion on the different variations of the DGA can be found in Section 2.6.

Provided fluctuations occur mainly in the shape of particle-hole fluctuations we can approximate the two-particle irreducible vertex Λ and the two-particle reducible vertex in the particle particle channel as *local* in the parquet equation via

$$\begin{aligned} F_D^{qkk'} &= \Lambda_D^{\omega\nu\nu'} + \Phi_{D,pp}^{\omega\nu\nu'} + \Phi_{D,ph}^{q\nu\nu'} + \Phi_{D,\overline{ph}}^{qkk'} \\ &= \Lambda_D^{\omega\nu\nu'} + \Phi_{D,pp}^{\omega\nu\nu'} + \Phi_{D,ph}^{\omega\nu\nu'} + \Phi_{D,\overline{ph}}^{\omega\nu\nu'} + \left(\Phi_{D,ph}^{q\nu\nu'} - \Phi_{D,ph}^{\omega\nu\nu'} \right) + \left(\Phi_{D,\overline{ph}}^{qkk'} - \Phi_{D,\overline{ph}}^{\omega\nu\nu'} \right) \\ &= F_D^{\omega\nu\nu'} + \left(\Phi_{D,ph}^{q\nu\nu'} - \Phi_{D,ph}^{\omega\nu\nu'} \right) + \left(\Phi_{D,\overline{ph}}^{qkk'} - \Phi_{D,\overline{ph}}^{\omega\nu\nu'} \right) \end{aligned} \quad (2.123)$$

By treating the ph and the \overline{ph} channel on equal footing we are able to enforce the crossing (CR) symmetry explicitly. Illustrated in Fig. 2.62, exchanging the in- or outgoing legs transforms diagrams between the ph and \overline{ph} channel

$$\Phi_{\overline{ph},lmm'l'}^{\omega\nu\nu'} \underset{\sigma\sigma'}{\stackrel{\text{CR}}{=}} -\Phi_{ph,ll'm'm}^{\nu-\nu')\nu(\nu-\omega)}, \quad (2.124a)$$

$$\underset{\sigma'\sigma}{\stackrel{\text{CR}}{=}} -\Phi_{ph,m'mll'}^{\nu'-\nu)(\nu'-\omega)\nu'}. \quad (2.124b)$$

Through this type of transformation we can express the transversal particle-hole channel in terms of

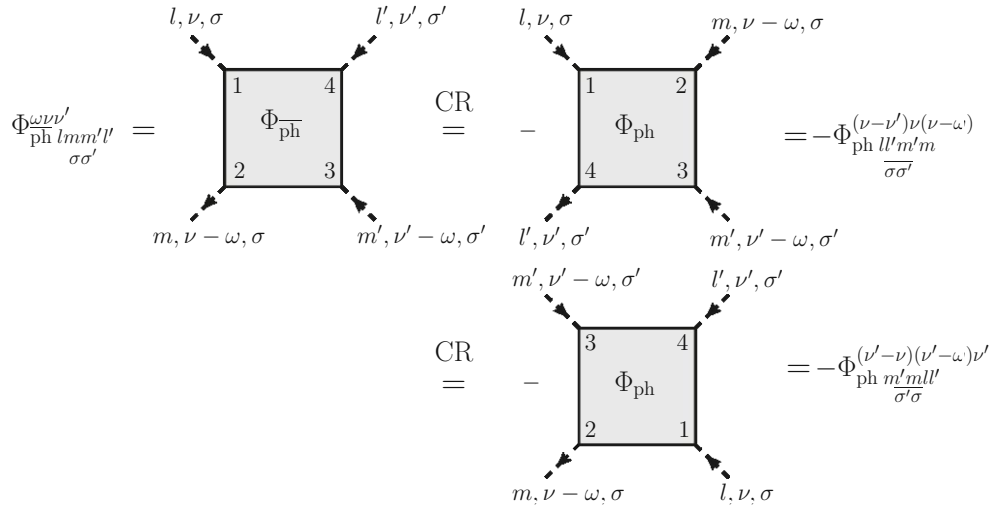


Figure 2.62: Crossing symmetric change from particle-hole transversal reducible (\overline{ph}), separable between internal pairs 14 — 23, to particle-hole reducible (ph), separable between internal pairs 12 — 34 by exchanging the outgoing (top line) or incoming lines (bottom line). The additional sign stems from the fermionic anti commutator where we employ the particle-hole notation throughout, see Appendix A.1.

the particle-hole channel

$$\begin{aligned}
\Phi_{\overline{ph},D}^{\omega\nu\nu'} &= \Phi_{\overline{ph},\uparrow\uparrow}^{\omega\nu\nu'} + \Phi_{\overline{ph},\uparrow\downarrow}^{\omega\nu\nu'} \\
&\stackrel{\text{CR}}{=} -\Phi_{\overline{ph},\uparrow\uparrow}^{(\nu'-\nu)(\nu'-\omega)\nu'} - \Phi_{\overline{ph},\uparrow\downarrow}^{(\nu'-\nu)(\nu'-\omega)\nu'} \\
&\stackrel{\text{SU}(2)}{=} -\Phi_{\overline{ph},\uparrow\uparrow}^{(\nu'-\nu)(\nu'-\omega)\nu'} - \Phi_{\overline{ph},\uparrow\downarrow}^{(\nu'-\nu)(\nu'-\omega)\nu'} + \Phi_{\overline{ph},\downarrow\downarrow}^{(\nu'-\nu)(\nu'-\omega)\nu'} \\
&= \frac{1}{2} \left(-\Phi_{\overline{ph},\uparrow\uparrow}^{(\nu'-\nu)(\nu'-\omega)\nu'} - \Phi_{\overline{ph},\uparrow\downarrow}^{(\nu'-\nu)(\nu'-\omega)\nu'} \right) + \frac{3}{2} \left(-\Phi_{\overline{ph},\uparrow\uparrow}^{(\nu'-\nu)(\nu'-\omega)\nu'} + \Phi_{\overline{ph},\uparrow\downarrow}^{(\nu'-\nu)(\nu'-\omega)\nu'} \right) \\
&= -\frac{1}{2} \Phi_{\overline{ph},D}^{(\nu'-\nu)(\nu'-\omega)\nu'} - \frac{3}{2} \Phi_{\overline{ph},M}^{(\nu'-\nu)(\nu'-\omega)\nu'}
\end{aligned} \tag{2.125a}$$

$$\begin{aligned}
\Phi_{\overline{ph},M}^{\omega\nu\nu'} &= \Phi_{\overline{ph},\uparrow\uparrow}^{\omega\nu\nu'} - \Phi_{\overline{ph},\uparrow\downarrow}^{\omega\nu\nu'} \\
&\stackrel{\text{CR}}{=} -\Phi_{\overline{ph},\uparrow\uparrow}^{(\nu'-\nu)(\nu'-\omega)\nu'} + \Phi_{\overline{ph},\uparrow\downarrow}^{(\nu'-\nu)(\nu'-\omega)\nu'} \\
&\stackrel{\text{SU}(2)}{=} -\Phi_{\overline{ph},\uparrow\uparrow}^{(\nu'-\nu)(\nu'-\omega)\nu'} + \Phi_{\overline{ph},\uparrow\downarrow}^{(\nu'-\nu)(\nu'-\omega)\nu'} - \Phi_{\overline{ph},\downarrow\downarrow}^{(\nu'-\nu)(\nu'-\omega)\nu'} \\
&= \frac{1}{2} \left(-\Phi_{\overline{ph},\uparrow\uparrow}^{(\nu'-\nu)(\nu'-\omega)\nu'} - \Phi_{\overline{ph},\uparrow\downarrow}^{(\nu'-\nu)(\nu'-\omega)\nu'} \right) + \frac{1}{2} \left(\Phi_{\overline{ph},\uparrow\uparrow}^{(\nu'-\nu)(\nu'-\omega)\nu'} - \Phi_{\overline{ph},\uparrow\downarrow}^{(\nu'-\nu)(\nu'-\omega)\nu'} \right) \\
&= -\frac{1}{2} \Phi_{\overline{ph},D}^{(\nu'-\nu)(\nu'-\omega)\nu'} + \frac{1}{2} \Phi_{\overline{ph},M}^{(\nu'-\nu)(\nu'-\omega)\nu'}
\end{aligned} \tag{2.125b}$$

and identically for the full momentum dependency

$$\Phi_{\overline{ph},D}^{qkk'} = -\frac{1}{2} \Phi_{\overline{ph},D}^{(k'-k)(k'-q)k'} - \frac{3}{2} \Phi_{\overline{ph},M}^{(k'-k)(k'-q)k'} \tag{2.126a}$$

$$\Phi_{\overline{ph},M}^{qkk'} = -\frac{1}{2} \Phi_{\overline{ph},D}^{(k'-k)(k'-q)k'} + \frac{1}{2} \Phi_{\overline{ph},M}^{(k'-k)(k'-q)k'}. \tag{2.126b}$$

where $k = (\mathbf{k}, \nu)$, $k' = (\mathbf{k}', \nu')$ and $q = (\mathbf{q}, \omega)$. The non-local corrections to the reducible vertices now can be rewritten to

$$\Phi_{\overline{D,ph}}^{q\nu\nu'} - \Phi_{\overline{D,ph}}^{\omega\nu\nu'} = \left(F_{\overline{D,ph}}^{q\nu\nu'} - \Gamma_{\overline{D,ph}}^{q\nu\nu'} \right) - \left(F_{\overline{D,ph}}^{\omega\nu\nu'} - \Gamma_{\overline{D,ph}}^{\omega\nu\nu'} \right) = F_{\overline{D,ph}}^{q\nu\nu',\text{nl}}, \tag{2.127}$$

and

$$\begin{aligned}
\Phi_{lmm'l'}^{qkk'} - \Phi_{lmm'l'}^{\omega\nu\nu'} &= -\frac{1}{2}\Phi_{m'mll'}^{(k'-k)(k'-q)k'} - \frac{3}{2}\Phi_{m'mll'}^{(k'-k)(k'-q)k'} + \frac{1}{2}\Phi_{m'mll'}^{(\nu'-\nu)(\nu'-\omega)\nu'} + \frac{3}{2}\Phi_{m'mll'}^{(\nu'-\nu)(\nu'-\omega)\nu'} \\
&= -\frac{1}{2}\left(F_{D,ph}^{(k'-k)(k'-q)k'} - \Gamma_{D,ph}^{(k'-k)(k'-q)k'}\right) - \frac{3}{2}\left(F_{M,ph}^{(k'-k)(k'-q)k'} - \Gamma_{M,ph}^{(k'-k)(k'-q)k'}\right) \\
&\quad + \frac{1}{2}\left(F_{D,ph}^{(\nu'-\nu)(\nu'-\omega)\nu'} - \Gamma_{D,ph}^{(\nu'-\nu)(\nu'-\omega)\nu'}\right) + \frac{3}{2}\left(F_{M,ph}^{(\nu'-\nu)(\nu'-\omega)\nu'} - \Gamma_{M,ph}^{(\nu'-\nu)(\nu'-\omega)\nu'}\right) \\
&= -\frac{1}{2}F_{D,ph}^{(k'-k)(\nu'-\omega)\nu',nl} - \frac{3}{2}F_{M,ph}^{(k'-k)(\nu'-\omega)\nu',nl}.
\end{aligned} \tag{2.128}$$

Inserted into the initial parquet equation gives us an expression that can be constructed with purely ph ladders in the density and magnetic channel

$$F_{lmm'l'}^{qkk'} = F_{lmm'l'}^{\omega\nu\nu'} + \underbrace{F_{lmm'l'}^{q\nu\nu',nl} - \frac{1}{2}F_{D,ph}^{(k'-k)(\nu'-\omega)\nu',nl} - \frac{3}{2}F_{M,ph}^{(k'-k)(\nu'-\omega)\nu',nl}}_{\text{constructed with non-local ph ladder}}, \tag{2.129}$$

The momentum dependent self-energy can be calculated via the Schwinger Dyson equation (equation of motion) resulting in one-particle Hartree Fock contributions Σ^{HF} and a connection between the one-particle and two-particle level Σ^{con}

$$\begin{aligned}
\Sigma_{mm'}^k &= \Sigma_{mm'}^{\text{kHF}} + \Sigma_{mm'}^{\text{kcon}} \\
&= \underbrace{\sum_{\substack{\mathbf{k}' \\ l_n \\ \sigma'}} U_{mlm'n} n_{l_n}^{\mathbf{k}'}}_{\text{Hartree}} - \underbrace{\sum_{lh} U_{mlhm'} n_{lh}^{\mathbf{k}-\mathbf{q}}}_{\text{Fock}} - \frac{1}{\beta} \underbrace{\sum_{\substack{qk' \\ lhn,rst}} U_{mlhn} \chi_{0,nlsr}^{qk'k'} F_{rstm'}^{qk'k} G_{ht}^{k-q}}_{\text{Connected}}
\end{aligned} \tag{2.130}$$

illustrated in Fig. 2.63 and Fig. 2.64. Please note that the numerical implementation of this equation is more elaborate and built on the basis of three-leg (boson - fermion) vertices [2]. They allow for a more efficient evaluation, details thereof (including possible non-local interactions) can be found in Refs. [33, 176].

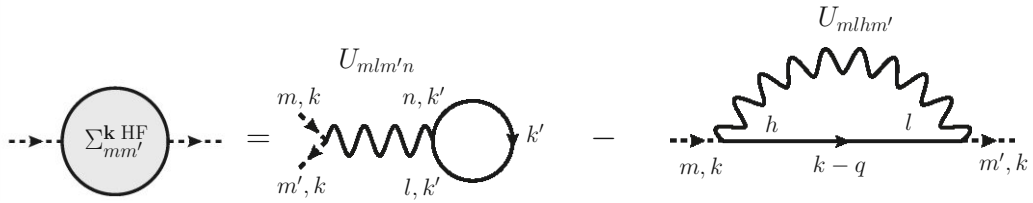


Figure 2.63: Diagrammatic representation of the Hartree and Fock contribution to the self-energy in Eq. (2.130). In the former, the occupation n_{ln} is represented by a fermionic loop from vertex n to l . In the latter, due to spin conservation the propagator $k - q$ must have the same spin as the implied incoming and outgoing propagators. The dashed propagators imply that they do not contribute to the diagram.

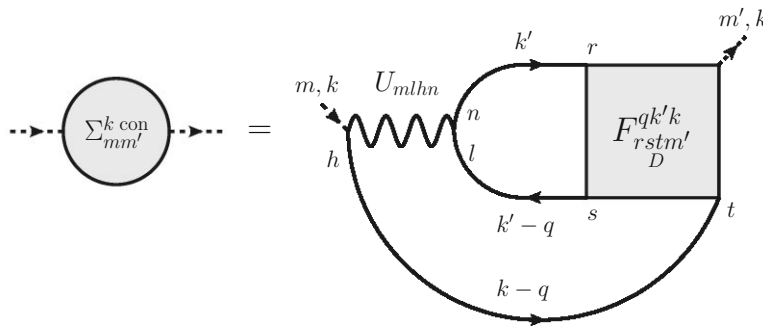


Figure 2.64: Diagrammatic representation of the connected contribution to the self-energy in Eq. (2.130) containing the full (density) vertex $F_D^{qk'k}$. The dashed propagators imply that they do not contribute to the diagram.

The following results were obtained via the `AbinitioDFA` package [2]. The local two-particle Green's function was sampled at DMFT self-consistency by continuous-time quantum Monte Carlo simulations in the hybridization expansion [97, 197] using `w2dynamics` [30] with worm sampling [96]. The DFA chemical potential was readjusted to fix the total number of electrons to the considered doping level. In this study we apply DFA in a *one-shot setting*, forgoing λ -corrections or self-consistency, see Ref. [4] and Section 2.6. Therefore, `AbinitioDFA` results can only be obtained where the DMFT is yet to be ordered $\lambda_r < 1$. The resulting, too large susceptibilities from DMFT, will lead to an overestimation of spectral renormalizations in DFA.

One-shot results however remain useful as a first “estimate” of the non-local physics as play. For example, the momentum selectivity of the pseudogap in the half-filled one-band Hubbard model in

the weak coupling regime can already be observed in the first D Γ A “shot” (not shown).

D Γ A Fermi surfaces are obtained from the Green’s function at imaginary time $\tau = \beta/2$ ($\beta = 1/k_B T$). This procedure corresponds to a spectral function $\overline{A(\mathbf{k}, \omega = 0)}$ that is averaged over a frequency-interval $\sim k_B T$ around the Fermi level, see Appendix A.2. We emphasize that our **AbinitioD Γ A** calculations are not self-consistent.

2.5.7.2 SrO termination

Fig. 2.65 shows the real and imaginary part of the **AbinitioD Γ A** self-energy in the vicinity of the DMFT phase transitions where non-local correlations become strong. Shown are the two inequivalent orbitals, xy (top) and xz (middle panel) as a function of Matsubara frequency ν_n . The yz orbital is equivalent to the xz orbital if the momenta are rotated by 90° rotated; the DMFT self-energy is shown for comparison. In the vicinity of half-filling, $n = 0.9$ and $n = 1.1$, AF spin fluctuations prevail with leading eigenvalue $\lambda_M(\pi, \pi) = 0.95$ and 0.79 , respectively, in the magnetic (M) channel at $\mathbf{q} = (\pi, \pi)$. Note, $\lambda = 1$ indicates a divergence of the susceptibility, i.e., an ordering instability. These AF spin fluctuations are driven by the xy orbital that is close to half filling, whereas the xz and yz orbitals rather act as passive bystanders [5]. Consequently, we see for $n = 0.9$ and $n = 1.1$ in Fig. 2.65 a pronounced momentum differentiation only for the xy orbital. The Matsubara frequency self-energy has the advantage that it does not require the ill-conditioned analytic continuation. Nonetheless, we can gain valuable information: The momentum differentiation of the real part of the self-energy in Fig. 2.65 between unoccupied [$\mathbf{k} = (0, 0)$, red] and occupied states [$\mathbf{k} = (\pi, \pi)$, green] signals that the quasi-particle poles at $\omega + \mu = \Re\Sigma + \epsilon_{\mathbf{k}}$ are pushed further away from the Fermi energy, causing an overall *enhancement* of the bandwidth. The momentum differentiation between $\mathbf{k} = (0, \pi)$ (blue) and $\mathbf{k} = (\pi/2, \pi/2)$ (orange) that are closer to the Fermi level, indicates a deformation of the Fermi surface for $n = 0.9$, but not for $n = 1.1$ which has a similar self-energy for these two \mathbf{k} -points. Indeed a deformation is observed in Fig. 2.66, where the electron-like DMFT Fermi surface (Fig. 2.60) turns into a hole-like one in D Γ A for $n = 0.9$. For $n = 1.3$ with strong FM fluctuations ($\lambda_M(0, 0) = 0.78$) and $n = 1.5$ with strong cOO fluctuations in the density (D) channel ($\lambda_D(\pi, \pi) = 0.98$), the momentum differentiation of $\Re\Sigma$ is less pronounced.

Let us now turn to $\Im\Sigma$ from which we can read off the scattering rate, as the $\nu_n \rightarrow 0$ -extrapolated value. Further, from its slope the quasi-particle renormalization $Z_{\mathbf{k}} = [1 - \partial\Im\Sigma(\mathbf{k}, i\nu)/\partial\nu|_{\nu \rightarrow 0}]^{-1}$ is accessible for a Fermi liquid phase. A positive slope of $\Im\Sigma(i\nu \rightarrow 0)$ indicates the crossover to a diverging (Mott-like) self-energy, which splits the spectrum and leads to an insulating gap. Clearly, for all four fillings shown in Fig. 2.65, there are momenta for which the system exhibits non-Fermi liquid

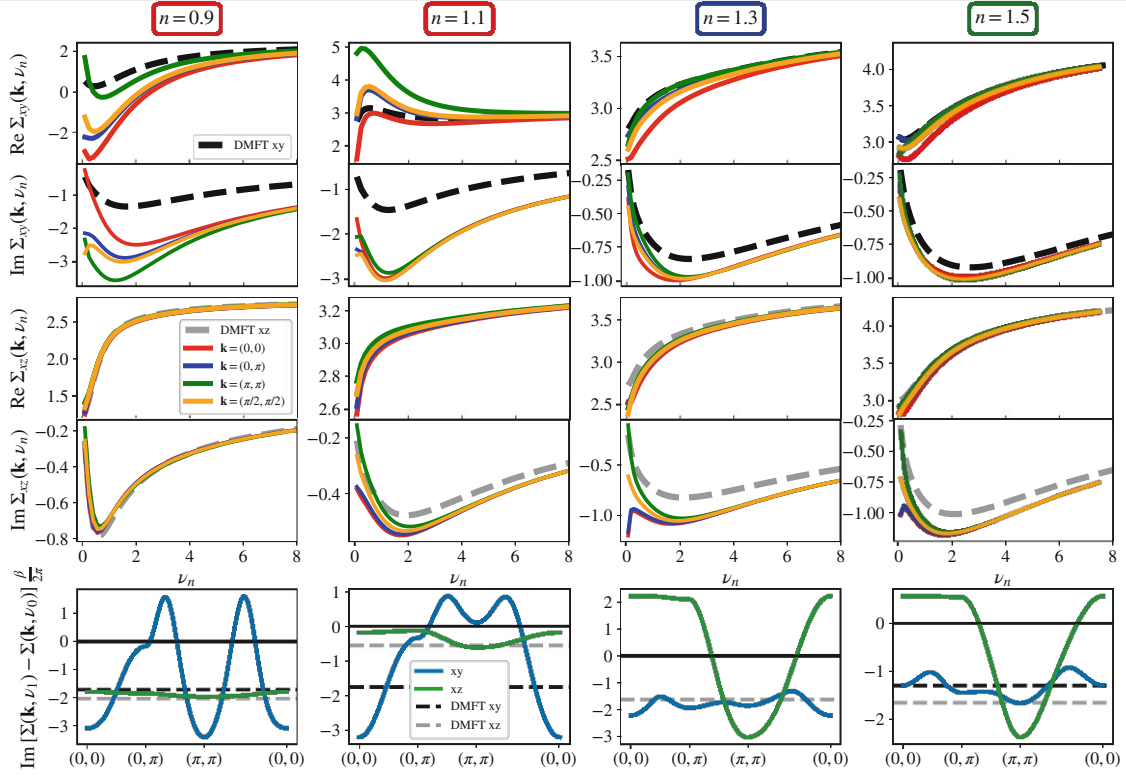


Figure 2.65: SrO-terminated monolayer – Momentum differentiation of the DΓA self-energy. Top 4 rows: real and imaginary parts for the xy and xz orbital at 4 different momenta, compared to DMFT, for the dopings and temperatures indicated in Fig. 2.55a. Bottom row: Slope of the imaginary part of the DΓA self-energy for a path through the Brillouin zone. Negative values correspond to a Fermi-liquid like self-energy, positive values indicate the formation of a (pseudo)gap.

behavior, identifiable by a kink and a downturn in $\Im\Sigma$ at low energies. In case of AF fluctuations ($n = 0.9$ and $n = 1.1$) this downturn is in the xy orbital, whereas it occurs in the xz (and yz) orbital which dominates the FM ($n = 1.3$) and cOO ($n = 1.5$) fluctuations. These kinks are salient indicators for the occurrence of a pseudogap state, and they get more pronounced when cooling the system toward the respective phase transition. Interestingly, in the vicinity of the AF phase, the structure of the scattering rate is *opposite* to the cuprates: It is larger for the diagonal (π, π) direction than for the $(0, \pi)$ direction. This momentum differentiation on the Fermi surface is, however, much less pronounced than the momentum dependence perpendicular to the Fermi surface, i.e., comparing occupied vs. unoccupied states. This can be seen in Fig. 2.65 (bottom), where we plot the slope between the first two positive Matsubara frequencies, i.e., $slope = (\Im\Sigma(i\nu_1) - \Im\Sigma(i\nu_0))\beta/(2\pi)$, along

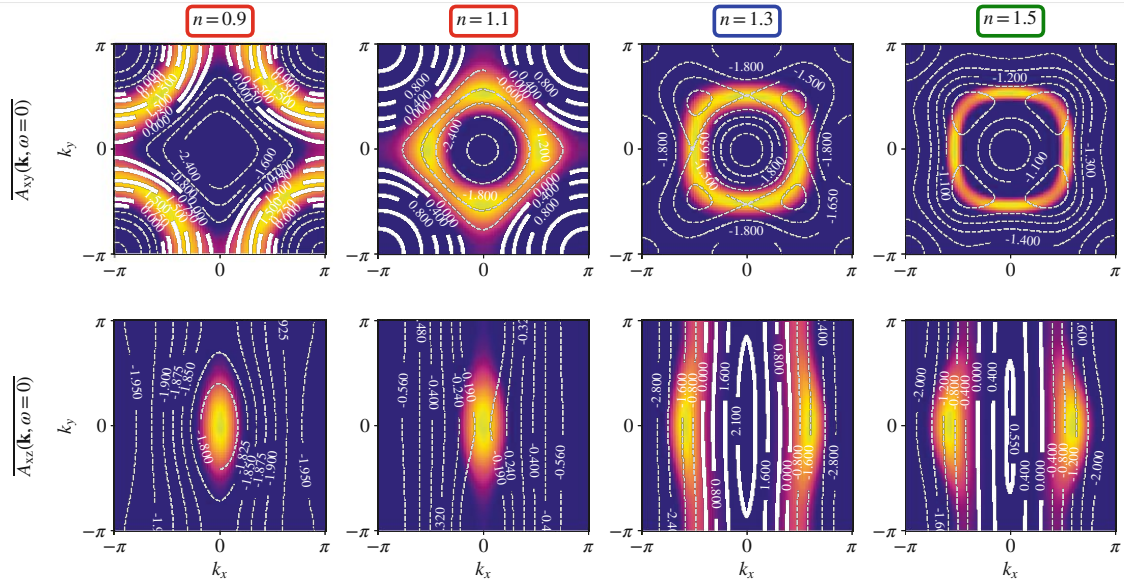


Figure 2.66: SrO-terminated monolayer – DΓA Fermi surfaces at the same dopings and T as in Fig. 2.60. The white lines represent isolines of the slope between the first two Matsubara frequencies of the imaginary part of Σ : Solid, fat lines indicate a *positive* slope, i.e., a kink in the self-energy, dashed, thin lines a *negative* value, suggestive of a Fermi-liquid-like state.

the indicated \mathbf{k} -path. Isolines of this slope are superimposed on the DΓA Fermi surfaces in Fig. 2.66, with the sign indicated by solid, fat (positive) and dashed, thin (negative) lines. In the electron doped regime, the slope in $\Im\Sigma$ is always negative on the Fermi surface, i.e., Fermi liquid-like. However, when moving away from the Fermi energy, we observe positive slopes, which corresponds to the kinks in Fig. 2.65;: at $n = 1.1$ for the unoccupied xy states above the Fermi level; and at $n = 1.3$ and $n = 1.5$ for the occupied xz states. In the hole doped regime, at $n = 0.9$, we find $\Im\Sigma$ isoline patterns similar to $n = 1.1$. However, owing to the larger xy -occupation in combination with the equally strong reconstruction through $\Re\Sigma$, negative slopes of $\Im\Sigma$ instead appear across the transformed xy Fermi surface. This insulating-like behavior is found only in the most relevant orbitals, i.e., the xy orbital for the AF fluctuations around $n = 1$, and the xz/yz orbitals where FM and cOO long-range fluctuations are dominant. The ancillary orbitals (xz/yz for $n = 1.1$ and xy for $n = 1.3, 1.5$) on the other hand exhibit only a comparatively minor momentum differentiation (see Fig. 2.65)—implying also a stark orbital differentiation.

2.5.7.3 VO₂ termination

The corresponding `AbinitioDΓA` results for the VO₂-terminated SrVO₃ monolayer for the self-energy and the Fermi surface are presented in Fig. 2.67 and Fig. 2.68, respectively.

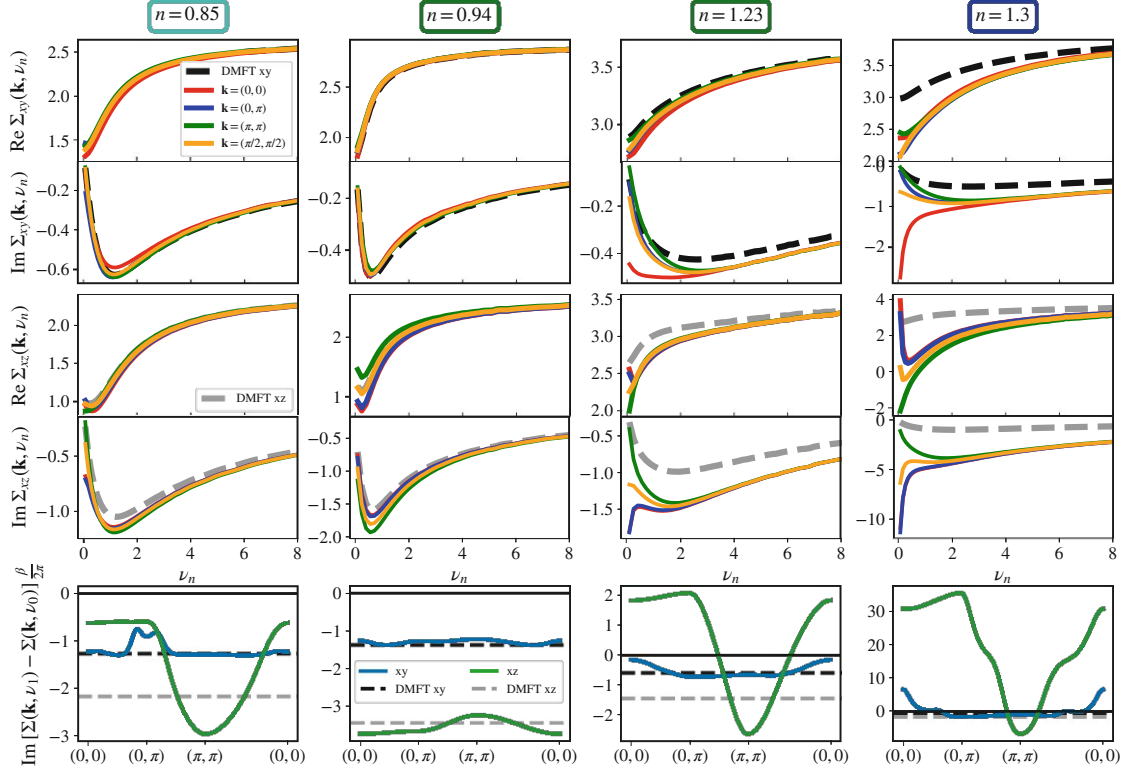


Figure 2.67: VO₂-terminated monolayer – momentum differentiation of the DΓA self-energy. Top 4 rows: real and imaginary parts for the xy and xz orbital for 4 different momenta (colors) and, for comparison, the DMFT self-energy (dashed) at the four dopings and T indicated by the “+” in Fig. 2.55b. Bottom row: Slope of the imaginary part of the DΓA self-energy for a momentum path through the Brillouin zone.

For cOO fluctuations at $n = 1.23$ ($\lambda_D(\pi, \pi) = 0.97$), the momentum differentiation of the self-energy and Fermi surface are qualitatively similar to the cOO results at $n = 1.5$ for the SrO-terminated layer. But for the cOO at $n = 0.94$ and sOO at $n = 0.85$, we only find a minor momentum differentiation of the self-energy, see Fig. 2.67. Correspondingly, the Fermi surface in Fig. 2.68 is similar to that of DMFT in Fig. 2.61, and there are no positive non-Fermi-liquid like slopes (solid lines in Fig. 2.68). This is surprising since the leading eigenvalue $\lambda_D(0, \pi) = \lambda_D(\pi, 0) = 0.985$ at

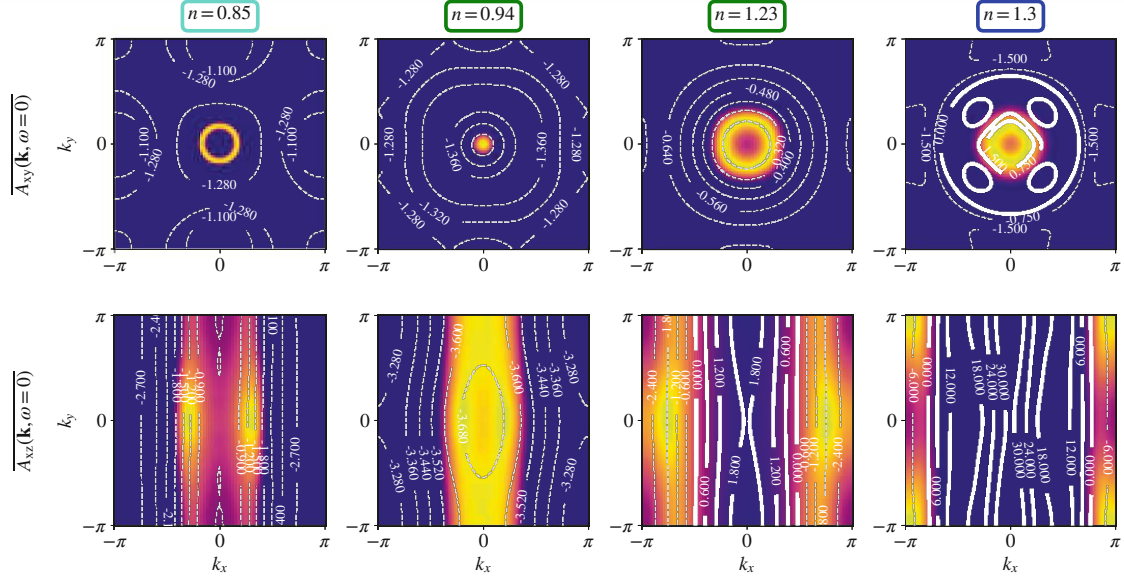


Figure 2.68: VO₂-terminated monolayer – DΓA Fermi surfaces at the same dopings and T as in Fig. 2.61. Isolines are again the low-energy slope of $\Im\Sigma$, where the solid, fat lines represent a positive, and the dashed, thin lines represent a negative value.

$n = 0.85$ and $\lambda_D(\pi, \pi) = 0.91$ at $n = 0.94$ is similarly close to 1 as for $n = 1.23$ or the SrO-termination, indicating that strong orbital ordering fluctuations are present. On the contrary, at $n = 1.3$, above iM order, we observe the by far strongest momentum differentiation in Fig. 2.67, even though $\lambda_M(\delta, \delta) = 0.97$ with $\delta \approx \pm\pi/4$ is again comparable to the strength of other fluctuations. A clear pole develops in the vicinity of the Fermi level not only for the xz and yz orbitals, that drive the iM ordering, but also for the xy orbital. This pole is so large that the spectrum splits into two parts, akin to the splitting into upper and lower Hubbard band; and it pushes the Fermi surface to $\mathbf{k} = (0, \pm\pi)$. However, the divergence occurs only for a region of the Brillouin zone that does not account for the Fermi surface of the respective orbital character.

2.5.8 Binaural fluctuation diagnostics

We now expose the connection between strong non-local two-particle fluctuations and the occurrence (or not) of large, momentum-selective corrections to one-particle spectral properties. To this end, we revisit the **Abinitio**DΓA equation of motion [33]: The self-energy of spin σ consists of the Hartree-Fock (“HF”) contribution and a term that includes all truly two-particle scattering events by linking the density vertex F_D with the interaction matrix U , the bare susceptibility χ_0 , and a Green’s function

G that closes the Feynman diagram

$$\Sigma_{\sigma}^k = \Sigma_{\sigma}^{\text{HF}} - \frac{1}{\beta^2} \sum_{\substack{qk' \\ lhn, rst}} U_{mlhn} \chi_{0, nlsr}^{qk'k'} F_{rstm'}^{qk'k} G_{ht}^{k-q}, \quad (2.131)$$

see also Eq. (2.130). In this notation, q, k, k' refer to compound indices consisting of pairs of momenta and Matsubara frequencies, $(\mathbf{q}, i\omega), (\mathbf{k}, i\nu), (\mathbf{k}', i\nu')$. In the ladder approximation employed in `AbinitioDΓA`, F_D is constructed from the Bethe-Salpeter equations in the particle-hole (“ph”) channel with an additional enforcement of crossing symmetry via the parquet equation [204, 33]. The resulting expression

$$\begin{aligned} F_{lm m' l'}^{qk k'} = & F_{lm m' l'}^{\omega \nu \nu'} + F_{lm m' l'}^{q \nu \nu', \text{nl}} \\ & - \frac{1}{2} F_{m' m l l'}^{(k'-k)(\nu'-\omega)\nu', \text{nl}} - \frac{3}{2} F_{M, \text{ph}}^{(k'-k)(\nu'-\omega)\nu', \text{nl}} \end{aligned} \quad (2.132)$$

contains both charge (density, “ D ”) and spin (magnetic, “ M ”) fluctuations. The non-local (nl) particle-hole (ph) vertices are calculated through the Bethe-Salpeter equation, and a local contribution with only frequency and orbital dependencies is subtracted to avoid a double counting. We can further decompose Eq. (2.131) into the DMFT self-energy and non-local corrections to it,

$$\Sigma_{\sigma}^k = \Sigma_{\sigma}^{\nu, \text{DMFT}} + \Sigma_{\sigma}^{k, \text{correction}} \quad (2.133)$$

as the purely local vertex of Eq. (2.132) combines with the Hartree-Fock contribution of Eq. (2.131) to the DMFT self-energy. The correction term, $\Sigma^{k, \text{correction}}$, then contains all non-local contributions and is efficiently implemented as a linear combination of various three-leg vertices, see Ref. [2]. For our purpose, we now transform internal momenta and frequencies in the corrections to DMFT by substituting $k'' = k - q$, leading to

$$\Sigma_{\sigma}^{k, \text{correction}} = \Sigma_{\sigma}^{\text{HF}} - \Sigma_{\sigma}^{\nu, \text{DMFT}} + \sum_{k''} \Xi_{mm'}(k, k'') \quad (2.134)$$

where we lumped all internal summations except that over k'' into

$$\Xi_{mm'}(k, k'') = -\frac{1}{\beta^2} \sum_{\substack{k' \\ lhn, rst}} U_{mlhn} \chi_{0, nlsr}^{(k''-k)k'k'} F_{rstm'}^{(k''-k), k'k} G_{ht}^{k''}. \quad (2.135)$$

Now, by selecting a specific momentum k of the self-energy correction, $\Sigma^{k, \text{correction}}$, we are able to identify the contributions stemming from momentum k'' via $\Xi(k, k'')$. This analysis allows highlighting the link between the electronic structure (encoded in $G^{k''}$) and non-local fluctuations (included in

F): In the vicinity of spontaneous instabilities, F_D will peak at zero (bosonic) energy transfer, $i\omega_m = i(\nu_n'' - \nu_n) = 0$, while the characteristic momentum transfer $\mathbf{Q} = \mathbf{k}'' - \mathbf{k}$ depends on the dominant type of fluctuations. Since we are interested in renormalizations at low energies, we limit the discussion to the lowest fermionic Matsubara frequency, $\nu_n = \nu_0 = \pi/\beta$, implying also $\nu_n'' = \pi/\beta$. Focusing then on the momentum dependence,

$$\Xi_{mm'}(\mathbf{k}, \mathbf{k}'') \equiv \Xi_{mm'}((\mathbf{k}, i\nu_0), (\mathbf{k}'', i\nu_0'')), \quad (2.136)$$

we note that (in the absence of nesting) the bare susceptibility χ_0 contributes only minimally to the \mathbf{k} -dependence. The momentum structure is, hence, dominantly generated from the interplay of the vertex $F_D^{(\mathbf{k}''-\mathbf{k})}$ and the Greens function $G^{\mathbf{k}''}$. We find a strong momentum variation in the *imaginary* part of the self-energy correction to originate from the *real* part of the vertex and the *imaginary* part of the Green's function. The latter is a direct reflection of the underlying Fermi surface, while the vertex's amplitude is driven by the dominant fluctuations. Essentially, large corrections to electronic lifetimes will be generated at Brillouin zone momenta \mathbf{k} if they can be connected to a Fermi surface via the transfer momentum \mathbf{Q} of the existing fluctuations. This connection does not need to be precise: First, deviations in the transfer momentum that are within the bounds of the (inverse) correlation length, ξ^{-1} , will still produce a large signature in Ξ [205]. Second, the (DMFT) scattering rate $\Gamma = Z\Im\Sigma(\omega = 0)$ allows excitations to contribute even if they are at a distance $\mathcal{O}(\Gamma/2)$ away from the Fermi surface.

Our decomposition of the equation of motion derives from previous approaches for the diagnostics of fluctuations [206, 207, 208]. Our contribution to the diagnostics tool box is two-fold: First, we supplemented the fluctuation diagnostics with a second layer of analysis: We plot the fluctuation diagnostics together with the Fermi surface, providing a link between the dominant fluctuation momentum \mathbf{Q} and spectral properties at \mathbf{k}'' for the studied momentum \mathbf{k} , see Fig. 2.69. This additional layer helps explaining when and why non-local renormalizations from particular fluctuations become large. We call this doubled-down analysis that pairs fluctuation diagnostics with spectral information: “binaural fluctuation diagnostics”. Second, we extended the domain of the fluctuation diagnostics from many-body models to realistic multi-orbital materials.

Using the above “binaural fluctuation diagnostics”, we now analyze the self-energy corrections shown in the left column of Fig. 2.69 for both surface terminations, various doping levels, hosting orbitals, and \mathbf{k} -points. The positions of three selected \mathbf{k} -points are indicated in the Brillouin zone plots in the three adjacent columns. There, the colored heat maps (blue: negative, red: positive, white: no correction) illustrate $\Im\Xi_{mm}(\mathbf{k}, \mathbf{k}'')$ from Eq. (2.136). The grey shaded overlay corresponds to the

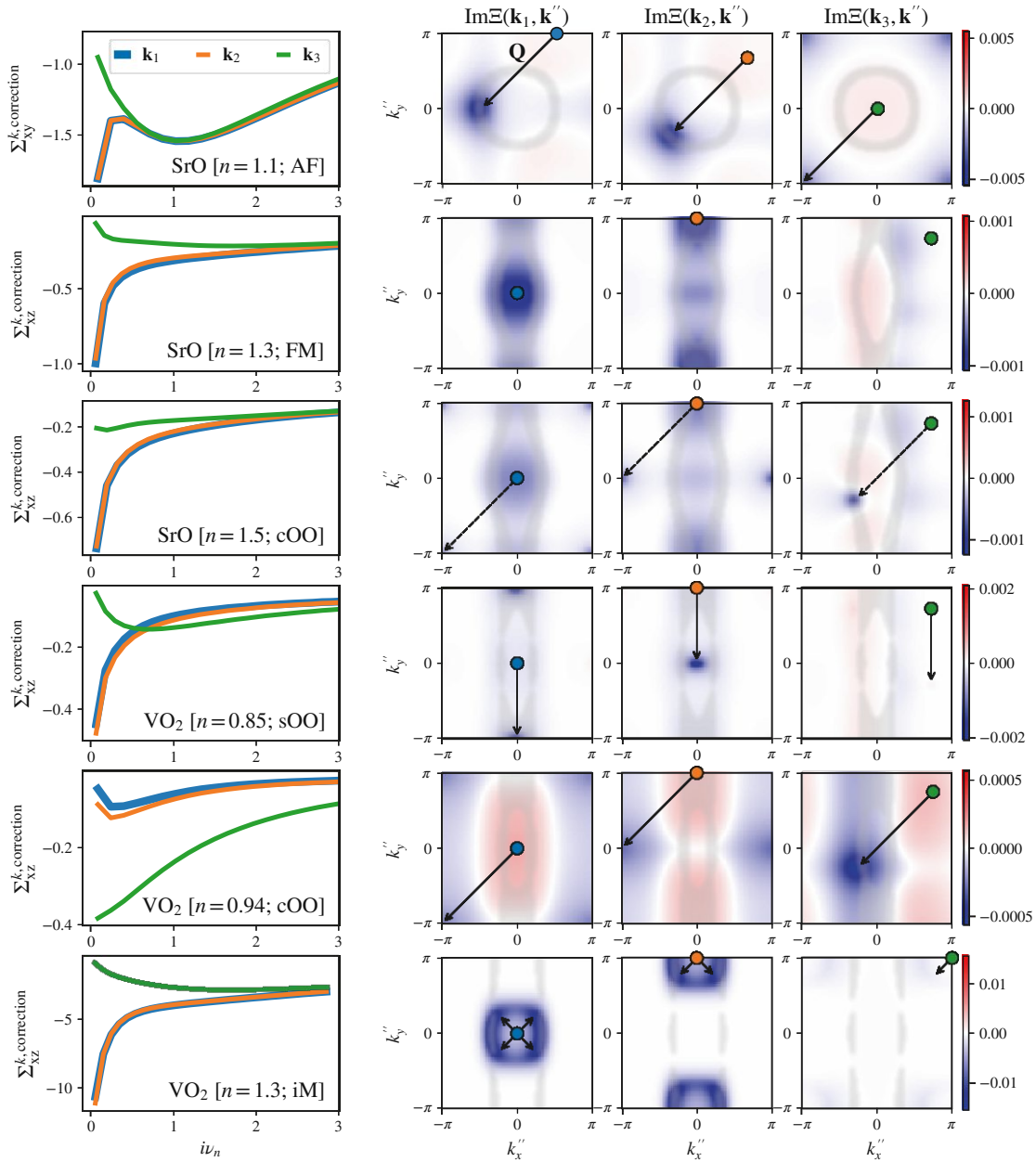


Figure 2.69: Binaural fluctuation diagnostics. Left: Self-energy correction to Σ_{DMFT} for six selected terminations, fillings, k-points and orbitals. Right: Binaural fluctuation diagnostics for these six cases, consisting of: (i) The corresponding momentum (k'') fluctuation diagnostics $\Im\Xi(\mathbf{k}, \mathbf{k}'')$ from Eq. (2.136) at the first positive fermionic and zeroth bosonic Matsubara frequency (three columns on the right). (ii) Marking the selected \mathbf{k} -points ($\mathbf{k}_1, \mathbf{k}_2, \mathbf{k}_3$) in the Brillouin zone plots as colored circles, indicating the dominant wave vector \mathbf{Q} (arrows) of a given type of fluctuations, and the Fermi surface (gray shaded area) of the same orbital. Strong corrections are a product of strong fluctuations (large $F_D^{\mathbf{Q}}$) where the momentum transfer \mathbf{Q} (arrows) connects the self-energy momentum \mathbf{k} to the Fermi surface (gray shaded area) of the same orbital. While antiferromagnetic fluctuations cause strong corrections at momenta *outside* the Fermi surface (top row), ferromagnetism and the observed incommensurate magnetism are prone to corrections *inside* the Fermi surface (second and last row). Orbital ordering on the other hand is different (third and fifth row): checkerboard fluctuations have little to no effect, while stripe ordering promotes moderate corrections. This analysis reveals that in the SrO-terminated structure at $n = 1.5$ (third row) the adjacent ferromagnetism is the root cause of the sizable renormalization, not the orbital order fluctuations that dominate the susceptibility.

Fermi surface of the selected orbital m . In close proximity to the antiferromagnetic DMFT phase transition (SrO termination; $n = 1.1$; top row) the momenta \mathbf{k}_1 and \mathbf{k}_2 display a pronounced kink in the correction to the xy self-energy. Our momentum diagnostics reveals that these momenta can indeed be connected to the xy Fermi surface via the AF ordering vector $\mathbf{Q} = (\pi, \pi)$, generating a large amplitude in $\Im\Xi(\mathbf{k}_{1,2}, \mathbf{k}_{1,2} - \mathbf{Q})$. Due to the shape and size of the Fermi surface, momenta—for which this constructive interplay with the AF fluctuations is possible—naturally lie in *unoccupied* regions of the Brillouin zone. Instead, *occupied* momenta, such as \mathbf{k}_3 , cannot be connected to the Fermi surface via the AF ordering vector: As a result, there is no kink in \mathbf{k}_3 's self-energy correction and the overall shape is Fermi liquid-like. This insight into the momentum-structure of the equation of motion thus explains the evidenced momentum asymmetry ($k > k_F$) in the scattering rate. While corrections at \mathbf{k}_3 are small compared to those at \mathbf{k}_1 and \mathbf{k}_2 , $-\Im\Sigma_{xy}^{\mathbf{k}_3, \text{correction}}(i\nu \rightarrow 0) \sim \mathcal{O}(0.5)\text{eV}$ is still larger than some of the corrections at other dopings, discussed below. The reason is the large (DMFT) scattering rate, $-\Im\Sigma_{xy}^{\nu=\pi/\beta, \text{DMFT}} \approx 0.7\text{eV}$, see Fig. 2.65: It causes incoherent spectral weight of bands slightly below E_F (cf. Fig. 2a in Ref. [5]) to spill to the Fermi level, thus contributing to $\Xi(\Gamma, M)$.

Larger electron doping at $n = 1.3$ favors ferromagnetism hosted by the xz/yz -orbitals (second row in Fig. 2.69). Here $\mathbf{Q} = (0, 0)$ (hence no arrow) naturally causes corrections to appear at the occupied states within the Fermi surface because it is rather narrow. The extent of the momentum region in which the FM-driven Ξ is large (see the diameter of the (blue) circular region) owes to the inverse correlation length ξ^{-1} that was found to be sizably larger than for dominant fluctuations at other dopings, see Fig. 6c in Ref. [5] for a comparison. The large ξ^{-1} enables the Γ -point, which manifestly is not on the Fermi surface, to significantly contribute to the self-energy corrections. Instead, \mathbf{k}_3 is far enough from the Fermi surface for corrections to be suppressed.

Doping further to $n = 1.5$, the xz/yz orbitals become close to quarter-filling and a checkerboard orbital ordering instability emerges (third row in Fig. 2.69). Interestingly, the corresponding characteristic vector $\mathbf{Q} = (\pi, \pi)$ of the cOO fluctuations, only plays a minor role in the lifetime differentiation: For \mathbf{k}_1 and \mathbf{k}_2 , (π, π) connects to a small region of finite intensity in Ξ far away from the Fermi surface. However, larger contributions to the self-energy correction manifestly still come from the high amplitude around $\mathbf{Q} = (0, 0)$, i.e., from the direct vicinity of the \mathbf{k}_1 and \mathbf{k}_2 momenta in Fig. 2.69: Spectral renormalizations are dominated by FM fluctuations although, at the current doping level, these are subleading in the susceptibility. This interpretation is further supported by looking at \mathbf{k}_3 , where FM contributions are absent: There, self-energy corrections from (π, π) -fluctuations are largest, as this momentum-transfer directly connects \mathbf{k}_3 to the Fermi surface. However, the resulting

corrections are nonetheless very small. One contributing factor is again the inverse correlation length, ξ^{-1} . It is smaller for cOO than for FM by one order of magnitude (cf. Fig. 6c in Ref. [5]), resulting in a smaller (k''_x, k''_y) -region with finite (blue) intensity to integrate over. We can motivate an additional factor: The OO susceptibility of two orbitals $l \neq m$ can be expanded into a linear combination of the density susceptibilities in which diagonal and offdiagonal components enter with *opposite* sign

$$\chi_{OO}^{lm} = 2\chi_D^{llll} + 2\chi_D^{mmmm} - 4\chi_D^{llmm}. \quad (2.137)$$

The entering diagonal and off-diagonal χ_D^{llmm} for $l, m \in \{xz, yz\}$ are displayed Fig. 2.70b. While χ_{OO}^{lm} for fixed $l \neq m$ is naturally large in an OO regime, we empirically find the density susceptibility, $\chi_D = 2 \sum_{lm} \chi_D^{llmm}$, in which the above terms are summed with the *same* (plus) sign, to be small, see Fig. 2.70d, suggestive of compensational effects. Similar to χ^D , also the equation of motion involves a summation over diagonal and off-diagonal components, this time of F :

$$\Sigma_{\sigma}^k \propto \sum_{qk'} U \left(\chi_{0,mmmm}^{qk'k'} F_{D}^{qk'k} + \chi_{0,llll}^{qk'k'} F_{D}^{qk'k} \right) G_{\sigma}^{k-q} + \mathcal{O}(J) \quad (2.138)$$

where we omitted terms involving the Hund's coupling J and restricted G and χ_0 to diagonal elements, G_{mm} and $\chi_{0,lmml}$, mostly warranted in the systems considered here. Large off-diagonal contributions are only expected where bands hybridize, e.g., where the xz and yz orbitals cross. The observation made for χ^D then suggests that also the orbital summation in the equation of motion results in an (at least partial) cancellation of terms headed by U . Quite intuitively for orbital fluctuations, leading corrections will then be driven by a smaller energy scale: the Hund's coupling J . These intricacies highlight that strong non-local fluctuations do not always translate 1-to-1 into large non-local renormalizations in spectral properties.

Similar arguments hold for the cOO regime at filling $n = 0.94$ for the film with VO₂ termination (fifths panel in Fig. 2.69). Additionally, there is a modulation in the \mathbf{k}'' -plane, with positive contributions compensating part of the self-energy enhancement from around $\mathbf{k} + \mathbf{Q}$.

The argument of compensations in F_D does not hold for stripe orbital ordering for filling $n = 0.85$ and VO₂-termination (fourth panel in Fig. 2.69): Similar to the ferromagnetic case, the $\mathbf{Q} = (0, \pi)$ nematic fluctuation vector supports a strong differentiation between occupied ($\mathbf{k}_1, \mathbf{k}_2$) and unoccupied states (\mathbf{k}_3) in the xz orbital. We speculate that the lower symmetry of the sOO state obviates cancellation effects in the equation of motion. Indeed, compared to the cOO regime, the sOO orbital-summed density susceptibility, χ^D , and the partial sum $\chi_D^{xz,xz} + \chi_D^{xz,yz}$ that mirrors the orbital combinations entering the equation of motion, Eq. (2.138), is one order of magnitude larger, cf. Fig. 2.70 panels (c) and (d). Note also that the sOO data point is much closer to its DMFT ordering temperature than

the cOO one (Eigenvalues: $\lambda_{sOO} = 0.985 > \lambda_{cOO} = 0.91$), suggestive of overall larger fluctuations.

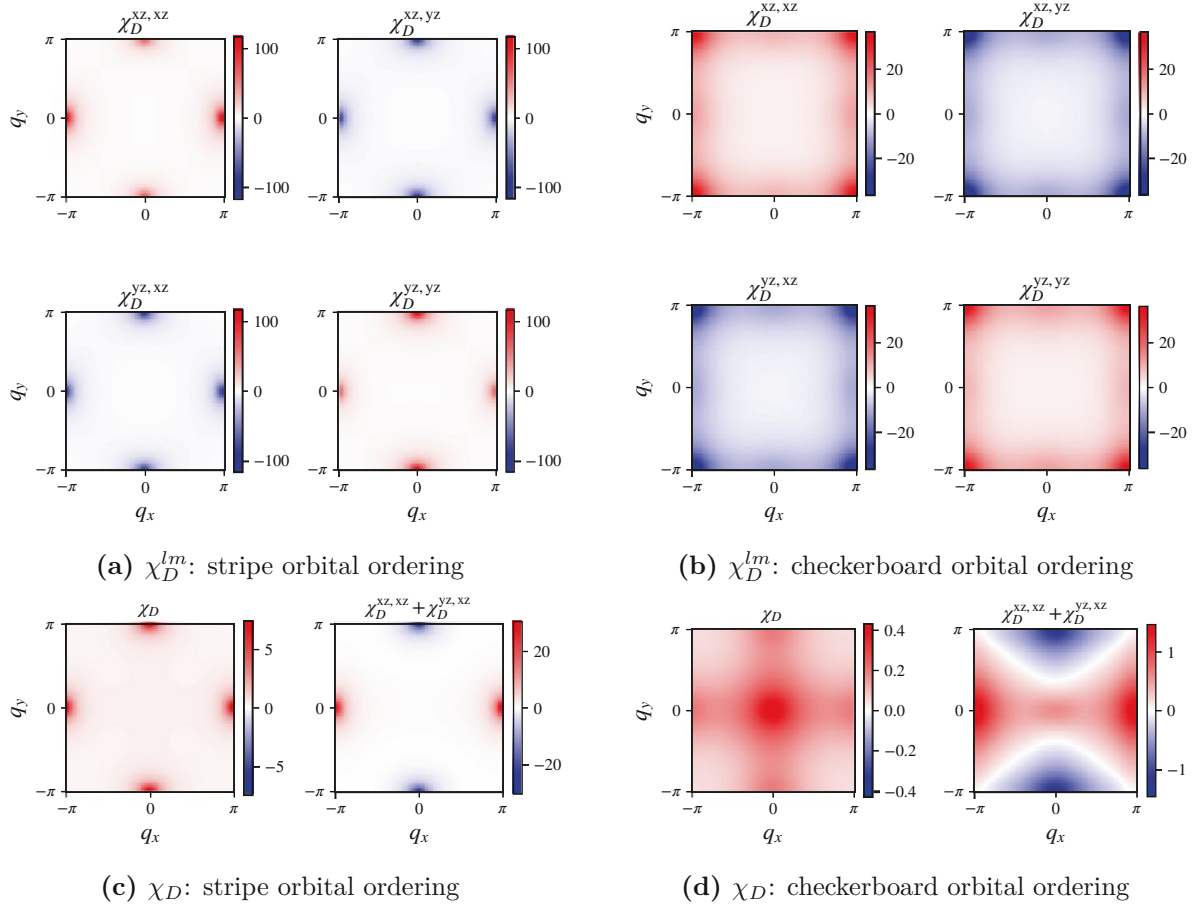


Figure 2.70: Density susceptibilities in the (q_x, q_y) -plane. (a) and (b): χ_D -matrix in the xz/yz -orbital space and the vicinity of stripe orbital ordering and checkerboard orbital ordering found in the VO₂ terminated monolayer at $n = 0.85$ and $n = 0.94$, respectively. The sOO response in (a) displays orbital asymmetry where $\chi_D^{xz,xz}(\pi, 0) > \chi_D^{xz,xz}(0, \pi)$ and vice versa for the yz orbital. The cOO response in (b) on the other hand is perfectly symmetric, i.e. $\chi_D^{xz,xz}(\pi, \pi) = \chi_D^{yz,yz}(\pi, \pi) = -\chi_D^{xz,yz}(\pi, \pi) = -\chi_D^{yz,xz}(\pi, \pi)$. (c) and (d): Orbital-summed density susceptibility $\chi_D = 2 \sum_{lm} \chi_D^{lm}$ and the non-symmetric sum $\chi_D^{xz,xz} + \chi_D^{yz,xz}$ motivated by Eq. (2.138). The aforementioned asymmetry manifests itself in a—for sOO fluctuations—large remainder in $\chi_D^{xz,xz} + \chi_D^{yz,xz}$, which is strongly attenuated in the vicinity of the cOO phase (note the different color scales).

Lastly, the incommensurate nature of the magnetic ordering at $n = 1.3$ in the VO₂-terminated structure is easily seen as the root cause of the massive self-energy corrections in the last row of Fig. 2.69: The $\mathbf{Q} = \delta \times \hat{\mathbf{e}}_Q$ vector is able to perfectly connect onto the Fermi surface for $k_x'' = 0$.

Due to the large $\delta \sim \pi/4$ also most other \mathbf{k} -points are able to—at least partially—connect onto the Fermi surface—with zone-boundary momenta, such as \mathbf{k}_3 , being the only exceptions. The momentum diagnostics hence provides an explanation for the wide range of positive slopes in $\Im\Sigma(i\nu)$ throughout the Brillouin zone, shown in Fig. 2.68. Incidentally, the onset of this magnetism is also the main driver of the corrections at slightly smaller doping $n = 1.23$ where, yet again, the cOO fails to contribute. Consequently both the D Γ A Fermi surfaces and low-energy slopes of $\text{Im}\Sigma$ are qualitatively identical for $n = 1.23$ and $n = 1.3$ in Fig. 2.68.

In all, we find that all types of *spin* fluctuations provide a path to strong non-local renormalizations. Our analysis further motivates the asymmetry with respect to the Fermi surface to be a direct consequence of the interplay of shape and size of the Fermi surface and the ordering vector \mathbf{Q} of the driving fluctuations. The impact of *orbital* fluctuations, instead, is more ambiguous. Our work suggests that checkerboard orbital fluctuations only produce a weak momentum differentiation in the self-energy, while stripe-orbital fluctuations have larger signatures. A simpler model should be studied to further elucidate spectral consequences of orbital fluctuations in the absence of other complications.

2.5.9 Discussion and perspective

Recapitulating, we have studied a SrVO₃ monolayer on a SrTiO₃ substrate with two different surface terminations, SrO and VO₂, to vacuum within DMFT and **AbinitioD Γ A**. Owing to the out-of-plane orbital truncation, undoped ($n = 1$) SrVO₃ monolayer is band width driven Mott insulating. Depending on the termination and filling we observe strong non-local fluctuations of magnetic and orbital-order type. These non-local fluctuations will suppress the mean-field DMFT ordering but also have pronounced effects on the self-energy, possibly deforming the Fermi surface, and quite generally can lead to a strong enhancement of $\Im\Sigma$. Strong non-local fluctuations can even cause the development of a pole in the self-energy, signaling the splitting of the spectrum into two parts—here not because of Mott physics but because of large non-local fluctuations. The latter is particularly strong for the incommensurate ferromagnetic phase of the VO₂-terminated SrVO₃ monolayer at $n = 1.3$ filling. First indications, i.e., downturns of the self-energy at the lowest Matsubara frequency are however ubiquitous for various dopings and both terminations.

For the cuprates, AF fluctuations lead to pseudogap physics with a momentum differentiation distinguishing between a Fermi liquid-like self-energy in the nodal direction on the Fermi surface, and a kink in the self-energy signaling the opening of a gap in the anti-nodal direction. Here, we also observe the joint presence of these two behaviors in the self-energy. However, the momentum differentiation is not realized *on* the Fermi surface but *perpendicular* to it: For the SrO-termination in

the electron-doped regime, AF fluctuations lead to a Fermi liquid-like behavior for momenta on the occupied side of the Fermi surface (“ $\mathbf{k} < \mathbf{k}_F$ ”) and a kink-like insulating behavior in the imaginary part of the self-energy on the unoccupied side (“ $\mathbf{k} > \mathbf{k}_F$ ”). In case of FM fluctuations, the momentum differentiation between occupied and unoccupied momenta is reversed. The tendency towards checkerboard orbital ordering, however, has no vital influence on the self-energy.

For the VO₂ termination, iM fluctuations at $n = 1.3$ lead to massive non-local correlations and a pole in the self-energy. In contrast to all other cases not only the xz/yz orbitals—driving the iM fluctuations—are affected but also the ancillary xy orbital. Around half-filling, again, the cOO fails to contribute significantly to the self-energy. Instead, sOO fluctuations do generate a momentum differentiation.

The imaginary part of the self-energy corresponds to the lifetimes and the broadening of the spectral function. Our results hence show that the lifetimes of an added hole or electron are extremely different. The hole-lifetime can be measured by angular resolved photoemission spectroscopy (ARPES); the electron lifetime by inverse photoemission spectroscopy, by ARPES at elevated temperatures, or in non-equilibrium situations (e.g., pump-probe measurements) in which states above the Fermi level become populated.

The differentiation between states above and below the Fermi surface that we observe is quite extreme. Technologically this might be exploited for thermoelectrics which rely on a strong electron-hole asymmetry [209, 210, 211, 212]. Particularly beneficial are sharp peaks in the spectral function on only one side of the Fermi level [209], as found for the SrO-terminated monolayer, see Fig. 2.60, within DMFT. There, *local* electronic correlations can enhance thermoelectricity through energy-dependent renormalizations that are different for electrons ($\omega > 0$) and holes ($\omega < 0$) [213, 210]. Our finding of a momentum-selectivity in the scattering rate may provide an *additional* route: A particle-hole asymmetry that is driven (or enhanced) by *non-local* renormalizations. Indeed, looking again at the SrO-terminated monolayer, dominant (sub-leading) FM fluctuations at $n = 1.3$ ($n = 1.5$), drive a dispersive scattering rate [214] that is larger for occupied momenta (“ $\mathbf{k} < \mathbf{k}_F$ ”) than for empty states (“ $\mathbf{k} > \mathbf{k}_F$ ”): Specifically, the downward kinks in the xz -component of $\Im\Sigma$, see Fig. 2.65, occur for $\mathbf{k} = (0, 0)$ and $\mathbf{k} = (0, \pi)$ which are inside the (DMFT) xz Fermi surface, see Fig. 2.60. For $\mathbf{k} = (\pi, \pi)$ and $\mathbf{k} = (\pi/2, \pi/2)$, which are outside the Fermi surface, the xz scattering rate instead decreases when approaching zero frequency. This electron-hole asymmetry of the scattering time will make the already electron-like DMFT thermopower even more negative, thus increasing its magnitude.

2.6 Self-consistent ladder dynamical vertex approximation

- The self-consistency and optical conductivity implementation are extensions of the `AbinitioDΓA` code. The latter was published as “The `AbinitioDΓA` Project v1.0: Non-local correlations beyond and susceptibilities within dynamical mean-field theory” by Anna Galler, Patrik Thunström, Josef Kaufmann, [Matthias Pickem](#), Jan M. Tomczak, and Karsten Held [2].
- The optical conductivities are computed based on the published DΓA data of “Self-consistent ladder dynamical vertex approximation” by Josef Kaufmann, Christian Eckhardt, [Matthias Pickem](#), Motoharu Kitatani, Anna Kauch, and Karsten Held [4] and were obtained in collaboration with Josef Kaufmann and Anna Kauch. Adopted figures have been marked accordingly.
- The reference parquet DΓA data for $U = 4$ has been kindly provided by Anna Kauch and is reproduced from Ref. [215].

Finalizing the Mott Chapter we turn to the two-dimensional one-band Hubbard model, one of the most studied models in the field of strongly correlated electron physics. We continue building on the self-consistent ladder dynamical vertex approximation method and extend it towards optical conductivities. First we briefly recap our newly developed “flavor” of the DΓA method introduced in Ref. [4], before deriving the multi-orbital (vertex-corrected) current-current correlation function necessary to compute optical conductivities.

2.6.1 Synopsis

The dynamical vertex approximation (DΓA) [204, 216] is a non-perturbative, diagrammatic extension [93] of dynamical mean-field theory [94] and presents a natural progression of the diagrammatic considerations thereof: DMFT considers the one-particle ($n = 1$) irreducible vertex, i.e. the self-energy Σ , to be local. DΓA assumes the two-particle ($n = 2$) irreducible vertex Λ to be local. Following this “series”, for $n \rightarrow \infty$, in principle, the exact solution will be recovered eventually [217].

DMFT is built on the solvability of an embedded impurity problem [97], allowing for an accurate description of local electronic correlations as all possible diagrams built from local propagators can be captured through the (numerically exact solution of the) single impurity Anderson model (SIAM). In the limit of infinite lattice dimensions, with proper scaling of the hopping amplitudes, DMFT

becomes exact [95]. The local self-energy of the (self-consistently determined) impurity problem then coincides with the self-energy of the lattice problem which is approximated to be momentum independent $\Sigma(\mathbf{k}, \omega) \rightarrow \Sigma(\omega)$. Due to DMFT's construction, non-local correlations on the one-particle level are per construction out of its reach. To this end, diagrammatic extensions have been developed that, at their heart, refine the DMFT approximation by instead approximating specific two-particle vertices. The dynamical vertex approximation, for example, a priori determines specific, channel-dependent two-particle *irreducible* vertices to be local (only their frequency structures are considered). Ladder D Γ A approaches commonly approximate Φ_{pp} to be local (building block: Γ_{ph}) to incorporate predominant spin and charge fluctuations, e.g. in the repulsive $U > 0$ Hubbard model. Other variants do however exist that treat the attractive $U < 0$ Hubbard model, that approximate Φ_{ph} instead to be local [218]. A less crude approximation is made in the parquet variant where only the *fully irreducible* two-particle vertex Λ is assumed to be local. As a result one is capable of treating all fluctuations on equal footing without a preliminary exclusion of specific channels. Due to the massive increase in complexity, the latter has hitherto only been successfully implemented for one-band models [219].

Non-local two-particle ladder diagrams are then generated using these local vertices as input. The resulting non-local full vertex F , inserted into the equation of motion, then yields non-local self-energies, see Section 2.5.7. Contrary to cluster extensions, diagrammatic approaches are not limited in the range of the incorporated fluctuations. This in principle allows for full compliance with the Mermin-Wagner theorem [220, 221, 222].

In this thesis we restrict ourselves to the ladder dynamical vertex approximation (Φ_{pp} local) [223], on which the *self-consistent* ladder dynamical vertex approximation (scD Γ A) approach is built upon. The main building block of the theory is the two-particle irreducible vertex in the particle-hole channel Γ_{ph} , allowing for an accurate description of spin and charge fluctuations [93]. In its original formulation, ladder-D Γ A relies on either one-shot results or posterior adjustments, e.g., via an application of so-called λ -corrections [224, 225]. One-shot calculations are sufficient if the resulting self-energies are close to the DMFT result [33], i.e. non-local correction terms are small or cancel out (as we have seen in the case of checkerboard orbital ordering in Section 2.5.7). In the vicinity of ordered phases, where deviations from DMFT tend to be large, one-shot results can only be used to gain information about qualitative tendencies. Due the increasingly large vertices at the ordering momenta, control over asymptotic behavior and orbital occupation is partially lost. The high-frequency behavior of the resulting momentum-dependent self-energies is modified, violating important vital sum rules, see Eqs. (2.142).

2.6.1.1 λ corrections

The “standard” ladder D Γ A approach relies on so-called λ -corrections to regulate the vertex contributions. At the heart of this regularization are the (physical) lattice susceptibilities $\chi_r(\mathbf{q})$ (channel $r \in \{D, M\}$) whose static contribution can be approximated by an Ornstein-Zernike form

$$\chi_r(\mathbf{q}, \omega = 0) \sim \frac{A}{(\mathbf{q} - \mathbf{Q})^2 + \xi^{-2}}, \quad (2.139)$$

in the vicinity of ordered phases. A denotes some proportionality factor, \mathbf{q} the momentum transfer vector, ω the transfer frequency and \mathbf{Q} the ordering vector of the instability. The coherence length ξ describes the propagation distance over which the described fluctuations maintain coherence. Naturally, ξ diverges when approaching the ordered phase either via cooling or non-temperature control parameters, such as a magnetic field or chemical doping. The λ -correction is then introduced as

$$\chi_r^\lambda(\mathbf{q}, \omega) = [(\chi_r^{-1}(\mathbf{q}, \omega) + \lambda_r)]^{-1}, \quad (2.140)$$

providing an upper boundary for the coherence length $\tilde{\xi} = [\xi^{-2} + \lambda_r]^{-1/2}$ and a suppression of the predominant fluctuations. Via Eq. (2.140), the relevant susceptibility sum rule can be constrained such that the summation over the non-local and local (impurity) quantities are identical [226]

$$\frac{1}{\beta} \sum_{\mathbf{q}, \omega_m} \chi_{\uparrow\uparrow}^{\text{lattice}}(\mathbf{q}, \omega_m) \stackrel{!}{=} \frac{1}{\beta} \sum_{\omega_m} \chi_{\uparrow\uparrow}^{\text{imp}}(i\omega_m) = \frac{n}{2} \left(1 - \frac{n}{2}\right). \quad (2.141)$$

The right side is valid for the one-band case and is connected to the band filling n . Due to the connection to the density and magnetic channel, “ $\uparrow\uparrow = \frac{1}{2}(D + M)$ ”, two separate conditions emerge (with different λ_r)

$$\frac{1}{\beta} \sum_{\mathbf{q}, \omega_m} \chi_D^{\text{lattice}}(\mathbf{q}, \omega_m) \stackrel{!}{=} \frac{1}{\beta} \sum_{\omega_m} \chi_D^{\text{imp}}(i\omega_m), \quad (2.142a)$$

$$\frac{1}{\beta} \sum_{\mathbf{q}, \omega_m} \chi_M^{\text{lattice}}(\mathbf{q}, i\omega_m) \stackrel{!}{=} \frac{1}{\beta} \sum_{\omega_m} \chi_M^{\text{imp}}(i\omega_m). \quad (2.142b)$$

Applied to three dimensional systems, this leads to a reduction of the transition temperature, e.g., a reduction of the antiferromagnetic Néel temperature in the Hubbard model [193]. In pure two dimension systems λ -corrections go a step further and are capable of fully suppressing the phase transition for finite temperatures fulfilling the Mermin-Wagner theorem [224, 225]. In short, systems of dimensionality $d \leq 2$ and with interactions that are sufficiently short-range, continuous symmetries cannot be spontaneously broken at finite temperatures $T > 0$. In these cases long range fluctuations (e.g. antiferromagnetic) proliferate, however never diverge for $T > 0$. In practice, real samples can

never resemble a perfect, infinite two dimensional model. Deviations thereof such as weak coupling in the third dimension, magnetic anisotropies, disorder, lattice defects, finite size effects, etc. eventually allow the occurrence of a phase transition at finite transition temperatures [227].

Thus far, this technique has only been applied to one-band systems. Once multiple correlated orbitals are necessary to represent the structure²⁶ the numerical complexity of λ -corrections quickly increases. As the λ regularization is introduced as susceptibility corrections, they inherit their general numerical features: A multi-orbital λ correction is therefore, per construction, a matrix with rank n^2 (n : number of correlated bands). Root-finding methods, e.g., applied in Ref. [224], become ill-conditioned, as the most optimal n^2 variables need to be determined in a safe manner. Furthermore, it is a priori not clear whether susceptibility corrections of the type given in Eq. (2.140) are universally applicable for a wide range of materials. While this form universally reflects the spin fluctuations of the one-band Hubbard model, even reproducing the expected critical exponents (the 3D Hubbard model is described by the 3D Heisenberg universality class, at least at half-filling [228, 229, 230]), a more complex interplay of fluctuation of different origin might require different modifications.

2.6.1.2 Self-consistent approach

The approach of the self-consistent ladder dynamical vertex approximation circumvents the λ complications altogether by instead allowing for a full feedback of the D Γ A self-energy back into the Bethe-Salpeter equations. The algorithmic flow was first introduced in Ref. [4] and is illustrated in Fig. 2.71: On top of the converged DMFT calculation we calculate a *one-shot* two-particle Green's function from which the irreducible vertex can be extracted (blue box). As described in Section 2.5.7, non-local corrections to the self-energy are calculated via the Bethe-Salpeter equations (BSE) and the Schwinger-Dyson equation (SDE). The main idea of the self-consistent approach is an “inner” feedback (green box) into the BSE + SDE sequence.²⁷ Here the irreducible vertex Γ_{ph} , extracted from the DMFT two-particle Green's function, remains untouched. The self-energy $\Sigma(\mathbf{k}, i\nu_n)$ and the adjusted chemical potential μ lead to new momentum dependent propagators G^k which are then used for the construction of a new self-energy. This cycle is iterated until convergence is reached. For a more complete description of the method, including the technical details regarding the updates of local quantities, please refer to Ref. [4] or Ref. [231]. In principle, an “outer” feedback can be

²⁶ Adding uncorrelated bands is less cumbersome as the corresponding sectors in the self-energy and vertices vanish, see, e.g., Ref. [225] for an application to the periodic Anderson model.

²⁷ If the underlying DMFT calculation shows diverging lattice susceptibilities, this inner feedback cannot be done in a straight forward way. The non-locality then needs to be introduced step-by-step by replacing the geometric sum $F_r^q = F_r^\omega [1 - \chi_0^{q,\text{nl}} F_r^\omega]^{-1}$, see Eq. (2.115) with a truncation of the infinite series $F_r^q = F_r^\omega [1 + \chi_0^{q,\text{nl}} F_r^\omega + (\chi_0^{q,\text{nl}} F_r^\omega)^2 + \dots]$. After the feedback has been introduced, the partial sum can be safely replaced by the geometric sum until convergence is reached. Evidently, this procedure only makes sense if the iteration cures the susceptibility divergence, i.e., a non-ordered state is restored.

introduced (gray arrow) where the converged self-energy leads to a change in the DMFT bath and consequently a new two-particle Green's function (and an updated Γ_{ph}). After the DMFT and the D Γ A are converged in unison outer self-consistency would be reached. This last step is, however, beyond the scope of this thesis.

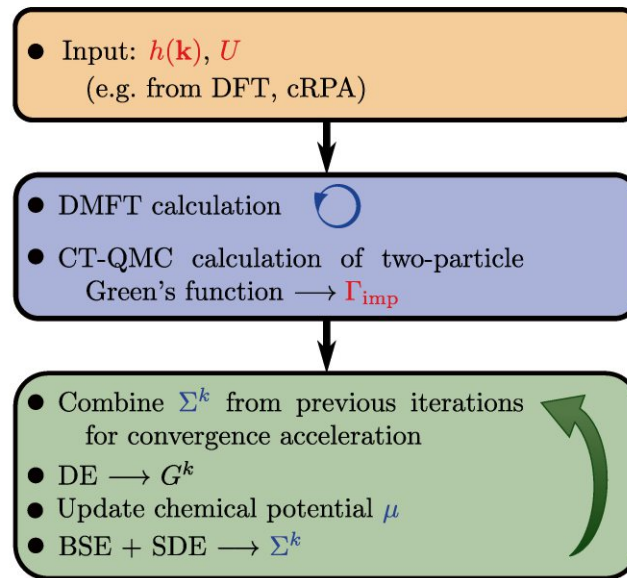


Figure 2.71: Flow chart of the self-consistent D Γ A (scD Γ A) method. The DMFT self-consistent cycle (blue box) is supplemented via a Hamiltonian $h(\mathbf{k})$ and interaction (matrix) U . The local two-particle vertex is sampled from the converged DMFT bath function, providing the pivotal input for the the scD Γ A (green box). In principle an outer self-consistency (gray arrow) could be enacted, updating Γ_{imp} . In this Section we stop at the “inner” scD Γ A convergence.

2.6.2 Optical conductivity

Motivated by a recent study of optical conductivities in strongly correlated systems we introduce the capability to compute optical conductivities for generalized multi-orbital systems into the scD Γ A approach: Kauch *et al.* [215] showcased that the optical spectrum is prone to strong modifications by vertex corrections corresponding to the newly encountered polariton — the π -ton, see Fig. 2.72. In the proximity of antiferromagnetism (e.g., half-filling in the two-dimensional Hubbard model), light ($\mathbf{q} \approx 0$) couples to the predominant fluctuations with transfer momentum $\mathbf{Q} = (\pi, \pi)$ in a non-trivial manner. As this coupling mechanism is intrinsically contained in the ladder D Γ A approach (crossing symmetric $\overline{\text{ph}}$ contribution), we extend the π -ton analysis to the the self-consistent dynamical vertex

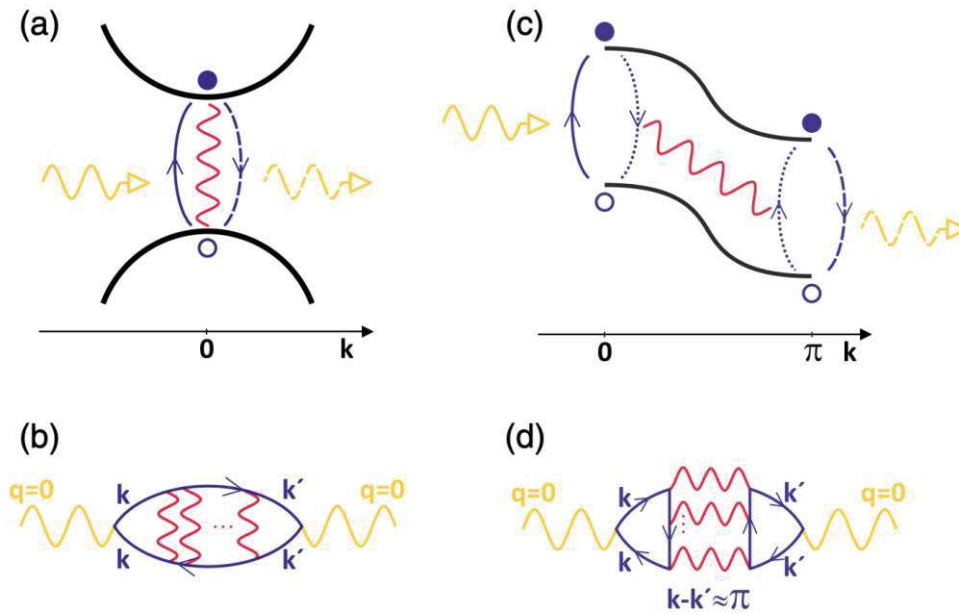


Figure 2.72: Differences between an exciton (a/b) and a π -ton (c/d). The physical process in energy and \mathbf{k} -space is sketched at the top while the corresponding Feynman diagrams are sketched at the bottom. In order to couple to antiferromagnetic fluctuations the π -tons, due to the vanishing transfer momentum \mathbf{q} of light, must couple to the transversal particle hole channel. [Reprinted with permission from Kauch *et al.*, Phys. Rev. Letters **124**, 047401 (2020). Copyright (2020) by the American Physical Society.] [215]

approximation. To this end, let us first introduce the optical conductivity.

The complex conductivity tensor σ relates the magnitude and phase of the current (density) \mathbf{J} to the applied electrical field \mathbf{E}

$$\mathbf{J}(\omega) = \sigma(\omega)\mathbf{E}(\omega). \quad (2.143)$$

The Maxwell equations then give rise to the connection to the absolute permittivity $\varepsilon(\omega)$ via

$$\varepsilon(\omega) = \varepsilon_0 + \frac{i\sigma(\omega)}{\omega}. \quad (2.144)$$

where $\varepsilon_0 = 1/(\mu_0 c^2)$ is the vacuum permittivity, connected to the vacuum magnetic permeability $\mu_0 \approx 4\pi \cdot 10^{-7} \text{H/m}$ and the speed of light c . The refraction index, which is how one commonly gains access to the optical conductivity in experiments [232, 233], then combines the (di)electric and magnetic response $\chi_M = \mu/\mu_0 - 1$, with μ as the permeability connecting the magnetic flux B and the magnetizing field H via $\mathbf{B} = \mu\mathbf{H}$

$$n(\omega) = \sqrt{\frac{\varepsilon(\omega)}{\varepsilon_0} \frac{\mu(\omega)}{\mu_0}}. \quad (2.145)$$

In generalized multi-orbital systems the real part of the conductivity tensor $\sigma_{\alpha\beta}$ is directly connected to the imaginary part of the electronic current-current correlation function χ^{jj} on the real frequency axis where $\alpha, \beta \in \{x, y, z\}$ represent the Cartesian directions

$$\Re\sigma_{\alpha\beta}(\omega) = \frac{\Im\chi_{\alpha\beta}^{jj}(\mathbf{q} = \mathbf{0}, i\omega_n \rightarrow \omega + i0^+)}{\omega}. \quad (2.146)$$

The current-current correlation function is commonly introduced on the imaginary time axis

$$\chi_{\alpha\beta}^{jj}(\mathbf{q} = \mathbf{0}, \tau) = \frac{1}{V} \lim_{\mathbf{q} \rightarrow 0} \langle T_\tau j_E^\alpha(\mathbf{q}, \tau) j_E^\beta(-\mathbf{q}, 0) \rangle \quad (2.147)$$

with the unit cell volume V and the (electronic) current operators

$$j_E^\alpha(\mathbf{q}, \tau) = -e \sum_{\mathbf{k}, l, m, \sigma} \gamma_{lm}^{\mathbf{k}-\mathbf{q}/2, \alpha} \hat{c}_{\mathbf{k}-\mathbf{q}, m\sigma}^\dagger(\tau) \hat{c}_{\mathbf{k}, l\sigma}(\tau) \quad (2.148)$$

with a positively defined elementary charge e and the coupling element in the Peierls approximation [234] in the form of the band velocities via the derivative of the band structure

$$\gamma_{lm}^{\mathbf{k}, \alpha} = \frac{1}{\hbar} \frac{\partial \varepsilon_{lm}^{\mathbf{k}}}{\partial k_\alpha}, \quad (2.149)$$

see Appendix A.3.2.1. The transition to bosonic Matsubara frequencies $i\omega_n$ is performed by a straight forward Fourier transform

$$\chi_{\alpha\beta}^{jj}(\mathbf{q}, i\omega_n) = \int_0^\beta d\tau \chi_{\alpha\beta}^{jj}(\mathbf{q}, \tau) e^{i\omega_n \tau}. \quad (2.150)$$

2.6.2.1 Multi-orbital derivation

The calculation of the optical conductivity via diagrammatic methods is done by calculating the bosonic correlation function χ^{jj} on the imaginary time τ or frequency axis $i\omega_m$, which is then analytically continued to the real frequency axis ω . The general expression of the current-current correlation function can be derived by inserting the current operators into the expectation value of χ^{jj} and connecting the resulting expression to the two-particle Green's function. As is common in model calculations, in the following we consider natural units, i.e. $e \equiv 1$ and $\hbar \equiv 1$.

$$\begin{aligned} \chi_{\alpha\beta}^{jj}(\mathbf{q} = \mathbf{0}, \tau) &= \sum_{\mathbf{k}, l, m, \sigma} \sum_{\mathbf{k}', m', l', \sigma'} \gamma_{lm}^{\mathbf{k}, \alpha} \gamma_{m'l'}^{\mathbf{k}', \beta} \langle T_\tau \hat{c}_{\mathbf{k}m\sigma}^\dagger(\tau) \hat{c}_{\mathbf{k}l\sigma}(\tau^+) \hat{c}_{\mathbf{k}'l'\sigma'}^\dagger(0) \hat{c}_{\mathbf{k}'m'\sigma'}(0^+) \rangle \\ &= \sum_{\mathbf{k}, l, m, \sigma} \sum_{\mathbf{k}', m', l', \sigma'} \gamma_{lm}^{\mathbf{k}, \alpha} \gamma_{m'l'}^{\mathbf{k}', \beta} G_{lmm'l'}^{\mathbf{q}=\mathbf{0} \mathbf{k}\mathbf{k}'}(\tau^+, \tau, 0^+), \end{aligned} \quad (2.151)$$

with the infinitesimal expressions $\tau^+ > \tau$ and $0^+ > 0$. By applying Wick contractions we are able to separate all two-particle diagrams into their connected and disconnected constituents

$$\begin{aligned} \chi_{\alpha\beta}^{jj}(\mathbf{q} = \mathbf{0}, \tau) &= \sum_{\mathbf{k}, lm, \sigma} \sum_{\mathbf{k}', m'l', \sigma'} \gamma_{lm}^{\mathbf{k}, \alpha} \gamma_{m'l'}^{\mathbf{k}', \beta} \left[G_{lm}^{\mathbf{k}}(\tau^+ - \tau) G_{m'l'}^{\mathbf{k}'}(0^+ - 0) \right. \\ &\quad \left. - \delta_{\mathbf{k}\mathbf{k}'} \delta_{\sigma\sigma'} G_{ll'}^{\mathbf{k}}(\tau^+ - 0) G_{m'm}^{\mathbf{k}'}(0^+ - \tau) + G_{lmm'l'}^{\mathbf{q}=\mathbf{0}}(\tau^+, \tau, 0^+) \right]. \end{aligned} \quad (2.152)$$

Fourier transforming these three terms leads to

$$\begin{aligned} \int_0^\beta d\tau e^{i\omega_n \tau} G_{lm}^{\mathbf{k}}(\tau^+ - \tau) G_{m'l'}^{\mathbf{k}'}(0^+ - 0) &= \int_0^\beta d\tau e^{i\omega_n \tau} G_{lm}^{\mathbf{k}}(0^+) G_{m'l'}^{\mathbf{k}'}(0^+) \\ &= \delta_{\omega_n, 0} \beta \left(n_{lm}^{\mathbf{k}} - \delta_{lm} \right) \left(n_{m'l'}^{\mathbf{k}'} - \delta_{m'l'} \right), \end{aligned} \quad (2.153a)$$

$$\begin{aligned} \int_0^\beta d\tau e^{i\omega_n \tau} G_{ll'}^{\mathbf{k}}(\tau^+ - 0) G_{m'm}^{\mathbf{k}'}(0^+ - \tau) &= \int_0^\beta d\tau e^{i\omega_n \tau} G_{ll'}^{\mathbf{k}}(\tau) G_{m'm}^{\mathbf{k}'}(-\tau) \\ &= \frac{1}{\beta} \sum_{\nu_a} G_{ll'}^{(\mathbf{k}, \nu_a)} G_{m'm}^{(\mathbf{k}', \nu_a - \omega_n)}, \end{aligned} \quad (2.153b)$$

$$\int_0^\beta d\tau e^{i\omega_n \tau} G_{lmm'l'}^{\mathbf{q}=\mathbf{0}}(\tau^+, \tau, 0^+) = \frac{1}{\beta^2} \sum_{\nu_a, \nu_b} G_{lmm'l'}^{(\mathbf{q}=\mathbf{0}, \omega_n)}(\mathbf{k}, \nu_a)(\mathbf{k}', \nu_b) \text{con}. \quad (2.153c)$$

where we employed the momentum dependent, multi-orbital occupation (see Section A.2)

$$n_{lm}^{\mathbf{k}} - \delta_{lm} \equiv G_{lm}^{\mathbf{k}}(\tau = 0^+) = \frac{1}{\beta} \sum_{\nu_n} G_{lm}^{\mathbf{k}}(i\nu_n) e^{-i\nu_n 0^+}, \quad (2.154)$$

and employed the frequency notation introduced for AbinitioDΓA in Ref. [33]. Inserting these identities back into Eq. (2.152) gives us

$$\begin{aligned} \chi_{\alpha\beta}^{jj}(\mathbf{q} = \mathbf{0}, i\omega_n) &= \sum_{\mathbf{k}, lm, \sigma} \sum_{\mathbf{k}', m'l', \sigma'} \gamma_{lm}^{\mathbf{k}, \alpha} \gamma_{m'l'}^{\mathbf{k}', \beta} \left[\delta_{\omega_n, 0} \beta \left(n_{lm}^{\mathbf{k}} - \delta_{lm} \right) \left(n_{m'l'}^{\mathbf{k}'} - \delta_{m'l'} \right) \right. \\ &\quad \left. - \delta_{\mathbf{k}\mathbf{k}'} \delta_{\sigma\sigma'} \frac{1}{\beta} \sum_{\nu_a} G_{ll'}^{(\mathbf{k}, \nu_a)} G_{m'm}^{(\mathbf{k}', \nu_a - \omega_n)} + \frac{1}{\beta^2} \sum_{\nu_a, \nu_b} G_{lmm'l'}^{(\mathbf{q}=\mathbf{0}, \omega_n)}(\mathbf{k}, \nu_a)(\mathbf{k}', \nu_b) \text{con} \right], \end{aligned} \quad (2.155)$$

which simplifies under the assumed paramagnetic phase to

$$\begin{aligned} \chi_{\alpha\beta}^{jj}(\mathbf{q} = \mathbf{0}, i\omega_n) &= \beta \delta_{\omega_n, 0} \sum_{\mathbf{k}\mathbf{k}', lmm'l', \sigma\sigma'} \gamma_{lm}^{\mathbf{k}, \alpha} \gamma_{m'l'}^{\mathbf{k}', \beta} \left(n_{lm}^{\mathbf{k}} - \delta_{lm} \right) \left(n_{m'l'}^{\mathbf{k}'} - \delta_{m'l'} \right) \\ &\quad - \frac{2}{\beta} \sum_{\mathbf{k}, lmm'l'} \gamma_{lm}^{\mathbf{k}, \alpha} \gamma_{m'l'}^{\mathbf{k}, \beta} \sum_{\nu_a} G_{ll'}^{(\mathbf{k}, \nu_a)} G_{m'm}^{(\mathbf{k}, \nu_a - \omega_n)} \\ &\quad + \frac{2}{\beta^2} \sum_{\mathbf{k}\mathbf{k}', lmm'l'} \gamma_{lm}^{\mathbf{k}, \alpha} \gamma_{m'l'}^{\mathbf{k}', \beta} \sum_{\nu_a, \nu_b} G_{lmm'l'}^{(\mathbf{q}=\mathbf{0}, \omega_n)}(\mathbf{k}, \nu_a)(\mathbf{k}', \nu_b) \text{con}. \end{aligned} \quad (2.156)$$

The first (diamagnetic) term is purely real and hence does not contribute to the conductivity. Expanding the connected Greens function according to Ref. [33] leads to equations that can be evaluated within `AbinitioDΓA`:

$$\begin{aligned}
\chi_{\alpha\beta}^{jj}(\mathbf{q} = \mathbf{0}, i\omega_n) &= \beta\delta_{\omega_n,0} \underbrace{\sum_{\mathbf{k}\mathbf{k}',lmm'l',\sigma\sigma'} \gamma_{lm}^{\mathbf{k},\alpha} \gamma_{m'l'}^{\mathbf{k}',\beta} \left(n_{lm}^{\mathbf{k}} - \delta_{lm} \right) \left(n_{m'l'}^{\mathbf{k}'} - \delta_{m'l'} \right)}_{\text{does not contribute to conductivity}} \quad (2.157) \\
&\quad - \underbrace{\frac{2}{\beta} \sum_{\mathbf{k},lmm'l'} \gamma_{lm}^{\mathbf{k},\alpha} \gamma_{m'l'}^{\mathbf{k},\beta} \sum_{\nu_a} G_{ll'}^{(\mathbf{k},\nu_a)} G_{m'm}^{(\mathbf{k},\nu_a-\omega_n)}}_{\text{bubble}} \\
&\quad + \underbrace{\frac{2}{\beta^2} \sum_{\mathbf{k}\mathbf{k}',lmm'l'} \gamma_{lm}^{\mathbf{k},\alpha} \gamma_{m'l'}^{\mathbf{k}',\beta} \sum_{\nu_a,\nu_b} \sum_{abcd} G_{la}^{(\mathbf{k},\nu_a)} G_{bm}^{(\mathbf{k},\nu_a)} F_{abcd}^{(\mathbf{q}=\mathbf{0},\omega_n)}(\mathbf{k},\nu_a)(\mathbf{k}',\nu_b) G_{m'c}^{(\mathbf{k}',\nu_b)} G_{d'l'}^{(\mathbf{k}',\nu_b)}}}_{\text{vertex correction}}
\end{aligned}$$

2.6.2.2 Implementation

The (spin-resolved) bubble evaluation is straight forward as only a combination of Green's functions and their corresponding optical elements need to be summed over

$$\chi_{\alpha\beta}^{jj,0}{}_{lmm'l'\sigma}(\mathbf{q} = \mathbf{0}, i\omega_n) = -\frac{1}{\beta N_{\mathbf{k}}} \sum_{\mathbf{k},\nu} \gamma_{lm}^{\mathbf{k},\alpha} \gamma_{m'l'}^{\mathbf{k},\beta} G_{ll'}^{(\mathbf{k},\nu)} G_{m'm}^{(\mathbf{k},\nu-\omega)}. \quad (2.158)$$

In this Section we show the exact numerical equations that have been implemented: For that reason here, and in the following, when summing over momenta in the Brillouin zone we explicitly denote the pre-factor that includes the number of \mathbf{k} -points $N_{\mathbf{k}}$. In any other Section this technical detail is implicitly assumed.

The physical response requires an additional orbital and spin summation such that only the external frequency and momentum transfer remains

$$\chi_{\alpha\beta}^{jj,0}(\mathbf{q} = \mathbf{0}, i\omega_n) = 2 \sum_{lmm'l'} \chi_{\alpha\beta}^{jj,0}{}_{lmm'l'}(\mathbf{q} = \mathbf{0}, i\omega_n), \quad (2.159)$$

The vertex correction of Eq. (2.156) is still in its most general form, in which an appropriate density vertex F_D must be inserted. Within `AbinitioDΓA` this vertex is constructed via

$$F_{lmm'l'}^{qkk'}{}_D = F_{lmm'l'}^{\omega\nu\nu'}{}_D + F_{lmm'l'}^{q\nu\nu',nl}{}_{D,ph} - \frac{1}{2} F_{m'mll'}^{(k'-k)(\nu'-\omega)\nu',nl}{}_{D,ph} - \frac{3}{2} F_{m'mll'}^{(k'-k)(\nu'-\omega)\nu',nl}{}_{M,ph}, \quad (2.160)$$

which was previously derived in Section 2.5.7.

Horizontal particle-hole channel

The first two terms of Eq. (2.160) are readily available in the **AbinitioDΓA** implementation and yield when plugged into Eq. (2.156) the contribution from the particle-hole channel

$$\chi_{\alpha\beta}^{jj,\text{ph}}{}_{lmm'l'\sigma}(\mathbf{q} = \mathbf{0}, i\omega_n) = \frac{1}{\beta^2 N_{\mathbf{k}}^2} \sum_{\mathbf{k}} \sum_{\mathbf{k}'\nu\nu'} \gamma_{lm}^{\mathbf{k},\alpha} \gamma_{m'l'}^{\mathbf{k}',\beta} \quad (2.161)$$

$$G_{la}^{(\mathbf{k},\nu)} G_{bm}^{(\mathbf{k},\nu-\omega)} G_{m'c}^{(\mathbf{k}',\nu'-\omega)} G_{dl'}^{(\mathbf{k}',\nu')} \left[F_{abcd}^{\omega\nu\nu'} + F_{abcd}^{(\mathbf{q}=\mathbf{0},\omega)\nu\nu',\text{nl}} \right],$$

see Fig. 2.72b. Again, a full orbital and spin summation is required to obtain the physical response

$$\chi_{\alpha\beta}^{jj,\text{ph}}(\mathbf{q} = \mathbf{0}, i\omega_n) = 2 \sum_{lmm'l'} \chi_{\alpha\beta}^{jj,\text{ph}}{}_{lmm'l'\sigma}(\mathbf{q} = \mathbf{0}, i\omega_n). \quad (2.162)$$

In this formulation, the spin summation leads to the same factor 2 as the density vertex is, per definition, SU(2) symmetric: $D \equiv \uparrow\uparrow + \uparrow\downarrow \stackrel{\text{SU}(2)}{=} \downarrow\downarrow + \downarrow\uparrow$. Let us note that for a one-band model this quantity must evaluate to zero: Within the Peierls approximation the optical elements are represented as derivatives of the energy levels $\gamma_{\mathbf{k}} = \frac{1}{\hbar} \frac{\partial \varepsilon(\mathbf{k})}{\partial \mathbf{k}}$ changing sign when moving from $\mathbf{k} \rightarrow -\mathbf{k}$. As the band structure $\varepsilon(\mathbf{k})$ is invariant under the same transformation (for a single band a consequence of Bloch's theorem), performing a full Brillouin zone summation necessarily cancels out all terms. In generalized multi-orbital systems this statement does not necessarily hold.

Transverse particle-hole channel

The last two terms of Eq. (2.160) correspond to the contribution of the transverse particle-hole channel, stemming from the enforced crossing symmetry of the vertex F . In order to evaluate the expression

$$\chi_{\alpha\beta}^{jj,\text{ph}}{}_{lmm'l'\sigma}(\mathbf{q} = \mathbf{0}, i\omega_n) = \frac{1}{N_{\mathbf{k}}^2 \beta^2} \sum_{\mathbf{k}} \sum_{\mathbf{k}'\nu\nu'} \gamma_{lm}^{\mathbf{k},\alpha} \gamma_{m'l'}^{\mathbf{k}',\beta} \quad (2.163)$$

$$G_{la}^{(\mathbf{k},\nu)} G_{bm}^{(\mathbf{k},\nu-\omega)} G_{m'c}^{(\mathbf{k}',\nu'-\omega)} G_{dl'}^{(\mathbf{k}',\nu')} \left[-\frac{1}{2} F_{cbad}^{(k'-k)(\nu'-\omega)\nu',\text{nl}} - \frac{3}{2} F_{cbad}^{(k'-k)(\nu'-\omega)\nu',\text{nl}} \right],$$

first a variable substitution for the momenta and frequencies (energies) must be performed

- $\mathbf{k}' - \mathbf{k} \rightarrow \tilde{\mathbf{q}}$,
- $\nu' - \nu \rightarrow \tilde{\omega}$.

The new “tilde” variables now correspond to the outer (bosonic) loop of **AbinitioDΓA**

$$\chi_{\alpha\beta}^{jj,\text{ph}}{}_{lmm'l'\sigma}(\mathbf{q} = \mathbf{0}, i\omega_n) = \frac{1}{N_{\mathbf{k}} N_{\tilde{\mathbf{q}}} \beta^2} \sum_{\tilde{\mathbf{q}}\tilde{\omega}\nu\nu'} \gamma_{lm}^{\mathbf{k}'-\tilde{\mathbf{q}},\alpha} \gamma_{m'l'}^{\mathbf{k}',\beta} \quad (2.164)$$

$$G_{la}^{(\mathbf{k}'-\tilde{\mathbf{q}},\nu'-\tilde{\omega})} G_{bm}^{(\mathbf{k}'-\tilde{\mathbf{q}},\nu'-\tilde{\omega}-\omega)} G_{m'c}^{(\mathbf{k}',\nu'-\omega)} G_{dl'}^{(\mathbf{k}',\nu')} \left[-\frac{1}{2} F_{cbad}^{(\tilde{\mathbf{q}},\tilde{\omega})(\nu'-\omega)\nu',\text{nl}} - \frac{3}{2} F_{cbad}^{(\tilde{\mathbf{q}},\tilde{\omega})(\nu'-\omega)\nu',\text{nl}} \right],$$

which we have easy access to in the numerical implementation. Again, an orbital and spin summation is required to obtain the contribution to the physical response

$$\chi_{\alpha\beta}^{jj,\overline{\text{ph}}}(\mathbf{q} = \mathbf{0}, i\omega_n) = 2 \sum_{lmm'l'} \chi_{\alpha\beta}^{jj,\overline{\text{ph}}}_{lmm'l'}(\mathbf{q} = \mathbf{0}, i\omega_n). \quad (2.165)$$

Let us emphasize that due to the variable transformation the transverse particle-hole contribution requires a full loop over all possible bosonic transfer frequencies $\tilde{\omega}$ and transfer momenta $\tilde{\mathbf{q}}$. Furthermore, from a technical point of view, care has to be taken when dealing with internal frequency summations: To achieve a consistent “box size effect” for all (external) bosonic transfer frequencies, the frequency range involved in $\sum_{\nu'}$ needs to be selected according to $\max i\omega_n$.

As per Eq. (2.157), the total current-current correlation function is then the sum over all considered terms

$$\chi_{\alpha\beta}^{jj}(\mathbf{q} = \mathbf{0}, i\omega_n) = \chi_{\alpha\beta}^{jj,0}(\mathbf{q} = \mathbf{0}, i\omega_n) + \chi_{\alpha\beta}^{jj,\text{ph}}(\mathbf{q} = \mathbf{0}, i\omega_n) + \chi_{\alpha\beta}^{jj,\overline{\text{ph}}}(\mathbf{q} = \mathbf{0}, i\omega_n). \quad (2.166)$$

2.6.2.3 Characteristics of the optical spectrum

Before analyzing the effects of vertex corrections, we first provide a brief introduction to the qualitative features of optical spectra. To this end we exploit the bubble contribution, which can be interpreted by rewriting the Green’s function via a Hilbert transformation, connecting the Matsubara axis with the real frequency axis

$$G^{\mathbf{k}}(i\nu_n) = \int_{-\infty}^{\infty} d\omega \frac{A(\mathbf{k}, \omega)}{i\nu_n - \omega}. \quad (2.167)$$

The resulting current-current correlation function (restricted to the one-orbital case here) evaluates to

$$\chi_{\alpha\beta}^{jj} \sigma(\mathbf{q} = \mathbf{0}, i\omega_m) = -\frac{1}{\beta N_{\mathbf{k}}} \sum_{\mathbf{k}, \nu_n} \gamma^{\mathbf{k},\alpha} \gamma^{\mathbf{k},\beta} \int_{-\infty}^{\infty} \int_{-\infty}^{\infty} d\omega' d\omega'' \frac{A(\mathbf{k}, \omega')}{i\nu_n - \omega'} \frac{A(\mathbf{k}, \omega'')}{i\nu_n - i\omega_m - \omega''} \quad (2.168)$$

which can be simplified by evaluating the Matsubara sum

$$-\frac{1}{\beta} \sum_{\nu_n} \frac{1}{i\nu_n - \omega'} \frac{1}{i\nu_n - i\omega_m - \omega''} = \frac{f_{FD}(\omega') - f_{FD}(\omega'')}{\omega'' - \omega' + i\omega_m}, \quad (2.169)$$

see Appendix A.2. The optical conductivity then results from the continuation to real frequency $i\omega_m \rightarrow \omega + i0^+$, see Eq. (2.146), which we can perform analytically

$$\begin{aligned} \sigma(\omega) &= \frac{\Im \chi(i\omega_m \rightarrow \omega + i0^+)}{\omega} \propto \Im \frac{1}{\omega} \int_{-\infty}^{\infty} \int_{-\infty}^{\infty} d\omega' d\omega'' A(\omega') A(\omega'') \frac{f_{FD}(\omega') - f_{FD}(\omega'')}{\omega'' - \omega' + \omega + i0^+} \\ &= \frac{\pi}{\omega} \int_{-\infty}^{\infty} d\omega' A(\omega') A(\omega + \omega') [f_{FD}(\omega') - f_{FD}(\omega' + \omega)] \end{aligned} \quad (2.170)$$

employing

$$\frac{1}{\omega'' - \omega' + \omega + i0^+} = \mathcal{P} \left(\frac{1}{\omega'' - \omega' + \omega} \right) - i\pi\delta(\omega'' - \omega' + \omega, 0) \quad (2.171)$$

where the Cauchy principal value does not contribute and the frequency constraint eliminates one of the integrals. In the direct current (DC) limit the selection window simplifies into the derivative of the Fermi function

$$\lim_{\omega \rightarrow 0^+} \frac{f_{FD}(\omega') - f_{FD}(\omega' + \omega)}{\omega} = -\frac{\partial f_{FD}(\omega')}{\partial \omega'}. \quad (2.172)$$

Ignoring momentum dependencies for a moment, the optical conductivity can thus be thought of as a convolution of spectral functions and a corresponding selection window, determined by the excitation frequency ω . As long as sharp momentum features are lost due to the Brillouin zone averaging, we are able to schematically understand the qualitative behavior of the optical spectrum $\sigma(\omega)$ from the *local* spectral function $A(\omega)$. This is presented in Fig. 2.73 where $A(\omega)$ and $\sigma(\omega)$ are shown for the metallic DMFT result of the two-dimensional Hubbard model on a square lattice with nearest neighbor hopping $t \equiv 1$, (weak) interaction $U = 2$ and temperature $T = 0.1$.

The optical spectrum mirrors the three distinct features of the shown spectral function: (i) The quasi-particle peak at the Fermi level translates to a dominant Drude peak around $\sigma(\omega = 0)$, naturally only present for metallic spectral functions. Its size provides information of the quasi-particle coherence at the Fermi level. The name is derived from the Drude model [235] whose steady-state solution connects the (complex) conductivity tensor to the mean free time τ between collisions of the excited electrons

$$\sigma^{\text{Drude}}(\omega) = \frac{ne^2\tau}{m_e} \frac{1}{1 - i\omega\tau}. \quad (2.173)$$

n , e , m_e refers to the particle density, the electron charge and the electron mass, respectively. The real part of Eq. (2.173), $\Re\sigma \propto 1/(1 + \omega^2\tau^2)$, then displays the same characteristic behavior around $\omega = 0$ as seen in Fig. 2.73e.

(ii) At intermediate frequencies ($\omega \approx 1.5$) we observe the so-called mid infrared (MIR) peak generated by optical transitions between the quasi-particle peak and satellite features, marked in the top panel. (iii) Finally, transitions between the Hubbard “bands” translate into a miniscule high-frequency feature, barely visible on a logarithmic scale. Increasing the interaction U will lead to a stronger renormalization, making the high-energy features more prominent. This simple picture will be modified by momentum dependencies and vertex corrections, leading to quantitative deviations and are not as easily interpretable. This demands a more thorough investigation which will be our task in the following.

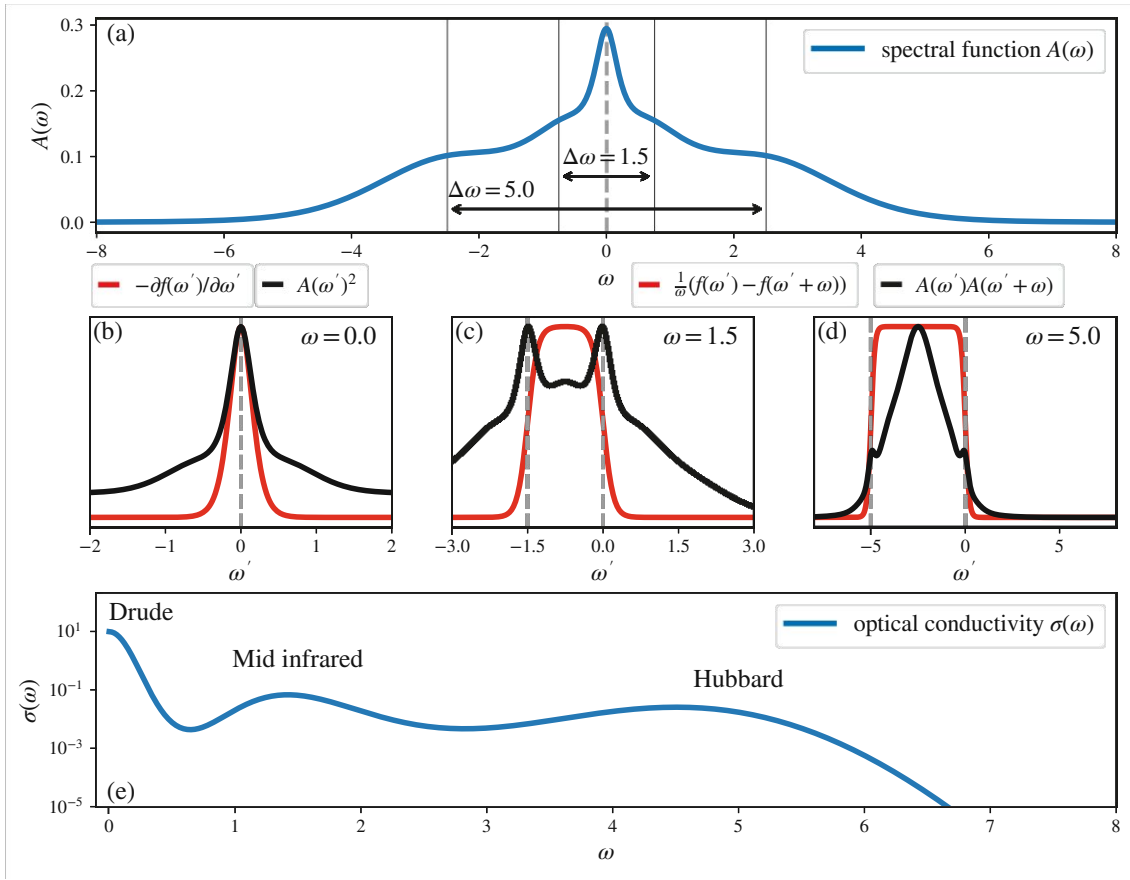


Figure 2.73: Schematic relation between the *local* electronic spectral function $A(\omega)$ (a) and the conductivity $\sigma(\omega)$ (e) via selection windows according to the equations in the main text (b-d, arbitrary y-axis scaling). The three distinct peaks of the optical spectrum, stemming from the features in $A(\omega)$, are referred to as Drude peak, mid infrared (MIR) peak and Hubbard peak. In realistic measurements peaks beyond are usually referred to as high frequency (HF) features. A particle-hole symmetric ($n = 1$) DMFT calculation of the two-dimensional Hubbard model with interaction $U = 2$ at temperature $T = 0.1$ was used for the spectral function and the optical conductivity.

2.6.2.4 Numerical analytic continuation

Once numerical data of Green's functions and vertex corrections has to be taken into consideration, conductivities on the real frequency axis must be obtained via a bosonic analytic continuation, similar to the fermionic continuation of Section 2.2.3. Here, the imaginary and real axis are related via the Kramers-Kronig relation [236]

$$\Re[\chi(i\omega_m)] = \frac{2}{\pi} \int_0^\infty d\omega \frac{\omega}{\omega^2 + \omega_m^2} \Im[\chi(\omega)], \quad (2.174)$$

resulting in the bosonic spectral function of

$$S_b(\omega) = \frac{2}{\pi} \frac{\Im[\chi(\omega)]}{\omega}. \quad (2.175)$$

Defining a corresponding kernel of

$$K_b(\omega, i\omega_m) = \frac{\omega^2}{\omega^2 + \omega_m^2}, \quad (2.176)$$

the connection between imaginary and real frequency axis is

$$\Re[\chi(i\omega_m)] = \int_0^\infty d\omega K_b(\omega, i\omega_m) S_b(\omega). \quad (2.177)$$

Analytic continuation via, e.g., the maximum entropy method then generates the *most likely* bosonic spectral function which is directly related to the (real part) of the conductivity, see Eq. (2.146)

$$\Re\sigma(\omega) = \frac{\pi}{2} S_b(\omega). \quad (2.178)$$

Let us note that throughout the rest of this Section we will restrict our discussion to this real part, which we will simply denote as $\sigma(\omega)$. From the above equations we can deduce that the f-sum rule of the conductivity can be connected to the static value of the susceptibility

$$\int_0^\infty d\omega \sigma(\omega) = \int_0^\infty d\omega \frac{\Im[\chi^{jj}(\mathbf{q}=0, \omega)]}{\omega} = \frac{\pi}{2} \Re[\chi^{jj}(\mathbf{q}=\mathbf{0}, i\omega_m=0)]. \quad (2.179)$$

To illustrate these connections, we present exemplary optical conductivities $\sigma(\omega)$ in Fig. 2.74, modelled phenomenologically via normal distributions

$$\sigma(\omega) \propto \exp\left(-\frac{1}{2} \frac{(\omega - \bar{\omega})^2}{\delta^2}\right) \quad (2.180)$$

for positive frequencies $\omega \geq 0$ that are normalized to $\int_0^\infty \sigma(\omega) = 1$. To illustrate complications from the interpretation of raw data on the Matsubara axis we look at two scenarios: (i) the formation of an optical gap by a shift of the center points $\bar{\omega}$ (top row), (ii) the widening of the Drude-like peak ($\bar{\omega} = 0$) via a scan over various standard deviations δ (bottom row). The resulting current-current correlation functions on the Matsubara axis are then calculated via Eq. (2.177). Both scenarios show a distinct increase of $\chi^{jj}(i\omega_m)$ at finite frequencies and for the case of a gap formation, a characteristic flattening of the response at the first two Matsubara frequencies whose slope vanishes once the gap has been fully formed. The Drude peak widening results in a similar, however way less pronounced, effect on these first two Matsubara frequencies. With this insight, the effects of vertex corrections onto the spectrum can then be classified at first glance according to their signatures on the Matsubara axis.

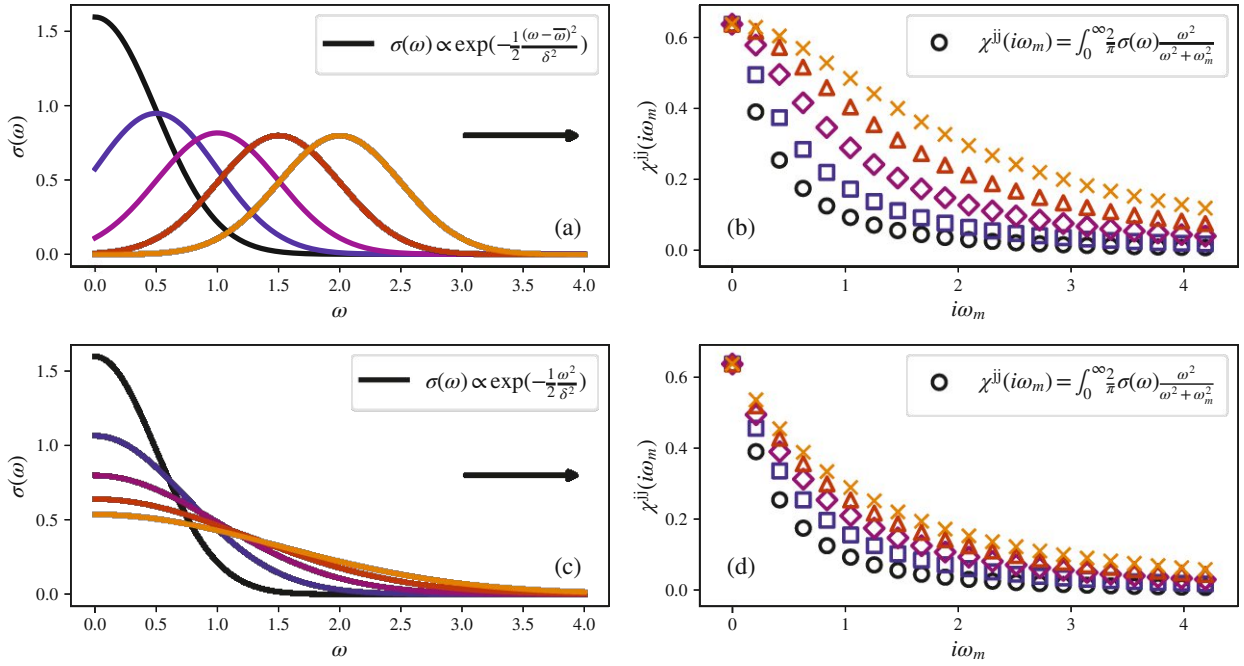


Figure 2.74: Exemplary behavior of the susceptibility χ^{jj} when opening an optical gap (a-b) and broadening the Drude-like peak (c-d). The optical conductivities $\sigma(\omega)$ (left) are modelled via normal distributions (panel a: standard deviation $\delta = 0.5$, center points $\bar{\omega} = \{0, 0.5, 1.0, 1.5, 2.0\}$; panel c: standard deviations $\delta = \{0.5, 0.75, 1.0, 1.25, 1.5\}$) normalized to $\int_0^{\infty} d\omega \sigma(\omega) = 1$. The resulting susceptibilities ($\beta = 30$) are the result of the integral given in Eq. (2.177). Due to the normalization of the Gaussian model $\sigma(\omega)$ the zeroth frequency $i\omega_m = 0$ is identical for all modelled conductivities, i.e. $\chi^{jj}(i\omega_m = 0) = 2/\pi$. The opening of the gap (increase of $\bar{\omega}$) coincides with a flattening of χ^{jj} at the lowest bosonic Matsubara frequencies, accompanied by a response increase for all finite frequencies. The same effects occur for a widening of the Drude peak, albeit less pronounced, i.e. a steep slope between zeroth and first Matsubara frequency remains.

Special attention must be given to the low frequency behavior, indicative of a loss/gain of coherence of the Drude peak and in the most extreme cases: the opening of an optical gap.

Let us note that conductivities must be related to a physical, i.e. positive, current-current correlation function. In order to analyze the effect of the vertex corrections, we therefore perform two separate continuations

$$\chi_{\text{scD}\Gamma\text{A}}^{\text{jj},0}(i\omega_m) \rightarrow \sigma_{\text{scD}\Gamma\text{A}}^0(\omega) \quad (2.181\text{a})$$

$$\chi_{\text{scD}\Gamma\text{A}}^{\text{jj},0}(i\omega_m) + \chi_{\text{scD}\Gamma\text{A}}^{\text{jj},\text{ph}}(i\omega_m) \rightarrow \sigma_{\text{scD}\Gamma\text{A}}(\omega) \quad (2.181\text{b})$$

from which we consider the correction as the difference

$$\sigma_{\text{scD}\Gamma\text{A}}^{\text{correction}}(\omega) = \sigma_{\text{scD}\Gamma\text{A}}(\omega) - \sigma_{\text{scD}\Gamma\text{A}}^0(\omega). \quad (2.182)$$

From a numerical point of view, this procedure makes the analysis on the real frequency axis slightly more error prone.

2.6.3 Two-dimensional Hubbard model

Defining the Hubbard model on a two-dimensional square lattice (with lattice vector lengths of $a = 1$), restricted to only nearest neighbor hopping

$$\mathcal{H} = -t \sum_{\langle i,j \rangle, \sigma} \hat{c}_{i\sigma}^\dagger \hat{c}_{j\sigma} + U \sum_i \hat{n}_{\uparrow,i} \hat{n}_{\downarrow,i} - \mu \sum_{i,\sigma} \hat{n}_{\sigma,i} \quad (2.183)$$

results in an kinetic energy diagonal in \mathbf{k} -space

$$\mathcal{H} = \sum_{\mathbf{k}, \sigma} \varepsilon_{\mathbf{k}} \hat{c}_{\mathbf{k}\sigma}^\dagger \hat{c}_{\mathbf{k}\sigma} + U \sum_i \hat{n}_{\uparrow,i} \hat{n}_{\downarrow,i} - \mu \sum_{i,\sigma} \hat{n}_{\sigma,i} \quad (2.184)$$

with an energy dispersion of

$$\varepsilon_{\mathbf{k}} = -2t [\cos(k_x) + \cos(k_y)]. \quad (2.185)$$

For the following considerations we set the hopping amplitude to $t = 1$, resulting in a band width of $W = 8$. The particle-hole symmetric, half-filling $\langle \hat{n}_{\uparrow} \rangle = \langle \hat{n}_{\downarrow} \rangle = 0.5$ of the energy dispersion Eq. (2.185) is generated via $\mu = 0$ in the non-interacting and $\mu = U/2$ in the interacting case²⁸ and results in a diamond shaped Fermi surface, see Fig. 2.75. Through the cosine dependence of the band structure, different points in the momentum space relate to each other

$$\varepsilon_{\mathbf{k}} = \varepsilon_{-\mathbf{k}}, \quad (2.186a)$$

$$\varepsilon_{\mathbf{k}} = -\varepsilon_{\mathbf{k}+\mathbf{\Pi}}, \quad (2.186b)$$

inducing a perfect nesting condition on the Fermi surface with nesting vector $\mathbf{q} = \mathbf{\Pi} = (\pi, \pi)$. The momenta responsible for the van-Hove singularity with its logarithmic divergence at the center of the density of states ($N(\varepsilon = 0) \rightarrow \infty$) are located in the antinodal (AN) directions: $\mathbf{k}_{\text{AN}} = (\pi, 0) \equiv (-\pi, 0) \equiv (0, \pi) \equiv (0, -\pi)$. In the context of optical spectra, the directional coupling element to the current operator in the Peierls approximation results in

$$\gamma^{\mathbf{k},x} = -2t \sin(k_x), \quad (2.187a)$$

$$\gamma^{\mathbf{k},y} = -2t \sin(k_y), \quad (2.187b)$$

see Eq. (2.149), modulating the contribution of each momentum to the current-current correlation function. Most prominently, the contribution of the antinodal direction to the bare response is fully

²⁸Given the energy dispersion of Eq. (2.185), this statement holds for any hopping amplitude t , temperature T , and interaction parameter U , and follows from the particle-hole transformation [193] of the Hamiltonian in Eq. (2.184).

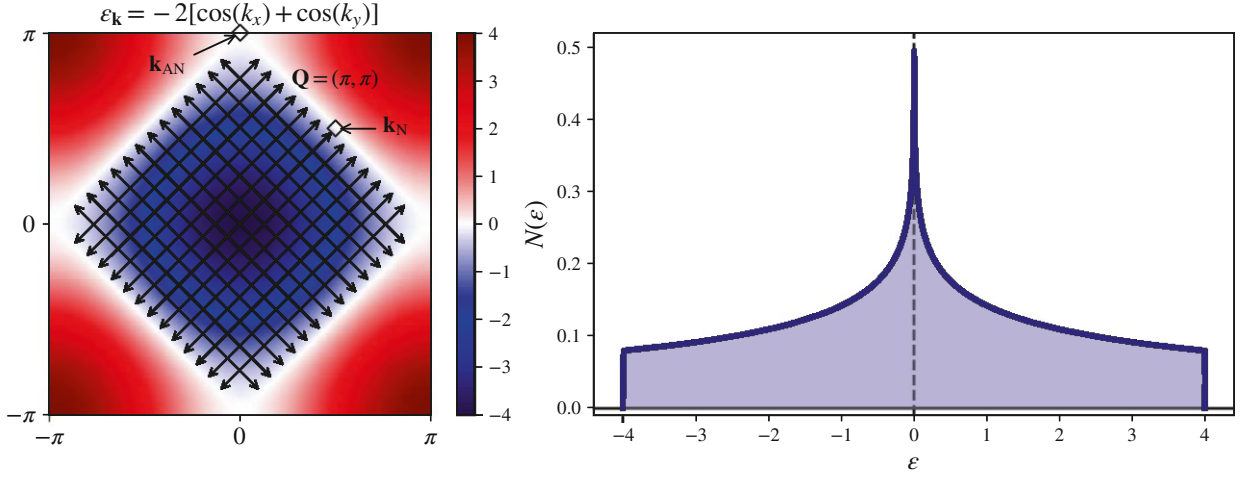


Figure 2.75: Energy distribution and density of states of the two-dimensional Hubbard model as described in Eq. (2.183) ($t \equiv 1$). The diamond shaped Fermi surface (left: white) for half-filling $n = 1$ causes a perfect nesting condition with $\mathbf{Q} = (\pi, \pi)$, indicated by arrows. The DOS features the logarithmic divergence at $\epsilon = 0$ stemming from the antinodal momenta $\mathbf{k}_{AN} = (0, \pi) \equiv (0, -\pi) \equiv (\pi, 0) \equiv (-\pi, 0)$. We numerically calculated the DOS with $10^5 \times 10^5$ k-points.

suppressed $\chi_{xx}^{jj,0}(\mathbf{k}_{AN}) = \chi_{yy}^{jj,0}(\mathbf{k}_{AN}) \equiv 0$, see Eq. (2.158). In the context of vertex corrections within scDFA, see Eq. (2.161) and Eq. (2.164), this momentum selectivity is more nuanced, since a pair of momenta $(\mathbf{k}, \mathbf{k}')$ contributes. Let us note that in all cases, the momentum summed response must obey the symmetry of the lattice (point group: C_{4v}), resulting in a directional equivalence of $\chi_{xx}^{jj} \equiv \chi_{yy}^{jj}$, whereas the response in the perpendicular direction of the applied field necessarily vanishes $\chi_{xy}^{jj} = \chi_{yx}^{jj} \equiv 0$.

Further, for the special case of these hyper-cubic lattices (square, cubic, etc.) we can connect the spectral weight of the (longitudinal — $j^x j^x$) optical conductivity to [237, 238]

$$\int_0^\infty d\omega \sigma(\omega) = \frac{\pi}{2} \sum_{\mathbf{k}} \sum_{\sigma} \frac{\partial^2 \epsilon_{\mathbf{k}}}{\partial k_x^2} \langle n_{\mathbf{k},\sigma} \rangle, \quad (2.188)$$

allowing us to retrieve an alternative expression for the static current-current correlation function through

$$\chi^{jj}(\mathbf{q} = \mathbf{0}, i\omega_m = 0) = \sum_{\mathbf{k}} \sum_{\sigma} \frac{\partial^2 \epsilon_{\mathbf{k}}}{\partial k_x^2} \langle n_{\mathbf{k},\sigma} \rangle. \quad (2.189)$$

For nearest neighbor hopping (nnh) this expression simplifies further, leading to a proportionality to the kinetic energy of the lattice fermions

$$\chi^{jj}(\mathbf{q} = \mathbf{0}, i\omega_m = 0) \stackrel{\text{nnh}}{=} -\frac{1}{2} \sum_{\mathbf{k}} \sum_{\sigma} \epsilon_{\mathbf{k}} \langle n_{\mathbf{k},\sigma} \rangle = -\frac{1}{2} E_{\text{kin}}. \quad (2.190)$$

Let us note that in the continuum formulation, that also includes all excitations beyond the low-energy dispersion, the f-sum rule instead connects the spectral weight to the total charge n in the system [35, 64]

$$\int_0^\infty d\omega \sigma(\omega) = \frac{\pi n e^2}{2 m_e} \quad (2.191)$$

where e is the elementary charge and m_e the mass of the electron. Eq. (2.191) is especially useful when tracking the redistribution of spectral weight as a function of temperature or pressure, etc.

2.6.3.1 Nesting induced antiferromagnetic instability

In the weak coupling regime the physics in the current setting is dominated by the perfect nesting condition: The non-interacting ($\Sigma \equiv 0$, $n = 1 \rightarrow \mu = 0$), momentum-dependent bare susceptibility χ_0 can be calculated analytically, see Appendix A.2, resulting in the well-known Lindhard expression

$$\begin{aligned} \chi_0(i\omega_m, \mathbf{q}) &= -\frac{1}{\beta} \sum_{\nu_n} \sum_{\mathbf{k}} \frac{1}{i\nu_n - \varepsilon_{\mathbf{k}}} \frac{1}{i\nu_n + i\omega_m - \varepsilon_{\mathbf{k}+\mathbf{q}}} \\ &= -\sum_{\mathbf{k}} \frac{f_{FD}(\varepsilon_{\mathbf{k}+\mathbf{q}}) - f_{FD}(\varepsilon_{\mathbf{k}})}{\varepsilon_{\mathbf{k}+\mathbf{q}} - \varepsilon_{\mathbf{k}} + i\omega_m} \end{aligned} \quad (2.192)$$

whose static contribution $i\omega_m = 0$ indeed exhibits fastest divergence for $\mathbf{q} = (\pi, \pi)$: $\chi_0^{(\pi, \pi)} \propto \ln(T)^2$ [239]. From a technical point of view, this behavior emerges since the (π, π) momentum transfer minimizes the denominator of Eq. (2.192) connecting every occupied \mathbf{k} -point to an unoccupied $\mathbf{k} + \mathbf{q}$ -point and vice versa. In contrast, for $\mathbf{q} = (0, 0)$ these non Fermi-surface contributions are comparatively suppressed, resulting in a slower divergence: $\chi_0^{(0,0)} \propto -\ln(T)$. An affirmation of this argument can be done in a straight forward manner for all possible \mathbf{q} -vectors via a numerical implementation of Eq. (2.192) (not shown).

Ordering at a finite critical temperature can be introduced via the random phase approximation (RPA). The Hubbard interaction constrains parts of the (spin-dependent) series to specific orders of U , resulting in the following geometric series²⁹, diagonal in transfer momentum \mathbf{q} and energy $i\omega_m$

$$\begin{aligned} \chi_{\uparrow\uparrow}^{\text{RPA}} &= \chi_0 + \chi_0 U \chi_0 U \chi_0 + \chi_0 U \chi_0 U \chi_0 U \chi_0 U \chi_0 + \dots \\ &= \chi_0 + \chi_0 U \chi_0 U \chi_0 \chi_{\uparrow\uparrow}^{\text{RPA}} = \frac{\chi_0}{1 - \chi_0 U \chi_0 U} \end{aligned} \quad (2.193a)$$

$$\begin{aligned} \chi_{\uparrow\downarrow}^{\text{RPA}} &= -\chi_0 U \chi_0 - \chi_0 U \chi_0 U \chi_0 U \chi_0 + \dots \\ &= -\chi_0 U (\chi_0 + \chi_0 U \chi_0 U \chi_0 + \dots) = -\chi_0 U \chi_{\uparrow\uparrow}^{\text{RPA}} \end{aligned} \quad (2.193b)$$

²⁹The sign of the different terms stem from the “standard” consideration of two-particle particle-hole reducible diagrams. The bare susceptibility χ_0 is defined via $-GG$, already including the minus sign of the loop. For each interaction U a separate minus sign must be included.

which can be combined to

$$\chi_D^{\text{RPA}} = \chi_{\uparrow\uparrow}^{\text{RPA}} + \chi_{\uparrow\downarrow}^{\text{RPA}} = \frac{\chi_0}{1 + \chi_0 U} \quad (2.194a)$$

$$\chi_M^{\text{RPA}} = \chi_{\uparrow\uparrow}^{\text{RPA}} - \chi_{\uparrow\downarrow}^{\text{RPA}} = \frac{\chi_0}{1 - \chi_0 U} \quad (2.194b)$$

valid in the weak coupling regime, i.e. small U . While the charge fluctuations become screened, the magnetic fluctuations eventually lead to nesting induced Slater antiferromagnetism, diverging for $\chi_0 U \geq 1$, appearing first for $\mathbf{q} = (\pi, \pi)$. DMFT susceptibilities then can be thought of as a generalization of the RPA concept by replacing the interaction U with the two-particle irreducible vertex in the ph channel $\Gamma_{r \in \{D, M\}}$, see Section 2.5.4.³⁰ A sketch of the resulting DMFT Néel temperature T_N , accompanied by the metal-insulator transition (MIT) is presented in Fig. 2.76.

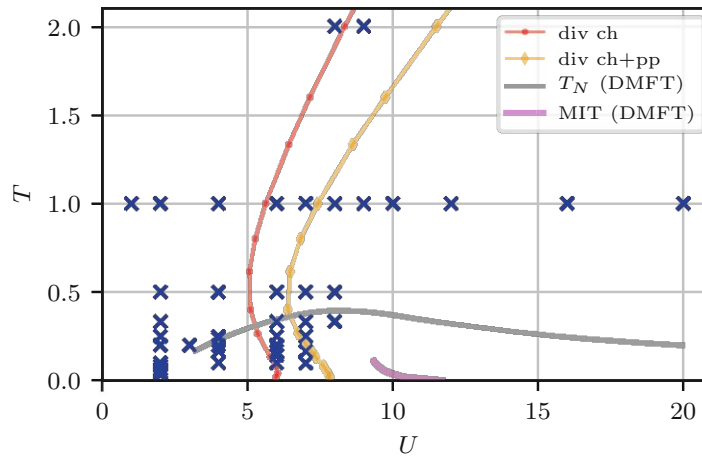


Figure 2.76: Phase diagram of the half-filled two-dimensional Hubbard model of Eq. (2.183). Blue crosses represent converged scDfA results of Ref. [215]. DMFT’s antiferromagnetic ordering temperature T_N and the metal-insulator transition line are indicated by a gray and pink line, respectively. Relevant local vertex divergences are indicated by a red and yellow line. These divergences mark the points where the local geometric series becomes ill-defined, i.e. the full vertex F can no longer be represented via $F = \Gamma + \Phi$. Numerically this is pinpointed by an inability to perform the inversion $\Gamma_r^\omega = F_r^\omega (1 + \chi_0 F_r^\omega)^{-1}$ [194, 240].

In this context, both RPA and DMFT violate the Mermin-Wagner theorem. The approximation of a static U or a local Γ as scattering matrices are thus too crude to fully capture the inherent (low temperature) physics of the model. Techniques beyond DMFT are essential to gain an understanding

³⁰The irreducible vertex Γ_{ph} via the parquet decomposition $\Gamma_{\text{ph}} = \Lambda + \Phi_{\text{pp}} + \Phi_{\text{ph}}$ contains to lowest order the interaction U itself (via Λ). The interaction contribution in the density and magnetic channel representation therefore leads to $\Gamma_D = +U$ and $\Gamma_M = -U$. By absorbing the sign into the vertex the susceptibilities can be written as $\chi_r = \chi_0 / (1 + \chi_0 \Gamma_r)$.

of the long range (magnetic) fluctuations and their effect onto the one-particle level (self-energy), present in the current setting.

2.6.3.2 Pseudogap emergence

Once genuine two-particle corrections are considered and properly fed back into the self-energy, as is the case in the self-consistent dynamical vertex approximation, the prominent antiferromagnetic fluctuations present in the Hubbard model may trigger the emergence of pseudogap physics. To illustrate this effect we show the temperature behavior of the self-energy on the Matsubara axis and the corresponding spectral function in the weak-coupling regime $U = 2$ for the prominent nodal (N) $\mathbf{k}_N = (\pi/2, \pi/2)$ and antinodal (AN) $\mathbf{k}_{AN} = (0, \pi)$ direction in Fig. 2.77. At elevated temperature $1/T = 1$ the system is in a fully incoherent state. Due to the strong thermal fluctuations a properly defined quasi-particle peak cannot establish itself. Coherence emerges first in the nodal direction at $1/T \approx 3$, signalled by an upturn of the lowest Matsubara frequency, followed by coherence in the antinodal direction at slightly lower T . At an intermediate temperature $1/T = 15$ the full Fermi surface becomes metallic. Whereas in DMFT this quasi-particle signature will only ever increase in coherence upon cooling, the feedback of the emerging antiferromagnetic fluctuations in scDfTA eventually induces a loss of spectral weight. This first occurs in the antinodal direction at $1/T_{AN}^* \approx 25$ in Fig. 2.77, marked by a significant downturn of the self-energy at the first Matsubara frequency, the signature of a gap opening. At the same temperature the nodal direction shows a similar behavior, there however, the slope of $\Sigma(i\nu_1) - \Sigma(i\nu_0)$ remains negative. Finally at $1/T_N^* \approx 30$ a (pseudo)gap is opened for all self-energies on the Fermi surface (for which the nodal momentum point is the proxy) which however remains quite momentum-selective. Due to long-range spin fluctuations the antiferromagnetic phase transition, observed in DMFT at finite temperatures, is pushed to $T \equiv 0$ compliant with Mermin-Wagner theorem and consistent with other diagrammatic methods [241]. The momentum selectivity, thought to be linked to the van Hove singularity in the antinodal direction, generates so-called Fermi arcs, similarly observed in copper oxides (cuprates) [242, 243]. Let us note however, that the underlying settings are different in cuprates: The cuprate parent compounds are Mott insulators, characterized by embedded CuO_2 planes as in LB-CO, YB-CO, BiS-CO, HGBC-CO, etc. The pseudogap regime is then observed via doping (away from the theoretical half-filled state) and is located next to the (strong-coupling) antiferromagnetic dome [244].

The momentum selective gap in the half-filled model, supported by diverging fluctuations upon cooling, eventually fully forms on the entire Fermi surface, transitioning the system to an insulator for all interaction strengths U , i.e. $U_c = 0$ at $T = 0$ [224]. Compared to DMFT, the emergence of the pseudogap strongly modifies the Fermi surface, and is expected to lead to strong renormalization of the optical spectrum. In the following, we will analyze the signatures of the pseudogap in optical

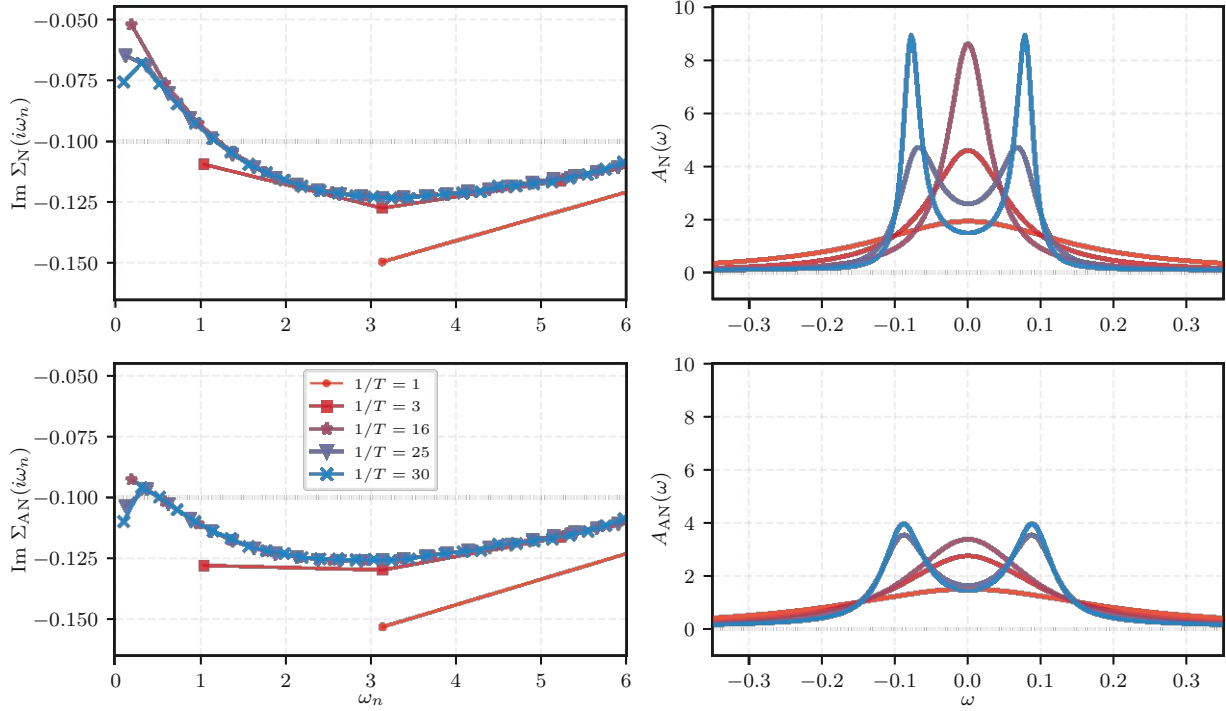


Figure 2.77: Imaginary part of the self-energy $\text{Im}\Sigma$ and corresponding spectral function $A(\omega)$ for the antinodal ($\mathbf{k} = (0, \pi)$, top) and nodal ($\mathbf{k} = (\pi/2, \pi/2)$, bottom) momenta for $U = 2$ and various temperatures. Coherence first emerges in the nodal direction (top) at $1/T = 3$ where throughout the coherence regime it displays less scattering rate than the antinodal direction. This is characterized by the more prominent quasi-particle peak in the spectral functions in the right panels. Due to strong antiferromagnetic fluctuations, Fermi surface weight is suppressed through the self-consistent vertex feedback resulting in a momentum-selective (pseudo)gap opening first appearing in the antinodal direction at $1/T = 25$. This is marked by a downturn of the self-energy at the first fermionic Matsubara frequency. Eventually, through a diverging correlation length, the Fermi surface will be fully suppressed and an insulator emerges for $T = 0$.

spectra and furthermore put an emphasis on the *explicit* effect of the dominant antiferromagnetic fluctuations via vertex corrections, as derived in Section 2.6.2.

For a detailed multi-method analysis of the underlying fluctuations and the pseudogap emergence, let us refer to Ref. [241].

2.6.3.3 Weak-coupling: $U = 2$

Having established characteristic pseudogap onset temperatures of $T_{\text{AN}}^* \approx 1/25$ and $T_{\text{N}}^* \approx 1/30$ for an interaction strength of $U = 2$, see Fig. 2.77, we turn our attention to the optical response. The

current-current correlation function $\chi^{jj}(i\omega_m)$ on the Matsubara axis and optical conductivities on the real frequency axis are depicted in Fig. 2.78, and Fig. 2.79, respectively.

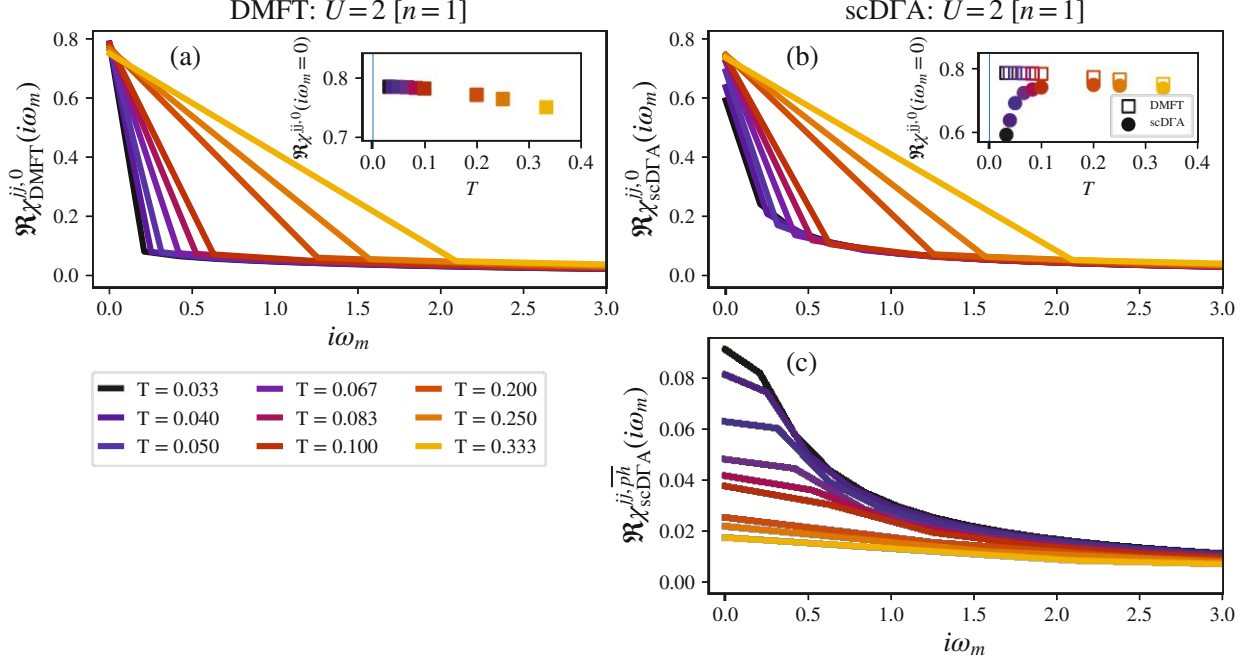


Figure 2.78: Current-current correlation functions for $U = 2$ at half-filling $n = 1$. (a) DMFT, (b) scDGA bubble contribution, (c) scDGA vertex contribution. Lowering the temperature leads to a monotonous increase of coherence in the DMFT response. The development of the pseudogap and the overall self-energy dampening reverses this trend in scDGA data. Cooling the system leads to a monotonous increase of the vertex corrections. Note that the values at the discrete Matsubara frequencies have been connected for clarity.

We present three different contributions to the correlation function in Fig. 2.78: In the panel (a) we show the DMFT bubble, in panel (b) the bubble contribution of scDGA and in panel (c) the vertex correction of the transverse particle-hole channel $\overline{\text{ph}}$. For the smallest shown temperatures the employed momentum grid was $k_x \times k_y = 80 \times 80$. Note that we connected the values at the discrete Matsubara frequencies $\omega_m = 2m\pi/\beta$ for clarity. The scDGA bubble contribution highlights the *implicit* effects of the antiferromagnetic fluctuations through the self-energy, directly comparable to the purely local correlations of DMFT. The vertex corrections on the other hand show the *explicit* effects through the direct evaluation of the transverse particle-hole BSE. Let us reiterate, that in this context (one band, $\mathbf{q} = \mathbf{0}$), particle-hole vertex corrections do not contribute due to the contrasting behavior of the band energies $\varepsilon(\mathbf{k}) = \varepsilon(-\mathbf{k})$ and band velocities as coupling elements $\gamma_{\mathbf{k}} = -\gamma_{-\mathbf{k}}$.

Within DMFT, all considered temperatures result in firm, Fermi liquid self-energy signatures

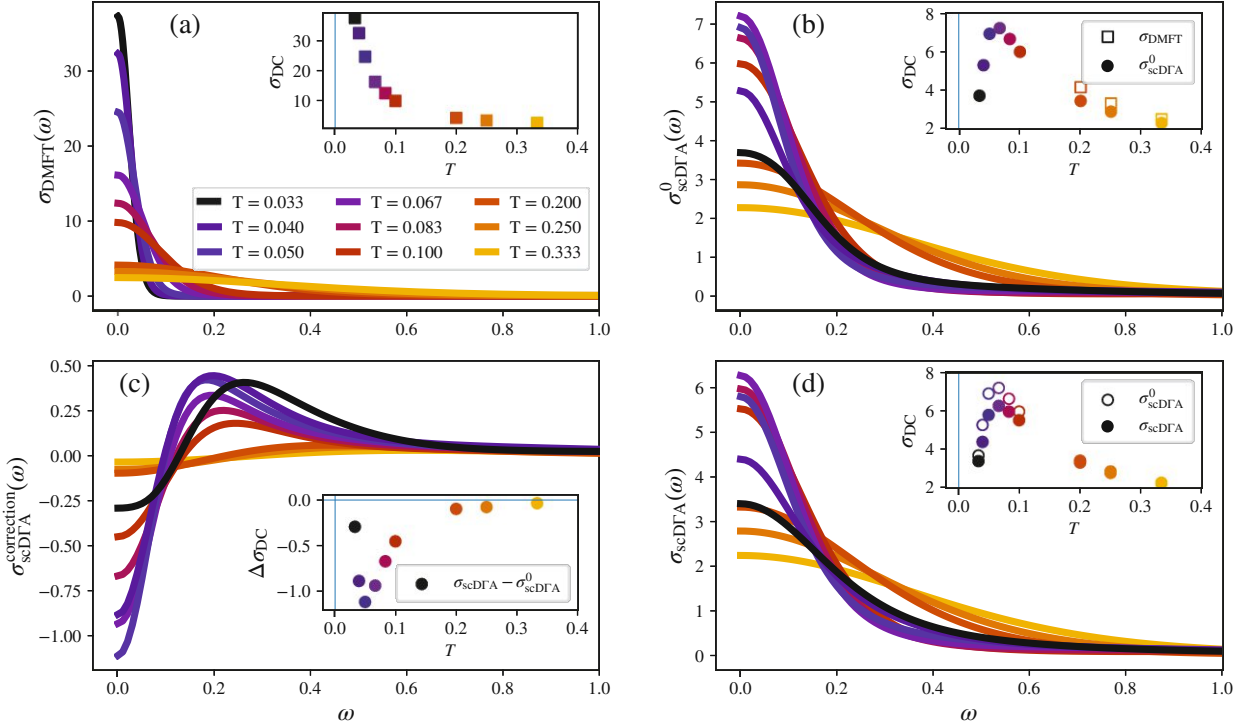


Figure 2.79: Optical conductivities for $U = 2$ at half-filling $n = 1$. (a) DMFT, (b) bare bubble scD Γ A, (c) vertex contribution to scD Γ A, (d) full scD Γ A. The insets illustrate the temperature dependence of the respective DC values. Cooling generates an increasingly coherent Drude peak within DMFT. This trend is broken in scD Γ A where a trend reversal is observed, followed by a continuous suppression of the Drude peak. Vertex correction, overall, lead to a broadening of the Drude peak by shifting weight toward the inflection point at $\omega = 0.25$.

where the characteristic scattering rate behavior $\Gamma = -\Im\Sigma(i\nu_n \rightarrow 0^+) \propto T^2$, however, can only be observed below $T = 0.067$ (not shown). With only local correlations at play, the current-current correlation functions and the resulting optical conductivities behave as expected: Upon cooling the static value $\chi^{jj}(i\omega_m = 0)$ increases monotonously (see inset), suggesting a kinetic energy increase through increased coherence, see Eq. (2.190). This is accompanied by a stark steepening of $\chi^{jj}(i\omega_m = 0) - \chi^{jj}(i\omega_m = 2\pi/\beta)$, due to the temperature behavior of the Matsubara axis: $(\omega_1 - \omega_0)$ decreases in size upon cooling. As the responses for finite transfer frequencies $i\omega_m > 0$ remain quite small, the optical spectrum (in real-frequencies) develops a dominant Drude peak contribution containing the majority of the spectral weight. The increased coherence then necessarily translates into a boost of the DC conductivity

$$\sigma_{\text{DC}} = \lim_{\omega \rightarrow 0^+} \sigma(\omega). \quad (2.195)$$

This temperature characteristic is plotted in the inset of Fig. 2.79a, mirroring the Fermi liquid sig-

natures at the lowest temperatures with $\rho \propto T^2$ (not shown).

Including non-local self-energies within scDΓA, unsurprisingly, induces significant changes in the bubble $\chi^{\text{jj},0}$: While the high temperature current-current correlation functions and conductivities for temperatures $T = 0.333$, $T = 0.25$, $T = 0.2$ still quantitatively mirror DMFT, upon cooling below $T \leq 0.100$ deviations become apparent. At these temperatures, the monotonous trend of the static response (inset of Fig. 2.78b) reverses, signalling the loss of kinetic energy through increased scattering. This is accompanied by a general broadening of the finite frequency response where $\chi_0^{\text{scD}\Gamma\text{A}}(i\omega_m) > \chi_0^{\text{DMFT}}(i\omega_m)$, see Fig. 2.78b, reflects in a broadened optical conductivity $\sigma_{\text{scD}\Gamma\text{A}}^0(\omega)$ whose DC value exhibit the same observed trend reversal. The DC value of the conductivity peaks at $T = 1/15 = 0.067$, significantly above the characteristic pseudogap temperatures $T_{\text{AN}}^* = 1/25 = 0.040$. In this regime the momentum-selective poles of the self-energy are not yet fully developed. The onset of the (pseudo)gap opening (see Fig. 2.77) is however significant enough to trigger a suppression of the states on the Fermi surface, the main contributors to the DC conductivity. Once the pseudogap has been established below $1/T = 25 = 0.040$ at all \mathbf{k} -points, the DC conductivity diminishes rapidly, necessarily being fully suppressed $\sigma(T \rightarrow 0) \rightarrow 0$ as an optical gap is formed and antiferromagnetic order sets in.

The $\overline{\text{ph}}$ vertex corrections in panel (c) of Fig. 2.78 are small compared to the bare susceptibility. In particular, at high temperatures $T \geq 0.200$ this contribution displays no significant, distinct features on the Matsubara axis, correcting the static response by no more than 3%. Cooling down monotonously boosts the vertex corrections until, eventually, below $T = 0.1$, a flat “kink” is formed at the first Matsubara frequency $i\omega_1 = 2\pi/\beta$. For the lowest considered temperature, deep in the pseudogap regime $T = 0.033$, vertex corrections result in an increase of the static value of the current-current correlation function $\chi^{\text{jj},0}(i\omega_0 = 0)$ by 15% and of the first finite frequency $\chi^{\text{jj},0}(i\omega_1 = 2\pi/\beta)$ by 40%. That is, the vertex corrections on the Matsubara axis show less frequency dependence than the bare response, especially at the lowest frequencies.

In the total conductivity in Fig. 2.79 ((d): $\sigma(\omega)$, (c): $\sigma(\omega) - \sigma^0(\omega)$) the vertex correction effects show a characteristic signature, do not, however, contribute in a major way. The flat “kink” formation in $\chi^{\text{jj},\overline{\text{ph}}}$ softens the Drude peak, i.e. weight is shifted from the peak ($\omega = 0$) to its inflection point at around $\omega = 0.25$. The temperature trend of this DC suppression $\Delta\sigma_{\text{DC}}$ is illustrated in the inset of panel (c) and shows a peak at $T = 0.05$, in between the DC maximum at $T = 0.067$ and $T_{\text{AN}}^* = 0.04$. Evidently, the vertex corrections are largest at the point where a fine balance is struck between Fermi surface suppression and the size of the antiferromagnetic fluctuations themselves. Once the self-energy effects become overwhelming and the development of the (pseudo)gap suppresses a majority of the Fermi surface states, the fluctuations become less effective. The result is a DC modification $\Delta\sigma(\omega = 0)$ that rapidly declines and necessarily vanishes for $\lim_{T \rightarrow 0} \Delta\sigma(\omega = 0) = 0$ due to the

(anticipated) gap formation at zero temperature.

In this regime, effects on the other parts of the spectrum (mainly the inflection of the Drude peak, less so the mid infrared peak and the Hubbard-to-Hubbard peaks) however remain present: The static value of the vertex corrections $\chi^{jj,\text{ph}}$, corresponding to the added spectral weight, continue to grow through cooling, inevitably affecting purely the satellite features of $\sigma(\omega)$. These type of corrections to (pseudo)gapped system are not surprising, as they have been shown to be more significant than in metals [215].

2.6.3.4 Intermediate-coupling: $U = 4$

Doubling the interaction strength from $U = 2$ to $U = 4$ results in the current-current correlation functions and optical conductivities illustrated in Fig. 2.80 and Fig. 2.81, respectively.

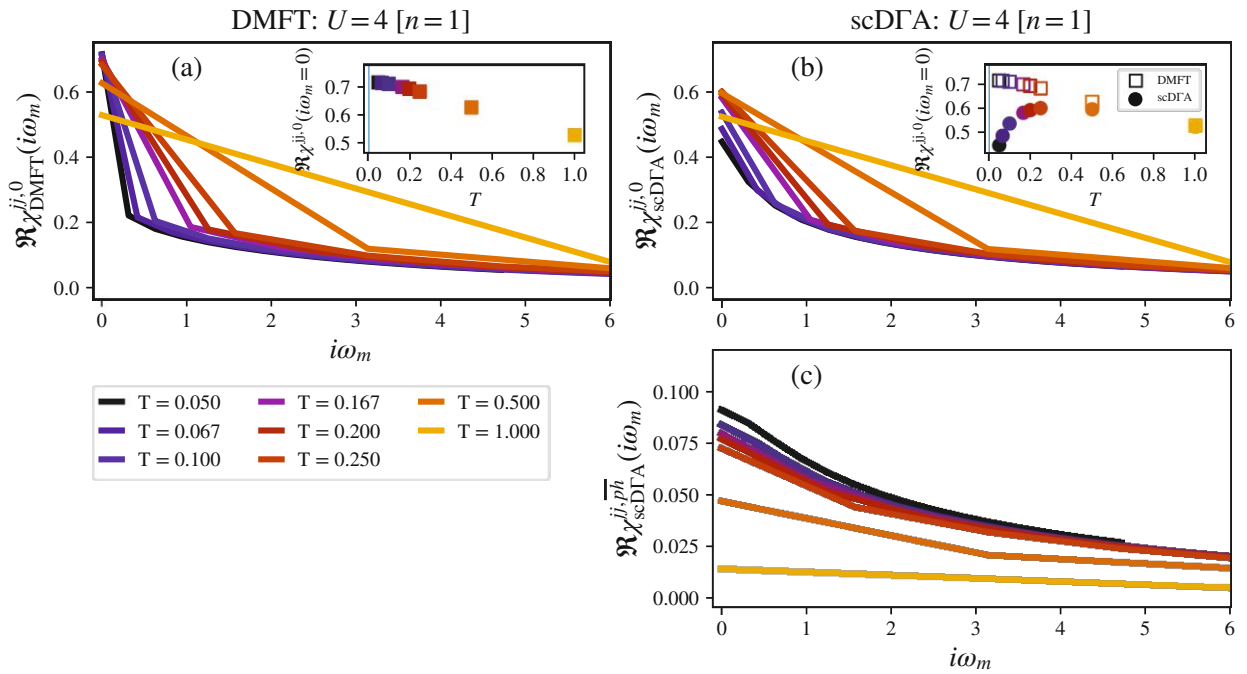


Figure 2.80: Current-current correlation functions for $U = 4$ at half-filling $n = 1$. (a) DMFT, (b) scDFA bubble contribution, (c) scDFA vertex contribution. We observe the same qualitative trends as for $U = 2$ where the size of the vertex correction are on par. The kink in the first Matsubara frequency is, due to the overall higher temperatures, on par.

Within DMFT, increased interaction strengths naturally lead to a stronger renormalization: The coherence temperature of $\Sigma(i\nu_n)$ is lowered, accompanied by increased scattering rates, $\Gamma = -\Im\Sigma(i\nu_n \rightarrow 0^+)$, and quasi-particle weights $m^*/m = 1/Z$. These effects are evident in the response data on the Matsubara axis: The static contribution (kinetic energy) is lowered $\chi^{jj,0}(i\omega_m =$

$0; U = 4) < \chi_{0,jj}(i\omega_m = 0; U = 2)$ and the response at finite frequencies becomes enhanced $\chi_{0,jj}(i\omega_m > 0; U = 4) > \chi^{jj,0}(i\omega_m > 0; U = 2)$. This effectively broadens the DMFT optical conductivity, which necessarily dampens the DC values, see inset of Fig. 2.79a.

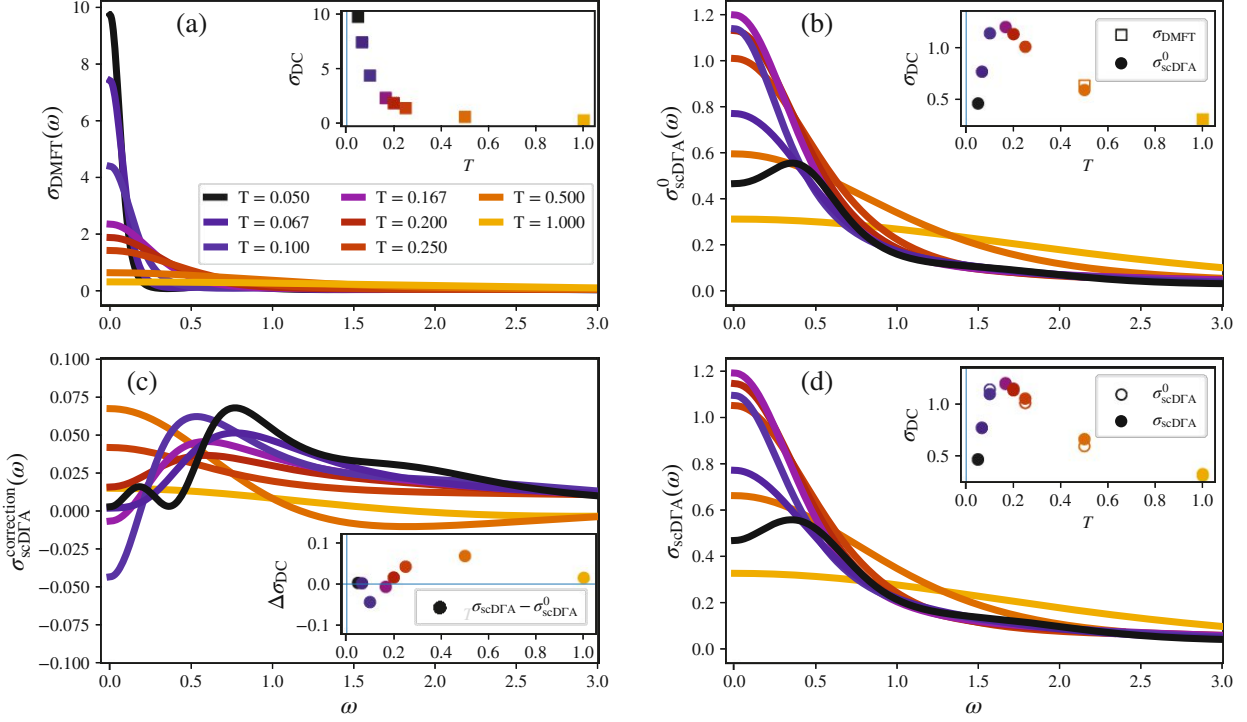


Figure 2.81: Optical conductivities for $U = 4$ at half-filling $n = 1$. (a) DMFT, (b) bare bubble scDfA, (c) vertex contribution to scDfA, (d) full scDfA. At the lowest temperature we see strong signs of an optical weight redistribution. The pseudogap causes a reshaping of the Drude peak where the maximum of the optical spectrum is no longer represented by the DC value. As the Drude peak is suppressed, its vertex induced correction incidentally also becomes smaller. The mid-infrared correction however remains somewhat large.

Turning to scDfA, the observed pseudogap phenomena become enhanced with the increased coupling strength. Congruent to expectations, we find larger characteristic pseudogap onset temperatures $T_N^* = 0.050$, $T_{AN}^* = 0.067$ (not shown), boosted by 50% as compared to $U = 2$. In combination with the stronger self-energy damping through stronger antiferromagnetic fluctuations, stark deviations from DMFT in the bubble $\chi^{jj,0}(i\omega_m)$ appear already at $T = 0.25$. Similarly, vertex corrections themselves increase in overall size. Despite doubling the interaction strength, however, their effect is less than naively anticipated: The vertex contributions $\chi_{jj,\overline{ph}}$ to the full response $\chi_{jj} = \chi_{jj,0} + \chi_{jj,\overline{ph}}$ are similar between $U = 2$ and $U = 4$, see Fig. 2.78 and Fig. 2.80. Most notable, however, is the lack of features in the correction term. The aforementioned kink at $U = 2$ is replaced by a much smoother,

unobtrusive continuation of the high frequency trend.

The optical conductivities in Fig. 2.81 reflect this behavior of Fig. 2.79 (b-d): In conformance with the enhanced pseudogap temperatures, we find a temperature at which the DC value reaches its maximum at $T^{\text{peak}} \approx 0.14$ (compared to $U = 2, T^{\text{peak}} \approx 0.07$). Contrary to $U = 2$, we now observe a second “regime change”: At the lowest temperature $T = 0.05$ the Drude peak subsides and the maximum of the optical response is shifted to $\omega > 0$, indicating the onset of the optical gap opening. This behavior aligns with our expectations of $\lim_{T \rightarrow 0} \sigma(\omega = 0, T) = 0$.

Vertex corrections, surprisingly, only play a minor role. Whereas at $U = 2$, the $\overline{\text{ph}}$ correction lead to a broadening of the Drude peak $\sigma_{\text{correction}}^{\text{scD}\Gamma\text{A}}(\omega = 0) < 0$, here a different picture emerges: The Drude peak is slightly enhanced at elevated temperatures $T > 0.200$, slightly suppressed at intermediate temperatures, and effectively unchanged by π -ton physics 2.72 at low temperatures. In accordance with the nearly featureless $\chi^{\text{jj},\overline{\text{ph}}}$ the main effect of these vertex corrections is an augmentation of the overall optical weight $\int_0^\infty d\omega \sigma(\omega)$.

Parquet D Γ A reference

In order to contextualize the results for $U = 4$ we perform a quantitative comparison of the scD Γ A simulations to parquet dynamical vertex approximation calculations from Ref. [215]. As the pD Γ A approximation is less crude (only the fully irreducible vertex Λ is approximated to be local), one gains access to all channel contributions $r \in \{\text{ph}, \overline{\text{ph}}, \text{pp}\}$ on equal footing. The comparison of the current-current correlation functions are illustrated in Fig. 2.82, the bare response $\chi_{0,jj}$ in the top row, the vertex corrections in the bottom row. The scD Γ A vertex corrections are comprised only of the transverse particle hole ($\overline{\text{ph}}$) whereas in pD Γ A, through the parquet equation, there are four contributions: $\Lambda, \Phi_{\text{ph}}, \Phi_{\overline{\text{ph}}}, \Phi_{\text{pp}}$. As Λ remains local throughout, its contribution to χ^{jj} necessarily vanishes. Due to the self-consistency all other vertices impact one another and gain full momentum dependencies, contributing to the full vertex F and the optical conductivity $\sigma(\omega)$.

Focusing first on the bare responses, we find a qualitatively different temperature behavior between the scD Γ A and the parquet method. In the given temperature range $\chi_{jj,0}(i\omega_m = 0)$ becomes strongly suppressed upon cooling within scD Γ A, whereas pD Γ A shows an insignificant temperature dependence, see top row of Fig. 2.82. This is *not* surprising, as the pseudogap onset temperature in scD Γ A is higher compared to the pD Γ A reference data, that was generated with a momentum grid of $k_x \times k_y = 6 \times 6$ in Ref. [215]. Please note that in principle, the characteristic pseudogap temperatures of scD Γ A should be smaller once the pD Γ A resolution is improved. Results from truncated unity parquet solver with 9 form factors [245], e.g., lead to $T_{\text{AN,pD}\Gamma\text{A}}^* = 0.100$ compared to $T_{\text{AN,scD}\Gamma\text{A}}^* = 0.067$. The latter was generated with a momentum grid of $k_x \times k_y = 80 \times 80$.

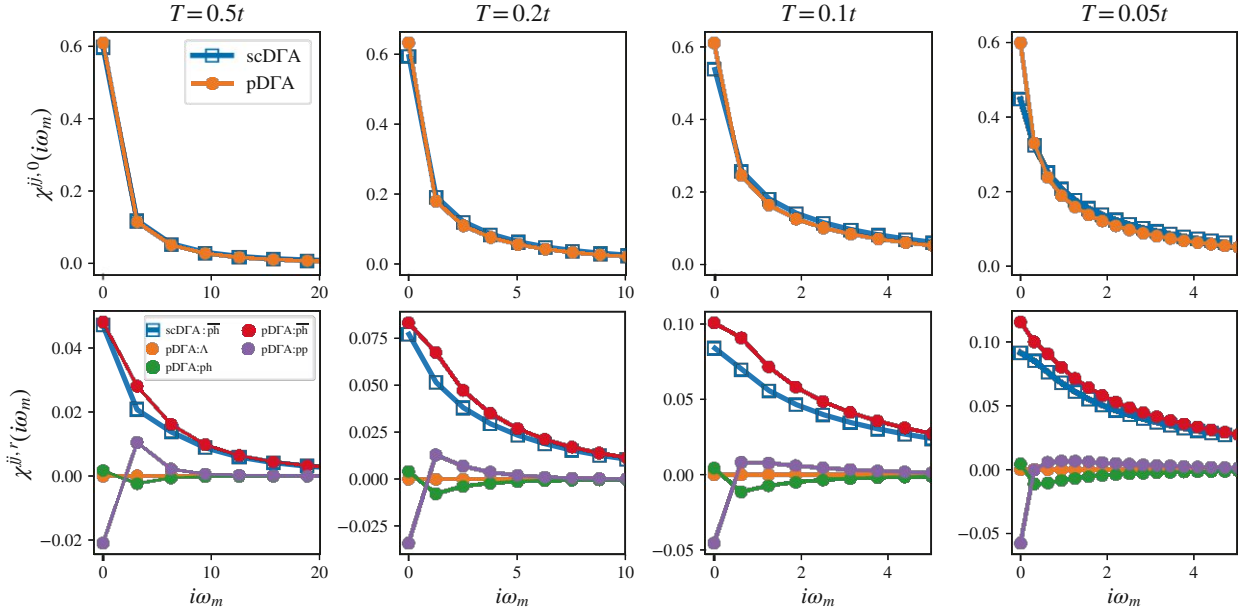


Figure 2.82: Contributions to the current-current correlation functions for $U = 4$ at half-filling $n = 1$. Top panels: bare contribution $\chi^{jj,0}$, bottom panels: channel dependent vertex correction $\chi^{jj,r}$. The pseudogap onset temperature within scDΓA is considerably higher than within pDΓA manifesting itself in a strong differentiation of $\chi_{0,jj}$ at low temperatures. Despite of this, the size of the $\overline{p\bar{h}}$ vertex corrections are similar. Due to the other three contributions, the lowest Matsubara frequencies are altered in a different fashion. As the system is cooled, the particle-particle contribution of pDΓA becomes increasingly more important.

Despite these differences in the static limit, the vertex corrections stemming from the $\overline{p\bar{h}}$ channel display quantitatively good agreement between the two methods at finite Matsubara frequencies where the overall size of $\Re\chi_{jj,\overline{p\bar{h}}}$ differs by less than 20%. While the overall corrections are dominated by the $\overline{p\bar{h}}$ channel, within pDΓA the feedback into the pp channel introduces a distinct low frequency signature, see bottom row of Fig. 2.82 (purple line). As we have ascertained in Section 2.6.2.4, such a downturn signifies that the current-current correlation function is closer to an “insulating” solution. In this case the conductivities, illustrated in Fig. 2.83, retain their metallic signature, however, the pp-correction induces a strong dampening of the Drude peak (bottom row: $\sigma_{\text{correction}}$).

In the incoherent regime $T = 0.5$, minor differences in the susceptibilities (top row) have somewhat large effects onto the optical conductivities (middle row). Here we cannot, however, preclude numerical inaccuracies w.r.t. box sizes and the analytic continuation. Nonetheless, a similar high temperature behavior has been observed in Ref. [246]. Due to the strong(er) self-energy renormalization in the coherent regime $T < 0.5$, scDΓA generates total susceptibilities that are consistently smaller than pDΓA. The additional pp corrections in the pDΓA, however, make these differences less

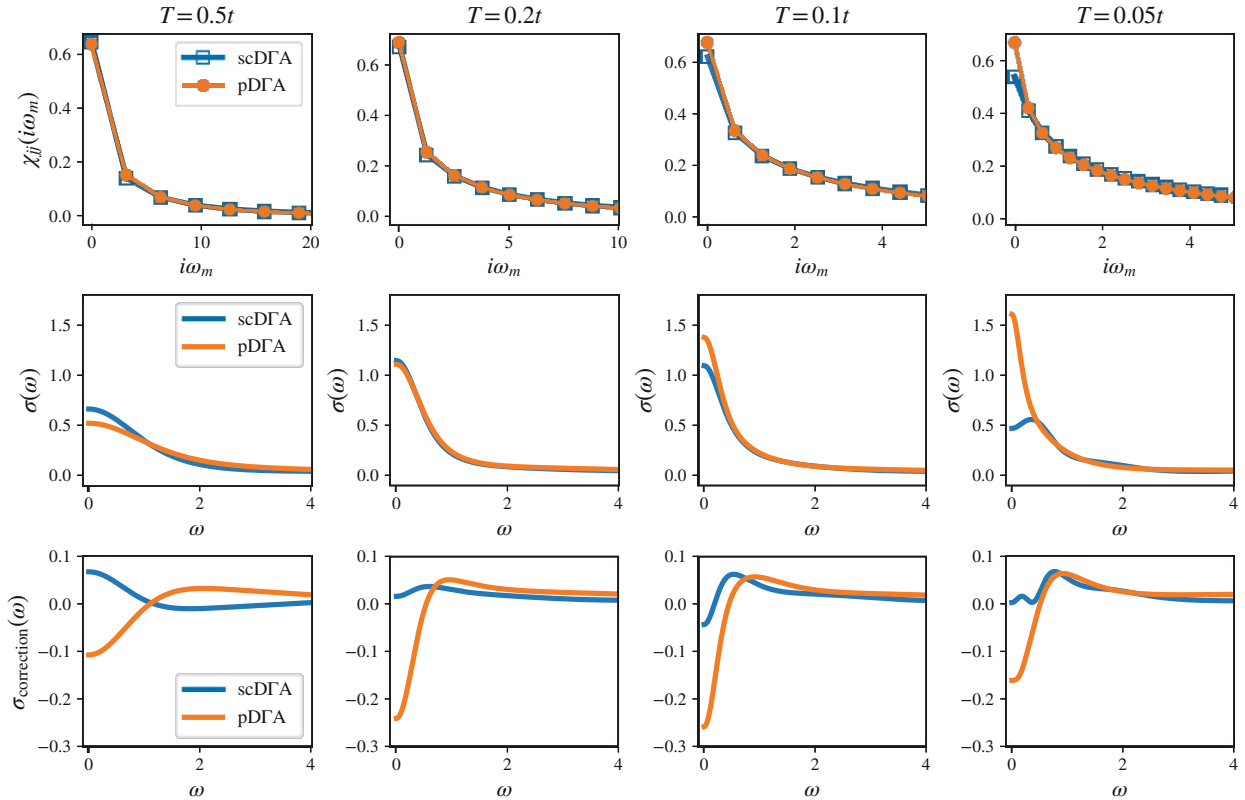


Figure 2.83: Current-current correlation functions (top panel) and the corresponding optical conductivities (middle panel) for $U = 4$ at half-filling $n = 1$. Vertex contributions to the conductivities are plotted in the bottom panel. Comparison between self-consistent D Γ A and parquet D Γ A. Due to the different characteristic pseudogap temperatures and self-energy dampening effects, the pD Γ A showcases a monotonous DC trend, while the scD Γ A already transitions towards the formation of an optical gap. The additional particle-particle contributions play a pivotal role in the Drude peak alteration within pD Γ A, a contribution completely absent in scD Γ A.

pronounced. The dampening of scD Γ A is especially noticeable in the vicinity of the pseudogap onset temperature $T = 0.05$: Whereas in scD Γ A the optical gap is starting to get formed, on the pD Γ A Fermi surface the antiferromagnetic fluctuations can operate more freely resulting in strong(er) corrections. In scD Γ A the pseudogap onset gets overshadowed by the increase in scattering, effectively suppressing the Drude peak. On this smeared-out Fermi surface, antiferromagnetic fluctuations have a smaller impact.

2.6.3.5 Towards strong-coupling: $U = 6$

As we increase the interaction further we slowly approach the Mott insulator transition of DMFT, located at $U_c \approx 9$, see Fig. 2.76. Accordingly, DMFT's antiferromagnetic ordering temperature is

increased, making the scDFA more cumbersome to converge. We require a denser momentum grid in combination with an increasingly large number of iterations in the self-consistency cycle to suppress the native antiferromagnetic fluctuations. Nonetheless, converged results can be obtained. For these, the current-current response functions and optical conductivities are illustrated in Fig. 2.84 and Fig. 2.85, respectively.

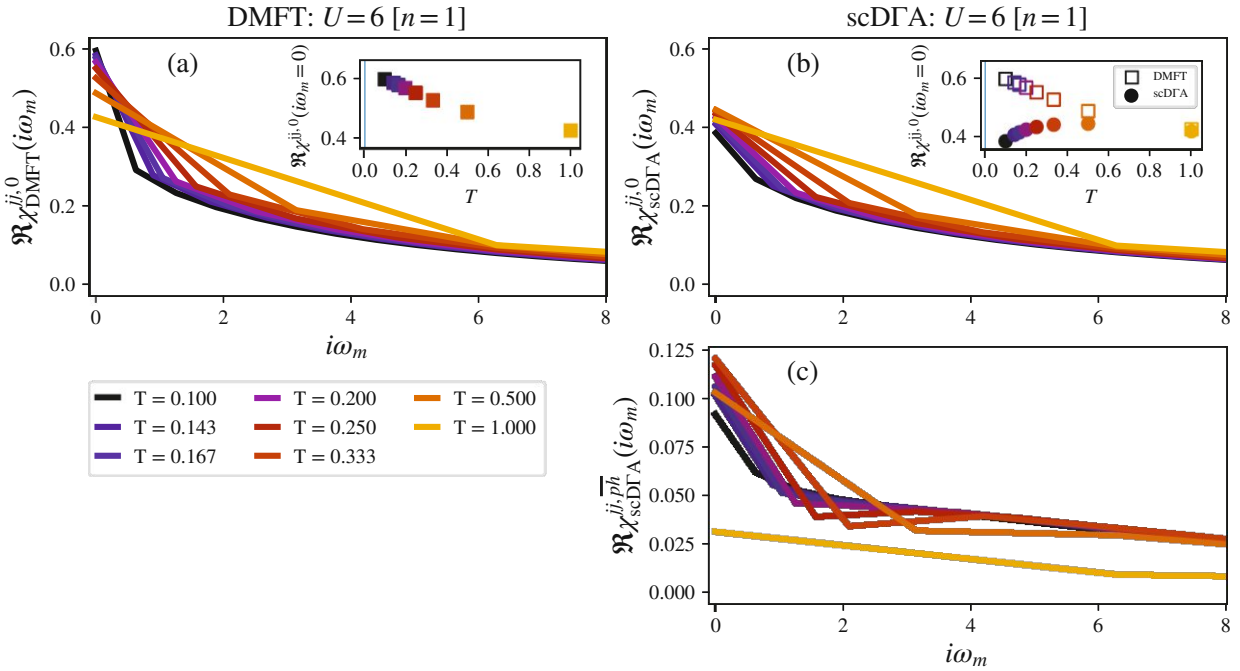


Figure 2.84: Current-current correlation functions for $U = 6$ at half-filling $n = 1$. (a) DMFT, (b) scDFA bubble contribution, (c) scDFA vertex contribution. As the interaction is pushed towards strong coupling qualitative changes yet again occur in the vertex corrections. There, steep “kinks” appear at lowest energies when linearly connecting the discrete Matsubara data. The increasingly large spin-fluctuation lead to a strong dampening of the self-energy, reflected in the sizes of the bare susceptibilities. Vertex corrections are large throughout and reach nearly a quarter of the size bare response.

The DMFT trends are unbroken towards strong coupling at $U = 6$ where the coherence temperature is further lowered and the electronic scattering rates are an order of magnitude larger compared to $U = 2$, see also Fig. 2.89. The increased correlation strength leads to less kinetic energy ($E_{\text{kin}} \propto \chi^{\text{jj}}(i\omega_m = 0)$, see Eq. (2.190)) and enhanced finite frequency responses. The increased renormalization is clearly reflected in the DC values of the optical conductivity, accompanied by an enhanced mid-infrared peak, stemming from the pronounced three-peak formation in the spectral function (not shown).

In scDFA, due to the aforementioned numerical obstacles, our considered temperature range is

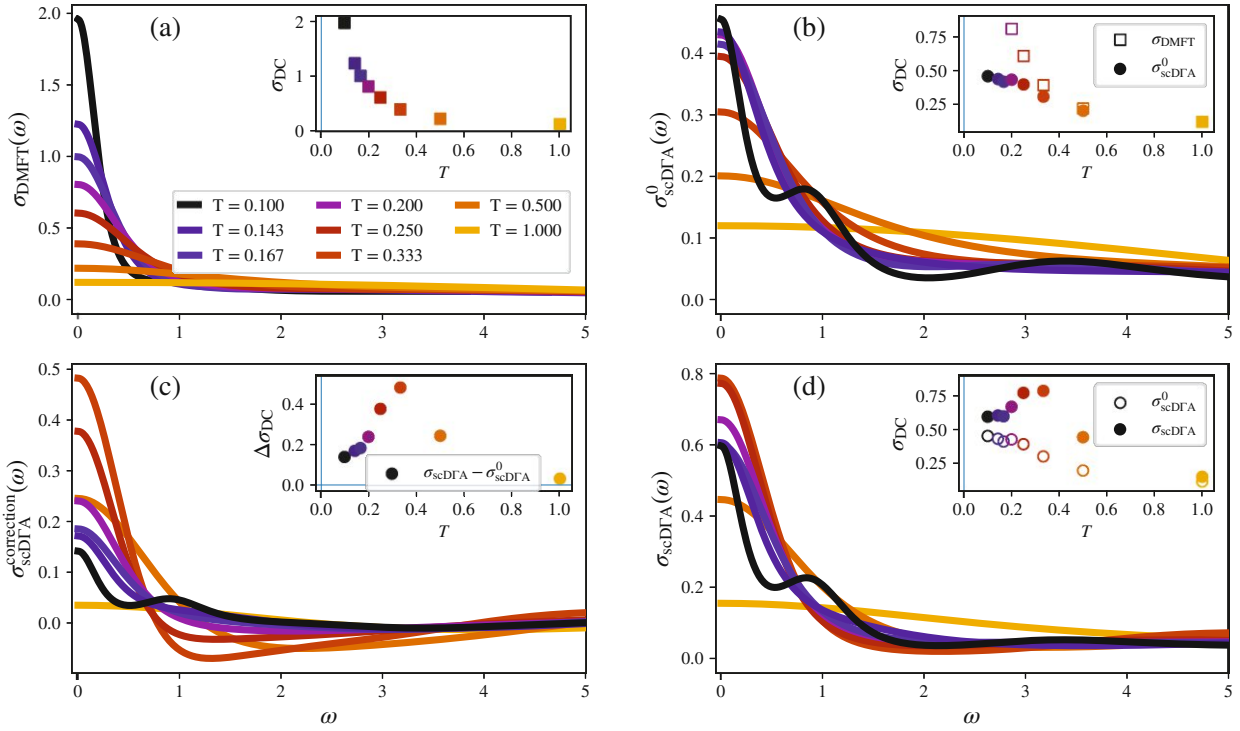


Figure 2.85: Optical conductivities for $U = 6$ at half-filling $n = 1$. (a) DMFT, (b) bare bubble scDGA, (c) vertex contribution to scDGA, (d) full scDGA. The enhanced corrections constitute half the size of the Drude peak of the optical conductivity. In order to still fulfill the sum rule, intermediate frequencies become suppressed.

located above the (expected) pseudogap onset temperature $T_{\text{AN}}^* < 0.100$. Nonetheless, large deviations from the static DMFT values ($i\omega_m = 0$) are already visible at $T = 0.5$ in χ_0^{scDGA} , see inset of Fig. 2.84b. Evidently, they are the result of the expected dampening of the predominant antiferromagnetic susceptibilities, whose size, in this regime, correlates with the interaction strength U . Translated to optical conductivities in Fig. 2.85b this, however, does not result in a maximum of $\sigma_{\text{DC}}(T)$, as we have seen at $U = 2$ and $U = 4$. We theorize that the momentum-selective pseudogap onset in the self-energy, when compared to the overall scattering rate, is too miniscule to be observable in the bubble contribution, as it involves a Brillouin zone average. The result is a tightening of the Drude peak, controlled purely by the temperature behavior of the scattering rate. Interestingly, at the lowest temperature, $T = 0.1$, the scDGA self-energy strongly promotes a satellite peak at $\omega = 1$, centered between the Drude and the mid-infrared peak ($\omega = 3.5$). This peak is already present in DMFT (barely visible in Fig. 2.85a), corresponding to a satellite feature of the spectral function at $\omega = \pm 0.5\text{eV}$ (not shown). Within scDGA we find a strong (momentum-selective) enhancement of this satellite with respect to the quasi-particle peak in $A(\mathbf{k}, \omega)$ on the Fermi surface (not shown), resulting

in the prominent satellite in $\sigma_{\text{scD}\Gamma\text{A}}(\omega)$.

Vertex corrections, unsurprisingly, increase in size at these elevated interaction strengths. We find that the static value of the bare response $\chi^{\text{jj},0}$ is altered by almost 25%, see Fig. 2.84. Qualitatively, the $\overline{\text{ph}}$ signatures are again modified when compared to $U = 2$ and $U = 4$. Linearly connecting the discrete Matsubara data, the slope between zeroth and first Matsubara frequency is almost flat at $U = 2$ (kink), slightly negative at $U = 4$, and steep for $U = 6$. The resulting corrections of the conductivities mirror the exemplary trends of Fig. 2.74 and lead to a strong increase of the DC conductivity $\Delta\sigma_{\text{DC}}$, see inset of Fig. 2.85c. At $T = 0.333$, the full DC conductivity $\sigma_{\text{scD}\Gamma\text{A}}$ more than triples in size with respect to the bare contribution $\sigma_{\text{scD}\Gamma\text{A}}^0$, see inset of Fig. 2.85d. At this point, weight from around the mid-infrared peak $\omega \approx 1.5$ has been transferred to the Drude peak as the spectrum augmentation is restricted by $\int d\omega \sigma_{\text{correction}} = \chi^{\text{jj},\overline{\text{ph}}}(i\omega_m = 0)$. Similar to $U = 2$ and $U = 4$, further cooling results in a stronger feedback of the antiferromagnetic fluctuation into the self-energy, making the vertex correction less effective, resulting in a trend towards $\lim_{T \rightarrow 0} \Delta\sigma_{\text{DC}} = 0$.

2.6.3.6 Strong coupling out of half-filling: $U = 8$

Having established a strong connection between perfect nesting, antiferromagnetic fluctuations and the pseudogap regime, our next goal is to distill the effect of vertex corrections when venturing away from half-filling. Hole-doping to $n = 0.85$ shifts the system away from the perfect nesting condition, removes the pseudogap phenomenon, and promotes incommensurate antiferromagnetism, see Fig. 2.86. The ordering vector of this (DMFT) magnetic instability takes the form of $\mathbf{q} = (\pi - \delta, \pi)$ with $\delta(T) > 0$, and is strongly temperature dependent. Doping away from half-filling also decreases both the magnitude of the self-energy correlations themselves (smaller scattering, smaller quasi-particle renormalization: not shown) and the overall amplitude of the resulting spin fluctuations, allowing us to perform calculations in the strong coupling regime at $U = 8$. Due to the broken particle-hole symmetry the Mott insulating conditions are no longer met: The lattice fermions gain itinerancy without the creation of double occupancies. As the ideal Heisenberg exchange description (in the strong coupling regime) no longer holds accurately, perfect (π, π) magnetic ordering, along with the overall (magnetic) susceptibility size is suppressed by doping. The resulting incommensurate antiferromagnetic response peaks around $(3\pi/4, \pi)$ and only reaches values of around 10eV^{-1} at the lowest considered temperature $T = 0.05$. Compared to the half-filled case at similar temperatures, this corresponds to a susceptibility (and coherence length) decrease by orders of magnitude. We show the resulting current-current correlation functions and optical conductivities in Fig. 2.87 and Fig. 2.88, respectively.

The DMFT responses are akin to all previous results, where cooling the system leads to increased coherence. Doping away from half-filling is counterbalanced by the increased interaction strength

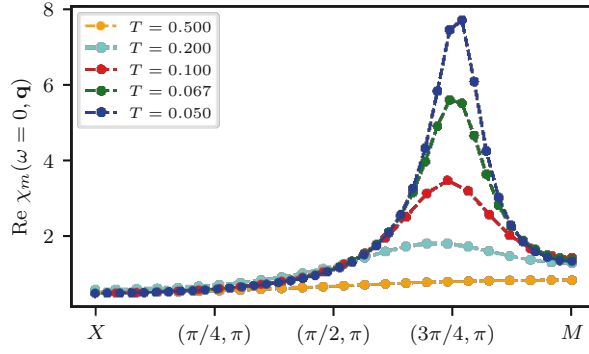


Figure 2.86: Static magnetic susceptibility χ_m of the hole-doped ($n = 0.85$, $U = 8$) one-band Hubbard model introduced in Eq. (2.183). χ_m peaks at $\mathbf{q} = (\pi, \pi - \delta)$ with a finite $\delta \approx 1/(4\pi)$, commonly referred to as incommensurate magnetic order.

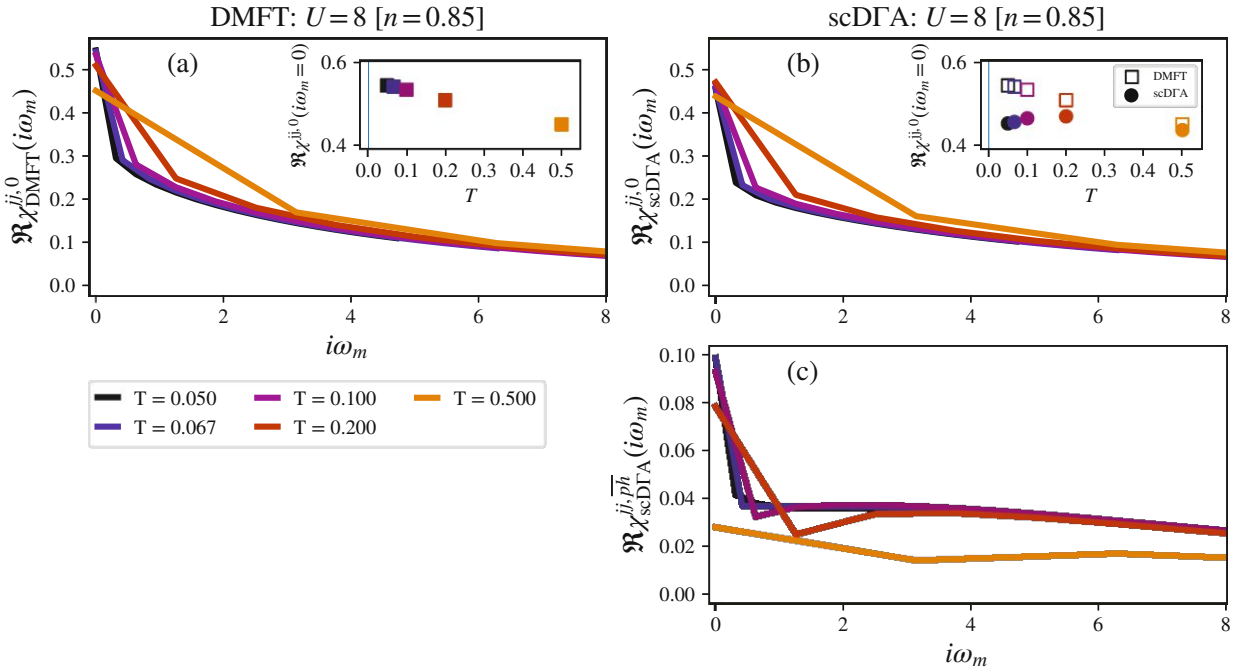


Figure 2.87: Current-current correlation functions for $U = 8$ at 15% hole-doping, i.e. $n = 0.85$. (a) DMFT, (b) scDGA bubble contribution, (c) scDGA vertex contribution. The qualitative features are similar to the half-filled case at $U = 6$, where the vertex corrections exhibit a distinct kink at the first Matsubara frequency. Contrary to the half-filled cases, the slope between zeroth and first frequency is heavily impacted.

resulting in DC values, comparable to the half-filled case of $U = 4$. The loss of nesting and the pseudogap phenomenon makes the differences between the bubbles of DMFT and scDGA less pro-

nounced. Still, as a function of temperature, scDFA exhibits a peak in $\chi^{jj,0}$ at $T = 0.2$, hinting at effects of the underlying incommensurate magnetic fluctuations. The scDFA optical conductivities are naturally very similar to DMFT. Quantitative differences are restricted to the loss of spectral weight, the decrease of the DC conductivity and a broadening of the Drude peak.

Despite the small magnetic susceptibilities, the vertex corrections are pronounced: Below $T = 0.2$ a steep slope develops between the zeroth and first Matsubara frequency, see Fig. 2.87c, if plotted with connecting lines. This results in a boost of the Drude peak by more than 30%, compared to the bare scDFA spectrum, see Fig. 2.88(c-d), accompanied by a slight suppression of the mid-infrared peak.

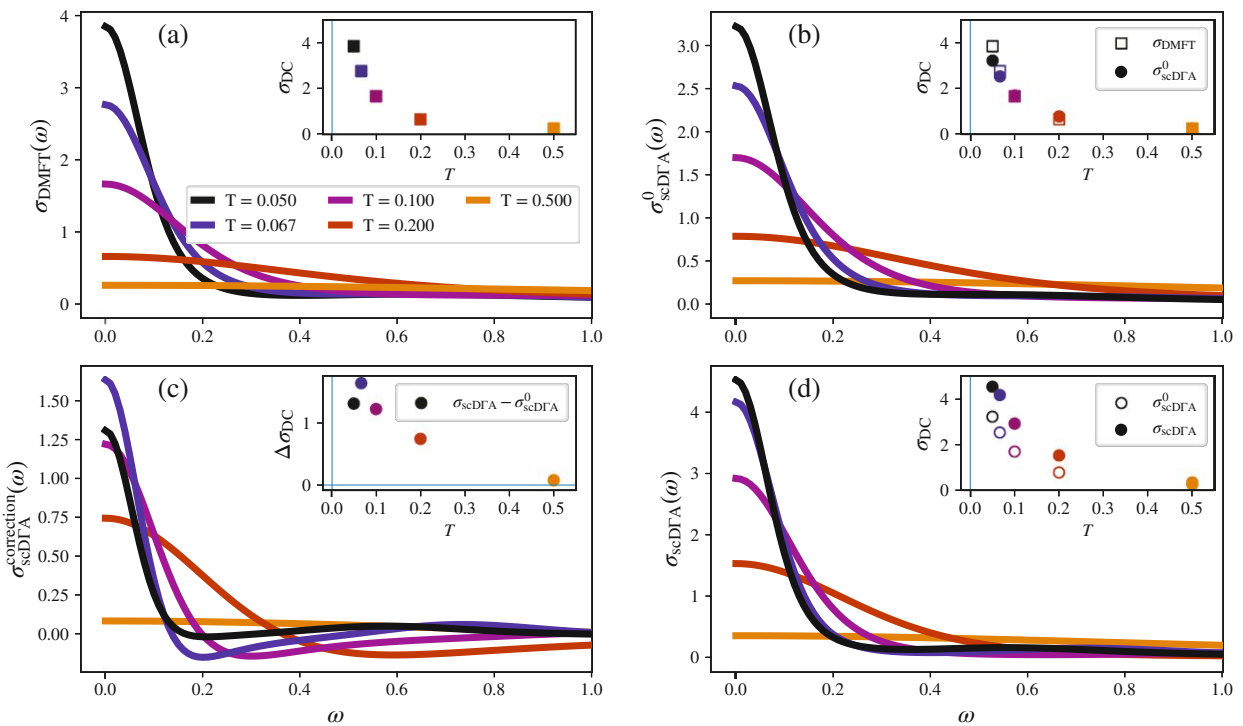


Figure 2.88: Optical conductivities for $U = 8$ at 15% hole-doping, i.e. $n = 0.85$. (a) DMFT, (b) bare bubble scDFA, (c) vertex contribution to scDFA, (d) full scDFA. The vertex induced slope changes have a major impact on the shape of the Drude peak where the DC values of the scDFA are boosted beyond its DMFT counterparts. As the relevant pseudogap physics are missing at this doping level the DC value trend is only slightly softened compared to DMFT.

2.6.3.7 Discussion

At half-filling the self-consistent ladder dynamical vertex approximation is capable of reproducing the essential phenomena of the two dimensional Hubbard model both on the one- (pseudogap) and

two-particle (suppression of magnetic phase transition) level. Compared to other (benchmark) diagrammatic methods (pD Γ A, λ -corrected D Γ A, diagrammatic Monte Carlo), scD Γ A evidently underestimates the onset temperature of the pseudogap and the amplitude of the predominant magnetic fluctuations [4, 241], the consequences of which are apparent in the optical responses. This can be traced back to the algorithm itself: As the two-particle irreducible vertex Γ remains fixed, the only mechanism to suppress fluctuations in scD Γ A is via a modification of the self-energy. To elucidate this mechanism, we illustrate the relevant momentum contributions in Fig. 2.89 where we compare the imaginary part of the DMFT self-energy (dashed line) with the Fermi surface average of the scD Γ A self-energy (solid line).

In the coherent temperature regime the scD Γ A leads to a dampening of the self-energy at the low to intermediate frequencies, i.e. $\Im\Sigma_{\text{scD}\Gamma\text{A}}(i\nu_n) < \Im\Sigma_{\text{DMFT}}(i\nu_n)$ resulting in enhanced electronic scattering rates $1/\tau = -\Im\Sigma(i\nu_n \rightarrow 0^+)$. Despite the Fermi surface averaging, we find a clear evidence of the pseudogap onset (T_{AN}^*) at $U = 2$ and $U = 4$, marked by a downturn at the first Matsubara frequency. At $U = 6$ the employed temperature range is above T_{AN}^* , hence no downturn is visible.

Once fluctuations arise through cooling, merely the onset of the pseudogap in combination with an overall dampening of the self-energy results in a trend reversal of the DC value of the optical spectrum (see Fig. 2.79, Fig. 2.81, Fig. 2.85) above the characteristic T_{AN}^* . In order to observe strong vertex corrections within scD Γ A a fine balance has to be struck between the amplitude of fluctuations and their effect onto the self-energy. Depending on the interaction strength, this interplay then may lead to a Drude peak sharpening ($U = 6$) or a Drude peak broadening ($U = 2$). Similar observations have been made in a study based on the RPA, see Ref. [6].

As we have seen in the comparison with the (more rigorous) pD Γ A at $U = 4$, other methods do not necessarily suffer from these obstacles, as (magnetic) fluctuations can be influenced by other means. In λ -corrected D Γ A, the vertex itself can be manipulated through a susceptibility regularization. In pD Γ A this can occur via the interplay of the various vertices through the parquet equation. Benchmarking against the latter, we were thus able to evidence large differences even though the intrinsic $\overline{\text{ph}}$ corrections were comparable. The comparison thus suggests that the consideration of the pp channel is vital in order to achieve an adequate description of the vertex corrections. As these corrections act on the low frequency domain (zeroth and first bosonic Matsubara frequency) they lead to a strong modification of the Drude peak.

To put these findings on a more technical footing, we analyze the pivotal f-sum rule, given in Eq. (2.190). The benchmark is illustrated in Fig. 2.90.

Whereas DMFT (left panel) achieves perfect agreement between the calculated kinetic energy and the one extracted from the static value of the current-current correlation function, strong deviations appear for the bare response of scD Γ A (right panel, dashed line) at half-filling. Once the $\overline{\text{ph}}$ correction

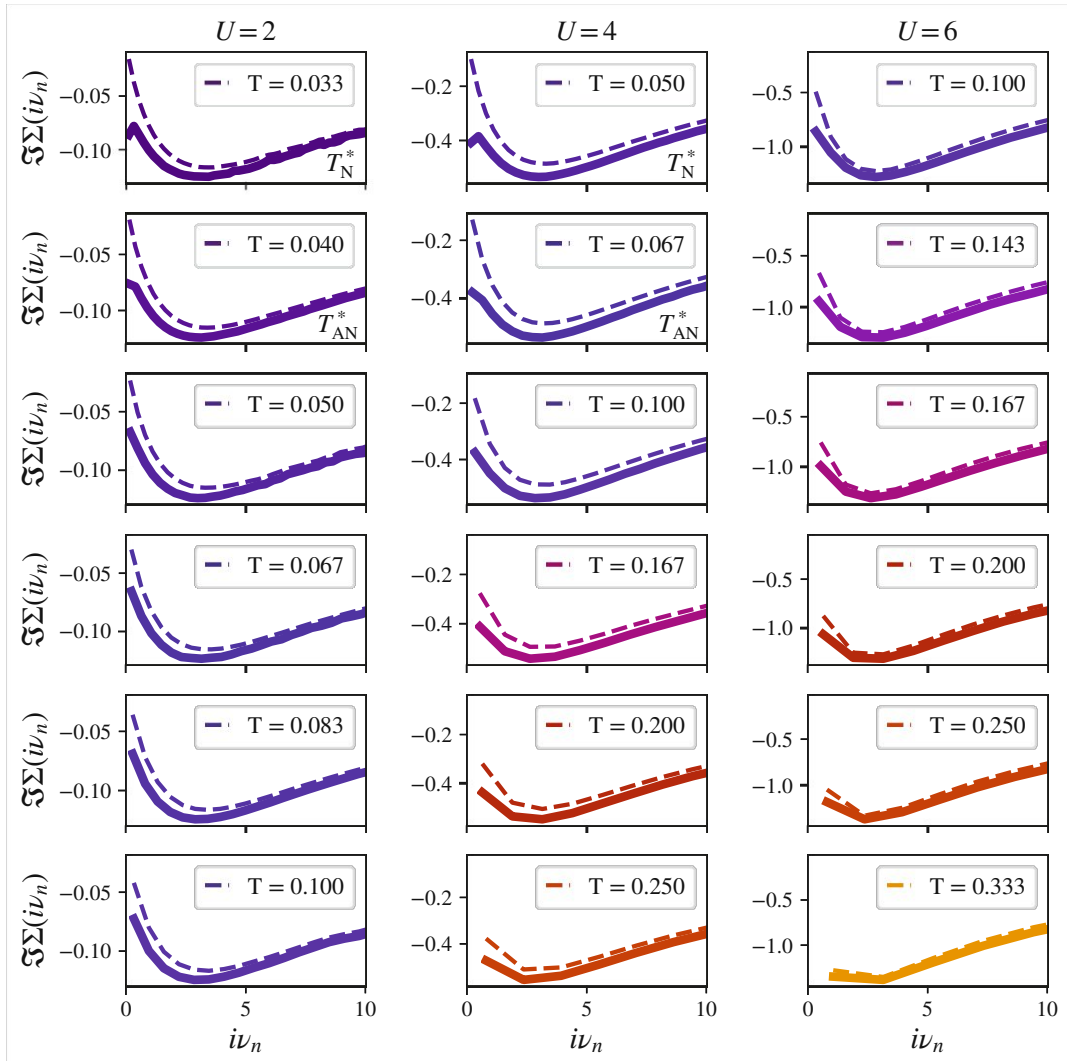


Figure 2.89: Comparison of the imaginary parts of the DMFT self-energy (dashed lines) and the DGA self-energy averaged over the Fermi surface $\sum_{\mathbf{k} \in \text{FS}} \Sigma_{\text{scDGA}}(\mathbf{k})$ (solid lines). The latter represents the most dominant contributions to the conductivity and illustrates the over-damping of the self-energy in the self-consistency approach. Left column: $U = 2$, Middle column: $U = 4$, Right column: $U = 6$ for various temperatures, indicated by the line color. The discrete Matsubara points have been connected to form a continuous line.

term is accounted for (solid line) we find reasonably good agreement for the temperature interval above the χ^{jj} downturn, i.e. where DMFT is not yet ordered $T > T_{\text{Néel}}^{\text{DMFT}}$ and represents a good approximation. Below that temperature χ^{jj} can no longer follow the monotonous increase of the kinetic energy: scDGA underestimates the optical spectral weight and violates the f-sum rule. Shifting away from half-filling ($U = 8$, $n = 0.85$), the perfect nesting is destroyed, the magnetic fluctuations

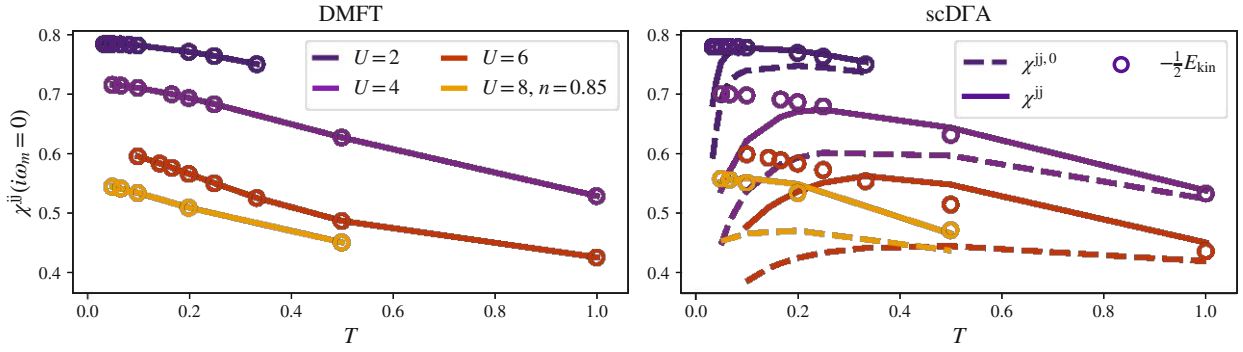


Figure 2.90: Sum rule benchmark via $\chi^{jj}(\mathbf{q} = \mathbf{0}, i\omega_m = 0) = -\frac{1}{2}E_{\text{kin}}$, see Eq. (2.190). Static current-current response are drawn as solid/dashed lines. Kinetic energies, see Eq. (2.190) $E_{\text{kin}} = \sum_{\mathbf{k}, \sigma} \varepsilon_{\mathbf{k}} n_{\mathbf{k}, \sigma}$ are marked as open circles. The two terms agree exactly within DMFT (left panel). In scDFA (right panel) the vertex correction must be taken into account to get a good approximation. The static value of χ^{jj} clearly exhibits a downturn, setting in at around the pseudogap onset temperature. Evidently, this behavior is not reflected in the direct evaluation of the kinetic energy. Without perfect nesting and the accompanied pseudogap phase out of half filling, we find reasonably good agreement even at a large interaction strength.

become suppressed and we find almost perfect agreement between the two terms of Eq. (2.189), at least for the considered temperature interval.

Let us note that at this moment, we have not yet properly investigated the convergence of the current-current correlation function with respect to the momentum grid, nor the frequency box size. Upon cooling into the pseudogap regime, the (antiferro)magnetic susceptibility quickly increases in size, accompanied by an increase of the corresponding coherence length ξ . For the lowest considered temperature at $U = 2$ ($T = 0.033$), e.g., we find an almost perfect Ornstein-Zernike fit, see Eq. (2.139), with a coherence length of roughly 50 unit cells (fit not shown). In this regime, improper \mathbf{q} -discretization, as is most likely the case for our employed momentum grid of $k_x \times k_y = 80 \times 80$, could lead to a major *underestimation* of the vertex contribution to χ^{jj} as the magnetic fluctuations are not sampled properly around the ordering vector $\mathbf{Q} = (\pi, \pi)$. Similarly, lower temperatures necessarily require larger (fermionic and bosonic) boxes. As the discrete fermionic frequencies inversely scale with temperature, a larger number of frequencies are necessary to encode the quintessential two-particle diagrams in F . Upon proper convergence, both the size and shape of $\chi^{jj, \text{ph}}$ at these low temperatures could change, leading also to quantitative changes to the presented $\sigma_{\text{scDFA}}^{\text{correction}}(\omega)$. The same, obviously, is also true for the pDFA data shown in Section 2.6.3.4: In the shown pDFA current-current correlation functions and optical conductivities, see Fig. 2.82 and Fig. 2.83, a larger (anticipated) pseudogap temperature, e.g., will lead to a smaller bare response $\chi^{jj, 0}(i\omega_m = 0)$, reducing the impact

of the vertex correction $\chi^{jj,r}$ and consequently reducing the magnitude of the corrections to the optical conductivity $\sigma_{\text{correction}}(\omega)$.

For the case of $U = 8$, $n = 0.85$ this problem is absent as neither size, nor coherence length of the incommensurate magnetic susceptibilities, see Fig. 2.86, are large. As a side remark: the (quantum Monte Carlo) quality of the (two-particle DMFT) data at $U = 6$ is worse than for $U = 2$ and $U = 4$, possibly causing deviations also at high temperature, see Fig. 2.90 (green line in the right panel).

Let us note that the response $\chi^{jj,0}(i\omega_m)$ does not suffer from these numerical problems, as the Green's functions can be easily extended to large frequency with an appropriate fit to the asymptotic behavior of Σ or G . We employed 2000 positive fermionic frequencies for the Matsubara sum, leading to a flawless compliance of the f-sum rule within DMFT.

Before answering the question whether the scD Γ A may be used as a reliable method in parameter regimes where non-local fluctuations dominate, it is thus important to perform further calculations that properly analyze the convergence of both the non-local self-energy as well as the contribution of the transverse particle-hole contribution to χ^{jj} . In fact, if the converged result still leads to a violation of the optical sum rule, the way the method is capable of fulfilling the Mermin-Wagner theorem has to be questioned. If the optical sum rule however can be fulfilled, the scD Γ A (in its current implementation) may provide an avenue of studying realistic (multi-orbital) systems even in the vicinity of phase transitions, provided they are of particle-hole nature.

With respect to the optical spectra, the comparison to the pD Γ A result has however shown that the explicit inclusion of the particle-particle channel is vital. Similar to the posterior evaluation of particle-particle channel with vertices generated from λ -corrected D Γ A to detect superconducting instabilities, see Refs. [247, 248, 249], it may be possible to perform a similar task in the context of the current-current correlation function. This is left for future work.

Chapter 3

Kondo materials and models thereof

In this second out of two primary results Chapters, we present those results that fall under the umbrella of “Kondo physics”. Whereas the previous Chapter was concerned with phenomena best described via the Hubbard model (quasi-particle renormalization, metal-insulator transition, etc.), here we will instead focus on the physics of materials which are best described via the so-called periodic Anderson model (PAM). The methodologies used throughout this Chapter are identical to the ones introduced in Chapter 2, namely Kohn Sham density functional theory and dynamical mean-field theory. In the following we first detail the characteristics and properties of the (three dimensional) PAM, which we will study both on the one- and two-particle level. We will then apply this knowledge and discuss the electronic structure and transport phenomena of the Kondo insulator $\text{Ce}_3\text{Bi}_4\text{Pt}_3$. Vis-à-vis transport measurements, we take a reductionist point of view and focus on gaining qualitative insights. After that we will flesh out this transport theory, extending it to all higher order transport kernel functions necessary for the description of (magneto) thermoelectric signatures. Finally, we will give a brief overview of the Linear Response Transport Centre **LINRETRACE** [11, 12], a program suite in which we have implemented this new transport methodology, and showcase some of its capabilities w.r.t. realistic Kondo materials and beyond.

3.1 Local moments and the formation of Kondo insulators

Materials classified as so-called “heavy-fermion systems” contain lanthanide or actinide elements with partially filled 4f or 5f orbitals [250], see Fig. 2.1 (pink box). If the corresponding bands are in the proximity of the Fermi level, various unusual physical phenomena may emerge at low temperature. Among them are specific heat coefficients that are orders of magnitude larger than expected from a free electron model, characteristic coherence temperatures observed in the (optical) conductivity, the emergence of non-Fermi liquid regimes, insulating behavior, magnetism, (unconventional) superconductivity, quantum criticality, etc. Typical heavy-fermion (HF) compounds include CeCu_6 (a

metal) [251], UBe_{13} (a superconductor) [252], $\text{Ce}_3\text{Bi}_4\text{Pt}_3$ (a Kondo insulator) [253], YbRh_2Si_2 (with field-tuned quantum critical point) [254], and SmB_6 , a mixed valence [255] (topological) insulator [256] whose Kondo nature is contentious [257].

The following Section presents a brief, and by no means exhaustive, theoretical introduction to field of Kondo physics with a strong focus towards Kondo insulators from the viewpoint of dynamical mean-field theory. In this context we will *not* review topological Kondo insulators. For the requisites necessary to stabilize a topological state please refer to the literature, e.g., Refs. [258, 259].

3.1.1 Local impurity: Kondo effect

3.1.1.1 Kondo's explanation

In order to fully appreciate the ramifications of the Kondo effect, we start from a historical point of view: Contrary to naive expectations, impure metallic systems can showcase a global minimum in their DC resistivity at finite temperatures $T > 0$. Ignoring the purely electronic Fermi liquid contribution, this resistance minimum can be recovered via contributions from residual scattering (constant in T), phonon scattering ($\propto T^5$) and the indispensable Kondo term that, phenomenologically, scales logarithmically with temperature

$$\rho(T) = \underbrace{\rho_0}_{\text{residual}} + \underbrace{AT^5}_{\text{phonons}} - \underbrace{B \ln(T)}_{\text{Kondo}}. \quad (3.1)$$

Evidently this description is sufficient at reproducing a resistivity minimum $T_{\min} = (B/(5A))^{(1/5)}$, however, as $\ln(T)$ diverges as $T \rightarrow 0$, it eventually breaks down. Modifying the impurity concentration, as well as their intrinsic magnetic moments, e.g., Refs. [260, 261] strongly affects the contribution of the pivotal Kondo term indicating a complex interplay of electronic and magnetic degrees of freedom. Kondo [262] showed that the logarithmic contribution can be rationalized via an s-d exchange interaction

$$\mathcal{H}^{s-d} = \sum_{k,\sigma} \varepsilon_k \hat{c}_{\mathbf{k},\sigma}^\dagger \hat{c}_{\mathbf{k},\sigma} + \frac{1}{2} \sum_{\mathbf{k},\mathbf{k}'} J_{\mathbf{k},\mathbf{k}'} \left[S^+ \hat{c}_{\mathbf{k},\downarrow}^\dagger \hat{c}_{\mathbf{k}',\uparrow} + S^- \hat{c}_{\mathbf{k},\uparrow}^\dagger \hat{c}_{\mathbf{k}',\downarrow} + S_z \left(\hat{c}_{\mathbf{k},\uparrow}^\dagger \hat{c}_{\mathbf{k}',\uparrow} - \hat{c}_{\mathbf{k},\downarrow}^\dagger \hat{c}_{\mathbf{k}',\downarrow} \right) \right]. \quad (3.2)$$

Here, the (non-interacting) conduction-band electrons ($c^{(\dagger)}$) may interact with the spin of a single impurity level ($d^{(\dagger)}$) through an exchange-interaction term $J_{\mathbf{k},\mathbf{k}'}$. The s-d Hamiltonian of Eq. (3.2) is conventionally expressed with the z -component of S as the measurement axis. The S_x and S_y components are then typically rewritten as spin raising and lower operators $S^\pm = S_x \pm iS_y$.

The interaction term is oftentimes further abbreviated in the literature in the form of a Heisenberg term without momentum dependence of the exchange-interaction parameter

$$\mathcal{H}^{KM} = \sum_{\mathbf{k},\sigma} \varepsilon_{\mathbf{k}} \hat{c}_{\mathbf{k},\sigma}^\dagger \hat{c}_{\mathbf{k},\sigma} + J \vec{S} \cdot \vec{s} \quad (3.3)$$

and vectorial spin operators

$$\begin{aligned}\vec{\hat{S}} &= \frac{1}{2} \sum_{\alpha\beta} \hat{d}_{\alpha}^{\dagger} \vec{\sigma}_{\alpha\beta} \hat{d}_{\beta}, \\ \vec{\hat{s}} &= \frac{1}{2} \sum_{\mathbf{k}, \mathbf{k}'} \sum_{\alpha\beta} \hat{c}_{\mathbf{k}, \alpha}^{\dagger} \vec{\sigma}_{\alpha\beta} \hat{c}_{\mathbf{k}', \beta},\end{aligned}\tag{3.4}$$

with the Pauli matrices $\vec{\sigma} = (\sigma_x, \sigma_y, \sigma_z)$. The resulting full Hamiltonian is then coined Kondo Model (KM). Let us note here that given the spin-operator definitions of Eq. (3.4), the factor 1/2 in Eq. (3.2) is necessary for a match of all considered interaction terms.

Indeed, treating the interaction term of Eq. (3.2) via a perturbation approach, one finds that for $S = \hbar \frac{1}{2}$ certain second order Feynman diagrams [263], see Fig. 3.1, give rise to the sought-after logarithmically diverging (inverse) lifetime τ . Taking all scattering processes up to second order into consideration, the resistance contribution solely from spin-scattering can be analytically calculated as [263]

$$R_{sd}(T) = \frac{3\pi m_e J^2 S(S+1)}{2e^2 \hbar \varepsilon_F} \left(1 - 4J\rho_0(\varepsilon_F) \ln\left(\frac{k_B T}{D}\right) \right),\tag{3.5}$$

assuming a band width D considerably larger than the Fermi energy $D \gg \varepsilon_F$. The (single) spin scatterer contributes both a temperature-independent term and the pivotal ‘‘Kondo term’’ that decreases the resistance logarithmically for an antiferromagnetic coupling $J > 0$.



Figure 3.1: Lowest order Feynman diagrams for the Hamiltonian in Eq. (3.2), that contribute to the logarithmic resistivity contribution. The solid line (with conserved spin) denotes the conduction electron propagator. The dashed line denotes the impurity spin. The Feynman diagrams are inspired by Ref. [264].

While this perturbative approach encodes the essential scattering mechanisms at finite temperatures, the logarithmic term, contrary to experimental observations, evidently diverges towards $T \rightarrow 0$. This unsurprisingly indicates a break down of perturbation theory at low temperatures. Abrikosov [265] was able to extend Kondo’s argument by summing up leading logarithmic terms, pushing the breakdown of the theory to finite temperatures instead. All relevant physical properties

were shown to diverge at the same temperature, the so-called *Kondo temperature*

$$k_B T_K \propto D \exp\left(-\frac{1}{2J\rho_0(\varepsilon_F)}\right). \quad (3.6)$$

Further insight was then obtained from renormalization group calculations [266], with a physical picture that emphasises a strong energy dependence: At intermediate to high temperatures, the spin of the impurity is unconstrained (free spin regime), resulting in the validity of the perturbative approach. Towards low temperatures, due to the suppressed thermal excitations, the exchange interactions dominate and lead to strong (energy reducing) coherent bonding of the spin with its surrounding environment (conduction electrons, $s_z = \pm\frac{1}{2}\hbar$): a Kondo singlet state is formed. The initial free spin ($S_z = \pm\frac{1}{2}\hbar$) is completely screened out, becomes confined and effectively behaves as a newly formed non-magnetic quasi-particle taking up Fermi-liquid behavior [267]. The spin scattering events leading to this effective bonding manifest themselves as resistivity contribution which, through the logarithmic temperature dependence, results in a global minimum of $\rho(T)$. The Kondo temperature T_K then can be thought of a *crossover temperature* from the unconstrained to the constrained spin regime also called local moment and strong coupling regime, respectively. The resulting screening cloud has an approximate radius [268]

$$\xi_{\text{Kondo}} \propto \frac{\hbar v_F}{k_B T_K}. \quad (3.7)$$

with v_F as the Fermi velocity $v_F \propto \partial\varepsilon_{\mathbf{k}}/\partial\mathbf{k}|_{\varepsilon_F}$. In general, due to the quite small Kondo temperatures and large Fermi velocities the relevant length scale may exceed several μm which allows for a macroscopic experimental observation of the phenomenon [269].

The Kondo effect can thus be effectively summarized as scattering events from impurities or ions which have low-energy quantum mechanical degrees of freedom [263]. In the context of realistic setups it is important to note that for larger spins $S > \frac{1}{2}\hbar$ the Kondo effect only emerges when the magnetocrystalline anisotropy (energy dependence of the spin orientation w.r.t. its environment) creates a degenerate ground state [270]. As it turns out, the Kondo effect has more far-reaching ramifications in solid-state physics as a whole. It is a key concept in understanding the quantitative behavior of metallic systems with strongly correlated electrons, cf. the three-peak structure in dynamical mean-field theory spectra in Sec. 2.2.3. In the next Section we will thus focus on a generalization of the Kondo model: the single impurity Anderson model. The latter encompasses the ingredients of the Kondo effect and is employed as the underlying impurity model in the DMFT cycle. This will provide us with the ground work for understanding Kondo materials and give us an alternate point of view of hitherto obtained DMFT results used to describe strongly correlated materials.

3.1.1.2 Quantum Monte Carlo treatment

In the context of the study of (Kondo) materials and most relevant to this thesis, we briefly scrutinize the Kondo effect via the single Anderson impurity model [263]

$$\mathcal{H}^{\text{SIAM}} = \sum_{\mathbf{k},\sigma} \varepsilon_{\mathbf{k}} \hat{c}_{\mathbf{k},\sigma}^\dagger \hat{c}_{\mathbf{k},\sigma} + \sum_{\sigma} \varepsilon_d \hat{d}_{\sigma}^\dagger \hat{d}_{\sigma} + U \hat{d}_{\uparrow}^\dagger \hat{d}_{\uparrow} \hat{d}_{\downarrow}^\dagger \hat{d}_{\downarrow} + \sum_{\mathbf{k},\sigma} \left(V_{\mathbf{k}} \hat{c}_{\mathbf{k},\sigma}^\dagger \hat{d}_{\sigma} + V_{\mathbf{k}}^* \hat{d}_{\sigma}^\dagger \hat{c}_{\mathbf{k},\sigma} \right), \quad (3.8)$$

where, the non-interacting conduction band electrons ($c^{(\dagger)}$) may only interact with the (localized) interacting impurity electrons ($d^{(\dagger)}$) through a hybridization term $V_{\mathbf{k}}$. While we have already discussed the importance of the SIAM in Section 2.2.3, it was merely treated as a necessary technicality in DMFT's embedding scheme. Its introduction hitherto was purely as a tool to compute correlations from a self-consistently determined (multi-orbital) hybridization function without attention to the finer details of the impurity itself, barring the local projection of the crystal structure and the accompanied crystal-field splitting. Here instead we focus on the behavior of the model itself: The SIAM and the Kondo model are, at half-filling and strong coupling U , inherently connected via a canonical Schrieffer-Wolff transformation [271]. The exchange terms of the Kondo model, see Eq. (3.3), are captured via virtual hopping processes from and to the conduction band, consolidated into an effective exchange-interaction determined via [263]

$$J_{\mathbf{k},\mathbf{k}'} = V_{\mathbf{k}}^* V_{\mathbf{k}'} \left(\frac{1}{\varepsilon_d + U - \varepsilon_{\mathbf{k}'}} + \frac{1}{\varepsilon_{\mathbf{k}} - \varepsilon_d} \right). \quad (3.9)$$

The equivalence of the two models can be obtained for large enough interaction strengths U and/or small enough hybridization V such that $J \propto V^2/U$ is sufficiently small. Given these parameters, the SIAM then must necessarily showcase the identical low temperature anomalies as the Kondo model. In fact, the pivotal local moment formation necessary for Kondo behavior to occur in the first place, takes place only for large enough interaction strengths $U > U_c = \pi^2 \rho_0 V^2$ (within a mean-field, i.e. Hartree-Fock, context) [239, 263, 272].

For the following considerations we define a *half-filled* SIAM via $\varepsilon_d = -U/2$, $\mu = 0$, a constant hybridization of $V_{\mathbf{k}} = V = 2$, a conduction band with a constant density of states with band width of $W = 2D = 10$: $\rho_0(\varepsilon) = 1/(2D)\Theta(D - |\varepsilon|)$ and an interaction strength of $U = 5.75$. Through this parameter set we ensure the formation of local moments as $U \gg U_c \approx 2$. For a more thorough discussion on a wider range of parameters of the SIAM, including different regimes of the (U, V) phase diagram, let us refer to Ref. [239]. Translated to ‘‘DMFT’’ input parameters, we now require an impurity hybridization function $\Delta(i\nu_n)$, here on the Matsubara axis, to fully define the non-interacting Green's function $G_0^{\nu_n}$. For the half-filled case one analytically integrates over the previously defined

flat density states, discovering a purely imaginary

$$\Delta(i\nu_n) = \sum_{\mathbf{k}} \frac{V^2}{i\nu_n - \varepsilon_{\mathbf{k}}} = \int_{-D}^D d\varepsilon \rho_0(\varepsilon) \frac{V^2}{i\nu_n - \varepsilon} = -i \frac{V^2}{D} \arctan\left(\frac{D}{\nu_n}\right). \quad (3.10)$$

The Kondo temperature of this model has been determined in Ref. [273] to be roughly $k_B T_K = 1/65$. Let us note that this temperature was determined via the method by Krishna-murthy *et al.* [274, 275], based on a comparison of the magnetic susceptibility to a universal renormalization group solution for a Kondo-Hamiltonian. This in turn can be affirmed by a comparison to the analytic result of the wide-band limit Kondo temperature solved by the Bethe Ansatz [239, 263].

3.1.1.3 Kondo singlet formation

In order to analyze the emerging energy ranges stemming from the Kondo effect we consider a temperature interval that ranges from below the extracted Kondo temperature $k_B T_K \approx 1/65$ up to the free orbital regime [274, 275]. The two-particle (magnetic and density) susceptibility responses are illustrated in Fig. 3.2. The formation of the Kondo resonance in the spectral function $A(\omega)$ and the (imaginary part of the) self-energy $\Sigma(i\nu_n)$ is shown in Fig. 3.3.

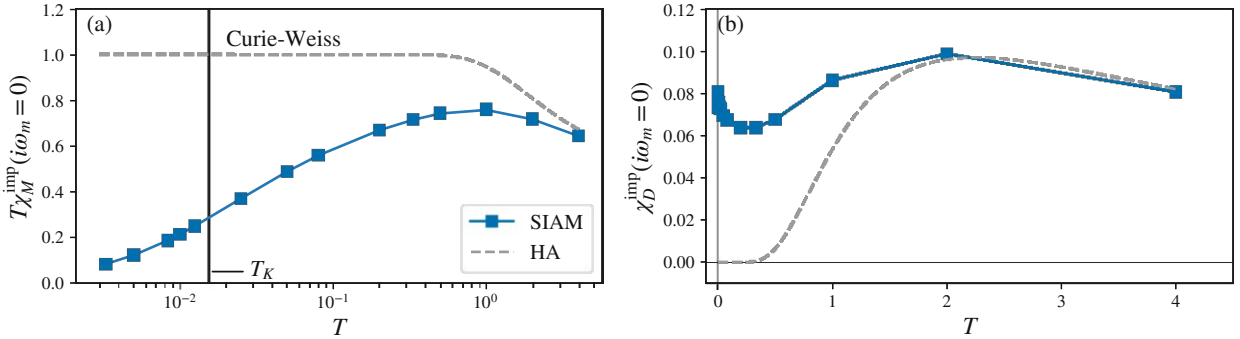


Figure 3.2: Magnetic ($T\chi_M^{\text{imp}}$) and charge (χ_D^{imp}) response of the single impurity Anderson model (SIAM, blue) compared to the Hubbard atom (HA, gray). (a) Static magnetic susceptibility times temperature showing a perfect Curie-Weiss behavior for the Hubbard atom ($T\chi_M \propto C$) which is getting screened by the Kondo effect present in the SIAM. (b) Static density susceptibility showing a full suppression of the charge fluctuations in the HM which are “kept alive” at low temperatures in the SIAM. The shown data has been kindly provided by Patrick Chalupa-Gantner, see Ref. [273].

At high temperatures, in the local moment regime, the spins are acting free, resulting in a Curie-like magnetic susceptibility $\chi_M^{\text{imp}}(T) \propto C/T$. The charge fluctuations are on par with the half-filled

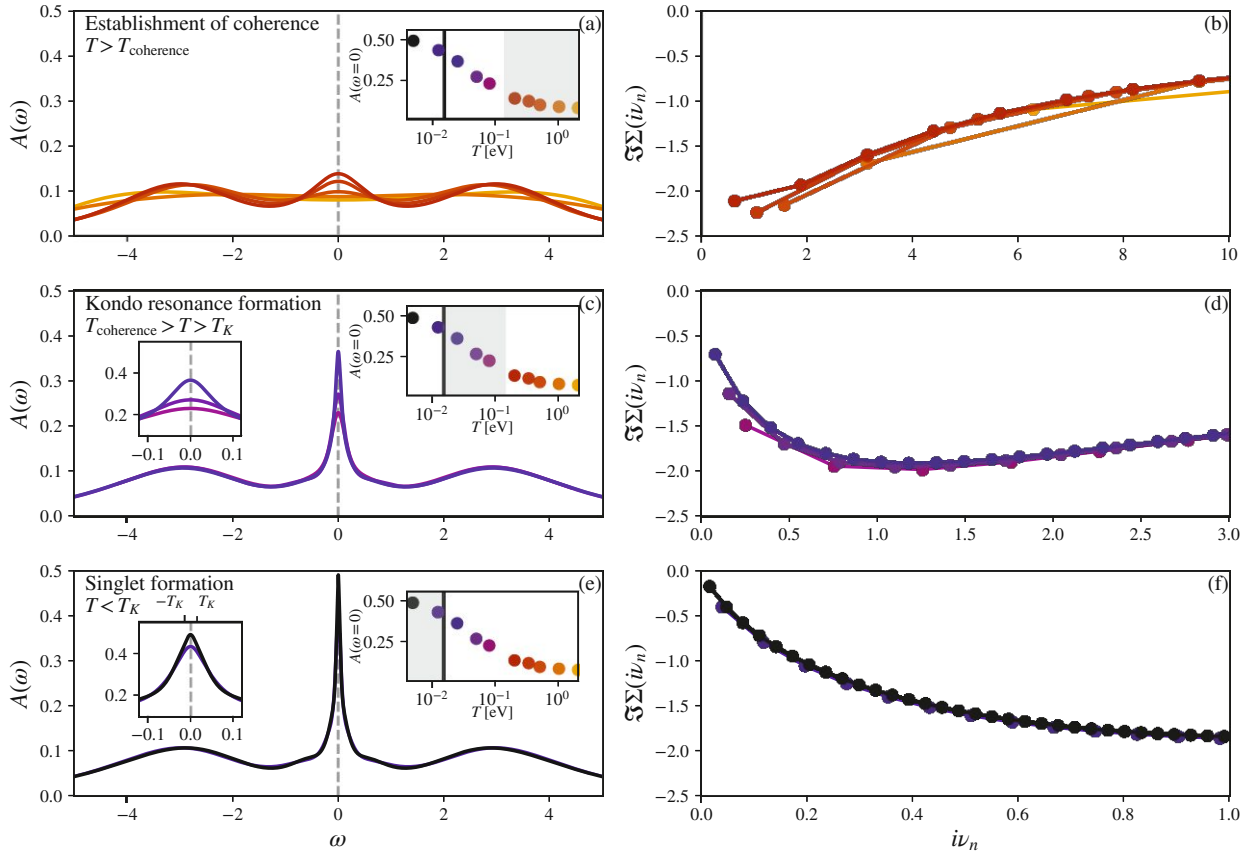


Figure 3.3: Formation of the Kondo resonance. Upon cooling, the system gains coherence signalled by an “upturn” of the imaginary part of the self-energy (right column). Above the Kondo temperature $k_B T_K \approx 1/65$, the Kondo resonance is formed by a stabilization of the metallic signature of the self-energy (reduction in electronic scattering rate), reflected in a strong peak formation of the spectral function at the Fermi level $\omega = 0$. Below the Kondo temperature, the local impurity becomes fully screened, forming a (non-magnetic) scattering center, resulting in a pronounced Kondo resonance at the Fermi level down to zero temperature.

Hubbard atom³¹ (see grey, dashed line). In this regime the coherence of the system is yet-to-be established signalled by a substantial imaginary part of the self-energy $\Im\Sigma(i\nu_n)$ on the Matsubara axis and the strongly broadened spectral function $A(\omega)$ on the real frequency axis, see Fig. 3.3a and Fig. 3.3b, respectively.

Upon cooling into the coherent regime $T < T_{\text{coherence}}$, the self-energy turns Fermi-liquid like and a

³¹The half-filled Hubbard atom represents the atomic limit of the single impurity Anderson model and is therefore fully described via $\mathcal{H}^{HA} = Un_\uparrow n_\downarrow - U/2(n_\uparrow + n_\downarrow)$, resulting in the magnetic response $\chi_M(i\omega_m = 0) = \int_0^\beta d\tau \langle (\hat{n}_\uparrow - \hat{n}_\downarrow)(\tau)(\hat{n}_\uparrow - \hat{n}_\downarrow) \rangle - \beta(n_\uparrow - n_\downarrow)^2 = \beta(1 + e^{-\beta U/2})^{-1}$, and the density response $\chi_D(i\omega_m = 0) = \int_0^\beta d\tau \langle (\hat{n}_\uparrow + \hat{n}_\downarrow)(\tau)(\hat{n}_\uparrow + \hat{n}_\downarrow) \rangle - \beta(n_\uparrow + n_\downarrow)^2 = \beta(1 + e^{\beta U/2})^{-1}$.

distinct Abrikosov-Suhl resonance [265, 276, 277, 278], in this context known as the Kondo resonance, is formed. The spectral function becomes increasingly pronounced around the Fermi level, see inset of Fig. 3.3c, until the Kondo temperature is reached, see Fig. 3.3e. Below T_K we find the characteristic suppression of the magnetic susceptibility in Fig. 3.2a where the free spin becomes gradually screened by the conduction sea to ultimately form a spinless singlet state. Apparent in Fig. 3.2b, the Kondo mechanism counteracts the suppression of charge fluctuations as seen in the Hubbard atom. Instead of a gradual suppression towards $\lim_{T \rightarrow 0} \chi_D^{\text{imp}}(i\omega_m = 0) = 0$, through the screening process the charge fluctuations are “kept alive” at low temperature leading to a non-monotonous behavior of $\chi_D^{\text{imp}}(i\omega_m = 0)$.

It is crucial to emphasize that the Kondo temperature does not represent a hard “cut-off” temperature visible in the illustrated one- and two-particle quantities. Instead, from this physical point of view, the Kondo temperature is best described as a crossover temperature with the Kondo effect as a primary example of the concept of asymptotic freedom. Below T_K the coupling becomes, as evidenced above, impossible to describe in a perturbative fashion. New quasi-particles are formed, acting as spinless scattering centers, gaining the properties of a Fermi-liquid. In this regime furthermore, in- [263] and out-of equilibrium [279] response quantities now follow a universal temperature scaling, with only T/T_K as the relevant (dimensionless) energy ratio.

3.1.2 Periodicity: Lattice Kondo effect

The previous considerations are valid for realistic situations that can be approximated by the Hamiltonian given in Eq. (3.8), i.e. single impurities and/or systems with an assortment of impurities that do not interact with one another in a meaningful fashion. The opposite end of this scenario is the case of an arrangement of free spins on a periodic lattice. This scenario is oftentimes realized once elements from the lanthanoids or actinoids are involved in the construction of a crystal structure. If their f-shell remains partially filled, the unpaired electrons may form freely acting moments that “inherit” the low temperature signatures of the Kondo effect, but that additionally form narrow bands. The latter is a direct consequence of the exceptionally localized (4f/5f) radial wave functions and a resulting suppression of inter-atomic wave function overlap between lattice sites. These compounds are hence usually referred to as Kondo materials or heavy-fermion systems [280]. Despite these narrow f-bands, interaction between the spins may develop indirectly via the interplay of the spins and separate conduction bands. Discovered by Ruderman, Kittel, Kasuya and Yosida [281, 282, 283] the so-called RKKY interaction allows, in principle, for long-range magnetic order whose effect we will discuss later in the context of DMFT.

3.1.2.1 One-particle considerations

In order to extract the most essential physics of these ubiquitous compounds one commonly employs a modelling of the underlying electronic structure via the periodic Anderson model (PAM) [272] that reads

$$\mathcal{H}^{\text{PAM}} = \sum_{\mathbf{k},\sigma} \varepsilon_{\mathbf{k}} \hat{c}_{\mathbf{k},\sigma}^\dagger \hat{c}_{\mathbf{k},\sigma} + \sum_{i,\sigma} \varepsilon_f \hat{f}_{i,\sigma}^\dagger \hat{f}_{i,\sigma} + U \sum_i \hat{n}_{i\uparrow}^f \hat{n}_{i\downarrow}^f + \sum_{i,\sigma} \left(V \hat{c}_{i,\sigma}^\dagger \hat{f}_{i,\sigma} + V^* \hat{f}_{i,\sigma}^\dagger \hat{c}_{i,\sigma} \right). \quad (3.11)$$

In this most basic form, the PAM describes the aforementioned localized f-electrons at the various lattice positions i with fixed energy ε_f , represented by *interacting* fermions $\hat{f}_{i,\sigma}^{(\dagger)}$ which are able to hybridize with *non-interacting* conduction electrons $\hat{c}_{i,\sigma}^{(\dagger)}$ whose energy dispersion is given by $\varepsilon_{\mathbf{k}}$. In realistic materials these conduction electrons are often provided by surrounding elements with, e.g., partially filled d-shells, in the simple equation above both orbitals are implicitly centered on the same lattice site. Experimentally this is, e.g., the situation for Ce where both 4f and 5d bands originate from the Ce atoms [284]. The PAM Hamiltonian can—to some degree—also be applied to “light-weight” systems where interacting d-electrons hybridize with p- or s-electrons, e.g., in FeSi [285].

Upon simultaneous occupation of both f-spins $\hat{n}_{i\sigma}^f = \hat{f}_{i,\sigma}^\dagger \hat{f}_{i,\sigma}$, an energy penalty in the form of the on-site repulsion U has to be paid. For the attentive reader it is obvious, that Eq. (3.11) is just a specialization of the multi-orbital Hubbard model of Eq. (2.18) where the non-interaction part of the Hamiltonian is given by

$$\mathcal{H}_0^{\text{PAM}} = \sum_{\mathbf{k},\sigma} \begin{bmatrix} \hat{c}_{\mathbf{k},\sigma}^\dagger & \hat{f}_{\mathbf{k},\sigma}^\dagger \end{bmatrix} \underbrace{\begin{bmatrix} \varepsilon_{\mathbf{k}} & V \\ V^* & \varepsilon_f \end{bmatrix}}_{H^{\text{PAM}}(\mathbf{k})} \begin{bmatrix} \hat{c}_{\mathbf{k},\sigma} \\ \hat{f}_{\mathbf{k},\sigma} \end{bmatrix} \quad (3.12)$$

where we employ the Fourier transformed $\hat{f}_{\mathbf{k}}^{(\dagger)}$ operators. The interaction matrix $U_{lmm'l'}$ is then limited to a single entry at $U_{\text{ff}} \equiv U$. In order to make the connection to the (single impurity) Anderson model manifest, it is however customary to introduce the Hamiltonian in the form of Eq. (3.11).

Hybridization gap

The first and foremost observation of the multi-orbital basis Eq. (3.12) is that, as a result of the hybridization V , the diagonal elements of the Hamiltonian H^{PAM} do not represent the eigenstates of the non-interacting system. For simplicity and for sake of illustration, we now assume a three-dimensional, particle-hole symmetric tight-binding Ansatz for the non-interacting conduction band

$$\varepsilon_{\mathbf{k}} = -2t \sum_{i \in x,y,z} \cos(k_i), \quad (3.13)$$

an energy of the f-sites of

$$\varepsilon_f = 0. \quad (3.14)$$

The ‘‘Kohn-Sham’’ basis of the formerly disconnected energy bands is now formed by two detached bands with energy dispersions

$$\varepsilon_{\mathbf{k}}^{\pm} = \frac{\varepsilon_{\mathbf{k}}}{2} \pm \sqrt{\frac{\varepsilon_{\mathbf{k}}^2}{4} + V^2}, \quad (3.15)$$

separated by a so-called *hybridization gap*, see Fig. 3.4.³² Let us note that if the hybridization gains a momentum dependence, the gap formation can be circumvented through which a nodal Kondo insulators may develop, see, e.g., Ref. [286]. For this to happen, from a technical point of view, the last term of Eq. (3.11) needs to be modified to include off-site hybridization terms, i.e. $\sum_{ij,\sigma} V_{ij} \hat{c}_{i,\sigma}^{\dagger} \hat{f}_{j,\sigma} + \text{h.c.}$

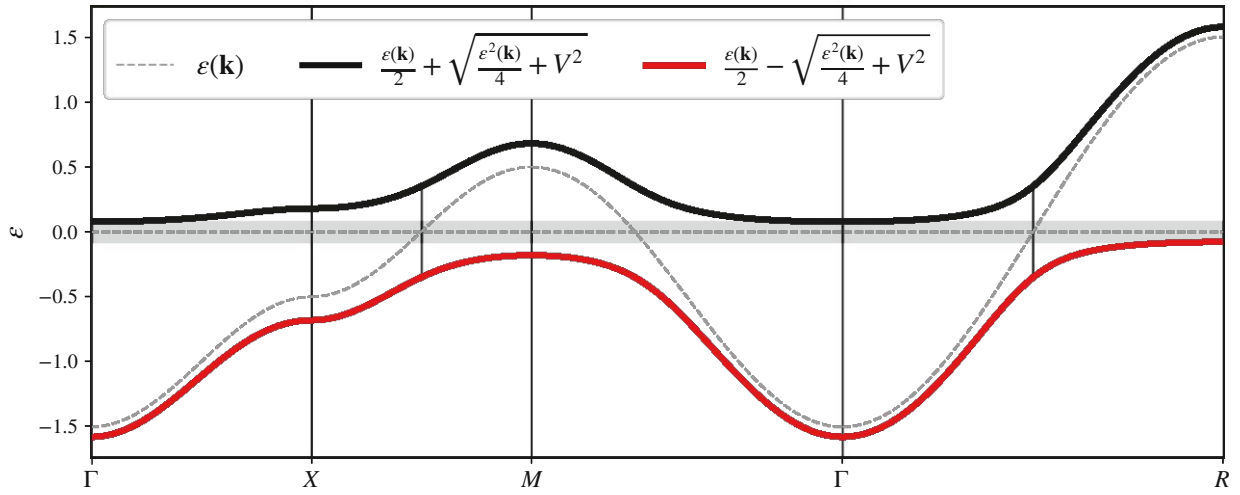


Figure 3.4: Band structure and density of states of the Periodic Anderson Model. Conduction band with a three-dimensional tight-binding Ansatz, see Eq. (3.13), with $t = 0.25\text{eV}$ and a hybridization to the flat band at $\varepsilon_f = 0$ with $V = 0.35\text{eV}$. The resulting indirect gap Δ_{indirect} is shaded in gray. The smallest direct gap is situated at $\mathbf{k} = (\pi/2, \pi, 0)$ with size of exactly $\Delta = 2V$. Through the injection of the f-state, two distinct van Hove singularities emerge on each of the hybridized bands: a cusp that was already present in the unhybridized conduction band (see dashed density of state $N(\varepsilon)$) and a newly formed divergence in the vicinity of the band gap. The density of states was calculated without broadening on a $5000 \times 5000 \times 5000$ k-grid.

Contrary to a structurally directed Bragg gap opening at the edge of the Brillouin zone, a hybridization gap originates from an avoided crossing. In our context the hybridization of the flat f-band

³²With a non particle-hole symmetric positioning of the energy ε_f , the bands become $\varepsilon_{\mathbf{k}}^{\pm} = \frac{\varepsilon_f + \varepsilon_{\mathbf{k}}}{2} \pm \sqrt{\frac{(\varepsilon_f + \varepsilon_{\mathbf{k}})^2}{4} + V^2 - \varepsilon_f \varepsilon_{\mathbf{k}}}$ maintaining an indirect gap of $\Delta_{\text{indirect}} = -6t + \varepsilon_f + \sqrt{9t^2 + 3t\varepsilon_f + V^2 + \varepsilon_f^2/4} + \sqrt{9t^2 - 3t\varepsilon_f + V^2 + \varepsilon_f^2/4}$. (asymmetrically) surrounding ε_f .

at $\varepsilon_f = 0$ and the conduction band $\varepsilon_{\mathbf{k}}$ generates an indirect gap of size

$$\begin{aligned}\Delta_{\text{indirect}} &= \varepsilon^+(\mathbf{k} = (0, 0, 0)) - \varepsilon^-(\mathbf{k} = (\pi, \pi, \pi)) \\ &= -6t + 2\sqrt{9t^2 + V^2}\end{aligned}\quad (3.16)$$

with the smallest direct gap found at the intersection of $\varepsilon_f = \varepsilon_{\mathbf{k}}$, i.e., at momentum $\mathbf{k} = (\frac{\pi}{2}, \pi, 0)$ and all momenta connected to it via symmetry, with size, see vertical bars in Fig. 3.4a,

$$\Delta_{\text{direct}} = (\varepsilon^+ - \varepsilon^-)\left(\mathbf{k} = \left(\frac{\pi}{2}, \pi, 0\right)\right) = 2V. \quad (3.17)$$

The two newly formed upper (“+”) and lower (“-”) branches maintain the symmetry of the conduction band Eq. (3.13) and are connected to one another via

$$\varepsilon_{\mathbf{k}}^{\pm} = -\varepsilon_{\mathbf{k}+\mathbf{\Pi}}^{\mp}, \quad (3.18)$$

with $\mathbf{\Pi} = (\pi, \pi, \pi)$ as the transfer vector.

Hybridized density of states

Upon the injection of the localized f-sites into the “conduction sea” (but still neglecting the f-f interaction), the density of states (DOS) is strongly modified already at the one-particle level: The new, renormalized, DOS $N^*(\varepsilon)$ now reflects the band separation with two distinct contributions

$$N_{\pm}^*(\varepsilon) = \sum_{\mathbf{k}} \delta(\varepsilon - \varepsilon_{\mathbf{k}}^{\pm}) \quad (3.19)$$

finite only above and below the indirect gap, see Fig. 3.4b. The hybridization splits the initial (tight-binding) DOS $N(\varepsilon) = \sum_{\mathbf{k}} \delta(\varepsilon - \varepsilon_{\mathbf{k}})$ and generates additional van Hove singularities in the vicinity of the gap. The cusp, already present in the conduction band (see dashed density of states) originates partially from the X-point on the lower branch ($N_-^*(\varepsilon)$) and the M-point for the upper branch ($N_+^*(\varepsilon)$), respectively. Through the transformation of the bands, displacement of this newly introduced weight of the flat band leads to the formation of a divergent van-Hove singularity whose k-point origin is reversed w.r.t. the cusp, i.e. the origin of $N_-^*(\varepsilon)$ is the M-point and of $N_+^*(\varepsilon)$ is the X-point. Its position on the energy spectrum then corresponds to

$$\text{van Hove : } N_+^* \left(\varepsilon^+[\mathbf{k} = (0, \pi, 0)] = -t + \sqrt{t^2 + V^2} \right) \quad (3.20a)$$

$$N_-^* \left(\varepsilon^-[\mathbf{k} = (\pi, \pi, 0)] = t - \sqrt{t^2 + V^2} \right) \quad (3.20b)$$

3.1.2.2 Heavy fermions and the Kondo insulating scenario

Within this thesis we will restrict our discussion to the cases where the chemical potential lies inside the hybridization gap.³³ These compounds are commonly referred to in the literature as *Kondo insulators* [287, 250, 212]. They are often based on Cerium — $\text{Ce}_3\text{Bi}_4\text{Pt}_3$ [288, 253] (see Section 3.2), CeNiSn [289], CeRu_4Sn_6 [290] — but can also derive from a wide variety of other lanthanoids — SmB_6 [291], YbB_{12} [292], YbRh_2Si_2 [293], actinoids — EuCd_2Sb_2 [294], $\text{U}_2\text{Ru}_2\text{Sn}$ [295], PuTe [296] or may be built up from “light-weight” d-elements such as iron — FeSi [297, 212], FeSb_2 [298, 299, 300].

Fundamentally, electron interactions in these materials strongly influence the one-particle picture at hand. Akin to the band width compression introduced in Section 2.2, the hybridization gap will become heavily renormalized which is accompanied by a Kondo resonance with width $k_B T_K \ll 2V$. Further, through the Kondo effect the magnetic response will transition from free spin behavior at high temperatures towards a spin gap (and charge gap) for $T \ll T_K$. We will discuss these “features” in the Section below.

Nonetheless the elementary picture painted by the one-particle considerations can be supported indirectly by various observations:

- (i) Since the involved hybridization between the localized and itinerant electrons is oftentimes small, the resulting band gaps are themselves small, too [301]. One can exploit this circumstance and show that it is possible to close this gap Δ with physically feasible magnetic fields, to first approximation $H \approx \Delta/(gJ\mu_B)$ [302, 303].
- (ii) Contrary to (most) ordinary semiconductors, hydrostatic pressure canonically leads to a widening of the hybridization gap (at least for Ce-based Kondo insulators).
- (iii) Kondo insulators usually have a fully itinerant semiconducting analog [304]. As these “*f*-less” itinerant counterparts have a wider radial extent of the wave function that is involved in the formation of the band hybridization, they commonly exhibit comparatively larger gaps and small effective masses. $\text{Ce}_3\text{Bi}_4\text{Pt}_3$ with a gap of around 10meV, see next Section, for example is isoelectronic to $\text{Th}_3\text{Sb}_4\text{Ni}_3$ which has a gap of around 70meV [304].³⁴
- (iv) Partial replacement of the magnetic rare-earth ion with its non-magnetic counterpart, e.g., $\text{Ce} \rightarrow \text{La}$, leads to an effective electronic doping effect through which a insulator-to-metal transition

³³If the chemical potential lies outside this gap, it is evident that the Fermi surface becomes modified and *expands* with respect to the non-interacting conduction band, see hypothetical Fermi surfaces in Fig. 3.4 via horizontal cuts. Through the strong modification of the DOS and the correlation-induced Abrikosov-Suhl resonance, these heavy-fermion systems experience strong modifications to their electronic signature with mass renormalizations oftentimes of the order of $\mathcal{O}(10^3)$.

³⁴Also the radial-extent of ligand-orbitals can be changed by isoelectronic substitutions to manipulate the hybridization to the *f*-states and thus the Kondo coupling [305].

can be enforced [306]. This can be also thought of as a dilution from the Kondo lattice model towards the (single impurity) Kondo model.

Heavy-fermion metals — to name a few: CeAl₃ [307], CeCu₂Si₂ [308], YbBiPt [309] — display vastly different characteristics compared to what is naively expected from ordinary metals. Through the occurrence of the Kondo effect, the low and high temperature behavior are almost fully detached from one another. At high temperatures, similar to Section 3.1.1, the decoupled magnetic moments generate magnetic susceptibilities that follow the Curie-Weiss law. Due to the complications of spin-orbit coupling and the surrounding crystal-field, quantitative predictions are however difficult. At low temperatures, below the Kondo (coherence) temperature T_K the spins become efficiently screened, leading to a rapid loss of spin entropy [304]. The scattering centres now form a coherent array, allowing Bloch waves to pass through. In turn, a strong decrease in the resistivity $\rho(T)$ sets in. Through the Kondo resonance a universal, highly renormalized, Fermi liquid is formed. For more detailed discussion on the characteristics and phenomena of heavy-fermion systems, please refer to the literature, e.g., to Ref. [280].

3.1.2.3 Kondo insulator within DMFT

So far we have discussed the implications of the hybridization of a flat band purely on the one-particle level, i.e. the modifications to the band structure and density of states. In order to advance towards realistic setups we now “turn on” the involved interactions and, again, resort to a dynamical mean-field theory treatment to analyze the many-body effects. At first we will ignore all possible non-local ordering tendencies.

In this short venture exploring “canonical” Kondo insulators, we will first restrict ourselves to a fixed on-site interaction U and hybridization strength V and perform a temperature scan similar to that in Section 3.1.1. The remaining parameters of the PAM Hamiltonian, see Eq. (3.11), are identical to the ones discussed in Section 3.1.2.1: a hopping amplitude of the (three-dimensional, nearest-neighbor) tight-binding conduction band of $t = 0.25\text{eV}$, an onsite repulsion of $U = 6t = 1.5\text{eV}$ and a fixed chemical potential $\mu = 0$ to enforce particle-hole symmetry.³⁵

The additional uncorrelated band expands the orbital subspace of the lattice systems, thus modifying the DMFT embedding self-consistency condition to

$$G_{\text{ff}}^{\text{imp}} \stackrel{!}{=} G_{\text{ff}}^{\text{lattice,loc}} = \left[\sum_{\mathbf{k}} G^{\mathbf{k}} \right]_{\text{ff}} \quad (3.21)$$

³⁵ Within DMFT, the necessary shift of the local level ε_f , necessary for the half-filling constraint of the interacting Hamiltonian, is performed by a double-counting correction that acts solely on the correlated band with size $\Sigma_{\text{DC}} = U/2$.

where the lattice Greens function $G^{\mathbf{k}}$ is defined in the two-orbital space, however only its projection onto the f-orbital enters the DMFT self-consistency condition. As the interaction terms only acts on the f-fermions, the self-energy is itself restricted to only the f-subspace

$$\Sigma^{\text{PAM}} = \begin{bmatrix} 0 & 0 \\ 0 & \Sigma_{\text{ff}} \end{bmatrix} \quad (3.22)$$

such that the momentum dependency of the interacting (lattice) Greens function

$$G^{\text{PAM}}(i\nu_n, \mathbf{k}) = \left[(i\nu_n + \mu)\mathbb{1} - H^{\text{PAM}}(\mathbf{k}) - \Sigma^{\text{PAM}}(i\nu_n) \right]^{-1} \quad (3.23)$$

stems purely from the conduction band.

Emerging lattice coherence

The result of the DMFT procedure is summarized for the considered temperature range in Fig. 3.5 where we plot the spectral function on the real-frequency axis and the imaginary part of the underlying self-energy of the DMFT impurity in the left and right column, respectively.

Similar to Section 3.1.1, we can distinguish three distinct energy (temperature) ranges:

(i) Above the coherence temperature $T_{\text{coherence}}$ (top row) the slope of the self-energy is clearly positive for all frequencies, indicating an incoherent state with localized spins. Cooling from the largest employed temperature ($T = 0.43$) results in a crossover from a fully incoherent spectral function to a spectral function with well defined satellites around $\omega = \pm 1\text{eV}$. The electronic scattering rate at high enough temperatures exceeds the (renormalized) one-particle gap, smearing out all remnants of the band, resulting in a Gaussian-like spectral function. Below a certain temperature threshold, the reduced scattering then allows for two split “bands” of the Kondo insulator to emerge, evidently leading to a drop-off of the spectral weight at the Fermi level $A(\omega = 0)$ (see inset).

(ii) Once quasi-particle coherence is reached below $T = 0.2\text{eV}$, the Kondo resonance, similar to the SIAM, emerges. Let us note that we find a Fermi liquid like upturn in the self-energy $-\Im\Sigma(i\nu_n \rightarrow 0^+) = \Gamma$ indicating growing coherence. The underlying spectrum, however, does not yet relate to a standard Fermi liquid: The four largest temperatures in panels (c-d) of Fig. 3.5 showcase a Kondo peak, the corresponding self-energy, however, is yet to conform to the “standard” Fermi liquid expansion on the Matsubara axis $\Im\Sigma(i\nu_n) \propto -\Gamma + (1 - Z^{-1})i\nu_n$, cf. Section 2.2.3.

(iii) Whereas in the SIAM the Kondo resonance remains stable down to zero temperature, here the low temperature behavior is expectedly different. Once the conditions for a fully formed Kondo resonance are met below $T = 0.025\text{eV}$, a spectral gap starts to open up. Due to the small size of the gap, at first we find large thermal weight (corresponding to the size of the scattering rate Γ) which eventually vanishes with $\lim_{T \rightarrow 0} A(\omega = 0) = 0$, see left inset in Fig. 3.5. With the employed

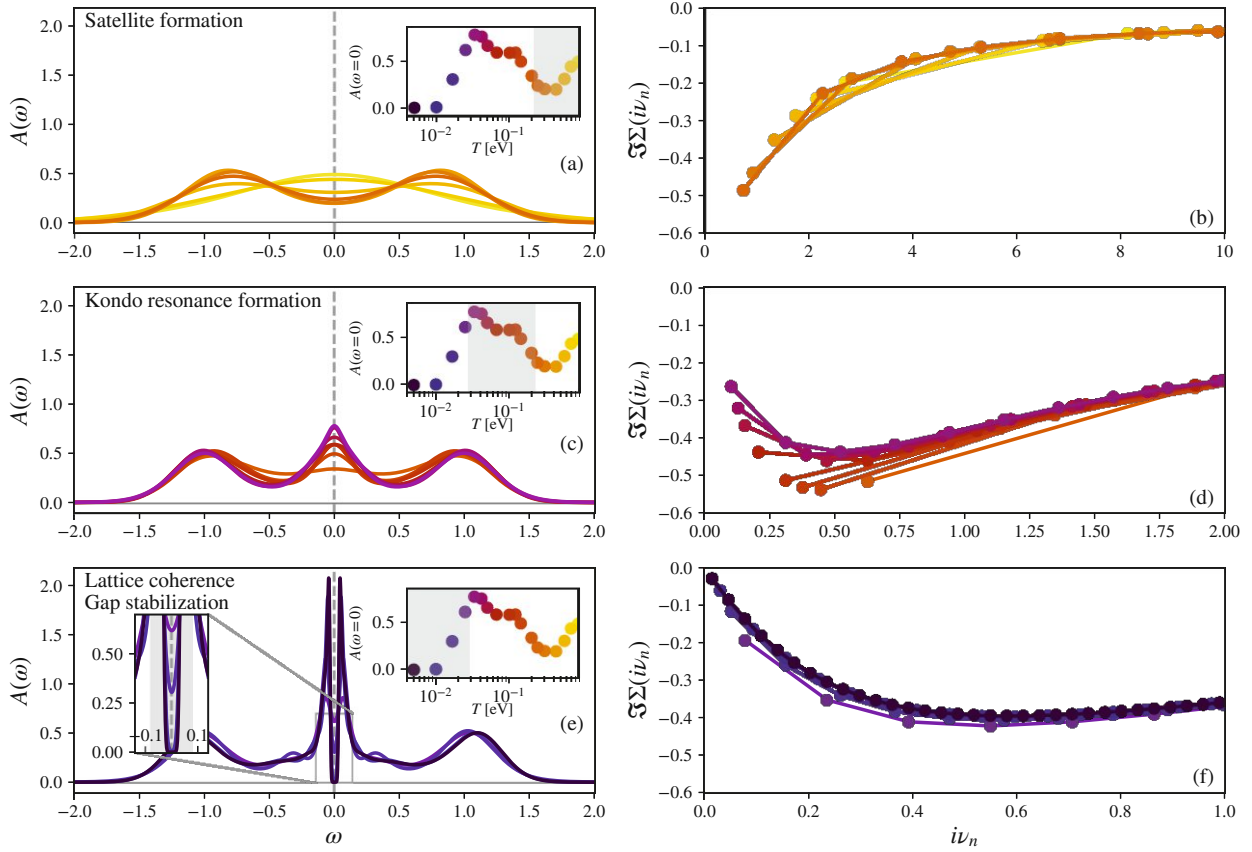


Figure 3.5: Temperature regimes of the (particle-hole symmetric) periodic Anderson model, see Eq. (3.11), within DMFT with $t = 0.25\text{eV}$, $U = 6t = 1.5\text{eV}$, and $V = 0.35\text{eV}$. The resulting band structure and density of states is shown in Fig. 3.4. Top panels: Full incoherence to satellite formation. Middle panels: Kondo peak formation via an upturn of the imaginary part of the self-energy at the lowest frequency. Bottom panels: Lattice coherence and a stabilization of the spectral gap. The self-energy (in the ff-sector) shows a (renormalized) Fermi-liquid behavior, which, in combination with the hybridization, opens a coherent gap in the local spectral function. For the lowest considered (inverse) temperature $\beta = 200\text{eV}^{-1}$ the opened DMFT gap, see inset, is roughly $\Delta^{\text{DMFT}} = 60\text{meV}$, compressed by a factor of 2.5 when compared to the indirect gap of $\Delta^{\text{indirect}} = 155\text{meV}$ (gray shading).

interaction strength $U = 6t$, the hybridization gap of the (one-particle) band structure ($\Delta = 155\text{meV}$, cf. Eq.(3.16)), becomes strongly renormalized, resulting in a DMFT band gap compression towards $\Delta_{\text{DMFT}} \approx Z\Delta = 60\text{meV}$. We find that this renormalization Z is in good agreement with the quasi-particle weight extracted from the Fermi liquid expansion of the self-energy (fit not shown).

Below the coherence (\propto Kondo) temperature, the self-energy of the DMFT impurity showcases comparable behavior to the single impurity case with fixed hybridization bath: In both scenarios the

self-energy is extraordinarily well described via a Fermi-liquid expansion and a residual scattering that is rapidly vanishing as we approach $T \rightarrow 0$. In the periodic Anderson model, from a technical point of view, the interplay of the lattice hybridization V and the fully coherent self-energy, see Eq. (3.23), necessarily opens a gap in the interacting Green's function. This mechanism is displayed in more detail via the DMFT band structure in Fig. 3.6: At high temperatures (top panel, $1/T = 4.14\text{eV}^{-1}$) we recover an in-tact (temperature broadened) conduction band $\varepsilon(\mathbf{k})$ with the previously mentioned satellite formation at around $\omega = \pm 1\text{eV}$. The Kondo resonance formation at $1/T = 10\text{eV}^{-1}$ is accompanied by an already strong modification of the band crossing which eventually leads to a partial gap opening at $1/T = 30\text{eV}^{-1}$. Whereas the gap is fully opened at the smallest direct gap $\mathbf{k} = (\pi, \pi/2, 0)$, the resonance remains fully formed at the Γ and R-point. Only below the coherence temperature $1/T = 30\text{eV}^{-1}$ do we also find a fully stabilized, indirect gap. Let us note that this band structure is a result from the analytic continuation of *both* the diagonal elements of the lattice Green's function, i.e. $\text{Tr}A(\mathbf{k}, \omega) = A_{\text{cc}}(\mathbf{k}, \omega) + A_{\text{ff}}(\mathbf{k}, \omega)$.

Insulator mechanism and coherence transition

Contrary to the signatures of the insulating solution discussed in Section 2.3.2 (suppression of charge fluctuations, i.e. a diminishing hybridization function, to achieve a Mott insulator), the canonical Kondo insulator, modelled via a half-filled periodic Anderson model, behaves quite differently. The local spectral functions of the DMFT impurity at particle-hole symmetry (where $\Re\Sigma = \Re\Delta \equiv 0$) are in essence only a product of the imaginary part of the self-energy $\Sigma(i\nu_n)$ and the (DMFT) hybridization function $\Delta(i\nu_n)$

$$G^{\text{imp}}(i\nu_n) = \frac{1}{i\nu_n - i\Im\Sigma(i\nu_n) - i\Im\Delta(i\nu_n)}. \quad (3.24)$$

The evidenced “metallic” self-energy renormalizes the non-interacting hybridization gap of Fig. 3.4, which we illustrate in Fig. 3.7. Along the coherence transition from $1/T = 30\text{eV}^{-1}$ towards $1/T = 200\text{eV}^{-1}$ the opening of the spectral gap is directly correlated with a strong upturn of the hybridization function at the first positive Matsubara point $i\nu_0 = i\pi/\beta$, see third column. Together, the imaginary part of the Green's function turns from metallic (positive slope on the Matsubara axis) to insulating (negative slope). The insulating gap within DMFT is therefore the consequence of an interplay between the emerging Kondo resonance and the lattice hybridization via the Dyson equation. For a classification of correlated insulators along these lines see Sec. 2.5 in Ref. [212].

Finally, before turning our attention towards the signatures encoded in the two-particle responses, we briefly showcase the behavior of the emergent lattice coherence in more detail in Fig. 3.8. We illustrate the transition at fixed (inverse) temperature while varying the hybridization strength V . The “critical hybridization” V_c for the given temperature behaves as expected: Cooling the system

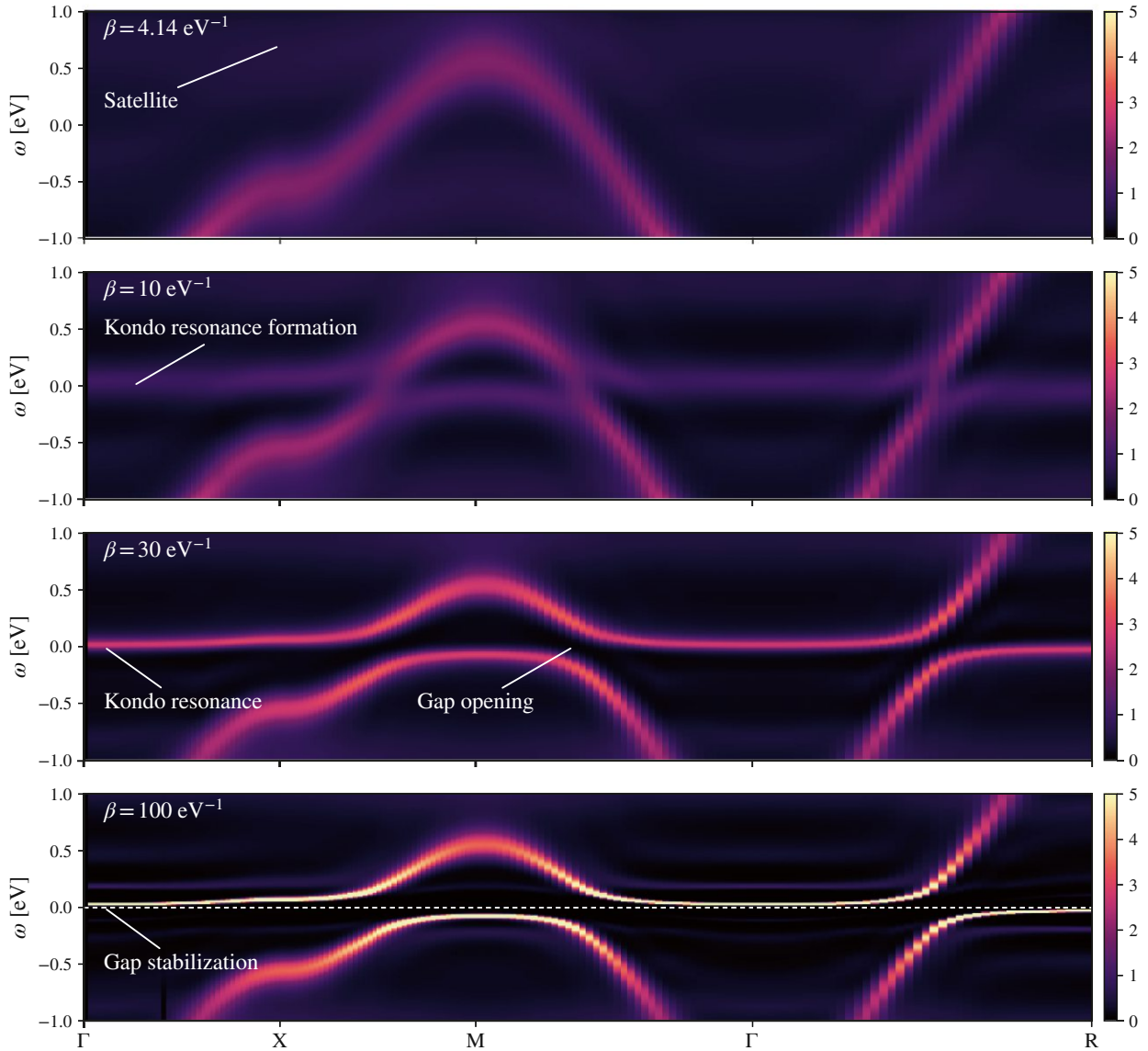


Figure 3.6: Renormalized (DMFT) band structure changes in the (particle-hole symmetric) periodic Anderson model upon temperature reduction $T = 1/\beta$, see Eq. (3.11) with $t = 0.25\text{eV}$, $U = 6t = 1.5\text{eV}$, and $V = 0.35\text{eV}$. The emergence of the Kondo peak, see Fig. 3.5, is reflected in a gain of coherence of the flat f -band ($\beta = 4.14\text{eV}^{-1} \rightarrow \beta = 10\text{eV}^{-1}$). Upon further cooling the Kondo peak sharpens ($\beta = 10\text{eV}^{-1}$) before being fully suppressed at low temperatures where instead a coherent gap is stabilized ($\beta = 100\text{eV}^{-1}$). The DMFT band structures result from the analytic continuation of the diagonal elements of the lattice Green's function, i.e. $A(\mathbf{k}, \omega) = A_{\text{cc}}(\mathbf{k}, \omega) + A_{\text{ff}}(\mathbf{k}, \omega)$.

(top panels towards bottom panels) reduces the size of the thermal fluctuations, lowering the necessary strength of the hybridization to the conduction bath in order to form a spectral gap. The affected

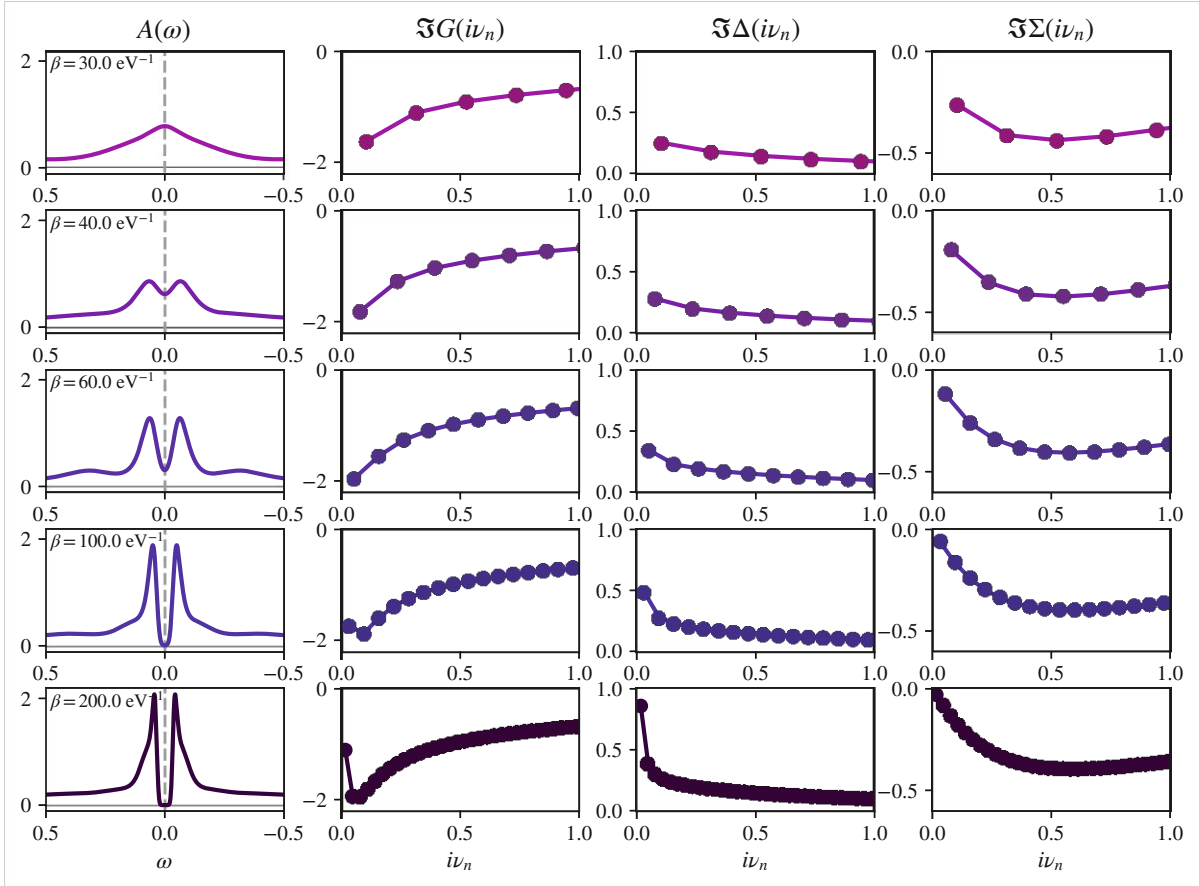


Figure 3.7: Stabilization of the insulating solution of the periodic Anderson model within DMFT. Rows: various (inverse) temperatures across the coherence temperature. Columns from left to right: Spectral function $A(\omega)$, imaginary part of the Green's function $\Im G(i\nu_n)$, imaginary part of the hybridization function $\Im \Delta(i\nu_n)$ and imaginary part of the self-energy $\Im \Sigma(i\nu_n)$. The self-energy turns metallic upon cooling, perfectly conforming to Fermi-liquid expectations. Through the hybridization function the Green's function turns insulating, i.e. a spectral gap forms despite the “metallic” self-energy.

energy range of the spectral function across the transition (width of the gap formation) becomes more narrow as we cool the system. Simultaneously, additional spectral satellite features emerge around $\omega = \pm 0.10\text{eV}$ at $\beta = 200\text{eV}^{-1}$ and $\omega = \pm 0.05\text{eV}$ at $\beta = 500\text{eV}^{-1}$, respectively, most likely corresponding to the additional van Hove singularity introduced through the coupling to the f-band, see Fig. 3.4 and Eq. (3.20). Overall, we find that the size of the coherence hybridization V_c necessary to drive the opening of a satisfactory spectral gap (which can roughly be defined via $\partial^2 A(\omega)/\partial\omega^2 > 0$ at $\omega = 0$) to be connected to the temperature $T \propto \exp(-A/V_c^2)$. This reemphasizes the close connection between the lattice coherence and the Kondo temperature expected from the single impurity Anderson Model with $T_K \propto \exp(-1/J)$, see Eq. (3.6).

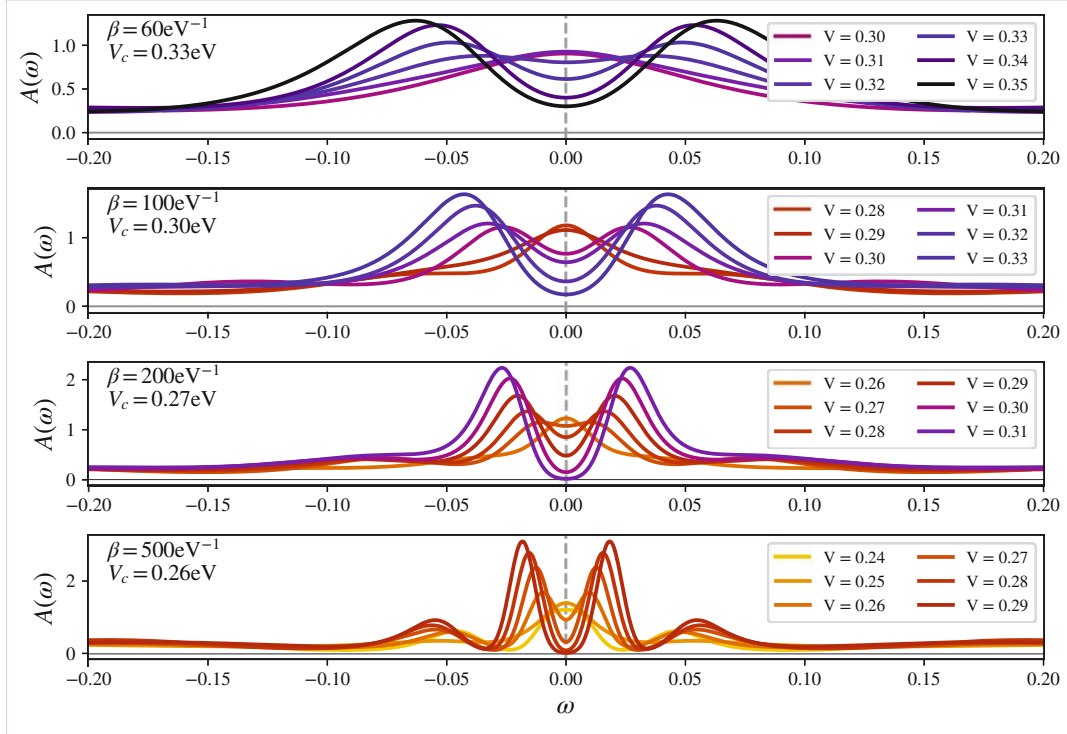


Figure 3.8: Lattice coherence of the periodic Anderson model via a variation of the hybridization strength V for a given (inverse) temperature. Lowering the temperature leads to suppression of the coherence hybridization V_c and a sharpening of spectral features surrounding the gap. Lower temperatures lead to a reduction of the necessary V_c to open the gap.

Mott vs. Kondo gap characteristic

Having explored the technical intricacies of the (spectral) Kondo gap formation within DMFT, we find it instructive to highlight the dichotomies between the Mott and Kondo insulating behavior. Hitherto we identified the opening of the gap via the spectral function $A(\omega)$, i.e. via the particle gap

$$E_p = E_0(N_\uparrow + 1, N_\downarrow) + E_0(N_\uparrow - 1, N_\downarrow) - 2E_0(N_\uparrow, N_\downarrow), \quad (3.25)$$

here explicitly denoted as the (combined) changes in ground-state energy E_0 necessary for adding and removing one particle from the system. Complementary, a powerful tool to differentiate the magnetic state of (Kondo) materials, is the spin gap

$$E_s = E_0(N_\uparrow + 1, N_\downarrow - 1) - E_0(N_\uparrow, N_\downarrow), \quad (3.26)$$

defined as the energy change necessary for a spin triplet excitation [310].³⁶ Spin gaps are commonly detected directly via, e.g., inelastic neutron scattering measuring the magnetic structure factor [312,

³⁶In the literature, see, e.g., Ref. [311] E_s is sometimes written in a symmetric fashion via $E_s = E_0(N_\uparrow + 1, N_\downarrow - 1) + E_0(N_\uparrow - 1, N_\downarrow + 1) - 2E_0(N_\uparrow, N_\downarrow)$, which can then be identified as spin stiffness $\partial^2 E_0 / \partial S^2$.

313] or indirectly via the temperature behavior of the response to a static magnetic field [314, 315]. The former is directly connected to spin fluctuations [316, 317] and can be thus calculated via the magnetic susceptibility on the real frequency axis $\Im\chi_M(\mathbf{q}, \omega)$ [318], the latter simply corresponds to the uniform, static magnetic susceptibility $\chi(\mathbf{q} = \mathbf{0}, i\omega_m = 0)$.

In the absence of magnetic ordering, a spin excitation of a Mott insulators is gapless as the process does not affect the electronic configuration of the system. This is different in a Kondo insulator where through the stabilization of the energy gap (already present at the one-particle level), charge and spin excitations require a finite amount of energy, see e.g., Ref. [288]. Here, Kondo insulators display a similar behavior when compared to correlated (hybridization-gap) band insulators [319, 320].

In principle, a second avenue of distinguishing the two types of materials is the response to hydrostatic pressure: all else being equal, pressure leads to a widening of the orbital overlap. In Mott insulators, the resulting widening of the band width leads to a reduction of the ratio between interaction strength and band width U/W and therefore a shrinkage of the spectral gap with a possibility to push the system towards metallicity [321, 322]. In Kondo insulators, increased overlap leads to an enhancement of the hybridization strength V and thus a widening of the hybridization gap. Naturally this only holds in the ideal picture: In realistic structures changes to the highly complex ionic environment may lead to more nuanced outcomes [323].

To extract the spin state of the of the periodic Anderson model, we calculate the magnetic susceptibility within DMFT: The relevant contributions to the spin-spin correlation function, see Section 2.5.4, are contained in

$$\chi_M^{\text{PAM}} = \begin{bmatrix} \chi_M^{\text{cc}} & \chi_M^{\text{cf}} \\ \chi_M^{\text{fc}} & \chi_M^{\text{ff}} \end{bmatrix}. \quad (3.27)$$

Let us note that Eq. (3.27) only contains contributions relating to the spin operator. Contrary to the Green's function or the self-energy definitions, here “cf”, e.g., is an abbreviation for the four-point orbital combination “cfff”.

In Fig. 3.9 we summarize our results where for a fixed hybridization strength V we varied the temperature T . We compare the static response of the underlying DMFT impurity, panels (a) and (b), with the uniform response of the lattice, panels (c) and (d).

In panels (a) and (c) we show the magnetic susceptibility of the ff-sector for which we find the expected high temperature, Curie-Weiss behavior $\chi_M \propto C/T$ in the impurity as well as the uniform lattice response. Cooling the system eventually breaks this trend, a peak is formed at intermediate temperatures, and a plateau is formed towards zero temperature.³⁷ Due to the small coherence

³⁷The (inverse) saturation value of the magnetic response of the impurity has previously been used to estimate the Kondo temperature in the infinite dimension limit [324].

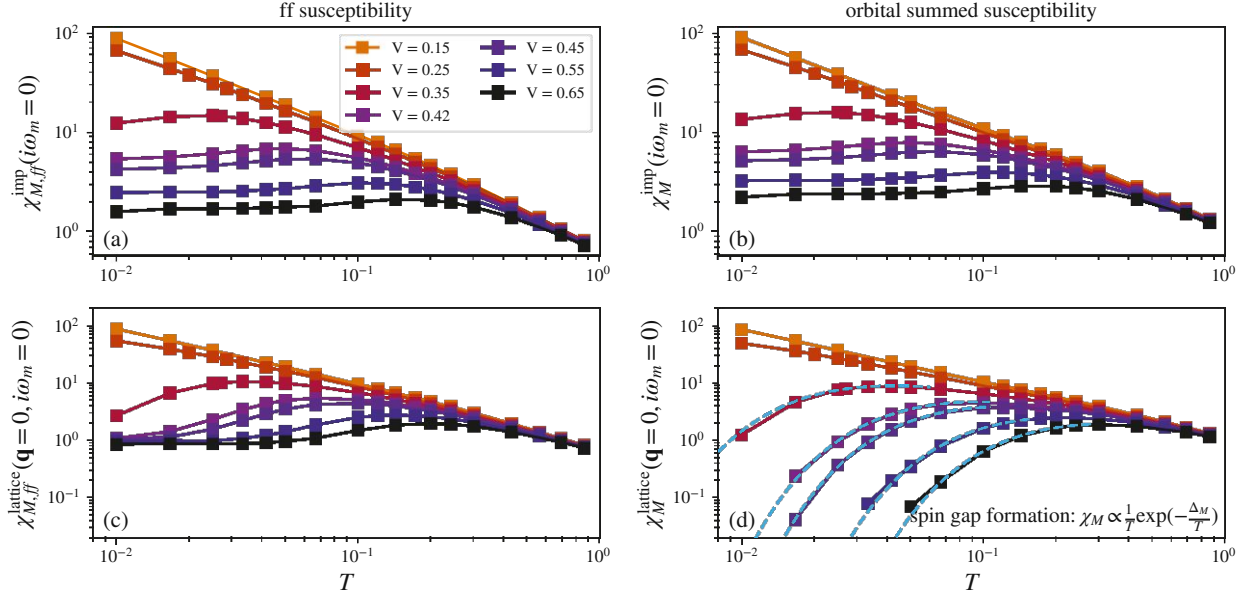


Figure 3.9: Orbital differentiation of the spin susceptibility χ_M for fixed hybridization strengths V (different colors) and varying temperature T . The impurity responses (panels a,b) showcase a transition from Curie-Weiss towards a plateau at low temperatures. The uniform lattice responses (panel d), on the other hand, display the anticipated activated behavior once all orbitals that form the physical response are included. The spin gaps are extracted by fitting the numerical data to $\chi_M \propto 1/T \exp(-\Delta_M/T)$, see main text.

temperatures this plateau is not yet fully formed for the smallest, considered hybridization strengths $V = 0.15\text{eV}$ and $V = 0.25\text{eV}$.

Panels (b) and (d) on the other hand show the physical susceptibilities which are constructed via a full orbital summation $\chi_M = 2 \sum_{lm} \chi_{M,llmm}$. The full impurity response highlights that the *local* correlations are fully captured within the ff-sector, i.e. the orbital sectors containing conduction electrons only induce a slight (positive) offset. The spin gap signature is exclusively present in the *physical* lattice response: Once the underlying fluctuations become suppressed, via the opening of the Kondo gap, we find an activated behavior that microscopically can be connected to the response of localized moment whose (non-magnetic) excited state is separated by Δ_M [285]. The magnetic susceptibility then follows as

$$\chi_M = \frac{N_A g_s^2 \mu_B^2}{3k_B T} \frac{S(S+1)(S+2)}{2S+1 + \exp(\Delta_M/(k_B T))} \quad (3.28)$$

whose low temperature behavior $k_B T < \Delta_M$ is recovered via

$$\chi_M \propto \frac{1}{k_B T} \exp\left(-\frac{\Delta_M}{k_B T}\right). \quad (3.29)$$

Here N_A is the Avogadro constant, g_s is the gyromagnetic ratio, μ_B is the Bohr magneton and S is the (total) spin of the local moment. The fits of $\chi_M^{\text{lattice}}(\mathbf{q} = \mathbf{0}, i\omega_m = 0)$ via Eq. (3.29) are illustrated in Fig. 3.9d as overlain, dashed lines.³⁸ We performed the fits on the 6 smallest temperatures, excluding susceptibilities with values below 10^{-1}eV^{-1} due to their numerical noise, and find excellent numerical agreement. From a technical point of view, the exponentially suppressed responses result from large, negative $\chi_M^{cf} \equiv \chi_M^{fc}$ contributions. Additionally, these contributions cause all finite frequencies responses $i\omega_m > 0$ to vanish for $\mathbf{q} = \mathbf{0}$ (not shown), i.e. the static value encodes the full spin information of the lattice. In short, this is simply a consequence of the conservation of the total spin [325].

Finally, one-particle hybridization gaps Δ_{indirect} , see Eq. (3.16), DMFT spectral gaps Δ_{DMFT} (extracted at $\beta = 100\text{eV}^{-1}$), and spin gaps Δ_M are listed vis-à-vis in Table 3.1.

V [eV]	Δ_{indirect} [eV]	Δ_{DMFT} [eV]	Δ_M [eV]
0.35	0.155	0.060	0.042
0.42	0.219	0.130	0.098
0.45	0.249	0.160	0.125
0.55	0.360	0.270	0.222
0.65	0.485	0.400	0.327

Table 3.1: Comparison of the most relevant gaps of the (symmetric) periodic Anderson model for $t = 0.25\text{eV}$, $\varepsilon_f = 0$ and $U = 6t = 1.5\text{eV}$ at half filling. The indirect gap follows directly from the band structure, see Eq. (3.16), the DMFT gap was estimated via the spectral function at $\beta = 100\text{eV}^{-1}$ (not shown). The extracted spin gap (Δ_M), was determined via a fit of Eq. (3.29) to the uniform magnetic response.

The local correlations included in DMFT are capable of strongly renormalizing the indirect hybridization gap. As we employ the same interaction strength $U = 6t$ throughout, this renormalization $\Delta_{\text{DMFT}} = Z\Delta_{\text{indirect}}$ is suppressed for large values of V . We find the extracted spin gap to be slightly smaller than the DMFT gap for all considered hybridization strengths V . Let us note however, that DMFT gaps extracted via the spectral function are prone to errors due to the thermal spillover.

3.1.3 The complication of magnetic ordering

Concluding the discussion on the periodic Anderson model, we now turn our attention to possible long-range order that competes with the intrinsic Kondo physics at play. As already alluded to earlier, the PAM is famous for hosting the Ruderman–Kittel–Kasuya–Yosida (RKKY) interaction [281, 282, 283].

³⁸Fits performed with a “semiconductor-esque” spin gap law $\chi_M \propto \exp(-\Delta_M/(2k_B T))$ [212, 285], often employed in experiment evaluation [314, 315], can only follow the numerical data for the lowest 2–3 data points and result in considerably worse coefficients of determination (not shown).

Within a metal, a magnetic moment generates Friedel oscillations in the spin density, the quantum analog to electric charge screening. If a second momentum is in the vicinity of this perturbation, these oscillations modify the total energy of the involved spins through an indirect spin-coupling. In the context of the three-dimensional PAM, the RKKY contribution

$$\mathcal{H}_{\text{RKKY}} = \frac{1}{2} \sum_{i,j} J_{\text{RKKY}}(\mathbf{r}_i, \mathbf{r}_j) \vec{S}_i \cdot \vec{S}_j \quad (3.30)$$

with

$$J_{\text{RKKY}}(\mathbf{r}_i, \mathbf{r}_j) \propto J^2 \rho \frac{\cos(2k_F |\mathbf{r}_i - \mathbf{r}_j|)}{|\mathbf{r}_i - \mathbf{r}_j|^3} \quad (3.31)$$

is already implicitly encoded via the hybridization terms between the two fermionic “species”.³⁹ J is therefore the effective exchange-interaction term introduced via the lattice hybridization as $J = V^2/U$, ρ is the conduction electron density of states per spin at the Fermi level and k_F is the Fermi wave vector (radius of the Fermi sphere). Through an indirect exchange via the non-interacting fermions the f -electrons therefore lower their energy by (anti)aligning their respective spins, depending on the sign of the exchange interaction.⁴⁰

In the absence of this long-range RKKY interaction the Kondo effect is screening the local moments: Below the Kondo temperature (coherence temperature) this screening is fully realized and the lattice coherent Kondo singlets are formed, stabilizing the gap of the Kondo insulator. Introducing magnetic fluctuation, a competition emerges: the Kondo effect attempts to form spin singlets, the RKKY interaction attempts to (anti)align them. This competition is famously encoded in the Doniach phase diagram [328] which we will reproduce later on.

The relevant energy scales of the two competing effects can be summarized via their critical temperatures. In second order perturbation theory in J , the RKKY ordering temperature scales via the square of the exchange-interaction strength [225]

$$T_{\text{RKKY}} = \frac{1}{4} J^2 \chi_0(i\omega_m = 0, \mathbf{Q} = (\pi, \pi, \pi)) \quad (3.32)$$

where χ_0 is the non-interacting susceptibility of the conduction bath. The underlying Kondo effect on the other hand is exponentially suppressed for small J where for the single-site Kondo model T_K scales with

$$T_K \propto \exp\left(-\frac{1}{2\rho J}\right). \quad (3.33)$$

Naturally, at small hybridization strengths the RKKY interaction dominates the system as $T_{\text{RKKY}} \gg T_K$: the system orders at finite T and towards zero temperature an antiferromagnetic insulator is

³⁹In order to reduce the complexity of the Hamiltonian, oftentimes the Kondo lattice model [326] is employed instead. Similar to the transformation of the SIAM to the Kondo Model, the hybridization terms are explicitly replaced with Eq. (3.30).

⁴⁰See, e.g., Ref. [327] for an experimental evidence of the magnetic Friedel oscillations on the Fe(001) surface.

stabilized. At large hybridization strengths the exponential scaling of the Kondo effect overcomes the magnetic ordering: beyond a critical V_c , a paramagnetic insulator is realized instead.

RKKY through DMFT feedback

In order to examine the RKKY phenomenon, we extend the analysis of the previously discussed uniform ($\mathbf{q} = \mathbf{0}$) magnetic susceptibilities to the antiferromagnetic ordering vector $\mathbf{q} = \mathbf{\Pi} = (\pi, \pi, \pi)$. As a starting point, we illustrate how the RKKY interaction gets introduced via the DMFT self-consistency cycle in Fig. 3.10.

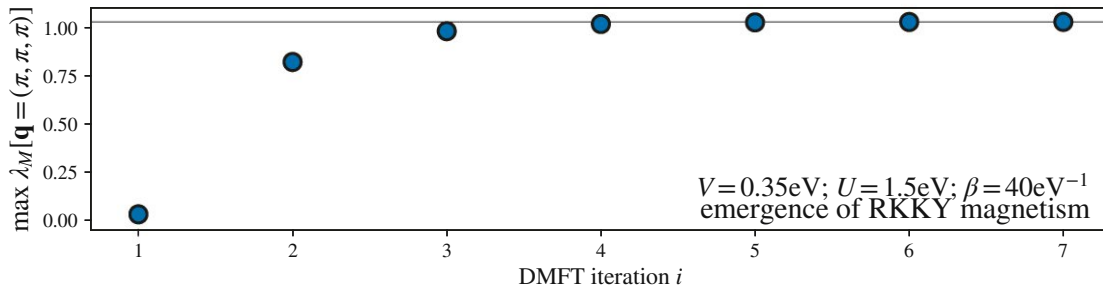


Figure 3.10: Leading magnetic eigenvalue development along the DMFT self-consistency cycle for the PAM defined via $V = 0.35\text{eV}$, $U = 6t = 1.5\text{eV}$ and $\beta = 40\text{eV}^{-1}$. Each step of the DMFT cycle corresponds to a valid impurity for which we calculated the two-particle response and the leading magnetic eigenvalue corresponding to antiferromagnetic ordering $\mathbf{q} = (\pi, \pi, \pi)$. DMFT convergence is reached at around step 6.

We show the evolution of the leading magnetic eigenvalue corresponding to antiferromagnetic ordering along the DMFT cycle for $V = 0.35\text{eV}$, $U = 6t = 1.5\text{eV}$ and $\beta = 40\text{eV}^{-1}$. The first iteration represents a prototypical single impurity Anderson model whose hybridization function is determined by the periodic model. A one-shot calculation can therefore only include the quintessential Kondo physics and the leading eigenvalue is, to good approximation, zero. Each additional iteration $i \rightarrow i+1$ includes the impurity self-energy from the previous iteration (we employ a full self-energy feedback, i.e. no mixing) as an ingredient in the determination of the new hybridization bath. Most of the RKKY feedback is obtained in the first three steps of the DMFT loop beyond which the leading eigenvalue slowly converges towards $\lambda_M = 1.026$. DMFT convergence is reached beyond iteration 6. The eigenvalue of $\lambda_M > 1$ signals that the system will order for the given parameter set.

Doniach phase diagram

Performing the same calculation on a wide range of parameter pairs (T, V) — temperature vs. hybridization strength — we find the phase diagram illustrated in Fig. 3.11. Let us note that in the

literature this phase diagram is oftentimes plotted with the effective exchange interaction $J = V^2/U$ as the x-axis instead.

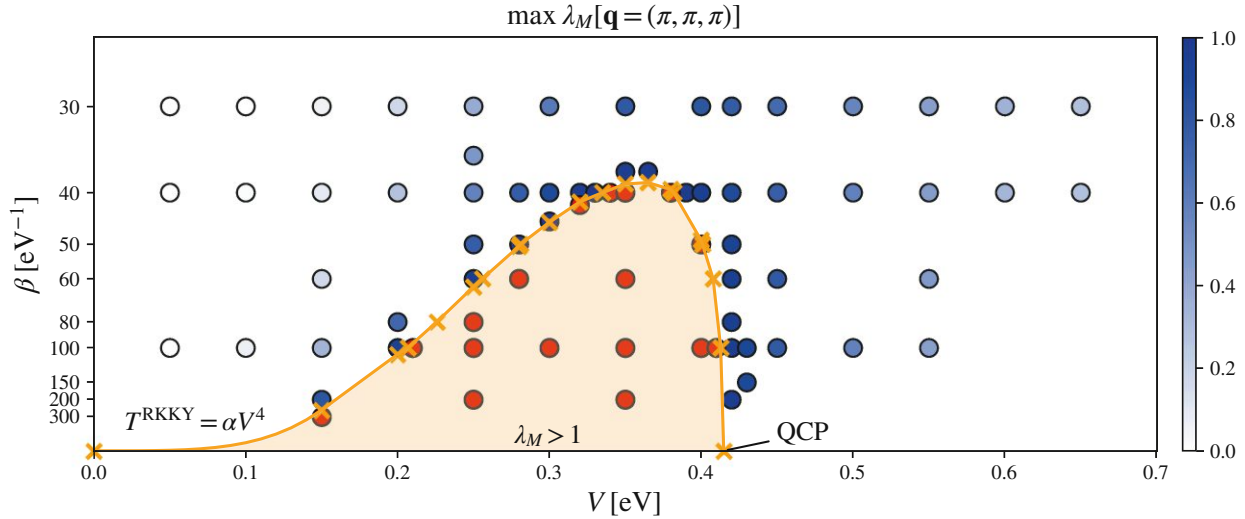


Figure 3.11: Magnetic phase diagram of the (particle-hole symmetric) periodic Anderson model with $t = 0.25\text{eV}$, $U = 6t = 1.5\text{eV}$. The competition between the RKKY interaction ($T^{\text{RKKY}} = \alpha V^4$) and the Kondo effect results in an antiferromagnetic dome (orange: leading magnetic eigenvalue $\mathbf{q} = (\pi, \pi, \pi) > 1$) and the emergence of a quantum critical point (QCP) at around $V = 0.415\text{eV}$. Surrounding this AF dome we show the magnitude of λ_M in the form of a blue color scale (see color bar). The AF transition points were estimated via extrapolations of the (inverse) susceptibilities (varying T) or the eigenvalues (varying V). The low V RKKY transition (below $V = 0.15$) is drawn as a guide to the eye, all other points are connected via straight lines.

Red and bluish circles signal an ordered and unordered solution, respectively. The former corresponds to $\lambda_M > 1$ whereas the color scale of the latter can be directly translated to the size of λ_M itself. From this data we extracted the magnetic dome (orange area): For small hybridization strength V , the boundary follows the perturbative result of the RKKY interaction: $T^{\text{RKKY}} = \alpha V^4$. Beyond $V = 0.15\text{eV}$ the Kondo temperature becomes significant enough to compete with the magnetic ordering, resulting in a deviation of the polynomial scaling, until, eventually, a temperature maximum around $V = 0.36\text{eV}$ is formed at around $\beta = 40\text{eV}^{-1}$. Going beyond, a further increase of the hybridization strength leads to a rapid suppression of the ordering temperature: The Kondo physics dominates the system and the magnetic dome vanishes. Through the competition of energy scales a quantum critical [329] point [225] emerges at around $V = 0.41\text{eV}$.⁴¹

⁴¹ When plotting the phase diagram as temperature vs. hybridization strength, see Fig. 3.11, variations in the interaction strength U have a major effect on the antiferromagnetic dome: increasing (decreasing) U leads to a suppression (boost) of the effective exchange-interaction strength $J = V^2/U$ which in turn leads to a amplification (diminishment) of the dome (since the Kondo scale is affected exponentially) in both its extent on the V -axis and T -axis.

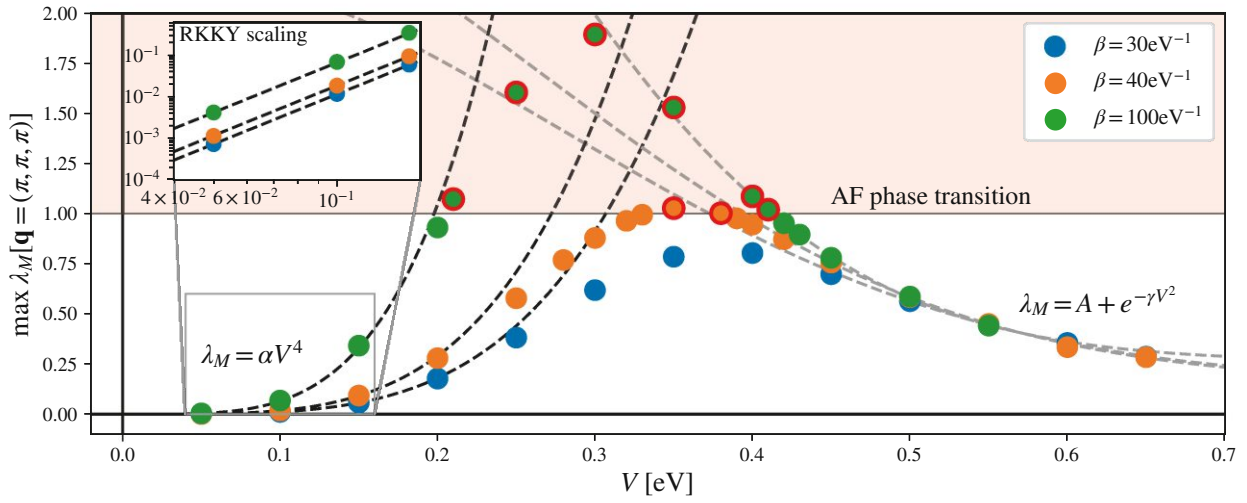


Figure 3.12: Leading magnetic eigenvalue for three (inverse) temperatures along the V -axis. We find three regimes: Small hybridization strengths V can be fitted via RKKY behavior $\lambda_M \propto \alpha V^4$, see inset. At intermediate hybridization a peak is formed formation that can be fitted via a Lorentzian. Large hybridization can be fitted proportional to Kondo behavior $\lambda_M \propto A + \exp(-\gamma V^2)$. Ordered points are marked with a red outline.

Evaluating the antiferromagnetic tendency in more detail by analyzing them at a fixed temperature in Fig. 3.12 we distinguish three regimes:

- (i) At small hybridization, the leading eigenvalue directly corresponds to the RKKY critical temperature $\lambda_M \propto \alpha V^4$, see polynomial fit in the top left inset of Fig. 3.12.
- (ii) In between the weak and strong hybridization regime, the balance between Kondo and RKKY physics leads to a smooth peak of Lorentzian form $\lambda_M \propto \frac{B}{(V - \bar{V}_{\max})^2 + C^2}$ centered at a crossover hybridization \bar{V}_{\max} (fit not shown).
- (iii) At large hybridization any RKKY ordering is fully suppressed leading to almost temperature independent eigenvalues beyond $V = 0.5$ with a V -dependence that can be fitted to $\lambda_M \propto A + \exp(-\gamma V^2)$ (“Kondo-esque” behavior).

Quantum critical point

Before discussing realistic Kondo insulators in Section 3.2, we briefly examine the behavior of the magnetic fluctuations around the quantum critical point. In Fig. 3.13 we show the inverse magnetic susceptibilities at the ordering vector for a wide temperature range.

In the left panel, we see the same Curie-Weiss behavior as already observed in the uniform ($\mathbf{q} = \mathbf{0}$) response, see Fig. 3.9. The right panel instead focuses on the low temperature regime for hybridization

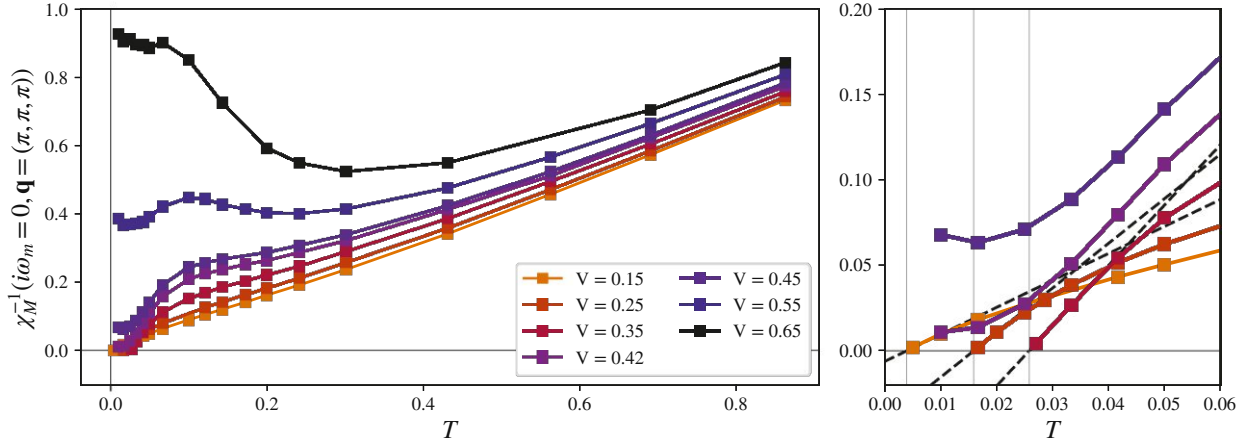


Figure 3.13: Inverse magnetic susceptibility for the ordering vector $\mathbf{q} = (\pi, \pi, \pi)$. The apparent Gaussian fluctuations $\chi^{-1} \propto (T - T_{\text{Néel}})^{-1}$ are upheld for all hybridization strength below the critical $V_c = 0.41\text{eV}$ (QCP). Beyond, the fluctuations become bounded and a plateau forms towards $T \rightarrow 0$.

strengths up to $V = 0.45\text{eV}$, i.e. a scan over the full magnetic dome going beyond the QCP. The main message is simple: the quantum critical point does not influence the Gaussian fluctuations expected from a bosonic mean-field theory such as DMFT [241, 330]. Below the critical V_c these fluctuations manifest themselves as a linear dependence of the inverse magnetic susceptibility above the finite Néel temperature: $\chi_M^{-1} \propto (T - T_{\text{Néel}})^{-\gamma}$ with $\gamma = 1$. In the considered regime we find a correlation between transition temperature and steepness of the $\chi^{-1}(T)$ curves. For a given temperature T , this implies larger magnetic fluctuations for a lower Néel temperature which could be explained via the suppression of the Kondo temperature for smaller hybridization values V . Indeed, in order to capture the effects induced by the QCP, a full two-particle feedback of the antiferromagnetic fluctuations is necessary, e.g., with the previously introduced dynamical vertex approximation [225].

Minimal deviations away from the QCP, beyond the AF dome ($V = 0.42\text{eV} > V_c$), lead to susceptibilities that at first come from a similar value at high T . At low enough temperatures the fluctuations become bounded and, instead of a vanishing χ^{-1} , a plateau forms. Beyond V_c , larger hybridization strengths V lead to a larger susceptibility boundary. Let us note that due to the difficulties involved in the sampling of the two-particle vertex at large hybridization strengths, the low temperature results are somewhat noisy. This noisiness is mostly apparent at $V = 0.65\text{eV}$ (black line in left panel of Fig. 3.13).

Summarizing, the periodic Anderson model represents a minimal multi-orbital model that encodes the essential ingredients for a Kondo insulator. The intrinsic Kondo effect that, at low enough temperatures, binds the semi-localized, asymptotically free spins to conduction electrons is also at the heart of the electronic phenomena in realistic materials with partially filled 4f or 5f shells. Through

the hybridization between localized and extended states a (one-particle) gap may form which, in combination with strong correlation effects, generates signatures in both spectral observables and in the spin (and charge) responses. The emergence of magnetic order through the RKKY interaction, strong spin-orbit couplings and complex crystal-field splittings provide additional energy scales and complications, and an overall complex platform for the realization of Kondo materials. To this end in the next Section, we finally transition to a realistic setup with the aim to describe the Kondo insulator $\text{Ce}_3\text{Bi}_4\text{Pt}_3$.

3.2 Resistivity saturation in $Ce_3Bi_4Pt_3$

- This Section is based on “Resistivity saturation in Kondo insulators” by [Matthias Pickem](#), Emanuele Maggio, and Jan M. Tomczak [7]. Adopted text passages are marked accordingly and have been, for the sake of readability, partially modified.
- Charge self-consistent DFT+DMFT and Kubo transport calculations have been performed by Jan M. Tomczak.
- Elements of the linear-response methodology that our data interpretation in this Section builds on, was first proposed in Ref. [331]. This methodology is developed into a comprehensive transport formalism in Sec. 3.3.

As introduced in Section 3.1, in Kondo insulators [287] the formation of bound-states between quasi-localized f -states and conduction electrons leads to the opening of a narrow hybridization gap at the Fermi level. When this hybridization is coherent, the resistivity exhibits an activation-type behaviour. This semiconductor-like regime has as upper bound the Kondo lattice temperature, above which the local f -moments break free, inducing an insulator-to-metal crossover. This Kondo effect has been exhaustively studied over the last decades [212, 250, 332]. A more recent focus is the experimental observation of a lower bound to the semiconductor compartment, see Fig. 3.14 for the example of $Ce_3Bi_4Pt_3$ [323, 333, 334]: Below an inflection temperature T^* the resistivity levels off from exponential rise and enters a saturation regime—indicative of residual conduction. Possible explanations include exhaustion regimes (where extrinsic impurities pin the chemical potential), off-stoichiometry and impurity-band conduction [306, 335], as well as, metallic surface states short-circuiting the gapped bulk. The latter can be an inevitable consequence of the non-trivial insulating bulk found in topological Kondo insulators [259].

Here, we develop an alternative mechanism in which residual conduction derives from finite lifetimes of intrinsic carriers of the (3D) bulk. We show that realistic many-body simulations, supplemented by a simple treatment for disorder, capture the puzzling resistivity in the (non-topological) Kondo insulator $Ce_3Bi_4Pt_3$. We then distil essential ingredients from a reductionist model, establish a microscopic understanding, and provide a phenomenological form of the resistivity with which experiments can be readily analyzed.

3.2.1 Experimental evidence

Cubic intermetallic $\text{Ce}_3\text{Bi}_4\text{Pt}_3$ is a 4f, 5d, prototypical Kondo insulator [212, 250, 253]: Spectroscopic [336, 337] and susceptibility [253] (also in high magnetic field [302, 338]) are consistent with the Kondo scenario [328, 339], see Section 3.1. While a topological bulk state has been envisaged [340], experiments argue against surface-dominated transport [323].⁴²

Magnetic susceptibility measurements [341] reveal a peak in χ_M at around 80K, below which, eventually, Kondo singlets are formed. Similar to many other Kondo materials [342, 343], $\text{Ce}_3\text{Bi}_4\text{Pt}_3$ retains a non-magnetic ground state for all considered temperatures, i.e. $T_K > T_{\text{RKKY}}$.

Further constraints for a theory of resistivity saturation in $\text{Ce}_3\text{Bi}_4\text{Pt}_3$ come from, see Fig. 3.14:

- (i) pressure-dependent measurements that show a substantial increase in the crossover temperature T^* , accompanied by a decrease of the saturation value $\rho(T \rightarrow 0)$
- (ii) radiation-damaged samples in which residual conduction is successively suppressed, while T^* is unaffected.

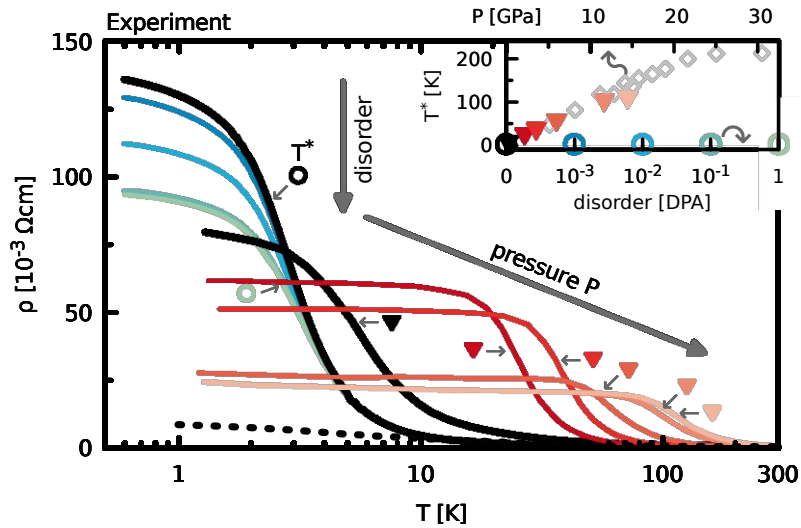


Figure 3.14: Experimental resistivity saturation in $\text{Ce}_3\text{Bi}_4\text{Pt}_3$. Below an inflection temperature T^* (indicated by small arrows), experimental resistivities $\rho(T)$ [333, 334, 323] deviate from activation-like behavior ($T > T^*$: $\rho \propto \exp(+\frac{\Delta}{2k_B T})$) and enter a regime of resistivity saturation ($T < T^*$). Pressure and disorder affect the resistivity and the crossover temperature T^* differently, see main text. Data reproduced from Refs. [333, 334, 344].

⁴² A topological surface state would lead to residual conduction, short circuiting the bulk, i.e. $\sigma_{\text{total}} = \sigma_{\text{surface}} + \sigma_{\text{bulk}}$. Below certain temperatures, the surface conductivity would dominate the thermally activated bulk contribution, leading to a resistivity saturation.

Below an inflection temperature T^* (indicated by small arrows), experimental resistivities $\rho(T)$ [333, 334, 323] deviate from activation-like behavior ($T > T^*$: $\rho \propto \exp(+\frac{\Delta}{2k_B T})$) and enter a regime of resistivity saturation ($T < T^*$). Pressure and disorder affect the resistivity differently: under pressure (black and shades of red; from Cooley *et al.* [333]) the crossover temperature T^* (labeled with colored triangles and reported in the inset) grows significantly and the saturation value $\rho(T \rightarrow 0)$ decreases. Radiation-induced disorder (black and blue to green; from Wakeham *et al.* [334]) only suppresses $\rho(T \rightarrow 0)$, while T^* (labeled with colored circles and reported in the inset) remains constant. Also shown are results at ambient from Katoh *et al.* [344] (dashed black line). Differences between black curves (solid and dashed) demonstrate a strong sample dependence. In the inset we illustrate the dependence of T^* on pressure (upper x axis; red-shaded triangles, gray diamonds from Campbell *et al.* [323]) and disorder (measured in displacements per atom (DPA); lower x axis; blue to green open circles) [334].

In the following, we will start off our analysis of $Ce_3Bi_4Pt_3$ via state-of-the art DFT+DMFT simulations, as introduced in Section 2.2.3. To this end we will analyze the structural details and the resulting electronic states of varying (hydrostatic) pressures. From them, we will calculate (dc) resistivities, as first introduced in Section 2.6, which we will use as a guide to construct a minimalist, microscopic theory.

3.2.2 Many-body corrections

3.2.2.1 Charge self-consistent approach

Using charge self-consistent DFT+DMFT, we simulate the bulk response of $Ce_3Bi_4Pt_3$ under pressure. DFT+DMFT [94] calculations are performed with the code of Haule *et al.* [32], including charge self-consistency, spin-orbit coupling, and using a continuous-time quantum Monte-Carlo solver. In the correlated subspace, rotationally invariant interactions for the Ce-4*f* shell were parametrized by a Hubbard $U = 5.5\text{eV}$ and Hund's $J = 0.68\text{eV}$ in conjunction with the nominal double-counting scheme [32]; Ce-4*f* hybridizations were allowed in an energy window of $\pm 10\text{eV}$ around the Fermi level. At ambient pressure, this setup yielded excellent results for spectral and optical properties [339] (see also Ref. [345]).

The concept of charge self-consistency extends the “DMFT on top of DFT” approach (employed in the previous Chapter) and effectively “marries” the two methods into DFT+DMFT. Self-consistency is reached whenever the self-energy corrected ground-state density of DFT leads to an projected/down-folded impurity, that generates the self-energy that initially corrects the electron density. That is, on top of the usual DMFT self-consistency (for the local Green's function), we require a self-consistency

on a “global” level (for the ground-state density). In practice this is done via:

- (i) Solving of the Kohn Sham equations with given exchange-correlation potential: electron density $\rho(\mathbf{r})$, Kohn Sham eigenvalues $\varepsilon_{\mathbf{k}n}$ and chemical potential μ_{KS} .
- (ii) Downfolding onto the correlated subspace: Hamiltonian $H(\mathbf{k})$ ⁴³ and computing the non-interacting impurity Green’s function G_0 and corresponding hybridization function Δ .
- (iii) Computing the interacting Green’s function of the DMFT impurity with impurity chemical potential: $G_0 \rightarrow G[\mu_{\text{DMFT}}]$.
- (iv) Upfolding of the interacting Green’s function / self-energy into the Kohn-Sham basis and calculating the feedback onto the electron density and updating the chemical potential: $\Delta\rho(\mathbf{r})$, μ_{KS} .
- (v) Iterating until self-consistency is reached.

For a more technical description of this procedure please refer to the literature, e.g., Refs. [32, 98, 99].

The full charge density can then be written as [346]

$$\rho(\mathbf{r}) = \rho_{\text{KS}}(\mathbf{r}) + \Delta\rho(\mathbf{r}) = \frac{1}{\beta} \sum_n \left(\langle \mathbf{r} | \hat{G}_{\text{KS}} | \mathbf{r} \rangle + \langle \mathbf{r} | \hat{G} - \hat{G}_{\text{KS}} | \mathbf{r} \rangle \right), \quad (3.34)$$

with \hat{G}_{KS} as the non-interacting Green’s function of the Kohn-Sham eigenvalues and chemical potential. As the self-consistently determined Kohn-Sham density ρ_{KS} already contains the full charge of the system, the charge correction must fulfill

$$\int d^3r \Delta\rho(\mathbf{r}) \stackrel{!}{=} 0. \quad (3.35)$$

Through this scheme, pivotal effects may occur in the crystal- and electronic structure:

- (i) Through the electron density feedback the orbital polarization of the correlated impurity and the electronic structure of the uncorrelated bands may be adjusted.
- (ii) Magnetic moments, effective exchange-interactions and total energy may change.
- (iii) The crystal structure may relax to a different ground state due to the changes to the electron density. This can effect both the unit cell volume and its internal atomic positions. Here, we do not include this effect.

Whereas in high symmetry structures, these effects are mostly minor in nature (strong orbital polarization, e.g., the previously discussed splitting of the t_{2g} orbitals in Section 2.3, tend to be weakened), they can be crucial when analyzing structural phase transitions [155].

⁴³The employed code of Haule (and other modern DFT+DMFT packages) does not compute maximally localized Wannier function and is, instead, based on projection/embedding. For more details, see Ref. [32].

3.2.2.2 Electronic structure and hybridization gap

We display the non-inversion symmetric crystal structure of $Ce_3Bi_4Pt_3$ in Fig. 3.15: Ce is bonded in a 12-coordinate geometry to four equivalent Pt and eight equivalent Bi atoms [288, 347]. We only highlight the Ce-Pt bond as connected (green-to-blue) lines. Whereas all Ce and Pt ions are spatially restricted by the symmetry of the $\bar{I}43d$ space group, Bi is essentially free to move along the internal (u, u, u) line. This internal parameter was previously assumed to be $u = 1/12$, see Refs. [339, 348].

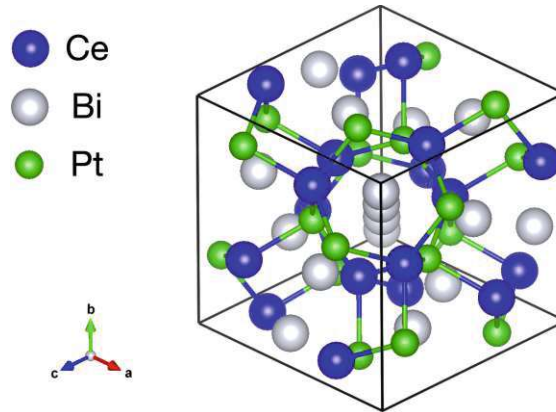


Figure 3.15: Crystal structure of cubic $Ce_3Bi_4Pt_3$ with Bismuth fixed to the $u = 1/12$ position, see main text. Cerium: blue, Bismuth: gray, Platinum: green spheres. The hybridization gap of the band structure stems from the overlap of the Ce 4f states with the 5d states of the neighboring Pt, indicated by the blue-to-green bond. Figure generated with VESTA [18].

For illustrative purposes, we show the band structure for this exact u -value calculated by a purely DFT calculation at zero pressure with PBE [23] as the exchange-correlation potential in Fig. 3.16. Additionally we also show the partial density of states of the most significant atomic character in the gap formation. The hybridization gap is mostly stemming from a mixture of Ce 4f and Pt 5d states generating a hybridization gap of size $\Delta_N = 180\text{meV}$. Cerium states both dominate the conduction and the valence band character with only a minimal Pt character involved (red). The situation is more involved around the edges of the (upper boundary) gap, see inset. Due to the additionally formed Γ -pocket, displaying a heavily mixed orbital character, the hybridization gap is reduced by almost a factor of 2.

The overall situation is similar to the periodic Anderson model of Section 3.1 in the sense that turning off the Ce-4f orbital hybridization to surrounding atoms, the band-structure becomes metallic, see Ref. [212]. Indeed, $La_3Bi_4Pt_3$ is a metal [253]. Interestingly, the situation is reversed in $R_3Bi_4Au_3$ with $R=La,Ce$. There, the one extra electron from the precious metal makes already $La_3Bi_4Au_3$ band-insulating, and yet another electron from Ce turns $Ce_3Bi_4Au_3$ (semi)metallic [349].

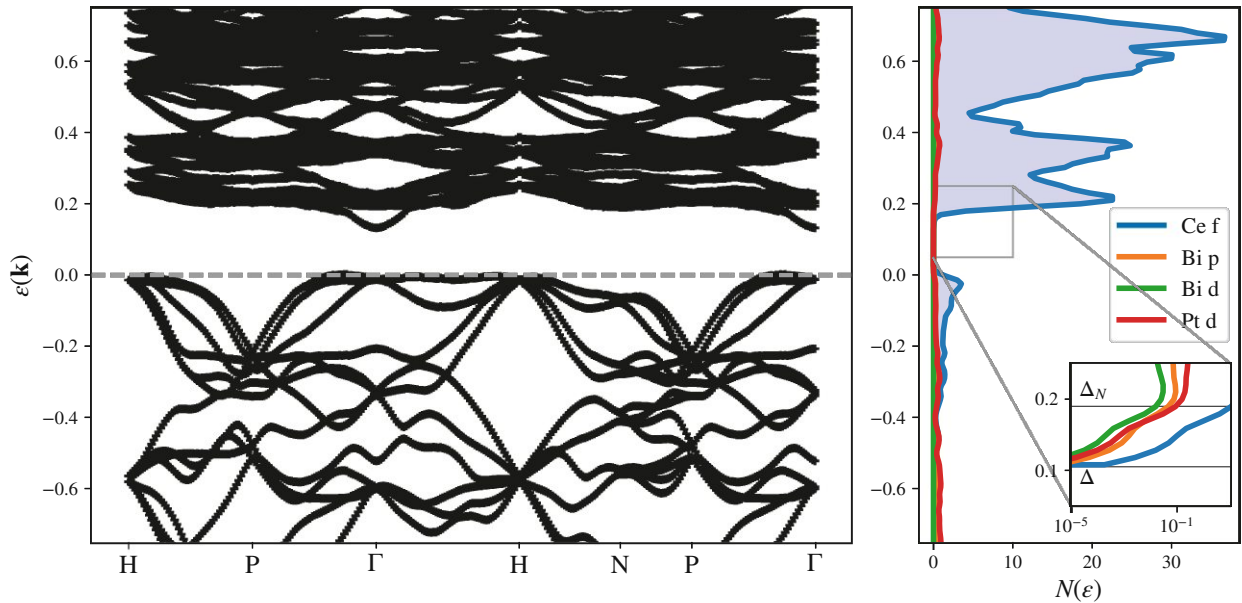


Figure 3.16: Exemprary $\text{Ce}_3\text{Bi}_4\text{Pt}_3$ band structure determined DFT calculation at zero pressure, Bismuth position at $u = 1/12$ (see main text) and PBE exchange-correlation potential (left) and its corresponding partial density of states. The hybridization gap ($\propto \Delta_N$) mostly stems from an interplay between Ce 4f (blue) and the Pt 5d states (red). The minimal gap Δ is, however, defined via the Γ -pocket which displays a heavily mixed orbital character (see inset). In order to circumvent this “problem” we define the relevant Kondo energy scale via the band gap at the N point Δ_N instead.

At finite pressures we use lattice constants from experimental fits to the third-order Birch-Murnaghan equation-of-state [323]. While the Wyckoff site 12a (12b) uniquely defines the placement of Ce (Pt) atoms, we relax the internal positions of Bi in density-functional theory (DFT) as implemented in WIEN2k [21, 22] using the PBE functional [23]. The essential band structure results are summarized in Fig. 3.17. The internal atomic position (u, u, u) of Bi (bottom panel) is critical for the (unrenormalized) DFT band gap Δ (top panel) as a function of pressure:

- (i) The often assumed position $u = 1/12$ (blue, used previously in Ref. [339]) leads to a monotonous increase of both the band gap Δ as well as the corresponding Δ_N that measures the gap from the valence-band maximum up to the conduction-band minimum at the N -point in the Brillouin zone, see Fig. 3.16 and also Ref. [305].
- (ii) The fully relaxed $u(P = 0)$ (green) applied to the full pressure range unsurprisingly shows consistent behavior compared to the $u = 1/12$ case.

(iii) The fully relaxed $u(P)$ (red) is qualitatively different: While Δ_N increases monotonously with pressure—indicative of boosted hybridizations—, the fundamental gap Δ decreases above a critical pressure of about $P_c \sim 15$ GPa. Beyond P_c , the centres of mass of conduction and valence states are still pushed apart, but a new dispersive conduction-band minimum emerges, that moves towards the Fermi level when increasing pressure further. Therewith the gap Δ ceases to be a good indicator for the hybridization strength (and hence the Kondo coupling) in this compound. For this reason, Ref. [305] introduced the gap Δ_N as measured up to the N -point in the Brillouin zone—a region unaffected by the new conduction-band minimum—as proxy for the Kondo coupling.

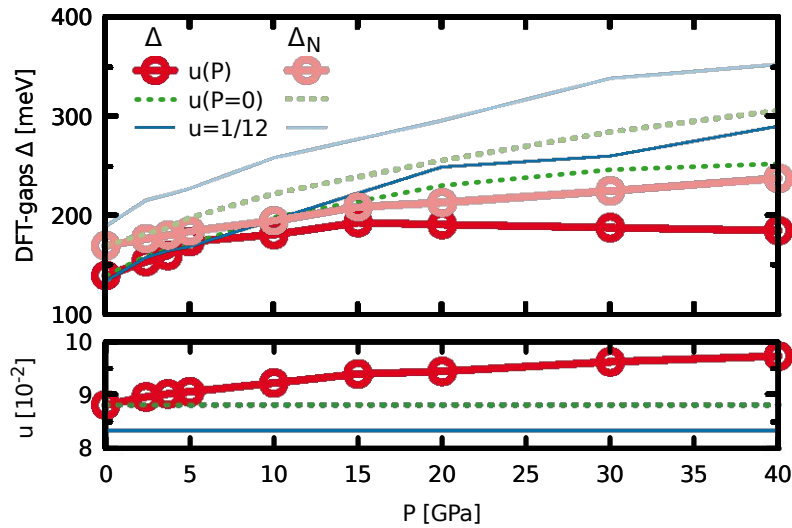


Figure 3.17: Band-gaps of $Ce_3Bi_4Pt_3$ in density functional theory (DFT). The top panel shows the DFT (=unrenormalized) band gap Δ of $Ce_3Bi_4Pt_3$ as a function of pressure (i.e., a varying unit-cell volume according to the experimental equation of state [323]) for different internal atomic positions (u, u, u) of Bi (indicated in the bottom panel): fully relaxed $u(P)$ (red), fixed to the relaxation at ambient pressure (green), and the often assumed position $u = 1/12$ (blue, used previously in Ref. [339]). Curves with faded colours indicate the corresponding Δ_N that measures the gap from the valence-band maximum up to the conduction-band minimum at the N -point in the Brillouin zone (see also Ref. [305]). While Δ_N increases monotonously with pressure—indicative of boosted hybridizations—, the fundamental gap Δ decreases above a critical pressure of about 15 GPa.

3.2.2.3 Spin-orbit coupling and N-fold degeneracy

Due to the large spin-orbit coupling present in rare-earth compounds, the spin (as has been assumed in Chapter 2) no longer represents a good basis or quantum number. Instead, we have to consider the total angular momentum J . In $\text{Ce}_3\text{Bi}_4\text{Pt}_3$, cerium obtains a nominal configuration of $4f^1$ with resulting total electronic spin $S = 1/2$, leading to

$$J = L - S = \frac{5}{2} \quad (3.36a)$$

$$J = L + S = \frac{7}{2} \quad (3.36b)$$

as “good” quantum numbers. In the absence of an external magnetic field, magnetic ordering or crystal-field the secondary total angular momentum quantum numbers remain degenerate

$$m_{J=5/2} \in \left\{ -\frac{5}{2}, -\frac{3}{2}, -\frac{1}{2}, +\frac{1}{2}, +\frac{3}{2}, +\frac{5}{2} \right\} \quad (3.37a)$$

$$m_{J=7/2} \in \left\{ -\frac{7}{2}, -\frac{5}{2}, -\frac{3}{2}, -\frac{1}{2}, +\frac{1}{2}, +\frac{3}{2}, +\frac{5}{2}, +\frac{7}{2} \right\} \quad (3.37b)$$

for each of the two juxtaposed J states. Once crystal-field induced multiplet effects come into play only the pairs $(m_J, -m_J)$ are, however, certain to be degenerate, assuming that no external field is applied or internal magnetic order is established.

Besides the obvious complications in the construction of the Hamiltonian and the sampling of the interacting Green’s function in the DMFT part of the DFT+DMFT approach, the larger number of $4f$ states with comparable energies in Kondo materials bring on further complications. Deducing “PAM-esque” one-particle parameters stemming from the bandwidth of the conduction band $W = \mathcal{O}(3-5)\text{eV}$, and the resulting band gap of $\Delta = \mathcal{O}(100-300)\text{meV}$ we find the hopping and hybridization strengths to be in the same energy range $V = \mathcal{O}(200-400)\text{meV}$. Furthermore, the larger on-site interaction of $U = 5.5\text{eV}$, should lead to a massive boost of antiferromagnetic fluctuations and thus a sizable increase of the AF dome in the temperature vs. hybridization phase diagram, see Section 3.1. Altogether, naively mapped to a one-orbital model these parameters always lead to an ordered magnetic state towards zero temperature.

Here is where the multi-orbital nature of cerium comes into play: through possible geometric frustration caused by the complex ion arrangement in the crystal structure, see Fig. 3.15, and the large number of involved $4f$ states, accompanied by strong spin-orbit coupling, the Kondo temperature may be orders of magnitude larger than what is anticipated from the one-band case. Indeed, systems displaying an (exact) N-fold degeneracy the exponential factor of the Kondo temperature becomes

significantly boosted [239]

$$T_K(N) \propto \exp\left(-\frac{1}{NJ\rho}\right) \quad (3.38)$$

where J and ρ are the effective exchange interaction and the density of states of the involved conduction band at the Fermi level, respectively. At high temperatures, due to the smearing of the energy levels modified by the spin-orbit coupling, cerium indeed acts as such an N -fold ($N = 6$ for the $J = 5/2$ states) degenerate ion. For low temperature, the physics is instead dominated by the lowest lying degenerate state, see next Section. This acts as stabilization of the local-moment lattice where the naively expected magnetic order is not apparent in experiment [350].

Let us also note, that strong antiferromagnetic fluctuations may also be strongly suppressed for non-integer filling. There the phenomenon of valence fluctuations leads to the demagnetisation [255].

3.2.2.4 Dynamical mean-field theory results

Having established an overview of the unrenormalized insulating characteristics, we turn our attention to many-body corrections treated within dynamical mean-field theory.

For illustrative purposes we showcase the imaginary part of the self-energy for varying pressure P of the dominant $J = 5/2$, $m_j = 5/2$ component at $\beta = 200 \text{ eV}^{-1}$ in the left panel of Fig. 3.18. The selected pressures $P = 0\text{GPa}$, $P = 5\text{GPa}$, and $P = 10\text{GPa}$ showcase the expected Fermi-Liquid behavior whose low-energy scattering rate can be extracted via a polynomial fit to $i\omega \rightarrow 0$ (see the zoom in the right panel). This dominant $4f$ contribution to the electronic state is thus a direct reflection of the observed flat band signature as observed in the periodic Anderson model in Section 3.1.2.3.

Naturally, in hybridization gap insulators, a smaller unit cell through increased pressure leads to stronger orbital hybridization and thus a larger gap opens up, see Eq. (3.16). In this context, the increased gap sizes are reflected in a smaller scattering rates $\Gamma = -\Im\Sigma(\omega = 0)|_{J=5/2, m_j=5/2}$ as the states contributing to the scattering at the Fermi level are pushed further away ($\Gamma \propto \omega^2$).

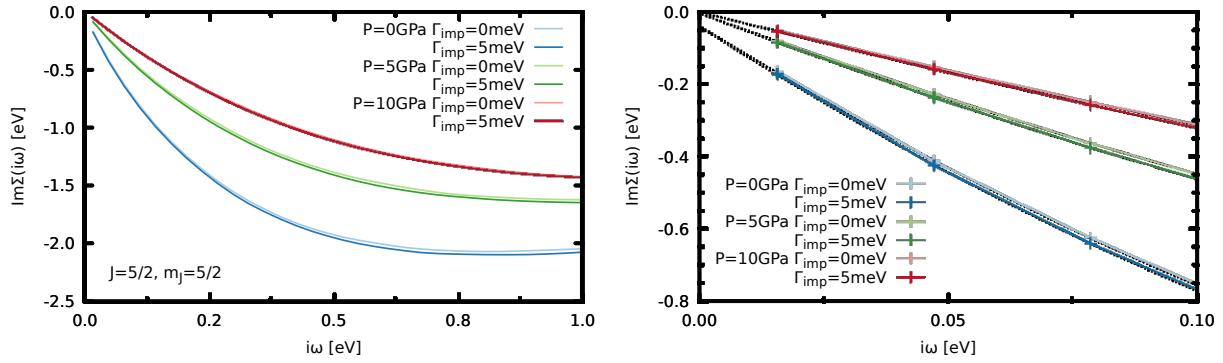


Figure 3.18: Including the impurity scattering rate in DMFT for $\text{Ce}_3\text{Bi}_4\text{Pt}_3$. For varying pressure P , we show the impact of including an impurity scattering rate $\Gamma_{imp} = 5\text{meV}$ already in the DMFT self-consistency for the dominant $J = 5/2$, $m_J = 5/2$ component of the self-energy at $\beta = 200/\text{eV}$. In the left panel we see a small enhancement of $\Im\Sigma(i\omega_n)$ when impurity scattering is included (compare dark to light colours). For all pressures the enhancement of scattering is smaller than the added impurity scattering rate. Further, at low pressure, $P = 0$, $\Delta\Im\Sigma(\omega = 0)$ is small against the total scattering rate $\Im\Sigma(\omega = 0) \approx 40\text{meV}$. At larger pressures, both the total scattering rate and the enhancement shrink drastically, as the gap in the spectral function increases and less carriers can scatter.

Non-canonical pressure dependence

Next, we briefly turn to $\text{Ce}_3\text{Bi}_4\text{Pt}_3$ at high pressures, where Campbell *et al.* [323] found an insulator-to-metal crossover, cf. Fig. 3.20b. Indeed pressure-induced metallic phases are rather common for correlated semiconductors, e.g., for SmB_6 [351, 352], CeRhSb [353] and FeSi [354]. We consider three candidate mechanisms: Changes in (1) correlation effects, (2) the valence, (3) structural aspects. (1) Our many-body calculations reveal that pressure reduces electronic correlations: Effective masses shrink from $m^*/m \sim 10$ at $P = 0$ (see also Ref. [339]) to a mere ~ 2 at $P = 40\text{GPa}$. Also electron-electron scattering becomes less prevalent: The rate Γ is—for all pressures—of the form γT^2 (see bottom panels of Fig. 3.19), with γ significantly decreasing with pressure. Reduced many-body renormalizations amplify the pressure enhancement of the non-interacting hybridization (see point (3), below), leading to larger gaps. In the absence of other factors, this is the canonical behaviour of Kondo insulators. (2) Changes in the f -valency drive metal-insulator transitions, e.g., in rare-earth monochalcogenides [355]. In $\text{Ce}_3\text{Bi}_4\text{Pt}_3$, congruent with experiment [333, 323], pressure decreases (increases) the simulated $4f$ -occupation n_f (valence $4 - n_f$) from $n_f = 1.05$ ($P = 0$) to 0.96 ($P = 40\text{GPa}$)—while temperature has little influence [356]. $4f^0$ ($J = 0$) admixtures augment with P —accounting for the larger valence. Yet, also $4f^2$ (and $4f^1$ with $J = 7/2$) contributions grow—

increasing the mixed valence character. Still, the probability of finding the system in a $4f^1$ -state with $J = 5/2$ merely decreases quantitatively from 80% ($P = 0$) to $\sim 55\%$ ($P = 40\text{GPa}$)—excluding a dominantly valence-driven metallization. (3) Instead, we unravel the non-monotonic transport to originate from two counter-acting structural trends within the confines of space group $I\bar{4}3d$: Globally, pressure shrinks the lattice, enhancing hybridization gaps. While the atomic coordinates of Ce and Pt are dictated by symmetry, the local Bi position (u, u, u) may vary. Minimizing total energies, we find $u = 0.088$ at $P = 0$ —in agreement with the experimental $u = 0.086$ [357]—and predict a much larger $u = 0.097$ at $P = 40\text{GPa}$, see Fig. 3.17. This seemingly minute modification drastically changes inter-atomic hybridizations: Instead of a monotonic increase (realized for $u = \text{const}$), a critical pressure emerges above which the gap decreases. Hence, $Ce_3Bi_4Pt_3$ exhibits a peculiar high-pressure behaviour, not canonical for Kondo insulators in general.

Explicit vs. implicit scattering rate

In order to avoid DMFT calculations for varying impurity scattering, the latter was only added to the transport simulations in the next Section. Before discussing these transport results however, we assess this approximation beforehand: We show the impact of including an impurity scattering rate $\Gamma_{imp} = 5\text{meV}$ already in the DMFT self-consistency for the dominant $J = 5/2$, $m_J = 5/2$ component of the self-energy at $\beta = 200/eV$. In the left panel of Fig. 3.18 we see a small enhancement of $\Im\Sigma(i\omega_n)$ when impurity scattering is included (compare dark to light colours). This is expected, as the impurity scattering leads to more incoherent spectral weight in the gap, which, in turn, provides carriers for further electron-electron scattering. This cooperation of different scattering rates enhances the lifetime signatures. The right panel shows a low-energy zoom of the left panel. There, the dotted black lines are polynomial fits to the Matsubara self-energy from which we extract an enhancement of low-energy scattering $\Delta\Im\Sigma(\omega = 0) = |\Im\Sigma_{\Gamma_{imp}=5\text{meV}}(\omega = 0)| - |\Im\Sigma_{\Gamma_{imp}=0}(\omega = 0)| = 3.7/1.5/0.3\text{meV}$ for $P = 0/5/10\text{GPa}$, respectively. For all pressures the enhancement of scattering is smaller than the added impurity scattering rate. Further, at low pressure, $P = 0$, $\Delta\Im\Sigma(\omega = 0)$ is small against the total scattering rate $\Im\Sigma(\omega = 0) \approx 40\text{meV}$. At larger pressures, both the total scattering rate and the enhancement shrink drastically, as the gap in the spectral function increases and less carriers can scatter. Thus, adding the impurity scattering rate to the DMFT self-consistency slightly enhances the effects that we are studying, while leaving all qualitative trends intact.

3.2.3 Conductivity tensor

Having established the intricacies of the non canonical Kondo insulating behavior of $Ce_3Bi_4Pt_3$ under pressure we finally turn our attention to the transport properties reported in Fig. 3.14 [333, 334, 344].

To quantitatively simulate the resistivity responses we employ the aforementioned DMFT results and (i) simulate disorder by an added impurity scattering in the self-energy, (ii) simulate pressure with the aforementioned crystal structures with reduced volume and optimize Bismuth position. To obtain the conductivity tensor, as first introduced in Section 2.6, we simply evaluate the corresponding multi-orbital equation (here expressed directly in terms of spectral functions $A(\omega)$) in the Kubo formalism, neglecting all vertex correction.

3.2.3.1 Kubo response

Contrary to the previous analysis where we focused on a sub selection of most dominant states, captured within the one-band Hubbard model, here the conductivity is calculated on the full energy range used within our DFT+DMFT setup. Neglecting vertex corrections⁴⁴, the generalized conductivity tensor in the Kubo formalism (in SI units) reads [64, 358, 359]

$$\Re\sigma_{\alpha\beta}(\omega) = \frac{2\pi e^2 \hbar}{V} \sum_{\mathbf{k}} \int_{-\infty}^{\infty} d\omega' \frac{f_{FD}(\omega') - f_{FD}(\omega' + \omega)}{\omega} \text{Tr} [v_{\alpha}(\mathbf{k})A(\mathbf{k}, \omega')v_{\beta}(\mathbf{k})A(\mathbf{k}, \omega' + \omega)]. \quad (3.39)$$

with $A(\mathbf{k}, \omega)$ corresponding to the spin- and momentum-resolved spectral function, v_{α} as the optical element in (Cartesian) direction α , and a prefactor consisting of the spin multiplicity 2, the elementary charge e and the volume of the unit cell V . Here the summation of all (internal and external) orbital degrees of freedom, as derived in Section 2.6.2, is replaced by an efficient evaluation of a trace over matrices in the orbital/band basis. Expressed as an Einstein summation the equivalence to the bubble becomes apparent: $\Re\sigma \propto \sum_{i=j,a,b,c} v_{ia}A_{ab}v_{bc}A_{cj}$. The optical conductivity then simplifies to the DC contribution in the dynamical limit

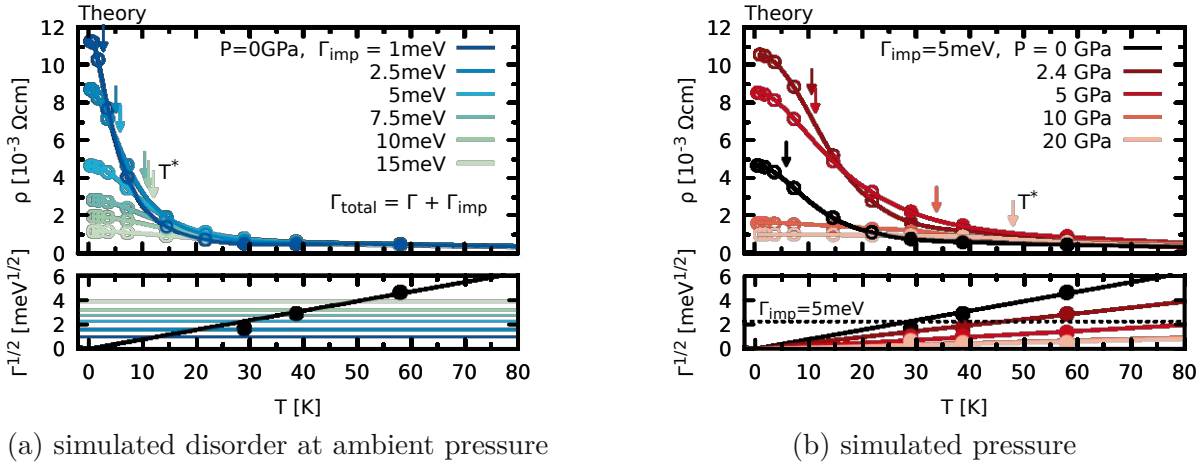
$$\begin{aligned} \Re\sigma_{\alpha\beta}^{DC} &= \lim_{\omega \rightarrow 0^+} \Re\sigma_{\alpha\beta}(\omega) \\ &= \frac{2\pi e^2 \hbar}{V} \sum_{\mathbf{k}} \int_{-\infty}^{\infty} d\omega' \left(-\frac{\partial f_{FD}}{\partial \omega'} \right) \text{Tr} [v_{\alpha}(\mathbf{k})A(\mathbf{k}, \omega')v_{\beta}(\mathbf{k})A(\mathbf{k}, \omega')]. \end{aligned} \quad (3.40)$$

The resulting resistivities for $\text{Ce}_3\text{Bi}_4\text{Pt}_3$ are illustrated in Figs. 3.19 for varying (a) disorder and (b) pressure P and are simulated with the full self-energy $\Sigma(\omega)$ as described in Ref. [320], using dipole transition matrix elements [360]. The extracted crossover temperature T^* and resistivity ratios on the other hand are illustrated in Fig. 3.20. We mimic the effect of disorder [361] with an added scattering term Γ_{imp} to the full self-energy $\Sigma(\omega)$ which was only included in the evaluation of Eq. (3.40) and

⁴⁴We can motivate that, here, vertex corrections do not change the qualitative picture: impurity corrections to the current vertex of intrinsic carriers via ladder diagrams mainly reduce the decay rate Γ in the response function's prefactor by filtering out forward scattering [239], i.e., they do not change the essential physics. Corrections from crossed diagrams can be important, e.g., in doped semiconductors where they may lead to metal-to-insulator transitions via localization. Here, instead, we are concerned with metallic signatures in an a priori insulating host.

not the DFT+DMFT itself.

The scattering rates Γ displayed in Fig. 3.19 (bottom) are obtained from the same self-energy $\Sigma(\omega)$ by averaging over the $J = 5/2$ components that dominate spectral weight near the Fermi level: $\Gamma = -\Im \langle \Sigma(\omega = 0) \rangle_{J=5/2}$. Finding that in all cases $\Gamma(T) \propto T^2$, we use this dependence to extrapolate the many-body scattering rate to temperatures beyond the reach of quantum Monte Carlo simulations, assuming that the frequency-dependence and the real-part do not change.



(a) simulated disorder at ambient pressure

(b) simulated pressure

Figure 3.19: Simulated resistivity of $Ce_3Bi_4Pt_3$. Resistivities $\rho(T)$ (a) at ambient pressure ($P = 0$) for varying impurity scattering Γ_{imp} and (b) at different pressures P for fixed impurity scattering $\Gamma_{imp} = 5\text{meV}$. Filled (open) circles in $\rho(T)$ indicate simulation (extrapolated) temperatures. Inflection points T^* in $\rho(T)$ are marked with vertical arrows. The simulations mirror the experimental trends: T^* varies significantly with pressure, but depends only weakly on disorder. In the bottom panels we illustrate the square root of $\Gamma = -\langle \Im \Sigma(\omega = 0) \rangle_{J=5/2}$; black and red-shaded lines are linear fits to $\Gamma^{1/2}$ of simulated points, suggesting that for all pressures: $\Gamma = \gamma T^2$; γ decreases notably under compression, indicative of weakening correlation effects.

In all cases we identify an inflection point T^* below which a saturation regime emerges: At ambient pressure, see Fig. 3.19a, a growing disorder (Γ_{imp}) causes T^* to only marginally increase. The saturation value $\rho(T \rightarrow 0)$, however, is notably suppressed as lifetimes shorten—congruent with experiments (Fig. 3.14). Applying pressure, see Fig. 3.19b, boosts T^* significantly, until it saturates between 20–30GPa. The extracted T^* , reported in Fig. 3.20a, is in qualitative agreement with experiment (Fig. 3.14 inset). Also the saturation limit $\rho(T \rightarrow 0)$ depends strongly on pressure. In experiments, the trend in $\rho(T \rightarrow 0)$ varies, however, significantly between samples [333] and setups [333, 323]. We therefore follow Campbell *et al.* [323] and reduce systematic errors by plotting in Fig. 3.20b the ratio ρ_{base}/ρ_{RT} of the simulated resistivity at the lowest (base) temperature ($T = 1\text{K}$)

and at room temperature (RT: $T = 290\text{K}$). In agreement with an experimental ratio at similar temperatures [323], we see an increase from $P = 0$ up to $P \sim 3\text{--}5\text{GPa}$ —the system becomes more insulating. For higher pressures, however, the ratio decreases again—mirroring the pressure-driven crossover to a bad insulator (cf. $\rho(T)$ in Fig. 3.19b). For this comparison we find the best quantitative agreement with experiment for $\Gamma_{\text{imp}} \sim 7.5\text{meV}$.

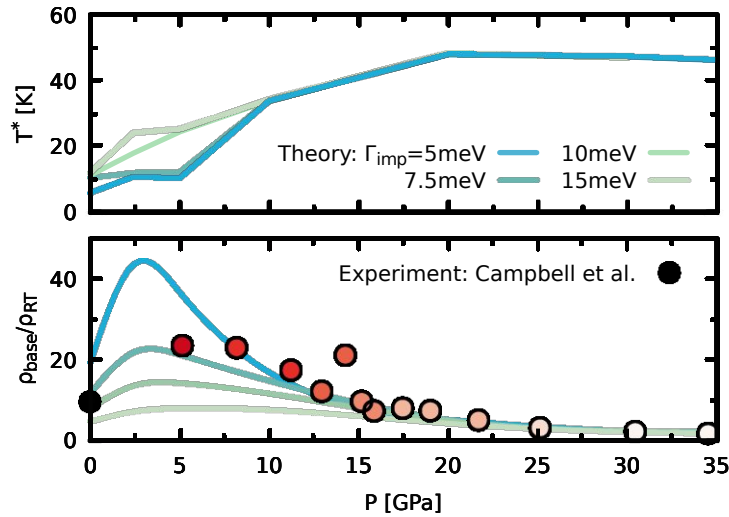


Figure 3.20: Crossover temperature T^* and resistivity ratio. (a) Inflection temperatures T^* as a function of pressure for different impurity-scatterings Γ_{imp} (lines shaded blue to green). At low pressures, T^* slightly depends on Γ_{imp} ; above $P = 5\text{GPa}$, the onset of saturation is insensitive to the magnitude of impurity scattering. (b) Ratio of the resistivity at base temperature, ρ_{base} , and at room temperature (RT), ρ_{RT} , for different impurity scatterings Γ_{imp} (lines shaded blue to green), compared to experiment (circles; from Ref. [323]). In the simulation (experiment [323]) the base and room temperatures were 1K and 290K (2K and 300K), respectively. The overall trend of the resistivity ratio with pressure is independent of the strength of impurity scattering. We find best quantitative agreement with experiment for $\Gamma_{\text{imp}} \sim 7.5\text{meV}$.

The simulations thus contain the necessary ingredients to account for the observed resistivity saturation in $\text{Ce}_3\text{Bi}_4\text{Pt}_3$, including its dependence on disorder and pressure.

3.2.3.2 Microscopic theory

In order to gain a better understanding of these Kubo simulations we resort to a minimalist model treatment with a linear-response conductivity that was first introduced in Ref. [331].

We consider a half-filled two-band ($n = 1, 2$) model with hopping t on the cubic lattice separated by a non-interacting gap Δ_0 : $\epsilon_{\mathbf{k}n}^0 = (-1)^n [2t \sum_{i=1,3} \cos(k_i) + (6t + \Delta_0/2)]$. We endow these dispersions with (i) a constant lifetime $\tau = \hbar/(2\Gamma_0)$ and (ii) a quasi-particle weight or mass enhancement $Z = m/m^* \leq 1$. The latter renormalizes the dispersion, $\epsilon_{\mathbf{k}n} = Z\epsilon_{\mathbf{k}n}^0$, yields the interacting gap $\Delta = Z\Delta_0$, and dresses the scattering rate $\Gamma = Z\Gamma_0$.

In the absence of particle-hole interactions, Eq. (3.40) still holds and can now be evaluated with the corresponding coherent part of the spectral function

$$A_{\mathbf{k}n}(\omega) = \frac{Z}{\pi} \frac{\Gamma}{(\omega - \epsilon_{\mathbf{k}n})^2 + \Gamma^2} \quad (3.41)$$

for which the linear-response conductivity can be calculated analytically (based on contour integration, see next Section 3.3):

$$\sigma(T) = \frac{2\pi e^2 \hbar}{V} \frac{Z^2}{4\pi^3} \frac{\beta}{\Gamma} \sum_{\mathbf{k}n} v_{\mathbf{k}n}^2 \left(\Re \Psi'(z) - \frac{\beta\Gamma}{2\pi} \Re \Psi''(z) \right) \quad (3.42)$$

with the inverse temperature $\beta = (k_B T)^{-1}$, the unit-cell volume V , (derivatives of) the digamma function $\psi(z)$ evaluated at $z = \frac{1}{2} + \frac{\beta}{2\pi} (\Gamma + i\epsilon_{\mathbf{k}n})$, and the Fermi velocities $v_{\mathbf{k}n} = 1/\hbar \partial \epsilon_{\mathbf{k}n}^0 / \partial \mathbf{k}$ obtained by applying the Peierls approximation in the band-basis. Indeed, this only accounts for intra-band transitions. In a more general framework [362] also inter-band transitions can be included within the Peierls philosophy. As far as the temperature dependence is concerned, inter- and intra-band contributions are very similar and the former have been omitted from the model for clarity (their analytic expressions and analysis can be found in Section 3.3). For a discussion of intra- and inter-orbital transitions in the realistic simulations for $Ce_3Bi_4Pt_3$, see the Supplementary information of Ref. [7].

Despite this minimalist assumptions the above formula is rich in physics: In the coherent limit $\Gamma \rightarrow 0$, Eq. (3.42) simplifies to the well-known Boltzmann expression in the constant relaxation-time approximation [363]

$$\sigma(T) \stackrel{\Gamma \rightarrow 0}{=} \frac{e^2 \hbar}{V} \frac{Z^2}{\Gamma} \sum_{\mathbf{k}n} v_{\mathbf{k}n}^2 (-\partial f / \partial \omega)_{\omega=\epsilon_{\mathbf{k}n}}, \quad (3.43)$$

with the Fermi function f —albeit with a renormalization Z^2 commonly not included. In this semi-classical regime, the conductivity is simply proportional to the lifetime $\tau = \hbar/(2\Gamma)$. Then, for $k_B T \ll \Delta$, the resistivity has an activated form $\rho(T) \propto \exp(\Delta/(2k_B T))$ that diverges for $T \rightarrow 0$. In fact, here, Δ is the only relevant energy scale: As epitomized by Arrhenius-plot analyzes, Δ single-handedly accounts for the archetypal $\rho(T)$ of semiconductors in the Boltzmann regime. There,

resistance can be approximately described through electrons with sharply-defined one-particle states (a band-structure $\epsilon_{\mathbf{k}n}$) that undergo collisions at a rate Γ , causing the charge current to decay on a timescale $\hbar/(2\Gamma)$. For sizable Γ , however, the broadening of the one-particle spectrum itself can no longer be neglected, see Section 3.3, spilling incoherent weight into the gap that contributes to conduction. This phenomenon is clearly beyond thermal activation across the gap. Still, Eq. (3.42) can be seen to retain an effective one-particle description (sharply defined dispersions), with many-body (lifetime) effects accounted for by a modified (Ψ -based) fermionic distribution function.

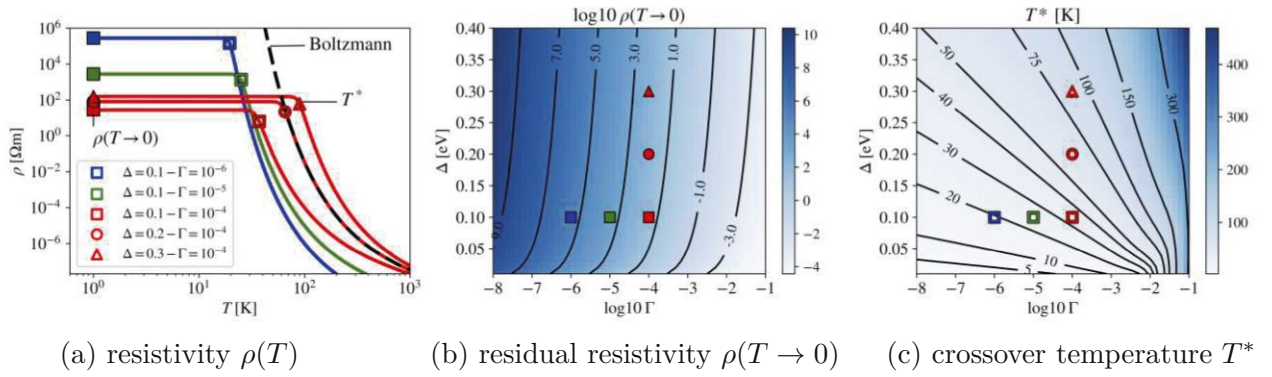


Figure 3.21: Prototypical resistivity in correlated narrow-gap semiconductors. For a minimal two-band model, the figure shows: (a) The resistivity (lines) as a function of temperature for different gaps Δ and scattering rates Γ (both measured in eV). Closed symbols indicate the saturation limit $\rho(T \rightarrow 0)$; open symbols mark the inflection point T^* —the lower (upper) bound of the semi-classical (quantum) regime. The semi-classical Boltzmann conductivity, Eq. (3.43), is shown as dashed black line. (b) The saturation limit $\rho(T \rightarrow 0)$ (coloured map; on a log-scale) as a function of Δ and Γ ; black lines are iso-curves for indicated values; colored symbols mark the choices of Δ and Γ from panel (a). (c) Crossover temperature T^* of the quantum regime. The data shows that T^* ($\rho(T \rightarrow 0)$) is dominantly controlled by Δ (Γ). Calculated for a three-dimensional half-filled two-band model with bare dispersions $\epsilon_{\mathbf{k}n}^0 = (-1)^n [2t \sum_{i=1,3} \cos(k_i) + (6t + \Delta_0/2)]$ ($n = 1, 2$), with hopping $t = 0.25\text{eV}$, a quasi-particle weight $Z = 1$, and a lattice constant $a = 1\text{\AA}$.

To characterize the transport signatures of $\Gamma > 0$, we compute the resistivity $\rho(T) = 1/\sigma(T)$ according to Eq. (3.42), see Fig. 3.21 within **LINRETRACE** (see Section 3.5). Akin to $\text{Ce}_3\text{Bi}_4\text{Pt}_3$, we see the emergence of a crossover temperature T^* below which $\rho(T)$ tends towards saturation. Since this phenomenon defies the semi-classical (Boltzmann) picture, we will label its domain the quantum regime. In conventional semiconductors, deviations from activated behaviour typically occur when an extrinsic in-gap density pins the chemical potential. In the current scenario, impurity states influence conduction merely by limiting the lifetime of intrinsic carriers. Importantly, already minute

scattering rates (mediated by impurities or other defects or couplings) lead to strong signatures at observable temperatures: In Fig. 3.21b and 3.21c we indicate, respectively, the saturation limit $\rho(T \rightarrow 0)$ and the characteristic temperature T^* for the resistivities of panel (a). In the relevant $\Gamma \ll \Delta$ regime, T^* changes more rapidly with Δ , whereas $\rho(T \rightarrow 0)$ is more sensitive to changes in Γ —as observed in experiments and simulations for $Ce_3Bi_4Pt_3$ (see above).

We can give more precise analytical insight: At low temperatures, the minimum (maximum) of conduction (valence) states dominates transport. For this leading contribution to Eq. (3.42), we neglect band-dispersions and consider two levels (2L) $\epsilon_n = (-1)^n \Delta/2$ ($n = 1, 2$) separated by a gap Δ . Then, with $z = 1/2 + \beta/(2\pi)(\Gamma + i\Delta/2)$,

$$\sigma_{2L}(T) \propto \frac{\beta}{\Gamma} \left[\Re\psi_1(z) - \frac{\beta\Gamma}{2\pi} \Re\psi_2(z) \right]. \quad (3.44)$$

This phenomenological quantum conductivity depends on two energy scales: Δ and Γ , and is very useful for analysing experimental data, as shown below. A low-temperature expansion of Eq. (3.44) to second order yields

$$\sigma_{2L}(T) \propto \frac{\Gamma^2}{(\Delta^2 + 4\Gamma^2)^2} \left(1 + \frac{8\pi^2}{3} \frac{5\Delta^2 - 4\Gamma^2}{(\Delta^2 + 4\Gamma^2)^2} (k_B T)^2 \right) \quad (3.45)$$

resulting—for finite Γ —in the residual conductivity

$$\sigma_{2L}(T = 0) \propto \frac{\Gamma^2}{(\Delta^2 + 4\Gamma^2)^2}. \quad (3.46)$$

Unlike conduction by surface states in topological insulators, the quantum-regime conductivity depends on the bulk values Δ and Γ . Therefore, as a paramount distinction, residual conduction can be manipulated by pressure, while topological surface conduction is oblivious to it [364]. A direct consequence of Eq. (3.46) is the existence of a temperature T^* below which $\rho(T)$ must depart from Boltzmann behaviour. Using Eq. (3.45), we can crudely estimate the dependencies of T^* via $\partial^2 \rho(T)/\partial T^2 = 0$, see Fig. 3.22:

$$k_B T^* = \frac{1}{\sqrt{10}\pi} \left(\frac{\Delta}{2} + \frac{11}{5} \frac{\Gamma^2}{\Delta} + \mathcal{O}(\Gamma^4) \right) \quad (3.47)$$

For $\Gamma \ll \Delta$, T^* is essentially controlled by Δ —consistent with our numerical results and available experiments.

The take-away message is this: If Γ/Δ is not vanishingly small, the lifetime of intrinsic charge carriers manifests as a relevant energy scale. It introduces a coherence temperature T^* , delimits

the applicability of Boltzmann theory from below, and leads to an algebraic saturation regime with residual conduction.

Here, we presented the residual conduction mediated by transitions within the same band (intra-band transitions). The methodology and implementation advanced in this thesis, however, also includes inter-band effects that become relevant in metals and solids with a very narrow gap. A particular case are extended (=finite) systems, such as molecules. There, transport is by construction driven by inter-orbital transitions. For a study of residual conduction in semi-conducting molecules, that builds on the methodologies developed here, see Ref. [365].

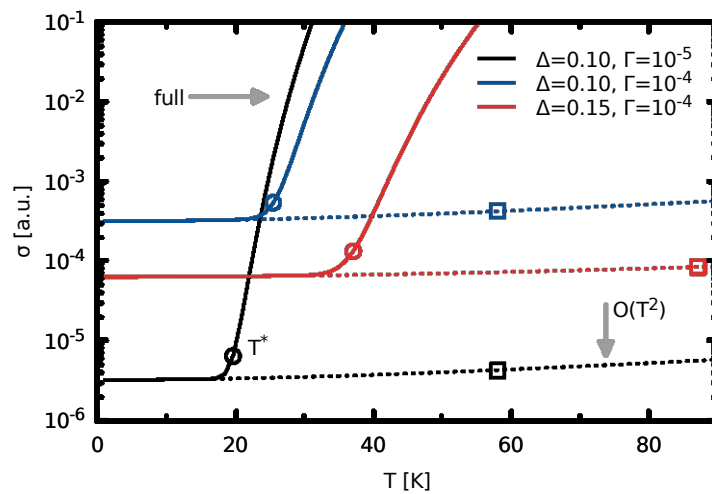


Figure 3.22: Comparison of Eq. (3.44) and Eq. (3.45): The quantum regime. The figure shows the regime of validity of the low temperature expansion, Eq. (3.45) (dotted lines), of the two-level approximation Eq. (3.44) of Eq. (3.42) (solid lines). The algebraic rise of $\sigma(T)$ is neatly captured by the quadratic approximation; higher order terms only become relevant in the direct vicinity of T^* (circles). Computing T^* from the approximate form Eq. (4) (squares), severely overestimates crossover temperatures. Still, the *qualitative* dependency on the size of the gap Δ and the scattering rate Γ is similar to the actual behaviour: T^* increases only marginally with Γ , but is strongly enhanced with growing Δ . However, we note that the limit $\Gamma \rightarrow 0$ —in which the true T^* vanishes by construction—is violated by the extraction from the derivative of the Taylor expansion.

3.2.3.3 The quantum regime in experiments

Returning to $Ce_3Bi_4Pt_3$, we anatomize the experimental conductivity vis-à-vis the characteristic temperature profile of the quantum regime established above. With the phenomenological conductivity, Eq. (3.44), we fit in Fig. 3.23 the data of (a) Cooley *et al.* [333] and (b) Wakeham *et al.* [334] and find near perfect agreement: Our Ansatz accurately reproduces the experimental temperature dependence for varying pressure and disorder.

We analyze trends in the fit parameters: As shown in the inset of Fig. 3.23a, we extract a gap $\Delta \sim 7.5\text{meV}$ at $P = 0$, which is largely enhanced for $P > 0$; also Γ increases with P . We extract smaller Γ s and Δ s for Wakeham *et al.*'s sample, see inset of Fig. 3.23b, owing to the overall smaller conductivity. Consistent with the degree of radiation damage, Γ increases with growing displacements per atom (DPA). The extracted Δ is congruent with activation-law fits above T^* [334] and increases only marginally under radiation. Note in Fig. 3.23a, for pressures $P > 4\text{GPa}$ and very low temperatures, deviations from the quantum regime occur. There, as shown in Ref. [333], $\sigma(T)$ matches 3D variable-range hopping (VRH) characteristics, $\propto \exp[(T/T_0)^{1/4}]$.

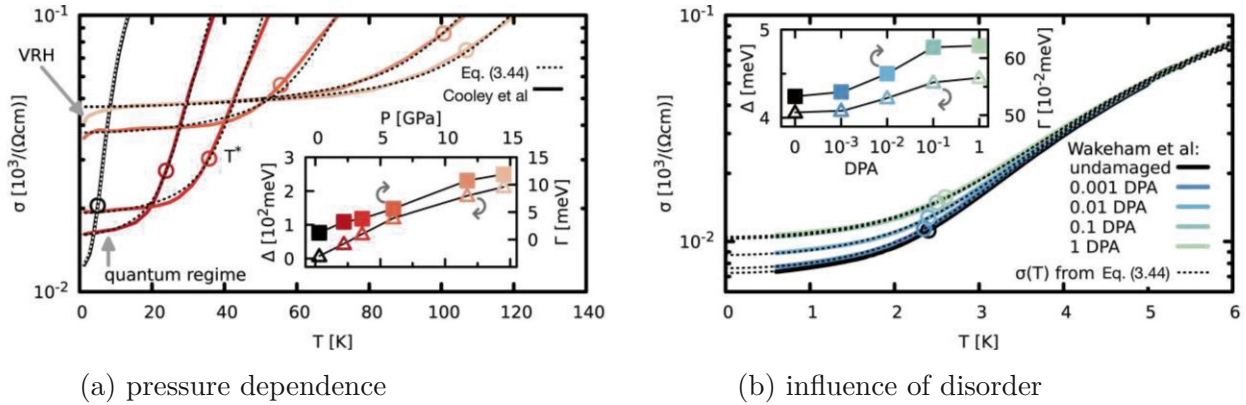


Figure 3.23: Analysis of the quantum regime in $Ce_3Bi_4Pt_3$. We fit the conductivity $\sigma(T) = 1/\rho(T)$ from (a) Cooley *et al.* [333] (coloured lines correspond to pressures indicated in the inset) and (b) Wakeham *et al.* [334] (coloured lines indicate the degree of disorder quantified in displacements per atom (DPA)) with the phenomenological quantum conductivity Eq. (3.44) (dashed lines). The agreement is excellent: From a finite residual value for $T \rightarrow 0$, the conductivity grows algebraically (see the quantum regime formula: Eq. (3.45)) up to the crossover temperature T^* (circles). Above, higher powers in T become relevant as $\sigma(T)$ enters the exponential (semi-classical) regime. For pressures $P > 4\text{GPa}$ and very low T , the experimental conductivity deviates from the quantum regime and instead matches 3D variable-range hopping (VRH) characteristics, $\propto \exp[(T/T_0)^{1/4}]$ [333]. The fit parameters Δ and Γ are given in the insets.

In Fig. 3.24 we perform a similar analysis for the bulk conductivity of the mixed-valence insulator SmB_6 [366], finding again excellent agreement. These results will be reviewed in the Discussion Section.

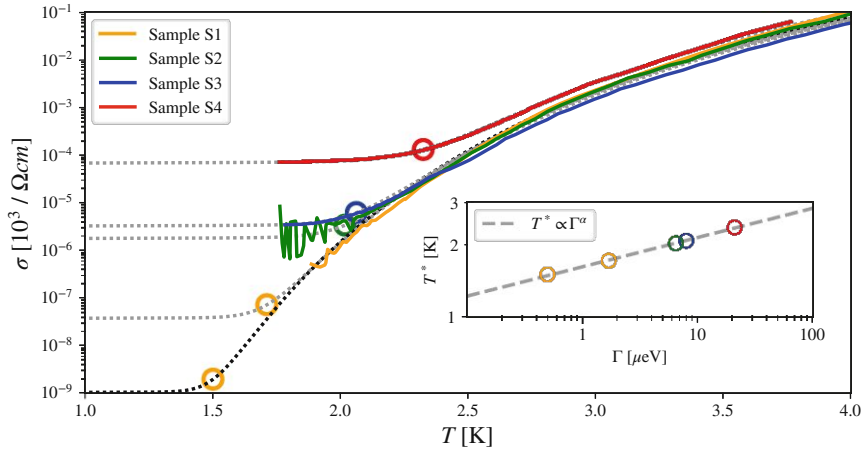


Figure 3.24: Quantum regime in the bulk conductivity of SmB_6 . In this figure we extend the analysis of the experimental *bulk* conductivity of SmB_6 obtained by Eo *et al.* [366] (shown in Fig. 6 of the manuscript for the samples S3 and S4) to their samples S1 and S2. Using the phenomenological Eq. (3) of the manuscript, we determine the crossover temperature T^* and extract the scattering rate Γ . Experimental data obtained for sample S2 (green) is noisy at low T , and our fit accordingly less reliable. For the sample S1 (yellow), the scattering rate is so low that the anticipated T^* moves outside the experimentally accessible temperature window. The available data is then insufficient to determine T^* . However, admissible combinations of fit parameters (e.g., the two yellow circles shown) suggest that $T^* \propto \Gamma^\alpha$ for all samples with $\alpha \approx 1/8$ (inset). Consistent with our theory, T^* vanishes in (unattainable) pure samples.

3.2.4 Discussion

The above results strongly suggest that electronic scattering is the microscopic driver of the resistivity saturation in $\text{Ce}_3\text{Bi}_4\text{Pt}_3$. Our mechanism is relevant also for other Kondo insulators. Indeed, iso-structural $\text{Ce}_3\text{Sb}_4\text{Pt}_3$ displays a $\rho(T)$ [367] consistent with our understanding: Different growth techniques (varying amounts of disorder) lead to largely different $\rho(T \rightarrow 0)$ while T^* changes little [367]. $\text{Ce}_3\text{Bi}_4\text{Pd}_3$, has recently been characterized as a semi-metal [368] or a Kondo insulator [341]. That the gap is next to non-existing [368, 341] has been ascribed to spin-orbit [368] or Kondo [305] coupling effects. Here, we conjecture that under compression a resistivity plateau devel-

ops in $Ce_3Bi_4Pd_3$. Future transport and susceptibility measurements could then elucidate whether pressurized $Ce_3Bi_4Pd_3$ mimics $Ce_3Bi_4(Pd_{1-x}Pt_x)_3$ for small x —(dis)favouring the (spin-orbit) Kondo scenario. Saturation tendencies have also been found in the Kondo insulators $CeFe_2Al_{10}$ [369] and pressurized $CeRu_4Sn_6$ [370, 371, 372]. However, Kondo physics is not a prerequisite for our mechanism. What makes these systems natural hosts for the quantum regime are their small gaps $\Delta \sim \mathcal{O}(\lesssim 50\text{meV})$. Correlation effects also drive narrow gaps in SmB_6 [291, 373, 374, 366], YbB_{12} [375], $U_3Sb_4Pt_3$ [376], or $FeSb_2$ [214], all of which exhibit saturation regimes, while rather belonging to the class of intermediate-valence insulators or d -electron intermetallics [212].

Yet, how can we ascertain that the presented microscopic scenario is at work in any such compound? Salient signatures of the quantum regime provide guidance: T^* correlates with the bulk gap and the residual conductivity increases with shrinking lifetimes. In $U_3Sb_4Pt_3$, the gap is unaffected by pressure, and—consistently—so is T^* [376]. In mixed-valence SmB_6 , however, the activation gap shrinks under pressure, while T^* is hardly affected [351, 352] and added disorder at first increases the resistivity [334]. Also in $CeRu_4Sn_6$ single crystals, pressure significantly increases activation energies, while T^* remains inert [372]. These observations are incompatible with our scenario and suggest a different origin to dominate residual conduction. Incidentally, for the latter two compounds conducting surface states of proposedly topological character [257, 377] have been evidenced [334, 366]. Note, however, that more disordered, polycrystalline samples of $CeRu_4Sn_6$ exhibit an additional inflection point in $\rho(T)$, which—consistent with our theory—moves up under compression [378]. Also for SmB_6 the situation is more complex: Using a special measurement setup, Eo *et al.* [366] were able to disentangle surface and bulk contributions to conduction. Crucially, the isolated bulk conductivity still exhibits a saturation regime—whose temperature profile defies all previous scenarios [366, 379]. As we demonstrate in Fig. 3.24, the phenomenological quantum conductivity Eq. (3.44) delivers an accurate description of the experimental data—providing strong evidence that the bulk resistivity in SmB_6 is lifetime-limited. Noteworthy, our theory shares its key ingredient with the scenario of Shen and Fu [380] that suggests finite lifetimes of Landau levels to account for quantum oscillations, e.g., in SmB_6 [381, 382].

In conclusion, we pinpoint finite lifetimes of intrinsic bulk carriers as a driver for residual conduction in semiconductors. Using a simple phenomenology, we demonstrated the characteristic temperature profile associated with this scenario to accurately match the saturation regimes in several materials. Possible microscopic sources for a finite scattering amplitude at low- T are impurities, other forms of disorder, and zero-point fluctuations. Indeed, the resistivity of no semiconductor in practice diverges for $T \rightarrow 0$. In the absence other factors (or, see SmB_6 , in combination with), signatures of the presented physics can therefore be expected to be ubiquitous in correlated narrow-gap semiconductors.

3.3 Thermoelectric transport coefficients generated by intrinsic life times

- This Section is based on the equations/derivations published in “Prototypical many-body transport phenomena in semiconductors” by [Matthias Pickem](#), Emanuele Maggio, and Jan M. Tomczak [9] and “The Linear Response Transport Centre” by [Matthias Pickem](#), Emanuele Maggio, and Jan M. Tomczak [11]. Adopted text passages have been marked accordingly.
- The theory is based on the Kubo methodology of our Ref. [7] which captures (in)coherence effects beyond the reach of semi-classical Boltzmann approaches.
- In this Section, we focus purely on the analytic derivation and the characterization of the transport kernels and coefficients. Numerical analysis is discussed in Section 3.4.
- This Section includes minor sign and prefactor fixes that occur in the published versions of Refs. [9] and [11]. We adjusted the relevant equations and figures accordingly.

In this Section, we lay out the setting in which we consider transport properties. The main purpose is to introduce the necessary correlation functions and notation enabling us to derive higher order (beyond the conductivity) Onsager coefficients. For more detailed derivations, the reader is referred to specialized literature [211, 358, 383]. The conceptual advances will be presented in Section 3.3.2 including the necessary contour integrations and Matsubara summations. After that, we will restrict ourselves to a general discussion of this new methodology. Realistic applications will be discussed in Section 3.4 and Section 3.5.

3.3.1 Methodological context: Onsager coefficients

Transport properties—such as resistivity (ρ), magneto-resistance (MR), thermal conductance (κ), and the coefficients of Hall, Seebeck and Nernst (R_H , S , ν)—are among the most widely investigated quantities in materials science. They provide essential information for characterizing new materials and for elucidating physical phenomena. To extract microscopic information from measurements requires a fundamental understanding of how carriers transport charge, heat and entropy. When simulating transport properties, an adequate inclusion of scattering processes is particularly crucial. These limit the lifetime of carriers, lead to a decay of currents, and can have various origins, such as electron-electron or electron-phonon interactions as well as defects or impurities.

To this end we are following the introduction to linear response theory (see Section 2.5.4.1) and are considering transport quantities that are based on correlation functions that specify measurable observables of a system in the presence of specific external perturbations (electric field, magnetic field, temperature gradient, etc.). Physical observables of transport processes are here described by charge and heat currents

$$j_E^\alpha = \mathcal{L}_{11}^{\alpha\beta} E^\beta + \frac{1}{T} \mathcal{L}_{12}^{\alpha\beta} \partial_\beta T \quad (3.48)$$

$$j_Q^\alpha = -\mathcal{L}_{21}^{\alpha\beta} E^\beta - \frac{1}{T} \mathcal{L}_{22}^{\alpha\beta} \partial_\beta T, \quad (3.49)$$

induced by electrons and generated by an external electric field \mathbf{E} and a temperature gradient ∇T perturbing the system. In our case these processes are described, on the imaginary time (τ) axis by

$$\chi_{\mathbf{j}_a \mathbf{j}_b}^{\alpha\beta}(\mathbf{q}, \tau) = \frac{1}{V} \left\langle T_\tau j_a^\alpha(\mathbf{q}, \tau) j_b^\beta(-\mathbf{q}, 0) \right\rangle \quad (3.50)$$

with the time-ordering operator T_τ , the charge ($a, b = 1$) and heat ($a, b = 2$) current operator \mathbf{j}_a^α in the Cartesian direction $\alpha, \beta \in \{x, y, z\}$, and V indicating the unit cell volume. From them, the usual (retarded) Onsager coefficients \mathcal{L} for dipolar transitions ($\mathbf{q} = \mathbf{0}$) are obtained by first Fourier transforming Eq. (3.50) into bosonic Matsubara frequencies

$$\chi_{\mathbf{j}_a \mathbf{j}_b}^{\alpha\beta}(\mathbf{q}, i\omega_n) = \int_0^\beta d\tau e^{i\omega_n \tau} \chi_{\mathbf{j}_a \mathbf{j}_b}^{\alpha\beta}(\mathbf{q}, \tau), \quad (3.51)$$

analytical continuation to real frequencies $i\omega_n \rightarrow \omega + i\delta$ and then taking the dynamic limit

$$\mathcal{L}_{ab}^{\alpha\beta} = \lim_{\omega \rightarrow 0^+} \frac{1}{\omega} \Im \left[\chi_{\mathbf{j}_a \mathbf{j}_b}^{\alpha\beta}(\mathbf{q} = \mathbf{0}, \omega) \right]. \quad (3.52)$$

In the presence of an external magnetic field B in direction $\gamma \in \{x, y, z\}$, one needs to instead evaluate the expectation value

$$\chi_{\mathbf{j}_a \mathbf{j}_b}^{B, \alpha\beta}(\mathbf{q}, \tau) = \frac{1}{V} \left\langle T_\tau j_a^\alpha(\mathbf{q}, \tau) j_b^\beta(\mathbf{0}, 0) \right\rangle_B \quad (3.53)$$

for the Hamiltonian that includes the field [384, 385, 386], and the resulting Onsager coefficients will be denoted as

$$\mathcal{L}_{ab}^{B, \alpha\beta\gamma} = \lim_{\omega \rightarrow 0^+} \frac{1}{\omega} \Im \left[\frac{\chi_{\mathbf{j}_a \mathbf{j}_b}^{B, \alpha\beta}(\mathbf{q} = \mathbf{0}, \omega)}{B^\gamma} \right]. \quad (3.54)$$

The coefficients $\mathcal{L}_{ab}^{B, \alpha\beta\gamma}$ are then the linear correction terms in the presence of a magnetic flux (\mathbf{B}) in the γ -direction. Employing the Onsager-Casimir relation

$$\mathcal{L}_{ab}^{\alpha\beta}(\mathbf{B}) = \mathcal{L}_{ba}^{\beta\alpha}(-\mathbf{B}) \quad (3.55)$$

on the expansion

$$\mathcal{L}_{ab}^{\alpha\beta}(\mathbf{B}) = \mathcal{L}_{ab}^{\alpha\beta} + \mathcal{L}_{ab}^{B,\alpha\beta\gamma} B^\gamma + \mathcal{O}(\mathbf{B}^2), \quad (3.56)$$

which we treat up to linear order in \mathbf{B} , one finds the symmetric and antisymmetric connections

$$\mathcal{L}_{ab}^{\alpha\beta} = \mathcal{L}_{ba}^{\beta\alpha} \quad (3.57a)$$

$$\mathcal{L}_{ab}^{B,\alpha\beta\gamma} = -\mathcal{L}_{ba}^{B,\beta\alpha\gamma} \quad (3.57b)$$

when the \mathbf{B} -field is the only source of time-reversal symmetry breaking.⁴⁵

From the Onsager coefficients, the electrical conductivity (σ), electrical resistivity (ρ), Peltier coefficient (Π), Seebeck coefficient (S), thermal conductivity (κ), Hall conductivity (σ^B), Hall coefficient (R_H), Nernst coefficient⁴⁶ (ν), Hall mobility (μ_H) and its analogue, the thermal mobility (μ_T) [214] can be calculated. Note that, here, we limit the transport kernels to symmetric contributions. Antisymmetric terms leading to anomalous transport from a non-trivial topological state [388, 389, 390, 391] are neglected. For a detailed dimensionality analysis of all involved quantities, see the Appendix of Ref. [11].

$$\sigma_{\alpha\beta} = \mathcal{L}_{11}^{\alpha\beta} = \left. \frac{j_E^\alpha}{E^\beta} \right|_{\Delta T=0} \quad (3.58)$$

$$\rho_{\alpha\beta} = \left(\mathcal{L}_{11}^{-1} \right)^{\alpha\beta} = (\sigma^{-1})^{\alpha\beta} \quad (3.59)$$

$$\Pi_{\alpha\beta} = - \left(\mathcal{L}_{11}^{-1} \right)^{\alpha i} \mathcal{L}_{21}^{\beta i} = \left. \frac{j_Q^\beta}{j_E^\alpha} \right|_{\Delta T=0} \quad (3.60)$$

$$S_{\alpha\beta} = -\frac{1}{T} \left(\mathcal{L}_{11}^{-1} \right)^{\alpha i} \mathcal{L}_{12}^{i\beta} = \left. \frac{E^\alpha}{\Delta_\beta T} \right|_{j_E=0} \quad (3.61)$$

$$\kappa_{\alpha\beta} = \frac{1}{T} \left[\mathcal{L}_{22}^{\alpha\beta} - \mathcal{L}_{21}^{\alpha i} \left(\mathcal{L}_{11}^{-1} \right)^{ij} \mathcal{L}_{12}^{j\beta} \right] = \left. \frac{j_Q^\alpha}{\Delta_\beta T} \right|_{j_E=0} \quad (3.62)$$

$$\sigma_{\alpha\beta\gamma}^B = \mathcal{L}_{11}^{B,\alpha\beta\gamma} \quad (3.63)$$

$$R_{H,\alpha\beta\gamma} = \left(\mathcal{L}_{11}^{-1} \right)^{\alpha i} \mathcal{L}_{11}^{B,ij\gamma} \left(\mathcal{L}_{11}^{-1} \right)^{j\beta} = \left. \frac{E^\alpha}{j_E^\beta B^\gamma} \right|_{\Delta T=0} \quad (3.64)$$

$$\nu_{\alpha\beta\gamma} = -\frac{1}{T} \left(\mathcal{L}_{11}^{-1} \right)^{\alpha i} \left[\mathcal{L}_{11}^{B,ij\gamma} \mathcal{L}_{12}^{jk} - \mathcal{L}_{12}^{B,ij\gamma} \mathcal{L}_{11}^{jk} \right] \left(\mathcal{L}_{11}^{-1} \right)^{k\beta} = \left. \frac{E^\alpha}{\Delta_\beta T B^\gamma} \right|_{j_E=0} \quad (3.65)$$

$$\mu_{H,\alpha\beta\gamma} = \left(\mathcal{L}_{11}^{-1} \right)^{\alpha i} \mathcal{L}_{11}^{B,i\beta\gamma} = R_{H,\alpha i\gamma} \sigma_{i\beta} \quad (3.66)$$

$$\mu_{T,\alpha\beta\gamma} = \left(\mathcal{L}_{12}^{-1} \right)^{\alpha i} \mathcal{L}_{12}^{B,i\beta\gamma} \quad (3.67)$$

⁴⁵In magnetized materials the Onsager relations take the form of $\mathcal{L}_{ba}^{\beta\alpha}(H, M) = \mathcal{L}_{ab}^{\alpha\beta}(-H, -M)$ instead (H : magnetic field strength; M : magnetization density), leading to the anomalous Hall effect and a linear magneto resistance [182, 387, 388].

⁴⁶We use the historical convention for the sign of the Nernst coefficient [392].

The connections to the Onsager coefficients are obtained via ratios (right hand side) of physical observables which include the induced electric current density j_E^α , the electric field E^α , measured as voltage difference along a direction $E^\alpha = -\Delta_\alpha V$, the induced heat current density j_Q^α and the magnetic field B_γ .

Let us comment on some connections and physical interpretations here: In systems where time reversal symmetry is maintained the Peltier coefficient simplifies to $\Pi_{\alpha\beta} = TS_{\alpha\beta}$ since $\mathcal{L}_{21}^{\beta i} = \mathcal{L}_{12}^{i\beta}$, see Eq. (3.57a), which is commonly known as the second Thomson relation [393]. The Seebeck coefficient itself can be understood as the entropy transported by the flow of electrons. The Hall coefficient R_H encodes the response to a transverse electric current in the presence of a magnetic field and can be thought of as a charge build-up perpendicular to an applied magnetic field (indicated by its unit m^3/C). Further it can be used as a direct measurement of the (inverse) concentration of available carriers. The sign of both the Seebeck and Hall coefficients signal the (dominant) type of charge carrier in the material: electrons lead to negative while holes lead to positive coefficients. The Nernst coefficient ν measures the electric response to a transverse thermal gradient and can be thus, similar to the Seebeck coefficient, understood as a transverse entropy flow [394].

Let us also note that the expressions for the Hall and Nernst coefficients, see Eqs. (3.64-3.65), correspond to the *intrinsically transverse* response, i.e. one has to employ the antisymmetric part of the $\mathcal{L}_{11}(\mathbf{B})$ and $\mathcal{L}_{12}(\mathbf{B})$ tensors to eliminate the symmetric off-diagonal elements [394, 395].

For model/materials whose unit cell's axes are orthogonal, as we are considering here, the Einstein summations over Cartesian directions simplify to a single expression, e.g., for an electric current in x -direction and a magnetic field in z -direction, the resulting Hall coefficient in y -direction is $R_{H,yxz} = (\mathcal{L}_{11}^{-1})^{yy} \mathcal{L}_{11}^{B,yxz} (\mathcal{L}_{11}^{-1})^{xx}$.

The transport observables, even when featuring one-particle currents \mathbf{j}_a^α ⁴⁷ in Eq. (3.50) and Eq. (3.53), probe multi-particle excitations. Diagrammatically, these can be described as the sum of all possible two-particle processes, with the leading term corresponding to the independent propagation of a particle-hole pair (bubble diagram). See Section 2.6 for the explicit consideration of vertex correction in the context of the optical conductivity. Magneto-transport quantities on the other hand stemming from Eq. (3.53) can be shown [385, 384, 386] to involve all possible three-particle processes.

Diagrams that (unlike the bubble) contain interconnected propagation lines, are commonly referred to as vertex-corrections [246, 397, 398, 399]. These can lead to collective phenomena such as excitons, π -tons [6, 215, 238] and other polaritons. In this derivation, following the spirit of the dynamical mean-field theory [94], we are neglecting vertex-corrections. In this approximation, which amounts

⁴⁷The heat-current $\mathbf{j}^Q = \mathbf{j}^2$ is only of one-particle nature when, as we assume here, interactions are local [359, 396].

to the infinite dimensional limit, vertex corrections vanish for all considered observables⁴⁸ [359, 396, 400, 401].

Assuming that the one-particle Green's function $G_{\mathbf{k}}(\omega)$ is diagonal in the chosen band or orbital basis, the current-current correlation functions entering Equations (3.52) and (3.54) can be evaluated directly by inserting the current operator

$$j_E^\alpha(\mathbf{q} = \mathbf{0}, \tau) = -e \sum_{\mathbf{k}, l, m, \sigma} \gamma_{lm}^{\mathbf{k}, \alpha} \left[\hat{c}_{\mathbf{k}m\sigma}^\dagger \hat{c}_{\mathbf{k}l\sigma} \right] (\tau) \quad (3.68)$$

and the heat-current operator

$$j_Q^\alpha(\mathbf{q} = \mathbf{0}, \tau) = \frac{1}{2} \sum_{\mathbf{k}, l, m, \sigma} \gamma_{lm}^{\mathbf{k}, \alpha} \left[\hat{c}_{\mathbf{k}m\sigma}^\dagger \dot{\hat{c}}_{\mathbf{k}l\sigma} - \dot{\hat{c}}_{\mathbf{k}m\sigma}^\dagger \hat{c}_{\mathbf{k}l\sigma} \right] (\tau) \quad (3.69)$$

with e as the (positively defined) elementary charge and $\gamma_{lm}^{\mathbf{k}, \alpha}$ as the coupling elements in both the charge and the heat current. These current expressions have been derived for the one-band Hubbard model in Ref. [359], but necessarily also hold under the assumption of a diagonal band/orbital basis. Let us note here, that we require different prefactors compared to the ones derived in Ref. [359]. We employ the definition of a positive electric current as the flow of negatively charged electrons, and the heat-current on the imaginary axis without a factor of i . Only with the definitions of Eqs. (3.68-3.69) do we find current-current correlation functions, see Appendix A.3, that are consistent with the definitions of physical observables in Eqs. (3.59-3.67).

One can then follow a similar derivation as shown in Section 2.6 while keeping in mind that the operator derivative occurring in the heat current must be evaluated like

$$\dot{\hat{c}}(\tau) = \partial_\tau \hat{c}(\tau) = \left[\mathcal{H}, \hat{c}(\tau) \right] \quad (3.70a)$$

$$\dot{\hat{c}}^\dagger(\tau) = \partial_\tau \hat{c}^\dagger(\tau) = \left[\mathcal{H}, \hat{c}^\dagger(\tau) \right] \quad (3.70b)$$

in the Heisenberg representation employed in the correlation functions of Eqs. (3.51) and (3.53). When neglecting vertex-corrections, the resulting current-current correlation functions expressed in terms of Green's functions [359, 386] and Appendix A.3, look as follows

$$\chi_{j_E j_E}(\mathbf{q} = \mathbf{0}, i\omega_m) \propto -\frac{1}{\beta} \sum_{\mathbf{k}, \nu_n} G(\mathbf{k}, i\nu_n) G(\mathbf{k}, i\nu_n + i\omega_m) \quad (3.71)$$

$$\chi_{j_Q j_E}(\mathbf{q} = \mathbf{0}, i\omega_m) \propto +\frac{1}{\beta} \sum_{\mathbf{k}, \nu_n} G(\mathbf{k}, i\nu_n) G(\mathbf{k}, i\nu_n + i\omega_m) \left(i\nu_n + \frac{i\omega_m}{2} \right) \quad (3.72)$$

$$\chi_{j_Q j_Q}(\mathbf{q} = \mathbf{0}, i\omega_m) \propto -\frac{1}{\beta} \sum_{\mathbf{k}, \nu_n} G(\mathbf{k}, i\nu_n) G(\mathbf{k}, i\nu_n + i\omega_m) \left(i\nu_n + \frac{i\omega_m}{2} \right)^2 \quad (3.73)$$

⁴⁸At least in the absence of multi-band effects [64]. For the vanishing of vertex corrections in infinite dimensions for massless fermions, see Ref. [402].

$$\chi_{j_E j_E}^B(\mathbf{q} = \mathbf{0}, i\omega_m) \propto \frac{1}{\beta} \sum_{\mathbf{k}, \nu_n} \left[G^2(\mathbf{k}, i\nu_n) G(\mathbf{k}, i\nu_n + i\omega_m) - G^2(\mathbf{k}, i\nu_n) G(\mathbf{k}, i\nu_n - i\omega_m) \right] \quad (3.74)$$

$$\chi_{j_Q j_E}^B(\mathbf{q} = \mathbf{0}, i\omega_m) \propto \frac{1}{\beta} \sum_{\mathbf{k}, \nu_n} \left[G^2(\mathbf{k}, i\nu_n) G(\mathbf{k}, i\nu_n + i\omega_m) \left(i\nu_n + \frac{i\omega_m}{2} \right) - G^2(\mathbf{k}, i\nu_n) G(\mathbf{k}, i\nu_n - i\omega_m) \left(i\nu_n - \frac{i\omega_m}{2} \right) \right] \quad (3.75)$$

$$\chi_{j_Q j_Q}^B(\mathbf{q} = \mathbf{0}, i\omega_m) \propto \frac{1}{\beta} \sum_{\mathbf{k}, \nu_n} \left[G^2(\mathbf{k}, i\nu_n) G(\mathbf{k}, i\nu_n + i\omega_m) \left(i\nu_n + \frac{i\omega_m}{2} \right)^2 - G^2(\mathbf{k}, i\nu_n) G(\mathbf{k}, i\nu_n - i\omega_m) \left(i\nu_n - \frac{i\omega_m}{2} \right)^2 \right] \quad (3.76)$$

Transforming the above expressions on the Matsubara axis into integrals over the real frequencies, the resulting Onsager coefficients can be written as

$$\mathcal{L}_{ab}^{\alpha\beta} = \frac{\pi \hbar e^{(4-a-b)}}{V} \sum_{\substack{n,m \\ \mathbf{k}, \sigma}} \mathcal{K}_{ab}(\mathbf{k}, n, m) M^{\alpha\beta}(\mathbf{k}, n, m) \quad (3.77)$$

$$\mathcal{L}_{ab}^{B, \alpha\beta\gamma} = \frac{2\pi^2 \hbar e^{(5-a-b)}}{3V} \sum_{\substack{n,m \\ \mathbf{k}, \sigma}} \mathcal{K}_{ab}^B(\mathbf{k}, n, m) M^{B, \alpha\beta\gamma}(\mathbf{k}, n, m) \quad (3.78)$$

with the (positively defined) elementary charge e , and the sums running over band-indices n, m , Brillouin zone momentum \mathbf{k} and spin σ . Here, the $M^{(B)}$ collect the dipolar transition matrix elements that depend on the Cartesian directions α, β (and γ) and are discussed in Section 3.3.4. The kernel functions $\mathcal{K}^{(B)}$, instead, contain the two(three)-particle expectation value of the fermionic operators that make up the currents \mathbf{j}^a . Neglecting vertex corrections (see above), they can be expressed as

$$\mathcal{K}_{ab}(\mathbf{k}, n, m) = \int_{-\infty}^{\infty} d\omega \omega^{(a+b-2)} \left(-\frac{\partial f}{\partial \omega} \right) A_{\mathbf{k}n}(\omega) A_{\mathbf{k}m}(\omega) \quad (3.79)$$

$$\mathcal{K}_{ab}^B(\mathbf{k}, n, m) = \int_{-\infty}^{\infty} d\omega \omega^{(a+b-2)} \left(-\frac{\partial f}{\partial \omega} \right) A_{\mathbf{k}n}^2(\omega) A_{\mathbf{k}m}(\omega) \quad (3.80)$$

where $A_{\mathbf{k}n}(\omega) = -1/\pi \Im G_{\mathbf{k}n}(\omega)$ is the spectral function associated with the retarded one-particle Green's function. Energies ω are measured with respect to the Fermi level μ . Thus, within our approximations, many-body (scattering) effects enter the transport properties only through the renormalization of the one-particle/hole propagators.

3.3.2 Kubo transport equations

3.3.2.1 Approximation: Linearized Self-energy

As seen in Eqs. (3.79-3.80), the derivative of the Fermi function assures that transport properties are dominated by energies close to the Fermi level.⁴⁹ Then, also in the quantity that encodes many-body renormalizations—the electron self-energy Σ —only the low-energy behaviour is relevant. Then, for the purpose of transport properties and in the absence of pole-like structures within several $k_B T$ of the Fermi level, the self-energy can be linearized, cf. Section 2.2.3:

$$\Sigma_{\mathbf{k}n}(\omega) \approx \Re\Sigma_{\mathbf{k}n}(0) + (1 - Z_{\mathbf{k}n}^{-1})\omega - i\Gamma_{\mathbf{k}n}^0 \quad (3.81)$$

In other words, the central assumption is that for transport properties the temperature dependence of renormalizations is more important than that on frequency. An implicit higher frequency dependence can, however, be included by linearizing the self-energy around the band-energies $\epsilon_{\mathbf{k}n}^0$. For the scattering rate, for instance, instead of evaluating $\Gamma_{\mathbf{k}n}^0 = -\Im\Sigma_{\mathbf{k}n}(\omega = 0)$ at the Fermi level, one can use $\Gamma_{\mathbf{k}n}^0 = -\Im\Sigma_{\mathbf{k}n}(\omega = \epsilon_{\mathbf{k}n}^0)$.

With Eq. (3.81), the retarded Green's function evaluates to

$$G_{\mathbf{k}n}^{\text{ret}}(\omega) = \left[\omega - \epsilon_{\mathbf{k}n}^0 + \mu - \Re\Sigma_{\mathbf{k}n}(0) - (1 - Z_{\mathbf{k}n}^{-1})\omega + i\Gamma_{\mathbf{k}n}^0 \right]^{-1} \quad (3.82)$$

from which the coherent part of the spectrum

$$A_{\mathbf{k}n}(\omega) = -\frac{1}{\pi} \Im G_{\mathbf{k}n}^{\text{ret}}(\omega) \quad (3.83)$$

results in a Lorentzian form of weight Z

$$A_{\mathbf{k}n}(\omega) = \frac{Z_{\mathbf{k}n}}{\pi} \frac{\Gamma_{\mathbf{k}n}}{(\omega - a_{\mathbf{k}n})^2 + \Gamma_{\mathbf{k}n}^2} \quad (3.84)$$

with $\Gamma_{\mathbf{k}n} = Z_{\mathbf{k}n}\Gamma_{\mathbf{k}n}^0$ and $a_{\mathbf{k}n} = Z_{\mathbf{k}n}(\epsilon_{\mathbf{k}n}^0 - \mu + \Re\Sigma_{\mathbf{k}n}(0))$, the renormalized scattering rate and dispersion, respectively. Employing the Hilbert transform of the self-energy

$$\Sigma_{\mathbf{k}n}(i\nu_n) = \Sigma_{\mathbf{k}n}(\omega \rightarrow \infty) - \frac{1}{\pi} \int_{-\infty}^{\infty} d\omega \frac{\Im\Sigma_{\mathbf{k}n}(\omega)}{z - \omega} \quad (3.85)$$

one additionally obtains a useful expression for a constant scattering rate on the Matsubara axis

$$\Sigma_{\mathbf{k}n}(i\nu_n) = \Sigma_{\mathbf{k}n}(\omega \rightarrow \infty) - i\Gamma_{\mathbf{k}n}^0 \text{sign}(\nu_n). \quad (3.86)$$

⁴⁹This is contrary to thermodynamic properties, such as the specific heat, where all energy scales contribute and self-energy sum rules have to be enforced.

Let us note however, that the Hilbert transform does not yield the expected $(1 - 1/Z)i\omega_n$ term, because the linearized self-energy violates the Kramers-Kronig relations. Restoring these relations requires taking into account the higher-energy, non-linear behaviour in $\Sigma(\omega)$. The restriction to the linear regime is not a problem for transport properties that only probe low energies.⁵⁰

3.3.2.2 Transport quantities for finite scattering

The central innovation of this Section is the observation that, in the current setting, the integrals in Eqs. (3.79-3.80) can be performed analytically—circumventing costly and (for small Γ) unstable numerical integrations. Indeed, also the evaluation of the particle number simplifies, one finds [331]

$$N = \sum_{\mathbf{k},n,\sigma} \int_{-\infty}^{\infty} d\omega f_{FD}(\omega) A_{\mathbf{k}n}(\omega) = \sum_{\mathbf{k},n,\sigma} \left(\frac{1}{2} - \frac{1}{\pi} \Im \psi(z_{\mathbf{k}n}) \right) \quad (3.87)$$

with the digamma function ψ evaluated at $z_{\mathbf{k}n} = \frac{1}{2} + \frac{\beta}{2\pi} [\Gamma_{\mathbf{k}n} + ia_{\mathbf{k}n}]$, where $\beta = 1/(k_B T)$ is the inverse temperature.⁵¹ Finite lifetimes (inverse scattering rate) explicitly enter through the digamma function—describing the thermal and lifetime smearing of excitations on an equal footing. Consequently, the energy states now obey a Γ -modified Fermi-Dirac statistic, displayed in Fig. 3.25. Crucially, even for $T = 0$ this distribution is not step-like—provided that $\Gamma > 0$. In Section 3.4.1.2, we explore the impact of the carrier density behaviour on the chemical potential and all derived transport properties.

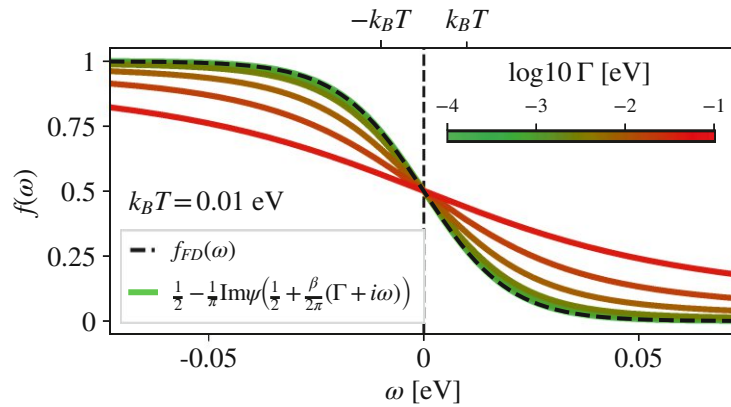


Figure 3.25: Lifetime enhanced broadening. Comparison between purely thermal broadening (dashed black line – Fermi function $f_{FD}(\omega)$) and lifetime enhanced broadening described by Eq. (3.87) for various scattering rates (solid colored lines).

⁵⁰In the occupation, the non-decaying behavior of the self-energy leads to lifetime smearing that generates contributions without an energy cut-off. This absence of a cut-off leads, e.g., to a divergence of the specific heat [403] in our formalism. Thus, one has to be mindful about this behavior when interpreting the resulting chemical potential.

The derivation of Eq. (3.87) is straight-forward: instead of an integral over the real frequency axis ω , we consider the Matsubara sum over the corresponding Green's function

$$n = \frac{1}{2} + \frac{1}{\beta} \sum_{\nu_m} \frac{1}{i\nu_m - a + i\Gamma \text{sign}(\nu_m)}, \quad (3.88)$$

where for brevity's sake we drop all band and momentum indices and consider only the purely imaginary part of the self-energy, $\Sigma(i\nu_m) = -i\Gamma \text{sign}(\nu_m)$. That is, we drop the Hartree term $\Sigma(\omega \rightarrow \infty)$ as we only consider lifetime broadening. Please see Appendix A.3 for a detailed explanation of the connection of the occupation to the Green's function and the necessary "convergence term" $\frac{1}{2}$. The Matsubara sum can now be rewritten into

$$\begin{aligned} \frac{1}{\beta} \sum_{\nu_m} \frac{1}{i\nu_m - a + i\Gamma \text{sign}(\nu_m)} &= \frac{1}{\beta} \sum_{m=-\infty}^{\infty} \frac{1}{i(2m+1)\frac{\pi}{\beta} - a + i\Gamma \text{sign}(2m+1)} \\ &= \frac{1}{2\pi i} \sum_{m=1}^{\infty} \left[\frac{1}{m - \frac{1}{2} + \frac{\beta}{2\pi}(\Gamma + ia)} - \frac{1}{m - \frac{1}{2} + \frac{\beta}{2\pi}(\Gamma - ia)} \right] \\ &\quad - \psi\left(\frac{1}{2} + \frac{\beta}{2\pi}(\Gamma + ia)\right) + \psi\left(\frac{1}{2} + \frac{\beta}{2\pi}(\Gamma - ia)\right) \\ &= -\frac{1}{\pi} \Im \psi\left(\frac{1}{2} + \frac{\beta}{2\pi}(\Gamma + ia)\right) \end{aligned} \quad (3.89)$$

where we used the series representation of the digamma function

$$\psi(z) = \sum_{m=1}^{\infty} \frac{1}{m} - \frac{1}{m+z-1} - \gamma \quad (3.90)$$

with the Euler-Mascheroni constant γ . To solidify the connection between the Fermi function and the digamma function, we provide a short proof that in the limit of $\Gamma \rightarrow 0^+$ one recovers an exact identity. The deviation of the Fermi function from $1/2$ (on the real axis) can be written as

$$\begin{aligned} f(a) - \frac{1}{2} &= -\frac{1}{2} \tanh\left(\frac{\beta a}{2}\right) \\ &= -2\beta a \sum_{k=1}^{\infty} \frac{1}{(1-2k)^2\pi^2 + (\beta a)^2} \end{aligned} \quad (3.91)$$

where the last identity only hold if $-\frac{1}{2} + \frac{i(\beta a)}{2\pi}$ is not an integer. Since we deal with arguments connected to the (inverse) temperature and energies a we can ensure the validity of the series representation at

⁵¹In this expression, the quasi-particle weight Z has been set to one, as, e.g., customary in slave-boson approaches. This procedure implicitly assumes the transfer of spectral weights, $1-Z$, to be symmetrical in the sense that it does not alter the chemical potential μ . In calculations where μ needs to be determined, we therefore solely employ renormalized energies and scattering rates in Eq. (3.87). Only in the transport kernels do we consider the full linearization of the self-energy, i.e. " Z -factors" emerge in the pre-factors of Eqs. (3.94-3.99).

all times. The deviation of the digamma function from $1/2$ on the other hand gives

$$\begin{aligned} -\frac{1}{\pi}\Im\psi\left(\frac{1}{2} + i\frac{\beta a}{2\pi}\right) &= \frac{1}{\pi}\Im\sum_{m=1}^{\infty}\frac{1}{m + \frac{1}{2} + i\frac{\beta a}{2\pi} - 1} = -\frac{1}{\pi}\sum_{m=1}^{\infty}\frac{\beta a}{2\pi}\frac{1}{(m - \frac{1}{2})^2 + \frac{(\beta a)^2}{4\pi^2}} \\ &= -2\beta a\sum_{m=1}^{\infty}\frac{1}{\pi^2(2m - 1)^2 + (\beta a)^2}, \end{aligned} \quad (3.92)$$

where we again used the series representation of the digamma function. Eq. (3.91) and Eq. (3.92) evidently agree with each other, term-by-term, i.e.

$$f(a) \equiv \frac{1}{2} - \frac{1}{\pi}\Im\psi\left(\frac{1}{2} + i\frac{\beta a}{2\pi}\right). \quad (3.93)$$

Turning our focus towards transport: For the intra-band kernels ($n \equiv m$) one finds with the polygamma function $\psi_{n'}(z)$ of order n' [404] evaluated at $z = z_{\mathbf{k}n} = \frac{1}{2} + \frac{\beta}{2\pi}(\Gamma_{\mathbf{k}n} + ia_{\mathbf{k}n})$

$$\mathcal{K}_{11}(\mathbf{k}, n) = \frac{Z^2\beta}{4\pi^3\Gamma}\left[\Re\psi_1(z) - \frac{\beta\Gamma}{2\pi}\Re\psi_2(z)\right], \quad (3.94)$$

$$\mathcal{K}_{12}(\mathbf{k}, n) = \frac{Z^2\beta}{4\pi^3\Gamma}\left[a\Re\psi_1(z) - \frac{a\Gamma\beta}{2\pi}\Re\psi_2(z) - \frac{\Gamma^2\beta}{2\pi}\Im\psi_2(z)\right], \quad (3.95)$$

$$\mathcal{K}_{22}(\mathbf{k}, n) = \frac{Z^2\beta}{4\pi^3\Gamma}\left[(a^2 + \Gamma^2)\Re\psi_1(z) + \frac{\beta}{2\pi}\Gamma(\Gamma^2 - a^2)\Re\psi_2(z) - \frac{\beta}{\pi}a\Gamma^2\Im\psi_2(z)\right], \quad (3.96)$$

$$\mathcal{K}_{11}^B(\mathbf{k}, n) = \frac{Z^3\beta}{16\pi^4\Gamma^2}\left[3\Re\psi_1(z) - \frac{3\Gamma\beta}{2\pi}\Re\psi_2(z) + \frac{\Gamma^2\beta^2}{4\pi^2}\Re\psi_3(z)\right], \quad (3.97)$$

$$\mathcal{K}_{12}^B(\mathbf{k}, n) = \frac{Z^3\beta}{16\pi^4\Gamma^2}\left[3a\Re\psi_1(z) - \frac{3a\Gamma\beta}{2\pi}\Re\psi_2(z) - \frac{\Gamma^2\beta}{2\pi}\Im\psi_2(z) + \frac{a\Gamma^2\beta^2}{4\pi^2}\Re\psi_3(z) + \frac{\Gamma^3\beta^2}{4\pi^2}\Im\psi_3(z)\right], \quad (3.98)$$

$$\begin{aligned} \mathcal{K}_{22}^B(\mathbf{k}, n) &= \frac{Z^3\beta}{16\pi^4\Gamma^2}\left[(\Gamma^2 + 3a^2)\Re\psi_1(z) - \frac{\beta\Gamma(\Gamma^2 + 3a^2)}{2\pi}\Re\psi_2(z) - \frac{\beta a\Gamma^2}{\pi}\Im\psi_2(z) \right. \\ &\quad \left. - \frac{\beta^2\Gamma^2(\Gamma^2 - a^2)}{4\pi^2}\Re\psi_3(z) + \frac{\beta^2 a\Gamma^3}{2\pi^2}\Im\psi_3(z)\right], \end{aligned} \quad (3.99)$$

where ψ_i is the i^{th} -derivative of the digamma function ψ evaluated at $z = \frac{1}{2} + \frac{\beta}{2\pi}(\Gamma + ia)$, with $a = \epsilon - \mu$. Momentum \mathbf{k} and band n indices of Z , Γ , and a have been omitted for “brevity”.

The (non-magnetic) inter-band ($n \neq m$) kernels become

$$\begin{aligned} \mathcal{K}_{11}(\mathbf{k}, n, m) &= \frac{Z_1 Z_2 \beta}{2\pi^3 [(a_1 - a_2)^2 + (\Gamma_1 - \Gamma_2)^2] [(a_1 - a_2)^2 + (\Gamma_1 + \Gamma_2)^2]} \times \\ &\times \left[\Re \left\{ [(a_1 - a_2)^2 + \Gamma_2^2 - \Gamma_1^2 - 2i\Gamma_1(a_2 - a_1)] \Gamma_2 \psi_1(z_1) \right\} \right. \\ &\left. + \Re \left\{ [(a_2 - a_1)^2 + \Gamma_1^2 - \Gamma_2^2 - 2i\Gamma_2(a_1 - a_2)] \Gamma_1 \psi_1(z_2) \right\} \right] \end{aligned} \quad (3.100)$$

$$\begin{aligned} \mathcal{K}_{12}(\mathbf{k}, n, m) &= \frac{Z_1 Z_2 \beta}{2\pi^3 [(a_1 - a_2)^2 + (\Gamma_1 - \Gamma_2)^2] [(a_1 - a_2)^2 + (\Gamma_1 + \Gamma_2)^2]} \times \\ &\times \left[\Re \left\{ (a_1 - i\Gamma_1) [(a_1 - a_2)^2 + \Gamma_2^2 - \Gamma_1^2 - 2i(a_2 - a_1)\Gamma_1] \Gamma_2 \psi_1(z_1) \right\} \right. \\ &\left. + \Re \left\{ (a_2 - i\Gamma_2) [(a_2 - a_1)^2 + \Gamma_1^2 - \Gamma_2^2 - 2i(a_1 - a_2)\Gamma_2] \Gamma_1 \psi_1(z_2) \right\} \right] \end{aligned} \quad (3.101)$$

$$\begin{aligned} \mathcal{K}_{22}(\mathbf{k}, n, m) &= \frac{Z_1 Z_2 \beta}{2\pi^3 [(a_1 - a_2)^2 + (\Gamma_1 - \Gamma_2)^2] [(a_1 - a_2)^2 + (\Gamma_1 + \Gamma_2)^2]} \times \\ &\times \left[\Re \left\{ (a_1 - i\Gamma_1)^2 [(a_1 - a_2)^2 + \Gamma_2^2 - \Gamma_1^2 - 2i(a_2 - a_1)\Gamma_1] \Gamma_2 \psi_1(z_1) \right\} \right. \\ &\left. + \Re \left\{ (a_2 - i\Gamma_2)^2 [(a_2 - a_1)^2 + \Gamma_1^2 - \Gamma_2^2 - 2i(a_1 - a_2)\Gamma_2] \Gamma_1 \psi_1(z_2) \right\} \right], \end{aligned} \quad (3.102)$$

where $\psi_1(z_{1/2})$ is evaluated at $z_{1/2} = \frac{1}{2} + \frac{\beta}{2\pi}(\Gamma_{1/2} + ia_{1/2})$. These kernels represent a generalization of Eqs. (3.94-3.96) and per Eq. (3.79) obey band-swapping symmetry $\mathcal{K}_{ab}(\mathbf{k}, n, m) \equiv \mathcal{K}_{ab}(\mathbf{k}, m, n)$.

The magnetic inter-band ($n \neq m$) kernels evaluate to

$$\begin{aligned} \mathcal{K}_{11}^B(\mathbf{k}, n, m) &= \frac{Z_1 Z_2^2 \Gamma_1 \Gamma_2^2 \beta}{2\pi^4} \times \left[\Re \left\{ \frac{1}{\Gamma_1} \psi_1(z_1) \frac{1}{[a_1 - a_2 - i(\Gamma_1 + \Gamma_2)]^2 [a_1 - a_2 - i(\Gamma_1 - \Gamma_2)]^2} \right\} \right. \\ &- \Re \left\{ \frac{\beta}{4\pi \Gamma_2^2} \psi_2(z_2) \frac{1}{[a_2 - a_1 - i(\Gamma_1 + \Gamma_2)] [a_2 - a_1 + i(\Gamma_1 - \Gamma_2)]} \right\} \\ &+ \Im \left\{ \frac{1}{\Gamma_2^2} \psi_1(z_2) \frac{(a_2 - a_1 - i\Gamma_2)}{[a_2 - a_1 - i(\Gamma_1 + \Gamma_2)]^2 [a_2 - a_1 + i(\Gamma_1 - \Gamma_2)]^2} \right\} \\ &\left. + \Re \left\{ \frac{1}{2\Gamma_2^3} \psi_1(z_2) \frac{1}{[a_2 - a_1 - i(\Gamma_1 + \Gamma_2)] [a_2 - a_1 + i(\Gamma_1 - \Gamma_2)]} \right\} \right], \end{aligned} \quad (3.103)$$

$$\begin{aligned}
\mathcal{K}_{12}^B(\mathbf{k}, n, m) = & \frac{Z_1 Z_2^2 \Gamma_1 \Gamma_2^2 \beta}{2\pi^4} \times \left[\Re \left\{ \frac{1}{\Gamma_1} \psi_1(z_1) \frac{(a_1 - i\Gamma_1)}{[a_1 - a_2 - i(\Gamma_1 + \Gamma_2)]^2 [a_1 - a_2 - i(\Gamma_1 - \Gamma_2)]^2} \right\} \right. \\
& - \Im \left\{ \frac{1}{2\Gamma_2^2} \psi_1(z_2) \frac{1}{[a_2 - a_1 - i(\Gamma_1 + \Gamma_2)] [a_2 - a_1 + i(\Gamma_1 - \Gamma_2)]} \right\} \\
& - \Re \left\{ \frac{\beta}{4\pi\Gamma_2^2} \psi_2(z_2) \frac{(a_2 - i\Gamma_2)}{[a_2 - a_1 - i(\Gamma_1 + \Gamma_2)] (a_2 - a_1 + i(\Gamma_1 - \Gamma_2))} \right\} \\
& + \Im \left\{ \frac{1}{\Gamma_2^2} \psi_1(z_2) \frac{(a_2 - i\Gamma_2)(a_2 - a_1 - i\Gamma_2)}{[a_2 - a_1 - i(\Gamma_1 + \Gamma_2)]^2 [a_2 - a_1 + i(\Gamma_1 - \Gamma_2)]^2} \right\} \\
& \left. + \Re \left\{ \frac{1}{2\Gamma_2^3} \psi_1(z_2) \frac{(a_2 - i\Gamma_2)}{[a_2 - a_1 - i(\Gamma_1 + \Gamma_2)] [a_2 - a_1 + i(\Gamma_1 - \Gamma_2)]} \right\} \right], \quad (3.104)
\end{aligned}$$

$$\begin{aligned}
\mathcal{K}_{22}^B(\mathbf{k}, n, m) = & \frac{Z_1 Z_2^2 \Gamma_1 \Gamma_2^2 \beta}{2\pi^4} \times \left[\Re \left\{ \frac{1}{\Gamma_1} \psi_1(z_1) \frac{(a_1 - i\Gamma_1)^2}{[a_1 - a_2 - i(\Gamma_1 + \Gamma_2)]^2 [a_1 - a_2 - i(\Gamma_1 - \Gamma_2)]^2} \right\} \right. \\
& - \Im \left\{ \frac{1}{\Gamma_2^2} \psi_1(z_2) \frac{(a_2 - i\Gamma_2)}{[a_2 - a_1 - i(\Gamma_1 + \Gamma_2)] [a_2 - a_1 + i(\Gamma_1 - \Gamma_2)]} \right\} \\
& - \Re \left\{ \frac{\beta}{4\pi\Gamma_2^2} \psi_2(z_2) \frac{(a_2 - i\Gamma_2)^2}{[a_2 - a_1 - i(\Gamma_1 + \Gamma_2)] (a_2 - a_1 + i(\Gamma_1 - \Gamma_2))} \right\} \\
& + \Im \left\{ \frac{1}{\Gamma_2^2} \psi_1(z_2) \frac{(a_2 - i\Gamma_2)^2 (a_2 - a_1 - i\Gamma_2)}{[a_2 - a_1 - i(\Gamma_1 + \Gamma_2)]^2 [a_2 - a_1 + i(\Gamma_1 - \Gamma_2)]^2} \right\} \\
& \left. + \Re \left\{ \frac{1}{2\Gamma_2^3} \psi_1(z_2) \frac{(a_2 - i\Gamma_2)^2}{[a_2 - a_1 - i(\Gamma_1 + \Gamma_2)] [a_2 - a_1 + i(\Gamma_1 - \Gamma_2)]} \right\} \right], \quad (3.105)
\end{aligned}$$

where for clarity we deliberately did not expand the imaginary and real part expressions.

3.3.2.3 Analytic evaluation of the transport kernels

Before discussing the consequences of the lifetime smearing and its effects on the low temperature behavior, we first give a detailed derivation of the transport kernels. The less technically involved reader may skip this Section and jump straight to the discussion in Section 3.3.5.

In this detailed derivation we will restrict ourselves to the intra-band case of Eqs. (3.79-3.80). We will “prove” the correctness of the inter-band expression by constructing the most general intra-band limit. For brevity we will abridge the notation and drop the full momentum and band dependence of the spectral function $A(\omega)$, quasi-particle weight Z , scattering rate Γ and energy $a = \epsilon - \mu$.

Contour integration

Starting from the generalized transport kernels ($a \in \{1, 2\}$, $b \in \{1, 2\}$) from Eq. (3.79)

$$\mathcal{K}_{ab}(\mathbf{k}, n) = \int_{-\infty}^{\infty} d\omega \omega^{(a+b-2)} \left(-\frac{\partial f_{FD}}{\partial \omega} \right) A^2(\omega) \quad (3.106)$$

we insert the Matsubara representation of the derivative of Fermi function

$$-\frac{\partial f_{FD}}{\partial \omega} = \lim_{\Omega \rightarrow 0^+} \frac{f_{FD}(\omega) - f_{FD}(\omega + \Omega)}{\Omega} = \lim_{\Omega \rightarrow 0^+} \frac{1}{\beta} \sum_m \frac{1}{\Omega} \left(\frac{1}{i\nu_m - \omega} - \frac{1}{i\nu_m - \omega - \Omega} \right)$$

as well as the (coherent part of the) spectral function

$$A_{\mathbf{k}n}(\omega) = \frac{Z\Gamma}{\pi} \frac{1}{(\omega - a)^2 + \Gamma^2} \quad (3.107)$$

where the fermionic Matsubara frequencies are $\nu_m = (2m+1)\frac{\pi}{\beta}$ with $m \in \mathbb{Z}$. The resulting expression

$$\begin{aligned} \mathcal{K}_{ab}(\mathbf{k}, n) &= \int_{-\infty}^{\infty} d\omega \frac{Z^2\Gamma^2}{\pi^2} \frac{\omega^{(a+b-2)}}{[(\omega - a)^2 + \Gamma^2]^2} \times \\ &\times \frac{1}{\beta} \sum_m \lim_{\Omega \rightarrow 0^+} \frac{1}{\Omega} \left(\frac{1}{i\nu_m - \omega} - \frac{1}{i\nu_m - \omega - \Omega} \right) \end{aligned} \quad (3.108)$$

can be abbreviated with

$$\mathcal{I}_{ab}(\mathbf{k}, n; \Omega; i\nu_m) = \int_{-\infty}^{\infty} d\omega \frac{(\omega - \Omega)^{(a+b-2)}}{[(\omega - a - \Omega)^2 + \Gamma^2]^2} \frac{1}{i\nu_m - \omega} \quad (3.109)$$

as

$$\mathcal{K}_{ab}(\mathbf{k}, n) = \frac{Z^2\Gamma^2}{\pi^2} \frac{1}{\beta} \lim_{\Omega \rightarrow 0^+} \left[\frac{1}{\Omega} \sum_m (\mathcal{I}_{ab}(\mathbf{k}, n; 0; i\nu_m) - \mathcal{I}_{ab}(\mathbf{k}, n; \Omega; i\nu_m)) \right] \quad (3.110)$$

For finite (positive) scattering rates, $\Gamma > 0$, Eq. (3.109) is an integral over a function with three distinct poles in the complex plane: $z = a + \Omega + i\Gamma$, $z = a + \Omega - i\Gamma$, and $z = i\nu_m$. This function decays with $z \rightarrow \infty$ as $\mathcal{O}(z^{a+b-7})$ which for all considered values of a and b is stronger than $\mathcal{O}(z^{-2})$, ensuring that any infinitely large arc in the complex plain will not contribute. Our desired integral, located on the real axis, can therefore be extended to a closed loop and thus be expressed as a sum of residues, see Fig. 3.26.

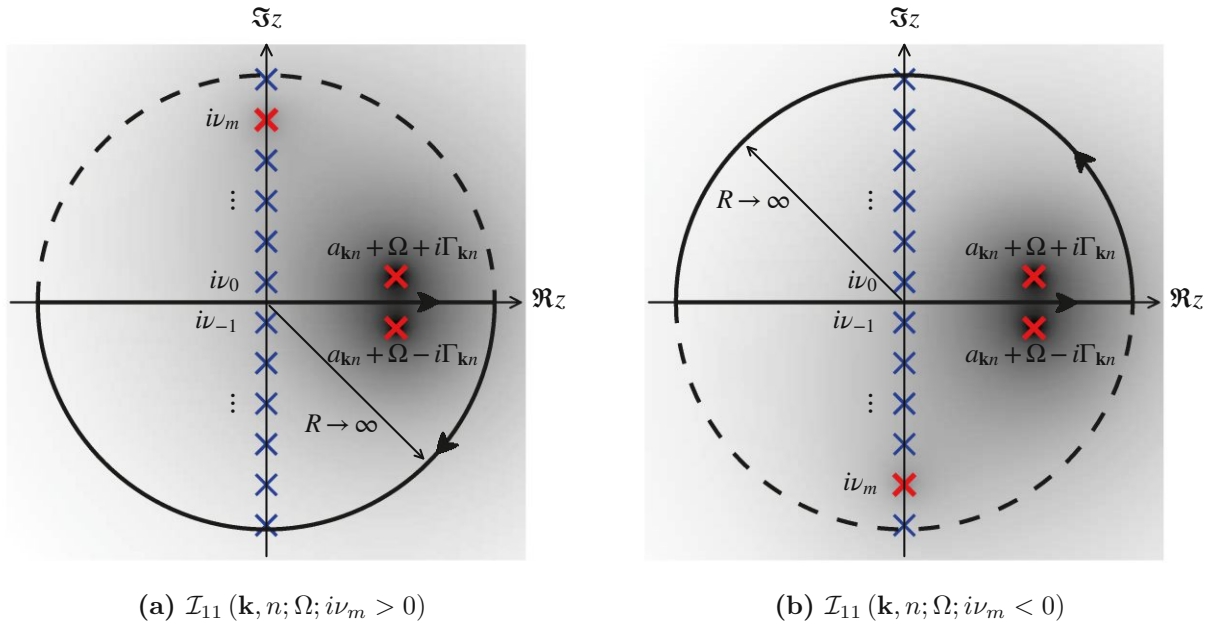


Figure 3.26: Contour integration. a) Extending the desired integral along $\omega = \Re z$ ($\Im z = 0$), the contour is closed via the *lower* half-plane for $\nu_m > 0$ or b) closed via the *upper* half-plane for $\nu_m < 0$. The poles of the Fermi function are located on the imaginary axis $z = i\nu_m = i\frac{\pi}{\beta}(2m + 1)$ while the poles of the spectral function are located at $z = a_{\mathbf{k}n} + \Omega \pm i\Gamma_{\mathbf{k}n}$. Due to functional decay $f(z) = \mathcal{O}(z^{a+b-7})$ (see text) in the limit of $R \rightarrow \infty$ the half-circles do not contribute. A straight-forward residue evaluation (inside the closed contour) is thus sufficient to calculate the initial integral.

By always choosing the half-circle opposite to the pole of the Matsubara frequency, see Fig. 3.26a and Fig. 3.26b respectively, we can restrict the evaluation to exactly one (higher order) pole

$$\begin{aligned}
 \mathcal{I}_{ab}(\mathbf{k}, n; \Omega; i\nu_m) &= \oint_{\mathcal{C}} dz \frac{(z - \Omega)^{(a+b-2)}}{[(z - a - \Omega)^2 + \Gamma^2]^2} \frac{1}{i\nu_m - z} \\
 &= -\text{sign}(\nu_m) 2\pi i \text{Res}_{z=(a+\Omega-i\text{sign}(\nu_m)\Gamma)} \frac{(z - \Omega)^{(a+b-2)}}{[(z - a - \Omega)^2 + \Gamma^2]^2} \frac{1}{i\nu_m - z}.
 \end{aligned} \tag{3.111}$$

Due to the different mathematical integration directions, positive and negative fermionic Matsubara frequencies result in differing prefactor signs.

Evaluating the residue at $z = (a + \Omega - i \operatorname{sign}(\nu_m)\Gamma)$ then results in the expressions

$$\mathcal{I}_{11}(\mathbf{k}, n; \Omega; i\nu_m) = \frac{\pi}{2\Gamma^3} \left[\frac{i\Gamma \operatorname{sign}(\nu_m)}{[i\nu_m - a - \Omega + i\Gamma \operatorname{sign}(\nu_m)]^2} + \frac{1}{[i\nu_m - a - \Omega + i\Gamma \operatorname{sign}(\nu_m)]} \right], \quad (3.112)$$

$$\mathcal{I}_{12}(\mathbf{k}, n; \Omega; i\nu_m) = \frac{\pi}{2\Gamma^3} \left[\frac{\Gamma^2 + i(a + \Omega)\Gamma \operatorname{sign}(\nu_m)}{[i\nu_m - a - \Omega + i\Gamma \operatorname{sign}(\nu_m)]^2} + \frac{(a + \Omega)}{[i\nu_m - a - \Omega + i\Gamma \operatorname{sign}(\nu_m)]} \right], \quad (3.113)$$

$$- \Omega \mathcal{I}_{11}(\mathbf{k}, n; \Omega; i\nu_m)$$

$$\mathcal{I}_{22}(\mathbf{k}, n; \Omega; i\nu_m) = \frac{\pi}{2\Gamma^3} \left[\frac{i(a + \Omega)^2 \Gamma \operatorname{sign}(\nu_m) + 2(a + \Omega)\Gamma^2 - i\Gamma^3 \operatorname{sign}(\nu_m)}{[i\nu_m - a - \Omega + i\Gamma \operatorname{sign}(\nu_m)]^2} + \frac{\Gamma^2 + (a + \Omega)^2}{[i\nu_m - a - \Omega + i\Gamma \operatorname{sign}(\nu_m)]} \right] - 2\Omega \mathcal{I}_{12}(\mathbf{k}, n; \Omega; i\nu_m) + \Omega^2 \mathcal{I}_{11}(\mathbf{k}, n; \Omega; i\nu_m). \quad (3.114)$$

Matsubara summations

The second step is to perform the Matsubara sums

$$\mathcal{I}_{ab}(\mathbf{k}, n; \Omega) = \frac{1}{\beta} \sum_{m=-\infty}^{\infty} \mathcal{I}_{ab}(\mathbf{k}, n; \Omega; i\nu_m). \quad (3.115)$$

Using, again, the series representation of the digamma and polygamma functions

$$\psi(z) = -\gamma + \sum_{n=1}^{\infty} \left(\frac{1}{n} - \frac{1}{n+z} \right) \quad (3.116a)$$

$$\psi_{m>0}(z) = (-1)^{m+1} m! \sum_{k=0}^{\infty} \frac{1}{(z+k)^{m+1}}, \quad (3.116b)$$

the summations appearing in Eqs. (3.112-3.114) result in

$$\frac{1}{\beta} \sum_{m=-\infty}^{\infty} \frac{1}{i\nu_m - a + i\Gamma \operatorname{sign}(\nu_m)} = -\frac{1}{\pi} \Im \psi(z) \quad (3.117)$$

$$\frac{1}{\beta} \sum_{m=-\infty}^{\infty} \frac{1}{[i\nu_m - a + i\Gamma \operatorname{sign}(\nu_m)]^2} = -\frac{\beta}{2\pi^2} \Re \psi_1(z) \quad (3.118)$$

$$\frac{1}{\beta} \sum_{m=-\infty}^{\infty} \frac{\operatorname{sign}(\nu_m)}{[i\nu_m - a + i\Gamma \operatorname{sign}(\nu_m)]^2} = -\frac{i\beta}{2\pi^2} \Im \psi_1(z) \quad (3.119)$$

$$\frac{1}{\beta} \sum_{m=-\infty}^{\infty} \frac{1}{[i\nu_m - a + i\Gamma \operatorname{sign}(\nu_m)]^3} = \frac{\beta^2}{8\pi^2} \Im \psi_2(z) \quad (3.120)$$

$$\frac{1}{\beta} \sum_{m=-\infty}^{\infty} \frac{\text{sign}(\nu_m)}{[i\nu_m - a + i\Gamma \text{sign}(\nu_m)]^3} = -\frac{i\beta^2}{8\pi^3} \Re\psi_2(z) \quad (3.121)$$

with $z = \frac{1}{2} + \frac{\beta}{2\pi}(\Gamma + ia)$. Then, the transport integrals simplify to

$$\mathcal{I}_{11}(\mathbf{k}, n; \Omega) = \frac{\pi}{2\Gamma^3} \left[\frac{\beta\Gamma}{2\pi^2} \Im\psi_1\left(z + \frac{i\beta\Omega}{2\pi}\right) - \frac{1}{\pi} \Im\psi\left(z + \frac{i\beta\Omega}{2\pi}\right) \right] \quad (3.122)$$

$$\begin{aligned} \mathcal{I}_{12}(\mathbf{k}, n; \Omega) = \frac{\pi}{2\Gamma^3} \left[-\frac{\Gamma^2\beta}{2\pi^2} \Re\psi_1\left(z + \frac{i\beta\Omega}{2\pi}\right) + \frac{(a + \Omega)\Gamma\beta}{2\pi^2} \Im\psi_1\left(z + \frac{i\beta\Omega}{2\pi}\right) \right. \\ \left. - \frac{(a + \Omega)}{\pi} \Im\psi\left(z + \frac{i\beta\Omega}{2\pi}\right) \right] - \Omega\mathcal{I}_{11}(\mathbf{k}, n; \Omega) \end{aligned} \quad (3.123)$$

$$\begin{aligned} \mathcal{I}_{22}(\mathbf{k}, n; \Omega) = \frac{\pi}{2\Gamma^3} \left[\frac{(a + \Omega)^2\Gamma\beta - \Gamma^3\beta}{2\pi^2} \Im\psi_1\left(z + \frac{i\beta\Omega}{2\pi}\right) - \frac{2(a + \Omega)\Gamma^2\beta}{2\pi^2} \Re\psi_1\left(z + \frac{i\beta\Omega}{2\pi}\right) \right. \\ \left. - \frac{\Gamma^2 + (a + \Omega)^2}{\pi} \Im\psi\left(z + \frac{i\beta\Omega}{2\pi}\right) \right] - 2\Omega\mathcal{I}_{12}(\mathbf{k}, n; \Omega) + \Omega^2\mathcal{I}_{11}(\mathbf{k}, n; \Omega). \end{aligned} \quad (3.124)$$

Dynamic limit

Taylor expanding the frequency-dependent di- and polygamma ($m > 0$) functions around z

$$\psi\left(z + \frac{i\beta\Omega}{2\pi}\right) = \psi(z) + \frac{i\beta\Omega}{2\pi}\psi_1(z) + \mathcal{O}(\Omega^2) \quad (3.125a)$$

$$\psi_m\left(z + \frac{i\beta\Omega}{2\pi}\right) = \psi_m(z) + \frac{i\beta\Omega}{2\pi}\psi_{m+1}(z) + \mathcal{O}(\Omega^2) \quad (3.125b)$$

and evaluating the limit

$$\mathcal{K}_{ab}(\mathbf{k}, n) = \frac{Z^2\Gamma^2}{\pi^2} \lim_{\Omega \rightarrow 0^+} \frac{1}{\Omega} [\mathcal{I}_{ab}(\mathbf{k}, n; 0) - \mathcal{I}_{ab}(\mathbf{k}, n; \Omega)] \quad (3.126)$$

we finally arrive at the intra-band equations

$$\mathcal{K}_{11}(\mathbf{k}, n) = \frac{Z^2\beta}{4\pi^3\Gamma} \left[\Re\psi_1(z) - \frac{\beta\Gamma}{2\pi} \Re\psi_2(z) \right], \quad (3.127)$$

$$\mathcal{K}_{12}(\mathbf{k}, n) = \frac{Z^2\beta}{4\pi^3\Gamma} \left[a\Re\psi_1(z) - \frac{a\Gamma\beta}{2\pi} \Re\psi_2(z) - \frac{\Gamma^2\beta}{2\pi} \Im\psi_2(z) \right], \quad (3.128)$$

$$\mathcal{K}_{22}(\mathbf{k}, n) = \frac{Z^2\beta}{4\pi^3\Gamma} \left[(a^2 + \Gamma^2)\Re\psi_1(z) + \frac{\beta}{2\pi}\Gamma(\Gamma^2 - a^2)\Re\psi_2(z) - \frac{\beta}{\pi}a\Gamma^2\Im\psi_2(z) \right]. \quad (3.129)$$

The equivalent calculation is easily performed for the magnetic kernel functions

$$\mathcal{K}_{ab}^B(\mathbf{k}, n) = \int_{-\infty}^{\infty} d\omega \omega^{(a+b-2)} \left(-\frac{\partial f}{\partial \omega} \right) A_{\mathbf{k}n}^3(\omega) \quad (3.130)$$

which only differ from their non-magnetic counterparts by an additional spectral function. The integrals

$$\mathcal{I}_{ab}^B(\mathbf{k}, n; \Omega; i\nu_m) = \int_{-\infty}^{\infty} d\omega \frac{(\omega - \Omega)^{(a+b-2)}}{[(\omega - a - \Omega)^2 + \Gamma^2]^3} \frac{1}{i\nu_m - \omega} \quad (3.131)$$

evaluate to

$$\mathcal{I}_{11}^B(\mathbf{k}, n; \Omega; i\nu_m) = \frac{i\pi}{8\Gamma^5} \left[\frac{2i\Gamma^2}{[i\nu_m - a - \Omega + i\Gamma \operatorname{sign}(\nu_m)]^3} + \frac{3\Gamma \operatorname{sign}(\nu_m)}{[i\nu_m - a - \Omega + i\Gamma \operatorname{sign}(\nu_m)]^2} + \frac{-3i}{[i\nu_m - a - \Omega + i\Gamma \operatorname{sign}(\nu_m)]} \right], \quad (3.132)$$

$$\mathcal{I}_{12}^B(\mathbf{k}, n; \Omega; i\nu_m) = \frac{i\pi}{8\Gamma^5} \left[\frac{2i(a + \Omega)\Gamma^2 + 2\Gamma^3 \operatorname{sign}(\nu_m)}{[i\nu_m - a - \Omega + i\Gamma \operatorname{sign}(\nu_m)]^3} + \frac{3(a + \Omega)\Gamma \operatorname{sign}(\nu_m) - i\Gamma^2}{[i\nu_m - a - \Omega + i\Gamma \operatorname{sign}(\nu_m)]^2} + \frac{-3i(a + \Omega)}{[i\nu_m - a - \Omega + i\Gamma \operatorname{sign}(\nu_m)]} \right] - \Omega \mathcal{I}_{11}^B(\mathbf{k}, n; \Omega; i\nu_m), \quad (3.133)$$

$$\mathcal{I}_{22}^B(\mathbf{k}, n; \Omega; i\nu_m) = \frac{i\pi}{8\Gamma^5} \left[\frac{2i(a + \Omega)^2\Gamma^2 + 4(a + \Omega)\Gamma^3 \operatorname{sign}(\nu_m) - 2i\Gamma^4}{[i\nu_m - a - \Omega + i\Gamma \operatorname{sign}(\nu_m)]^3} + \frac{-2i(a + \Omega)\Gamma^2 + \Gamma^3 \operatorname{sign}(\nu_m) + 3(a + \Omega)^2\Gamma \operatorname{sign}(\nu_m)}{[i\nu_m - a - \Omega + i\Gamma \operatorname{sign}(\nu_m)]^2} + \frac{-i\Gamma^2 - 3i(a + \Omega)^2}{[i\nu_m - a - \Omega + i\Gamma \operatorname{sign}(\nu_m)]} \right] - 2\Omega \mathcal{I}_{12}^B(\mathbf{k}, n; \Omega; i\nu_m) + \Omega^2 \mathcal{I}_{11}^B(\mathbf{k}, n; \Omega; i\nu_m). \quad (3.134)$$

Performing the Matsubara sums and taking the dynamical limit, the transport kernels results in the magnetic transport kernels

$$\mathcal{K}_{11}^B(\mathbf{k}, n) = \frac{Z^3\beta}{16\pi^4\Gamma^2} \left[3\Re\psi_1(z) - \frac{3\Gamma\beta}{2\pi}\Re\psi_2(z) + \frac{\Gamma^2\beta^2}{4\pi^2}\Re\psi_3(z) \right], \quad (3.135)$$

$$\mathcal{K}_{12}^B(\mathbf{k}, n) = \frac{Z^3\beta}{16\pi^4\Gamma^2} \left[3a\Re\psi_1(z) - \frac{3a\Gamma\beta}{2\pi}\Re\psi_2(z) - \frac{\Gamma^2\beta}{2\pi}\Im\psi_2(z) + \frac{a\Gamma^2\beta^2}{4\pi^2}\Re\psi_3(z) + \frac{\Gamma^3\beta^2}{4\pi^2}\Im\psi_3(z) \right], \quad (3.136)$$

$$\mathcal{K}_{22}^B(\mathbf{k}, n) = \frac{Z^3 \beta}{16\pi^4 \Gamma^2} \left[(\Gamma^2 + 3a^2) \Re\psi_1(z) - \frac{\beta\Gamma(\Gamma^2 + 3a^2)}{2\pi} \Re\psi_2(z) - \frac{\beta a \Gamma^2}{\pi} \Im\psi_2(z) \right. \\ \left. - \frac{\beta^2 \Gamma^2 (\Gamma^2 - a^2)}{4\pi^2} \Re\psi_3(z) + \frac{\beta^2 a \Gamma^3}{2\pi^2} \Im\psi_3(z) \right]. \quad (3.137)$$

3.3.2.4 Inter- to intra-band limit

Due to the number of involved terms, we only show the Kubo derivation for the intra-band transport kernels. When considering the inter-band form of Eqs. (3.100-3.102) one has to instead consider the explicit evaluation of two residues, located at $z_1 = a_1 \pm i\Gamma_1$ and $z_2 = a_2 \pm i\Gamma_2$ in the complex plane, as two distinct spectral functions contribute to the integrals (3.79-3.80). For brevity, we only illustrate the consistency between all provided inter- and intra-band formulas when taking the degenerate limit. Later on, we will see that this “trivial” property has critical consequences on approximations constructed from our new Kubo equations.

The compliance with this limit is especially important when evaluating the inter-band kernels *numerically*. To this end one has to do thorough checks of the involved energies $a_{1/2}$ and scattering rates $\Gamma_{1/2}$: If these parameters are too close to each other in the complex plane, the numerical evaluation becomes unstable.

This is apparent when evaluating, e.g., \mathcal{K}_{11} for a constant scattering rate $\Gamma = \Gamma_1 = \Gamma_2$ in the vicinity of a band crossing, see Eq. (3.100):

$$\mathcal{K}_{11}(\mathbf{k}, n, m) = \frac{Z_1 Z_2 \beta}{2\pi^3 (a_1 - a_2)^2 [(a_1 - a_2)^2 + 4\Gamma^2]} \times \quad (3.138) \\ \times \Re \left\{ \left[(a_1 - a_2)^2 - 2i\Gamma(a_2 - a_1) \right] \Gamma \psi_1(z_1) + \left[(a_2 - a_1)^2 - 2i\Gamma(a_1 - a_2) \right] \Gamma \psi_1(z_2) \right\}$$

which evaluates to something that is close to “0/0”. Naturally this numerical problem can be circumvented by instead evaluating the intra-band limit for these edge cases.

To “prove” the consistency, we construct the most general limit via a vectorial difference of the contributing poles in the upper half of the complex plane stemming from the spectral functions of Eq. (3.79):

$$\bar{z} = (a_2 + i\Gamma_2) - (a_1 + i\Gamma_1) \equiv R e^{i\Phi} \quad (3.139)$$

We can now express the “2” variables via the “1” variables

$$a_2 = a_1 + R \cos(\Phi) \quad (3.140a)$$

$$\Gamma_2 = \Gamma_1 + R \sin(\Phi) \quad (3.140b)$$

$$\psi_1(z_2) = \psi_1 \left(\frac{1}{2} + \frac{\beta}{2\pi} (\Gamma_1 + ia_1) + \frac{\beta}{2\pi} R \sin(\Phi) + i \frac{\beta}{2\pi} R \cos(\Phi) \right). \quad (3.140c)$$

and expand Eq. (3.140c) around $R = 0$:

$$\begin{aligned} & \psi_1 \left(\frac{1}{2} + \frac{\beta}{2\pi} (\Gamma_2 + ia_2) \right) = \\ & \psi_1 \left(\frac{1}{2} + \frac{\beta}{2\pi} (\Gamma_1 + ia_1) \right) + \psi_2 \left(\frac{1}{2} + \frac{\beta}{2\pi} (\Gamma_1 + ia_1) \right) \frac{\beta R}{2\pi} (\sin(\Phi) + i \cos(\Phi)) + \mathcal{O}(R^2) \end{aligned} \quad (3.141)$$

Setting $Z_1 = Z_2 = Z$, $a_1 = a$, $\Gamma_1 = \Gamma$, and expanding \mathcal{K}_{11} then results in

$$\begin{aligned} \mathcal{K}_{11}(\mathbf{k}, n, m) &= \frac{Z^2 \beta}{2\pi^3 R^2 [R^2 + 4\Gamma^2 + 4\Gamma R \sin(\Phi)]} \times \\ & \times \left[\Re \left\{ \left[R^2 + 2\Gamma R \sin(\Phi) - 2i\Gamma R \cos(\Phi) \right] (\Gamma + R \sin(\Phi)) \psi_1(z) \right\} \right. \\ & \left. + \Re \left\{ \left[R^2 (\cos^2(\Phi) - \sin^2(\Phi)) - 2\Gamma R \sin(\Phi) + 2i\Gamma R \cos(\Phi) + 2iR^2 \sin(\Phi) \cos(\Phi) \right] \Gamma \times \right. \right. \\ & \left. \left. \times \left[\psi_1(z) + \psi_2(z) \frac{\beta R}{2\pi} (\sin(\Phi) + i \cos(\Phi)) + \mathcal{O}(R^2) \right] \right\} \right]. \end{aligned} \quad (3.142)$$

To lowest order, the prefactor term scales with $\mathcal{O}(R^{-2})$, so in order to recover all non-vanishing terms we have to check the square bracket for terms up to $\mathcal{O}(R^2)$:

$$\begin{aligned} \mathcal{K}_{11}(\mathbf{k}, n, m) &= \left[\frac{Z^2 \beta}{8\pi^3 R^2 \Gamma^2} + \mathcal{O}(R^{-1}) \right] \times \\ & \times \left[R \underbrace{\left\{ 2\Gamma^2 \sin(\Phi) \Re \psi_1(z) + 2\Gamma^2 \cos(\Phi) \Im \psi_1(z) - 2\Gamma^2 \sin(\Phi) \Re \psi_1(z) - 2\Gamma^2 \cos(\Phi) \Im \psi_1(z) \right\}}_{\equiv 0} \right. \\ & \left. + R^2 \left\{ \Gamma \Re \psi_1(z) + 2\Gamma \sin^2(\Phi) \Re \psi_1(z) + 2\Gamma \cos(\Phi) \sin(\Phi) \Im \psi_1(z) \right. \right. \\ & \quad \left. \left. + (\cos^2(\Phi) - \sin^2(\Phi)) \Gamma \Re \psi_1(z) - 2 \sin(\Phi) \cos(\Phi) \Gamma \Im \psi_1(z) \right. \right. \\ & \quad \left. \left. + -2\Gamma^2 \sin^2(\Phi) \frac{\beta}{2\pi} \Re \psi_2(z) + 2\Gamma^2 \sin(\Phi) \cos(\Phi) \frac{\beta}{2\pi} \Im \psi_2(z) \right. \right. \\ & \quad \left. \left. - 2\Gamma^2 \cos(\Phi) \sin(\Phi) \frac{\beta}{2\pi} \Im \psi_2(z) - 2\Gamma^2 \cos^2(\Phi) \frac{\beta}{2\pi} \Re \psi_2(z) \right\} + \mathcal{O}(R^3) \right] \end{aligned} \quad (3.143)$$

As expected, the terms scaling with $\mathcal{O}(R)$ cancel exactly while the $\mathcal{O}(R^2)$ terms neatly recover the intra-band expression

$$\begin{aligned}
\mathcal{K}_{11}(\mathbf{k}, n, n) &= \lim_{R \rightarrow 0^+} \mathcal{K}_{11}(\mathbf{k}, n, m) = \frac{Z^2 \beta}{8\pi^3 \Gamma^2} \times \tag{3.144} \\
&\times \left[\Re \psi_1(z) \underbrace{\left[\Gamma + 2\Gamma \sin^2(\Phi) + \Gamma(\cos^2(\Phi) - \sin^2(\Phi)) \right]}_{\equiv 2\Gamma} + \Im \psi_1(z) \underbrace{\left[2\Gamma \cos(\Phi) \sin(\Phi) - 2\Gamma \sin(\Phi) \cos(\Phi) \right]}_{\equiv 0} \right] \\
&+ \Re \psi_2(z) \underbrace{\left[-2\Gamma^2 \sin^2(\Phi) \frac{\beta}{2\pi} - 2\Gamma^2 \cos^2(\Phi) \frac{\beta}{2\pi} \right]}_{\equiv -\frac{\Gamma^2 \beta}{\pi}} + \Im \psi_2(z) \underbrace{\left[2\Gamma^2 \sin(\Phi) \cos(\Phi) \frac{\beta}{2\pi} - 2\Gamma^2 \cos(\Phi) \sin(\Phi) \frac{\beta}{2\pi} \right]}_{\equiv 0} \Big]. \\
&= \frac{Z^2 \beta}{4\pi^3 \Gamma} \left[\Re \psi_1(z) - \frac{\beta \Gamma}{2\pi} \Re \psi_2(z) \right]
\end{aligned}$$

The other, non-magnetic, kernels follow in a similar fashion, see Appendix of Ref. [11]. For the inter-band magnetic kernels, the polygamma function has to be expanded to the third order

$$\begin{aligned}
\psi_1 \left(\frac{1}{2} + \frac{\beta}{2\pi} (\Gamma_2 + ia_2) \right) &= \psi_1 \left(\frac{1}{2} + \frac{\beta}{2\pi} (\Gamma_1 + ia_1) \right) \\
&+ \psi_2 \left(\frac{1}{2} + \frac{\beta}{2\pi} (\Gamma_1 + ia_1) \right) \frac{\beta R}{2\pi} (\sin(\Phi) + i \cos(\Phi)) + \tag{3.145} \\
&+ \psi_3 \left(\frac{1}{2} + \frac{\beta}{2\pi} (\Gamma_1 + ia_1) \right) \frac{\beta^2 R^2}{8\pi^2} (\sin(\Phi) + i \cos(\Phi))^2 + \mathcal{O}(R^3).
\end{aligned}$$

All generic limits have been also confirmed via *Mathematica*. The relevant notebook files can be verified at <https://github.com/mpickem/lrtclimit>.

3.3.3 Semiclassical Boltzmann limit

Besides providing us with expressions that can be evaluated with arbitrary accuracy at any given temperature, the expressions Eq. (3.94-3.105) can be exploited to derive the semiclassical Boltzmann transport equations.

By expanding the polygamma functions of order n around $\Gamma = 0$

$$\psi_n \left(\frac{1}{2} + \frac{\beta}{2\pi} (\Gamma + ia) \right) = \psi_n \left(\frac{1}{2} + \frac{i\beta a}{2\pi} \right) + \frac{\beta \Gamma}{2\pi} \psi_{n+1} \left(\frac{1}{2} + \frac{i\beta a}{2\pi} \right) + \mathcal{O}(\Gamma^2), \tag{3.146}$$

and recognizing that (see Section 3.3.2.2 above)

$$f_{\text{FD}}(a) = \frac{1}{2} - \frac{1}{\pi} \Im \psi \left(\frac{1}{2} + \frac{i\beta a}{2\pi} \right), \quad (3.147a)$$

$$-\partial_a f_{\text{FD}}(a) = \frac{\beta}{2\pi^2} \Re \psi_1 \left(\frac{1}{2} + \frac{i\beta a}{2\pi} \right). \quad (3.147b)$$

The Boltzmann intra-band expressions are then recovered from the expansions as the leading terms in the scattering rate Γ .

The limit for the \mathcal{K}_{11} kernel reads explicitly

$$\begin{aligned} \mathcal{K}_{11}(\mathbf{k}, n) &= \frac{Z^2 \beta}{4\pi^3 \Gamma} \left[\Re \psi_1 \left(\frac{1}{2} + \frac{\beta}{2\pi} (\Gamma + ia) \right) - \frac{\beta \Gamma}{2\pi} \Re \psi_2 \left(\frac{1}{2} + \frac{\beta}{2\pi} (\Gamma + ia) \right) \right] \\ &= \frac{Z^2 \beta}{4\pi^3 \Gamma} \left[\underbrace{\Re \psi_1 \left(\frac{1}{2} + \frac{i\beta a}{2\pi} \right)}_{-\frac{2\pi^2}{\beta} f'(a)} + \mathcal{O}(\beta^2 \Gamma^2) \right] \end{aligned} \quad (3.148)$$

which ignores terms of the order $(\beta\Gamma)^2$ and higher. Our quantum mechanical formalism thus contains the semi-classical description as the coherent (infinite lifetime) limit.

$$\mathcal{K}_{11}^{\text{Boltzmann}}(\mathbf{k}, n) = -\frac{Z^2}{2\pi\Gamma} \partial_a f_{\text{FD}}(a), \quad (3.149)$$

$$\mathcal{K}_{12}^{\text{Boltzmann}}(\mathbf{k}, n) = -\frac{aZ^2}{2\pi\Gamma} \partial_a f_{\text{FD}}(a), \quad (3.150)$$

$$\mathcal{K}_{22}^{\text{Boltzmann}}(\mathbf{k}, n) = -\frac{(a^2 + \Gamma^2) Z^2}{2\pi\Gamma} \partial_a f_{\text{FD}}(a), \quad (3.151)$$

$$\mathcal{K}_{11}^{\text{Boltzmann},B}(\mathbf{k}, n) = -\frac{3Z^3}{8\pi^2 \Gamma^2} \partial_a f_{\text{FD}}(a), \quad (3.152)$$

$$\mathcal{K}_{12}^{\text{Boltzmann},B}(\mathbf{k}, n) = -\frac{3aZ^3}{8\pi^2 \Gamma^2} \partial_a f_{\text{FD}}(a), \quad (3.153)$$

$$\mathcal{K}_{22}^{\text{Boltzmann},B}(\mathbf{k}, n) = -\frac{(3a^2 + \Gamma^2) Z^3}{8\pi^2 \Gamma^2} \partial_a f_{\text{FD}}(a). \quad (3.154)$$

Let us note that the two Boltzmann kernels describing heat-current-heat-current correlation functions $\mathcal{K}_{22}^{\text{Boltzmann},(B)}$ contain terms beyond the leading $1/\Gamma$ ($1/\Gamma^2$) order, see Eqs. (3.151,3.154). These higher-order terms are necessary, if one wants to ensure that the Boltzmann inter-band kernels reduce consistently to the Boltzmann intra-band expressions in the limit of degenerate states (with the same lifetime).

If the Boltzmann approximation only takes into account the leading terms, the limit $a_1 \rightarrow a_2; \Gamma_1 \rightarrow \Gamma_2$ will yield inconsistent results. To our knowledge this ensemble of inter-band Boltzmann expressions

has not been derived previously:

$$\begin{aligned} \mathcal{K}_{11}^{\text{Boltzmann}}(\mathbf{k}, n, m) &= -\frac{Z_1 Z_2}{\pi [(a_1 - a_2)^2 + (\Gamma_1 - \Gamma_2)^2] [(a_1 - a_2)^2 + (\Gamma_1 + \Gamma_2)^2]} \times \\ &\times \left[\left[(a_1 - a_2)^2 + \Gamma_2^2 - \Gamma_1^2 \right] \Gamma_2 \partial_{a_1} f_{\text{FD}}(a_1) \right. \\ &\left. + \left[(a_2 - a_1)^2 + \Gamma_1^2 - \Gamma_2^2 \right] \Gamma_1 \partial_{a_2} f_{\text{FD}}(a_2) \right] \end{aligned} \quad (3.155)$$

$$\begin{aligned} \mathcal{K}_{12}^{\text{Boltzmann}}(\mathbf{k}, n, m) &= -\frac{Z_1 Z_2}{\pi [(a_1 - a_2)^2 + (\Gamma_1 - \Gamma_2)^2] [(a_1 - a_2)^2 + (\Gamma_1 + \Gamma_2)^2]} \times \\ &\times \left[\left\{ \left[(a_1 - a_2)^2 + \Gamma_2^2 - \Gamma_1^2 \right] a_1 - 2\Gamma_1^2(a_1 - a_2) \right\} \Gamma_2 \partial_{a_1} f_{\text{FD}}(a_1) \right. \\ &\left. + \left\{ \left[(a_2 - a_1)^2 + \Gamma_1^2 - \Gamma_2^2 \right] a_2 - 2\Gamma_2^2(a_2 - a_1) \right\} \Gamma_1 \partial_{a_2} f_{\text{FD}}(a_2) \right] \end{aligned} \quad (3.156)$$

$$\begin{aligned} \mathcal{K}_{22}^{\text{Boltzmann}}(\mathbf{k}, n, m) &= -\frac{Z_1 Z_2}{\pi [(a_1 - a_2)^2 + (\Gamma_1 - \Gamma_2)^2] [(a_1 - a_2)^2 + (\Gamma_1 + \Gamma_2)^2]} \times \\ &\times \left[\left\{ \left[(a_1 - a_2)^2 + \Gamma_2^2 - \Gamma_1^2 \right] (a_1^2 - \Gamma_1^2) - 4\Gamma_1^2 a_1(a_1 - a_2) \right\} \Gamma_2 \partial_{a_1} f_{\text{FD}}(a_1) \right. \\ &\left. + \left\{ \left[(a_2 - a_1)^2 + \Gamma_1^2 - \Gamma_2^2 \right] (a_2^2 - \Gamma_2^2) - 4\Gamma_2^2 a_2(a_2 - a_1) \right\} \Gamma_1 \partial_{a_2} f_{\text{FD}}(a_2) \right] \end{aligned} \quad (3.157)$$

$$\begin{aligned} \mathcal{K}_{11}^{\text{Boltzmann},B}(\mathbf{k}, n, m) &= -\frac{Z_1 Z_2^2}{2\pi^2 \Gamma_2} \times \\ &\times \left[\Re \left\{ \frac{2\Gamma_2^3}{[a_1 - a_2 - i(\Gamma_1 + \Gamma_2)]^2 [a_1 - a_2 - i(\Gamma_1 - \Gamma_2)]^2} \right\} \partial_{a_1} f_{\text{FD}}(a_1) \right. \\ &+ \Im \left\{ \frac{2\Gamma_1 \Gamma_2 (a_2 - a_1 - i\Gamma_2)}{[a_2 - a_1 - i(\Gamma_1 + \Gamma_2)]^2 [a_2 - a_1 + i(\Gamma_1 - \Gamma_2)]^2} \right\} \partial_{a_2} f_{\text{FD}}(a_2) \\ &\left. + \Re \left\{ \frac{\Gamma_1}{[a_2 - a_1 - i(\Gamma_1 + \Gamma_2)] [a_2 - a_1 + i(\Gamma_1 - \Gamma_2)]} \right\} \partial_{a_2} f_{\text{FD}}(a_2) \right] \end{aligned} \quad (3.158)$$

$$\begin{aligned}
\mathcal{K}_{12}^{\text{Boltzmann},B}(\mathbf{k}, n, m) &= -\frac{Z_1 Z_2^2}{2\pi^2 \Gamma_2} \times \\
&\times \left[\Re \left\{ \frac{2\Gamma_2^3 (a_1 - i\Gamma_1)}{[a_1 - a_2 - i(\Gamma_1 + \Gamma_2)]^2 [a_1 - a_2 - i(\Gamma_1 - \Gamma_2)]^2} \right\} \partial_{a_1} f_{\text{FD}}(a_1) \right. \\
&- \Im \left\{ \frac{\Gamma_1 \Gamma_2}{[a_2 - a_1 - i(\Gamma_1 + \Gamma_2)] [a_2 - a_1 + i(\Gamma_1 - \Gamma_2)]} \right\} \partial_{a_2} f_{\text{FD}}(a_2) \\
&+ \Im \left\{ \frac{2\Gamma_1 \Gamma_2 (a_2 - i\Gamma_2) (a_2 - a_1 - i\Gamma_2)}{[a_2 - a_1 - i(\Gamma_1 + \Gamma_2)]^2 [a_2 - a_1 + i(\Gamma_1 - \Gamma_2)]^2} \right\} \partial_{a_2} f_{\text{FD}}(a_2) \\
&\left. + \Re \left\{ \frac{\Gamma_1 (a_2 - i\Gamma_2)}{[a_2 - a_1 - i(\Gamma_1 + \Gamma_2)] [a_2 - a_1 + i(\Gamma_1 - \Gamma_2)]} \right\} \partial_{a_2} f_{\text{FD}}(a_2) \right] \quad (3.159)
\end{aligned}$$

$$\begin{aligned}
\mathcal{K}_{22}^{\text{Boltzmann},B}(\mathbf{k}, n, m) &= -\frac{Z_1 Z_2^2}{2\pi^2 \Gamma_2} \times \\
&\times \left[\Re \left\{ \frac{2\Gamma_2^3 (a_1 - i\Gamma_1)^2}{[a_1 - a_2 - i(\Gamma_1 + \Gamma_2)]^2 [a_1 - a_2 - i(\Gamma_1 - \Gamma_2)]^2} \right\} \partial_{a_1} f_{\text{FD}}(a_1) \right. \\
&- \Im \left\{ \frac{2\Gamma_1 \Gamma_2 (a_2 - i\Gamma_2)}{[a_2 - a_1 - i(\Gamma_1 + \Gamma_2)] [a_2 - a_1 + i(\Gamma_1 - \Gamma_2)]} \right\} \partial_{a_2} f_{\text{FD}}(a_2) \\
&+ \Im \left\{ \frac{2\Gamma_1 \Gamma_2 (a_2 - i\Gamma_2)^2 (a_2 - a_1 - i\Gamma_2)}{[a_2 - a_1 - i(\Gamma_1 + \Gamma_2)]^2 [a_2 - a_1 + i(\Gamma_1 - \Gamma_2)]^2} \right\} \partial_{a_2} f_{\text{FD}}(a_2) \\
&\left. + \Re \left\{ \frac{\Gamma_1 (a_2 - i\Gamma_2)^2}{[a_2 - a_1 - i(\Gamma_1 + \Gamma_2)] [a_2 - a_1 + i(\Gamma_1 - \Gamma_2)]} \right\} \partial_{a_2} f_{\text{FD}}(a_2) \right] \quad (3.160)
\end{aligned}$$

To illustrate the problem of an inconsistent intra-band limit, we compare the evaluation of Eq. (3.155) to the “naive” inter-band expression, where only the leading Γ -terms are considered

$$\begin{aligned}
\mathcal{K}_{11}^{\text{Boltzmann leading}}(\mathbf{k}, n, m) &= -\frac{Z_1 Z_2}{\pi [(a_1 - a_2)^2 + (\Gamma_1 - \Gamma_2)^2] [(a_1 - a_2)^2 + (\Gamma_1 + \Gamma_2)^2]} \times \\
&\times \left[[(a_1 - a_2)^2] \Gamma_2 \partial_{a_1} f_{\text{FD}}(a_1) + [(a_2 - a_1)^2] \Gamma_1 \partial_{a_2} f_{\text{FD}}(a_2) \right] \quad (3.161)
\end{aligned}$$

in Fig. 3.27, where we employed $a_1 = 0$, $\Gamma_1 = 2 \cdot 10^{-4} \text{eV}$ and varied a_2 and Γ_2 around these fixed values. Note that we restricted the heatmap to $\pm 2\%$ around the intra-band expression of Eq. (3.149).

When all necessary leading and higher order terms are considered, see Fig. 3.27a, approaching the degenerate state via $\Gamma_2 \rightarrow \Gamma_1$ and $a_2 \rightarrow a_1$ becomes directional-independent: irrespective of how the limit is performed, the inter-band value approaches the intra-band value in a smooth fashion. If

only the leading orders are considered, see Fig. 3.27b, one obtains a directional dependence

$$\mathcal{K}_{11}^{\text{Boltzmann leading}}(\mathbf{k}, n, m \rightarrow n) = \frac{Z_1 Z_2}{2\pi\Gamma} \cos(\Theta)^2 \quad (3.162)$$

when employing the same vectorial difference as used in Eq. (3.139) and taking the $R \rightarrow 0^+$ limit. In the leading order formulation of Eq. (3.161) the intra-band limit to Eq. (3.149) is thus only valid if both scattering rates are identical $\Gamma_1 = \Gamma_2$ and the limit is taken with respect to the energies ($\Theta \in \{0, \pi\}$). Despite the agreement in this specific limit, the two expressions differ vastly away from the degenerate state, see Fig. 3.27: Setting $a_1 = a_2$ and approaching the center via $\Gamma_2 \rightarrow \Gamma_1$, the leading order kernel does not seem to approach the white-shaded degenerate limit at all. Further, even when moving a sizable distance away from the center, considerable differences can be noticed.

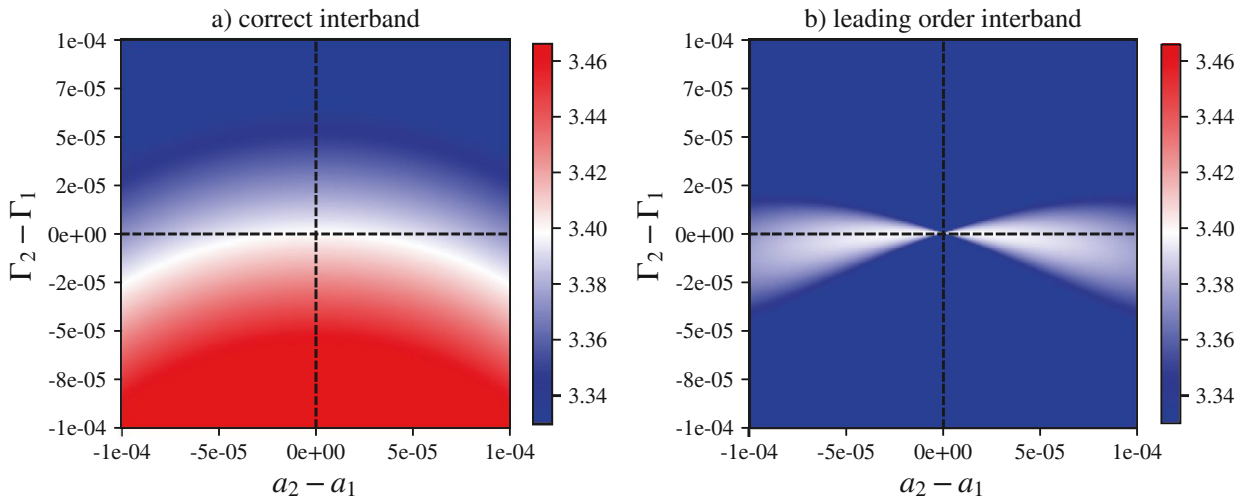


Figure 3.27: Numerical evaluation of the inter-band limit. The heatmaps show the evaluation of the Boltzmann inter-band kernels with $\Gamma_1 = 2 \cdot 10^{-4} \text{eV}$ and $a_1 = 0$ of a) Eq. (3.155) and b) Eq. (3.161). Approaching the degenerate state in the centre ($\Gamma_2 = \Gamma_1$, $a_2 = a_1$), we find a directional independence in the former and a strong directional dependence in the latter.

Following these considerations, the inter-band Boltzmann kernels of Eqs. (3.155-3.160) contain most terms of the Kubo kernels of Eqs. (3.100-3.105) and a reduction in complexity is nearly impossible. Furthermore, only when considering non-intuitive higher-order-in- Γ contributions in Eqs. (3.151,3.154) do we then also find compatibility with the above inter-band kernels. The relevant *Mathematica* notebooks showing this analytic connection (for all six inter-band quantities), can be also found at <https://github.com/mpickem/lrtclimit>.

3.3.4 Transition-matrix elements

To finalize the discussion of the Onsager coefficients, a few comments on the transition-matrix elements are in order.

3.3.4.1 Dipole optical elements

With band-theory (for WIEN2k's implementation see Ref. [360]), the coupling elements in the evaluation of the Onsager coefficients Eqs. (3.77-3.78) can be calculated via the corresponding Fermi velocities (matrix elements of the momentum operator)

$$v_{\mathbf{k}n'n}^\alpha = \frac{1}{m} \langle \mathbf{k}n' | \mathcal{P}_\alpha | \mathbf{k}n \rangle = v_{\mathbf{k}n'n}^{\alpha*} \quad (3.163)$$

with α indicating a Cartesian direction, m the electron mass, and $\langle \mathbf{r} | \mathbf{k}n \rangle = \chi_{\mathbf{k}n}(\mathbf{r})$ a band-momentum basis. The amplitude of optical dipole ($\mathbf{q} = \mathbf{0}$) transitions is then given by

$$M^{\alpha\beta}(\mathbf{k}, n, m) = v_{\mathbf{k}nm}^{\alpha*} v_{\mathbf{k}mn}^\beta \quad (3.164)$$

3.3.4.2 Peierls approximation

In tight-binding or model settings, in which there is no access to wavefunctions, the above matrix elements cannot be calculated. Instead, one couples the electromagnetic vector potential directly to the lattice fermions using the Peierls substitution approach [234]. Following this (approximate) procedure [64, 359, 362, 405], Fermi velocities are momentum-derivatives of the (one-particle) Hamiltonian. Performing the derivative in the band-basis, there are only intra-band velocities, $v_{\mathbf{k}nm}^\alpha \propto \delta_{nm} v_{\mathbf{k}n}^\alpha$, for which

$$v_{\mathbf{k}n}^\alpha = \frac{1}{\hbar} \partial_{k_\alpha} \varepsilon_n(\mathbf{k}), \quad (3.165)$$

and

$$M^{\alpha\beta}(\mathbf{k}, n, n) = v_{\mathbf{k}n}^\alpha v_{\mathbf{k}n}^\beta. \quad (3.166)$$

In a more general framework [384, 359] also inter-band transitions can be included in a Peierls-like fashion.

Using the band-curvatures $c_k^{\alpha\beta} = 1/\hbar \partial_{k_\alpha} \partial_{k_\beta} \varepsilon(\mathbf{k})$, also the matrix elements for magnetic quantities can be derived. One finds [386]

$$M^{B,\alpha\beta\gamma}(\mathbf{k}, n, n) = \varepsilon_{\gamma ij} v_{\mathbf{k}n}^\alpha c_{\mathbf{k}n}^{\beta j} v_{\mathbf{k}n}^i \quad (3.167)$$

with ε_{ijk} the Levi-Civita symbol in three dimensions.

Clearly, however, taking momentum-derivatives does not commute with a general basis transformation U : $\partial_k U^\dagger(\mathbf{k})H(\mathbf{k})U(\mathbf{k}) \neq U^\dagger(\mathbf{k})(\partial_k H(\mathbf{k}))U(\mathbf{k})$. Therefore, transport properties using the Peierls approach will be basis-dependent [405]. One can show [362] that the Peierls approximation is best (closest to the true dipole element) the more localized the basis is. In the tight-binding and Wannier mode, we therefore perform the momentum-derivative in the local/Wannier basis $\chi_{\mathbf{R}l}(\mathbf{r}) = \langle \mathbf{r} | \mathbf{R}l \rangle$:

$$v_{\mathbf{k}l'l'}^\alpha = \frac{1}{\hbar} \partial_{k_\alpha} H^{ll'}(\mathbf{k}) - i(\rho_{l'}^\alpha - \rho_l^\alpha) H^{ll'}(\mathbf{k}) \quad (3.168)$$

where $H(\mathbf{k})$ is the Fourier transform of $H(\mathbf{R})$. In this generalized Peierls approach [362], the second term arises for unit-cells with more than one atom, with intra-cell coordinates ρ_l of the atom hosting orbital l . This extra-term in particular assures that an arbitrary extension of the unit-cell (conventional cell or equivalent supercells) gives the same result as calculations for the primitive unit-cell. Velocities evaluated in the local basis (orbitals indexed with l) are then rotated into the band-basis (band-index n). Because of the mentioned non-commutation of momentum-derivative and basis-transformation, the generalized Peierls approach may yield inter-band transitions à la Eq. (3.164) that are absent in Eq. (3.165).

3.3.5 Discussion

The general feature that can be observed when treating thermal (β) and lifetime (Γ) smearing on equal footing is a departure from a transport description with decoupled energy scales. Within the Boltzmann approximation, see Section 3.3.3, the kernels scale “trivially” with the (inverse) lifetime and their selection window is determined purely by the thermal fluctuations. Here instead, we find an overarching description with highly non-trivial prefactors and functional arguments which no longer act independently from one another.

The inclusion of finite lifetimes in Eqs. (3.94)-(3.99) leads to

- (i) An effectively different statistic: the Fermi function is replaced with a digamma function in which thermal broadening is supplemented by an energy smearing Γ corresponding to finite lifetimes (cf. Fig. 3.25).
- (ii) All transport kernels have, beyond the explicitly leading terms (e.g., $1/\Gamma \Re \Psi_1$ in \mathcal{K}_{11}), contributions from higher order polygamma functions Ψ_n .

While the Eqs. (3.94-3.99) are quite involved, they are, in fact, on par with Boltzmann approaches employing the relaxation time approximation in terms of numerical complexity and evaluation speed.

In fact, many Boltzmann codes [406, 407, 408, 409, 410, 411, 412] could readily upgrade their electronic transport capabilities by switching to the kernels presented here.

3.3.5.1 Polygamma functions

The Polygamma functions, naturally occurring through the required (internal, fermionic) Matsubara summations (see Section 3.3.2.3), are the $(m+1)$ th derivative of the logarithm of the Gamma function

$$\psi_m(z) = \frac{d^{m+1}}{dz^{m+1}} \ln \Gamma(z). \quad (3.169)$$

The digamma function ($m = 0$) and its higher order derivatives are thus

$$\psi(z) = \psi_0(z) = \frac{\Gamma'(z)}{\Gamma(z)} \quad (3.170a)$$

$$\psi_{m>0} = \frac{d^m}{dz^m} \psi(z). \quad (3.170b)$$

Sometimes helpful in numerical libraries, the polygamma functions ($m > 0$) can be also connected to the Hurwitz zeta function

$$\zeta(s, a) = \sum_{n=0}^{\infty} \frac{1}{(n+a)^s} \quad (3.171)$$

(Riemann zeta function: $s = 1$) via

$$\psi_m(z) = (-1)^{m+1} m! \zeta(m+1, z). \quad (3.172)$$

Through the connection to the Gamma function, the polygamma functions are holomorphic everywhere except at non-positive integers. There, a pole of order $m+1$ occurs, see Eq. (3.171). Evaluating the polygamma functions at $z = 1/2 + \beta/(2\pi)(\Gamma + ia)$ avoids any problematic regions in the complex plane and all functions are well-behaved.

In order to evaluate the low temperature behavior we exploit the Taylor expansion around $\bar{z} = \infty$ of the digamma function

$$\Psi \left(\frac{1}{2} + \bar{z} \right) = \ln(\bar{z}) + \frac{1}{24\bar{z}^2} - \frac{7}{960\bar{z}^4} + \mathcal{O}(\bar{z}^{-6}), \quad (3.173)$$

and all higher order polygamma functions

$$\Psi_1 \left(\frac{1}{2} + \bar{z} \right) = \frac{1}{\bar{z}} - \frac{1}{12\bar{z}^3} + \frac{7}{240\bar{z}^5} + \mathcal{O}(\bar{z}^{-7}), \quad (3.174a)$$

$$\Psi_2 \left(\frac{1}{2} + \bar{z} \right) = -\frac{1}{\bar{z}^2} + \frac{1}{4\bar{z}^4} - \frac{7}{48\bar{z}^6} + \mathcal{O}(\bar{z}^{-8}), \quad (3.174b)$$

$$\Psi_3 \left(\frac{1}{2} + \bar{z} \right) = \frac{2}{\bar{z}^3} - \frac{1}{\bar{z}^5} + \frac{7}{8\bar{z}^7} + \mathcal{O}(\bar{z}^{-9}). \quad (3.174c)$$

Eqs. (3.94-3.99) then become

$$\mathcal{K}_{11} = \frac{Z^2}{\pi^2} \frac{\Gamma^2}{(a^2 + \Gamma^2)^2} \left[1 + \frac{2\pi^2}{3} \frac{5a^2 - \Gamma^2}{(a^2 + \Gamma^2)^2} (k_B T)^2 + \mathcal{O}(T^4) \right] \quad (3.175)$$

$$\mathcal{K}_{12} = \frac{4Z^2}{3} \frac{a\Gamma^2}{(a^2 + \Gamma^2)^3} \left[(k_B T)^2 + \frac{7\pi^2}{5} \frac{5a^2 - 3\Gamma^2}{(a^2 + \Gamma^2)^2} (k_B T)^4 + \mathcal{O}(T^6) \right] \quad (3.176)$$

$$\mathcal{K}_{22} = \frac{Z^2}{3} \frac{\Gamma^2}{(a^2 + \Gamma^2)^2} \left[(k_B T)^2 + \frac{14\pi^2}{5} \frac{5a^2 - \Gamma^2}{(a^2 + \Gamma^2)^2} (k_B T)^4 + \mathcal{O}(T^6) \right] \quad (3.177)$$

$$\mathcal{K}_{11}^B = \frac{Z^3}{\pi^3} \frac{\Gamma^3}{(a^2 + \Gamma^2)^3} \left[1 + \pi^2 \frac{7a^2 - \Gamma^2}{(a^2 + \Gamma^2)^2} (k_B T)^2 + \mathcal{O}(T^4) \right] \quad (3.178)$$

$$\mathcal{K}_{12}^B = \frac{2Z^3}{\pi} \frac{a\Gamma^3}{(a^2 + \Gamma^2)^4} \left[(k_B T)^2 + \frac{28\pi^2}{15} \frac{7a^2 - 3\Gamma^2}{(a^2 + \Gamma^2)^2} (k_B T)^4 + \mathcal{O}(T^6) \right] \quad (3.179)$$

$$\mathcal{K}_{22}^B = \frac{Z^3}{3\pi} \frac{\Gamma^3}{(a^2 + \Gamma^2)^3} \left[(k_B T)^2 + \frac{21\pi^2}{5} \frac{7a^2 - \Gamma^2}{(a^2 + \Gamma^2)^2} (k_B T)^4 + \mathcal{O}(T^6) \right] \quad (3.180)$$

Therefore for any $\lim_{T \rightarrow 0} \Gamma(T) > 0$ the resistivity as well as the Hall coefficient will saturate. Furthermore the Seebeck coefficient, the Nernst coefficient as well as the thermal conductivity will tend to 0 in a linear fashion, cf. Section 3.3.1.

3.3.5.2 Quasi-particle renormalizations

The above equations also allow for a simple symmetry analysis. For instance, we see that \mathcal{K}_{12} is odd with respect to a . As a consequence, electron and hole contributions to the Seebeck coefficient, Eq. (3.61), have opposite signs. \mathcal{K}_{11}^B , instead, is even in a . Therefore, the Hall coefficient R_H , Eq. (3.64), actually does not distinguish electron and hole contributions through their energies (the sign of a), but thanks to the sign of the dispersion's curvature entering the matrix element M^B in Eq. (3.167). Manifestly, the above kernel functions are far more complicated than the familiar expressions of the semi-classical Boltzmann approach in the constant relaxation time approximation (cf., e.g., Refs. [363, 406, 407, 408, 413]). However, the latter are recovered from the above formulae as the leading terms in the limit of infinite lifetimes, see Section 3.3.3. Besides the broadening effects, we also derived renormalization factors that are commonly not included in Boltzmann approaches.

The kernel expressions in Sec. 3.3.2, based on the self-energy linearization Eq. (3.81), clearly exhibit a non-trivial dependency on the quasi-particle renormalization: Z -factors emerge, both, as part of the overall prefactor (à la Boltzmann) as well as in the argument of the polygamma functions via a renormalization of the energy (a) and the scattering (Γ):

Consider a *metallic* system with bare dispersion $\varepsilon_0(\mathbf{k})$ and a bare scattering rate Γ_0 at temperatures where the Boltzmann approximation is accurate. If the same quasi-particle renormalizations is applied to all states, a partial cancellation of the prefactors in Eqs. (3.149-3.154) occurs due to renormalization of the scattering rate $\Gamma = Z\Gamma_0$. The Boltzmann response kernels then verify

$$\mathcal{K}_{ij}^{(B)} \propto Z a^{i+j-2} \partial_a f_{\text{FD}}(a). \quad (3.181)$$

The conductivity kernel ($i = j = 1$) that is even in the energy $a = Z\varepsilon_0$ is to good approximation unaffected by Z due to a compensation of two effects: Z simultaneously decreases the weights of the selected states, and pushes more states into the (thermal) selection window through band-narrowing.⁵²

Odd kernels (\mathcal{L}_{12} , \mathcal{L}_{12}^B) on the other hand distinguish between electron and hole contributions via the sign of a . Through this differentiation the overall summation will be tilted to either direction depending on the asymmetry of the system. Energy renormalization in this context then can be thought of as an amplification of this asymmetry, increasing the non-interacting signal⁵³

$$\mathcal{K}_{12}^{(B)}(Z) \propto \frac{1}{Z} \mathcal{K}_{12}^{(B)}(Z = 1) \quad (3.182)$$

providing a correlation mechanism to boost the Seebeck [414, 415] and Nernst coefficient, realized, e.g., in heavy-fermion systems [416]. The above arguments in general do not hold for insulating systems where we find a more nuanced interplay of band gap, energies, chemical potential and quasi-particle renormalization. At the very least $Z < 1$ will result in a band gap reduction $\Delta = Z\Delta_0$, which affects thermal activation, and hence conduction, exponentially.

⁵²This is exact for $0 < Z \leq 1$, in the limit of infinite bandwidth and a flat density of states. In realistic scenarios, however, there can be a notable Z -dependence for strong renormalizations and narrow band-widths, elevated temperatures, or a strongly energy-dependent density of states.

⁵³By assuming a linearized density of states centered around the thermal selection window, $D(\varepsilon) = D_0 + \alpha\varepsilon$, it is apparent that only the linear (constant) term is responsible for finite values of kernels that are odd (even) in the energy a . Quasi-particle renormalizations drop out for the constant term and amplify the effect of the linear term, leading to the increase of $\frac{1}{Z}$ of Eq. (3.182).

3.4 Many-body transport phenomena in semiconductors

- This Section is based on the results published in “Prototypical many-body transport phenomena in semiconductors” by [Matthias Pickem](#), Emanuele Maggio, and Jan M. Tomczak [9]. Adopted text passages have been marked accordingly.
- In this Section we focus purely on the numerical analysis and characterization of the transport tensors in gapped systems (semiconductors). The present results were computed with `LINRETRACE` version 1.0. Here, the aforementioned sign and pre-factor fixes have been adopted and the relevant figures have been adjusted accordingly.
- The implementation details and applications beyond “simple” semiconductors of `LINRETRACE` are discussed in Section 3.5.

Here, we establish the prototypical signatures of finite electronic lifetimes in transport properties of (narrow-gap) semiconductors [212, 363]. To this end, we build on the Kubo methodology of Section 3.2, based on Ref. [7], which captures (in)coherence effects beyond the reach of semi-classical Boltzmann approaches [406, 407, 408], while incurring a comparable numerical cost. Our theory reveals that the scattering is a *relevant energy scale*: Through its interplay with the gap-energy, a rich temperature profile emerges in all observables. In this scenario, *extrinsic* effects only enter indirectly, by limiting the lifetimes of *intrinsic* carriers. Previous semi-classical techniques—where scattering merely scales the amplitude of conduction—often require explicit in-gap states to provide additional carriers so as to mimic the experimental temperature dependence.

We highlight this insight in Fig. 3.28 for a simple two-band modeling of the colossal-thermopower material FeSb_2 [214, 300, 417, 418]. The large *magnitude* of its S and ν originates from the phonon-drag effect [331, 419, 420, 421, 422, 423]⁵⁴. Here, we focus on the *characteristic temperatures* that mark features across various observables [214]: For instance, inflection points in the resistivity ρ and the Seebeck coefficient S correlate with maxima in the Hall and Nernst coefficient, R_H , ν . This intriguing—but by no means uncommon [212, 424, 425]—temperature profile, was previously advocated to derive from *extrinsic* in-gap states [421, 422, 423, 426, 427, 428].

⁵⁴ The phonon-enhancement of the electron diffusion is expected to be smooth in temperature, i.e., it does not introduce characteristic features. Further, a suppression of the phonon-drag in polycrystalline samples yields Seebeck coefficients [419, 420, 429, 430] comparable to our modelling.

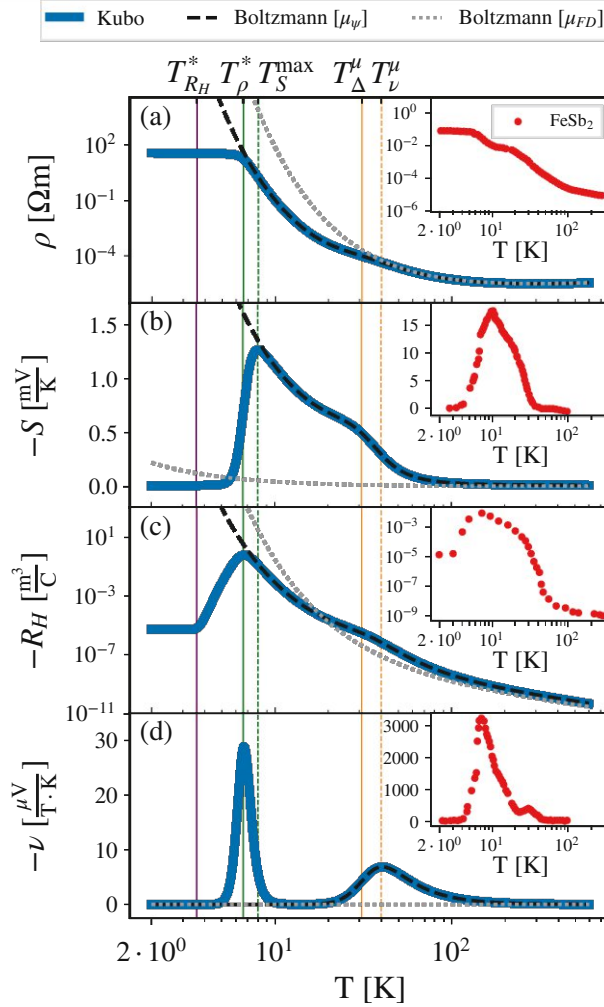


Figure 3.28: Prototypical transport in semiconductors. Comparing an asymmetric two-band model, $\epsilon_{\mathbf{k}n}^0 = -\sum_{i=x,y,z} 2t_n \cos(k_i) + (-1)^n(6t_n + \Delta_0/2)$, ($\alpha = |t_2/t_1| = 1.06$), with $t_1=250\text{meV}$, $t_2=-265\text{meV}$, bandgap $\Delta_0 = 60\text{ meV}$; effective mass $Z^{-1} = 2$, scattering rate $\Gamma(T) = (5 \cdot 10^{-5} + 10^{-7}/\text{K}^2 \cdot T^2)\text{ eV}$ to experiments on FeSb_2 [214] (insets): a) resistivity, coefficients of b) Seebeck, c) Hall, and d) Nernst *without* impurity in-gap states. Vertical lines mark characteristic temperatures (from left to right): Saturation onset of the Hall coefficient T_{RH}^* and the resistivity T_ρ^* , the maximal Seebeck coefficient T_S^{max} , onset of second activated regime T_Δ^μ , and the high-temperature Nernst peak T_ν^μ . Dashed black (grey) lines show Boltzmann results using a chemical potential, μ_ψ (μ_{FD}), that accounts for lifetime and thermal (only thermal) broadening.

Here, instead, we reproduce all qualitative temperature features in FeSb_2 in the absence of explicit in-gap levels, exclusively by endowing the *intrinsic* valence and conduction carriers with a *finite scattering rate*, $\Gamma(T) = \Gamma_0 + \gamma T^2$. Our findings establish a new phenomenology for transport properties

in semiconductors: Below a temperature T_ρ^* , ρ saturates [7] instead of growing exponentially (see the Boltzmann result (dashed line) in Fig. 3.28). R_H also saturates (below $T_{R_H}^* < T_\rho^*$), indicating that residual scattering leads to a finite density of states even at absolute zero. Finite lifetimes also mend the violation of the 3rd law of thermodynamics of Boltzmann's relaxation time approximation: Instead of diverging, the Seebeck coefficient S vanishes linearly for $T \rightarrow 0$. Combined to the powerfactor $S^2\sigma$ and the figure of merit zT , our findings have practical relevance for thermoelectric applications: In narrow-gap semiconductors, these quantities exhibit large values at intermediate to low temperatures when scattering processes are properly accounted for. Material surveys based on Boltzmann approaches for coherent band structure instead fail to even qualitatively describe $S^2\sigma$ and zT . Finally, in congruence with experiment, a sharp low- T feature emerges in the Nernst coefficient that, again, has no analogue in the Boltzmann treatment.

Looking at the available experimental literature, we find a number of narrow-gap semiconductors [212] that exhibit qualitatively similar temperature profiles as the ones displayed in Fig. 3.28. For instance, other marcasite compounds (FeAs₂, RuSb₂ [424, 431, 432, 433], CrSb₂ [434]), silicides (FeSi [320, 435, 436], RuSi [437, 438, 439]), Heusler systems (e.g., Fe₂VAl [440, 441, 442, 443, 444]), other intermetallic compounds [445] (e.g., FeGa₃, RuGa₃ [425, 446, 447]), as well as Kondo insulators (e.g., Ce₃Bi₄Pt₃ [253, 323, 333, 334, 339, 344])—strongly suggesting that our scenario based on carriers with finite lifetimes is prototypical for a wide array of different systems.

3.4.1 A new phenomenology of transport in semiconductors

3.4.1.1 Low-temperature expansion

Signatures of finite electronic lifetimes are most pronounced at low-temperatures, where qualitative deviations from Boltzmann behaviour are especially pronounced. Our first goal therefore is to provide *simple* phenomenological formulae for transport observables at low temperatures. To this end we first expand the polygamma functions $\psi_i(1/2 + \bar{z})$ in the intra-band kernel Eqs. (3.94-3.99), derived in Section 3.3, around $\bar{z} = \infty$, i.e. $T = 0$. Second, we assume a simplistic electronic structure; indeed, we note that in metals and semi-metals only states in the direct vicinity of the Fermi level contribute sizably to conduction of charge and heat. In gapped systems, instead, transport will be dominated by the conduction (valence) band minimum (maximum). Both constraints effectively limit the parts of the Brillouin zone relevant to transport. To gain a qualitative insight, we therefore radically forgo the momentum integration in Eqs. (3.77-3.78): We consider a single non-dispersive level at an energy ϵ and constant transition matrix elements $M^{(B)}$. Assuming further a scattering rate Γ independent of temperature, we obtain the following prototypical dependencies

$$\sigma \propto e^2 \frac{Z^2}{\pi^2} \frac{\Gamma^2}{(a^2 + \Gamma^2)^2} \left[1 + \frac{2\pi^2}{3} \frac{5a^2 - \Gamma^2}{(a^2 + \Gamma^2)^2} \times (k_B T)^2 + \mathcal{O}(T^4) \right] \quad (3.183)$$

$$\sigma^B \propto e^3 \frac{2Z^3}{3\pi^3} \frac{\Gamma^3}{(a^2 + \Gamma^2)^3} \left[1 + \pi^2 \frac{7a^2 - \Gamma^2}{(a^2 + \Gamma^2)^2} \times (k_B T)^2 + \mathcal{O}(T^4) \right] \quad (3.184)$$

$$S \propto -\frac{k_B}{e} \frac{4\pi^2}{3} \frac{a}{a^2 + \Gamma^2} \left[k_B T + \frac{\pi^2}{15} \frac{55a^2 - 53\Gamma^2}{(a^2 + \Gamma^2)^2} (k_B T)^3 + \mathcal{O}(T^5) \right] \quad (3.185)$$

$$R_H \propto \frac{2\pi}{3e} \frac{1}{Z\Gamma} \left[a^2 + \Gamma^2 + \frac{\pi^2}{3} (k_B T)^2 + \mathcal{O}(T^4) \right] \quad (3.186)$$

$$\kappa \propto \frac{Z^2}{3} \frac{\Gamma^2}{(a^2 + \Gamma^2)^2} \left[k_B T - \frac{16\pi^2 a^2}{3(a^2 + \Gamma^2)^2} (k_B T)^3 + \mathcal{O}(T^5) \right] \quad (3.187)$$

$$\nu \propto -\frac{4\pi^2}{9} k_B \frac{aZ\Gamma}{(a^2 + \Gamma^2)^2} \left[k_B T - \frac{4\pi^2}{3} \frac{8a^2 - \Gamma^2}{(a^2 + \Gamma^2)^2} (k_B T)^3 + \mathcal{O}(T^5) \right] \quad (3.188)$$

where $a = \epsilon - \mu$ indicates the position of the renormalized level $\epsilon = Z\epsilon^0$ with respect to the chemical potential μ . We now discuss the above asymptotic behavior and compare to Boltzmann approaches in the relaxation time approximation, see Table 3.2 for a summary of the $T \rightarrow 0$ limit. Note that the above equations describe the low- T response for a single level. If several states are contributing, terms can be simply added up for the conductivities. For composite quantities, such as the Seebeck or the Hall coefficient, however, contributions to the Onsager coefficients, Eq. (3.52), have to be summed before they are combined into the observable quantities.

$\lim T \rightarrow 0$	LinReTraCe	Boltzmann
ρ	ρ_{sat}	∞
S	0	∞
κ	0	0
R_H	$R_{H,\text{sat}}$	∞
$\nu = \nu_1 - \nu_2$	0	0
$\nu_{1/2}$	0	∞

Table 3.2: Zero temperature limits of transport properties in stoichiometric gapped systems for a finite scattering rate Γ . Eqs. (3.183, 3.186) lead to saturation in the resistivity and the Hall coefficient, while the Boltzmann signal diverges. Entropy transport complies with the laws of thermodynamics (Seebeck $S \rightarrow 0$ for $T \rightarrow 0$), while S unphysically diverges in the relaxation time approximation. $\nu_{1/2}$ denote the two contributions to the Nernst coefficient, Eq. (3.65). All limiting behaviors of LINRETRACE are congruent with experiments, see Fig. 3.37 and Fig. 3.28.

Charge transport

One of the main observations is that in the zero temperature limit $T \rightarrow 0$ the electrical (σ) and Hall conductivity (σ^B) remain finite in the presence of residual scattering ($\Gamma > 0$). In Eqs. (3.79-3.80) the derivative of the Fermi function becomes increasingly narrow with decreasing temperature. Alone, this temperature-dependent energy cut-off would lead to the typical activated behavior and is well-described in Boltzmann theory. However, for $\Gamma > 0$, the Lorentzian shape of the spectral function, Eq. (3.84), allows states away from the Fermi level to still contribute to conduction even at $T = 0$, as incoherent spectral weight spills into the gap, see Fig. 3.29b and cf. the effective particle distribution function in Fig. 3.25. This residual conductivity is at the heart of the resistivity saturation in (non-topological) Kondo insulators and has been discussed in detail in Ref. [7]. Similarly, the Hall conductivity in Eq. (3.63) and, hence, the Hall coefficient in Eq. (3.64) saturate for $\Gamma > 0$. The Boltzmann approximation, see Section 3.3.3, on the other hand relies solely on the Fermi function to select states with sharply defined energies ϵ . Then, conductivities must strictly approach zero in gapped systems for $T \rightarrow 0$. Since the electrical and the Hall conductivity have the identical temperature scaling, Eq. (3.64) implies a diverging Hall coefficient in Boltzmann's relaxation time approximation, see Fig. 3.28c⁵⁵.

Thermoelectric transport

In essence the Seebeck and Nernst effect can be understood as entropy carried by charged currents [211, 383, 394]. The third law of thermodynamics states that at zero temperature the entropy S_0 of the system must be minimal. In a perfect crystal lattice without ground state degeneracy this minimal value must be 0 since there is only one possible microstate ($S_0 = k_B \ln(\Omega); \Omega = 1$), requiring the Seebeck as well as the Nernst coefficient to vanish for $T \rightarrow 0$. This is respected in our framework: Similar to the case of metals [416], we find $S \sim T$ ($T \rightarrow 0$) in a semiconductor with finite lifetimes. As discussed in more detail in Section 3.4.1.2, it is residual conduction from incoherent states that leads to a weakly metal-like Seebeck coefficient. In the Boltzmann limit, instead, S unphysically diverges in a semiconductor: $S(T) \propto \frac{1}{T}$.

⁵⁵The higher order kernels $\mathcal{K}_{12}^{(B)}$ and $\mathcal{K}_{22}^{(B)}$ are accompanied by an additional ω - and ω^2 -factor in Eqs. (3.79-3.80), respectively. Therefore, the active energy window is additionally suppressed, causing these kernels to vanish for $T \rightarrow 0$. The exact temperature scaling is crucial (see Appendix 3.3.5.1) since an additional $1/T$ -factor must be considered for some transport tensors in Eqs. (3.58-3.65). Then, in our formalism, the thermal conductivity κ and the Seebeck coefficient S vanish for $T \rightarrow 0$.

The Nernst coefficient vanishes in both formalisms. In the Boltzmann case, this is hidden in the two terms making up Eq. (3.65) ($\nu = \nu_1 - \nu_2$): While both ν_i ($i = 1, 2$) diverge, they cancel exactly when combined. In the Kubo formalism, both terms ν_i separately approach 0. Further, for finite Γ , $\nu \propto T$ at lowest temperatures—again akin to the behaviour of metals [392] and (see Section 3.4.1.2) connected to conduction from intrinsic, but incoherent in-gap states.

In all, Eqs. (3.183-3.188) establish a low-temperature phenomenology of transport in semiconductors. The derived asymptotic behavior overcomes limitations of semi-classical descriptions and is congruent with experimental observations (see Fig. 3.28 above and Fig. 3.37 below).

3.4.1.2 Prototypical transport properties of narrow-gap systems

In this Section we leave the low temperature limit and study the full temperature dependence of the transport observables from Eqs. (3.58-3.65). Motivated by experimental transport measurements of intermetallic hybridization-gap semiconductors—such as FeSb₂, FeAs₂, FeSi, FeGa₃, their Ru-analogues and others—we consider a simple, asymmetric two-band electronic structure

$$\epsilon_{\mathbf{k}n}^0 = - \sum_{i=x,y,z} 2t_n \cos(k_i) + (-1)^n (6t_n + \Delta_0/2) \quad (3.189)$$

with $n = 1, 2$ for the valence and conduction band, respectively, and fix the filling to $N = 2$ (half-filling). We use a generic lattice constant $a_{\text{lattice}} = 1\text{\AA}$ and $60 \times 60 \times 60$ ($200 \times 200 \times 200$) k -points for the Kubo (Boltzmann) calculations to achieve k -grid convergence. Particle-hole asymmetry is introduced by hopping parameters, t_n , that are different for the valence band (VB; $n = 1$) and the conduction band (CB; $n = 2$). We measure the degree of asymmetry via

$$\alpha = \left| \frac{t_2}{t_1} \right|. \quad (3.190)$$

The two bands of the narrow-gap semiconductor are then additionally endowed with the same, finite and—for the time being—temperature-independent scattering rate Γ , while we set the quasi-particle weight to unity, $Z = 1$. This setup generalizes the symmetric ($\alpha = 1$) two-band model for which we studied the resistivity in Ref. [7]. An example electronic structure is displayed in Fig. 3.29. Even though motivated by said materials, we keep the electronic structure deliberately simple, so as to isolate qualitative trends and the prototypical temperature dependencies of transport properties. A more realistic setup with a temperature-dependent scattering rate will be introduced in Section 3.4.1.2.

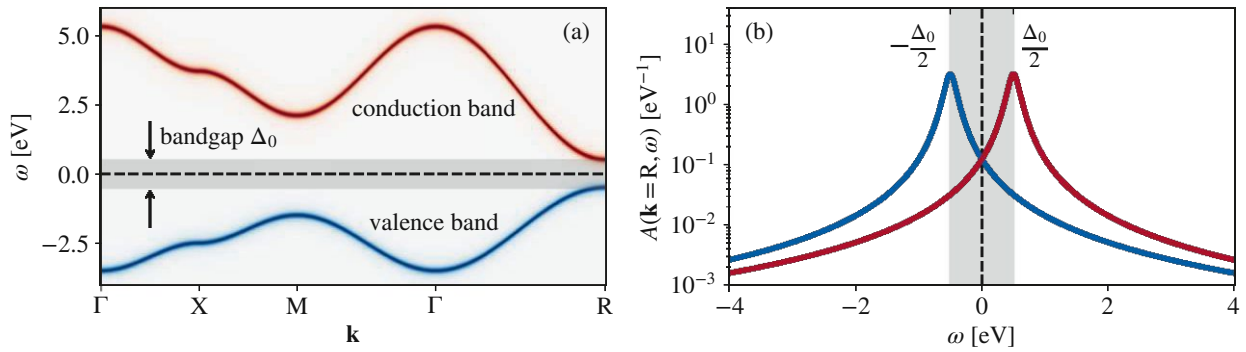


Figure 3.29: Model electronic structure. (a) Broadened band structure $\epsilon_{\mathbf{k}n}^0 = -\sum_{i=x,y,z} 2t_n \cos(k_i) + (-1)^n (6t_n + \Delta_0/2)$ with $t_1 = 0.25\text{eV}$, $t_2 = -0.40\text{eV}$ and $\Delta_0 = 1.0\text{eV}$. The broadening $\Gamma = 0.1\text{eV}$ is exaggerated in order to illustrate the effects. (b) Spectral functions at $\mathbf{k} = \mathbf{R} = (\pi, \pi, \pi)$ where the direct gap is exactly Δ_0 . The Lorentzian form, Eq. (3.84), of the spectral functions causes weight to spill-over into the bandgap. As a consequence, for $T \rightarrow 0$, transport properties exhibit metal-like signatures, such as residual conduction (=resistivity saturation) and a linear-in- T Seebeck coefficient.

The three parameters that describe the transport equations of our model are the bandgap Δ_0 , the band asymmetry α and the scattering rate Γ . As a first step we simply scan through each parameter individually while keeping the other two fixed. The results for these parameter sweeps are shown in Fig. 3.30. The clear protagonist of transport properties beyond Boltzmann results based on band structures is the scattering rate Γ . It influences transport in two ways: First, $\Gamma > 0$ leads—in a particle-hole asymmetric system—to a non-trivial temperature dependence of the chemical potential, which, in turn, influences charge and energy transport. Boltzmann approaches that use band structures as input fully miss this ingredient as only thermal (not lifetime) broadening is included in the chemical potential search. Second, contributions to the transport kernels, Eqs. (3.94-3.99), are—contrary to Boltzmann approaches in the relaxation-time approximation—not simply proportional to the carrier lifetime, $1/\Gamma$, but exhibit an intricate Γ -dependence that influences the temperature profile of transport properties. In the following, we will disentangle these two ingredients.

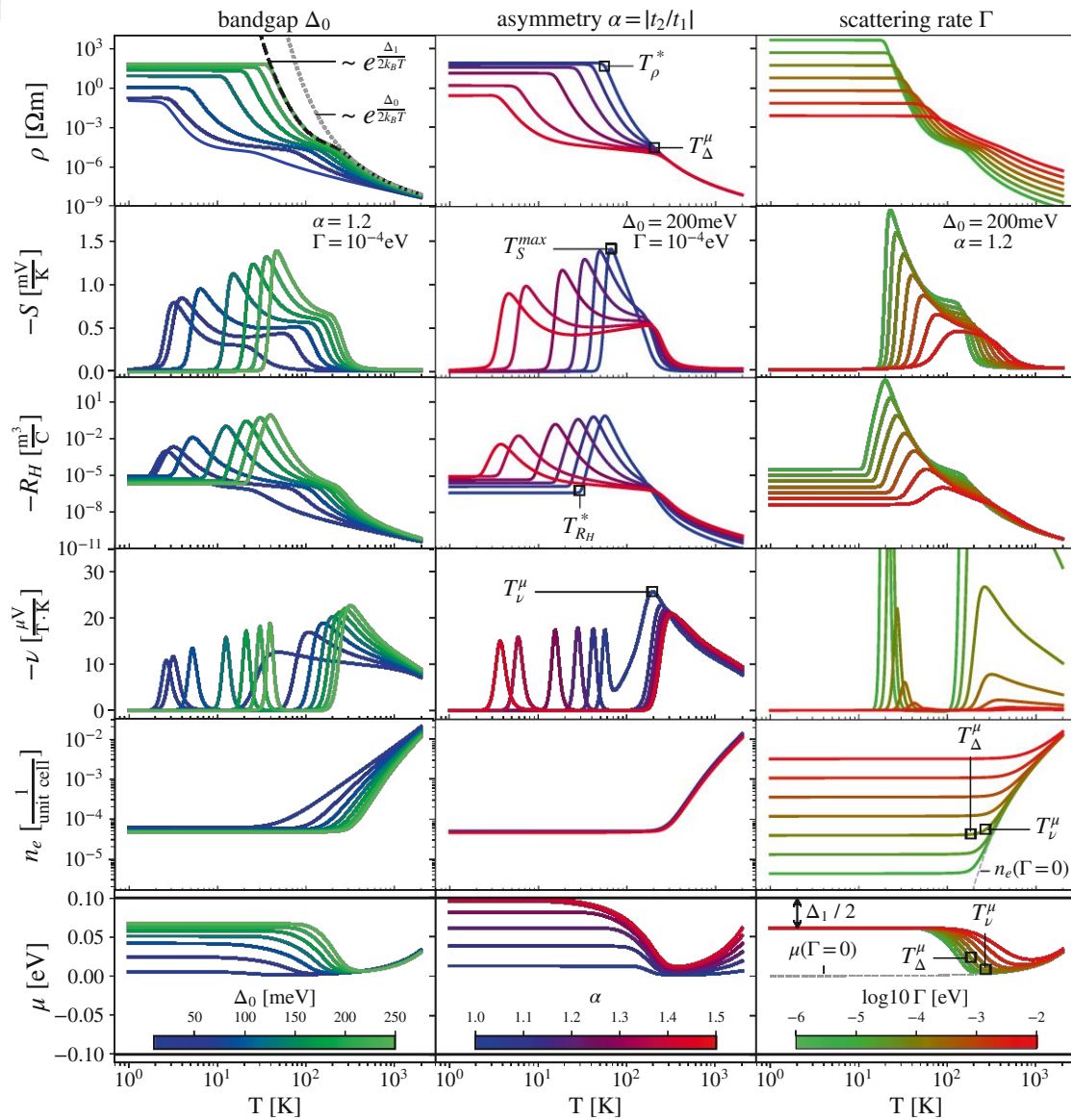


Figure 3.30: Transport in semiconductors: A parameter scan. Left column: varying bandgaps Δ_0 for fixed hopping $t_1 = 0.25\text{eV}$ and $t_2 = -0.30\text{eV}$ (asymmetry $\alpha = 1.2$) and scattering rate $\Gamma = 10^{-4}\text{eV}$; middle column: varying asymmetries α for fixed bandgap $\Delta_0 = 200\text{meV}$ and scattering rate $\Gamma = 10^{-4}\text{eV}$; right column: varying scattering rate Γ for fixed $\Delta_0 = 200\text{meV}$ and $\alpha = 1.2$. Throughout, a quasi-particle weight $Z = 1$ is used. From top to bottom we show the resistivity ρ , the coefficients of Seebeck S , Hall R_H , Nernst ν , the activated number of electrons n_e (holes $n_h = n_e$), and the chemical potential μ . Notable characteristics: For finite Γ , the asymmetry α leads to a chemical potential that does not converge to the gap mid-point for $T \rightarrow 0$. This Γ -induced deviation in μ causes the high temperature features at T_Δ^μ and T_ν^μ . There, the resistivity transitions between an activated regime corresponding to the fundamental gap Δ_0 to one with a reduced energy Δ_1 , given by twice the distance between $\mu(T \rightarrow 0)$ and the nearest band edge. The characteristic T_S^{max} , T_ρ^* and T_{RH}^* instead are driven by the quantum kernels and the importance of higher order polygamma functions in them: The resistivity and the Hall coefficient saturate at T_ρ^* and T_{RH}^* , respectively. The latter signals a finite density of carriers at the Fermi level even at absolute zero, congruent with $n_e > 0$. The Seebeck coefficient is suppressed and vanishes for $T \rightarrow 0$ in accordance with the laws of thermodynamics. The Nernst coefficient peaks one more time before also trending to zero for $T \rightarrow 0$.

Chemical potential and activated carriers

For sharply defined valence and conduction states $\epsilon_{\mathbf{k}}$, i.e. $\Gamma = 0$, the position of the chemical potential μ is driven through the thermal broadening of the Fermi function. In particular, one can show (see, e.g., Ref. [331]) that μ approaches the middle of the gap for $T \rightarrow 0$, with a temperature slope that depends on the particle-hole asymmetry. If the lifetime of valence and conduction states is finite, this description is no longer valid. Indeed, determined via Eq. (3.87), the chemical potential is intrinsically dependent on the scattering rate. Fig. 3.29b, that displays a spectral function at a selected k -point, illustrates why this is the case: The Lorentzian width of the spectral function results in small but finite weight of incoherent in-gap states that the chemical potential has to account for. As seen in the bottom panel of Fig. 3.30, μ follows the result of the Fermi function at high temperatures, where thermal broadening dominates over the Lorentzian in-gap weight. Below a temperature T_{ν}^{μ} , however, μ starts to strongly deviate. In particular, it no longer extrapolates to the midgap point (here set to zero), but to a finite value that increases with growing particle-hole asymmetry α and bandgap Δ_0 , while being only weakly dependent on the residual scattering Γ . This behavior can be rationalized through the low temperature expansion of the occupation in Eq. (3.87), which, for a state at $a = \epsilon - \mu$, yields

$$N = \frac{1}{2} - \frac{1}{\pi} \Im \ln(\Gamma + ia) + \frac{\pi}{3} \frac{a\Gamma}{(a^2 + \Gamma^2)^2} (k_B T)^2 + \mathcal{O}(T^4). \quad (3.191)$$

Given that, in a semiconductor, the scattering rate Γ is orders of magnitude smaller than the band energies, changes in the band structure ($a = \epsilon - \mu$) will dominate the chemical potential at low temperatures. Noteworthy, the evolution of the chemical potential μ shown in the lower panels of Fig. 3.30—its deviation from the intrinsic Fermi-Dirac result (gray dashed in bottom right panel) at T_{ν}^{μ} , its inflection point T_{Δ}^{μ} , and the eventual saturation at a finite position—is reminiscent of the exhaustion and extrinsic regime in semiconductors with impurity-derived in-gap states [448]. There, changes in the chemical potential are driven by donated electrons or holes, i.e. a change in the total number of charge carriers. In our scenario instead, the total number of electrons stays constant, but the finite lifetimes of intrinsic carriers causes excitations to widen, spilling incoherent spectral weight into the gap, so that the chemical potential has to adapt. Consequently, even at lowest temperatures, the number of activated carriers

$$n_e = \sum_{\mathbf{k}, n \geq \text{CB}, \sigma} \left(\frac{1}{2} - \frac{1}{\pi} \Im \psi(z_{\mathbf{k}n}) \right) \quad (3.192a)$$

$$n_h = \sum_{\mathbf{k}, n \leq \text{VB}, \sigma} \left(\frac{1}{2} + \frac{1}{\pi} \Im \psi(z_{\mathbf{k}n}) \right) \quad (3.192b)$$

must remain finite for $\Gamma > 0$, as shown in the Fig. 3.30 (second panel row from the bottom). In more detail, at any temperature, the number of activated electrons n_e and holes n_h (per unit-cell) necessarily balance each other, $n_e = n_h$, in the stoichiometric (half-filled) case considered here. At high temperatures n_e follows the result for the coherent ($\Gamma = 0$) band structure (indicated in dashed gray). In this regime, dominated by thermal activation across the gap Δ_0 , n_e is exponentially suppressed upon cooling; for $k_B T \ll \Delta_0$: $n_e(\Gamma = 0; T) \sim e^{-\Delta_0/k_B T}$. For finite Γ , the discussed deviations in the chemical potential reflect in the carriers available for conduction: At the temperature T_ν^μ , n_e no longer shrinks exponentially and, at T_Δ^μ , transitions into a regime in which the number of available carriers is virtually independent of temperature. In this low-temperature regime the dominant control parameter for the number of carriers is the scattering rate Γ , whereas asymmetry and the size of the gap hardly affect $n_e(T \rightarrow 0)$ on the shown exponential scale.

Electric resistivity

Signatures of the described evolution of the number of carriers available for conduction are readily seen in the resistivity in the top row of Fig. 3.30. The activated behavior above T_ν^μ —purely determined by the bandgap Δ_0 —transitions into a second activated regime realized below T_Δ^μ , with an effectively reduced bandgap $\Delta_1 < \Delta_0$. As indicated in Fig. 3.30 (bottom right panel), Δ_1 measures (twice) the distance between the saturated $\mu(T \lesssim T_\Delta^\mu)$ and the nearest band edge (for $\alpha > 1$: the conduction band). Again, this behavior is reminiscent of an impurity-driven extrinsic regime. There, Δ_1 would measure the difference between the extrinsic impurity level on the one hand and the conduction or valence band on the other. In both scenarios—extrinsic in-gap states vs. intrinsic states with finite lifetimes—changes in conduction reflect a modification in the chemical potential. Here, our theory provides a complementary microscopic origin for the appearance of the chemical potential-driven characteristic temperature scales T_ν^μ and T_Δ^μ . Note that for particle-hole symmetric systems, where the chemical potential is temperature independent, no such crossover exists and there is only one activation-like regime [7].

Cooling further, also the second activated regime is bounded from below: At a temperature T_ρ^* , the resistivity enters a saturation regime. Contrary to the features at higher temperatures, T_ρ^* has no signature in the chemical potential, but derives entirely from the physics encoded in the kernel function Eq. (3.94). As discussed in detail in Ref. [7] the crossover temperature T_ρ^* and the saturation value $\rho(T \rightarrow 0)$ strongly depend on the scattering rate and the bandgap. Noteworthy, the influence of Γ inverts as a function of temperature: At high T , a larger scattering rate increases the resistivity. This is the conventional behavior, also realized in metals. At low T , however, where conduction is driven by incoherent spectral weight inside the gap, the resistivity understandably *decreases* with a

growing scattering rate (see top right panel in Fig. 3.30). Here, we extend the previous analysis [7] and demonstrate that also the band asymmetry α has a strong effect on the conduction. In the asymmetric case, the chemical potential must be positioned closer to the conduction ($\alpha > 1$) or valence ($\alpha < 1$) band so that the correct number of electrons in the system is occupied. Therewith, the majority of carriers—those that reside in the centres of the Lorentz-broadened peaks in the spectral function—conduct more and freeze out at a lower temperature, i.e. T_ρ^* and the corresponding saturation value $\rho(T \rightarrow 0)$ decreases with α .

To summarize, the resistivity of an *intrinsic* narrow-gap semiconductor with a finite scattering rate has four regimes:

- (i) $T > T_\nu^\mu$: the activated high-temperature region that is well-described in Boltzmann theory.
- (ii) $T_\Delta^\mu < T < T_\nu^\mu$: a narrow regime in which the chemical potential starts to sense the incoherent spectral weight inside the gap and adjusts accordingly.
- (iii) $T_\rho^* < T < T_\Delta^\mu$: a regime at intermediate temperatures in which the (Γ -imposed) chemical potential shift has led to a reduced activation energy for valence ($\alpha < 1$) or conduction ($\alpha > 1$) carriers.
- (iv) $T < T_\rho^*$: a regime of resistivity saturation in which thermal activation is frozen out but a residual conductivity, driven by incoherent in-gap weight, remains finite.

Seebeck coefficient

The three temperatures, $T_\rho^* < T_\Delta^\mu < T_\nu^\mu$, that separate the four regimes in the electrical resistivity also account for features in the Seebeck coefficient (second row in Fig. 3.30): The increase of S starting from high temperatures is interrupted by the crossover of the chemical potential at T_ν^μ . Depending on the parameters, the transition to the maximum amplitude at lower temperatures can then either be smooth (large scattering rate) and monotonous (large gap) or be accompanied by a significant shoulder (large bandgap, small scattering rates). In extreme cases this shoulder transforms into a local peak (small gap, strong asymmetry), i.e. the temperature dependence is non-monotonous. The temperature at which the Seebeck coefficient has its global maximum amplitude S^{\max} is linked to T_ρ^* . In fact, S peaks at T_S^{\max} , consistently slightly above the onset of the resistivity saturation regime ($T_S^{\max} \gtrsim T_\rho^*$). Below this global peak temperature, the Seebeck coefficient drops rather abruptly. In the zero temperature limit, it follows the metal-like linear behavior $S(T) \sim T$, anticipated in Section 3.4.1.1.

This rich structure is *absent* when the Boltzmann approach is applied to the band structure $\epsilon_{\mathbf{k}n}^0$

of Eq. (3.189): The features associated with T_{Δ}^{μ} and T_{ν}^{μ} are missed if finite lifetimes are unaccounted for in the search of the chemical potential; the characteristic features further below are absent owing to the simple structure of the Boltzmann transport kernels. Indeed, for a momentum- and state-independent scattering rate Γ , the kernels \mathcal{L}_{11} and \mathcal{L}_{12} in the Boltzmann approximation are both merely proportional to Γ^{-1} . Then, given by their ratio, Eq. (3.61), Boltzmann's Seebeck coefficient is independent of the scattering rate. Manifestly, this approximation is a severe oversimplification even for extremely small Γ (see Fig. 3.30: right column, second panel from the top).

Next, we will comment on two approximate tools that are popular for the analysis of thermoelectric measurements or simulations.

The Goldsmid-Sharp gap

Goldsmid and Sharp [449] motivated that the size of a semiconductor's gap could be gauged from the peak amplitude of the Seebeck coefficient:

$$\Delta \approx 2e|S^{\max}| \cdot T_S^{\max}. \quad (3.193)$$

This estimate works decently for both n - and p -type semiconductors [449], although deviations of the order of a factor of two are not uncommon. The relation is used as a coarse analysis tool [450, 451, 452] in simulations and experiments and even as a descriptor in high-throughput materials discovery studies [453]. Eq. (3.193) was deduced for a coherent, large gap, particle-hole symmetric semiconductor in which impurity states move the chemical potential so as to optimize the Seebeck coefficient [331, 449]. Allowing for particle-hole asymmetry, the Seebeck coefficient can, however, be larger, while it is always bounded by $|S| \leq |\Delta/(eT) + S(\infty)|$, where $S(\infty)$ is the comparatively small high temperature limit ($|S(\infty)| = \mathcal{O}(k_B/e)$) [331]. Since the original argument [449] relies on replacing the Fermi-Dirac with the classical Maxwell-Boltzmann statistics, further deviations occur if $k_B T_S^{\max} \not\ll \Delta$ [454].

Here, we scrutinize the Goldsmid-Sharp relation, Eq. (3.193), for our two-band model: In Fig. 3.31 we report $|S^{\max}| \cdot T_S^{\max}$ extracted from the parameter scans of Fig. 3.30 as well as for an additional scan for an almost particle-hole symmetric system, $\alpha = 1.04$ (open circles in the main panel). For the latter, the Goldsmid-Sharp gap indeed provides a very accurate estimation of the fundamental gap Δ_0 . For systems with more asymmetrical electronic structures, however, Eq. (3.193) yields poor results: $|S^{\max}| \cdot T_S^{\max}$ largely underestimates the charge gap (filled circles). Looking at the corresponding resistivities, Seebeck coefficients and the chemical potential in Fig. 3.30 reveals the reason: The thermopower is largest at the lower end of the second activated regime of the resistivity,

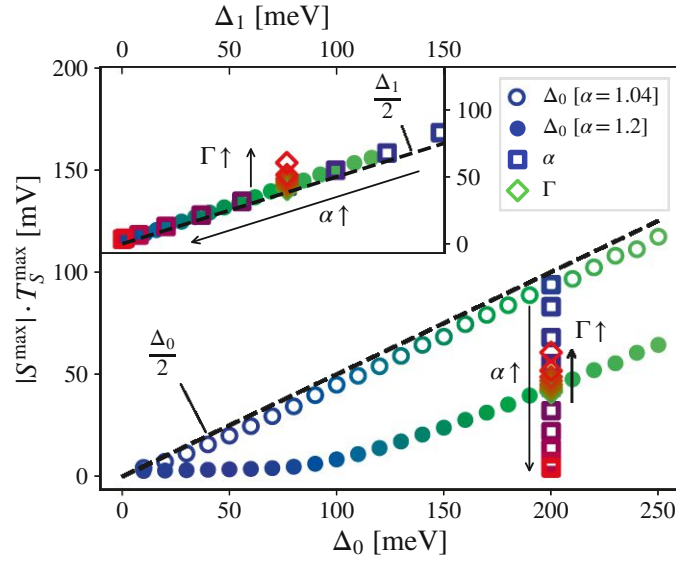


Figure 3.31: Goldsmid-Sharp gap. We display the gap-estimate $|S^{\max}| \cdot T_S^{\max}$ for scans of the bandgap Δ_0 for asymmetries $\alpha = 1.04$ (open circles) and $\alpha = 1.2$ (closed circles). Also shown is a scan of the asymmetry (open squares) and of the scattering rate (open diamonds), using the same parameters as in Fig. 3.30. The expression $|S^{\max}| \cdot T_S^{\max}$ deviates strongly from $\Delta_0/2$ (dashed line) when the system's asymmetry is at least moderate. Only in the vicinity of particle-hole symmetry ($\alpha = 1.04$, open circles) do we find good agreement for Eq. (3.193). An increase in asymmetry leads to a suppression of $|S^{\max}| \cdot T_{\max}$ while different scattering rates have minimal effects. Instead, plotting $|S^{\max}| \cdot T_{\max}$ against the effective gap Δ_1 (cf. $\rho(T)$ in Fig. 3.30), the various scans collapse onto the $\Delta_1/2$ line (see inset): The Goldsmid-Sharp gap expression reliably estimates the effective gap Δ_1 .

$T_\rho^* \lesssim T_S^{\max} < T_\Delta^\mu$. This regime emerges when a finite scattering rate pushes the chemical potential towards the lighter band (in our case the conduction band). As a consequence, the crucial gap, as apparent in the resistivity, is the effective Δ_1 , not Δ_0 . This observation suggests that the Goldsmid-Sharp gap does not monitor the bandgap Δ_0 but the effective gap Δ_1 . This hypothesis is confirmed in the inset of Fig. 3.31: plotted as a function of the emergent Δ_1 , the scatter plot of $|S^{\max}| \cdot T_S^{\max}$ collapses onto a single line indicating $\Delta_1/2$. This statement is largely independent of the scattering rate: $|S^{\max}| \cdot T_S^{\max}$ only slightly increases with Γ , leading to a mild overestimation of Δ_1 .

In all, in the realistic presence of a scattering rate, the Goldsmid-Sharp expression quite accurately gauges the effective gap Δ_1 that controls transport at intermediate temperatures—but which can be significantly smaller than the true bandgap Δ_0 .

The Mott formula

In metals, conduction is largely dominated by states in the vicinity of the chemical potential. Then, performing a low temperature Sommerfeld expansion of the conductivity is justified. Doing so for the Boltzmann relaxation-time approximation, see Section 3.3.3, yields a convenient expression for the Seebeck coefficient

$$S \approx -\frac{\pi^2}{3e} k_B^2 T \frac{\partial \ln \sigma(\mu)}{\partial \mu}, \quad (3.194)$$

which is a simplified version of the so-called *Mott formula* of the thermopower [455, 456]. Here, $\sigma(\mu)$ is the electrical conductivity for varying chemical potential μ . Clearly, the above approximation is inaccurate for *coherent* semiconductors, where conduction is driven by conduction and/or valence states that are far (more than several $k_B T$) from the chemical potential. Manifestly, our general kernel functions therefore do not verify Eq. (3.194). However, as we demonstrated [7], finite lifetimes may drive residual conduction in semiconductors, leading to resistivity saturation. The incoherent in-gap states associated with this phenomenon might provide the metallicity required to justify expanding the derivative of the Fermi function around the chemical potential (Sommerfeld expansion). Therefore, Eq. (3.194) is expected to hold in the saturation regime, where conduction is dominated by said incoherent in-gap weight. Evaluating Eq. (3.194) for the residual term of the conductivity given in Eq. (3.183), indeed yields the lowest-order expression of the low-T Seebeck coefficient, Eq. (3.185). This validity of the Mott formula for metals in the resistivity saturation regime of a semiconductor provides a direct link between residual charge conduction ($\sigma(T \rightarrow 0) > 0$) and a metal-like linear-in- T thermoelectric Seebeck signal ($S(T \rightarrow 0) \propto T$).

Hall coefficient

From high temperatures down to its maximum, the Hall coefficient R_H (third panel in Fig. 3.30) exhibits a qualitatively similar dependency on Δ_0 , α , and Γ as the Seebeck coefficient. However, R_H peaks at a slightly smaller temperature that matches T_ρ^* from the resistivity. Also, instead of vanishing, R_H saturates below a temperature $T_{R_H}^*$ ($< T_\rho^*$), in agreement with the low- T expansion Eq. (3.186) and experiment, see Fig. 3.28 and Fig. 3.37. This temperature arrangement is expected since the spectral function enters Eq. (3.80) to higher order compared to Eq. (3.79). Therefore, the \mathcal{K}_{11}^B kernel effectively senses a smaller amount of incoherent in-gap weight than \mathcal{K}_{11} . Consequently, the temperature, below which the thermal selection of valence and conduction carriers via $\left(-\frac{\partial f}{\partial \omega}\right)$ can be neglected in comparison to the incoherent in-gap weight that drives the residual conduction, is effectively reduced. At large temperatures ($T > T_V^\mu$, Boltzmann regime), R_H is dominantly controlled

by the bandgap and the particle-hole asymmetry, while the dependence on the scattering rate is weak. Instead, at low T , it is mostly the scattering rate that controls, both, the peak value and the saturation limit $R_H(T \rightarrow 0)$.

Nernst coefficient

The Nernst coefficient exhibits the most dramatic features⁵⁶. Starting from high temperature, ν increases and reaches a first peak at T_ν^μ where the chemical potential starts to transition towards its saturation regime. The Nernst then quickly drops to zero (unless the asymmetry is very small) and remains suppressed in the intermediate regime ($T_\rho^* < T < T_\Delta^\mu$; the second activation regime of ρ). The transition into the ρ -saturation regime at T_ρ^* is then accompanied by a second large and sharp peak in ν before it finally converges linearly to zero for $T \rightarrow 0$. Similar to the Hall coefficient, the biggest changes in the temperature profile of ν are achieved by varying the bandgap and the asymmetry, while absolute values are mostly controlled by the scattering rate.

Focusing on (a) the large low-temperature peak and (b) the $T \rightarrow 0$ limit, we analyze the fabric of the Nernst coefficient through different representations.

Hall and thermal mobilities

Using the expression Eq. (3.61) of the Seebeck coefficient, we can rewrite the Nernst coefficient Eq. (3.65) as

$$\nu = S(\mu_H - \mu_T) \quad (3.195)$$

where $\mu_H = \mathcal{L}_{11}^B/\mathcal{L}_{11}$ is the Hall mobility, and $\mu_T = \mathcal{L}_{12}^B/\mathcal{L}_{12}$ its thermal analogue, introduced by Sun *et al.* [214]. From this point of view, a finite Nernst signal can only appear when there is a mismatch in the mobilities. The two mobilities, μ_H and μ_T , are shown in Fig. 3.32 for varying (a) bandgap, (b) asymmetry, and (c) scattering rate. At large T , $-\mu_T \gg -\mu_H$, resulting in a sizeable Nernst coefficient. At intermediate temperatures, both mobilities exhibit a temperature- and gap-independent plateau of *equal* magnitude: The Nernst signal vanishes. At low T there is again a mobility mismatch, $-\mu_T > -\mu_H$, which is responsible for the pronounced low temperature peak. Qualitatively, this behavior mirrors the analysis of the experimental mobilities of FeSb₂ from Ref. [214] that we reproduce in the inset of Fig. 3.37h: Also in experiment, the mobility mismatch is sizable at low and high temperatures, while in between they almost match.

⁵⁶Our survey of the Nernst coefficient can be compared to the semi-classical relaxation-time approximation pioneered recently in Ref. [413] that includes effects to leading order in $1/\Gamma$.

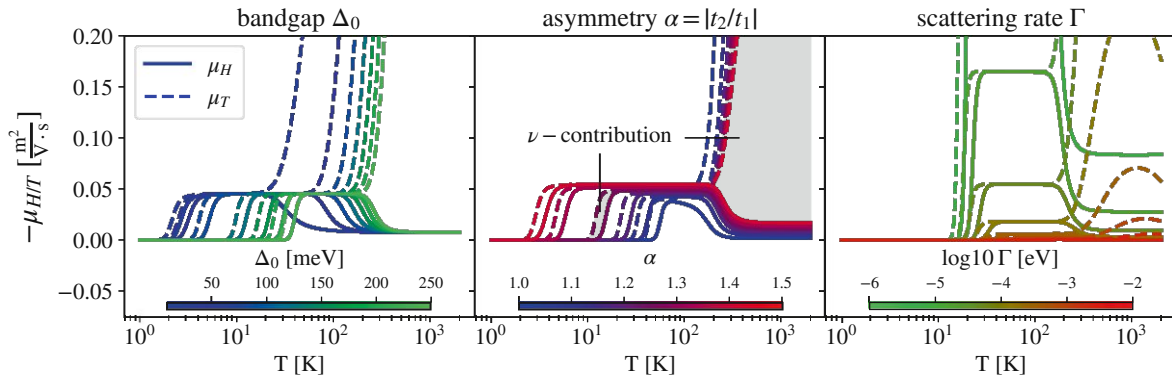


Figure 3.32: Hall and thermal mobilities. Both mobilities vanish in the zero temperature limit and coincide with each other at intermediate temperatures, marking the ranges where the Nernst coefficient vanishes in Fig. 3.30. This transition however takes place at slightly different temperature between μ_H and μ_T giving rise to the low temperature ν -contribution at roughly T_{ρ^*} (first shaded area). At large temperature the two mobilities diverge from each other. μ_T increases drastically while μ_H gets suppressed, marking the second ν -contribution which is peaked at T_{ν}^{μ} (second shaded area).

Mott formula for the Nernst coefficient

Analogous to the Mott formula of the Seebeck coefficient, Eq. (3.194), a Sommerfeld expansion can be used to obtain an approximate formula for the Nernst coefficient. Using $\mathcal{L}_{12}^B \approx \frac{\pi^2 k_B^2 T^2}{3e} \frac{\partial \mathcal{L}_{11}^B(\mu)}{\partial \mu}$, valid at low T for Boltzmann-derived Onsager coefficients of metals [457], one finds [458]

$$\nu \approx -\frac{\pi^2}{3e} k_B^2 T \frac{\partial \mu_H}{\partial \mu} \quad (3.196)$$

where $\mu_H = \mathcal{L}_{11}^B / \mathcal{L}_{11}$ is again the Hall mobility (This “Mott formula” for the Nernst coefficient is often written using the Hall angle $\tan(\theta_H)/B = \mu_H$ with the magnetic field B .)⁵⁷. As for the Seebeck coefficient, we find the link Eq. (3.196) between transport of charge (μ_H) and entropy (ν) to hold in the low- T saturation regime (in this case $T < T_{R_H}^*$). In other words, the lowest order terms in the low temperature expansions, Eqs. (3.183-3.184), fulfill Eq. (3.196). In this sense, the saturation of both σ_{xx} and σ_{xy}^B dictates the Nernst coefficient to vanish linearly for $T \rightarrow 0$. This behavior—otherwise typical for metals [392]—is indeed experimentally observed in correlated narrow-gap semiconductors, see Fig. 3.37h for the example of FeAs₂. In metals, however, the variation of the charge and Hall conductivities with the chemical potential is usually small. Then, Eq. (3.196) means that also the Nernst coefficient will be very small—a statement referred to as Sondheimer

cancellation [392, 457, 459]. Instead, as we have seen here, a changing chemical potential can notably manipulate the residual conductivities of an incoherent semiconductor.

Thermal conductivity and Lorenz ratio

Next, we discuss the electronic contribution to the thermal conductivity κ . In the low temperature ρ -saturation regime we find the linear behavior from Eq. (3.187). Increasing the temperature results in various kinks and shoulders. Again, we can separate the influence of a changing chemical potential from the inner structure of the transport kernel functions: While the pure \mathcal{L}_{22} -contribution (first term in Eq. (3.62); dashed lines in Fig. 3.33) only experiences the transition stemming from the chemical potential, the shoulders in the intermediate regime derive from the \mathcal{L}_{12} -contribution (second term in Eq. (3.62)). Combined to the Lorenz ratio

$$L = \frac{\kappa}{\sigma T}, \quad (3.197)$$

we find a complex temperature dependence: In the zero temperature limit $L(T)$ clearly converges to the Sommerfeld value of the Lorenz number $L_0 = \frac{\pi^2 k_B^2}{3e^2}$. This can also be confirmed via the low- T expansion

$$L = L_0 + \left(\frac{k_B}{e}\right)^2 \frac{16\pi^4}{45} \frac{5a^2 - 2\Gamma^2}{(a^2 + \Gamma^2)^2} k_B^2 T^2 + \mathcal{O}(T^4). \quad (3.198)$$

This result is expected, since in our theory both the electrical and heat current are transported by the same carriers, subject to the same elastic scattering mechanism. If inelastic scattering effects, e.g., via an electron-phonon coupling, were to be included, this unison will be jeopardized [461]. Then, the Wiedemann-Franz law can be strongly violated at low (but finite) temperatures, with L being notably suppressed [462].

In the opposite limit, $T \rightarrow \infty$, we find $L(T \rightarrow \infty) = 0$. Note that this result assumes a temperature-independent scattering rate. For specific conditions on $\Gamma(T)$, the Lorenz ratio converges to L_0 at high temperatures, as will be discussed in Section 3.4.1.2.

⁵⁷ Alternatively, the temperature-derivative of the Hall mobility can be seen as a source for a finite Nernst signal, $\propto T \partial \mu_H / \partial T$ [460].

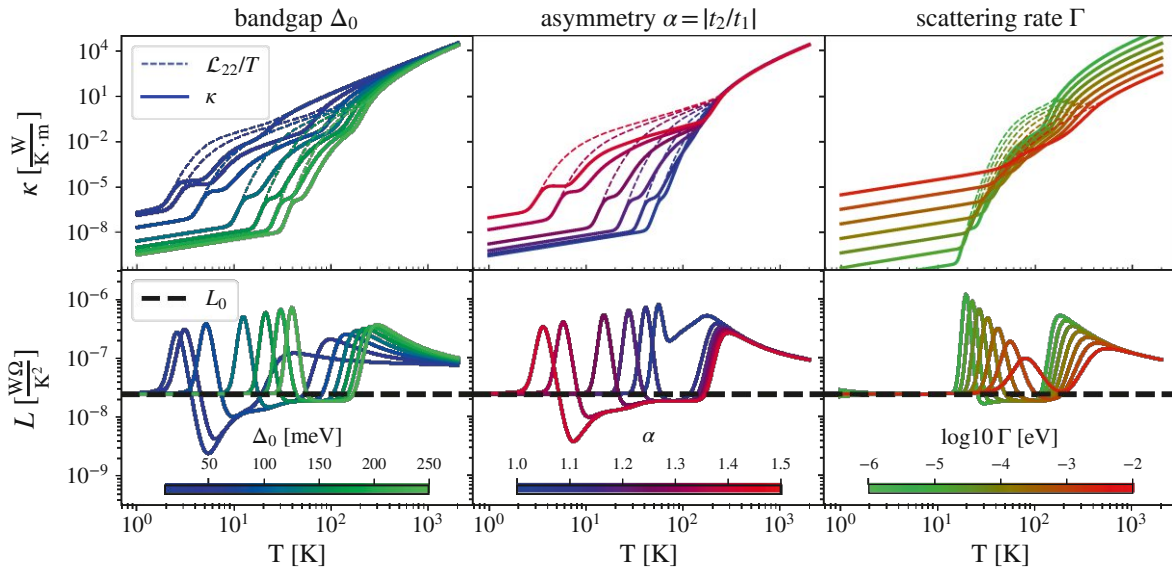


Figure 3.33: Thermal conductivity and Wiedemann Franz law. The same parameter sets as in Fig. 3.30 are used. In addition to the total thermal conductivity κ (top row) we plot also the contribution \mathcal{L}_{22}/T (dashed) individually. The Lorenz ratio (bottom row) converges to $L(T \rightarrow 0) = L_0 = \frac{\pi^2 k_B^2}{3e^2}$ (see text for details).

Power factor and figure of merit

Finally, we consider the thermoelectric power factor $S^2\sigma$ and the figure of merit zT , given by

$$PF = S^2\sigma \quad (3.199)$$

and

$$zT = \frac{S^2\sigma T}{\kappa}, \quad (3.200)$$

shown in Fig. 3.34. Furthermore, in order to achieve somewhat realistic zT values we add a (dominant) phonon contribution to the thermal conductivity $\kappa = \kappa_e + \kappa_{\text{ph}}$ using an optimistic $\kappa_{\text{ph}} = 10 \frac{\text{W}}{\text{K}^2 \cdot \text{m}}$. First, we note that $S^2\sigma$ is seemingly large at the upper end of the shown temperature window. However, this behavior again originates from the temperature-independence of the scattering rate—that we assume here for illustrative purposes. Indeed, $\Gamma = \text{const.}$ causes (for large T) a very small resistivity, see top row of Fig. 3.30, that overcompensates the drop in the Seebeck coefficient. In practice, the scattering rate itself is typically temperature dependent. As explained below, see Section 3.4.1.2, a reasonable $\Gamma(T)$ causes, both, the powerfactor and zT to vanish quite rapidly at large temperatures,

see Fig. 3.35 (lowest two panels). We therefore focus on the lower temperature structure in $S^2\sigma$ and zT in Fig. 3.34, that is equally present when a realistic $\Gamma(T)$ is used. The displayed peak in the powerfactor and zT is the result of the usual compromise [211, 383] between large S and small ρ^{58} . We find the optimal power factor to occur in the vicinity of T_ν^μ , the onset of the high-temperature crossover from the first into the second activated- ρ regime. Peak temperatures move up (down) for a growing bandgap (scattering rate), while peak amplitudes benefit from larger gaps, larger asymmetry, but a smaller scattering rate.

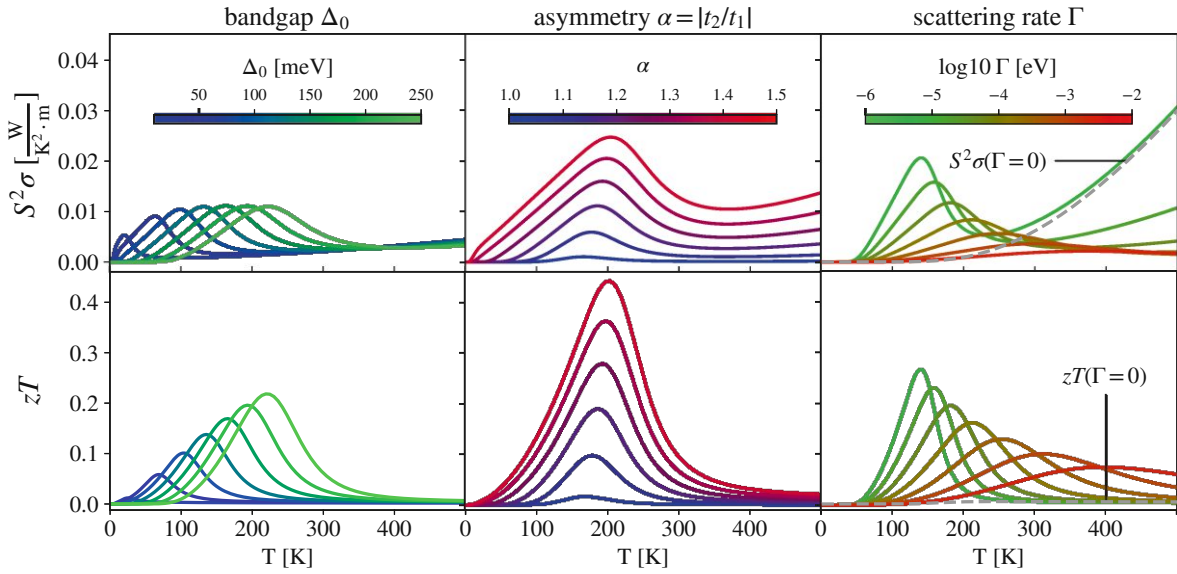


Figure 3.34: Power factor and figure of merit. The power factor $S^2\sigma$ (top row) is peaked at the transition of the first into the second activated regime of $\rho = 1/\sigma$. For $T \rightarrow 0$, $S^2\sigma$ is suppressed due to the low temperature limit of $S(T) \sim T$. At intermediate temperatures, $S^2\sigma$ develops an important peak that is undetectable in Boltzmann theory (gray, dashed line). The high temperature increase in the powerfactor is nonphysical and disappears when a T -dependent scattering is included (see Section 3.4.1.2). The figure of merit zT (bottom row) shows similar features but—due to the thermal-conductivity weighing—peak sizes are affected differently. Note: In zT we included a constant phonon contribution of $\kappa_{\text{ph}} = 10 \frac{\text{W}}{\text{K}^2 \cdot \text{m}}$. Again, the low temperature peak zT , indicative of potential merit in thermoelectric devices is completely missing in the Boltzmann regime (gray, dashed line).

As the ratio of powerfactor and thermal conductivity, zT inherits its structure from the former, while the latter modulates the overall magnitude. Indeed, bandgap variations keep the peak amplitude of $S^2\sigma$ essentially unchanged but move the peak position. The maximal zT then increases for larger bandgaps, as the (here: electrical) thermal conductivity dwindles. Variations of the band asymmetry,

instead, only change the size of the zT maximum, while increasing scattering rates lower the peak amplitude and shift it to higher temperatures.

Importantly, the just described peak in, both, $S^2\sigma$ and zT is *absent* when the Boltzmann approach is applied to the band structure (dashed grey lines in the right panels of Fig. 3.34). Indeed, we find that maximal thermoelectric performance is realized in the temperature range delimited by T_{Δ}^{μ} and T_{ν}^{μ} . These characteristic scales are driven (see above) by changes in the chemical potential μ , caused by the finite lifetimes of conduction and valence states—an effect beyond mere thermal activation. As a consequence, assessing the potential of narrow-gap semiconductors for thermoelectric applications on the basis of Boltzmann theory applied to coherent electronic band structures is virtually meaningless. A (high-throughput) screening of materials [463, 464, 465] that neglects finite electronic lifetimes of intrinsic carriers may miss potentially favorable compounds.

Temperature dependent scattering rate

In the previous Section, we held the scattering rate Γ constant to unravel the prototypical variations of transport observables with respect to gap, particle-hole asymmetry and the scattering rate itself. Setting $\Gamma(T) = \Gamma_0$ led to some effects not observed in experiments. In particular, the resistivity became vanishingly small in the intermediate to high temperature regime ($\frac{\rho(T < T_p^*)}{\rho(T > T_p^*)} \sim 10^5$). Indeed, only when temperature reaches a value greater than the system's band-width, the resistivity starts again to increase (not shown). Experiments probing narrow-gap semiconductors, however, witness an insulator-to-metal crossover above a temperature that is still small with respect to the charge gap [212]. In FeSi ($\Delta \sim 50\text{meV} = k_B \times 580\text{K}$), for example, the slope of the resistivity turns positive above 300K [467], while in optical spectroscopy for FeSb₂ ($\Delta \sim 30\text{meV} = k_B \times 350\text{K}$) a Drude-like peaks starts developing at around 100K [468, 469]. Clearly this metallization is beyond mere thermal activation of carriers across the charge gap. Theoretically, this phenomenon has been attributed to incoherent spectral weight spilling into the gap and was advocated to derive from electronic correlation effects [320] or thermal disorder [470, 471]. In the correlations' picture, the Hund's rule coupling drives a scattering rate that grows quadratically with temperature [320, 439]. Therefore, we will restrict ourselves in the following to scattering rates with a polynomial temperature dependence.

⁵⁸Interestingly, this conventional trade-off was recently found to be broken in an ultra-thin oxide film near its Mott transition [466].

General considerations

Without a growing scattering rate the Lorenz ratio L approaches zero in the high temperature limit and an unreasonably large power factor $S^2\sigma$ appears in the intermediate temperature regimes, see the high- T upturn in Fig. 3.34. If, instead, we consider a residual scattering rate plus a term with a polynomial temperature dependence, $\Gamma(T) = \Gamma_0 + \gamma T^\eta$, where $\gamma > 0$, $\eta > 0$, the argument z of the polygamma functions $\psi_i(z)$ becomes

$$z(T) = \frac{1}{2} + \left[\frac{\Gamma_0 + ia}{2\pi k_B T} + \frac{\gamma T^\eta}{2\pi k_B T} \right]. \quad (3.201)$$

Scattering rates that increase slower than linearly ($\eta < 1$) lead to arguments that converge to $z(T \rightarrow \infty) = \frac{1}{2}$; exact linear behavior leads to $z(T \rightarrow \infty) = \frac{1}{2} + \frac{\gamma}{2\pi k_B}$ while $\eta > 1$ leads to a diverging $z(T)$.

In the first two cases the Lorenz ratio simplifies in leading order to $L(T) \sim \mathcal{O}(T^{2\eta-2})$. $\eta < 1$ therefore implies a vanishing Lorenz ratio while $\eta = 1$ implies some saturation value $L(\gamma)$, which, numerically, is generally orders of magnitude smaller than L_0 . If the scattering rate increases faster ($\eta > 1$), the same Taylor series of the polygamma functions that was applied in the zero temperature limit (see Section 3.3.5.1) can be employed. Consequently, the high temperature limit is identical to the low temperature limit and thus $L(T \rightarrow \infty) = L_0$.

Fermi liquid-like scattering

Dynamical mean-field theory calculations suggest that the scattering rate evolves quadratically with temperature for, both, Kondo insulators [7] and d -electron-based narrow-gap semiconductors [320, 439]. From here on, we therefore assume a Fermi-liquid-like

$$\Gamma(T) = \Gamma_0 + \gamma T^2. \quad (3.202)$$

Fig. 3.35 illustrates how the additional scattering term changes the transport for a range of γ -values (shades green to red) compared to $\gamma = 0$ (dashed black line), for a fixed bandgap $\Delta_0 = 200\text{meV}$, residual scattering $\Gamma_0 = 10^{-4}\text{eV}$, and asymmetry $\alpha = 1.2$.

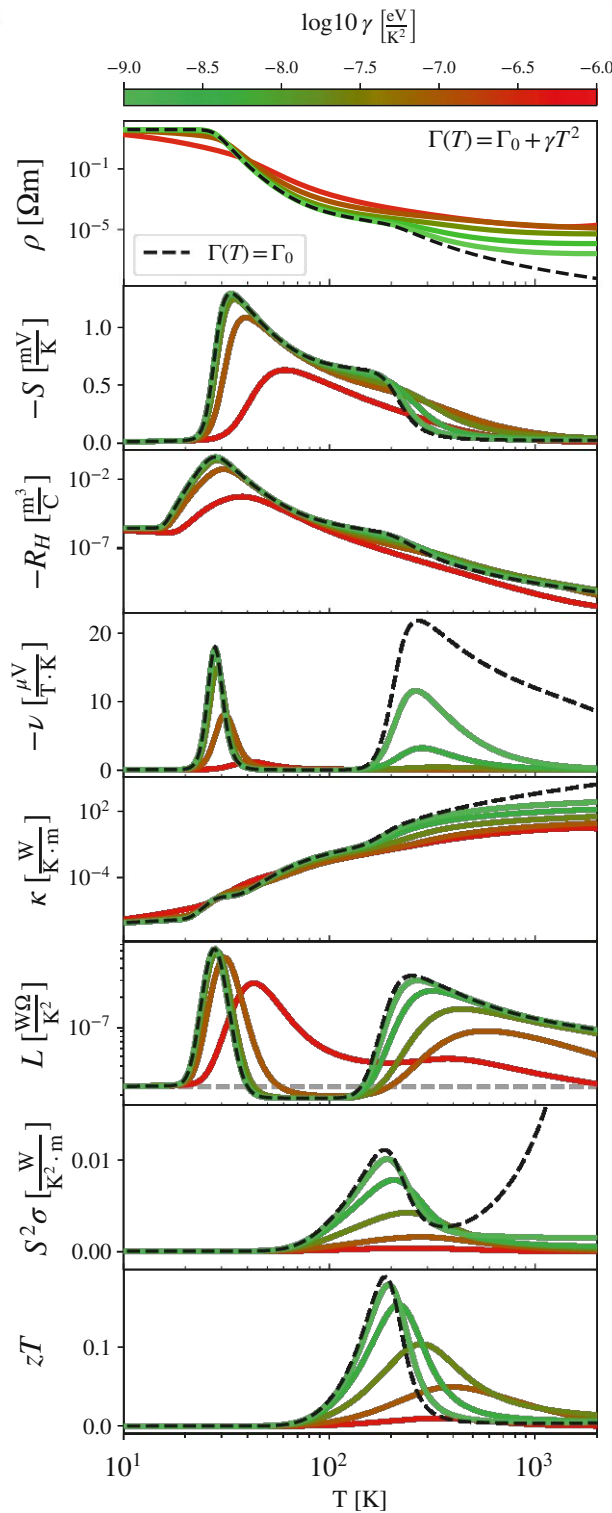


Figure 3.35: Temperature dependent scattering rate. Effects of $\Gamma(T) = \Gamma_0 + \gamma T^2$, with residual scattering $\Gamma_0 = 10^{-4} \text{eV}$ and varying γ , for fixed bandgap $\Delta_0 = 200 \text{meV}$ and asymmetry $\alpha = 1.2$. The dashed black lines are results for $\gamma = 0$. The additional temperature dependence causes a resistivity upturn at high temperatures which also results in a smoothed Seebeck and Hall coefficient. This metallic trend directly removes the nonphysical upturn in the power factor while simultaneously causing the Lorenz factor L to converge towards L_0 (horizontal, dashed, gray line).

Overall, the increased scattering smoothes all considered quantities. A minimal γ is sufficient to suppress the high temperature shoulder in ρ at T_ν^μ and causes a slight upturn at high temperatures. The saturation regime is instead stable up to rather large γ . Naturally, the added scattering term only notably influences transport above temperatures for which $\gamma T^2 \sim \Gamma_0$. In this vein the high-temperature shoulder of the Seebeck coefficient is smoothed out and parts of the signal is pushed up in temperature. Quite generally, the increased scattering leads to less pronounced peaks which are shifted to higher temperatures. Since the shoulder in S at T_Δ^μ was responsible for the strong signal in the power factor and the figure of merit (see above), significant qualitative changes are expected for $\gamma > 0$: Besides the suppression of the nonphysical increase of the power factor at high temperatures, both $S^2\sigma$ and zT are equally attenuated for $\gamma > 0$ and their peaks shift up in temperature, as expected. Again, we included in zT a phonon contribution, $\kappa_{\text{ph}} = 10 \frac{\text{W}}{\text{K}^2 \cdot \text{m}}$, to the thermal conductivity. As already seen in the Γ_0 -scan in Fig. 3.30, a noticeable suppression is observed for the high-temperature peak of the Nernst coefficient. The second, low- T peak in the Nernst coefficient (that is absent in Boltzmann approaches) is instead relatively stable with γ as it occurs at low enough temperatures $T \sim T_\rho^*$. As discussed in Section 3.4.1.2 the Fermi-liquid like scattering rate enforces that the high-temperature limit of the Lorenz ratio converges to L_0 . This is evident in Fig. 3.35: For the largest scattering rate, L reaches L_0 within the shown temperature window.

3.4.2 Modeling materials

Having established an understanding of how relevant parameters drive changes in transport observables, we now turn to material specific simulations. While still focusing on a minimal description, we attempt to reproduce the temperature profiles of transport properties in selected narrow-gap semiconductors, as well as trends among them.

3.4.2.1 FeSb₂: Characteristic temperature scales without impurity states

First, we discuss the result for FeSb₂ shown in the front Fig. 3.28. FeSb₂ is a correlated semiconductor [214, 300, 417, 468] with a narrow gap of $\Delta \gtrsim 30\text{meV}$, as extracted from activation-law fits of the resistivity [214, 417] or the magnetic susceptibility [472, 473]. Consistent with GW and $GW+DMFT$ simulations [331, 418], we model FeSb₂ with a non-interacting gap $\Delta_0 = 60\text{meV}$ and an effective mass enhancement $Z^{-1} = 2$. We find that a small asymmetry $\alpha = 1.06$ mimics the material well. Finally, we assume a scattering rate of the form Eq. (3.202), where the parameters of the residual scattering Γ_0 and the prefactor γ of the quadratic term are adjusted by hand. We find that best agreement with experiment is reached for $\Gamma(T) = 5 \cdot 10^{-5}\text{eV} + 10^{-7} \frac{\text{eV}}{\text{K}^2} T^2$, see Fig. 3.28. This scat-

tering rate is quite realistic: Dynamical mean-field calculations for the related correlated narrow-gap semiconductor FeSi [320, 439] yield comparable values. Having optimized the electronic structure parameters so that the simulated resistivity qualitatively follows the experiment, the temperature profiles of all other transport observables for FeSb₂ automatically fall into place, see Fig. 3.28. The approach therewith in particular verifies the experimentally observed correlation between features in different response functions:

At low temperatures, the onset of resistivity saturation at T_ρ^* is accompanied by a peak in, both, the Hall and the Nernst coefficient at the identical temperature and a peak in the Seebeck coefficient at a slightly higher temperature—all of which is congruent with experiment. This low- T behavior of transport properties is encoded in the linear response kernel functions. Agreement with experiment confirms that our approximations for the kernels—linearized self-energy, omission of vertex corrections—conserves the essential physics. Instead, in previous modelings of FeSb₂, based on semi-classical approaches [421, 422, 423], resistivities and the Hall coefficient either diverged at low T or had to be suppressed by impurity states, e.g., by forcing the chemical potential into the conduction band. An alternative scenario for residual conduction in FeSb₂ could be provided by the recent observation of metallic surface states [418, 474]. Whether these weakly dispersive states can account for the typical low- T characteristics across all transport observables remains to be seen. We also note that for the topological insulator SmB₆ conduction by surface states and residual bulk conduction from finite lifetimes coexist [7].

Moving to higher temperatures, the resistivity exhibits two distinct activation regimes. We find the shoulder in between, $T_\Delta^\mu < T < T_\nu^\mu$, to be driven by changes in the chemical potential. Therefore, if the chemical potential only accounts for the thermal broadening of excitations—as commonly done in the context of Boltzmann approaches for band theory methods—all structure at intermediate temperatures is lost (gray, dotted lines in Fig. 3.28). If instead, the chemical potential, e.g., via Eq. (3.87), accounts for the scattering rate, Boltzmann simulations do capture the intermediate- T features (see black, dashed lines in Fig. 3.28). Alternatively, the temperature dependence of the chemical potential can be engineered by assuming in-gap impurity states [421, 422, 423]. Given that transport observables exhibit three to four distinct regimes, phenomenological modellings actually used up to three impurity levels to properly guide the chemical potential [421]. In our description, no impurity states are required: According to the presented phenomenology for transport in narrow-gap semiconductors, the intriguing temperature dependence in FeSb₂ exclusively originates from its *intrinsic* electronic structure. Instead of being set by *explicit* energy levels inside the gap, characteristic temperatures emerge through the interplay of relevant energy scales: the gap, the hopping, temperature, and—crucially—the scattering rate.

In the following Section, we investigate the influence of potential impurity states in more detail for FeSb₂. Thereafter, we will see that *explicit* impurity states are not fully out of the picture for other materials, but likely account for at least some aspects of conduction at intermediate temperatures in semiconductors with gaps $\Delta > 50\text{meV}$.

Before, however, a few comments regarding thermoelectricity in FeSb₂ are in order. While our approach neatly captures the *temperature profile* of transport observables, we do not reproduce the large *amplitude* of the Seebeck and Nernst coefficient. In fact, this is expected, as FeSb₂ violates the upper bound, $|S| \leq \Delta/T$, for a thermopower exclusively driven by electron diffusion [331]. As alluded to in the introduction, this riddle was successfully solved [331, 419, 420, 421, 422, 423] by attributing the colossal amplitude to the phonon-drag effect. Simply speaking, the thermal gradient also leads to a non-equilibrium phonon distribution. Working to equilibrate the thermal gradient, phonons then scatter with electrons dominantly towards the cold end of the sample, which is also the direction of the net electronic diffusion. Thereby momentum is constructively injected into the electronic subsystem, significantly boosting thermoelectric effects. This well-known phenomenon [475] continues to receive renewed interest, in the context of electronic correlations [212, 421, 423] (the effect is large when coupling to heavy electrons), the phonon-engineering pathway to efficient thermoelectrics [476], or both [477]. Crucially for our argument here, this phonon-enhancement of the electric response is expected to be smooth in temperature, so as to not produce additional features in transport observables. Indeed, while experimental peak-amplitudes cover almost an order of magnitude, $S^{\text{max}} \sim 5 - 45 \frac{\text{mV}}{\text{K}}$ across different samples [214, 417, 424, 428], the corresponding characteristic temperature profiles are almost identical. Crucially, Pokharel *et al.* [419] and Takahashi *et al.* [420] demonstrated that the phonon-drag in FeSb₂ can be consistently suppressed by geometric constraints. With their severely limited phonon mean-free path, polycrystalline samples are then expected to yield Seebeck amplitudes compatible with the purely electronic diffusion simulated here. Indeed, experimental peak-amplitudes for polycrystalline samples, $S^{\text{max}} \sim \mathcal{O}(0.1 - 1) \frac{\text{mV}}{\text{K}}$ [419, 420, 429, 430] are comparable to our modelling, see Fig. 3.28. With the phonon-drag thus mainly scaling the amplitude of the thermoelectric response, previous modellings including this effect had to explicitly introduce in-gap impurity levels [421, 422, 423], to generate the experimentally evidenced characteristic temperature scales. Here, we showed that the electron diffusion part of the Seebeck and Nernst coefficient has the correct temperature profile without the need for *ad hoc* in-gap levels—provided that finite lifetimes of intrinsic carriers are accounted for consistently.

3.4.2.2 FeSb₂: Explicit impurity states?

To strengthen the argument that in-gap impurity states are not crucial for an understanding of transport properties of FeSb₂, we study the explicit inclusion of such states. In Fig. 3.36 (bottom panel) we compare several ways to obtain the needed chemical potential: (i) μ_ψ (solid blue) indicates an occupation determined via Eq. (3.87), that accounts for, both, thermal broadening and the finite lifetimes of valence and conduction states (data reproduced from Fig. 3.28); (ii) μ_{FD} (black) that only includes thermal broadening via the Fermi-Dirac distribution; (iii) $\mu_{FD} + \text{imp}$ (pink dashed) in which an in-gap impurity level has been designed to mimic μ_ψ ; and (iv) $\mu_\psi + \text{imp}$ (green dashed) in which the same impurity level is added in the presence of finite lifetimes of intrinsic states.

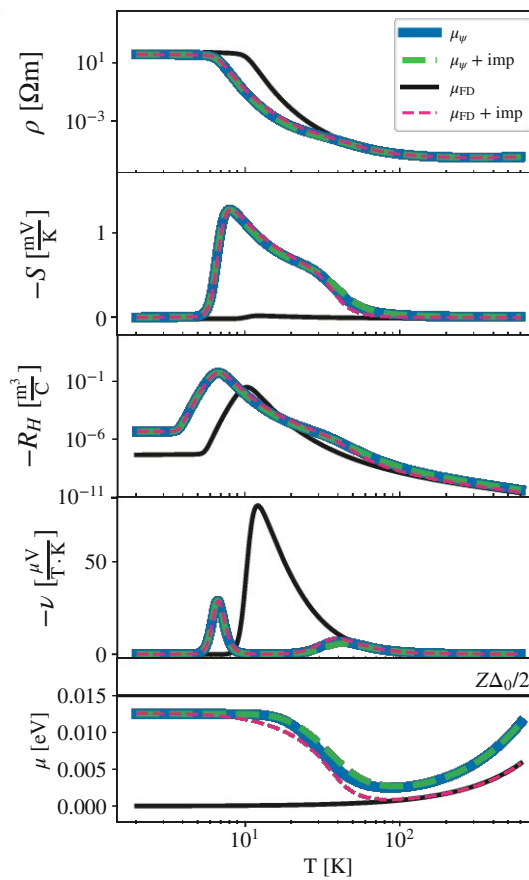


Figure 3.36: FeSb₂ and impurity in-gap states. Imitation of the chemical potential determined via Eq. (3.87)— μ_ψ —with the Fermi-Dirac distribution through the presence of an explicit impurity level— $\mu_{FD} + \text{imp}$ —in the vicinity of the conduction band. We employ the same parameters as in Fig. 3.28. The impurity is modelled by a donor at $E_D = 26\text{meV}$ below the conduction band with density $\rho_D = 5 \cdot 10^{-6} \frac{1}{\text{unit cell}}$. For comparison we also show μ solely determined via the Fermi-Dirac distribution— μ_{FD} —and the digamma-computed chemical potential with the impurity— $\mu_\psi + \text{imp}$.

Clearly, the Fermi-Dirac description of the chemical potential (black), in which the chemical potential converges towards the mid-gap point (origin of energy) for $T \rightarrow 0$, yields very different transport functions (upper panels). Their temperature profiles do not agree with experiment, cf. Fig. 3.28 (insets). Still, the resistivity and the Hall coefficient saturate (albeit at values different than in the “ μ_ψ ” scenario) and the Nernst and Seebeck coefficient vanish for $T \rightarrow 0$, since these low temperature properties stem from the employed **LINRETRACE** kernels, Eqs. (3.94-3.99). As a consequence, if the chemical potential μ_ψ —that drives both, the features at intermediate temperatures and influences the saturation values—could be mimicked by other means, transport properties will be very similar to the intrinsic “ μ_ψ ” picture. And, indeed, imitating the temperature dependence of μ_ψ through the inclusion of a single explicit donor level (at an energy $E_D = 26\text{meV}$, degeneracy $g = 1$ and density $\rho_D = 5 \cdot 10^{-6}$ per unit-cell), these “ $\mu_{FD} + \text{imp}$ ”-results (pink dashed) are very close to the μ_ψ results. In turn, if we include the same impurity level on top of the lifetime effects that drive μ_ψ (a combination labelled “ $\mu_\psi + \text{imp}$ ” (green dashed) in Fig. 3.36), nothing much happens. In other words: if finite lifetimes of intrinsic valence and conduction states are properly accounted for, extrinsic in-gap states have little on transport properties in FeSb_2 . This finding strengthens our alternative scenario in which the driver of the characteristic temperature profile in transport properties is the scattering rate.

3.4.2.3 Related materials: FeAs_2 , FeGa_3 , RuSb_2

We now extend our transport study to other materials. In the right column of Fig. 3.37 we reproduce experimental data of various intermetallic semiconductors. In order of increasing gap: FeSb_2 [214], FeAs_2 [214], RuSb_2 [424] and FeGa_3 [425, 446]. For all considered compounds, the charge gap can be extracted directly from the high-temperature behavior of the resistivity (or optical data). With the exception of FeSb_2 ($Z^{-1} = 2$), we do not apply a quasi-particle renormalization ($Z = 1$). Indeed, larger hybridization-gap semiconductors are expected to exhibit less correlation signatures [212] and also the substitution of a $3d$ transition-metal with its $4d$ homolog will reduce correlation effects [439], as explicitly shown for $\text{Fe}_{1-x}\text{Ru}_x\text{Sb}_2$ [433, 478].

While the resistivity of FeSb_2 only displays a shoulder at $T \sim T_\Delta^\mu$ (successfully modelled with $\Gamma(T)$), a distinct peak can be observed in the three other materials. The metallic slope, $\partial\rho/\partial T > 0$, at temperatures below said peak *cannot* be replicated with a chemical potential that is driven by finite lifetimes through Eq. (3.87) alone. Indeed, the transition of the chemical potential must occur more abruptly in temperature, making explicit impurity states a necessity to achieve agreement with experiment. We find that deploying a single donor level near the conduction band allows us to reproduce the qualitative behavior of all considered materials across all considered transport observables.

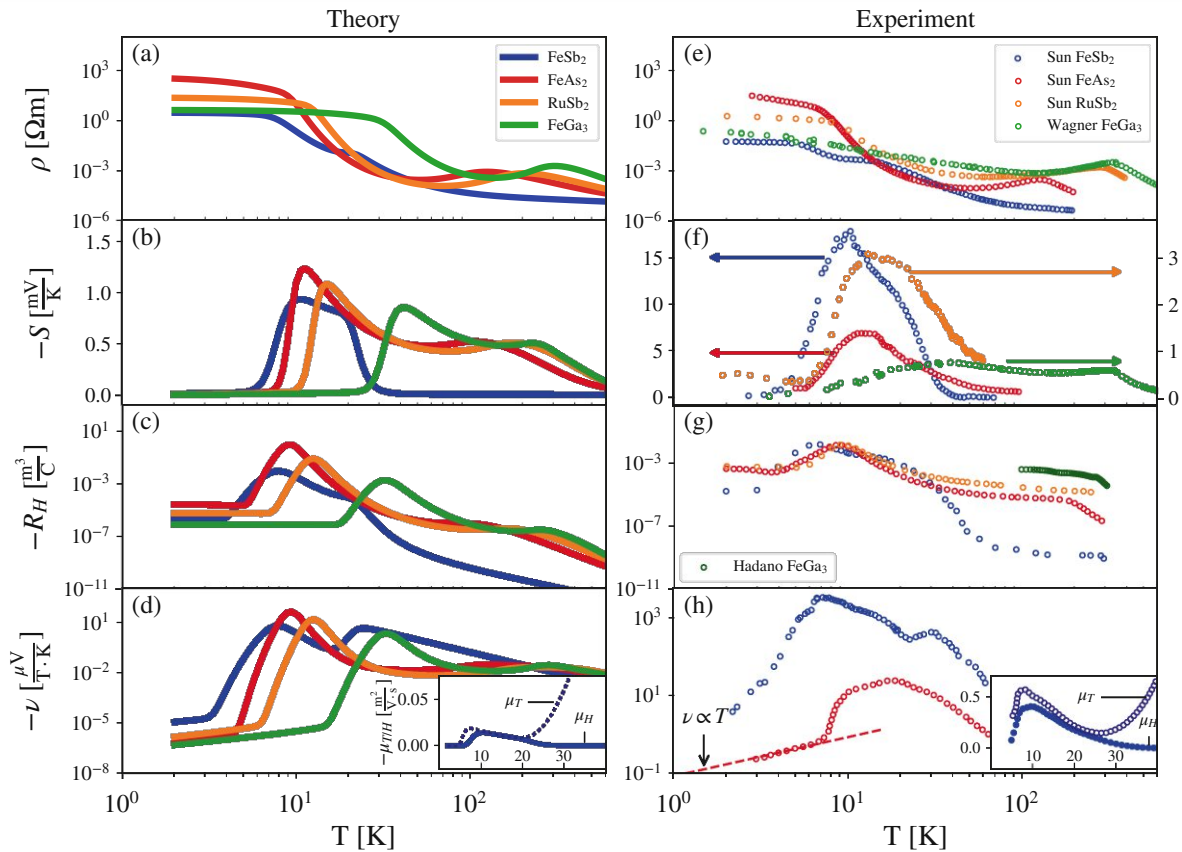


Figure 3.37: Modelling of intermetallic narrow-gap semiconductors. The experimental temperature profile of transport observables of FeSb₂ [214], FeAs₂ [214], RuSb₂ [424] and FeGa₃ ([100] orientation) [425, 446] is simulated with finite lifetimes and a single donor level at a distance E_D below the conduction band. Lifetimes dominantly determine transport at intermediate to low temperatures. Instead, the donor level virtually only affects higher temperatures near T_{Δ}^{μ} and T_{ν}^{μ} . In particular, in congruence with experiment, the level accounts for the metallic slope in the resistivity seen in all materials other than FeSb₂. To limit the number of adjustable parameters, bandgaps were fixed to experimental values: using $Z = 0.5$ for $\Delta_{\text{FeSb}_2} = Z \times \Delta_{0,\text{FeSb}_2} = 30\text{meV}$ and $Z = 1$ in $\Delta_{\text{FeAs}_2} = 200\text{meV}$; $\Delta_{\text{RuSb}_2} = 290\text{meV}$; $\Delta_{\text{FeGa}_3} = 500\text{meV}$. All modelling parameters are listed in Table 3.3. Jointly, finite lifetimes and the impurity level yield an accurate description without the need for other electronic structure details.

Resistivity

For FeSb₂ this leads to minor improvements in T_{Δ}^{μ} and T_{ν}^{μ} of the initial fit (Fig. 3.28). For Fe/RuAs₂ and FeGa₃ the engineered chemical potential causes the resistivity to decrease when cooling below

their T_ν^μ (metallic slope), before it rises again to enter the second activated region and, eventually, the saturation regime below T_ρ^* . The overall agreement is astounding: with a single impurity level characteristic temperatures, qualitative features and even relative amplitudes between various materials can be accurately modelled.⁵⁹

Seebeck coefficient

Unsurprising from the previous analysis and the optimal parameters listed in Table 3.3 the magnitude of the theoretical Seebeck coefficients (Fig. 3.37b) do not differ significantly in the modelling. For all materials considered we observe a peak amplitude in the range of $|S^{\max}| = 0.8 - 1.3 \frac{\text{mV}}{\text{K}}$ positioned at a respective T_S^{\max} slightly above the saturation temperatures T_ρ^* of Fig. 3.37a. While lacking the phonon-drag boost to the Seebeck magnitude, our treatment still captures quite well, both, the dominant peak's position at T_S^{\max} and the high temperature shoulder (peak) at T_Δ^μ for FeSb₂ (FeGa₃). Unfortunately, no data for FeAs₂ and RuSb₂ is available for higher temperatures: For them, we anticipate an additional Seebeck feature where the respective resistivities are peaked.

Hall coefficient

The agreement to experiment for the Hall coefficient, Fig. 3.37g, is comparable to that of the resistivity: As in the experiments, the position of the peak in R_H virtually coincides with the T_ρ^* crossover in the resistivity. Equally the hierarchy across materials is captured for the saturation value, $R_H(T \rightarrow 0)$, and also the decay at higher temperatures mirrors the experiment. Clearly, the high-temperature shoulder is connected to the resistivity peak at T_Δ^μ . We therefore expect R_H of RuSb₂ to similarly drop if temperatures slightly beyond the shown experimental range were probed.

Nernst coefficient

For the Nernst coefficient less experimental data is available, see Fig. 3.37h. For the cases of FeSb₂ and FeAs₂ the qualitative agreement between simulation and measurements is reasonably good. Of course, what has been said about the Seebeck coefficient of FeSb₂ also applies to its Nernst signal: It is substantially boosted by the phonon drag [421, 423], limiting us to discussing the qualitative temperature profile⁶⁰. Not suffering from this intricacy, clearer agreement is seen for FeAs₂: There, the experimental low temperature signal neatly follows the linear behavior $\nu \propto T$ (dashed line) as derived in Eq. (3.188) and illustrated in Fig. 3.37d.

⁵⁹The only noticeable deviation constitutes FeGa₃ where the chosen experiment exhibits a less clear transition between an activated and a saturated region. See, however, the c-axis resistivity in Ref. [446].

For FeSb₂, we also indicate the Hall and thermal mobilities of Eq. (3.195) in the insets of Fig. 3.37d/h. The experimental data [214] qualitatively matches the theoretical prediction: At high temperatures a divergence between μ_T and μ_H is observed, giving rise to FeSb₂'s smaller Nernst peak at $T \approx 40\text{K}$. Below, at intermediate temperatures, $T \approx 20\text{K}$, the two mobilities almost coincide (i.e., ν is suppressed). At low temperatures, $T \approx 10\text{K}$, again a slight mismatch occurs, giving rise to the prominent low temperature peak.

	Z	Δ_0 [meV]	α	Γ_0 [eV]	γ [$\frac{\text{eV}}{\text{K}^2}$]	E_D [meV]	ρ_D [$\frac{1}{\text{unit.cell}}$]
FeSb ₂	0.5	60	1.02	$1.5 \cdot 10^{-4}$	$8 \cdot 10^{-7}$	20	$6 \cdot 10^{-8}$
FeAs ₂	1	200	1.12	$1.5 \cdot 10^{-5}$	$3 \cdot 10^{-7}$	15	$1.5 \cdot 10^{-4}$
RuSb ₂	1	290	1.12	$7 \cdot 10^{-5}$	$2 \cdot 10^{-7}$	18	$3.5 \cdot 10^{-4}$
FeGa ₃	1	500	1.04	$3 \cdot 10^{-4}$	$2 \cdot 10^{-7}$	40	$1.5 \cdot 10^{-3}$

Table 3.3: Electronic structure parameters for simulated materials. Quasi-particle renormalization Z , bandgap Δ_0 , band asymmetry $\alpha = |t_2/t_1|$, scattering rate coefficients in $\Gamma(T) = \Gamma_0 + \gamma T^2$ and a single donor level of concentration ρ_D positioned at a distance E_D below the conduction band. Gap sizes, $\Delta = Z\Delta_0$, are kept fixed to experimental values during the (manual) optimization procedure.

3.4.2.4 Perspective

The previous Section made clear that with reasonable scattering rates and (for larger gap systems) an explicit impurity in-gap level, all experimental transport coefficients can be qualitatively matched with an essentially featureless band structure. This emphasizes the notion that most—if not all—of the relevant transport physics in narrow-gap semiconductors is purely determined by the interplay of the gap, the chemical potential profile (shaped by temperature, carrier lifetimes and, potentially, impurity states) and the scattering rate. Electronic structure intricacies, such as details of the band structure beyond the gap value and optical transition elements, all seem to play only a secondary role. Further, we evidenced that, at low temperatures ($T_{RH}^* < T_\rho^* < T_S^{\max}$), features are controlled by the scattering rate through the (quantum = beyond-Boltzmann) transport kernels, whereas the higher-temperature features ($T_\Delta^\mu < T_\nu^\mu$) are determined through the behavior of the chemical potential, which can be driven by the scattering rate of intrinsic carriers as well as by extrinsic impurity in-gap states.

⁶⁰ Contrary to S , ν depends on the lattice constant and scales according to $\nu \propto a_{\text{lattice}}$, see Appendix of Ref. [9]. Using instead of our generic $a = 1\text{\AA}$, a realistic lattice constant, FeSb₂'s Nernst amplitude is, in principle, not out of reach of the electron diffusion picture.

Future extensions of the presented formalism (and software package [11]) could include the ability to describe phonon-drag contributions to thermoelectric observables. This advance could remedy our current inability to quantitatively match the amplitude of the Seebeck coefficient, in particular of single crystalline FeSb₂. Furthermore, an inclusion of (topological) surface conduction and in-depth comparisons of their importance vis-à-vis the discussed bulk conduction is desirable, also in view of FeSb₂ [418, 474]. Finally, also anomalous bulk contributions could be included, following, e.g., the recent Ref. [391].

3.4.3 Summary

Summarizing Section 3.3 and Section 3.4, we conceptualized an efficient linear response transport formalism: A low-energy expansion of quasi-particle renormalizations enabled performing frequency integrations in dominant Feynman diagrams *analytically* which we applied to narrow-gap semiconductors and established a comprehensive phenomenology of their transport properties:

First, we analytically extracted low-temperature characteristics of various transport observables: In congruence with experiments, both, the resistivity and the Hall coefficient saturate at finite values for $T \rightarrow 0$. The Seebeck and Nernst coefficients, instead, vanish linearly in the zero temperature limit, consistent with thermodynamic expectations. These behaviours are beyond the reach of semi-classical approaches like Boltzmann theory in the relaxation time approximation, highlighting the importance of a fully quantum mechanical description.

Next, we simulated transport properties as a function of temperature for varying bandgap, particle-hole asymmetry and scattering rate. This survey establishes the prototypical temperature dependence of transport in narrow-gap semiconductors to be structured by five emergent characteristic temperatures: $T_{RH}^* < T_{\rho}^* < T_S^{\max} < T_{\Delta}^{\mu} < T_{\nu}^{\max}$: At high temperatures, $T > T_{\nu}^{\mu}$, the shape of all observables is controlled by the bandgap Δ_0 and our equations yield results identical to Boltzmann approaches. Upon cooling, $T_{\Delta}^{\mu} < T < T_{\nu}^{\mu}$, the system experiences a crossover from the activated, Boltzmann-like regime to a renormalized activation region, $T_{\rho}^* < T < T_{\Delta}^{\mu}$, with an associated energy $\Delta_1 < \Delta_0$. We find this crossover to be driven by the chemical potential: Finite lifetimes of valence and conduction states cause incoherent spectral weight to spill into the gap. Below a characteristic temperature, these incoherent carriers can no longer be neglected with respect to the charges that are thermally activated across the gap Δ_0 . In particle-hole asymmetrical systems, the chemical potential then has to adapt to preserve charge neutrality by moving to a position separated by only Δ_1 from the top (or bottom) of the valence (or conduction) band. This *intrinsic* mechanism provides an explanation alternative to the common *extrinsic* scenario in which the moving of the chemical potential (and the associated shoulder in the resistivity) is attributed to the presence of impurity in-gap

states. Finally, at low enough temperature, $T < T_\rho^*$ ($T < T_{RH}^*$) the system enters the aforementioned lifetime-dominated regimes in which the resistivity (the Hall coefficient) saturates and thermoelectric observables vanish linearly.

In semi-classical approaches, the lifetime of excitations appears as a mere prefactor of, say, the conductivity. In the quantum formulation derived here, instead, the scattering rate is a relevant control parameter that can compete with other energy scales of the problem. Indeed, the emergence of all characteristic transport features is a direct consequence of the interplay of the charge gap and the scattering rate. In other words, in our transport equations, thermal and lifetime broadening are described on an equal footing.

Let us note that recently, Eo *et al.* [298] provided strong evidence for surface states in FeSb₂ and FeSi (previously also found in Refs. [299, 474]), and, importantly, extracted a bulk resistivity that rises exponentially over up to 9 orders of magnitude down to lowest temperatures. These results suggest that topologically protected surface states short-circuit the bulk in a standard four-point resistivity measurement and lead to the observed residual conduction. To further distinguish the different scenarios, it will be enlightening to perform measurements on crystals with different types and concentrations of defects. It could be that our lifetime-scenario only comes to light for less pure samples.

Nonetheless, our phenomenology seems to be prototypical in a wider context of narrow-gap semiconductors [212]. Indeed, all considered hybridization-gap semiconductor showed reasonably good qualitative agreement where FeAs₂ even showcasing the linear temperature dependence of the Nernst coefficient, one of the hallmarks of residual conduction within our theory, see Fig. 3.37. Further, in Ce₃Bi₄Pt₃, our other main target material, residual conduction was shown to be indeed a bulk property [334].

In the next, final results Section, we will give a brief overview of the `LINRETRACE` package used to generate the results shown in this Section. In the context of the models and materials studied so far, we will highlight some important, hitherto ignored, technical details and showcase some potential future avenues of research.

3.5 The Linear Response Transport Centre

- This Section is based on “LinReTraCe: The linear response transport centre” by [Matthias Pickem](#), Emanuele Maggio, and Jan M. Tomczak [11]. Adopted text passages have been marked accordingly.
- In this Section we detail the numerical implementation of the methodology introduced in Section 3.3. To this end we emphasize certain technical details which were necessary in the applications to narrow gap semiconductors as well as (realistic) applications that go beyond the insulating scenario. Similar to Section 3.4, the aforementioned sign and pre-factor fixes have been adopted and the relevant figures have been adjusted accordingly.
- For a practical userguide (installation, configuration, execution) of the code package, please refer to the original publication [11]. The live repository can be found at Ref. [12].

Finalizing our discussion on transport properties of narrow-gap semiconductors, we detail the implementation of the Linear Response Transport Centre **LINRETRACE** (github.com/linretrace), a software package that facilitates the computation of a variety of transport observables. The unique feature of **LINRETRACE** is the treatment of thermal and lifetime broadening on an equal footing [7, 9], while still incurring numerical costs as low as semi-classical Boltzmann approaches in the relaxation-time approximation. We exploit that linearizing the dynamics of many-body renormalizations (self-energy) allows for a semi-analytical (instead of numerical) evaluation of leading contributions in Kubo’s linear response theory [7, 9, 331], see the previous Sections. **LINRETRACE**’s principle input are electronic excitation energies and associated quasi-particle weights and lifetimes, as well as optical transition matrix elements. Being agnostic to the input’s origin, **LINRETRACE** can be used in a variety of settings, including electronic structures from tight-binding or Wannier projections [63], density functional theory (DFT) [479], many-body perturbation theory [480, 481], dynamical mean-field theory (DMFT) [94, 482], or approaches beyond [74, 93]. Scattering amplitudes and many-body renormalizations can be phenomenological, extracted from electronic self-energies (obtained, e.g., from DMFT), or could incorporate results



Figure 3.38: LINRETRACE [11]
<https://github.com/linretrace>

from electron-phonon codes [409, 410, 412, 483, 484, 485, 486]. In this release we include interfaces to the DFT codes **WIEN2k** [21, 22] and **VASP** [26], the band interpolation tool of **BoltzTraP2** [406, 407], maximally localized Wannier functions of **Wannier90** [29], as well as tools for general tight-binding systems. We further provide templates for the implementation of interfaces to other codes. With an emphasis on numerical accuracy and scalability, **LINRETRACE** will be of value also for high-throughput studies [465, 487, 488, 489, 490, 491] and for tight-binding descriptions of very large unit-cells.

3.5.1 Methodological context

To highlight the merits of **LINRETRACE**, let us group previous packages for electronic transport properties of solids into two categories: semi-classical Boltzmann and Kubo linear response codes. Owing to their numerical efficiency and ease of handling, Boltzmann codes [406, 407, 408, 409, 410] have become popular tools. Typically, they are used in conjunction with band-theory, i.e., they utilize well-defined excitation energies. The selection of carriers participating in conduction is then solely determined from the *thermal* broadening (activation) via the Fermi function. In the usually employed relaxation-time approximation (RTA), electron scattering then only results in amplitude-scaling prefactors for a given momentum \mathbf{k} and state n , e.g., for the conductivity $\sigma \propto \sum_{\mathbf{k}n} \Gamma_{\mathbf{k}n}^{-1} \times \dots$, cf. Eq. (3.149). Often, the scattering rate Γ is moreover assumed to be equal for all states and momenta. Then, the lifetime $\tau = \frac{\hbar}{2\Gamma}$ scales the Boltzmann conductivity globally, while the Seebeck and Hall coefficient become independent of τ . With this assumption, insight into electronic transport can be gained without explicit knowledge of scattering amplitudes and their physical origin. As a consequence, Boltzmann transport kernels are relatively simple and the algorithmic complexity of, e.g., **BoltzTraP** [406, 407] and **BoltzWann** [408] (and the difference between them), lies in how they achieve convergence in the sampling of the Brillouin zone.

There are however circumstances, when the approximations inherent to band theory and the semi-classical treatment of transport fail. Inadequacies of band-theory for strongly correlated materials are well-documented: Examples not only include Mott insulators, where correlation effects fully invalidate the band-picture [59]. Also the electronic structure of correlated metals [416, 492, 493, 494] and correlated narrow-gap semiconductors [212, 250] are severely altered and have to be accounted for with methodologies that include dynamical renormalizations (self-energies). However, even if such many-body corrections are captured on the level of electronic structure theory, plugging them into a semi-classical transport methodology may still lead to severe pathologies: Irrespective of the size of the scattering rate, the resistivity, the Seebeck, and the Hall coefficient of a clean semiconductor diverge in the zero temperature limit within Boltzmann's relaxation time approximation. A diverging activation law for the $T \rightarrow 0$ resistivity is physically admissible—but it is never observed. A diverging

Seebeck coefficient, $|S(T \rightarrow 0)| \rightarrow \infty$, instead, violates the third law of thermodynamics (there can be no entropy transport at $T = 0$ for non-degenerate ground-states).

A quantum mechanical description of transport using Kubo's linear response theory [191] overcomes these artefacts by correctly treating effects of finite lifetimes (incoherence) of charge carriers [7, 9, 320]. To allow, beyond the *thermal*, also for a *lifetime* broadening of excitations, Kubo formulas require an integration over energies. This evaluation may become expensive for large systems and is hazardous at low temperatures and when the scattering rate is small. With **LINRETRACE** we conquer this bottleneck by performing frequency integrations *analytically* instead of numerically. This step becomes possible after linearizing the dynamics of many-body renormalizations (the self-energy Σ), yielding the **LINRETRACE** input: the scattering rate Γ , the quasi-particle weight Z , and possible static offsets $\Re\Sigma$. This approximation is warranted as the self-energy typically varies slowly inside the narrow energy-window probed by transport (a few $k_B T$), unless there are relevant pole-like structures in the self-energy, as is the case in Mott insulators. Following common practice of Kubo implementations [32, 362, 492, 493, 494, 495, 496, 497, 498, 499, 500], **LINRETRACE** neglects particle-hole scattering, so-called vertex corrections. The ensuing analytical transport functions are then not only numerically inexpensive and stable, they also reveal valuable microscopic information: In particular they show that the scattering is not a mere prefactor (scaling the amplitude of conduction), but a relevant energy scale that has a complex interplay with other energies of the system, e.g., the charge gap in a semiconductor [9]. In all, **LINRETRACE** combines the best of both (Boltzmann & Kubo) worlds: an efficient and stable evaluation of transport observables that treats thermal and lifetime broadening on an equal footing.

3.5.2 Implementation

Programming languages

— Fortran 95 and Python 3

Required dependencies

— HDF5 ($\geq 1.12.1$), h5py, numpy, scipy, ase ($\geq 3.18.0$), spglib ($\geq 1.9.5$)

Optional dependencies

— MPI (Fortran 95), matplotlib, boltztrap2 ($\geq 20.7.1$), cmake

LINRETRACE calculations follow the flow chart of Fig. 3.39 and require two mandatory files: an energy file and a config file. The former is a direct result of one of the various interfaces and contains all the necessary energies $\varepsilon(\mathbf{k}, n)$, optical elements $M^{(B),\alpha\beta(\gamma)}$, and other auxiliary data. Depending on the data source only some of these optical elements can be generated, as, e.g., the magnetic field optical elements require the existence of band velocities and curvatures, not available in stand-alone WIEN2k

calculations. The transport calculation itself is configured via a config text file for which `lconfig` provides a minimal starting point. More elaborate options, e.g., impurity states, need to be added by hand. In the config file one has access to simplistic scattering rate (and quasi-particle weight) dependencies, i.e., polynomial behaviors in temperature. More control over these dependencies can be gained via a scattering file where one has the option to specify all available data points individually. The results of the transport calculation are then saved in the HDF5 output file containing all the Onsager coefficients $\mathcal{L}_{ab}^{\alpha\beta}$, $\mathcal{L}_{ab}^{B,\alpha\beta\gamma}$ among other auxiliary information, including the configuration, structure information, etc. `lprint` provides easy access to these data containers as well as their combinations that form the physical transport quantities.

As it does not contribute to this thesis in a significant manner: For a detailed installation instructions, a thorough discussion on the interfaces (green boxes), the various executables (red boxes), the resulting files (blue boxes) and the configuration options, please refer to the original publication in Ref. [11]. Instead, here we will focus purely on technical details relevant to the previously shown results and advance the discussion towards inter-band contributions and applications to exemplary, realistic material calculations.

3.5.3 Technical details

3.5.3.1 Matrix elements on irreducible grids

Periodic unit cells can be assigned a point group that is commonly represented by a set of n square matrices P_i ($\det P_i = \pm 1$) that describe all applicable symmetry operations acting in real space. In reciprocal space this can be exploited as one can reduce the number of momenta necessary to represent the full Brillouin zone (for a symmetry reduction algorithm scaling linearly with the number of points see [501]). Each so-called irreducible \mathbf{k} -point \mathbf{k}_{irr} then represents a set of momenta $\{\mathbf{k}_i\}$ that are all connected to each other via the transposed matrices P_i^T

$$\mathbf{k}_i = P_i^T \mathbf{k}_{irr}. \quad (3.203)$$

The number of unique momenta generated from \mathbf{k}_{irr} is called its multiplicity m , where each point in the set will be generated exactly $\frac{n}{m}$ times. Naturally, the energies within this set remain unchanged

$$\forall i, \mathbf{k}_{irr} : \varepsilon(\mathbf{k}_{irr}) = \varepsilon(P_i^T \mathbf{k}_{irr}) \quad (3.204)$$

which then also applies to the kernel functions Eqs. (3.79-3.80). Crucially, owing to their directionality, this does not hold for the associated optical elements, band velocities and band curvatures, hence Eqs. (3.77-3.78) must not be evaluated directly on the irreducible grid. Instead, matrix elements have

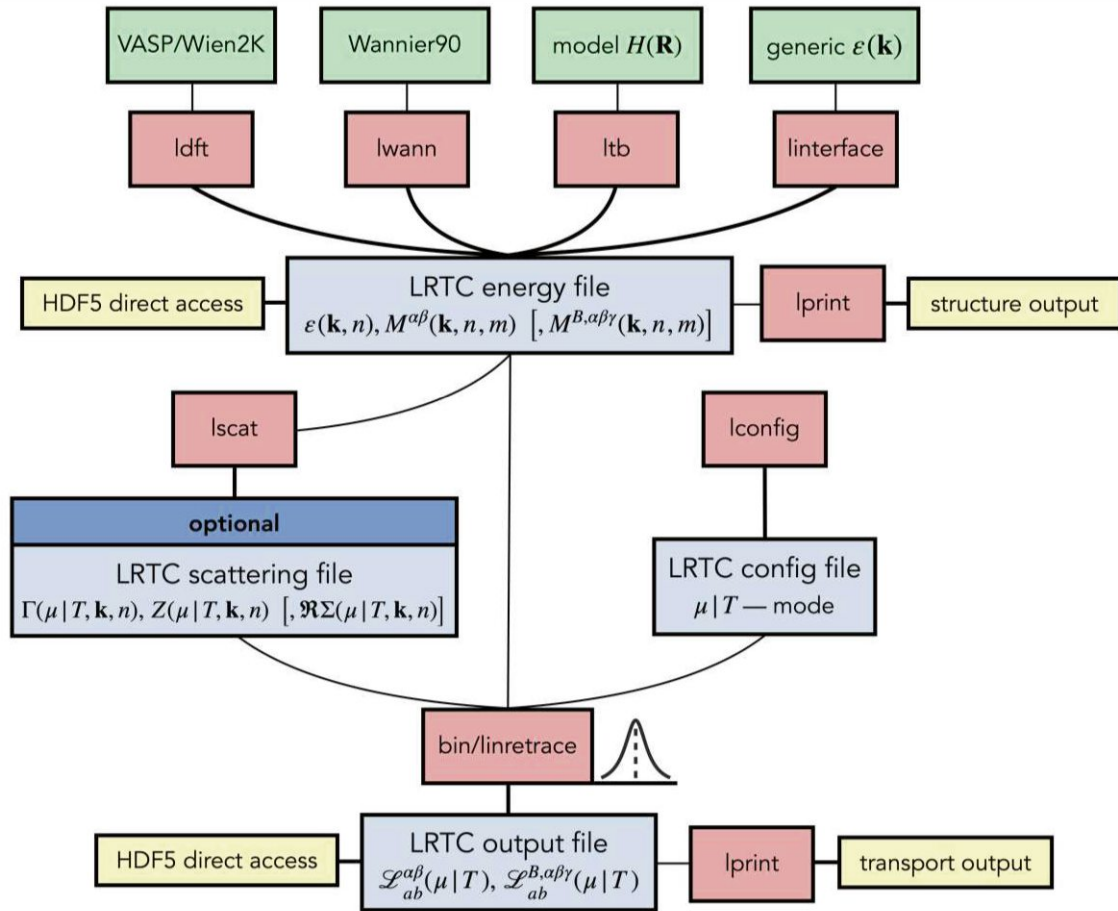


Figure 3.39: Flow chart of the LINRETRACE package: The energy file can be generated by interfacing various electronic structure codes or modelling your own dependencies. Combined with a config file and, *optionally*, full scattering dependencies, this constitutes the input of the core program `bin/linretrace`. The HDF5 output file can either be accessed effortlessly by `lprint` or via any external HDF5 library.

to be symmetrized: By averaging over all connected optical elements

$$M_{opt}^{\text{symmetrized}}(\mathbf{k}_{\text{irr}}) = \frac{1}{n} \sum_{i=1}^n M_{opt}(P_i^T \mathbf{k}_{\text{irr}}) \quad (3.205)$$

one is able to absorb all the required symmetry information. Please note that these schemes require the momentum mesh to respect the same point group symmetries as the unit cell itself, e.g., a cubic crystal structure requires $n_{kx} = n_{ky} = n_{kz}$. If this were not the case, $P_i^T \mathbf{k}_{\text{irr}}$ generates points outside the initial grid.⁶¹

While density functional theory codes like WIEN2k provide dipole matrix elements on an irreducible grid, optical elements as listed in Sec. 3.3.4.2 need to be symmetrized explicitly. Since Eq. (3.205) relies on information from the full Brillouin, the symmetrization is implemented via real-space rotations. Band velocities then transform as

$$v(P_i^T \mathbf{k}_{\text{irr}}) = [K^{-1} P_i^{-1} K] v(\mathbf{k}_{\text{irr}}) \quad (3.206)$$

whereas band curvatures c transform as

$$c(P_i^T \mathbf{k}_{\text{irr}}) = [K^{-1} P_i^{-1} K] c(\mathbf{k}_{\text{irr}}) [K^{-1} P_i^{-1} K]^T \quad (3.207)$$

as they correspond to a single and twofold momentum derivative, respectively. In the same vein the optical elements M themselves transform as the curvatures in Eq. (3.207). Here K is the matrix formed by the reciprocal lattice vectors (the rows of K). This transforms the point group matrix into Cartesian directions and is explicitly necessary for non-orthogonal unit cells. The generated velocities and curvatures are then combined to optical elements via Eqs. (3.166-3.167), over which the symmetrization is performed.

Let us emphasize that Eqs. (3.206-3.207) only hold in the band-basis. In the context of (non-diagonal) Wannier basis (coming from Wannier90 or tight-binding parameters), the symmetrization must be performed explicitly. That is, one is forced to generate all connected reducible points via $P_i^T \mathbf{k}_{\text{irr}}$, and calculate the multi-orbital Hamiltonian and its derivatives (velocities v and curvatures c)⁶²

$$H_W(\mathbf{k}) = \sum_{\mathbf{R}} e^{i\mathbf{k}\cdot\mathbf{R}} H_W(\mathbf{R}), \quad (3.208a)$$

$$H_W^{v,\alpha}(\mathbf{k}) = i \sum_{\mathbf{R}} R^\alpha e^{i\mathbf{k}\cdot\mathbf{R}} H_W(\mathbf{R}), \quad (3.208b)$$

$$H_W^{c,\alpha\beta}(\mathbf{k}) = - \sum_{\mathbf{R}} R^\alpha R^\beta e^{i\mathbf{k}\cdot\mathbf{R}} H_W(\mathbf{R}), \quad (3.208c)$$

on these connected set of momenta. Here R^α is the Cartesian component $\alpha \in \{x, y, z\}$ of the unit-cell vector \mathbf{R} . One then has to perform the diagonalization to the band basis on each of these momentum points via

$$\varepsilon(\mathbf{k}) = U^{-1}(\mathbf{k}) H(\mathbf{k}) U(\mathbf{k}) \quad (3.209)$$

separately, as the Hamiltonian matrices do not necessarily have to coincide – only their respective

⁶¹ An incommensurate reducible grid could still be reduced, by deselecting invalid momenta. Also an exact symmetry mapping of every single irreducible \mathbf{k} -point to all m connected momenta would solve this issue. Our current implementation, however, requires the user to make a sensible choice for the grid.

⁶² In unit cells with more than one atom we employ the Peierls correction as derived in Ref. [362]. The velocities are corrected by a second term according to $v_{kl'}^\alpha = \frac{1}{\hbar} \partial_{k_\alpha} H^{ll'}(\mathbf{k}) - i(\rho_l^\alpha - \rho_{l'}^\alpha) H^{ll'}(\mathbf{k})$.

eigenvalues. Finally, the symmetrization is then performed over the optical elements $M^{(B),\alpha\beta(\gamma)}$, see Section 3.3.4, which consist of a combination of velocities and curvatures that have similarly been transformed to the band basis with the transformation matrices $U^{(-1)}(\mathbf{k})$.

To showcase the validity of these equations and our symmetrization routine we compare a graphene-inspired honeycomb lattice on a reducible and corresponding irreducible momentum grid, see Fig. 3.40.

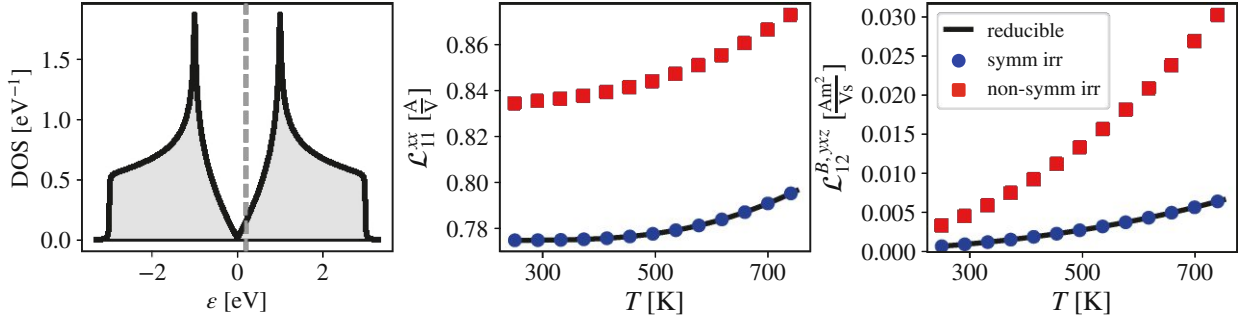


Figure 3.40: Reducible calculations compared to calculations on an irreducible grid with and without optical element symmetrization. Left: Density of states of the honeycomb lattice with hopping of $t_{AB} = t_{BA} = 1\text{eV}$ and lattice length $|a| = 1\text{\AA}$. Middle and right: Onsager coefficients \mathcal{L}_{11}^{xx} and \mathcal{L}_{12}^{yz} performed for 180×180 reducible (8191 irreducible) \mathbf{k} -points at a constant chemical potential of $\mu = 0.20\text{eV}$ (vertical dashed line) and scattering rate $\Gamma = 10^{-5}\text{eV}$. Only a properly symmetrized irreducible grid leads to consistent data. Note that for this 2D system, Onsager coefficients needed to be multiplied with the (fictitious) c -lattice constant to yield proper units, as, e.g., \mathcal{L}_{11} is linked to a conductance $[\sigma^{2D}] = 1/\Omega$ instead of a conductivity $[\sigma] = 1/(\Omega m)$.

3.5.3.2 Chemical potential search

Determining the chemical potential is a common root finding problem where the numerical search of μ can be represented by

$$N - \sum_{\mathbf{k},n} f(\varepsilon_{\mathbf{k},n} - \mu) \stackrel{!}{=} 0. \quad (3.210)$$

For the case of no band renormalizations ($Z \equiv 1$) the occupation $f(\varepsilon_{\mathbf{k},n} - \mu)$ is either determined from the Fermi function

$$f(\varepsilon_{\mathbf{k},n} - \mu) = f_{\text{FD}}(\varepsilon_{\mathbf{k},n} - \mu) = \frac{1}{1 + e^{\beta(\varepsilon_{\mathbf{k},n} - \mu)}} \quad (3.211)$$

or from the lifetime-broadened spectrum Eq. (3.84), entailing

$$f(\varepsilon_{\mathbf{k},n} - \mu) = \frac{1}{\pi} - \Im\psi\left(\frac{1}{2} + \frac{\beta}{2\pi}(\Gamma_{\mathbf{k},n} + i(\varepsilon_{\mathbf{k},n} - \mu))\right). \quad (3.212)$$

In some cases, employing root-finding algorithms on Eq. (3.210) can lead to severe problems. While metallic systems suffer mostly from too coarse momentum grids, gapped systems tend to exhibit massive numerical instabilities.⁶³ Due to the additional Γ -smearing in our formalism, this problem is absent for reasonably large scattering rates ($\Gamma \geq 10^{-6}\text{eV}$) and reasonable band gaps ($\Delta < 10\text{eV}$) at all temperatures when using Eq. (3.212). Using the Fermi-Dirac distribution for insulators, on the other hand, the root-finding is strongly restricted in the temperatures that can be safely captured, irrespective of the numerical accuracy, see double and quadruple precision calculations (blue and green lines) in Fig. 3.41, respectively.

In order to circumvent this problem the root-finding problem can be reformulated to

$$\underbrace{\sum_{\mathbf{k},n \geq \text{CB}} f(\varepsilon_{\mathbf{k},n} - \mu)}_{\text{activated electrons}} - \underbrace{\sum_{\mathbf{k},n \leq \text{VB}} f(-(\varepsilon_{\mathbf{k},n} - \mu))}_{\text{activated holes}} \stackrel{!}{=} 0 \quad (3.213)$$

in fully gapped systems with μ inside the gap: The chemical potential is determined by balancing the electrons in the conduction bands with the holes in valence bands. As a consequence one is not limited by machine precision anymore and can exploit the full floating point range. Nonetheless, due to finite bit length, temperatures are still bounded. The lowest possible achievable temperature corresponds to resolving density contributions down to the smallest positive number representable in quadruple precision: 2^{-16494} . If the occupation is determined via the Fermi function and the chemical potential is in the middle of the band gap Δ , it follows from

$$\frac{1}{e^{\beta\varepsilon} + 1} \approx e^{-\beta\varepsilon} = e^{-\beta\frac{\Delta}{2}} \quad (3.214)$$

that the lowest temperature bound is

$$T_{\text{bound}}^{\mu}[\text{K}] = \frac{\Delta[\text{eV}]}{2 \ln(2) 16494 k_B} \approx 0.5\Delta[\text{eV}]. \quad (3.215)$$

The chemical potential determined via this refined root-finding problem is also illustrated in Fig. 3.41.

⁶³Which is why Boltzmann codes typically use a fixed chemical potential instead of searching for it.

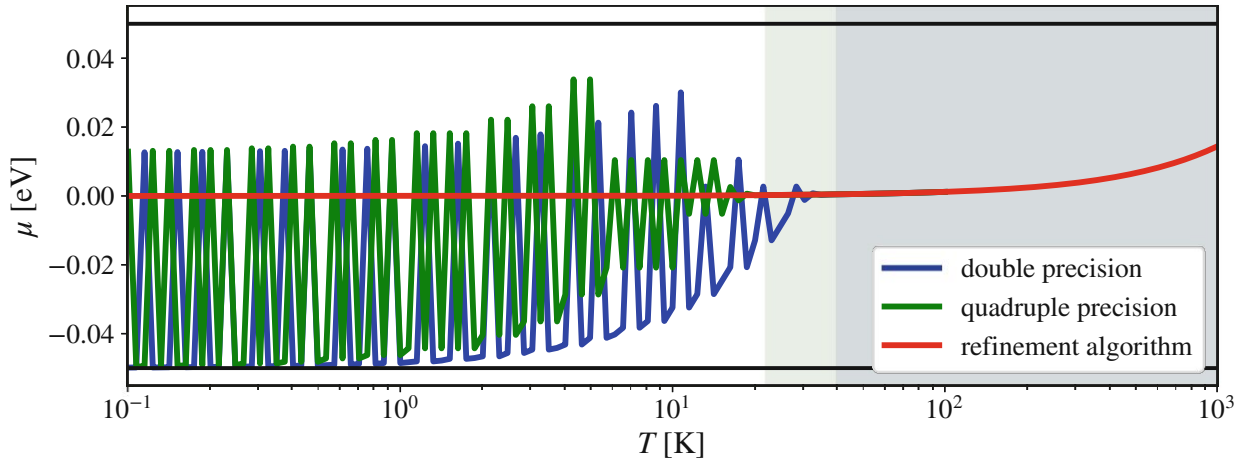


Figure 3.41: Chemical potentials in a gapped system determined via Eq. (3.210) with double (blue) and quadruple precision (green) compared to the chemical potential via the reformulated Eq. (3.213) (red). In all three cases the Fermi distribution is used. For the given band gap $\Delta = 0.1\text{eV}$ the “standard” root finding breaks down below $T = 40\text{K}$ and $T = 10\text{K}$ as the floating point accuracy is exhausted at double and quadruple precision, respectively. The reformulated problem on the other hand is stable down to $T = 0.05\text{K}$ (below plotted range), see text.

Impurity levels

LINRETRACE allows the inclusion of passive impurity states: Neglecting explicit contributions to the transport functions, the charge of these extra states affects the transport data merely through the position of the chemical potential. The above refinement algorithm is especially important when employing impurity states inside the gap. Without them, one could approximate the chemical potential obtained via the Fermi function, by extrapolating μ towards the band-gap mid-point at $T = 0$ [331].

Including impurity states is straight forward:

- (i) calculate (intrinsic) electron occupation $f(\mu)$ according to Eq. (3.211) or Eq. (3.212)
- (ii) calculate (extrinsic) impurity contribution n_{imp} according to Eq. (3.217a) or Eq. (3.217b)
- (iii) calculate total occupation: $n(\mu) = f(\mu) - n_{\text{imp}}^D + n_{\text{imp}}^A$ (given a donor (acceptor) level, the chemical potential has to increase (decrease) to compensate)
- (iv) determine μ according to Eq. (3.210) or Eq. (3.213)

Please note that the reformulated root-finding problem of Eq. (3.213) then becomes

$$\sum_{\mathbf{k}, n \in \text{CB}} f(\varepsilon_{\mathbf{k}, n} - \mu) - \sum_{\mathbf{k}, n \in \text{VB}} f(-(\varepsilon_{\mathbf{k}, n} - \mu)) - n_{\text{imp}}^D + n_{\text{imp}}^A \stackrel{!}{=} 0. \quad (3.216)$$

Here the impurity contribution differs between donor (D) and acceptor (A) levels

$$n_{\text{imp}}^D = \frac{\rho_D}{1 + g e^{\beta(\mu - E_{\text{imp}}^D)}} \quad (3.217a)$$

$$n_{\text{imp}}^A = \frac{\rho_A}{1 + g e^{\beta(E_{\text{imp}}^A - \mu)}} \quad (3.217b)$$

where $\rho^{D/A}$ is the impurity density, g is the impurity degeneracy and E_{imp} is the impurity position. For a donor level in the vicinity of the conduction band edge the chemical potential has to increase to compensate for the additional impurity occupation. Fig. 3.42 illustrates the effect for varying impurity densities. Using the Fermi distribution for intrinsic states, the chemical potential approaches the center point between the impurity level E_{imp}^D and the closest conduction state (instead of the band-gap middle point, realized for $\rho_D = 0$). From a transport perspective the effective band gap transforms from $\Delta = E_c - E_v$ at high temperatures to $\Delta = E_c - E_{\text{imp}}$ at low temperatures. The transition temperature is controlled by the impurity density and partially by the degeneracy of the impurity level. In addition to single impurity levels **LINRETRACE** also offers finite-size impurity bands with various shapes including box (constant), half-circle, and squared sine, see the Appendix of Ref. [11].

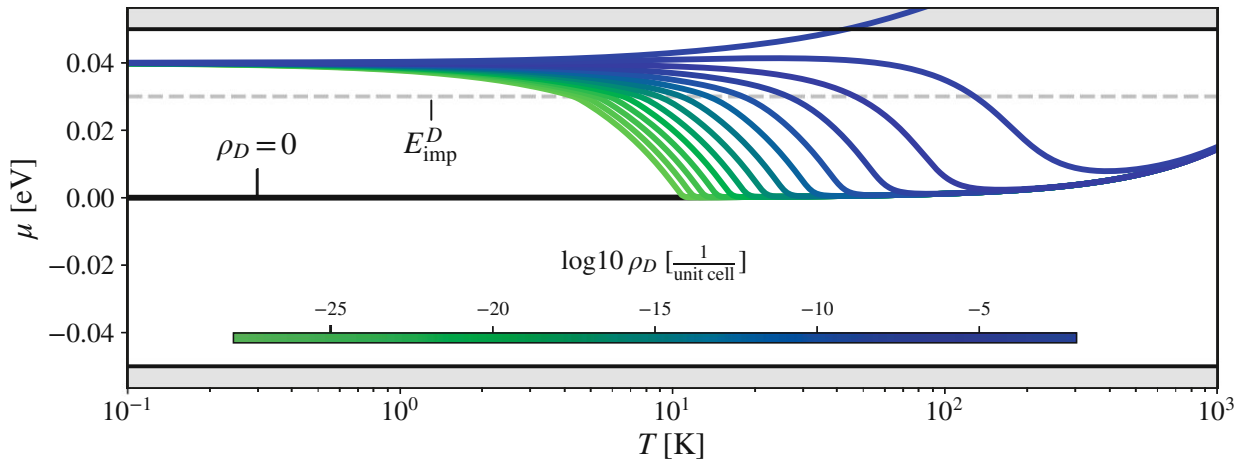


Figure 3.42: Comparison of the chemical potential for different impurity densities ρ_D for a donor level located at E_{imp}^D inside a semiconducting gap of 100meV. Intrinsic states were chosen to be described by the Fermi distribution ($\Gamma = 0$).

Homogeneous doping

Besides explicit impurity states, **LINRETRACE** also supports generic doping. Contrary to impurity levels where the chemical potential converges for $T \rightarrow 0$ to a point inside the gap, any global doping forces the chemical potential eventually to move outside the gap. Leading up to this, the root finding works identical as in Sec. 3.5.3.2. Here the “impurity contribution” is simply the doping which, now, is not affected by temperature and the position of the chemical potential. Please note that, technically, this kind of doping is more nuanced than a simple change of the total electron occupation. For the refinement algorithm to work inside the gap, an underlying integer filling is mandatory. Thus instead of changing the filling, one has to employ an explicit `Doping` keyword in the config, see Appendix of the original publication [11].

In Fig. 3.43 we showcase the same underlying band-structure as in Sec. 3.5.3.2 with various electron doping levels. Note the differences to Fig. 3.42: For the largest shown doping level ($\delta_e = 10^{-6}$) the crossing into the conduction band (shaded gray) already happens at around $T = 100\text{K}$.

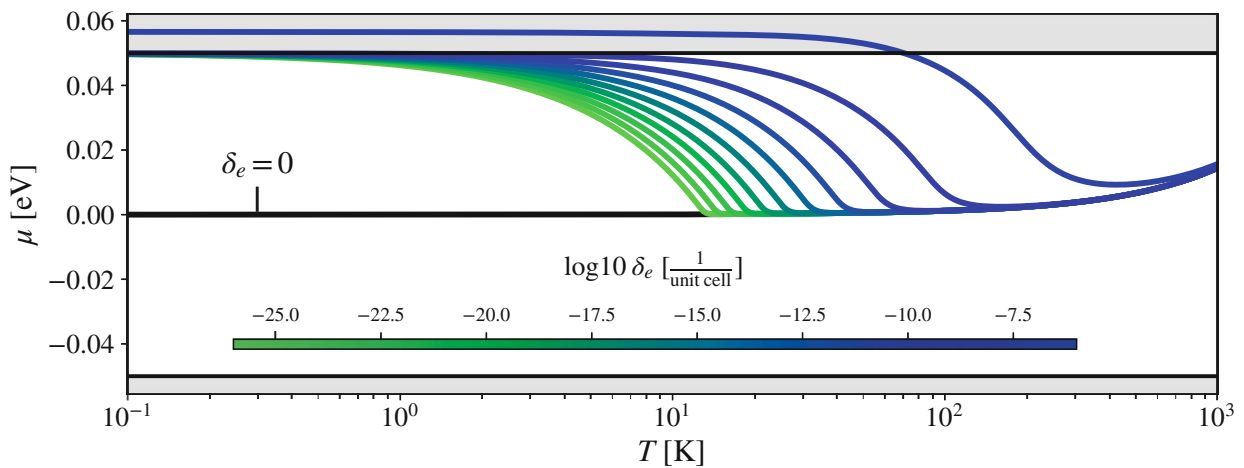


Figure 3.43: Comparison of the chemical potential for different levels of electron doping δ_e in a semiconductor. This example uses the Fermi distribution ($\Gamma = 0$) to find the chemical potential.

3.5.3.3 Polygamma evaluation

While all Fermi-function related equations can be implemented efficiently with native Fortran functions up to quadruple precision, the evaluation of the digamma and polygamma functions is more delicate. The digamma function is the derivative of the natural logarithm of the Gamma function

whose series representation is closely related to the harmonic numbers

$$\psi(z) = \frac{d}{dz} \ln \Gamma(z) = \frac{\Gamma'(z)}{\Gamma(z)} \quad (3.218a)$$

$$\psi(z) = -\gamma + \sum_{n=1}^{\infty} \left(\frac{1}{n} - \frac{1}{n+z-1} \right) \quad (3.218b)$$

where γ is the Euler–Mascheroni constant. The polygamma function ψ_m ($m > 0$) is the m^{th} derivative of the digamma function whose series expansion follows directly from the differentiation

$$\psi_m(z) = \frac{d^m}{dz^m} \psi(z) \quad m \in \mathbb{N}^+ \quad (3.219a)$$

$$\psi_m(z) = (-1)^{m+1} m! \sum_{n=1}^{\infty} \frac{1}{(n+z-1)^{m+1}}. \quad (3.219b)$$

Eqs. (3.218b,3.219b) are used extensively in our analytic derivation of the transport kernels [9]. Numerical implementations instead use different expressions depending on the location of the argument z in the complex plane. In particular, for large $\Re(z)$, an asymptotic Bernoulli expansion makes the evaluation very efficient [404]:

$$\psi(z) = \ln(z) - (2z)^{-1} - \sum_{k=1}^{n-1} \frac{B_{2k}}{2k} z^{-2k} + \mathcal{O}(z^{-2n}) \quad |\arg(z)| \leq \pi - \epsilon, \epsilon > 0 \quad (3.220)$$

with the Bernoulli numbers B_{2k} . In **LINRETRACE**, we adapt the cernlib [502] Fortran routine **wpsigp** (v1.2) for polygamma functions with complex argument, originally described by Kölbig [503]. We upgraded the routine to quadruple precision and commensurately increased the Bernoulli expansion order (to up to $k = 16$).⁶⁴

3.5.3.4 Code scaling

As the code is meant to be a hybrid—designed to solve models *and* large realistic materials—the scaling behavior of the parallelization is important: **LINRETRACE** is parallelized over the number of Brillouin zone momenta n_k (see Sec. 3.5.4.1 for a momentum convergence test). The resulting scaling is illustrated in Fig. 3.44. As expected, a purely linear behavior (runtime $t \propto n_k$) emerges.⁶⁵ While a single core installation experiences almost no overhead, the MPI implementation requires roughly 200 data points per core to become efficient. The quadruple precision evaluation of kernels roughly doubles the runtime.

⁶⁴At $T = 5.8\text{K}$ and $\Gamma = 0$ this setting reproduces the analytical Fermi function $f_{FD}(\omega)$ with an error of less than 10^{-27} for any ω .

In intra-band calculations the runtime will necessarily further scale linearly with the number of bands, while the inter-band portion of the code will scale with the square of the number of bands, as each band permutation must be evaluated. In normal circumstances, i.e., for small primitive unit cells, the number of bands is usually limited to between $\mathcal{O}(10)$ and $\mathcal{O}(100)$ where necessarily the momentum mesh must remain dense. On the contrary, in super cells one reallocates the computational load from the momentum mesh to the number of bands. The increased unit cell size requires fewer momenta to achieve convergence, which is counterbalanced by an increased number of atoms in the cell and thus an increased number of bands. To combat this intrinsic scaling problem one is encouraged to truncate the number of bands to a specific energy range around the Fermi level. Super cells especially benefit from this drastic decrease of the number of bands while maintaining numerical accuracy.

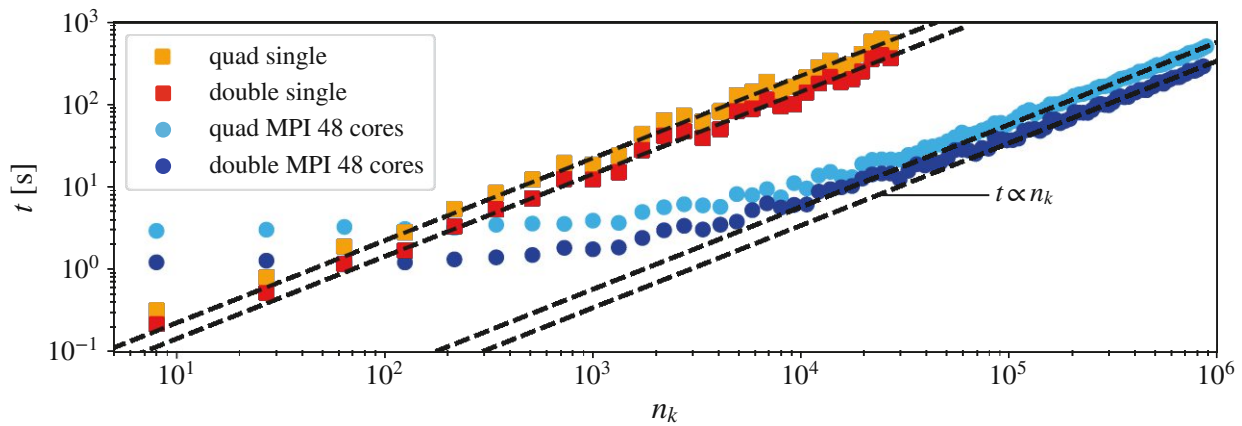


Figure 3.44: Runtime t of a one-band model over a wide range of momentum grids with n_k points. A clear linear scaling emerges which is somewhat delayed in the MPI runs due to the communication and input overhead. “quad” and “double” indicate the employed internal precision.

3.5.4 Applications

In this Section we are going to apply the previously described transport methodology. Our aim is to highlight some of the features implemented in **LINRETRACE** on systems that cover a wide range of phenomena, without, however, exhausting the code’s full functionality. We start off with simple models in Sec. 3.5.4.1, Sec. 3.5.4.3 and Sec. 3.5.4.4 and transition to realistic crystal structures in

⁶⁵The calculations contain 100 temperature steps and were performed on a single node of the Vienna Scientific Cluster 4. Each node consists of two sockets with one Intel Xeon Platinum 8174 Processor @ 3.1 GHz (formerly Skylake) on each socket, leading to 48 physical cores. We used the Intel Fortran compiler ifort and mpiifort (2020 release) for the single core and multi core installation, respectively, with -O3 optimization.

Sec. 3.5.4.5 and Sec. 3.5.4.6. Input and configuration files of all examples can be found in the github.com/linretrace/linretrace_examples repository.⁶⁶

3.5.4.1 Convergence: One-band metal

We consider the simple electronic structure

$$\epsilon_{\mathbf{k}n}^0 = -2t \sum_{\alpha=x,y} \cos(k_\alpha) \quad (3.221)$$

with hopping amplitude $t = 0.25\text{eV}$, lattice spacing $a_x = a_y = 1\text{\AA}$ and optical elements determined with the Peierls approximation. In order to introduce particle-hole asymmetry (to generate a finite thermopower) we set the system's charge to $N = 1.2$ and determine the chemical potential with the digamma occupation Eq. (3.212). Figure 3.45 shows the conductivity and Seebeck coefficient for a temperature-independent scattering rate $\Gamma = 10^{-4}\text{eV}$, no quasi-particle renormalization $Z = 1$, and various momentum grids. Once \mathbf{k} -convergence is reached, the conductivity is essentially temperature independent. Then, as expected from the Mott formula [456], see Section 3.4.1.2, a linear-in- T behaviour appears in the Seebeck coefficient. As the system is above half-filling, the carriers are of hole-type, and the Seebeck coefficient is positive. Unsurprisingly, a dense momentum grid is required to reach convergence at low temperatures. For the largest momentum grid employed here ($n_k = n_{k_x} \times n_{k_y} = 5000 \times 5000$) the results are converged down to approximately $T_c = 6\text{K}$. Please note that due to the chemical potential search, discrepancies for coarse \mathbf{k} -meshes are the results of a mixture of chemical potential and kernel sampling errors. In all, even if the \mathbf{k} -convergence in **LINRETRACE** is more stable than in Boltzmann codes, a thorough check of the Brillouin-zone discretization is *mandatory*—at least when the response is metallic.

3.5.4.2 Inter-band: Multi-atomic cells

Besides “intrinsic” inter-band contributions, stemming from multi-orbital dipole elements, see Section 3.3.4, inter-band contribution can be artificially brought into play by considering multi-atomic cells or supercells: We again assume a simple nearest-neighbor hopping setup

$$\epsilon_{\mathbf{k}n}^0 = -2t \cos(k_x), \quad (3.222)$$

this time only in the x-direction, with an atomic spacing of the primitive unit cell of $a = 1\text{\AA}$. Moving to an equivalent non-primitive unit cell of size $n \cdot a$, the boundary of the resulting band structure becomes

⁶⁶For storage reasons, the hosted HDF5 input files contain data on a coarser momentum mesh than that used for the results shown here. For the model systems, however, the user can directly reproduce our results by generating their own HDF5 input files using the number of \mathbf{k} -points specified in the text. The same is possible for the material test cases, but requires performing ones own DFT calculations.

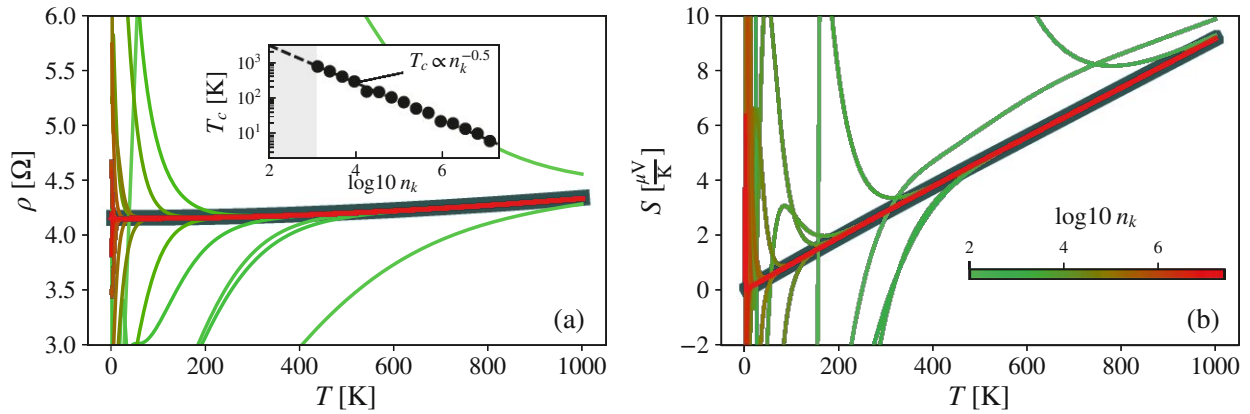


Figure 3.45: (a) Resistivity and (b) Seebeck coefficient for the two-dimensional electronic structure of Eq. (3.221) with $\Gamma = 10^{-4}$ eV, system charge $N = 1.2$ and various numbers of \mathbf{k} -points n_k . The convergence temperature T_c (inset in (a)) scales as $T_c \propto n_k^{-0.5} = n_{k_x}^{-1}$ (fitted, dashed line). A dense momentum grid is required to reach convergence (fat gray line) for reasonably low temperatures. There, we observe an almost temperature independent resistivity and a linear-in- T behavior of the Seebeck coefficient. The identical behavior is observed in the three dimensional equivalent where instead the convergence temperature scales as $T_c \propto n_k^{-0.33} = n_{k_x}^{-1}$ (not shown).

restricted, see Fig. 3.46, which results in a backfolding effect. This is the result of the modified real-space Hamiltonian where additional “bands” are introduced: The on-site term $H(\mathbf{R} = \mathbf{0})$ becomes a symmetric, tridiagonal $n \times n$ matrix

$$H(\mathbf{R} = \mathbf{0}) = \begin{bmatrix} 0 & t & 0 & \dots \\ t & 0 & t & \ddots \\ 0 & t & 0 & \ddots \\ \vdots & \ddots & \ddots & \ddots \end{bmatrix} \quad (3.223)$$

and the nearest-neighbor matrix is reduced to a single $H_{1n}(\mathbf{R} = -a) = t$, $H_{n1}(\mathbf{R} = +a) = t$.

Total conductivities now contain intra- and inter-band contributions, see Fig. 3.46b, which were all calculated with a fixed scattering rate $\Gamma = 10^{-4}$ eV and no quasi-particle renormalization $Z = 1$. Combining intra and inter-band contributions, we find perfect numerical agreement compared to the intra-band-only contribution of the primitive unit cell: The differences $\Delta\mathcal{L}_{11}^{xx}(T)$ are plotted in the inset and are evidently below the double precision accuracy employed in the calculations. As we chose a particle-hole symmetric chemical potential $\mu = 0$, we obtain a strong differentiation between even and odd numbered unit cells: Through the band folding of the unit cells with an even number of atoms (that occurs exactly at the Fermi level), their inter-band contribution are significantly boosted compared to their odd numbered counterparts.

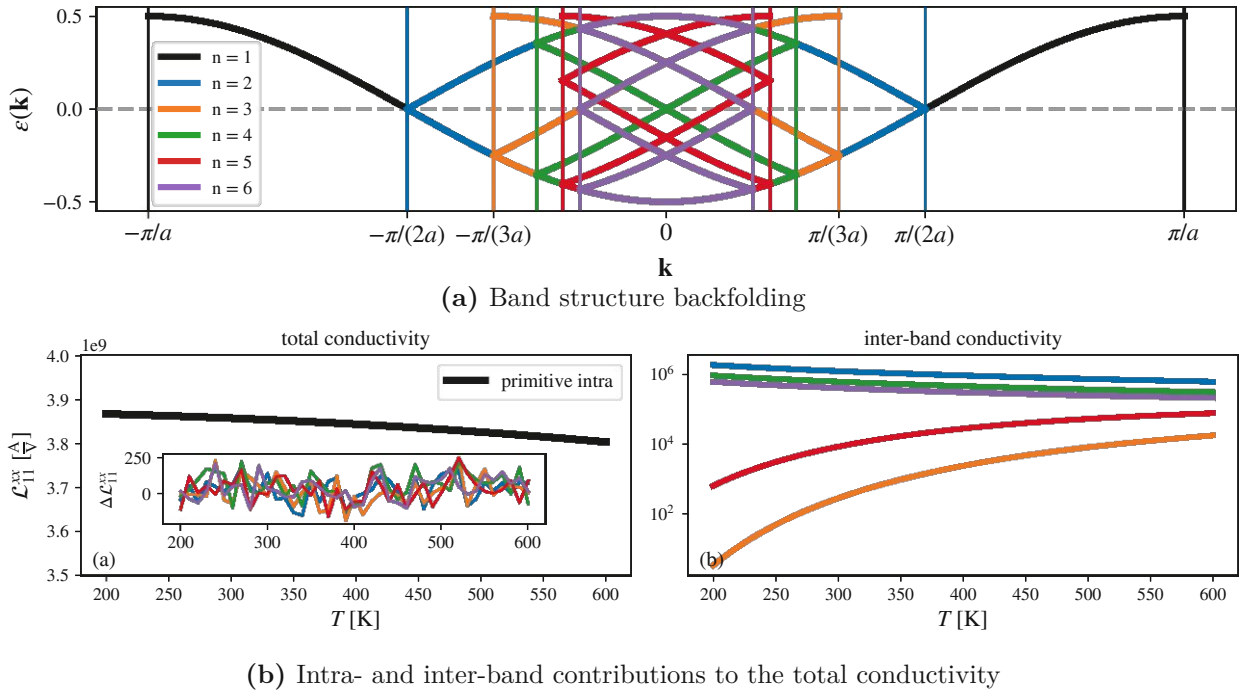


Figure 3.46: Transition from primitive cell (black lines) to a multi-atomic cell via a larger unit cell (colors). At particle-hole symmetry ($\mu = 0$) the back-folding induces a strong differentiation between even and odd numbered unit cells. An even number of atoms results in a band crossing exactly at the Fermi level, boosting the inter-band contribution. Note the different scales of the plots.

3.5.4.3 Kernels: Two-band insulator

For this Section to be somewhat self-contained we consider the two-band electronic structure used in Section 3.4

$$\epsilon_{\mathbf{k}n}^0 = - \sum_{\alpha=x,y,z} 2t_n \cos(k_\alpha) + (-1)^n (6t_n + \Delta_0/2) \quad (3.224)$$

with valence band hopping amplitude $t_1 = 0.25\text{eV}$ and lattice spacing $a_x = a_y = a_z = 1\text{\AA}$. Here, we use the Peierls approach in the band-basis, see Eq. (3.166), to compute matrix elements, limiting the response to intra-band transitions. For the temperature scan we use a conduction band hopping $t_2 = -0.30\text{eV}$ and a band gap of $\Delta_0 = 0.1\text{eV}$ while for the chemical potential scan we use $t_2 = -0.25\text{eV}$ and $\Delta_0 = 1\text{eV}$. On the calculated temperature range, full momentum-grid convergence is achieved for $60 \times 60 \times 60$ \mathbf{k} -points. Contrary to the metallic system, the transport coefficients of this insulator *must* be evaluated with quadruple precision for $\Gamma > 0$ in order to avoid numeric instabilities in the polygamma functions at low temperatures. Instead, evaluating the Boltzmann kernels, a much denser

momentum grid, that scales similarly to the metallic system of Sec. 3.5.4.1 is required for convergence (not shown). Therefore, the more proper treatment of scattering amplitudes in our formalism actually facilitates the numerical evaluation with respect to semi-classical approaches.

Temperature scan

The introduced band asymmetry leads to an imbalance of electronic carriers as the chemical potential lies above $\mu = 0$, see bottom panel of Fig. 3.47a. The thermal activation across the gap is reflected in all considered physical observables where one finds $\rho, R_H \propto e^{+\frac{\Delta_0}{2k_B T}}$ and $S, \nu \propto \frac{1}{T}$ at high temperatures.

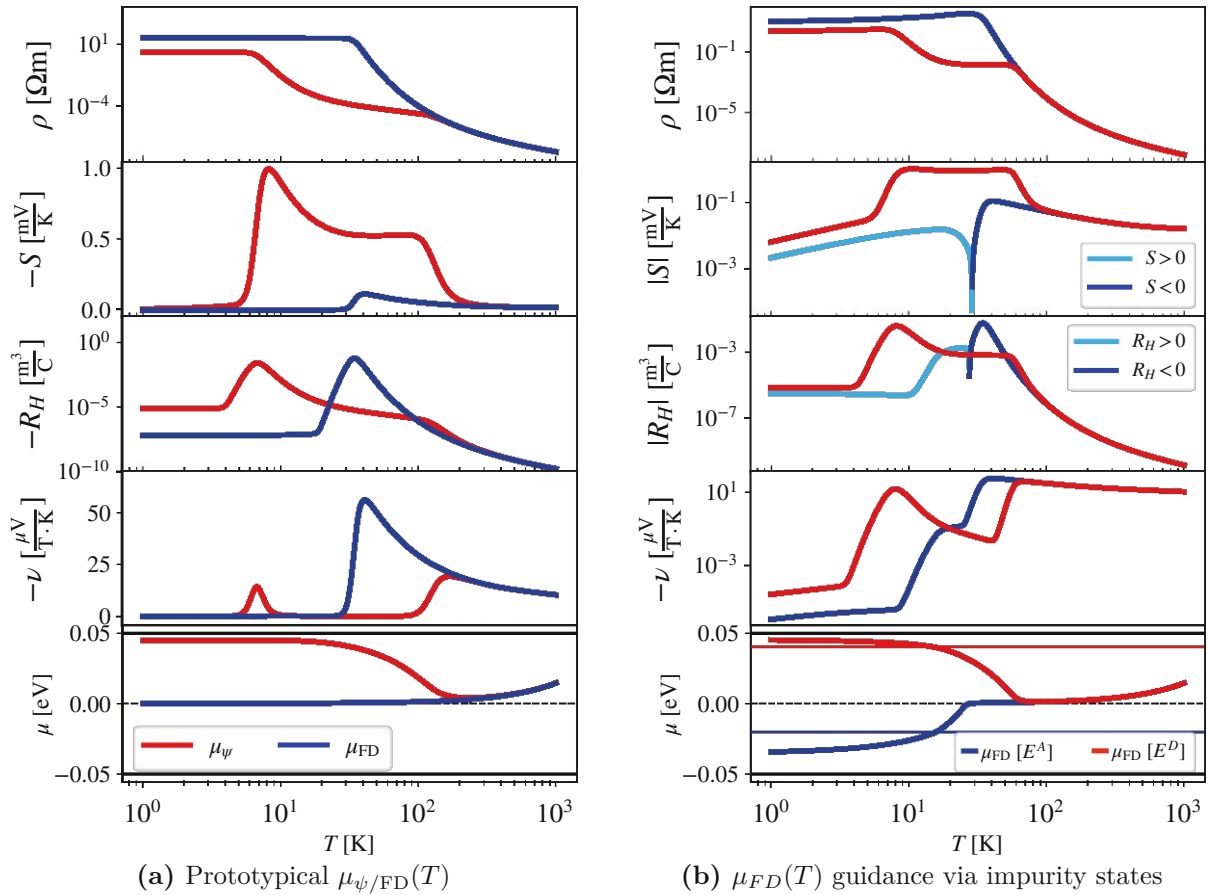


Figure 3.47: Temperature dependencies in a semiconductor of the resistivity ρ (top), the coefficients of Seebeck S , Hall R_H , and Nernst ν (second to fourth panel), as well as the chemical potential (bottom; band gap delimited by thick black lines): (a) Effects stemming purely from the occupation distribution (Fermi-Dirac “FD” or digamma “ ψ ”). (b) Effects achievable by guiding the chemical potential with impurity states. Red: donor level $E^D = 0.04\text{eV}$, $\rho_D = 10^{-8} \frac{1}{\text{unit cell}}$; Blue: acceptor level $E^A = -0.02\text{eV}$, $\rho_A = 10^{-14} \frac{1}{\text{unit cell}}$. In all cases $\Delta_0 = 100\text{meV}$, $\Gamma = 10^{-4}\text{eV}$; $Z = 1$.

At low enough temperatures, however, a saturation regime is observed in ρ and R_H , stemming from the Kubo transport kernels, see Ref. [9] for details. Further, entropy transport is thermodynamically consistent, as $S \propto T$ and $\nu \propto T$ towards absolute zero. Taking lifetime broadening into account also for the occupation, the chemical potential $\mu_\psi(T)$ is necessarily (since $|t_2| > |t_1|$) forced towards the conduction band from which a second activated regime is generated below 100K, see Fig. 3.47a (top panel). This *intrinsic* chemical potential behavior can also be achieved, in principle, through a guidance of $\mu_{\text{FD}}(T)$ via *explicit* impurity states, see Fig. 3.47b. Here, sharper transitions between regimes and even changes in the dominant type of carriers can be generated. Please note the different plotting scales and the sign changes of the Seebeck and Hall coefficient, consistent with the change of dominant charge carriers.

Chemical potential scan

The chemical potential scans in Fig. 3.48 illustrate the in-gap behavior of the (intra-band) conductivity and the (intra-band) Seebeck coefficient. For small scattering rates and elevated temperatures (Fig. 3.48a), we recover the usual “S”-shaped curve for the Seebeck coefficient: S crosses zero at $\mu = 0$, where the system is particle-hole symmetric. Slightly above (below) a minimum (maximum) develops, corresponding to the dominant type of carriers ($\mu > 0$: electrons; $\mu < 0$: holes). In the “Boltzmann” regime we find perfect agreement with the Goldsmid rule $2eS_{\text{max}}T = \Delta_0$ [449], relating the maximal Seebeck coefficient S_{max} to the system’s gap. At lower temperatures, however, deviations from this behavior can be observed as a plateau around $\mu = 0$ develops that expands as we lower the temperature further. This effect stems from the Kubo kernels Eqs. (3.94-3.99) and signals the transition from the activated to a saturation regime. For a detailed discussion, see Ref. [9]. Larger scattering rates (Fig. 3.48b) already lead to a deviation from the “Boltzmann” behavior at the highest temperatures, where we additionally find a strong suppression towards the band edges at $\mu = \pm 0.5\text{eV}$.

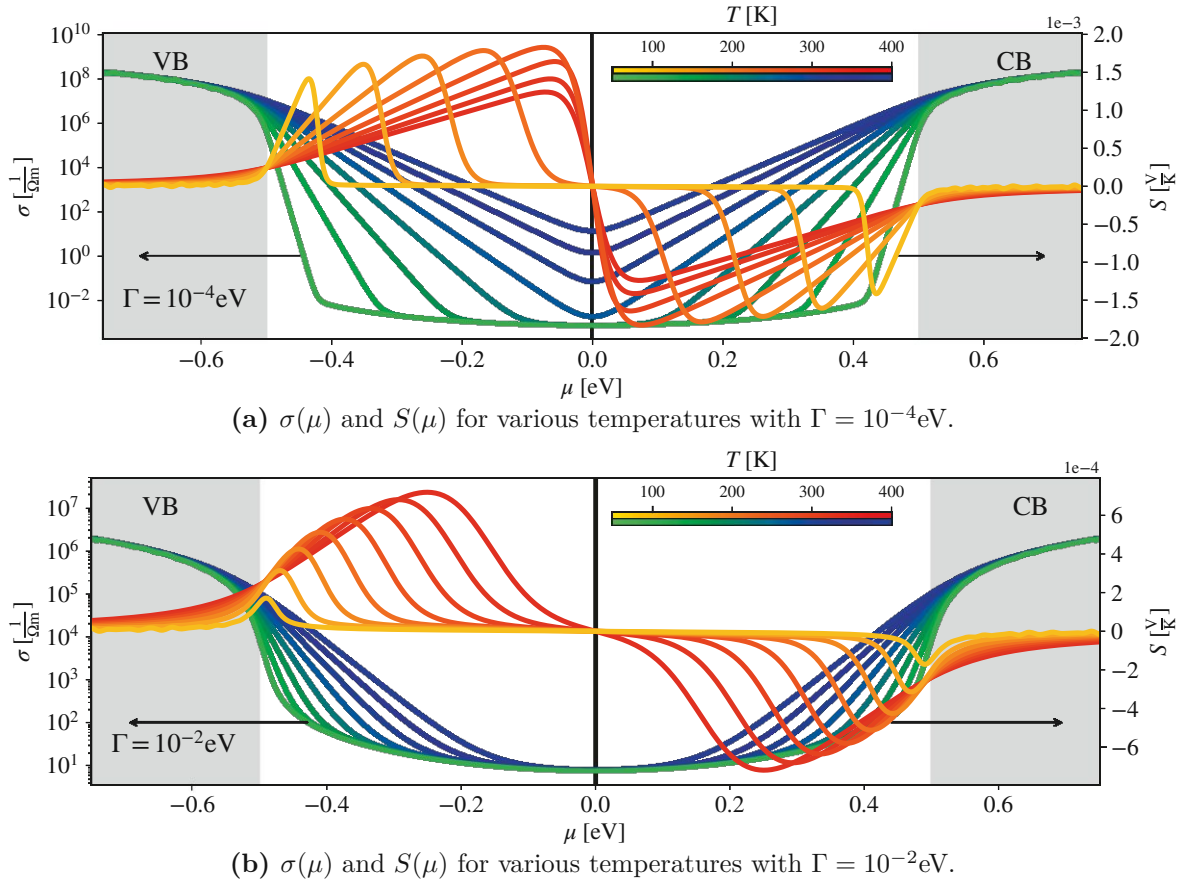


Figure 3.48: Chemical potential scans for the symmetric insulator $t_1 = -t_2 = 0.25$ eV for (a) small $\Gamma = 10^{-4}\text{eV}$ and (b) large $\Gamma = 10^{-2}\text{eV}$ scattering rates. Blue-to-green shades represent conductivities; red-to-orange shades Seebeck coefficients. In the Boltzmann temperature regime ($\Gamma = 10^{-4}\text{eV}$; $T > 250\text{K}$) we find perfect agreement with the Goldsmid rule $2eS_{\text{max}}T = \Delta_0$. Lower temperatures and increased scattering leads to a departure of the Boltzmann regime and the transport responses qualitatively change shape. The white (grey shaded) background indicates the gap (valence/conduction band region). The gap is $\Delta_0 = 1\text{eV}$ and we used $Z = 1$.

3.5.4.4 Interplay of band velocities and curvatures

In order to illustrate the effect of velocities and curvatures in a detailed way, we consider tight-binding Hamiltonians constructed for a honeycomb and kagome lattice, see Fig. 3.49. Both types of lattices are based on the same underlying hexagonal unit cell, only differentiated from one another by the internal atomic positions. The honeycomb lattice can be constructed the equivalent $(1/3, 1/3) - (2/3, 2/3)$, and the kagome lattice via the equivalent $(0.25, 0.25) - (0.75, 0.25) - (0.25, 0.75)$.

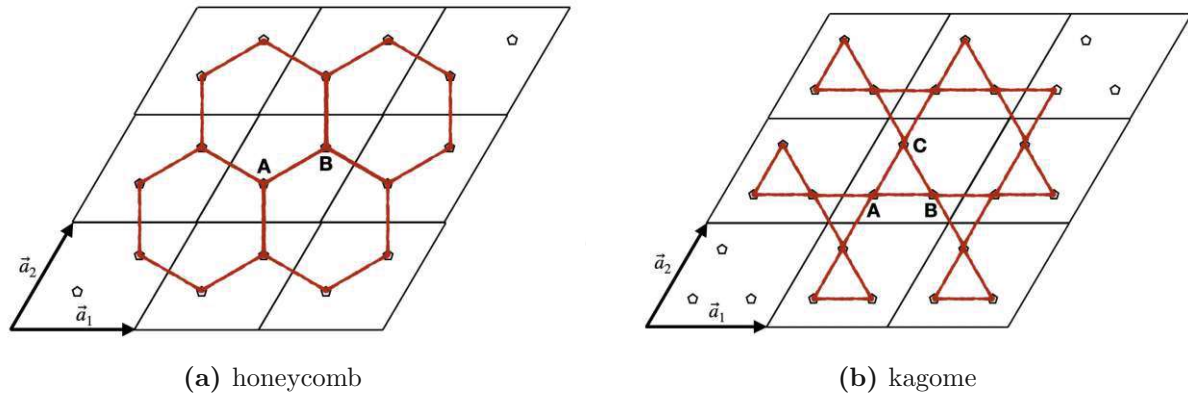


Figure 3.49: Honeycomb and kagome lattice generated by an identical, underlying hexagonal unit cell with different (equivalent) atomic positions. The A-B positions of the former lie on the long unit cell diagonal forming a bipartite lattice. The A-B-C positions of the latter form “triangles”. We draw lines stemming from the central unit cells and connect nearest neighbors.

For both the honeycomb and the kagome we define the identical lattice vectors of length 1\AA via

$$\vec{a}_1 = \begin{pmatrix} 1 \\ 0 \end{pmatrix}; \vec{a}_2 = \frac{1}{2} \begin{pmatrix} 1 \\ \sqrt{3} \end{pmatrix} \quad (3.225)$$

resulting in the reciprocal lattice vectors

$$\vec{b}_1 = \frac{2\pi}{\sqrt{3}} \begin{pmatrix} \sqrt{3} \\ -1 \end{pmatrix}; \vec{b}_2 = \frac{4\pi}{\sqrt{3}} \begin{pmatrix} 0 \\ 1 \end{pmatrix}, \quad (3.226)$$

fulfilling $\vec{a}_i \cdot \vec{b}_j = 2\pi\delta_{i,j}$. The special points K and K' (see Fig. 3.52) are then located at

$$K = \frac{2}{3}\vec{b}_1 + \frac{1}{3}\vec{b}_2 \quad (3.227a)$$

$$K' = \frac{1}{3}\vec{b}_1 + \frac{2}{3}\vec{b}_2 \quad (3.227b)$$

hence momentum grids that are divisible by three in each direction are required to include them. We choose $n_{k_x} \times n_{k_y} = 300 \times 300$ with nearest neighbor hopping $t = 1\text{eV}$.

The required tight-binding hopping parameters, mirroring the connections drawn from the central unit cell in Fig. 3.49, can be found in the `templates` folder of the `LINRETRACE` repository. The resulting band structures and density of states are illustrated in Fig. 3.50.

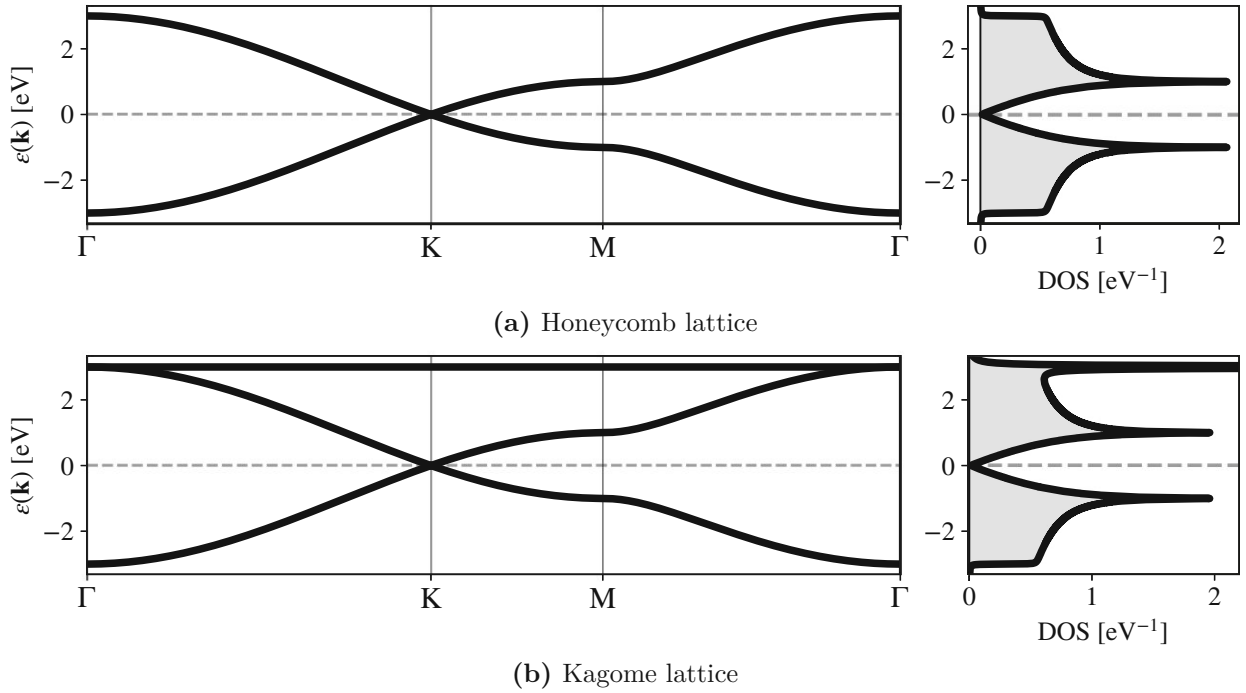


Figure 3.50: Band structure along a high-symmetry path and corresponding density of states for the (a) honeycomb lattice and (b) kagome lattice. The dispersive bands (and their contribution to the density of states) are identical between the two lattices. The latter however also generates a flat band at the upper edge of the dispersive bands which, due to the (numerical) broadening, spills slightly into the rest of the density of states.

The relevant *band velocities* and *band curvatures* are generated via a rotation of the derivatives (evaluated analytically in real space) of the multi-orbital Hamiltonian, see Eqs. (3.208a-3.208c),

$$v^\alpha(\mathbf{k}) = U^{-1}(\mathbf{k})H^{v,\alpha}(\mathbf{k})U(\mathbf{k}) \quad (3.228a)$$

$$c^{\alpha\beta}(\mathbf{k}) = U^{-1}(\mathbf{k})H^{c,\alpha\beta}(\mathbf{k})U(\mathbf{k}) \quad (3.228b)$$

which results in a peculiar disparity between the two models.

In both the honeycomb and kagome lattice, the particle-hole symmetry of the dispersive bands around $\varepsilon = 0$ results in symmetric transport properties that only include band velocities, $\mathcal{L}_{ab}^{\alpha\beta}(+\mu) = \mathcal{L}_{ab}^{\alpha\beta}(-\mu)$, see Fig. 3.51a and 3.51b.

Indeed, in the band-basis, a flat band yields a vanishing group velocity: $\partial\varepsilon_{\mathbf{k}}/\partial\mathbf{k}_\alpha \equiv 0$. Although we compute the velocity in the local Wannier basis *before* rotating it into the band basis, the flat band of this model neither contributes itself to conduction, nor does it modify the intra-band conductivities

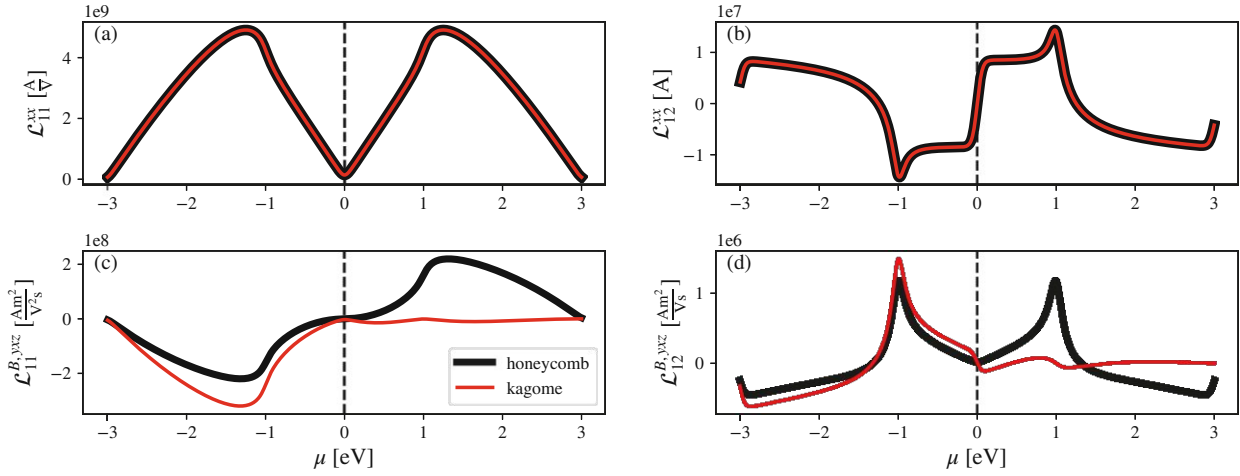


Figure 3.51: Effects of evaluating the velocities and curvatures in the Wannier basis before rotating into the band basis. The responses connected purely to the velocities (\mathcal{L}_{11} ; top row) remain identical for both models, whereas responses connected to the curvatures (\mathcal{L}_{11}^B ; bottom row) develop a significant asymmetry in μ in the presence of the flat band. Instead, if the velocities and curvatures had been evaluated in the band basis, all responses would be symmetric around $\mu = 0$.

of the other bands. Once curvatures come into play, however, the flat band does in fact play a role: magnetic corrections to the Onsager coefficients $\mathcal{L}_{ab}^{B,yxz}$ obtain a strong asymmetry around $\mu = 0$, indicating a modification of the (magnetic) matrix elements of the dispersive bands. For a positive chemical potential, the presence of the flat band strongly suppresses the response in the presence of a magnetic field as compared to the honeycomb lattice. Instead, for negative chemical potentials, the response is somewhat enhanced.

Lastly, we illustrate the interplay of the velocities in the momentum space explicitly in Fig. 3.52. The left column shows the momentum-resolved optical elements $M^{\alpha\beta} \propto v_\alpha v_\beta$ in and around the Brillouin zone. Combined with the kernel function \mathcal{K}_{11} (middle), evaluated at $\mu = 0.8\text{eV}$ we can capture how each point in the Brillouin zone contributes to the conductivity $\sigma_{\alpha\beta} = \sum_{\mathbf{k} \in \text{BZ}} \sigma_{\alpha\beta}(\mathbf{k})$ (right panel). Via an interplay of symmetry, the sign, and the values of the optical elements we find the anticipated result: $\sigma_{xx} = \sigma_{yy}$ and $\sigma_{xy} = \sigma_{yx} \equiv 0$.

Let us note that, through the aforementioned reasoning and observations, Fig. 3.52 reflects both the honeycomb and the kagome lattice identically.

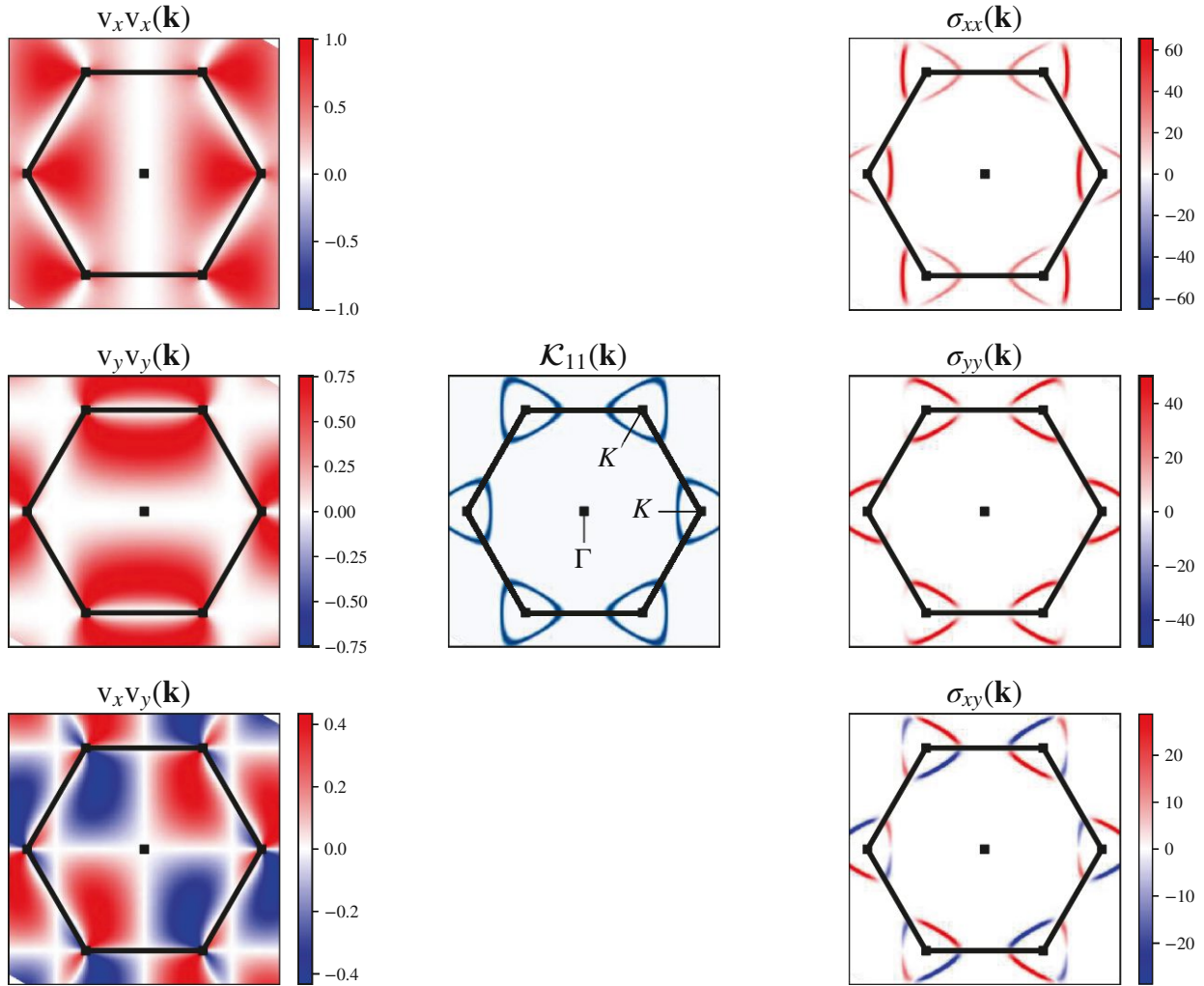


Figure 3.52: Momentum analysis of the honeycomb lattice. Left: Optical elements for the xx (top), yy (middle) and xy (bottom) Cartesian directions in units of $[\text{eV}^2 \text{\AA}^2]$. Middle: Kernel function \mathcal{K}_{11} , reflecting the Fermi surface at $\mu = 0.8\text{eV}$. Right: Momentum resolved conductivity $\sigma(\mathbf{k})$ in units of $[\frac{1}{\Omega}]$ which is the left and middle column multiplied with each other. The resulting \mathbf{k} -summed quantities result in $\sigma_{xx} = \sigma_{yy}$ and $\sigma_{xy} \equiv 0$.

3.5.4.5 Material: FeAs₂

As a realistic crystal structure we first consider FeAs₂, a hybridization-gap semiconductor. Band-theory yields a gap of around $\Delta_0 = 0.275\text{eV}$ when using the PBE exchange-correlation potential [331, 504]. The top panel of Fig. 3.53 shows the ensuing density of states (DOS) for a wide energy range, with the gap centered at $\mu = 0$. The states near the gap edges are dominantly of iron character.

The bottom panel shows the resulting conductivities σ calculated for $T = 300\text{K}$, using a scattering rate $\Gamma_0 = 10^{-5}\text{eV}$. Comparing the intra-band conductivity using the WIEN2k dipole matrix elements (yellow) with that employing group velocities constructed from the BoltzTraP2 band interpolation (blue) illustrates the accuracy of the Peierls approximation for simple unit cells.⁶⁷ With the full dipole matrix element, we have access also to inter-band contributions to the conductivity (green). As expected, inter-band contributions only play a subsidiary role at these elevated temperatures: They are two orders of magnitude smaller than the intra-band contributions.

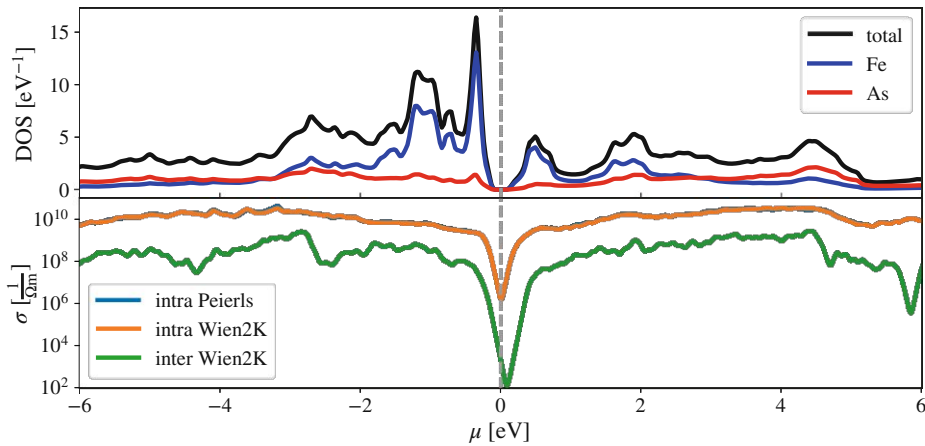


Figure 3.53: Hybridization-gap semiconductor FeAs_2 via a WIEN2k calculation (PBE; $20 \times 20 \times 40$ k-points). The DOS around the gap ($\Delta = 0.275\text{eV}$) is dominated by Fe-character. (top) total and partial density of states (DOS), (bottom) intra- and inter-band conductivities in the x -direction and as a function of the chemical potential μ . The Peierls approximation to the optical elements leads to intra-band results (blue) virtually indistinguishable to using the full dipole matrix elements (yellow). For the given temperature ($T = 300\text{K}$) and scattering rate ($\Gamma = 10^{-5}\text{eV}$) the intra-band contributions dominate over inter-band effects (green).

Translating the μ -axis into carrier concentrations $n = (N(\mu) - N)/V$ results in the behavior shown in Fig. 3.54. For the given temperature, the shaded gray area marks the region, where the chemical potential has moved inside the conduction band. Upon entering said region, the conductivity increases rapidly, while the Seebeck coefficient has its peak amplitude for μ inside the gap, cf. Figure 3.48.

⁶⁷ We cross-checked our result with BoltzTraP2: Differences are small. We note that BoltzTraP2 calculates transport distribution functions that are based on an artificially broadened density of states, leading to a numerical smearing of the gap edges. At its core, LINRETRACE is designed to stay numerically exact and avoids unphysical broadening of any transport quantity. If desired, however, the user can apply a Gaussian broadening of a chemical potential scan in the post-processing. For explicit comparisons, the BoltzTraP2 conductivities σ/τ_0 [$\frac{1}{\Omega\text{ms}}$] have to be multiplied with $\tau_0 = \frac{\hbar}{2\Gamma_0}$, $\hbar = 6.58211956 \cdot 10^{-16}\text{eVs}$.

Indeed, the behavior of σ and S is typically [505], but not always [466], antagonistic. The response is polarization dependent, with the powerfactor $S^2\sigma$ being most sensitive on the crystal orientation. Note that we only compute thermoelectric properties from pure electron diffusion. Phonon-drag enhancements—relevant, e.g., for the related narrow-gap semiconductors FeSb_2 [421, 422, 423] and CrSb_2 [434, 506]—are not included.

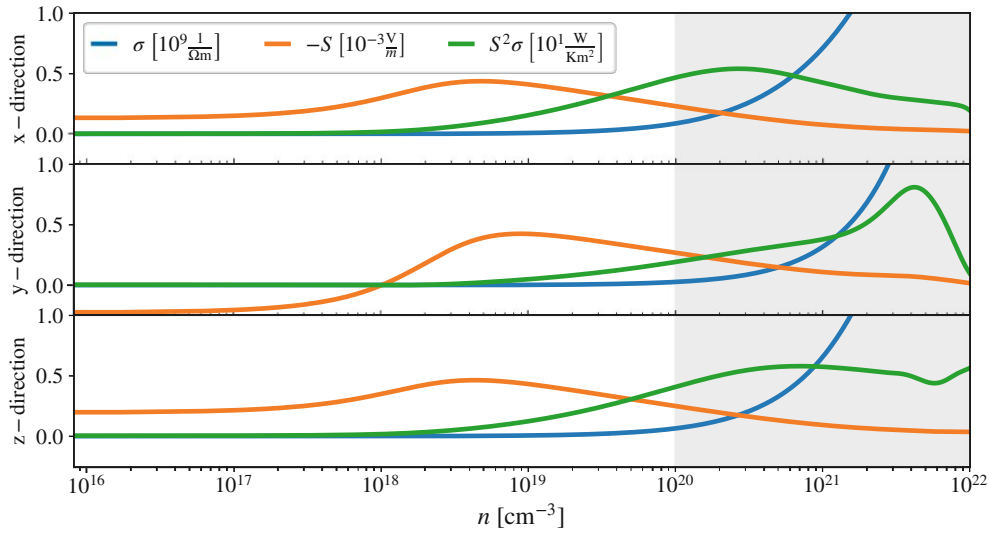


Figure 3.54: FeAs_2 : WIEN2k intra-band conductivity (σ), Seebeck coefficient (S) and power factor ($S^2\sigma$) for the same temperature ($T = 300\text{K}$) and scattering rate ($\Gamma = 10^{-5}\text{eV}$) as in Fig. 3.53. Here, we instead show the dependency on the electron doping $n = \frac{N(\mu) - N_{\text{neutral}}}{V}$. The gray, shaded area indicates doping levels where the chemical potential has moved inside the conduction band.

Finally, we add an in-gap impurity state and showcase the ensuing temperature behavior of transport observables in comparison to experiment [214, 431] in Fig. 3.55. Due to the additional electrons provided by the donor level, located in the vicinity of the conduction band, the system experiences a transition from activated behavior with the intrinsic gap Δ_0 at high temperatures to a second regime controlled by a reduced gap Δ_1 , determined by the position of the impurity, cf. Fig. 3.42 and Ref. [9]. At still lower temperatures, and akin to Sec. 3.5.4.3, the prototypical saturation regimes set in: The resistivity and the Hall coefficient saturate, while the Seebeck and Nernst coefficients tend towards zero in a linear fashion. Due to the three distinct crystal directions in FeAs_2 , the Hall and Nernst coefficients behave differently depending on the direction of the applied magnetic field.

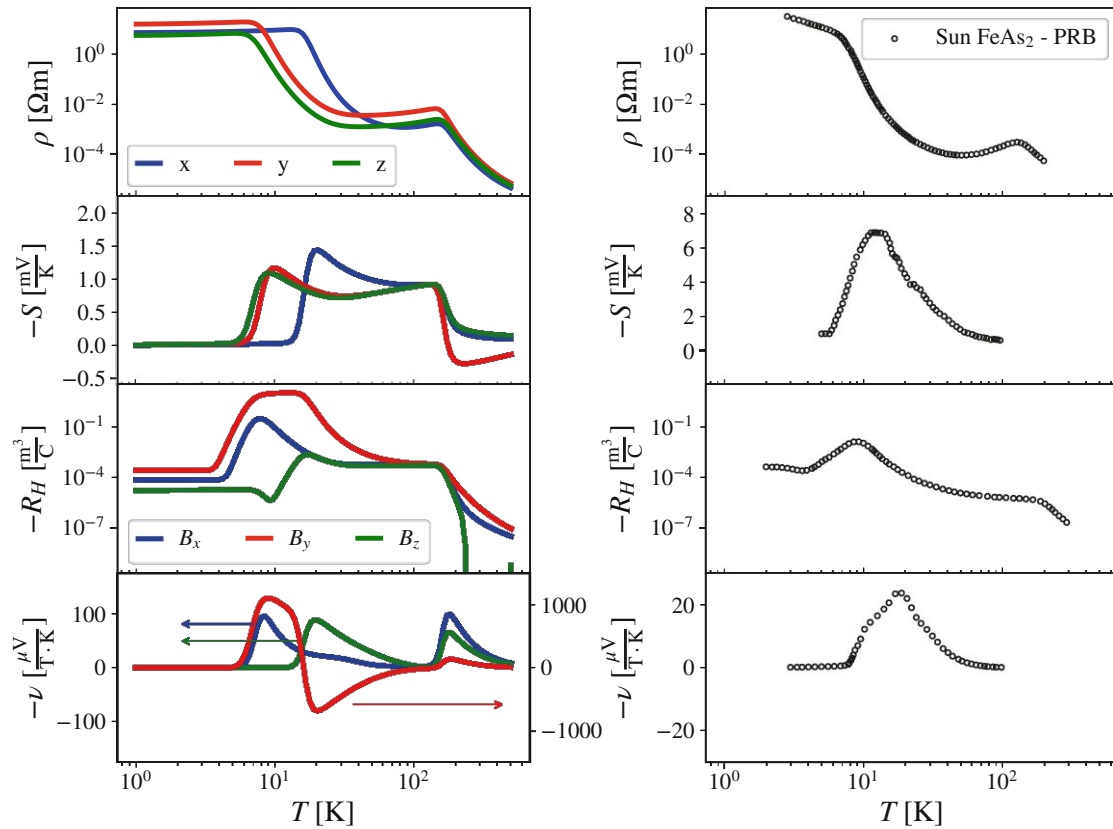


Figure 3.55: FeAs₂: Intra-band resistivity ρ , Seebeck coefficient S , Hall coefficient R_H and Nernst coefficient ν (left) compared to experimental data (right) [214]. We show results for all three Cartesian directions. The chemical potential was determined by the Fermi Dirac function and altered by a donor level (at $E_D = 0.015\text{eV}$ below the conduction band with $\rho = 2 \cdot 10^{-6} \frac{1}{\text{unit cell}}$), chosen so that the resistivity approximates the experimental behavior. The scattering rate includes only polynomial terms: $\Gamma(T) = 7 \cdot 10^{-5} + 5 \cdot 10^{-9}T^2$ in eV. Note that we underestimate S and overestimate ν . All shown data use the intra-band Peierls approximation.

3.5.4.6 Material: Tl-doped PbTe

As a final test material we consider Tl-doped PbTe, a prime example for the enhancement of thermoelectric transport by resonance states [507]. In a broader context, through the Tl-doping, a superconductivity instability emerges at $T = \mathcal{O}(1)\text{K}$, accompanied by apparent signatures of the so-called “charge Kondo effect”, thought to be supported by the introduced, degenerate Tl valence states [508, 509, 510]. Here we restrict ourselves, however, to the for thermoelectricity relevant temperature scale: We model the doping by explicitly constructing a $4 \times 4 \times 4$ supercell of PbTe and substituting a single Pb atom with a Tl one. Internal positions of the resulting $\text{Tl}_{0.004}\text{Pb}_{0.996}\text{Te}$ are

then fully relaxed before extracting the `LINRETRACE` input. In order to gain access to both the Seebeck and the Nernst coefficient, we employ the `BoltzTraP2` interpolation scheme to obtain Peierls velocities. As the prepared super cell does not match the experimental stoichiometry, we are mainly aiming for qualitative aspects.

Through the Tl-(hole)doping an increase of the density of states in the vicinity of the valence-band edge appears, see Figure 3.56 and the emerging resonance pins the chemical potential.

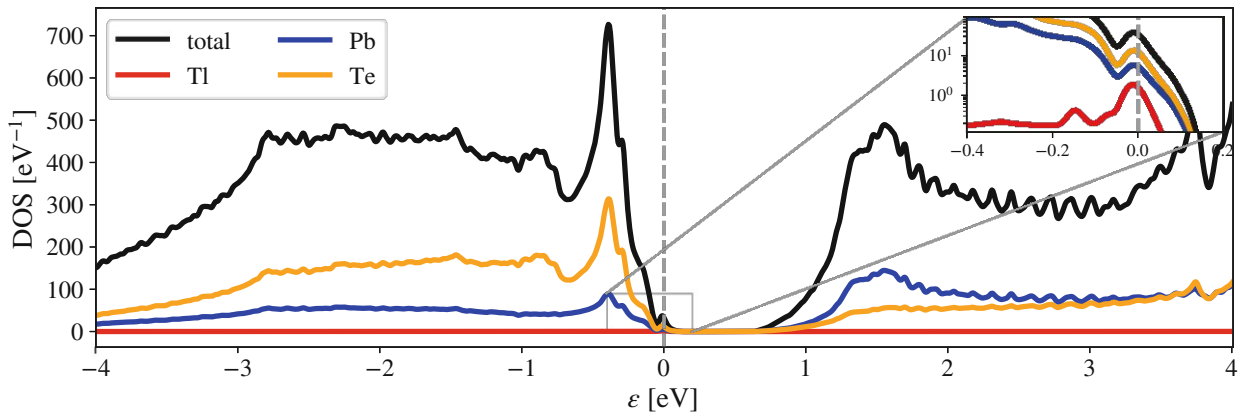


Figure 3.56: Tl-doped PbTe: Density of states using the LDA exchange-correlation potential and $17 \times 17 \times 17$ \mathbf{k} -points. Introducing a single $\text{Tl} \leftrightarrow \text{Pb}$ substitutional impurity results in a distorted electronic structure and additional states appear near the valence-band edge, pinning the chemical potential. The zoomed inset illustrates the non-trivial nature of the resonance to which all three elements contribute in some part.

Consequently, the Tl-doping cause a semiconductor-to-metal transition. Supplementing the electronic structure with a phenomenological, band-independent $\Gamma(T) = 20\text{meV} + 6 \cdot 10^{-5}\text{meV}/\text{K}^2 T^2$ results in the resistivity, Seebeck, and Nernst coefficient shown in Fig. 3.57. Comparing to experimental results [507], plotted on the same scale, we find good agreement for the resistivity at elevated temperature. However, we do not capture the resonance's signature below 200K. This finding suggests that the resistivity in that temperature range is not controlled by band-structure effects. Instead, the scattering rate might be markedly different for the resonance than for other states and display a more complex temperature dependence. We hence expect that—with scattering rates obtained from more sophisticated (beyond band-theory) electronic structure methodologies—`LINRETRACE` could capture the resistivity also below 200K. Alternatively, a reverse engineering approach could be employed within `LINRETRACE` to *extract* a phenomenological but band-dependent scattering rate that reproduces the experimental resistivity.

The Seebeck and Nernst coefficient, instead, are well reproduced (albeit slightly underestimated) within our setting without any additional input, suggesting a simple electronic picture of thermoelectric transport to hold. Indeed, in the case of metals, the Seebeck coefficient is—to a first approximation—insensitive to the scattering rate. The congruence to experiment for S then supports the above claim that the temperature profile of the resistivity below 200K is controlled by an intricate scattering rate. The metallic nature of the transport poses the previously discussed challenges for the Brillouin-zone discretization. While the resistivity and the Seebeck coefficient are, for all practical purposes, convergent with the largest \mathbf{k} -mesh used, the Nernst coefficient is notably more sensitive: The shown data provides a good approximation for the Nernst coefficient above 200K, while below the result is clearly not yet converged. Indeed, the Nernst coefficient must vanish for $T \rightarrow 0$ [9]. We stress that these limitations regarding the number of usable \mathbf{k} -points are on the side of the electronic structure methodology, while **LINRETRACE** could handle larger meshes at acceptable costs.

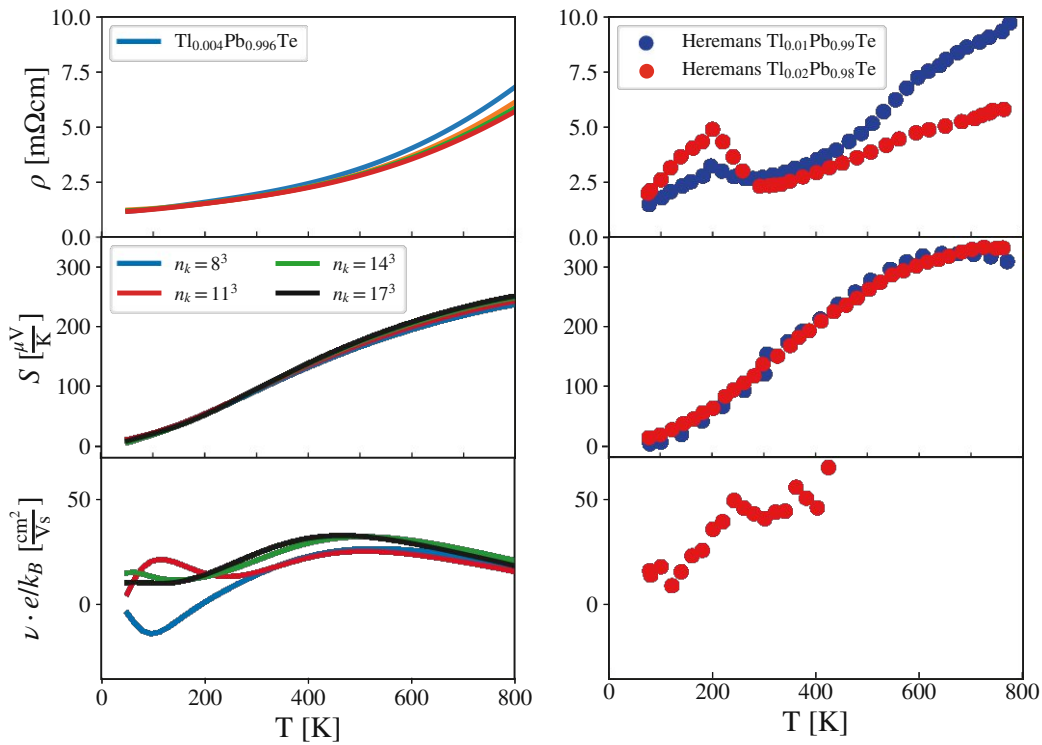


Figure 3.57: Tl-doped PbTe: Resistivity (top) and coefficients of Seebeck (middle) and Nernst (bottom) within **LINRETRACE** (left) compared to experiment [507] (right). Despite the resonance feature of the resistivity not being reproducible with our phenomenological scattering rate, the Seebeck and Nernst coefficients are close to the experimental values. There are opposing conventions for the sign of the Nernst coefficient [392]. Since our Hall signal (not shown) has the same sign as the experiment [507], but not the Nernst coefficient, we multiplied the experimental ν with (-1) .

3.5.5 Possible extensions

Having established a framework for thermoelectric transport, that can be reasonably well connected to various electronic structure codes and is capable of producing high precision results for tight-binding kind of inputs, we mention here future avenues that **LINRETRACE** can and will be developed towards.

Beyond purely electronic transport

As established in Section 3.4, certain thermoelectric materials such as FeSb₂ experience a significant boost to their thermopower via the help of phonon contributions (phonon-drag effect). Hitherto, all derived transport equations have been obtained with a purely electron/hole-induced current in mind, see Section 3.3.1. A first step towards more realistic simulations is therefore the inclusion of phonons. For a given phonon-mode, electron-phonon contributions to the Hamiltonian can be summarized with the additional terms

$$\mathcal{H}_{ph-ph} = \sum_{\mathbf{q}} \hbar\omega_{\mathbf{q}} \hat{a}_{-\mathbf{q}}^{\dagger} \hat{a}_{\mathbf{q}} \quad (3.229a)$$

$$\mathcal{H}_{e-ph} = \sum_{\mathbf{k}, \mathbf{q}, \sigma} g_{\mathbf{q}} \hat{c}_{\mathbf{k}+\mathbf{q}, \sigma}^{\dagger} \hat{c}_{\mathbf{k}, \sigma} (\hat{a}_{\mathbf{q}} + \hat{a}_{-\mathbf{q}}^{\dagger}) \quad (3.229b)$$

with $\hat{a}_{\mathbf{q}}^{(\dagger)}$ as the annihilation (creation) operator of a phonon at momentum \mathbf{q} and energy $\omega_{\mathbf{q}}$ and the coupling constant $g_{\mathbf{q}}$. The thermal phonon current

$$j_{Q,ph}^{\alpha} = \sum_{\mathbf{q}} \hbar\omega_{\mathbf{q}} \frac{\partial\omega_{\mathbf{q}}}{\partial q_{\alpha}} \hat{a}_{\mathbf{q}}^{\dagger} \hat{a}_{\mathbf{q}}, \quad (3.230)$$

see, e.g., Refs. [422, 511], then may allow us to perform a similar analytic evaluation of the phonon-electron correlation function

$$\chi_{\mathbf{j}_Q, \mathbf{j}_E}^{\alpha\beta}(i\Omega_m) = \frac{1}{V} \int_0^{\beta} d\tau e^{i\Omega_m\tau} \langle T_{\tau} j_{Q,ph}^{\alpha}(\tau) j_E^{\beta} \rangle. \quad (3.231)$$

The lowest order Feynman diagrams to consider, as derived, e.g., in Ref. [512], stem from the second-order perturbation expansion in \mathcal{H}_{e-ph} , which, through Wick contractions, results in an interplay of phonon propagators, $D(\mathbf{q}, \tau) = -\langle T_{\tau} \hat{a}_{\mathbf{q}}(\tau) \hat{a}_{\mathbf{q}}^{\dagger} \rangle$ (drawn as dashed line), and electron propagator, $G(\mathbf{k}, \tau) = -\langle T_{\tau} \hat{c}_{\mathbf{k}, \sigma}(\tau) \hat{c}_{\mathbf{k}, \sigma}^{\dagger} \rangle$ (drawn as solid line),

$$\begin{aligned} \chi_{\mathbf{j}_Q, \mathbf{j}_E}^{\alpha\beta}(i\Omega_m) &\propto \sum_{\substack{\mathbf{q}, \mathbf{k} \\ \omega_g, \nu_n}} g_{\mathbf{q}}^2 \hbar \frac{\partial\omega_{\mathbf{q}}}{\partial q_{\alpha}} \omega_{\mathbf{q}} e\nu_{\mathbf{k}}^{\beta} D(\mathbf{q}, \omega_g) D(\mathbf{q}, \omega_g - \Omega_m) \times \\ &\times \left[G(\mathbf{k}, \nu_n) G(\mathbf{k}, \nu_n - \Omega_m) G(\mathbf{k} - \mathbf{q}, \nu_n - \omega_g) + G(\mathbf{k}, \nu_n - \Omega_m) G(\mathbf{k}, \nu_n) G(\mathbf{k} + \mathbf{q}, \nu_n + \omega_g - \Omega_m) \right], \end{aligned} \quad (3.232)$$

with the bosonic phonon frequency ω_g , transfer frequency Ω_m and fermionic frequency ν_n . Here, the electronic current couples, in the Peierls approximation, via the band velocities $v_{\mathbf{k}}$, see Section 3.3.4. Eq. (3.232) is illustrated in Fig. 3.58 and highlights the relevant electronic “triangle” diagram, similarly occurring in linear response in the presence of an external magnetic field, see Appendix A.3.

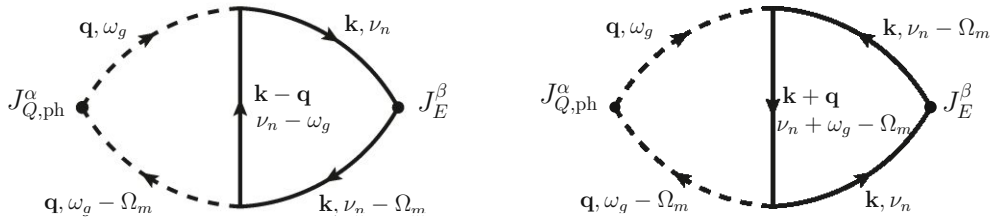


Figure 3.58: Lowest order Feynman diagrams contributing to the phonon heat-current, electric current correlation function, illustrating Eq. (3.232). Dashed (solid) line represents phonon (electron) propagators. Dots at the left and right hand side of the diagrams correspond to coupling elements. Diagrams inspired by Ref. [512] which we chose to modify in order to keep a consistent frequency notation within this thesis.

In a similar vein, contributions of magnons to the thermopower could be treated, see Ref. [513].

Anomalous transport quantities

A different avenue represents anomalous transport. The anomalous Hall conductivity typically occurs in solids with broken time-reversal symmetry. Its intrinsic contribution to the Hall conductivity (without the presence of a magnetic field) in the band picture from linear response reads

$$\sigma_{\alpha\beta} = -\epsilon_{\alpha\beta\gamma} \frac{e^2}{\hbar} \sum_n \int \frac{d^3k}{(2\pi)^d} f_{FD}(\epsilon_n^{\mathbf{k}}) \Omega_n^\gamma(\mathbf{k}) \quad (3.233)$$

where $\epsilon_{\alpha\beta\gamma}$ is the Levi-Civita symbol, $\Omega_n(\mathbf{k}) = \nabla_{\mathbf{k}} \times \mathcal{A}_n(\mathbf{k})$ the Berry curvature, determined from the Berry connection $\mathcal{A}_n(\mathbf{k}) = i\langle n, \mathbf{k} | \nabla_{\mathbf{k}} | n, \mathbf{k} \rangle$ [514], with n indexing band eigenstates and Greek indices label Cartesian directions, as before. The same result can be obtained from a semi-classical treatment of electron transport, where the Berry phase enters through an anomalous (group) velocity of the wave-package, $\hbar \dot{\mathbf{r}} = \nabla \epsilon_n^{\mathbf{k}} - \mathbf{E} \times \Omega_n(\mathbf{k})$, when an electrical field \mathbf{E} is applied. Details can be found, e.g., in the review by Nagasosa *et al.* [388] and references therein.

Then, a natural extension of the formalism advanced in this thesis is the inclusion of said anomalous velocities and Berry curvatures. An upgrade along these lines would also allow studying the effect of finite lifetimes of *non-trivial* bulk states onto the surface conduction they generate in topologically non-trivial systems. On the model level, such effects have been studied numerically (i.e., without a semi-analytical evaluation of transport kernels) in two dimensions, e.g., by Mitscherling *et al.* [390].

Chapter 4

Conclusion

Summary: Mott materials and models thereof

The state-of-the-art [density functional theory](#) + [dynamical mean-field approach](#) is capable of reproducing the hallmarks of a strongly correlated metal, the formation of Hubbard bands and the renormalization of the quasi-particle peak in the spectral function of [bulk SrVO₃](#). Through the quantum impurity projection and subsequent self-consistent embedding into the lattice itself, local correlations can be captured in a non-perturbative fashion with DMFT. We employed this DFT+DMFT approach in the study of materials in both their bulk form and in restricted geometries which have seen a recent boost in interest due to improvements in modern atomic layer-by-layer deposition techniques.

In a first project, we showcased how a [thick film of SrVO₃ deposited on a substrate](#), is capable of undergoing a metal-to-insulator transition: Deforming the cubic perovskite structure leads to a reduction in crystal symmetry, causing the formation of a crystal-field splitting between the three initially degenerate t_{2g} states. Beyond a critical deformation threshold, this splitting, in combination with the large on-site repulsion present at the vanadium site, triggers a sudden breakdown of the Fermi-liquid state and the emergence of a Mott insulator. Our simulated temperature vs. out-of-plane lattice constant phase diagram highlights how such a “simple” setup is capable of yielding a highly complex separation between metallic and insulating phases. With our approach, we are able to quantitatively reproduce the characteristics of thick films whose *c*-axis have been tuned via helium implantation. To be more precise, transport measurements display a similarly sharp metal-insulator transition as seen within our DMFT calculations.

In a second project we used this knowledge and applied it to the scenario of [thin films protected by surface passivation](#). We showed that a similar metal-to-insulator transition can be achieved via quantum confinement. Reducing the number of deposited layers below a critical threshold, we were able to reason that the same kind of crystal-field splitting is capable of triggering the Mott transition. Here we find that the crystal-field splitting, in combination with the auxiliary effects of reduced

band-widths, is a sufficient ingredient to reproduce the critical thickness of 5 – 6 seen in experiments. Due to the ideal d^1 occupation (V^{4+} valence) the Mott scenario can be supported despite an almost bulk-esque electronic state with respect to the band width.

In a third project we revisited the [surface phenomena of \$SrVO_3\$ thin films without passivation](#), i.e. where, per se, a clean film termination cannot be provided. Through the pulse-laser deposition growth process our collaborators found strong evidence for a thickness dependent coverage of excess, apical surface oxygen. This additional oxygen generates domains on the surface, with a maximal coverage of one oxygen for every other surface vanadium atom, resulting in a $\sqrt{2} \times \sqrt{2}$ surface reconstruction. The resulting, unprotected samples display a massively reduced critical thickness of 2 – 3 instead. In our theoretical efforts, we restricted ourselves to pristine VO_2 terminated structures and supercell structures that possess the aforementioned surface reconstruction. Within DFT+DMFT above the critical thickness, both scenarios lead to definite metallic solutions. For the structures mimicking the domains with apical oxygen, however, we find complete neutralization of the outermost vanadium sites (d^0): an electronic dead layer emerges. Through the reduction of actively contributing layers, a reduction of quantum well state ensues when compared to an identically sized structure with a clean surface, in agreement with angle-resolve photoemission spectroscopy measurements. Revisiting the metal-insulator transition [86] with these (remedied) surface terminations, we find a critical thickness of 2 – 3 in agreement with PES measurements: Supported by magnified crystal-field splittings induced by the severing of the surface VO_6 octahedrons and accompanied by vacuum-induced crystal distortions, the Mott insulating state can be found in both considered scenarios: “Clean” samples turn metallic above 2 layers, samples with a reconstructed surface above 3 layers. Interestingly, here the dead-layer is kept in tact independently of whether the system turns insulating or not. Suffice it to say, these simulations only scratch the surface of the physics at play. From the theoretical point of view, a multitude of questions remain regarding other effects of the apical oxygen and notably also the influence of the substrate.

In a more theoretically motivated study we discuss [non-local fluctuations and their signatures in pristine \$SrVO_3\$ monolayers](#), a scenario that is in fact quite difficult to realize experimentally. Through the reduction to a (quasi-) two-dimensional system, the shape and kinetic energy of the involved orbitals is drastically modified leading to an exceptionally stable Mott insulator with respect to variations of the on-site interaction U . Despite this stability, doping away from the realized d^1 Mott insulator is relatively uncomplicated in DMFT: Within our explored range of vanadium site occupation, in principle achievable by chemical doping or by applying a gate voltage, we find a wide variety of spin and charge ordered phases: antiferromagnetism, ferromagnetism, incommensurate magnetism, checkerboard orbital ordering and stripe orbital ordering. We employ the dynamical vertex approximation, to scrutinize the effect of these various types of fluctuations onto the self-

energy above the ordering temperatures. In order to refine our evaluation, we developed an improved “binaural” diagnostic tool, effectively allowing us to pinpoint the origins of self-energy modification and connect them to the spectral properties of the system.

Finalizing the Mott Chapter, we return to the “basics” and consider the [one-band, two-dimensional Hubbard model](#). We advance the [self-consistent ladder dynamical vertex approximation](#) method for which we derive and implement a multi-orbital expression for the vertex-corrected optical conductivity. In the weak to strong coupling regimes, we analyze the effect of the predominant antiferromagnetic fluctuations, and provide some quantitative comparisons to the parquetDΓA method.

Summary: Kondo materials and models thereof

We started off our discussion on Kondo materials with an analysis of the differences between the Kondo effect present in the [single impurity Anderson model](#) and its pendant, the lattice Kondo effect in the [periodic Anderson model](#). Whereas the SIAM can be (numerically exactly) solved by an impurity solver, we employed the aforementioned dynamical mean-field theory for the PAM which, in the symmetric, half-filled case, can be seen as a “canonical” Kondo insulator. That is, as in Ce-based systems, hydrostatic pressure leads to a widening of the (hybridization) gap. Upon cooling of the SIAM, the Kondo effect leads to a screening out of the free, local spin which, through scattering processes, generates a magnified resonance at the Fermi level. This so-called Kondo resonance is “kept alive” down to the lowest temperature, leading to a suppression of local moment fluctuations. Within the half-filled PAM, on the other hand, the hybridization of the f- and the d-levels the Kondo resonance instead leads to the formation of a (lattice) coherent state in which a (spectral) gap is eventually stabilized. Beyond the analysis of this coherence transition, we provided further insight in the mechanism and characteristics of the magnetic fluctuations associated with the RKKY interaction.

In the next step, we turned our attention towards a more realistic manifestation of a [Kondo insulator in the form of Ce₃Bi₄Pt₃](#). Via a charge self-consistent DMFT treatment we extracted the intricacies of the atomic make-up of the crystal structure and its resulting electronic structure. Due to the freedom of the bismuth positioning inside the unit cell the emergent hybridization gap experiences a “non-canonical” pressure dependence. Moving onto transport properties, we were able to qualitatively reproduce the phenomenon of resistivity saturation. Employing a full Kubo computation of the conductivity tensor we find that the trends upon applying pressure and adding disorder is consistent with experimental transport measurements. With this validation, we developed a minimal, microscopic theory that is capable of reproducing this behavior: A simple two-band tight-binding model supplemented with a static scattering rate, solved (analytically) within linear response. We find that finite lifetimes of intrinsic valence and conduction states spill incoherent weight into the

gap, introducing a lower bound on the residual conductivity, leading to a saturation of the resistivity. Within this minimalist model our explored bandgap vs. scattering rate phase diagrams reproduce the experimental trends of the observed saturation values and crossover temperatures quite well.

Based on the same premise of intrinsic, finite lifetimes, obtained from a linearized self-energy, we derived the [higher order transport kernels](#) that are necessary for the computation of a wider range of thermoelectric and magnetotransport observables, such as the Seebeck, Hall, and Nernst coefficient. Using contour integration and Matsubara summation, we obtain semi-analytical expressions that effectively “interpolate” between a simple relaxation-time approximation within a Boltzmann approach and the full Kubo response. While leading to qualitative improvements over the former, the computational precision and speed are essentially identical. From the derived set of intra- and inter-band expressions, we also show how the Boltzmann kernel functions can be consistently extended to inter-band transitions (that are not included in some Boltzmann packages).

In the next project we illustrated the transport signatures of [many-body phenomena in semiconductors](#). Analyzing a simple, asymmetric two-band model, encoding the essential features of a wide range of gapped systems, we performed parameter scans over the band gap, band asymmetry, and electronic lifetime. We find hard temperature cut-offs, below which the Boltzmann-esque behavior ceases to be valid. Indeed, at sufficiently low temperatures, the scattering rate associated with the finite electronic lifetimes becomes a relevant energy scale, in that it determines the temperature profile of transport observables, leading to drastic modification vis-à-vis semi-classical expectations. Incoherence of intrinsic states modifies the chemical potential, seemingly akin to extrinsic in-gap states. More importantly, however, a residual (Hall) conduction emerges which in turn leads to “metal-like” Seebeck $S(T) \propto T$ and Nernst coefficients $\nu(T) \propto T$ in the low temperature limit, while the resistivity $\rho(T)$ and the Hall coefficient $R_H(T)$ saturate. Contrary to the Boltzmann approximation, in which $S(T) \propto \frac{1}{T}$, our theory thus respects the quintessential laws of thermodynamic: $S \rightarrow 0 (T \rightarrow 0)$.

Finally, we discussed [LINRETRACE](#), our full-fledged implementation of the derived transport kernels which is capable of interfacing to modern electronic structure codes and has the ability to handle generalized tight-binding Hamiltonians. Focusing on technical details that are critical for a stable and efficient numerical evaluation of observables for models and realistic crystal structures, we provide an overview of the program structure, explore some of the code’s capabilities, and illustrate future research avenues.

Outlook on future avenues

Metal-insulator transitions in transition metal oxides

Starting with potential candidates in the material class of transition-metal oxide heterostructures: The “ingredient” of crystal-field splitting is a rather generic and easy to realize mechanism in thin films. Currently, discussions are ongoing whether the metal-to-insulator transitions in thin film setups should be ascribed to correlation or localization/impurity effects. Having presented a strong argument towards correlation effects, further experimental confirmation of the painted picture is required. This may include the effect of uniaxial pressure on the protected thin film layers or polarized (AR)PES measurements in order to detect the predicted strong orbital polarization. Similarly, theoretical analyses in related (perovskite) materials are in order: It is yet to see, how easy it is to generalize the idealized t_{2g}/d^1 scenario towards (i) other (integer) fillings, (ii) more complex projections such as $t_{2g}+e_g$ or $d+p$, (iii) more complex local crystal environments, or (iv) how critical changes to the, in principle, layer-dependent on-site interaction values are. Potential projects include the study of CaVO_3 (which includes tilting of the VO_6 octahedra), SrRuO_3 , LaNiO_3 , etc.

In our detailed theoretical and experimental analysis of “unprotected” thin films, we further revealed a far more intricate surface that has hitherto been modelled within DFT+DMFT approaches. To gain further insight into this, heavily environmentally influenced, metal-insulator transition further studies are required. Unanswered questions include: (i) How different surface domains interact with one another and how possible delocalized apical oxygen may affect the local electronic structure and the overall insulating (metallic) state found below (above) a critical thickness. (ii) Whether the hypothesized hole-doping is present below the critical thickness and if so, how does it influence the theorized Mott insulating state.

Bethe-Salpeter equations

In order to achieve more “realism”, the two-particle analysis via the Bethe-Salpeter equations should be extended towards (i) general hybridization functions such that spin-orbit coupling may be included on the susceptibility level and a (ii) general (non-symmetrized) spin description such that a treatment of symmetry-broken phases becomes possible [236, 515]. In such a framework, explicit computations of, e.g., the generalized spin/charge susceptibility of $\text{Ce}_3\text{Bi}_4\text{Pt}_3$ or other related Kondo compounds would become possible.

Self-consistent dynamical vertex approximation

The developed self-consistent dynamical vertex approximation including its extension towards optical conductivities shows promising results. One apparent avenue is an extension of the scDFA approach

towards outer self-consistency, i.e. one also updates the two-particle irreducible Γ_{ph} such that not only the self-energy acts as a “suppressor” of fluctuations. Before that, however, additional benchmarking and a wider range of test cases are in order: (i) More accurate calculations for the existing two-dimensional Hubbard model, especially with respect to momentum grid convergence. This is necessary to achieve properly converged optical conductivities in the employed temperature range shown in this thesis. In doing so, a quantitative comparison of the vertex contribution to similar methods such as the parquet D Γ A and the λ -corrected D Γ A becomes feasible. (ii) The study of critical exponents of the dominant antiferromagnetic fluctuations of the Hubbard model [228]. (iii) An application towards the periodic Anderson model [225]: This includes the effect on the antiferromagnetic dome and the study of optical conductivities in the vicinity said dome and/or the quantum critical point. (iv) An application to generalized multi-orbital systems that display vastly different orbital fluctuations (such as the investigated SrVO₃ monolayer). In a first step one could, e.g., screen how the self-energy feedback affects orbital polarization, ordering phases and temperatures.

LINRETRACE

Continuing with the derived transport methodology, further avenues are represented by the possibilities of (i) analyzing anomalous transport effects [388], (ii) the inclusion of phonon [516] and/or magnon drag [517] contributions in order to gain an improved understanding of the qualitative and quantitative signatures of colossal thermopowers found in some thermoelectrics [460], (iii) moving towards non-linear transport by further expanding the magnetoresistance [518] beyond linear order or by considering higher order correlation functions that are necessary to describe high harmonic generation [519], and (iv) considering higher order Feynman diagrams within the employed “ Γ -approximation” where one could envisage modelling vertex corrections that include e.g., forward scattering processes [520] that further renormalize transport kernels.

Appendices

A.1 Many-body Green's functions

A.1.1 Matsubara Green's functions

The general n -particle Green's function in imaginary time corresponds to the correlation function measuring the addition and removal of n -particles to a system in thermal equilibrium

$$G_{i_1, \dots, i_{2n}}^{(n)}(\tau_1, \dots, \tau_{2n}) = (-1)^n \left\langle T_\tau \left[\hat{c}_{i_1}(\tau_1) \hat{c}_{i_2}^\dagger(\tau_2) \dots \hat{c}_{i_{2n-1}}(\tau_{2n-1}) \hat{c}_{i_{2n}}^\dagger(\tau_{2n}) \right] \right\rangle. \quad (\text{A.1})$$

Here, the time-dependent fermionic annihilation / creation operators have specific identifiers $i_1 \dots i_{2n}$ (orbitals, momentum, spin, etc.) and are expressed in the Heisenberg representation

$$\hat{c}^{(\dagger)}(\tau) = e^{\mathcal{H}\tau} \hat{c}^{(\dagger)} e^{-\mathcal{H}\tau} \quad (\text{A.2})$$

with the full Hamiltonian \mathcal{H} entering the time evolution operators. When evaluating the Green's functions, we employ the grand-canonical expectation value⁶⁸

$$\langle \dots \rangle = \text{Tr} \langle \rho \dots \rangle = \frac{1}{Z} \text{Tr} \left(e^{-\beta \mathcal{H}} \dots \right) = \frac{1}{Z} \sum_n \langle n | e^{-\beta \mathcal{H}} \dots | n \rangle. \quad (\text{A.3})$$

with ρ as the density matrix and Z as the partition function defined by

$$\rho = \frac{e^{-\beta \mathcal{H}}}{Z}, \quad (\text{A.4a})$$

$$Z = \text{Tr} \left(e^{-\beta \mathcal{H}} \right) = \sum_n \langle n | e^{-\beta \mathcal{H}} | n \rangle, \quad (\text{A.4b})$$

respectively. Here the trace corresponds to a sum over all possible eigenstates $|n\rangle$ with corresponding eigenvalue E_n via

$$\mathcal{H} |n\rangle = E_n |n\rangle. \quad (\text{A.5})$$

Finally, the time ordering operator T_τ orders the fermionic operators from left to right according to their imaginary time argument (from largest to smallest)

$$T_\tau \left[c_1^{(\dagger)}(\tau_1) c_2^{(\dagger)}(\tau_2) \right] = \left[c_1^{(\dagger)}(\tau_1) c_2^{(\dagger)}(\tau_2) \right] \Theta(\tau_1 - \tau_2) - \left[c_2^{(\dagger)}(\tau_2) c_1^{(\dagger)}(\tau_1) \right] \Theta(\tau_2 - \tau_1). \quad (\text{A.6})$$

This ordering is done by switching operator positions which is accompanied by an additional (-1) for each exchange.

A.1.1.1 Boundaries

Without loss of generality we can assume that the operators are ordered from largest to smallest imaginary time $\tau_1 > \dots > \tau_{2n}$

$$\begin{aligned} G_{i_1, \dots, i_{2n}}^{(n)}(\tau_1, \dots, \tau_{2n}) &= \frac{(-1)^n}{Z} \sum_m \langle m | e^{-\beta \mathcal{H}} \hat{c}_{i_1}(\tau_1) \hat{c}_{i_2}^\dagger(\tau_2) \dots \hat{c}_{i_{2n-1}}(\tau_{2n-1}) \hat{c}_{i_{2n}}^\dagger(\tau_{2n}) | m \rangle \\ &= \frac{(-1)^n}{Z} \sum_m e^{(-\beta + \tau_1 - \tau_{2n}) E_m} \langle m | \hat{c}_{i_1} e^{-\mathcal{H} \tau_1} \hat{c}_{i_2}^\dagger(\tau_2) \dots \hat{c}_{i_{2n-1}}(\tau_{2n-1}) e^{\mathcal{H} \tau_{2n}} \hat{c}_{i_{2n}}^\dagger | m \rangle. \end{aligned} \quad (\text{A.7})$$

With the evaluation of the outermost operators one arrives at a pre-factor of $e^{(-\beta + \tau_1 - \tau_{2n}) E_m}$. Since the eigenvalues E_m of an infinitely large system may also become infinitely large, one has to ensure that this pre-factor is of suppressing nature by requiring

$$-\beta + \tau_1 - \tau_{2n} < 0, \quad (\text{A.8})$$

which can be rewritten into

$$\tau_{2n} + \beta > \tau_1 > \dots > \tau_{2n}. \quad (\text{A.9})$$

In other words: All time arguments have to be within an interval of the length of β . Using the cyclic property of the trace ($\text{Tr}[ABCD] = \text{Tr}[DABC] = \dots$) one finds

$$\begin{aligned} G_{i_1, \dots, i_{2n}}^{(n)}(\tau_1, \dots, \tau_{2n}) &= \frac{(-1)^n}{Z} \sum_m \langle m | e^{-\beta \mathcal{H}} \hat{c}_{i_1}(\tau_1) \hat{c}_{i_2}^\dagger(\tau_2) \dots \hat{c}_{i_{2n-1}}(\tau_{2n-1}) \hat{c}_{i_{2n}}^\dagger(\tau_{2n}) | m \rangle \\ &= \frac{(-1)^n}{Z} \sum_m \langle m | e^{-\beta \mathcal{H}} \hat{c}_{i_2}^\dagger(\tau_2) \dots \hat{c}_{i_{2n}}^\dagger(\tau_{2n}) e^{-\beta \mathcal{H}} \hat{c}_{i_1}(\tau_1) e^{\beta \mathcal{H}} | m \rangle \\ &= \frac{(-1)^n}{Z} \sum_m \langle m | e^{-\beta \mathcal{H}} \hat{c}_{i_2}^\dagger(\tau_2) \dots \hat{c}_{i_{2n}}^\dagger(\tau_{2n}) \hat{c}_{i_1}(\tau_1 - \beta) | m \rangle \\ &= -\frac{(-1)^n}{Z} \sum_m \langle m | e^{-\beta \mathcal{H}} \hat{c}_{i_1}(\tau_1 - \beta) \hat{c}_{i_2}^\dagger(\tau_2) \dots \hat{c}_{i_{2n-1}}(\tau_{2n-1}) \hat{c}_{i_{2n}}^\dagger(\tau_{2n}) | m \rangle \\ &= -G_{i_1, \dots, i_{2n}}^{(n)}(\tau_1 - \beta, \dots, \tau_{2n}), \end{aligned} \quad (\text{A.10})$$

⁶⁸In the grand-canonical ensemble the weighting factor is $e^{-\beta(\mathcal{H} - \mu \mathcal{N})}$ and not $e^{-\beta \mathcal{H}}$. In order to be more concise, we implicitly mean $\mathcal{H} - \mu \mathcal{N}$ when writing \mathcal{H} from now on.

$$\begin{aligned}
G_{i_1, \dots, i_{2n}}^{(n)}(\tau_1, \dots, \tau_{2n}) &= \frac{(-1)^n}{Z} \sum_m \langle m | e^{-\beta \mathcal{H}} \hat{c}_{i_1}(\tau_1) \hat{c}_{i_2}^\dagger(\tau_2) \dots \hat{c}_{i_{2n-1}}(\tau_{2n-1}) \hat{c}_{i_{2n}}^\dagger(\tau_{2n}) | m \rangle \\
&= \frac{(-1)^n}{Z} \sum_m \langle m | e^{-\beta \mathcal{H}} e^{\beta \mathcal{H}} \hat{c}_{i_{2n}}^\dagger(\tau_{2n}) e^{-\beta \mathcal{H}} \hat{c}_{i_1}(\tau_1) \dots \hat{c}_{i_{2n-1}}(\tau_{2n-1}) | m \rangle \\
&= \frac{(-1)^n}{Z} \sum_m \langle m | e^{-\beta \mathcal{H}} \hat{c}_{i_{2n}}^\dagger(\tau_{2n} + \beta) \hat{c}_{i_1}(\tau_1) \dots \hat{c}_{i_{2n-1}}(\tau_{2n-1}) | m \rangle \quad (\text{A.11}) \\
&= -\frac{(-1)^n}{Z} \sum_m \langle m | e^{-\beta \mathcal{H}} \hat{c}_{i_1}(\tau_1) \hat{c}_{i_2}^\dagger(\tau_2) \dots \hat{c}_{i_{2n-1}}(\tau_{2n-1}) \hat{c}_{i_{2n}}^\dagger(\tau_{2n} + \beta) | m \rangle \\
&= -G_{i_1, \dots, i_{2n}}^{(n)}(\tau_1, \dots, \tau_{2n} + \beta),
\end{aligned}$$

the so-called Kubo-Martin-Schwinger (KMS) boundary conditions.

A.1.1.2 Matsubara frequencies

In order to get a more convenient notation, we exploit the KMS boundary conditions further. Since $G(\tau)$ is restricted to an interval of the size β it can be represented in terms of a Fourier series [521]

$$G_{i_1, \dots, i_{2n}}^{(n)}(\tau_1, \dots, \tau_{2n}) = \frac{1}{\beta 2^n} \sum_{\{\nu_i\}} e^{i(-\nu_1 \tau_1 + \nu_2 \tau_2 - \dots + \nu_{2n} \tau_{2n})} G_{i_1, \dots, i_{2n}}^n(\nu_1, \dots, \nu_{2n}). \quad (\text{A.12})$$

The frequency representation $G_{i_1, \dots, i_{2n}}^{(n)}(\nu_1, \dots, \nu_{2n})$ therefore reproduces our original time-dependent Green's function and the associated properties. Consequently, we get this representation by performing the Fourier transform

$$G_{i_1, \dots, i_{2n}}^{(n)}(\nu_1, \dots, \nu_{2n}) = \int_0^\beta d\tau_1 \dots \int_0^\beta d\tau_{2n} e^{i(\nu_1 \tau_1 - \nu_2 \tau_2 + \dots - \nu_{2n} \tau_{2n})} G_{i_1, \dots, i_{2n}}^{(n)}(\tau_1, \dots, \tau_{2n}). \quad (\text{A.13})$$

Due to the antiperiodicity⁶⁹ we get the so-called (fermionic) Matsubara frequencies of the form

$$\nu_n = \frac{(2n+1)\pi}{\beta}, \quad n \in \mathbb{Z}. \quad (\text{A.14})$$

Alongside this definition one defines the bosonic variant, obtained from a periodic function, as the even multiples of π/β

$$\omega_m = \frac{2m\pi}{\beta}, \quad m \in \mathbb{Z}. \quad (\text{A.15})$$

⁶⁹ A general antiperiodic function fulfills the condition $-f(x) = f(x + np)$ with $n = 1, 3, 5, \dots$ and the periodicity p . This property is created by the KMS boundary conditions with a periodicity of $p = \beta$.

A.1.1.3 Symmetries

Given a Hamiltonian that is both time-independent and has an underlying lattice translational invariance, the frequency and momentum dependence of the n -particle Green's function simplifies: Energy conservation leads to a restriction of the frequency arguments

$$G_{i_1, \dots, i_{2n}}^{(n)}(\nu_1, \dots, \nu_{2n}) = \beta \delta_{(\nu_1 - \nu_2 + \dots + \nu_{2n-1}), \nu_{2n}} G_{i_1, \dots, i_{2n}}^{(n)}(\nu_1, \dots, \nu_{2n-1}), \quad (\text{A.16})$$

requiring us to only list $2n - 1$ frequency arguments. In the same way, momentum conservation leads to a restriction of the momentum arguments

$$G_{i_1, \dots, i_{2n}}^{(n)} = \frac{(2\pi)^d}{V} \delta_{(\mathbf{k}_1 - \mathbf{k}_2 + \dots + \mathbf{k}_{2n-1}), \mathbf{k}_{2n}} G_{i_1, \dots, i_{2n}}^{(n)}, \quad (\text{A.17})$$

where V is the volume of the unit cell and d is the dimensionality of the system.

The other commonly employed symmetries in this thesis are the crossing (CR) and the swapping (SW) symmetry. By exchanging a pair of annihilation or creation operators in the general n -particle Green's function

$$G_{i_1, \dots, i_{2n}}^{(n)}(\tau_1, \dots, \tau_{2n}) = (-1)^n \left\langle T_\tau \left[\hat{c}_{i_1}(\tau_1) \hat{c}_{i_2}^\dagger(\tau_2) \dots \hat{c}_{i_{2n-1}}(\tau_{2n-1}) \hat{c}_{i_{2n}}^\dagger(\tau_{2n}) \right] \right\rangle, \quad (\text{A.18})$$

we have to perform $(2k - 1)$ swapping operations resulting in an additional factor (-1) . Subsequently we get

$$G_{i_1, \dots, i_i, \dots, i_j, \dots, i_{2n}}^{(n)}(\tau_1, \dots, \tau_i, \dots, \tau_j, \dots, \tau_{2n}) \stackrel{\text{CR}}{=} -G_{i_1, \dots, i_j, \dots, i_i, \dots, i_{2n}}^{(n)}(\tau_1, \dots, \tau_j, \dots, \tau_i, \dots, \tau_{2n}). \quad (\text{A.19})$$

Swapping symmetry on the other hand is often used in the context of two-particle Green's functions. By applying crossing symmetry on both the incoming and outgoing particles, accompanied with the pre-factor $(-1)^2$, we get

$$G_{i_1, i_2, i_3, i_4}^{(2)}(\tau_1, \tau_2, \tau_3, \tau_4) \stackrel{\text{SW}}{=} G_{i_3, i_4, i_1, i_2}^{(2)}(\tau_3, \tau_4, \tau_1, \tau_2). \quad (\text{A.20})$$

Let us note that from here on out, we omit the superscript denoting the particle-number as the number of arguments (frequencies or imaginary times) are a sufficient identifier for the given quantity.

A.1.1.4 One-particle properties

The (fermionic) one-particle Green's function naturally presents the simplest case, while also displaying some interesting features. $G_{i_1, i_2}(\tau)$ is defined in the time interval $(-\beta, \beta)$ while the negative (positive) arguments can be restored via the KMS condition of Eqs. (A.10-A.11)

$$-G_{i_1, i_2}(\tau - \beta) = G_{i_1, i_2}(\tau) \quad (\text{A.21a})$$

$$-G_{i_1, i_2}(\beta - \tau) = G_{i_1, i_2}(-\tau) \quad (\text{A.21b})$$

with $\tau \in [0, \beta)$. The function takes, depending on the involved (compound) indices, a step of size 1 when τ changes from negative to positive

$$\begin{aligned} G_{i_1, i_2}(0^+) &= -\left\langle T_\tau \left[\hat{c}_{i_1}(0^+) \hat{c}_{i_2}^\dagger(0) \right] \right\rangle \\ &= -\left\langle \hat{c}_{i_1}(0) \hat{c}_{i_2}^\dagger(0) \right\rangle = n_{i_2, i_1} - \delta_{i_1, i_2} \end{aligned} \quad (\text{A.22a})$$

$$\begin{aligned} G_{i_1, i_2}(0^-) &= -\left\langle T_\tau \left[\hat{c}_{i_1}(0^-) \hat{c}_{i_2}^\dagger(0) \right] \right\rangle, \\ &= \left\langle \hat{c}_{i_2}^\dagger(0) \hat{c}_{i_1}(0) \right\rangle = n_{i_2, i_1}, \end{aligned} \quad (\text{A.22b})$$

resulting in

$$G_{i_1, i_2}(0^-) - G_{i_1, i_2}(0^+) = \delta_{i_1, i_2}. \quad (\text{A.23})$$

As previously introduced, the Fourier transform to the fermionic Matsubara axis is performed via

$$G_{i_1, i_2}(i\nu_n) = \int_0^\beta d\tau e^{i\nu_n \tau} G_{i_1, i_2}(\tau). \quad (\text{A.24})$$

Since the Green's function on the imaginary time axis is a purely real quantity, the real (imaginary) part of the Matsubara Green's function becomes even (odd) w.r.t. $i\nu_n \leftrightarrow -i\nu_n$. Furthermore, due to the antiperiodicity of the Green's function, the integration interval $[0, \beta)$ can be shifted arbitrarily

$$\begin{aligned} \int_{-\tau_1}^{\beta-\tau_1} d\tau e^{i\nu_n \tau} G_{i_1, i_2}(\tau) &= \int_{0^+}^{\beta-\tau_1} d\tau e^{i\nu_n \tau} G_{i_1, i_2}(\tau) + \int_{-\tau_1}^{0^-} d\tau e^{i\nu_n \tau} G_{i_1, i_2}(\tau) \\ &= \int_{0^+}^{\beta-\tau_1} d\tau e^{i\nu_n \tau} G_{i_1, i_2}(\tau) + \int_{\beta-\tau_1}^{\beta} d\tau e^{i\nu_n(\tau-\beta)} G_{i_1, i_2}(\tau - \beta) \\ &= \int_{0^+}^{\beta-\tau_1} d\tau e^{i\nu_n \tau} G_{i_1, i_2}(\tau) + \int_{\beta-\tau_1}^{\beta} d\tau (-e^{i\nu_n \tau}) (-G_{i_1, i_2}(\tau)) = G_{i_1, i_2}(i\nu_n) \end{aligned} \quad (\text{A.25})$$

with $\tau_1 \in [0, \beta)$ and $e^{\pm i\nu_n \beta} = (-1)$. Let us note that the same argument holds for bosonic quantities that are intrinsically periodic along the imaginary time axis, $\chi(-\tau) = \chi(\beta - \tau)$ for $\tau \in [0, \beta)$.

A.1.1.5 Two-particle frequency notations

As shown in Appendix A.1.1.2, we are now able to represent a general two-particle Green's function in the more convenient frequency notation by performing a Fourier transform from the (imaginary) time space into the frequency space. This transformation reads

$$G_{ijkl}^{\nu_1 \nu_2 \nu_3 \nu_4} = \int d\tau_1 d\tau_2 d\tau_3 d\tau_4 G_{ijkl}(\tau_1, \tau_2, \tau_3, \tau_4) e^{i\nu_1 \tau_1} e^{-i\nu_2 \tau_2} e^{i\nu_3 \tau_3} e^{-i\nu_4 \tau_4}. \quad (\text{A.26})$$

Due to time translational symmetry not all times are independent from each other: We can translate the Green's function by τ_4 such that the last time argument is 0. Subsequent substitutions

$$\tau'_i = \tau_i - \tau_4 \quad \text{with } i \in \{1, 2, 3\}$$

and an integration over τ_4 gives⁷⁰

$$\begin{aligned}
G_{ijkl}^{\nu_1\nu_2\nu_3\nu_4} &= \int_0^\beta d\tau_1 d\tau_2 d\tau_3 d\tau_4 G_{ijkl}(\tau_1 - \tau_4, \tau_2 - \tau_4, \tau_3 - \tau_4, 0) e^{i\nu_1\tau_1} e^{-i\nu_2\tau_2} e^{i\nu_3\tau_3} e^{-i\nu_4\tau_4} \\
&= \int_0^\beta d\tau'_1 d\tau'_2 d\tau'_3 d\tau_4 G_{ijkl}(\tau'_1, \tau'_2, \tau'_3, 0) e^{i\nu_1\tau'_1} e^{-i\nu_2\tau'_2} e^{i\nu_3\tau'_3} e^{i(\nu_1 - \nu_2 + \nu_3 - \nu_4)\tau_4} \\
&= \underbrace{\int_0^\beta d\tau'_1 d\tau'_2 d\tau'_3 G_{ijkl}(\tau'_1, \tau'_2, \tau'_3, 0) e^{i\nu_1\tau'_1} e^{-i\nu_2\tau'_2} e^{i\nu_3\tau'_3}}_{\equiv G_{ijkl}^{\nu_1\nu_2\nu_3}} \underbrace{\int d\tau_4 e^{i(\nu_1 - \nu_2 + \nu_3 - \nu_4)\tau_4}}_{\beta\delta_{(\nu_1 - \nu_2 + \nu_3 - \nu_4), 0}},
\end{aligned} \tag{A.27}$$

These three frequencies ν_1, ν_2, ν_3 are now commonly written as a combination of two fermionic frequencies and one bosonic, transfer frequency. Depending on the way this transfer frequency is employed, one refers to the frequency notation as particle-hole (ph), transverse particle-hole ($\overline{\text{ph}}$) and particle-particle (pp) notation

$$\nu_1 = \nu_{ph} = \nu_{\overline{ph}} = \nu_{pp} \tag{A.28}$$

$$\nu_2 = \nu_{ph} - \omega_{ph} = \nu'_{ph} = \omega_{pp} - \nu'_{pp} \tag{A.29}$$

$$\nu_3 = \nu'_{ph} - \omega_{ph} = \nu'_{\overline{ph}} - \omega_{\overline{ph}} = \omega_{pp} - \nu_{pp} \tag{A.30}$$

$$\nu_4 = \nu'_{ph} = \nu_{\overline{ph}} - \omega_{\overline{ph}} = \nu'_{pp} \tag{A.31}$$

and are illustrated in Fig. A.1. Let us note that annihilation (creation) operators correspond to ingoing (outgoing) arrows.

In the main text, we restrict ourselves to the ph-notation which then explicitly reads

$$G_{ijkl}^{\omega\nu\nu'} = \int d\tau_1 d\tau_2 d\tau_3 e^{i\nu_n\tau_1} e^{-i(\nu_n - \omega_m)\tau_2} e^{i(\nu'_n - \omega_m)\tau_3} G_{ijkl}(\tau_1, \tau_2, \tau_3, 0), \tag{A.32}$$

see Section 2.5.4.2.

⁷⁰The substitution also shift the integral interval from $[0, \beta]$ to $[-\tau_4, \beta - \tau_4]$. Similar to Appendix A.1.1.4, both the prefactor $e^{i\nu_j\tau_j}$ and the Green's function itself is antiperiodic with respect to τ_j and subsequently any integral of the length β is equal to the integral from 0 to β .

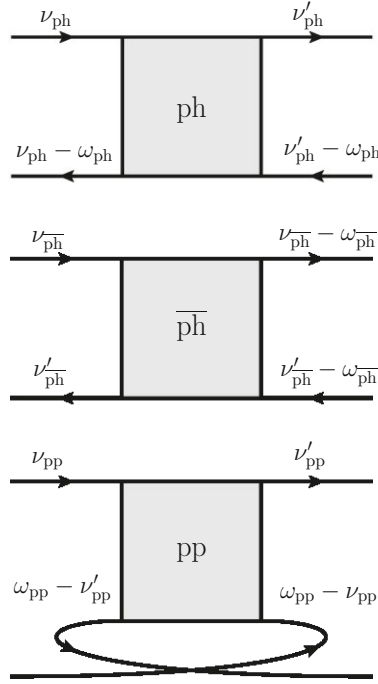


Figure A.1: The three different frequency notations: In the top panel the particle-hole (ph) notation, in the middle panel the transverse particle-hole ($\overline{\text{ph}}$) notation and in the bottom panel the particle-particle (pp) notation. These notations naturally appear when considering the Bethe-Salpeter equations in the ph, $\overline{\text{ph}}$ and pp channel. Of course, a two-particle Green's function can be equivalently represented in all three frequency notations.

A.1.2 Equation of motion

In order to arrive at the Green's function expressions used in the main text, one starts with the derivative of the (one-particle) one-particle Green's function with respect to its imaginary time argument. For a lattice Hamiltonian separated into a one-particle and a two-particle part via

$$\mathcal{H} = \underbrace{\sum_{\mathbf{k}, \sigma} \sum_{lm} h_{lm}^{\mathbf{k}} \hat{c}_{\mathbf{k}l, \sigma}^{\dagger} \hat{c}_{\mathbf{k}m, \sigma}}_{\mathcal{H}_0} + \underbrace{\frac{1}{2} \sum_{\substack{\mathbf{q} \mathbf{k} \mathbf{k}' \\ l' m m' \\ \sigma \sigma'}} U_{lm' m l} \hat{c}_{\mathbf{k}' - \mathbf{q}, m' \sigma}^{\dagger} \hat{c}_{\mathbf{k}, l \sigma'}^{\dagger} \hat{c}_{\mathbf{k} - \mathbf{q}, m \sigma} \hat{c}_{\mathbf{k}', l' \sigma'}}_{\mathcal{U}}, \quad (\text{A.33})$$

where we Fourier transformed the on-site interaction term of Eq. (2.18), we exploit the expression of the derivative of a Heisenberg operator

$$\partial_{\tau} \hat{c}_{\mathbf{k}, \sigma}(\tau) = \partial_{\tau} \left(e^{\tau \mathcal{H}} \hat{c}_{\mathbf{k}, \sigma} e^{-\tau \mathcal{H}} \right) = \left[\mathcal{H}, \hat{c}_{\mathbf{k}, \sigma}(\tau) \right]. \quad (\text{A.34})$$

Performing the derivative explicitly one finds the so-called Schwinger-Dyson equation

$$\begin{aligned}
\frac{d}{d\tau} G_{mm'}^{\mathbf{k}}(\tau) &= -\frac{d}{d\tau} \left\langle T_{\tau} \left[\hat{c}_{\mathbf{k}m\sigma}(\tau) \hat{c}_{\mathbf{k}m'\sigma}^{\dagger}(0) \right] \right\rangle \\
&= -\frac{d}{d\tau} \left[\Theta(\tau) \left\langle \hat{c}_{\mathbf{k}m\sigma}(\tau) \hat{c}_{\mathbf{k}m'\sigma}^{\dagger}(0) \right\rangle - \Theta(-\tau) \left\langle \hat{c}_{\mathbf{k}m'\sigma}^{\dagger}(0) \hat{c}_{\mathbf{k}m\sigma}(\tau) \right\rangle \right] \\
&= -\delta(\tau) \left\langle \hat{c}_{\mathbf{k}m\sigma}(\tau) \hat{c}_{\mathbf{k}m'\sigma}^{\dagger}(0) \right\rangle - \Theta(\tau) \left\langle \left[\mathcal{H}, \hat{c}_{\mathbf{k}m\sigma}(\tau) \right] \hat{c}_{\mathbf{k}m'\sigma}^{\dagger}(0) \right\rangle \\
&\quad - \delta(\tau) \left\langle \hat{c}_{\mathbf{k}m'\sigma}^{\dagger}(0) \hat{c}_{\mathbf{k}m\sigma}(\tau) \right\rangle + \Theta(-\tau) \left\langle \hat{c}_{\mathbf{k}m'\sigma}^{\dagger}(0) \left[\mathcal{H}, \hat{c}_{\mathbf{k}m\sigma}(\tau) \right] \right\rangle \\
&= -\delta(\tau) \delta_{mm'} - \left\langle T_{\tau} \left[\left[\mathcal{H}, \hat{c}_{\mathbf{k}m\sigma}(\tau) \right] \hat{c}_{\mathbf{k}m'\sigma}^{\dagger}(0) \right] \right\rangle \\
&= -\delta(\tau) \delta_{mm'} - \underbrace{\left\langle T_{\tau} \left[\left[\mathcal{H}_0, \hat{c}_{\mathbf{k}m\sigma}(\tau) \right] \hat{c}_{\mathbf{k}m'\sigma}^{\dagger}(0) \right] \right\rangle}_{[\Sigma G]_{mm'}^{\mathbf{k}}},
\end{aligned} \tag{A.35}$$

where σ is the spin-index, m, m' are the orbital indices and \mathbf{k} is the momentum vector. In this first step, we focus on the derivation of the non-interacting Green's function, i.e. we focus purely on the $[\mathcal{H}_0, \hat{c}_{\mathbf{k}m\sigma}(\tau)]$ commutator.

A.1.2.1 Lattice Green's function

With the general (anti-)commutator rules

$$\begin{aligned}
[AB, C] &= A[B, C] + [A, C]B \\
&= A\{B, C\} - \{A, C\}B,
\end{aligned} \tag{A.36}$$

we obtain the two emerging commutator expressions

$$\begin{aligned}
[\hat{c}_1^{\dagger} \hat{c}_2, \hat{c}_3] &= \hat{c}_1^{\dagger} \{\hat{c}_2, \hat{c}_3\} - \{\hat{c}_1^{\dagger}, \hat{c}_3\} \hat{c}_2 \\
&= -\delta_{1,3} \hat{c}_2
\end{aligned} \tag{A.37}$$

and

$$\begin{aligned}
[\hat{c}_1^{\dagger} \hat{c}_2^{\dagger} \hat{c}_3 \hat{c}_4, \hat{c}_5] &= -\{\hat{c}_5, \hat{c}_1^{\dagger}\} \hat{c}_2^{\dagger} \hat{c}_3 \hat{c}_4 + \hat{c}_1^{\dagger} \{\hat{c}_5, \hat{c}_2^{\dagger}\} \hat{c}_3 \hat{c}_4 - \hat{c}_1^{\dagger} \hat{c}_2^{\dagger} \{\hat{c}_5, \hat{c}_3\} \hat{c}_4 + \hat{c}_1^{\dagger} \hat{c}_2^{\dagger} \hat{c}_3 \{\hat{c}_5, \hat{c}_4\} \\
&= -\delta_{5,1} \hat{c}_2^{\dagger} \hat{c}_3 \hat{c}_4 + \hat{c}_1^{\dagger} \delta_{5,2} \hat{c}_3 \hat{c}_4.
\end{aligned} \tag{A.38}$$

We can therefore calculate the commutator with \mathcal{H}_0 from Eq. (2.131)

$$\begin{aligned}
[\mathcal{H}_0, \hat{c}_{\mathbf{k}m\sigma}(\tau)] &= \sum_{\substack{\mathbf{a} \\ xy \\ \rho}} h_{xy}^{\mathbf{a}} \left[\hat{c}_{\mathbf{a},x\rho}^{\dagger} \hat{c}_{\mathbf{a}y\rho}, \hat{c}_{\mathbf{k}m\sigma}(\tau) \right] \\
&= -\sum_{\substack{\mathbf{a} \\ xy \\ \rho}} h_{xy}^{\mathbf{k}} \delta_{\mathbf{a},\mathbf{k}} \delta_{x,m} \delta_{\rho,\sigma} \hat{c}_{\mathbf{a}y\rho}(\tau) = -\sum_y h_{my}^{\mathbf{k}} \hat{c}_{\mathbf{k}y\sigma}(\tau).
\end{aligned} \tag{A.39}$$

Inserting this relation back in (2.131) we get

$$\begin{aligned} \frac{d}{d\tau} G_{0,mm'}^{\mathbf{k}}(\tau) &= -\delta(\tau)\delta_{mm'} - \left\langle T_{\tau} \left[\left[\mathcal{H}_0, \hat{c}_{\mathbf{k}m\sigma}(\tau) \right] \hat{c}_{\mathbf{k}m'\sigma}^{\dagger}(0) \right] \right\rangle \\ &= -\delta(\tau)\delta_{mm'} + \sum_y h_{my}^{\mathbf{k}} \left\langle T_{\tau} \left[\hat{c}_{\mathbf{k}y\sigma}(\tau) \hat{c}_{\mathbf{k}m'\sigma}^{\dagger}(0) \right] \right\rangle = -\delta(\tau)\delta_{mm'} - \sum_y h_{my}^{\mathbf{k}} G_{0,ym'}^{\mathbf{k}}(\tau). \end{aligned} \quad (\text{A.40})$$

Applying the Fourier transform with respect to the imaginary time τ to both sides of the equation we get to an explicit expression for the Green's function. The derivative is transformed by

$$\begin{aligned} \mathcal{F} \left[\frac{d}{d\tau} G_{mm'}^{\mathbf{k}}(\tau) \right] &= \int_0^{\beta} e^{i\nu_n \tau} \frac{d}{d\tau} \left(G_{mm'}^{\mathbf{k}}(\tau) \right) d\tau = \left[e^{i\nu_n \tau} G_{mm'}^{\mathbf{k}}(\tau) \right]_{0^-}^{\beta^-} - \int_0^{\beta} \frac{d}{d\tau} \left(e^{i\nu_n \tau} \right) G_{mm'}^{\mathbf{k}}(\tau) d\tau \\ &= \underbrace{-G_{mm'}^{\mathbf{k}}(\beta) - G_{mm'}^{\mathbf{k}}(0^-)}_{\equiv 0 \text{ (KMS)}} - i\nu_n \int_0^{\beta} e^{i\nu_n \tau} G_{mm'}^{\mathbf{k}}(\tau) d\tau = -i\nu_n \mathcal{F} \left[G_{mm'}^{\mathbf{k}}(\tau) \right] = -i\nu_n G_{mm'}^{\mathbf{k}} \end{aligned} \quad (\text{A.41})$$

and we finally arrive at

$$-i\nu_n G_{0,mm'}^{\mathbf{k}} = -\delta_{mm'} - \sum_y h_{my}^{\mathbf{k}} G_{0,ym'}^{\mathbf{k}} \quad (\text{A.42})$$

which reads in matrix form

$$\sum_y \left[(i\nu_n + \mu) \delta_{my} - h_{my}^{\mathbf{k}} \right] G_{0,ym'}^{\mathbf{k}} = \delta_{mm'}. \quad (\text{A.43})$$

We expanded $\varepsilon_{\mathbf{k}m_y} \rightarrow \varepsilon_{\mathbf{k}m_y} - \mu\delta_{m_y}$ in conformance with the abbreviated grand canonical form of $\mathcal{H} \rightarrow \mathcal{H} - \mu\mathcal{N}$ and arrived at the non-interacting Green's function G_0 in the orbital basis. For the sake of illustration, the matrix equation for two orbitals reads

$$\left(\begin{bmatrix} i\nu_n + \mu & 0 \\ 0 & i\nu_n + \mu \end{bmatrix} - \begin{bmatrix} h_{11}^{\mathbf{k}} & h_{12}^{\mathbf{k}} \\ h_{21}^{\mathbf{k}} & h_{22}^{\mathbf{k}} \end{bmatrix} \right) \times \begin{bmatrix} G_{11}^{\mathbf{k}} & G_{12}^{\mathbf{k}} \\ G_{21}^{\mathbf{k}} & G_{22}^{\mathbf{k}} \end{bmatrix}_0 = \begin{bmatrix} 1 & 0 \\ 0 & 1 \end{bmatrix}. \quad (\text{A.44})$$

A.1.2.2 Self-energy via ΣG

From the Dyson equation

$$G = G_0 + G_0 \Sigma G \quad (\text{A.45})$$

we can deduct that the hitherto ignored interaction term, see Eq. (2.131), represents the self-energy contribution $[\Sigma G]_{mm'}^{\mathbf{k}}$

$$\begin{aligned} -i\nu_n G_{mm'}^{\mathbf{k}} &= -\delta_{mm'} - \sum_y h_{my}^{\mathbf{k}} G_{ym'}^{\mathbf{k}} - \underbrace{[\Sigma G]_{mm'}^{\mathbf{k}}}_{\text{from } \mathcal{U} \text{ commutator}} \\ \implies \sum_y \left[(i\nu_n + \mu) \delta_{my} - h_{my}^{\mathbf{k}} - \Sigma_{my}^{\mathbf{k}} \right] G_{ym'}^{\mathbf{k}} &= \delta_{mm'}. \end{aligned} \quad (\text{A.46})$$

With \mathcal{U} expressed in a general, local, multi-orbital form, see Section 2.2.2, let us now explicitly calculate this contribution. With the emerging commutator simplified via Eq. (A.38)

$$\left[\mathcal{U}, \hat{c}_{\mathbf{k}m\sigma}(\tau) \right] = \frac{1}{2} \sum_{\substack{\mathbf{a}\mathbf{b}\mathbf{b}' \\ x'yy' \\ \rho\rho'}} U_{xy'yx'} \underbrace{\left[\hat{c}_{\mathbf{b}'-\mathbf{a},y'\rho}^\dagger \hat{c}_{\mathbf{b}x\rho'}^\dagger \hat{c}_{\mathbf{b}-\mathbf{a},y\rho'} \hat{c}_{\mathbf{b}'x'\rho'} \hat{c}_{\mathbf{k}m\sigma}(\tau) \right]}_{-\delta_{\mathbf{b}'-\mathbf{a},\mathbf{k}} \delta_{y',m} \delta_{\rho,\sigma} \hat{c}_{\mathbf{b}x\rho'}^\dagger \hat{c}_{\mathbf{b}-\mathbf{a},y\rho'} \hat{c}_{\mathbf{b}'x'\rho'} + \hat{c}_{\mathbf{b}'-\mathbf{a},y'\rho}^\dagger \delta_{\mathbf{b},\mathbf{k}} \delta_{x,m} \delta_{\rho',\sigma} \hat{c}_{\mathbf{b}-\mathbf{a},y\rho'} \hat{c}_{\mathbf{b}'x'\rho'}}, \quad (\text{A.47})$$

the first term of the commutator simplifies to

$$\begin{aligned} -\frac{1}{2} \sum_{\substack{\mathbf{a}\mathbf{b}\mathbf{b}' \\ x'yy' \\ \rho\rho'}} U_{xy'yx'} \left(\delta_{\mathbf{b}'-\mathbf{a},\mathbf{k}} \delta_{y',m} \delta_{\rho,\sigma} \hat{c}_{\mathbf{b}x\rho'}^\dagger \hat{c}_{\mathbf{b}-\mathbf{a},y\rho'} \hat{c}_{\mathbf{b}'x'\rho'} \right) (\tau) &= -\frac{1}{2} \sum_{\substack{\mathbf{a}\mathbf{b} \\ xx'y \\ \rho'}} U_{xmyx'} \left(\hat{c}_{\mathbf{b}x\rho'}^\dagger \hat{c}_{\mathbf{b}-\mathbf{a},y\rho'} \hat{c}_{\mathbf{k}+\mathbf{a},x'\sigma} \right) (\tau) \\ &= -\frac{1}{2} \sum_{\substack{\mathbf{q}\mathbf{k}' \\ lh'n \\ \sigma'}} U_{lmnh} \left(\hat{c}_{\mathbf{k}'-\mathbf{q},l\sigma'}^\dagger \hat{c}_{\mathbf{k}'n\sigma'} \hat{c}_{\mathbf{k}-\mathbf{q},h\sigma} \right) (\tau) \\ &= -\frac{1}{2} \sum_{\substack{\mathbf{q}\mathbf{k}' \\ lh'n \\ \sigma'}} U_{mlhn} \left(\hat{c}_{\mathbf{k}'-\mathbf{q}',l\sigma'}^\dagger \hat{c}_{\mathbf{k}'n\sigma'} \hat{c}_{\mathbf{k}-\mathbf{q},h\sigma} \right) (\tau), \end{aligned} \quad (\text{A.48})$$

where in the second line we renamed $x \rightarrow l$, $y \rightarrow n$, $x' \rightarrow h$, $\mathbf{a} \rightarrow -\mathbf{q}$, $\mathbf{b} \rightarrow \mathbf{k}' - \mathbf{q}$ and $\rho' \rightarrow \sigma'$ and in the third line exploited $U_{lmhn} \equiv U_{mlnh}$. The second term of the commutator simplifies to

$$\begin{aligned} \frac{1}{2} \sum_{\substack{\mathbf{a}\mathbf{b}\mathbf{b}' \\ x'yy' \\ \rho\rho'}} U_{xy'yx'} \left(\hat{c}_{\mathbf{b}'-\mathbf{a},y'\rho}^\dagger \delta_{\mathbf{b},\mathbf{k}} \delta_{x,m} \delta_{\rho',\sigma} \hat{c}_{\mathbf{b}-\mathbf{a},y\rho'} \hat{c}_{\mathbf{b}'x'\rho'} \right) (\tau) &= \frac{1}{2} \sum_{\substack{\mathbf{a}\mathbf{b}' \\ x'yy' \\ \rho}} U_{my'yx'} \left(\hat{c}_{\mathbf{b}'-\mathbf{a},y'\rho}^\dagger \hat{c}_{\mathbf{k}-\mathbf{a},y\sigma} \hat{c}_{\mathbf{b}'x'\rho} \right) (\tau) \\ &= \frac{1}{2} \sum_{\substack{\mathbf{q}\mathbf{k}' \\ lh'n \\ \sigma'}} U_{mlhn} \left(\hat{c}_{\mathbf{k}'-\mathbf{q},l\sigma'}^\dagger \hat{c}_{\mathbf{k}-\mathbf{q},h\sigma} \hat{c}_{\mathbf{k}'n\sigma'} \right) (\tau), \end{aligned} \quad (\text{A.49})$$

where in the last line we renamed $\mathbf{a} \rightarrow \mathbf{q}$, $\mathbf{b}' \rightarrow \mathbf{k}'$, $y' \rightarrow l$, $y \rightarrow h$, $x' \rightarrow n$ and $\rho \rightarrow \sigma'$. Thus, we find two identical terms that can be directly inserted into our initial equation

$$\begin{aligned} [\Sigma G]_{mm'}^{\mathbf{k}}(\tau) &= \sum_{\substack{\mathbf{q}\mathbf{k}' \\ lh'n \\ \sigma'}} U_{mlhn} \left\langle T_\tau \left[\hat{c}_{\mathbf{k}'-\mathbf{q}',l\sigma'}^\dagger(\tau^+) \hat{c}_{\mathbf{k}-\mathbf{q},h\sigma}(\tau) \hat{c}_{\mathbf{k}'n\sigma'}(\tau) \hat{c}_{\mathbf{k}m'\sigma}^\dagger(0) \right] \right\rangle \\ &= \sum_{\substack{\mathbf{q}\mathbf{k}' \\ lh'n \\ \sigma'}} U_{mlhn} \left\langle T_\tau \left[\hat{c}_{\mathbf{k}'n\sigma'}(\tau) \hat{c}_{\mathbf{k}'-\mathbf{q}',l\sigma'}^\dagger(\tau^+) \hat{c}_{\mathbf{k}-\mathbf{q},h\sigma}(\tau) \hat{c}_{\mathbf{k}m'\sigma}^\dagger(0) \right] \right\rangle \\ &= \lim_{\tau' \rightarrow \tau^+} \sum_{\substack{\mathbf{q}\mathbf{k}' \\ lh'n \\ \sigma'}} U_{mlhn} G_{nlhm'}^{\mathbf{q}\mathbf{k}'\mathbf{k}}(\tau, \tau', \tau), \end{aligned} \quad (\text{A.50})$$

where we employed the SU(2) symmetric notation of the two-particle Green's function $G_{\sigma'\sigma} \equiv G_{\sigma'\sigma'\sigma\sigma}$. We also introduced the imaginary time limit in order to perform a separate evaluation of the disconnected terms

$$\begin{aligned} [\Sigma G]_{mm'}^{\mathbf{k}}(\tau) &= \lim_{\tau' \rightarrow \tau^+} \sum_{\substack{\mathbf{q}\mathbf{k}' \\ lh\bar{n} \\ \sigma'}} U_{mlhn} \left[G_{nlhm'}^{\mathbf{q}\mathbf{k}'\mathbf{k} \text{ con}}(\tau, \tau', \tau) \right. \\ &\quad \left. + \delta_{\mathbf{q}\mathbf{0}} G_{nl}^{\mathbf{k}'}(\tau - \tau') G_{hm'}^{\mathbf{k}}(\tau) - \delta_{\mathbf{k}\mathbf{k}'} \delta_{\sigma\sigma'} G_{nm'}^{\mathbf{k}'}(\tau) G_{hl}^{\mathbf{k}-\mathbf{q}}(\tau - \tau') \right] \\ &= \sum_{\substack{\mathbf{q}\mathbf{k}' \\ lh\bar{n} \\ \sigma'}} U_{mlhn} \left[G_{nlhm'}^{\mathbf{q}\mathbf{k}'\mathbf{k} \text{ con}}(\tau, \tau, \tau) + \delta_{\mathbf{q}\mathbf{0}} n_{lh}^{\mathbf{k}'} G_{hm'}^{\mathbf{k}}(\tau) - \delta_{\mathbf{k}\mathbf{k}'} \delta_{\sigma\sigma'} G_{nm'}^{\mathbf{k}'}(\tau) n_{lh}^{\mathbf{k}-\mathbf{q}} \right], \end{aligned} \quad (\text{A.51})$$

where we used the relation to the occupation number

$$\begin{aligned} \lim_{\tau' \rightarrow \tau^+} G_{nl}^{\mathbf{k}'}(\tau - \tau') &= - \lim_{\tau' \rightarrow \tau^+} \langle T_{\tau} [\hat{c}_{\mathbf{k}'n\sigma'}(\tau) \hat{c}_{\mathbf{k}'l\sigma'}^{\dagger}(\tau')] \rangle \\ &= \lim_{\tau' \rightarrow \tau^+} \langle \hat{c}_{\mathbf{k}'l\sigma'}^{\dagger}(\tau') \hat{c}_{\mathbf{k}'n\sigma'}(\tau) \rangle = n_{lh}^{\mathbf{k}'}. \end{aligned} \quad (\text{A.52})$$

When applying the Fourier transform to both sides of the equation we exploit the fact that transforming the equal-time object is equivalent to a summation over one fermionic and the bosonic frequency.

$$\int_0^{\beta} d\tau e^{i\nu_n \tau} G_{nlhm'}^{\mathbf{q}\mathbf{k}'\mathbf{k} \text{ con}}(\tau, \tau, \tau) = G_{nlhm'}^{\mathbf{q}\mathbf{k}'\mathbf{k} \text{ con}} = \frac{1}{\beta^2} \sum_{\omega_m \nu_n} G_{nlhm'}^{\mathbf{q}\mathbf{k}'\mathbf{k} \text{ con}}. \quad (\text{A.53})$$

Thus, we get the expression

$$[\Sigma G]_{mm'}^{\mathbf{k}} = \frac{1}{\beta^2} \sum_{\substack{\mathbf{q}\mathbf{k}' \\ lh\bar{n} \\ \sigma'}} U_{mlhn} G_{nlhm'}^{\mathbf{q}\mathbf{k}'\mathbf{k} \text{ con}} + \sum_{\substack{\mathbf{q}\mathbf{k}' \\ lh\bar{n} \\ \sigma'}} U_{mlhn} \left[\delta_{\mathbf{q}\mathbf{0}} n_{lh}^{\mathbf{k}'} G_{hm'}^{\mathbf{k}} - \delta_{\mathbf{k}\mathbf{k}'} \delta_{\sigma\sigma'} G_{nm'}^{\mathbf{k}} n_{lh}^{\mathbf{k}-\mathbf{q}} \right], \quad (\text{A.54})$$

from which we can extract the connected (first line) and the Hartree-Fock self-energy contribution (second line) by dividing off the right hand Green's function (the term "connected" originates from the connected part of the two-particle Green's function which might be misleading at first glance)

$$\begin{aligned} \Sigma_{mm'}^{\mathbf{k}} &= \sum_{l'} [\Sigma G]_{ml'}^{\mathbf{k}} [G^{-1}]_{l'm'}^{\mathbf{k}} \\ &= \Sigma_{mm'}^{\mathbf{k} \text{ con}} + \Sigma_{mm'}^{\mathbf{k} \text{ HF}} \end{aligned} \quad (\text{A.55})$$

with

$$\begin{aligned}
\Sigma_{mm'}^{\mathbf{k}\text{ HF}} &= \sum_{\substack{\mathbf{q}\mathbf{k}' \\ l'lh'n \\ \sigma'}} U_{mlhn} \left[\delta_{\mathbf{q}\mathbf{0}} n_{ln}^{\mathbf{k}'} G_{hl'}^{\mathbf{k}} - \delta_{\mathbf{k}\mathbf{k}'} \delta_{\sigma\sigma'} G_{nl'}^{\mathbf{k}} n_{lh}^{\mathbf{k}-\mathbf{q}} \right] \left[G^{-1} \right]_{l'm'}^{\mathbf{k}} \\
&= \sum_{\substack{\mathbf{q}\mathbf{k}' \\ l'lh'n \\ \sigma'}} U_{mlhn} \delta_{\mathbf{q}\mathbf{0}} n_{ln}^{\mathbf{k}'} \underbrace{G_{hl'}^{\mathbf{k}}}_{\delta_{hm'}} \left[G^{-1} \right]_{l'm'}^{\mathbf{k}} - \sum_{\substack{\mathbf{q}\mathbf{k}' \\ l'lh'n \\ \sigma'}} U_{mlhn} \delta_{\mathbf{k}\mathbf{k}'} \delta_{\sigma\sigma'} \underbrace{G_{nl'}^{\mathbf{k}}}_{\delta_{nm'}} \left[G^{-1} \right]_{l'm'}^{\mathbf{k}} n_{lh}^{\mathbf{k}-\mathbf{q}} \\
&= \underbrace{\sum_{\substack{\mathbf{k}' \\ ln \\ \sigma'}} U_{mlm'n} n_{ln}^{\mathbf{k}'}}_{\text{Hartree}} - \underbrace{\sum_{\substack{\mathbf{q} \\ lh}} U_{mlhm'} n_{lh}^{\mathbf{k}-\mathbf{q}}}_{\text{Fock}}
\end{aligned} \tag{A.56}$$

and

$$\begin{aligned}
\Sigma_{mm'}^{\mathbf{k}\text{ con}} &= \frac{1}{\beta^2} \sum_{\substack{\mathbf{q}\mathbf{k}' \\ l'lh'n \\ \sigma'}} U_{mlhn} \left[G_{nlhl'}^{\mathbf{q}\mathbf{k}'\mathbf{k}\text{con}} \right] \left[G^{-1} \right]_{l'm'}^{\mathbf{k}} = -\frac{1}{\beta^2} \sum_{\substack{\mathbf{q}\mathbf{k}' \\ l'lh'n, rstu \\ \sigma'}} U_{mlhn} \left[\chi_{0, nlsr}^{\mathbf{q}\mathbf{k}'\mathbf{k}'} F_{rstu}^{\mathbf{q}\mathbf{k}'\mathbf{k}} G_{ul'}^{\mathbf{k}} G_{ht}^{\mathbf{k}-\mathbf{q}} \right] \left[G^{-1} \right]_{l'm'}^{\mathbf{k}} \\
&= -\frac{1}{\beta^2} \sum_{\substack{\mathbf{q}\mathbf{k}' \\ lhn, rst \\ \sigma'}} U_{mlhn} \chi_{0, nlsr}^{\mathbf{q}\mathbf{k}'\mathbf{k}'} F_{rstm'}^{\mathbf{q}\mathbf{k}'\mathbf{k}} G_{ht}^{\mathbf{k}-\mathbf{q}} = -\frac{1}{\beta^2} \sum_{\substack{\mathbf{q}\mathbf{k}' \\ lhn, rst}} U_{mlhn} \chi_{0, nlsr}^{\mathbf{q}\mathbf{k}'\mathbf{k}'} F_{rstm'}^{\mathbf{q}\mathbf{k}'\mathbf{k}} G_{ht}^{\mathbf{k}-\mathbf{q}},
\end{aligned} \tag{A.57}$$

where we employed the “ β -notation” $\chi_0^{\mathbf{q}\mathbf{k}\mathbf{k}} = -G^{\mathbf{k}} G^{\mathbf{k}-\mathbf{q}}$, as introduced in Section 2.5.4.5. Let us note that in the more commonplace one-orbital derivation, the interaction term of the Hamiltonian \mathcal{U} is set up as $U n_{\uparrow} n_{\downarrow}$ which results in an expression for the connected part of the self-energy with full vertex $F_{\uparrow\downarrow}$, see, e.g., Ref. [93]. In the one-orbital case, the numerical evaluation of the $F_{\uparrow\uparrow}$ part of the density vertex F_D cancels due to crossing symmetry. Furthermore, for one orbital (without non-local interaction $V^{\mathbf{q}}$), the Hartree-Fock contributions collapse onto a single term $\Sigma_{\sigma}^{\text{HF}} = U n_{\sigma}$.

A.1.2.3 Impurity Green's function

In this derivation of the impurity Green's function we rely on the Hamiltonian of the single impurity Anderson model, used in the main text

$$\begin{aligned}
\mathcal{H}_{\text{SIAM}} &= \sum_{lm, \sigma} \tilde{\epsilon}_{lm} \hat{d}_{l, \sigma}^{\dagger} \hat{d}_{m, \sigma} + \underbrace{\frac{1}{2} \sum_{\substack{l'm'm' \\ \sigma\sigma'}} U_{lm'm'} \hat{d}_{m', \sigma}^{\dagger} \hat{d}_{l', \sigma'}^{\dagger} \hat{d}_{m, \sigma'} \hat{d}_{l', \sigma}}_{\text{impurity}} \\
&\quad + \underbrace{\sum_{\mathbf{k}, \sigma} \sum_{lm} h_{lm}^{\mathbf{k}} \hat{c}_{\mathbf{k}l, \sigma}^{\dagger} \hat{c}_{\mathbf{k}m, \sigma}}_{\text{bath}} + \underbrace{\sum_{\mathbf{k}, \sigma} \sum_{lm} V_{lm}^{\mathbf{k}} \hat{c}_{\mathbf{k}l, \sigma}^{\dagger} \hat{d}_{m, \sigma} + (V_{lm}^{\mathbf{k}})^* \hat{d}_{m, \sigma}^{\dagger} \hat{c}_{\mathbf{k}l, \sigma}}_{\text{hybridization}}.
\end{aligned} \tag{A.58}$$

The different “fermionic” species generate four distinct Green's function

$$G_{mm'}^{dd}(\tau) = -\left\langle T_\tau \left[\hat{d}_{m\sigma}(\tau) \hat{d}_{m'\sigma}^\dagger(0) \right] \right\rangle, \quad (\text{A.59})$$

$$G_{mm'}^{k,cd}(\tau) = -\left\langle T_\tau \left[\hat{c}_{\mathbf{k}m\sigma}(\tau) \hat{d}_{m'\sigma}^\dagger(0) \right] \right\rangle, \quad (\text{A.60})$$

$$G_{mm'}^{k,dc}(\tau) = -\left\langle T_\tau \left[\hat{d}_{m\sigma}(\tau) \hat{c}_{\mathbf{k}m'\sigma}^\dagger(0) \right] \right\rangle, \quad (\text{A.61})$$

$$G_{mm'}^{k,cc}(\tau) = -\left\langle T_\tau \left[\hat{c}_{\mathbf{k}m\sigma}(\tau) \hat{c}_{\mathbf{k}m'\sigma}^\dagger(0) \right] \right\rangle. \quad (\text{A.62})$$

Exploiting the equation of motion we find

$$\frac{d}{d\tau} G_{mm'}^{dd}(\tau) = -\delta(\tau) \delta_{mm'} - \left\langle T_\tau \left[[\mathcal{H}, \hat{d}_{m\sigma}(\tau)] \hat{d}_{m'\sigma}^\dagger(0) \right] \right\rangle, \quad (\text{A.63})$$

$$\frac{d}{d\tau} G_{mm'}^{k,cd}(\tau) = -\left\langle T_\tau \left[[\mathcal{H}, \hat{c}_{\mathbf{k}m\sigma}(\tau)] \hat{d}_{m'\sigma}^\dagger(0) \right] \right\rangle, \quad (\text{A.64})$$

$$\frac{d}{d\tau} G_{mm'}^{k,dc}(\tau) = -\left\langle T_\tau \left[[\mathcal{H}, \hat{d}_{m\sigma}(\tau)] \hat{c}_{\mathbf{k}m'\sigma}^\dagger(0) \right] \right\rangle, \quad (\text{A.65})$$

$$\frac{d}{d\tau} G_{mm'}^{k,cc}(\tau) = -\delta(\tau) \delta_{mm'} - \left\langle T_\tau \left[[\mathcal{H}, \hat{c}_{\mathbf{k}m\sigma}(\tau)] \hat{c}_{\mathbf{k}m'\sigma}^\dagger(0) \right] \right\rangle, \quad (\text{A.66})$$

where $\delta(\tau)$ is only generated for the “operator diagonal” Green's function through the anticommutator $\{\hat{c}_{\mathbf{k},m\sigma}, \hat{c}_{\mathbf{k},m'\sigma}^\dagger\} = \{\hat{d}_{m\sigma}, \hat{d}_{m'\sigma}^\dagger\} = \delta_{mm'}$, which necessarily vanishes for any other permutation. The commutator with the *non-interacting* part of the Hamiltonian results in

$$[\mathcal{H}_0, \hat{d}_{m,\sigma}(\tau)] = -\sum_y \tilde{\varepsilon}_{my} \hat{d}_{y,\sigma}(\tau) - \sum_{\mathbf{k}y} (V_{ym}^{\mathbf{k}})^* \hat{c}_{\mathbf{k},y\sigma}(\tau), \quad (\text{A.67})$$

$$[\mathcal{H}_0, \hat{c}_{\mathbf{k},m\sigma}(\tau)] = -\sum_y h_{my}^{\mathbf{k}} \hat{c}_{\mathbf{k},y\sigma}(\tau) - \sum_y V_{my}^{\mathbf{k}} \hat{d}_{y\sigma}(\tau). \quad (\text{A.68})$$

Inserted in the original set of equations and applying a Fourier transform on both sides of the equations generates an interconnected set of non-interacting Green's functions

$$-i\nu_n G_{0,mm'}^{\nu_n,dd} = -\delta_{mm'} - \sum_y \tilde{\varepsilon}_{my} G_{0,ym'}^{\nu_n,dd} - \sum_{\mathbf{k}y} (V_{ym}^{\mathbf{k}})^* G_{0,ym'}^{k,cd}, \quad (\text{A.69})$$

$$-i\nu_n G_{0,mm'}^{k,cd} = -\sum_y h_{my}^{\mathbf{k}} G_{0,ym'}^{k,cd} - \sum_y V_{my}^{\mathbf{k}} G_{0,ym'}^{\nu_n,dd}, \quad (\text{A.70})$$

$$-i\nu_n G_{0,mm'}^{k,dc} = -\sum_y \tilde{\varepsilon}_{my} G_{0,ym'}^{k,dc} - \sum_{\mathbf{k}y} (V_{ym}^{\mathbf{k}})^* G_{0,ym'}^{k,cc}, \quad (\text{A.71})$$

$$-i\nu_n G_{0,mm'}^{k,cc} = -\delta_{mm'} - \sum_y h_{my}^{\mathbf{k}} G_{0,ym'}^{k,cc} - \sum_y V_{my}^{\mathbf{k}} G_{0,ym'}^{k,dc}, \quad (\text{A.72})$$

from which we calculate the (non-interacting) impurity Green's function G_0^{dd} . This is easier done in matrix form ($\tilde{\varepsilon}_{lm} \rightarrow \tilde{\varepsilon}$, $h_{lm} \rightarrow H$, $G_{mm'} \rightarrow G$, $V_{lm} \rightarrow V$) which reads

$$[(i\nu_n + \mu)\mathbb{1} - \tilde{\varepsilon}] G_0^{\nu_n, dd} = \mathbb{1} + \sum_{\mathbf{k}} \overline{(V^{\mathbf{k}})^T} G_0^{k, cd}, \quad (\text{A.73})$$

$$[(i\nu_n + \mu)\mathbb{1} - H^{\mathbf{k}}] G_0^{k, cd} = V^{\mathbf{k}} G_0^{\nu_n, dd}. \quad (\text{A.74})$$

Here $\overline{(V^{\mathbf{k}})^T}$ is the conjugate transpose of $V^{\mathbf{k}}$ and μ is the chemical potential that acts on both species of electrons simultaneously and was thus added to both the local energy levels $\tilde{\varepsilon}_{lm} \rightarrow \tilde{\varepsilon}_{lm} - \mu\delta_{lm}$ as well as the bath $h_{lm}^{\mathbf{k}} \rightarrow h_{lm}^{\mathbf{k}} - \mu\delta_{lm}$. Combining Eqs. (A.73-A.74) then results in

$$G_0^{\nu_n, dd} = \left[(i\nu_n + \mu)\mathbb{1} - \tilde{\varepsilon} - \underbrace{\sum_{\mathbf{k}} \overline{(V^{\mathbf{k}})^T} [(i\nu_n + \mu)\mathbb{1} - H^{\mathbf{k}}]^{-1} V^{\mathbf{k}}}_{\Delta(i\nu_n)} \right]^{-1}. \quad (\text{A.75})$$

In the single orbital case ($H_{\mathbf{k}} \rightarrow \varepsilon_{\mathbf{k}}$), this gives the well-known expression for the hybridization function

$$\Delta(i\nu_n) = \sum_{\mathbf{k}} \frac{|V^{\mathbf{k}}|^2}{i\nu_n + \mu - \varepsilon_{\mathbf{k}}}. \quad (\text{A.76})$$

Finalizing the discussion on Green's functions, let us emphasize that the impurity self-energy is derived identically to the lattice self-energy. For brevity's sake, we forgo the detailed derivation, as it does not provide further information. The commutator of the interaction matrix with the impurity annihilation operator leads to

$$[\Sigma G]_{mm'}_{\sigma}(\tau) = \left\langle T_{\tau} \left[[\mathcal{U}, \hat{d}_{m\sigma}(\tau)] \hat{d}_{m'\sigma}^{\dagger}(0) \right] \right\rangle \quad (\text{A.77})$$

which naturally results in a connection of the momentum-independent self-energy with the purely local, impurity two-particle Green's function

$$[\Sigma G]_{mm'}_{\sigma}(\tau) = \lim_{\tau' \rightarrow \tau^+} \sum_{lh\eta} U_{mlh\eta} G_{nlhm'}_{\sigma'\sigma}(\tau, \tau', \tau), \quad (\text{A.78})$$

which can be, again, separated into its disconnected parts (Hartree and Fock) and its connected part. Expanding Eq. (A.63) with ΣG , modifies Eq. (A.69) to

$$-i\nu_n G_{mm'}_{\sigma}^{\nu_n, dd} = -\delta_{mm'} - \sum_y \tilde{\varepsilon}_{my} G_{ym'}_{\sigma}^{\nu_n, dd} - \sum_{\mathbf{k}y} (V_{ym}^{\mathbf{k}})^* G_{ym'}_{\sigma}^{k, cd} - \sum_y \Sigma_{my} G_{ym'}_{\sigma}^{\nu_n, dd}, \quad (\text{A.79})$$

which recovers the Dyson equation of the impurity propagator in the resolved matrix expression

$$G^{\nu_n, dd} = [(i\nu_n + \mu)\mathbb{1} - \tilde{\varepsilon} - \Sigma^{\nu_n} - \Delta^{\nu_n}]^{-1} \equiv \left[[G_0^{\nu_n, dd}]^{-1} - \Sigma^{\nu_n} \right]^{-1}. \quad (\text{A.80})$$

A.2 Matsubara summation technique

In this Section we go over the basic properties of Green's functions used throughout the main text of this thesis. Furthermore we showcase the technique of Matsubara summations, including its pitfalls, that lead to some of the "shorthand transformations" used throughout the main text.

A.2.1 Spectral function

The purely real valued, one-particle Green's function in imaginary times

$$G(\tau) = \frac{1}{\beta} \sum_{\nu_n} e^{-i\nu_n\tau} G(i\nu_n), \quad (\text{A.81})$$

see Fig. A.2 for an example, can be connected to the spectral function $A(\omega)$ via the Hilbert transform

$$G(z) = -\frac{1}{\pi} \int_{-\infty}^{\infty} d\omega \frac{\Im G(\omega)}{z - \omega} \quad (\text{A.82})$$

resulting in

$$G(\tau) = \frac{1}{\beta} \sum_{\nu_n} e^{-i\nu_n\tau} \int_{-\infty}^{\infty} d\omega \frac{A(\omega)}{i\nu_n - \omega}. \quad (\text{A.83})$$

In order to generate the Matsubara sum in Eq. (A.83) we exploit the Fermi function f_{FD} whose poles are all possible fermionic Matsubara frequencies. We define two distinct, generating functions

$$\oint_{R \rightarrow \infty^+} dz \frac{e^{-z\tau}}{z - \omega} f_{FD}(z) \stackrel{!}{=} 0 \quad \tau < 0 \quad (\text{A.84a})$$

$$\oint_{R \rightarrow \infty^+} dz \frac{e^{-z\tau}}{z - \omega} f_{FD}(-z) \stackrel{!}{=} 0 \quad \tau > 0 \quad (\text{A.84b})$$

which, following Jordan's lemma, necessarily have to possess a sufficient decay behavior, such that the integral $\oint_{R \rightarrow \infty^+}$ vanishes: For *negative* imaginary times the Fermi function delivers the exponential suppression in $z \rightarrow \infty^+$ while $e^{-z\tau}$ delivers the suppression towards $z \rightarrow \infty^-$. For *positive* imaginary times, the roles are reversed: the Fermi function delivers the exponential suppression in $z \rightarrow \infty^-$ while $e^{-z\tau}$ results in exponential suppression towards $z \rightarrow \infty^+$.

Applying the residue theorem by evaluating all residues of the complex plane we find for $\tau < 0$

$$\oint_{R \rightarrow \infty^+} dz \frac{e^{-z\tau}}{z - \omega} f_{FD}(z) \stackrel{!}{=} 0 = 2\pi i \left[-\frac{1}{\beta} \sum_{\nu_n} \frac{e^{-i\nu_n\tau}}{i\nu_n - \omega} + e^{-\omega\tau} f_{FD}(\omega) \right] \quad (\text{A.85a})$$

$$G(\tau < 0) = \int_{-\infty}^{\infty} d\omega A(\omega) e^{-\omega\tau} f_{FD}(\omega), \quad (\text{A.85b})$$

and for $\tau > 0$

$$\oint_{R \rightarrow \infty^+} dz \frac{e^{-z\tau}}{z - \omega} f_{FD}(-z) \stackrel{!}{=} 0 = 2\pi i \left[\frac{1}{\beta} \sum_{\nu_n} \frac{e^{-i\nu_n\tau}}{i\nu_n - \omega} + e^{-\omega\tau} f_{FD}(-\omega) \right] \quad (\text{A.86a})$$

$$G(\tau > 0) = - \int_{-\infty}^{\infty} d\omega A(\omega) e^{-\omega\tau} f_{FD}(-\omega), \quad (\text{A.86b})$$

where we employed $\text{Res} f_{FD}(z) = \lim_{z \rightarrow i\nu_n} (z - i\nu_n) f_{FD}(z) = -1/\beta$ and similarly, $\text{Res} f_{FD}(-z) = 1/\beta$. Eqs. (A.85b) and (A.86b) can be validated via the KMS boundary conditions (see Section A.1.1) of the Green's function

$$G(\beta - \tau) = -G(-\tau) \quad \tau > 0 \quad (\text{A.87})$$

yielding

$$\begin{aligned} G(\beta - \tau) &= - \int_{-\infty}^{\infty} d\omega A(\omega) e^{-\omega(\beta - \tau)} f_{FD}(-\omega) \\ &= - \int_{-\infty}^{\infty} d\omega A(\omega) e^{\omega\tau} f_{FD}(\omega) = -G(-\tau). \end{aligned} \quad (\text{A.88})$$

Properties of the imaginary time axis

The integral identities can be exploited to determine the curvature of the Green's function in imaginary times

$$\left. \frac{d^2 G(\tau)}{d\tau^2} \right|_{\tau < 0} = \int_{-\infty}^{\infty} d\omega A(\omega) \omega^2 e^{-\omega\tau} f_{FD}(\omega) \geq 0, \quad (\text{A.89a})$$

$$\left. \frac{d^2 G(\tau)}{d\tau^2} \right|_{\tau > 0} = - \int_{-\infty}^{\infty} d\omega A(\omega) \omega^2 e^{-\omega\tau} f_{FD}(-\omega) \leq 0. \quad (\text{A.89b})$$

The occupation of the band/orbital described via the Green's function can be read off directly from the imaginary axis through

$$n = G(\tau = 0^-) = - \langle T_\tau [\hat{c}(0^-) \hat{c}^\dagger(0)] \rangle = \int_{-\infty}^{\infty} d\omega A(\omega) f_{FD}(\omega). \quad (\text{A.90})$$

On the other hand, the Green's function evaluated in the limit $\tau \rightarrow 0^+$ leads to to the expected discontinuity with step size 1

$$n - 1 = G(\tau = 0^+) = - \langle T_\tau [\hat{c}(0^+) \hat{c}^\dagger(0)] \rangle = - \int_{-\infty}^{\infty} d\omega A(\omega) f_{FD}(-\omega). \quad (\text{A.91})$$

Besides the exact connection to the occupation, one can employ the Green's function to directly check for metallic/insulating behavior. Evaluated for $\tau = -\beta/2$ one finds

$$\begin{aligned} G(\tau = -\frac{\beta}{2}) &= \int_{-\infty}^{\infty} d\omega A(\omega) e^{\omega\beta/2} f_{FD}(\omega) \\ &= \int_{-\infty}^{\infty} d\omega A(\omega) \frac{1}{2 \cosh(\frac{\beta\omega}{2})} = \frac{\pi}{\beta} \overline{A(\omega = 0)}. \end{aligned} \quad (\text{A.92})$$

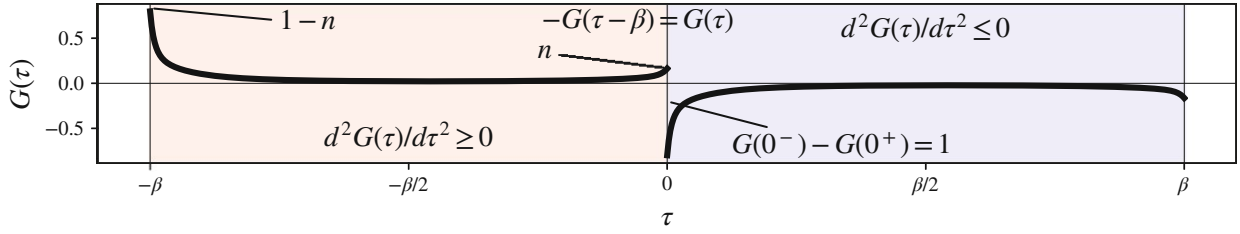


Figure A.2: Exemplary, metallic Green's function on the imaginary time axis τ with (spin-dependent) occupation $n = 0.167$. Through the KMS boundary condition, the Green's function is antiperiodic w.r.t. $\tau \leftrightarrow \tau - \beta$. The metallicity can be ascertained via the finite $G(\tau = -\beta/2) > 0$.

That is, the Green's function evaluated at imaginary time $\tau = -\frac{\beta}{2}$ is representative of the thermal average of the spectral function around the Fermi level. In the zero temperature limit ($T \rightarrow 0$, $\beta = \frac{1}{k_B T} \rightarrow \infty$) this relation becomes exact

$$\lim_{\beta \rightarrow \infty} \int_{-\infty}^{\infty} d\omega A(\omega) \frac{1}{2 \cosh(\frac{\beta\omega}{2})} \frac{\beta}{\pi} = \int_{-\infty}^{\infty} d\omega A(\omega) \delta(\omega) = A(\omega = 0). \quad (\text{A.93})$$

A summary of these properties are illustrated in an exemplary (weakly metallic) Green's function $G(\tau)$ in Fig. A.2.

A.2.2 Occupation

While the connection of the occupation to the imaginary time axis and the spectral function is useful in principle, more often than not we determine the occupation via a Matsubara sum over numerical data. To this end one has to perform the sum

$$n = G(\tau = 0^-) = \frac{1}{\beta} \sum_{\nu_n} e^{-i\nu_n 0^-} G(i\nu_n). \quad (\text{A.94})$$

Numerically this is quite challenging, if not impossible, given the slow decay behavior of the Green's function ($1/n$ with increasing Matsubara frequency). In order to circumvent numerical instabilities, one resorts to the workaround

$$\begin{aligned} n &= \frac{1}{\beta} \sum_{\nu_n} e^{-i\nu_n 0^-} \left[G(i\nu_n) - \frac{1}{i\nu_n} \right] + \frac{1}{\beta} \sum_{\nu_n} e^{-i\nu_n 0^-} \frac{1}{i\nu_n} \\ &= \frac{1}{\beta} \sum_{\nu_n} [\Re G(i\nu_n)] + f_{FD}(0). \end{aligned} \quad (\text{A.95})$$

By removing and adding an identical $1/i\nu_n$ term one splits the summation into two terms: (i) A numerically, stable term ($\propto 1/n^2$) that now no longer requires the explicit inclusion of the exponential factor. Through the functional evenness (oddness) of the real (imaginary) part of the Matsubara

Green's function, it is sufficient to only consider the real part in the summation. (ii) A numerically, unstable term that we evaluate analytically. To this end, one integrates over the contour

$$\begin{aligned} 0 &\stackrel{!}{=} \oint_{R \rightarrow \infty} dz f_{FD}(z) e^{-z0^-} \frac{1}{z - \varepsilon} = 2\pi i \sum_{\text{Res}} f_{FD}(z) e^{-z0^-} \frac{1}{z - \varepsilon} \\ &= 2\pi i \left[f_{FD}(\varepsilon) - \frac{1}{\beta} \sum_{\nu_n} e^{-i\nu_n 0^-} \frac{1}{i\nu_n - \varepsilon} \right], \end{aligned} \quad (\text{A.96})$$

illustrated in Fig. A.3a, which provides the (more generalized) Matsubara sum

$$\frac{1}{\beta} \sum_{\nu_n} e^{-i\nu_n 0^-} \frac{1}{i\nu_n - \varepsilon} = f_{FD}(\varepsilon). \quad (\text{A.97})$$

The combined terms of Eq. (A.96) are here sufficiently suppressed in all directions such that the circular integral $\oint dz$ in the infinite radius limit vanishes. Let us emphasize that convergence is only upheld with $e^{-z0^-} \equiv e^{z0^+}$. The suppression for $\Re z < 0$ is then naturally accompanied by an ordinary complex phase via

$$e^{z0^+} = e^{R \cos(\Phi)0^+} e^{iR \sin(\Phi)0^+} \quad \text{with} \quad \Phi \in \left(\frac{\pi}{2}, \frac{3\pi}{2} \right), \quad R > 0. \quad (\text{A.98})$$

The Matsubara sum of Eq. (A.97) can then be used in the expanded term of Eq. (A.95), generating a ‘‘correction term’’ of $f_{FD}(0) = 1/2$. Evidently, Eq. (A.97) provides the expression for the occupation of a non-interacting Green's function, as $G_0(i\nu_n) = (i\nu_n - \varepsilon)^{-1}$, see Eq. (A.94).

A.2.3 Bare susceptibility

Another commonly employed ‘‘shorthand transformation’’ concerns the bare susceptibility

$$\begin{aligned} \chi_0(\mathbf{q}, i\Omega_m) &= -\frac{1}{\beta} \sum_{\mathbf{k}, \nu_n} G(\mathbf{k}, \nu_n) G(\mathbf{k}-\mathbf{q}, \nu_n - \Omega_m) \\ &= -\frac{1}{\beta} \sum_{\mathbf{k}, \nu_n} \frac{1}{i\nu_n - \varepsilon_{\mathbf{k}}} \frac{1}{i\nu_n - i\Omega_m - \varepsilon_{\mathbf{k}-\mathbf{q}}}. \end{aligned} \quad (\text{A.99})$$

Given non-interacting Green's functions G , the term in the Matsubara sum can be generated via

$$\begin{aligned} 0 &\stackrel{!}{=} \oint_{R \rightarrow \infty} dz f_{FD}(z) \frac{1}{z - \varepsilon_{\mathbf{k}}} \frac{1}{z - i\Omega_m - \varepsilon_{\mathbf{k}-\mathbf{q}}} = 2\pi i \sum_{\text{Res}} f_{FD}(z) \frac{1}{z - \varepsilon_{\mathbf{k}}} \frac{1}{z - i\Omega_m - \varepsilon_{\mathbf{k}-\mathbf{q}}} \\ &= 2\pi i \left[\frac{f_{FD}(\varepsilon_{\mathbf{k}})}{\varepsilon_{\mathbf{k}} - i\Omega_m - \varepsilon_{\mathbf{k}-\mathbf{q}}} + \frac{f_{FD}(\varepsilon_{\mathbf{k}-\mathbf{q}} + i\Omega_m)}{\varepsilon_{\mathbf{k}-\mathbf{q}} + i\Omega_m - \varepsilon_{\mathbf{k}}} - \frac{1}{\beta} \sum_{\nu_n} \frac{1}{i\nu_n - \varepsilon_{\mathbf{k}}} \frac{1}{i\nu_n - i\Omega_m - \varepsilon_{\mathbf{k}-\mathbf{q}}} \right] \end{aligned} \quad (\text{A.100})$$

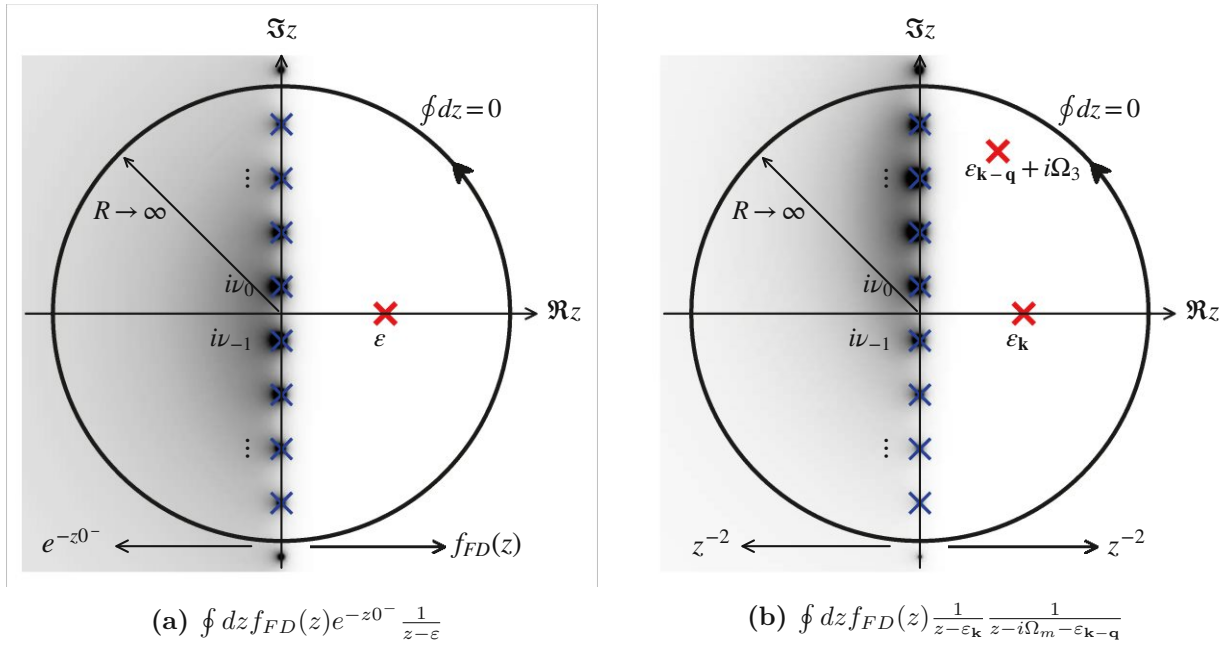


Figure A.3: Exemplary contour integration that generates the (a) occupation and (b) bare susceptibility. The (grayish= background color corresponds to the absolute value of employed complex functions, see Eqs. (A.96) and (A.100), with poles marked by “x”. For the evaluation of the occupation, the “convergence factor” e^{-z0^-} is essential to ensure a functional decay larger than the required z^{-2} .

which we illustrated in Fig. A.3b. Employing $f_{FD}(\varepsilon_{\mathbf{k}-\mathbf{q}} + i\Omega_m) = f_{FD}(\varepsilon_{\mathbf{k}-\mathbf{q}})$, since $e^{i\beta\Omega_m} \equiv 1$, we find the well-known Lindhard expression

$$\begin{aligned} \chi_0(\mathbf{q}, i\Omega_m) &= \sum_{\mathbf{k}} -\frac{f_{FD}(\varepsilon_{\mathbf{k}})}{\varepsilon_{\mathbf{k}} - i\Omega_m - \varepsilon_{\mathbf{k}-\mathbf{q}}} - \frac{f_{FD}(\varepsilon_{\mathbf{k}-\mathbf{q}})}{\varepsilon_{\mathbf{k}-\mathbf{q}} + i\Omega_m - \varepsilon_{\mathbf{k}}} \\ &= -\sum_{\mathbf{k}} \frac{f_{FD}(\varepsilon_{\mathbf{k}-\mathbf{q}}) - f_{FD}(\varepsilon_{\mathbf{k}})}{\varepsilon_{\mathbf{k}-\mathbf{q}} - \varepsilon_{\mathbf{k}} + i\Omega_m}. \end{aligned} \quad (\text{A.101})$$

Let us emphasize here that Eq. (A.99) *must not* be decomposed in a partial sum. In doing so, one would separate a convergent sum ($\propto 1/(\nu_n)^2$) into two terms whose Matsubara sum $\sum_{\nu_n} 1/(\nu_n - \varepsilon)$ maps to the Green’s function evaluated at exactly $\tau = 0$. As we have previously ascertained, $G(\tau)$ is only defined in the limit of $G(\tau = 0^+)$ and $G(\tau = 0^-)$, see Eq. (A.95), constituting this “shortcut” as flawed.

A.3 Two-particle correlation functions

In this Section, we provide more insights into correlation functions that have not hitherto been derived in the main text (for the connection of the current-current correlation function to the optical conductivity via the spectral representation of the Green's function, see Section 2.6). We focus on correlation functions including heat-currents (relevant for the Seebeck and Nernst coefficients) and the effect of a weak, static magnetic field describable within linear response theory.

A.3.1 Heat currents

For the following we consider the heat-current [359]

$$j_Q^\alpha(\mathbf{q} = \mathbf{0}, \tau) = \frac{1}{2} \sum_{\mathbf{k}, l, m, \sigma} \gamma_{lm}^{\mathbf{k}, \alpha} \left[\hat{c}_{\mathbf{k}m\sigma}^\dagger \dot{\hat{c}}_{\mathbf{k}l\sigma} - \dot{\hat{c}}_{\mathbf{k}m\sigma}^\dagger \hat{c}_{\mathbf{k}l\sigma} \right] (\tau), \quad (\text{A.102})$$

and the electric current on the imaginary axis

$$j_E^\alpha(\mathbf{q} = \mathbf{0}, \tau) = -e \sum_{\mathbf{k}, l, m, \sigma} \gamma_{lm}^{\mathbf{k}, \alpha} \left[\hat{c}_{\mathbf{k}m\sigma}^\dagger \hat{c}_{\mathbf{k}l\sigma} \right] (\tau) \quad (\text{A.103})$$

with e as the (positively defined) elementary charge and $\gamma_{lm}^{\mathbf{k}, \alpha}$ as the transition element in the Cartesian α direction. With the equation of motions

$$\dot{\hat{c}}_{\mathbf{k}\sigma}(\tau) = [\mathcal{H}_0, \hat{c}_{\mathbf{k}\sigma}(\tau)] = -\varepsilon_{\mathbf{k}} \hat{c}_{\mathbf{k}\sigma}(\tau) \quad (\text{A.104a})$$

$$\dot{\hat{c}}_{\mathbf{k}\sigma}^\dagger(\tau) = [\mathcal{H}_0, \hat{c}_{\mathbf{k}\sigma}^\dagger(\tau)] = \varepsilon_{\mathbf{k}} \hat{c}_{\mathbf{k}\sigma}^\dagger(\tau), \quad (\text{A.104b})$$

we can evaluate the operator derivative for a non-interacting Hamiltonian \mathcal{H}_0 . Without loss of generality we take one specific time derivative of the two-particle Green's function

$$\begin{aligned} \langle T_\tau \hat{c}_1(\tau_1) \hat{c}_2^\dagger(\tau_2) \dot{\hat{c}}_3(\tau_3) \hat{c}_4^\dagger(\tau_4) \rangle &= \frac{1}{\text{Tr} [e^{-\beta \mathcal{H}_0} S(\beta)]} \text{Tr} \left[e^{-\beta \mathcal{H}_0} T_\tau \hat{c}_1(\tau_1) \hat{c}_2^\dagger(\tau_2) \dot{\hat{c}}_3(\tau_3) \hat{c}_4^\dagger(\tau_4) S(\beta) \right] \\ &= \frac{-\varepsilon_3}{\text{Tr} [e^{-\beta \mathcal{H}_0} S(\beta)]} \text{Tr} \left[e^{-\beta \mathcal{H}_0} T_\tau \hat{c}_1(\tau_1) \hat{c}_2^\dagger(\tau_2) \hat{c}_3(\tau_3) \hat{c}_4^\dagger(\tau_4) S(\beta) \right] \end{aligned} \quad (\text{A.105})$$

and exploit the S-matrix to rewrite the two-particle Green's function into an expectation value w.r.t. the non-interacting system. Here $S(\beta)$ is the S-matrix defined by $S(\tau) = S(\tau_1 - \tau_2) = e^{\mathcal{H}_0 \tau_1} e^{\mathcal{H}(\tau_1 - \tau_2)} e^{-\mathcal{H}_0 \tau_2}$ that builds the theoretical basis upon which one is able generate all possible Feynman diagrams in a perturbation approach.⁷¹

In this expectation value with respect to the non-interacting system, we are allowed to evaluate the derivatives of the operators and perform the necessary Wick contractions that ultimately generate

⁷¹This is done by "solving" the S-matrix via $S(\tau) = T_\tau \exp(-\int_0^\tau d\tau' (\mathcal{H} - \mathcal{H}_0)(\tau'))$, expanding the exponential inside the expectation value and evaluating the expectation value with respect to the non-interacting system [522, 523].

the dressed bubble diagram we are interested in. After this separation of terms we may “reabsorb” the generated energies of Eqs. (A.104) to restore the operator derivative. In short, Wick contractions may be applied to operator derivatives in the same way as “regular” creation/annihilation operators.

A.3.1.1 Heat-current-current

With this property in mind the heat-current-current correlation function can be expanded to

$$\begin{aligned}
\chi_{21}^{\alpha\beta}(\mathbf{q} = \mathbf{0}, \tau) &= \left\langle T_\tau j_Q^\alpha(\mathbf{q} = \mathbf{0}, \tau_1) j_E^\beta(\mathbf{q} = \mathbf{0}, \tau_2) \right\rangle \\
&= -\frac{e}{2} \sum_{\substack{\mathbf{k}, \mathbf{k}', \sigma, \sigma' \\ l m m' l'}} \gamma_{lm}^{\mathbf{k}, \alpha} \gamma_{m'l'}^{\mathbf{k}', \beta} \left\langle T_\tau \left[\hat{c}_{\mathbf{k}m\sigma}^\dagger \hat{c}_{\mathbf{k}l\sigma} - \hat{c}_{\mathbf{k}m\sigma}^\dagger \hat{c}_{\mathbf{k}l\sigma} \right] (\tau_1) \left[\hat{c}_{\mathbf{k}', l' \sigma'}^\dagger \hat{c}_{\mathbf{k}', m' \sigma'} \right] (\tau_2) \right\rangle \\
&= -\frac{e}{2} \sum_{\substack{\mathbf{k}, \mathbf{k}', \sigma, \sigma' \\ l m m' l'}} \gamma_{lm}^{\mathbf{k}, \alpha} \gamma_{m'l'}^{\mathbf{k}', \beta} \left[\left\langle T_\tau \hat{c}_{\mathbf{k}m\sigma}^\dagger (\tau_1) \hat{c}_{\mathbf{k}l\sigma} (\tau_1) \hat{c}_{\mathbf{k}', l' \sigma'}^\dagger (\tau_2) \hat{c}_{\mathbf{k}', m' \sigma'} (\tau_2) \right\rangle \right. \\
&\quad \left. - \left\langle T_\tau \hat{c}_{\mathbf{k}m\sigma}^\dagger (\tau_1) \hat{c}_{\mathbf{k}l\sigma} (\tau_1) \hat{c}_{\mathbf{k}', l' \sigma'}^\dagger (\tau_2) \hat{c}_{\mathbf{k}', m' \sigma'} (\tau_2) \right\rangle \right]
\end{aligned} \tag{A.106}$$

where the time argument τ is short form for $\tau = \tau_1 - \tau_2$. Employing the aforementioned Wick contractions to generate (dressed) bubble diagrams we find

$$\begin{aligned}
\chi_{21}^{\alpha\beta}(\mathbf{q} = \mathbf{0}, \tau) &= -\frac{e}{2} \sum_{\substack{\mathbf{k}, \mathbf{k}', \sigma, \sigma' \\ l m m' l'}} \gamma_{lm}^{\mathbf{k}, \alpha} \gamma_{m'l'}^{\mathbf{k}', \beta} \left[- \left\langle T_\tau \hat{c}_{\mathbf{k}', m' \sigma'} (\tau_2) \hat{c}_{\mathbf{k}m\sigma}^\dagger (\tau_1) \right\rangle \left\langle T_\tau \hat{c}_{\mathbf{k}l\sigma} (\tau_1) \hat{c}_{\mathbf{k}', l' \sigma'}^\dagger (\tau_2) \right\rangle \right. \\
&\quad \left. + \left\langle T_\tau \hat{c}_{\mathbf{k}', m' \sigma'} (\tau_2) \hat{c}_{\mathbf{k}m\sigma}^\dagger (\tau_1) \right\rangle \left\langle T_\tau \hat{c}_{\mathbf{k}l\sigma} (\tau_1) \hat{c}_{\mathbf{k}', l' \sigma'}^\dagger (\tau_2) \right\rangle \right] \\
&= -\frac{e}{2} \sum_{\substack{\mathbf{k}, \mathbf{k}', \sigma, \sigma' \\ l m m' l'}} \gamma_{lm}^{\mathbf{k}, \alpha} \gamma_{m'l'}^{\mathbf{k}', \beta} \left[- G_{m'm, \sigma}^{\mathbf{k}}(\tau_2 - \tau_1) \partial_{\tau_1} G_{l'l', \sigma}^{\mathbf{k}}(\tau_1 - \tau_2) \delta_{\mathbf{k}, \mathbf{k}'} \delta_{\sigma, \sigma'} \right. \\
&\quad \left. + \partial_{\tau_1} G_{m'm, \sigma}^{\mathbf{k}}(\tau_2 - \tau_1) G_{l'l', \sigma}^{\mathbf{k}}(\tau_1 - \tau_2) \delta_{\mathbf{k}, \mathbf{k}'} \delta_{\sigma, \sigma'} \right]
\end{aligned} \tag{A.107}$$

where we neglected the $\delta(\tau)$ terms stemming from the Green’s function derivatives

$$\partial_{\tau_1} G_{lm, \sigma}^{\mathbf{k}}(\tau_1, \tau_2) = -\delta(\tau_1 - \tau_2) \delta_{lm} - \left\langle T_\tau \partial_{\tau_1} \hat{c}_{\mathbf{k}, l\sigma} (\tau_1) \hat{c}_{\mathbf{k}, m\sigma}^\dagger (\tau_2) \right\rangle, \tag{A.108a}$$

$$\partial_{\tau_2} G_{lm, \sigma}^{\mathbf{k}}(\tau_1, \tau_2) = \delta(\tau_1 - \tau_2) \delta_{lm} - \left\langle T_\tau \hat{c}_{\mathbf{k}, l\sigma} (\tau_1) \partial_{\tau_2} \hat{c}_{\mathbf{k}, m\sigma}^\dagger (\tau_2) \right\rangle, \tag{A.108b}$$

allowing us to only consider the physically relevant (dressed) bubble diagrams. The δ terms would lead to corrections corresponding to orbital occupations since $G(\tau = 0^\pm) \propto n$. Strictly speaking, these

processes do not contribute as they are purely real valued and the Onsager coefficient corresponds to $\Im\chi$. Finally, the Fourier transform results in

$$\begin{aligned}
\chi_{21}^{\alpha\beta}(\mathbf{q} = \mathbf{0}, i\Omega_m) &= \int_0^\beta d\tau e^{i\Omega_m\tau} \chi_{21}^{\alpha\beta}(\mathbf{q} = \mathbf{0}, \tau) \\
&= -\frac{e}{2} \sum_{\substack{\mathbf{k}, \sigma \\ lmm'l'}} \gamma_{lm}^{\mathbf{k}, \alpha} \gamma_{m'l'}^{\mathbf{k}, \beta} \int_0^\beta e^{i\Omega_m\tau} \frac{1}{\beta^2} \sum_{\nu_n, \nu'_n} \left[-e^{i\nu_n\tau} G_{m'm, \sigma}^{(\mathbf{k}, \nu_n)}(-i\nu'_n) e^{-i\nu'_n\tau} G_{ll', \sigma}^{(\mathbf{k}, \nu'_n)} + (i\nu_n) e^{i\nu_n\tau} G_{m'm, \sigma}^{(\mathbf{k}, \nu_n)} e^{-i\nu'_n\tau} G_{ll', \sigma}^{(\mathbf{k}, \nu'_n)} \right] \\
&= -\frac{e}{2} \sum_{\substack{\mathbf{k}, \sigma \\ lmm'l'}} \gamma_{lm}^{\mathbf{k}, \alpha} \gamma_{m'l'}^{\mathbf{k}, \beta} \frac{1}{\beta} \sum_{\nu_n} \left[G_{m'm, \sigma}^{(\mathbf{k}, \nu_n)} G_{ll', \sigma}^{(\mathbf{k}, \nu_n + \Omega_m)} (i\nu_n + i\Omega_m) + G_{m'm, \sigma}^{(\mathbf{k}, \nu_n)} G_{ll', \sigma}^{(\mathbf{k}, \nu_n + \Omega_m)} (i\nu_n) \right] \\
&= -e \sum_{\substack{\mathbf{k}, \sigma \\ lmm'l'}} \gamma_{lm}^{\mathbf{k}, \alpha} \gamma_{m'l'}^{\mathbf{k}, \beta} \frac{1}{\beta} \sum_{\nu_n} G_{m'm, \sigma}^{(\mathbf{k}, \nu_n)} G_{ll', \sigma}^{(\mathbf{k}, \nu_n + \Omega_m)} (i\nu_n + \frac{i\Omega_m}{2}), \tag{A.109}
\end{aligned}$$

where we re-inserted the condition $\tau = \tau_1 - \tau_2$ with $\partial_{\tau_1} = \partial_\tau$ and $\partial_{\tau_2} = -\partial_\tau$, respectively.

The current-heat-current correlation function does not require a full calculation as its connected via

$$\begin{aligned}
\chi_{12}^{\alpha\beta}(\mathbf{q} = \mathbf{0}, \tau) &= \left\langle T_\tau j_E^\alpha(\mathbf{q} = \mathbf{0}, \tau) j_Q^\beta(\mathbf{q} = \mathbf{0}, \tau = 0) \right\rangle \\
&= -\frac{e}{2} \sum_{\substack{\mathbf{k}, \mathbf{k}', \sigma, \sigma' \\ lmm'l'}} \gamma_{lm}^{\mathbf{k}, \alpha} \gamma_{m'l'}^{\mathbf{k}', \beta} \left\langle T_\tau \hat{c}_{\mathbf{k}, m\sigma}^\dagger(\tau) \hat{c}_{\mathbf{k}, l\sigma}(\tau) \left[\hat{c}_{\mathbf{k}'l'\sigma'}^\dagger \dot{\hat{c}}_{\mathbf{k}'m'\sigma'} - \dot{\hat{c}}_{\mathbf{k}'l'\sigma'}^\dagger \hat{c}_{\mathbf{k}'m'\sigma'} \right] \right\rangle \\
&= -\frac{e}{2} \sum_{\substack{\mathbf{k}, \mathbf{k}', \sigma, \sigma' \\ lmm'l'}} \gamma_{lm}^{\mathbf{k}, \alpha} \gamma_{m'l'}^{\mathbf{k}', \beta} \left[\left\langle T_\tau \hat{c}_{\mathbf{k}m\sigma}^\dagger(\tau) \hat{c}_{\mathbf{k}l\sigma}(\tau) \hat{c}_{\mathbf{k}'l'\sigma'}^\dagger \dot{\hat{c}}_{\mathbf{k}'m'\sigma'} \right\rangle - \left\langle T_\tau \hat{c}_{\mathbf{k}m\sigma}^\dagger(\tau) \hat{c}_{\mathbf{k}l\sigma}(\tau) \dot{\hat{c}}_{\mathbf{k}'l'\sigma'}^\dagger \hat{c}_{\mathbf{k}'m'\sigma'} \right\rangle \right] \\
&\equiv \chi_{21}^{\beta\alpha}(\mathbf{q} = \mathbf{0}, -\tau). \tag{A.110}
\end{aligned}$$

The Fourier transform then instead reads

$$\begin{aligned}
\chi_{12}^{\alpha\beta}(\mathbf{q} = \mathbf{0}, i\Omega_m) &= \int_0^\beta d\tau e^{i\Omega_m\tau} \chi_{21}^{\beta\alpha}(\mathbf{q} = \mathbf{0}, -\tau) = \chi_{21}^{\beta\alpha}(\mathbf{q} = \mathbf{0}, -i\Omega_m) \\
&= -e \sum_{\substack{\mathbf{k}, \sigma \\ lmm'l'}} \gamma_{lm}^{\mathbf{k}, \beta} \gamma_{m'l'}^{\mathbf{k}, \alpha} \frac{1}{\beta} \sum_{\nu_n} G_{m'm, \sigma}^{(\mathbf{k}, \nu_n)} G_{ll', \sigma}^{(\mathbf{k}, \nu_n - i\Omega_m)} (i\nu_n - \frac{i\Omega_m}{2}). \tag{A.111}
\end{aligned}$$

A.3.1.2 Heat-current-heat-current

In the same vein, the heat-current-heat-current correlation functions with imaginary time argument $\tau = \tau_1 - \tau_2$ results in

$$\begin{aligned}
\chi_{22}^{\alpha\beta}(\mathbf{q} = \mathbf{0}, \tau) &= \left\langle T_\tau j_Q^\alpha(\mathbf{q} = \mathbf{0}, \tau_1) j_Q^\beta(\mathbf{q} = \mathbf{0}, \tau_2) \right\rangle \\
&= \frac{1}{4} \sum_{\substack{\mathbf{k}, \mathbf{k}', \sigma, \sigma' \\ lmm'l'}} \gamma_{lm}^{\mathbf{k}, \alpha} \gamma_{m'l'}^{\mathbf{k}', \beta} \left\langle T_\tau \left[\hat{c}_{\mathbf{k}m\sigma}^\dagger \hat{c}_{\mathbf{k}l\sigma} - \hat{c}_{\mathbf{k}m\sigma}^\dagger \hat{c}_{\mathbf{k}l\sigma} \right] (\tau_1) \left[\hat{c}_{\mathbf{k}'l'\sigma'}^\dagger \dot{\hat{c}}_{\mathbf{k}'m'\sigma'} - \dot{\hat{c}}_{\mathbf{k}'l'\sigma'}^\dagger \hat{c}_{\mathbf{k}'m'\sigma'} \right] (\tau_2) \right\rangle
\end{aligned}$$

$$\begin{aligned}
&= \frac{1}{4} \sum_{\substack{\mathbf{k}, \mathbf{k}', \sigma, \sigma' \\ lmm'l'}} \gamma_{lm}^{\mathbf{k}, \alpha} \gamma_{m'l'}^{\mathbf{k}', \beta} \\
&\left[\left\langle T_\tau \hat{c}_{\mathbf{k}m\sigma}^\dagger(\tau_1) \hat{c}_{\mathbf{k}l\sigma}(\tau_1) \hat{c}_{\mathbf{k}'l'\sigma'}^\dagger(\tau_2) \hat{c}_{\mathbf{k}'m'\sigma'}(\tau_2) \right\rangle - \left\langle T_\tau \hat{c}_{\mathbf{k}m\sigma}^\dagger(\tau_1) \hat{c}_{\mathbf{k}l\sigma}(\tau_1) \hat{c}_{\mathbf{k}'l'\sigma'}^\dagger(\tau_2) \hat{c}_{\mathbf{k}'m'\sigma'}(\tau_2) \right\rangle \right. \\
&\quad \left. - \left\langle T_\tau \hat{c}_{\mathbf{k}m\sigma}^\dagger(\tau_1) \hat{c}_{\mathbf{k}l\sigma}(\tau_1) \hat{c}_{\mathbf{k}'l'\sigma'}^\dagger(\tau_2) \hat{c}_{\mathbf{k}'m'\sigma'}(\tau_2) \right\rangle + \left\langle T_\tau \hat{c}_{\mathbf{k}m\sigma}^\dagger(\tau_1) \hat{c}_{\mathbf{k}l\sigma}(\tau_1) \hat{c}_{\mathbf{k}'l'\sigma'}^\dagger(\tau_2) \hat{c}_{\mathbf{k}'m'\sigma'}(\tau_2) \right\rangle \right] \\
&= \frac{1}{4} \sum_{\substack{\mathbf{k}, \mathbf{k}', \sigma, \sigma' \\ lmm'l'}} \gamma_{lm}^{\mathbf{k}, \alpha} \gamma_{m'l'}^{\mathbf{k}', \beta} \\
&\left[- \left\langle T_\tau \hat{c}_{\mathbf{k}'m'\sigma'}(\tau_2) \hat{c}_{\mathbf{k}m\sigma}^\dagger(\tau_1) \right\rangle \left\langle T_\tau \hat{c}_{\mathbf{k}l\sigma}(\tau_1) \hat{c}_{\mathbf{k}'l'\sigma'}^\dagger(\tau_2) \right\rangle + \left\langle T_\tau \hat{c}_{\mathbf{k}'m'\sigma'}(\tau_2) \hat{c}_{\mathbf{k}m\sigma}^\dagger(\tau_1) \right\rangle \left\langle T_\tau \hat{c}_{\mathbf{k}l\sigma}(\tau_1) \hat{c}_{\mathbf{k}'l'\sigma'}^\dagger(\tau_2) \right\rangle \right. \\
&\quad \left. + \left\langle T_\tau \hat{c}_{\mathbf{k}'m'\sigma'}(\tau_2) \hat{c}_{\mathbf{k}m\sigma}^\dagger(\tau_1) \right\rangle \left\langle T_\tau \hat{c}_{\mathbf{k}l\sigma}(\tau_1) \hat{c}_{\mathbf{k}'l'\sigma'}^\dagger(\tau_2) \right\rangle - \left\langle T_\tau \hat{c}_{\mathbf{k}'m'\sigma'}(\tau_2) \hat{c}_{\mathbf{k}m\sigma}^\dagger(\tau_1) \right\rangle \left\langle T_\tau \hat{c}_{\mathbf{k}l\sigma}(\tau_1) \hat{c}_{\mathbf{k}'l'\sigma'}^\dagger(\tau_2) \right\rangle \right] \\
&= \frac{1}{4} \sum_{\substack{\mathbf{k}, \mathbf{k}', \sigma, \sigma' \\ lmm'l'}} \gamma_{lm}^{\mathbf{k}, \alpha} \gamma_{m'l'}^{\mathbf{k}', \beta} \delta_{\mathbf{k}, \mathbf{k}'} \delta_{\sigma, \sigma'} \\
&\left[- \partial_{\tau_2} G_{m'm, \sigma}^{\mathbf{k}}(\tau_2 - \tau_1) \partial_{\tau_1} G_{ll', \sigma}^{\mathbf{k}}(\tau_1 - \tau_2) + G_{m'm, \sigma}^{\mathbf{k}}(\tau_2 - \tau_1) \partial_{\tau_1} \partial_{\tau_2} G_{ll', \sigma}^{\mathbf{k}}(\tau_1 - \tau_2) \right. \\
&\quad \left. + \partial_{\tau_1} \partial_{\tau_2} G_{m'm, \sigma}^{\mathbf{k}}(\tau_2 - \tau_1) G_{ll', \sigma}^{\mathbf{k}}(\tau_1 - \tau_2) - \partial_{\tau_1} G_{m'm, \sigma}^{\mathbf{k}}(\tau_2 - \tau_1) \partial_{\tau_2} G_{ll', \sigma}^{\mathbf{k}}(\tau_1 - \tau_2) \right] \quad (\text{A.112})
\end{aligned}$$

where we, again, neglected all $\delta(\tau)$ terms stemming from the Green's function derivatives and consider only bubble diagrams. To be more precise, here we also neglect the double derivative

$$\partial_{\tau_1} \partial_{\tau_2} G_{lm, \sigma}^{\mathbf{k}}(\tau_1, \tau_2) = -\partial_{\tau_2} \delta(\tau_1 - \tau_2) \delta_{lm} - \delta(\tau_1 - \tau_2) \delta_{lm} - \left\langle T_\tau \partial_{\tau_1} \hat{c}_{\mathbf{k}, l\sigma}(\tau_1) \partial_{\tau_2} \hat{c}_{\mathbf{k}, m\sigma}^\dagger(\tau_2) \right\rangle. \quad (\text{A.113})$$

Finally we Fourier transform to Matsubara frequencies where we re-insert $\tau = \tau_1 - \tau_2$ with $\partial_{\tau_1} = \partial_\tau$ and $\partial_{\tau_2} = -\partial_\tau$

$$\begin{aligned}
\chi_{22}^{\alpha\beta}(\mathbf{q} = \mathbf{0}, i\Omega_m) &= \int_0^\beta d\tau e^{i\Omega_m \tau} \chi_{22}^{\alpha\beta}(\mathbf{q} = \mathbf{0}, \tau) \\
&= \frac{1}{4} \sum_{\substack{\mathbf{k}, \sigma \\ lmm'l'}} \gamma_{lm}^{\mathbf{k}, \alpha} \gamma_{m'l'}^{\mathbf{k}, \beta} \int_0^\beta d\tau e^{i\Omega_m \tau} \frac{1}{\beta^2} \sum_{\nu_n, \nu'_n} \\
&\quad \left[(i\nu_n) e^{i\nu_n \tau} G_{m'm, \sigma}^{(\mathbf{k}, \nu_n)}(-i\nu'_n) e^{-i\nu'_n \tau} G_{ll', \sigma}^{(\mathbf{k}, \nu'_n)} - e^{i\nu_n \tau} G_{m'm, \sigma}^{(\mathbf{k}, \nu_n)}(-i\nu'_n)^2 e^{-i\nu'_n \tau} G_{ll', \sigma}^{(\mathbf{k}, \nu'_n)} \right. \\
&\quad \left. - (i\nu_n)^2 e^{i\nu_n \tau} G_{m'm, \sigma}^{(\mathbf{k}, \nu_n)} e^{-i\nu'_n \tau} G_{ll', \sigma}^{(\mathbf{k}, \nu'_n)} + (i\nu_n) e^{i\nu_n \tau} G_{m'm, \sigma}^{(\mathbf{k}, \nu_n)}(-i\nu'_n) e^{-i\nu'_n \tau} G_{ll', \sigma}^{(\mathbf{k}, \nu'_n)} \right]
\end{aligned}$$

$$\begin{aligned}
&= \frac{1}{4} \sum_{\substack{\mathbf{k}, \sigma \\ lmm'l'}} \gamma_{lm}^{\mathbf{k}, \alpha} \gamma_{m'l'}^{\mathbf{k}, \beta} \frac{1}{\beta} \sum_{\nu_n} G_{m'm, \sigma}^{(\mathbf{k}, \nu_n)} G_{l'l, \sigma}^{(\mathbf{k}, \nu_n + \Omega_m)} \left(-4(i\nu_n)^2 - 4(i\nu_n)(i\Omega_m) - (i\Omega_m)^2 \right) \\
&= - \sum_{\substack{\mathbf{k}, \sigma \\ lmm'l'}} \gamma_{lm}^{\mathbf{k}, \alpha} \gamma_{m'l'}^{\mathbf{k}, \beta} \frac{1}{\beta} \sum_{\nu_n} G_{m'm, \sigma}^{(\mathbf{k}, \nu_n)} G_{l'l, \sigma}^{(\mathbf{k}, \nu_n + \Omega_m)} \left(i\nu_n + \frac{i\Omega_m}{2} \right)^2
\end{aligned} \tag{A.114}$$

A.3.1.3 Integral equations

The translation of the Matsubara sums to an integral spanning the real-frequency axis, can either be done by the spectral representation of the Green's function, see Section 2.6 or follow the contour integration sketched in Ref. [359]. The Matsubara sum occurring in the expression for the Onsager coefficients \mathcal{L}_{ab} with $a, b \in \{1, 2\}$ ⁷² can be connected to the integral⁷³

$$\frac{1}{2\pi i} \oint dz f_{FD}(z) G(z) G(z + i\Omega_m) \left(z + \frac{i\Omega_m}{2} \right)^{(a+b-2)} \stackrel{!}{=} - \frac{1}{\beta} \sum_{\nu_n} G(i\nu_n) G(i\nu_n + i\Omega_m) \left(i\nu_n + \frac{i\Omega_m}{2} \right)^{(a+b-2)}. \tag{A.115}$$

Through a deformation of the (anticircular) integral such that possible branch cuts stemming from the Green's functions $G(z)$ and $G(z + i\Omega_m)$ are avoided, see Fig. A.4 we find

$$\begin{aligned}
&\frac{1}{2\pi i} \oint dz f_{FD}(z) G(z) G(z + i\Omega_m) \left(z + \frac{i\Omega_m}{2} \right)^{(a+b-2)} \\
&= \frac{1}{2\pi i} \int_{-\infty}^{\infty} d\varepsilon \left[f_{FD}(\varepsilon + i0^+) G(\varepsilon + i0^+) G(\varepsilon + i\Omega_m + i0^+) \left(\varepsilon + i0^+ + \frac{i\Omega_m}{2} \right)^{(a+b-2)} \right. \\
&\quad - f_{FD}(\varepsilon - i0^+) G(\varepsilon - i0^+) G(\varepsilon + i\Omega_m - i0^+) \left(\varepsilon - i0^+ + \frac{i\Omega_m}{2} \right)^{(a+b-2)} \\
&\quad + f_{FD}(\varepsilon - i\Omega_m + i0^+) G(\varepsilon - i\Omega_m + i0^+) G(\varepsilon + i0^+) \left(\varepsilon + i0^+ - \frac{i\Omega_m}{2} \right)^{(a+b-2)} \\
&\quad \left. - f_{FD}(\varepsilon - i\Omega_m - i0^+) G(\varepsilon - i\Omega_m - i0^+) G(\varepsilon + i0^+) \left(\varepsilon - i0^+ - \frac{i\Omega_m}{2} \right)^{(a+b-2)} \right] \\
&= - \int_{-\infty}^{\infty} d\varepsilon f_{FD}(\varepsilon) A(\varepsilon) \left[G(\varepsilon + i\Omega_m) \left(\varepsilon + \frac{i\Omega_m}{2} \right)^{(a+b-2)} + G(\varepsilon - i\Omega_m) \left(\varepsilon - \frac{i\Omega_m}{2} \right)^{(a+b-2)} \right]
\end{aligned} \tag{A.116}$$

⁷²To be more precise, the integral form of Eq. (A.115) works for \mathcal{L}_{11} , \mathcal{L}_{21} and \mathcal{L}_{22} . For \mathcal{L}_{12} , see Eq. (A.111), the complex integral is instead performed over $f_{FD}(z) G(z) G(z - i\Omega_m) (z - i\Omega_m/2)$. After performing the analytic continuation and taking the DC limit, one however finds the identical end result as for \mathcal{L}_{21} (with reversed directional dependence).

⁷³The resulting Matsubara sum is not strictly convergent for all a and b values due to the insufficient decay behavior for $a + b > 3$. We however still follow this "symbolic" transformation, also commonly used in the literature, see, e.g., Ref. [359, 456]. What is saving the day is that, in the end, we are only interested in the *imaginary* part of χ on the *real*-axis, for which the expression turns out to be convergent.

where we used

$$G_{\text{ret}}(\varepsilon) = G(\varepsilon + i0^+), \quad (\text{A.117a})$$

$$G_{\text{adv}}(\varepsilon) = G(\varepsilon - i0^+) = G_{\text{ret}}^*(\varepsilon), \quad (\text{A.117b})$$

$$A(\varepsilon) = -1/\pi \Im G_{\text{ret}}(\varepsilon). \quad (\text{A.117c})$$

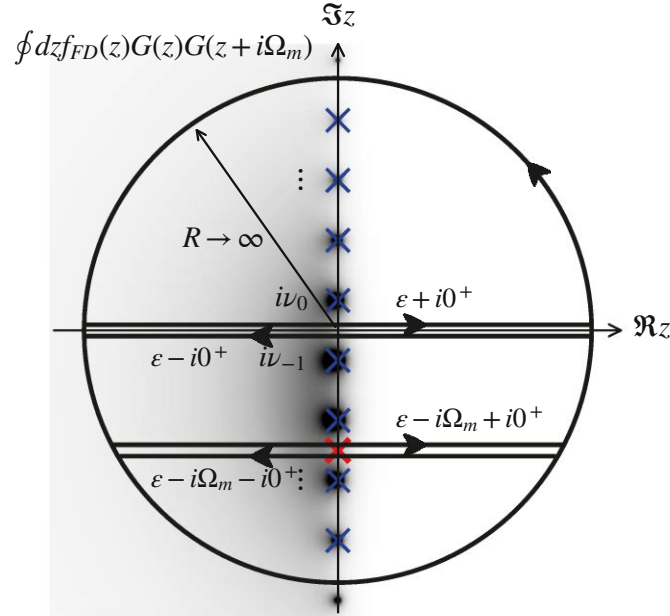


Figure A.4: Contour integration that generates the Matsubara sum occurring in various Onsager coefficients. The anticircular integral is rewritten into four integrals that avoid possible branch cuts of the Green's functions $G(z)$ and $G(z + i\Omega_m)$ at ε and $\varepsilon - i\Omega_m$, respectively.

We can now perform the analytic continuation $i\Omega_m \rightarrow \omega + i0^+$ and taking the limit towards

$$\mathcal{L}_{ab} = \lim_{\omega \rightarrow 0^+} \frac{\Im \chi_{ab}(i\Omega_m \rightarrow \omega + i0^+)}{\omega}, \quad (\text{A.118})$$

which results in

$$\begin{aligned} & - \lim_{\omega \rightarrow 0^+} \frac{1}{\omega} \Im \int_{-\infty}^{\infty} d\varepsilon f_{FD}(\varepsilon) A(\varepsilon) \left[G_{\text{ret}}(\varepsilon + \omega) \left(\varepsilon + \frac{\omega}{2} \right)^{(a+b-2)} + G_{\text{adv}}(\varepsilon - \omega) \left(\varepsilon - \frac{\omega}{2} \right)^{(a+b-2)} \right] \\ & = \lim_{\omega \rightarrow 0^+} \frac{\pi}{\omega} \int_{-\infty}^{\infty} d\varepsilon f_{FD}(\varepsilon) A(\varepsilon) \left[A(\varepsilon + \omega) \left(\varepsilon + \frac{\omega}{2} \right)^{(a+b-2)} - A(\varepsilon - \omega) \left(\varepsilon - \frac{\omega}{2} \right)^{(a+b-2)} \right] \\ & = \lim_{\omega \rightarrow 0^+} \pi \int_{-\infty}^{\infty} d\varepsilon A(\varepsilon) A(\varepsilon + \omega) \left(\varepsilon + \frac{\omega}{2} \right)^{(a+b-2)} \left[\frac{f_{FD}(\varepsilon) - f_{FD}(\varepsilon + \omega)}{\omega} \right] \\ & = \pi \int_{-\infty}^{\infty} d\varepsilon A^2(\varepsilon) \varepsilon^{(a+b-2)} \left(-\frac{df_{FD}}{d\varepsilon} \right). \end{aligned} \quad (\text{A.119})$$

In a system responding to a temperature gradient, the resulting Onsager coefficient $\mathcal{L}_{21}^{\alpha\beta} = \mathcal{L}_{12}^{\beta\alpha}$ will therefore be *positive* for negative charge carriers. Consider a thermally filled band above the Fermi level where $\varepsilon > 0$ with a negative temperature gradient along a chosen axis α : The resulting, positive \mathcal{L}_{12} will generate an electric current that will generate a displaced charge distribution until an energetic counter-balance is created that opposes to the externally applied temperature gradient exactly. Once this steady-state is achieved, the corresponding Seebeck coefficient will then be, per definition, negative, see Eq. (3.61).

A.3.2 Linear response in magnetic field

This Section follows the derivation of the Hall conductivity of Ref. [386]. Since minor typos and errors occur throughout the referenced text, we include the full verbose derivation with its notation adapted to this thesis. The derivations of the higher order linear response terms follow in a similar vein, are however beyond the scope of this Appendix.

Our goal is to calculate the magnetic correction term to the Onsager coefficient

$$\mathcal{L}_{11}^{B,\alpha\beta\gamma} = \lim_{\omega \rightarrow 0^+} \frac{1}{\omega} \Im \left[\frac{\chi_{\mathbf{j}_E \mathbf{j}_E}^{B,\alpha\beta}(\mathbf{q} = \mathbf{0}, \omega)}{B^\gamma} \right] \quad (\text{A.120})$$

through the correlation function

$$\chi_{\mathbf{j}_E \mathbf{j}_E}^{B,\alpha\beta}(\mathbf{q}, \tau) = \frac{1}{V} \left\langle T_\tau j_E^\alpha(\mathbf{q}, \tau) j_E^\beta(\mathbf{0}, 0) \right\rangle_B \quad (\text{A.121})$$

where the expectation value is taken in the presence of an external, static, magnetic field B .

A.3.2.1 Vector potential expansion

Our starting point is the minimal coupling approach where the (magnetic) vector potential corrects the kinetic term of the Hamiltonian: In the lattice notation within the Peierls approximation, this procedure translates to a modification of the hopping term⁷⁴

$$t_{ij} \rightarrow t_{ij} \exp \left(-\frac{ie}{\hbar} \int_j^i \mathbf{A}(\mathbf{r}) \cdot d\mathbf{r} \right) \quad (\text{A.122})$$

which results in a geometric sum for the quadratic part of the Hamiltonian

$$\mathcal{H}_t = \sum_{\langle i,j \rangle} t_{ij} \sum_{n=0}^{\infty} \frac{1}{n!} \left(\frac{ie}{\hbar} \right)^n (\mathbf{A}(\mathbf{R}_{ij}) \cdot \mathbf{r}_{ij})^n \hat{c}_{i\sigma}^\dagger \hat{c}_{j\sigma} \quad (\text{A.123})$$

⁷⁴This procedure holds only for unit cells with one atom. If the unit cell is of multi-atomic nature, the substitution must account for inter-atomic hopping [64, 362]. This is done by a modification of the integration boundaries. Per construction, the Peierls approximation always neglects intra-atomic optical transitions [405].

with the (positively defined) elementary charge e , the vector potential \mathbf{A} evaluated at the center point $\mathbf{R}_{ij} = (\mathbf{r}_i + \mathbf{r}_j)/2$ and the integral length as the lattice difference $\mathbf{r}_{ij} = (\mathbf{r}_j - \mathbf{r}_i)$. Let us note that this kind of integral evaluation is only justified in the long wavelength limit, i.e. the vector potential is varying slowly in space (transfer momentum \mathbf{q} is small).

Now we Fourier transform the kinetic term into momentum space by inserting

$$\hat{c}_{i\sigma}^\dagger = \sum_{\mathbf{p}} e^{i\mathbf{p}\mathbf{r}_i} \hat{c}_{\mathbf{p},\sigma}^\dagger, \quad (\text{A.124a})$$

$$\hat{c}_{j\sigma} = \sum_{\mathbf{p}} e^{-i\mathbf{p}\mathbf{r}_j} \hat{c}_{\mathbf{p},\sigma}, \quad (\text{A.124b})$$

$$\mathbf{A}(\mathbf{R}_{ij}) = \sum_{\mathbf{q}} e^{-i\mathbf{q}\mathbf{R}_{ij}} \mathbf{A}_{\mathbf{q}}, \quad (\text{A.124c})$$

resulting in

$$\mathcal{H}_t = \sum_{\mathbf{p}} \varepsilon_{\mathbf{p}} \hat{c}_{\mathbf{p}\sigma}^\dagger \hat{c}_{\mathbf{p}\sigma} - \frac{e}{\hbar} \sum_{\mathbf{p},\mathbf{q}} \hat{c}_{\mathbf{p}\sigma}^\dagger \hat{c}_{\mathbf{q}\sigma} \varepsilon_{\mathbf{p}/2+\mathbf{q}/2}^\alpha A_{\mathbf{p}-\mathbf{q}}^\alpha + \frac{1}{2} \left(\frac{e}{\hbar} \right)^2 \sum_{\mathbf{p},\mathbf{q},\mathbf{q}_1} \hat{c}_{\mathbf{p}\sigma}^\dagger \hat{c}_{\mathbf{q}\sigma} \varepsilon_{\mathbf{p}/2+\mathbf{q}/2}^{\alpha\beta} A_{\mathbf{q}_1}^\alpha A_{\mathbf{p}-\mathbf{q}-\mathbf{q}_1}^\beta + \mathcal{O}(A^3) \quad (\text{A.125})$$

where for each term we can recognize the momentum conservation via $\mathbf{p} = \mathbf{q} + \sum_i \mathbf{q}_i$ for all occurring $A_{\mathbf{q}_i}$ and where we employed the energy dispersion (in a band-diagonal basis)

$$\varepsilon_{\mathbf{p}} = \sum_{\mathbf{r}_{ij}} t_{ij} e^{-i\mathbf{p}\cdot\mathbf{r}_{ij}} \quad (\text{A.126})$$

with its derivatives in short-form notation

$$\varepsilon_{\mathbf{p}}^\alpha = \frac{\partial \varepsilon_{\mathbf{p}}}{\partial p_\alpha} \quad (\text{A.127a})$$

$$\varepsilon_{\mathbf{p}}^{\alpha\beta} = \frac{\partial^2 \varepsilon_{\mathbf{p}}}{\partial p_\alpha \partial p_\beta}, \quad (\text{A.127b})$$

and so on. Let us note that the sign convention of Eq. (A.126) is consistent with the main text, see Eq. (2.26), due to the definition of \mathbf{r}_{ij} . The (spin-dependent) current operator is now calculated via the functional derivative

$$J_{\mathbf{q}}^\gamma = \frac{\delta \mathcal{H}_t}{\delta A_{-\mathbf{q}}^\gamma} = \underbrace{-\frac{e}{\hbar} \sum_{\mathbf{p}} \hat{c}_{\mathbf{p}-\mathbf{q},\sigma}^\dagger \hat{c}_{\mathbf{p},\sigma} \varepsilon_{\mathbf{p}-\mathbf{q}/2}^\gamma}_{J_{\mathbf{q}}^{0,\gamma}} + \underbrace{\left(\frac{e}{\hbar} \right)^2 \sum_{\mathbf{p},\mathbf{q}_1} \hat{c}_{\mathbf{p}-\mathbf{q}+\mathbf{q}_1,\sigma}^\dagger \hat{c}_{\mathbf{p},\sigma} \varepsilon_{\mathbf{p}-\mathbf{q}/2+\mathbf{q}_1/2}^{\gamma\alpha} A_{\mathbf{q}_1}^\alpha}_{J_{\mathbf{q}}^{1,\gamma}} + \mathcal{O}(A^2), \quad (\text{A.128})$$

which we consider up to linear order in the vector potential A . Here A encodes both the external magnetic $\mathbf{B} = \nabla \times \mathbf{A}$ and electric field $\mathbf{E} = -\partial_t \mathbf{A}$.

A.3.2.2 Current-current correlation function

Having derived the current operator, we are now able to compute the correlation function

$$\chi_{j_E j_E}^{B, \alpha \beta}(\tilde{\mathbf{q}}, i\Omega_m) = \int_0^\beta e^{i\Omega_m \tau} \langle T_\tau J_{\tilde{\mathbf{q}}}^\alpha(\tau) J_{\mathbf{0}}^\beta \rangle_B \quad (\text{A.129})$$

where we consider the three contributions that are of linear order in A

$$\chi_1^{B, \alpha \beta}(\tilde{\mathbf{q}}, i\Omega_m) = \int_0^\beta e^{i\Omega_m \tau} \langle T_\tau J_{\tilde{\mathbf{q}}}^{1, \alpha}(\tau) J_{\mathbf{0}}^{0, \beta} \rangle, \quad (\text{A.130})$$

$$\chi_2^{B, \alpha \beta}(\tilde{\mathbf{q}}, i\Omega_m) = \int_0^\beta e^{i\Omega_m \tau} \langle T_\tau J_{\tilde{\mathbf{q}}}^{0, \alpha}(\tau) J_{\mathbf{0}}^{1, \beta} \rangle, \quad (\text{A.131})$$

$$\chi_3^{B, \alpha \beta}(\tilde{\mathbf{q}}, i\Omega_m) = - \int_0^\beta e^{i\Omega_m \tau} \langle T_\tau S_1 J_{\tilde{\mathbf{q}}}^{0, \alpha}(\tau) J_{\mathbf{0}}^{0, \beta} \rangle. \quad (\text{A.132})$$

In χ_3 the vector potential is introduced via the correction term in the action

$$S_1 = \int_0^\beta d\tau' \left(-\frac{e}{\hbar} \right) \sum_{\mathbf{p}, \mathbf{q}} \hat{c}_{\mathbf{p}+\mathbf{q}, \sigma}^\dagger(\tau') \hat{c}_{\mathbf{p}, \sigma}(\tau') \varepsilon_{\mathbf{p}+\mathbf{q}/2}^\alpha A_{\mathbf{q}}^\alpha, \quad (\text{A.133})$$

which stems from the path integral reformulation $\chi \propto \int D[\bar{c}c] e^{-S_B} J_{\tilde{\mathbf{q}}}^\alpha(\tau) J_{\mathbf{0}}^\beta(0) / \int D[\bar{c}c] e^{-S_B}$. Here, one expands the action $S_B = S_0 + S_1$ where S_0 is the action in the absence of the external magnetic field. Let us emphasize here, that the evaluation of Eqs. (A.130-A.132) now follows the usual Kubo procedure, where we take the expectation value with respect to the unperturbed system.

χ_1 evaluation

$$\begin{aligned} \chi_1^{B, \alpha \beta}(\tilde{\mathbf{q}}, i\Omega_m) &= -\frac{e^3}{\hbar^3} \sum_{\mathbf{p}', \mathbf{q}, \mathbf{q}_1} \varepsilon_{\mathbf{p}-\tilde{\mathbf{q}}/2+\mathbf{q}_1/2}^{\gamma \alpha} \varepsilon_{\mathbf{p}'}^\beta A_{\mathbf{q}_1}^\gamma \int_0^\beta d\tau e^{i\Omega_m \tau} \underbrace{\langle T_\tau \hat{c}_{\mathbf{p}-\tilde{\mathbf{q}}+\mathbf{q}_1}^\dagger(\tau) \hat{c}_{\mathbf{p}}(\tau) \hat{c}_{\mathbf{p}'}^\dagger(0) \hat{c}_{\mathbf{p}'}(0) \rangle}_{-G^{\mathbf{P}}(\tau) \delta_{\mathbf{p}, \mathbf{p}'} G^{\mathbf{P}'}(-\tau) \delta_{\mathbf{p}', \mathbf{p}-\tilde{\mathbf{q}}+\mathbf{q}_1}} \\ &= \frac{e^3}{\hbar^3} \sum_{\mathbf{p}} \varepsilon_{\mathbf{p}}^{\gamma \alpha} \varepsilon_{\mathbf{p}}^\beta A_{\tilde{\mathbf{q}}}^\gamma \int_0^\beta d\tau e^{i\Omega_m \tau} G^{\mathbf{P}}(\tau) G^{\mathbf{P}}(-\tau) \\ &= \frac{e^3}{\hbar^3} \sum_{\mathbf{p}} \varepsilon_{\mathbf{p}}^{\gamma \alpha} \varepsilon_{\mathbf{p}}^\beta A_{\tilde{\mathbf{q}}}^\gamma \frac{1}{\beta} \sum_{\nu_n} G^{(\mathbf{p}, \nu_n + \Omega_m)} G^{(\mathbf{p}, \nu_n)} \stackrel{!}{=} 0 \end{aligned} \quad (\text{A.134})$$

The last line vanishes due to the involved band structure derivatives: An inversion of the (internal) momentum \mathbf{p} leads to a sign change $-\varepsilon_{-\mathbf{p}}^{\gamma \alpha} \varepsilon_{-\mathbf{p}}^\beta$ (the Green's functions $G^{\mathbf{P}}$ are unaffected by this transformation), assuming a band-diagonal basis. In the first line we only consider the Wick contractions leading to the dressed bubble diagram and disregard “non-physical” equal-time density corrections. We also neglect vertex corrections. In the second line we performed the momentum selection and in the last line we computed the Fourier transform from imaginary time to the Matsubara frequencies.

This is the result of the following transformation

$$\begin{aligned} \int_0^\beta d\tau e^{i\Omega_m\tau} G^{\mathbf{P}}(\tau) G^{\mathbf{P}}(-\tau) &= \int_0^\beta d\tau e^{i\Omega_m\tau} \frac{1}{\beta} \sum_{\nu_n} e^{-i\nu_n\tau} G^{(\mathbf{P},\nu_n)} \frac{1}{\beta} \sum_{\nu'_n} e^{i\nu'_n\tau} G^{(\mathbf{P},\nu'_n)} \\ &= \beta \sum_{\nu_n, \nu'_n} \delta_{\Omega_m - \nu_n + \nu'_n, 0} \frac{1}{\beta} G^{(\mathbf{P},\nu_n)} \frac{1}{\beta} G^{(\mathbf{P},\nu'_n)} = \frac{1}{\beta} \sum_{\nu_n} G^{(\mathbf{P},\nu_n + \Omega_m)} G^{(\mathbf{P},\nu_n)}. \end{aligned} \quad (\text{A.135})$$

Let us note, that all future Fourier transforms are performed similarly. For brevity's sake we will however skip the explicit calculation and simply show the end result.

χ_2 evaluation

$$\begin{aligned} \chi_2^{B,\alpha\beta}(\tilde{\mathbf{q}}, i\Omega_m) &= -\frac{e^3}{\hbar^3} \sum_{\mathbf{p}, \mathbf{p}', \mathbf{q}_1} \varepsilon_{\mathbf{p}-\tilde{\mathbf{q}}/2}^\alpha \varepsilon_{\mathbf{p}'+\mathbf{q}_1/2}^{\beta\gamma} A_{\mathbf{q}_1}^\gamma \int_0^\beta d\tau e^{i\Omega_m\tau} \underbrace{\langle T_\tau \hat{c}_{\mathbf{p}-\tilde{\mathbf{q}}}^\dagger(\tau) \hat{c}_{\mathbf{p}}(\tau) \hat{c}_{\mathbf{p}'+\mathbf{q}_1}^\dagger(0) \hat{c}_{\mathbf{p}'}(0) \rangle}_{-G^{\mathbf{P}}(\tau) \delta_{\mathbf{p}, \mathbf{p}'+\mathbf{q}_1} G^{\mathbf{P}'}(-\tau) \delta_{\mathbf{p}', \mathbf{p}-\tilde{\mathbf{q}}}} \\ &= \frac{e^3}{\hbar^3} \sum_{\mathbf{p}} \varepsilon_{\mathbf{p}-\tilde{\mathbf{q}}/2}^\alpha \varepsilon_{\mathbf{p}-\tilde{\mathbf{q}}/2}^{\beta\gamma} A_{\tilde{\mathbf{q}}}^\gamma \int_0^\beta d\tau e^{i\Omega_m\tau} G^{\mathbf{P}}(\tau) G^{\mathbf{P}-\tilde{\mathbf{q}}}(-\tau) \\ &= \frac{e^3}{\hbar^3} \sum_{\mathbf{p}} \varepsilon_{\mathbf{p}+\tilde{\mathbf{q}}/2}^\alpha \varepsilon_{\mathbf{p}+\tilde{\mathbf{q}}/2}^{\beta\gamma} A_{\tilde{\mathbf{q}}}^\gamma \int_0^\beta d\tau e^{i\Omega_m\tau} G^{\mathbf{P}+\tilde{\mathbf{q}}}(\tau) G^{\mathbf{P}}(-\tau) \\ &= \frac{e^3}{\hbar^3} \sum_{\mathbf{p}} \varepsilon_{\mathbf{p}+\tilde{\mathbf{q}}/2}^\alpha \varepsilon_{\mathbf{p}+\tilde{\mathbf{q}}/2}^{\beta\gamma} A_{\tilde{\mathbf{q}}}^\gamma \frac{1}{\beta} \sum_{\nu_n} G^{(\mathbf{P}+\tilde{\mathbf{q}}, \nu_n + \Omega_m)} G^{(\mathbf{P}, \nu_n)} \end{aligned} \quad (\text{A.136})$$

In the first line we performed the Wick contraction to the bubble diagram, in the second line we performed the momentum selection, in the third line shifted the momentum sum $\mathbf{p} \rightarrow \mathbf{p} + \tilde{\mathbf{q}}$, and in the fourth line we performed the Fourier transform.

Now we expand all terms in $\tilde{\mathbf{q}}$ up to linear order in $\tilde{\mathbf{q}}$ via

$$\varepsilon_{\mathbf{p}+\tilde{\mathbf{q}}/2}^\alpha \varepsilon_{\mathbf{p}+\tilde{\mathbf{q}}/2}^{\beta\gamma} G^{(\mathbf{P}+\tilde{\mathbf{q}}, \nu_n + \Omega_m)} \rightarrow \left[\varepsilon_{\mathbf{p}}^\alpha + \varepsilon_{\mathbf{p}}^{\alpha\delta} \frac{\tilde{\mathbf{q}}^\delta}{2} \right] \left[\varepsilon_{\mathbf{p}}^{\beta\gamma} + \varepsilon_{\mathbf{p}}^{\beta\gamma\delta} \frac{\tilde{\mathbf{q}}^\delta}{2} \right] \left[G^{(\mathbf{P}, \nu_n + \Omega_m)} + \left[G^{(\mathbf{P}, \nu_n + \Omega_m)} \right]^2 \varepsilon_{\mathbf{p}}^\delta \tilde{\mathbf{q}}^\delta \right]$$

where the Green's function expansion (in the band basis) employs

$$G^{(\mathbf{P}, \nu_n)} = (i\nu_n + \mu - \varepsilon_{\mathbf{p}} - \Sigma^{(\mathbf{P}, \nu_n)})^{-1}, \quad \frac{\partial}{\partial p_\delta} G^{(\mathbf{P}, \nu_n)} = (i\nu_n + \mu - \varepsilon_{\mathbf{p}} - \Sigma^{(\mathbf{P}, \nu_n)})^{-2} \frac{\partial \varepsilon_{\mathbf{p}}}{\partial p_\delta} = \left[G^{(\mathbf{P}, \nu_n)} \right]^2 \varepsilon_{\mathbf{p}}^\delta$$

where we neglect the correction induced by the momentum derivative of the self-energy. Inserted into χ_2 , we only consider terms up to linear order in $\tilde{\mathbf{q}}$

$$\begin{aligned} \chi_2^{B,\alpha\beta}(\tilde{\mathbf{q}}, i\Omega_m) &= \frac{e^3}{\hbar^3 \beta} \sum_{\mathbf{p}, \nu_n} \left[\underbrace{\varepsilon_{\mathbf{p}}^\alpha \varepsilon_{\mathbf{p}}^{\beta\gamma} A_{\tilde{\mathbf{q}}}^\gamma G^{(\mathbf{P}, \nu_n + \Omega_m)} G^{(\mathbf{P}, \nu_n)}}_{\equiv 0} + \varepsilon_{\mathbf{p}}^{\alpha\delta} \frac{\tilde{\mathbf{q}}^\delta}{2} \varepsilon_{\mathbf{p}}^{\beta\gamma} A_{\tilde{\mathbf{q}}}^\gamma G^{(\mathbf{P}, \nu_n + \Omega_m)} G^{(\mathbf{P}, \nu_n)} \right. \\ &\quad \left. + \varepsilon_{\mathbf{p}}^\alpha \varepsilon_{\mathbf{p}}^{\beta\gamma\delta} \frac{\tilde{\mathbf{q}}^\delta}{2} A_{\tilde{\mathbf{q}}}^\gamma G^{(\mathbf{P}, \nu_n + \Omega_m)} G^{(\mathbf{P}, \nu_n)} + \varepsilon_{\mathbf{p}}^\alpha \varepsilon_{\mathbf{p}}^{\beta\gamma} A_{\tilde{\mathbf{q}}}^\gamma \left[G^{(\mathbf{P}, \nu_n + \Omega_m)} \right]^2 \varepsilon_{\mathbf{p}}^\delta \tilde{\mathbf{q}}^\delta G^{(\mathbf{P}, \nu_n)} + \mathcal{O}(\tilde{\mathbf{q}}^2) \right], \end{aligned} \quad (\text{A.137})$$

where the first term vanishes due to its antisymmetry with respect to \mathbf{p} in the band-diagonal basis. Integrating the third term by parts with respect \mathbf{p}

$$\begin{aligned}
& \sum_{\mathbf{p}} \varepsilon_{\mathbf{p}}^{\alpha} \varepsilon_{\mathbf{p}}^{\beta\gamma\delta} \frac{\tilde{\mathbf{q}}^{\delta}}{2} A_{\tilde{\mathbf{q}}}^{\gamma} G^{(\mathbf{p}, \nu_n + \Omega_m)} G^{(\mathbf{p}, \nu_n)} = \\
& = \underbrace{\sum_{\mathbf{p}} \frac{\partial}{\partial p_{\delta}} \left[\varepsilon_{\mathbf{p}}^{\alpha} \varepsilon_{\mathbf{p}}^{\beta\gamma} G^{(\mathbf{p}, \nu_n + \Omega_m)} G^{(\mathbf{p}, \nu_n)} \right]}_{\equiv 0} \frac{\tilde{\mathbf{q}}^{\delta}}{2} A_{\tilde{\mathbf{q}}}^{\gamma} - \underbrace{\sum_{\mathbf{p}} \varepsilon_{\mathbf{p}}^{\alpha} \varepsilon_{\mathbf{p}}^{\beta\gamma} \frac{\tilde{\mathbf{q}}^{\delta}}{2} A_{\tilde{\mathbf{q}}}^{\gamma} G^{(\mathbf{p}, \nu_n + \Omega_m)} G^{(\mathbf{p}, \nu_n)}}_{\text{cancels with second term of Eq. (A.137)}} \\
& - \underbrace{\sum_{\mathbf{p}} \varepsilon_{\mathbf{p}}^{\alpha} \varepsilon_{\mathbf{p}}^{\beta\gamma} \frac{\tilde{\mathbf{q}}^{\delta}}{2} A_{\tilde{\mathbf{q}}}^{\gamma} \left[G^{(\mathbf{p}, \nu_n + \Omega_m)} \right]^2}_{\text{partial cancellation with fourth term of Eq. (A.137)}} \varepsilon_{\mathbf{p}}^{\delta} G^{(\mathbf{p}, \nu_n)} - \sum_{\mathbf{p}} \varepsilon_{\mathbf{p}}^{\alpha} \varepsilon_{\mathbf{p}}^{\beta\gamma} \frac{\tilde{\mathbf{q}}^{\delta}}{2} A_{\tilde{\mathbf{q}}}^{\gamma} G^{(\mathbf{p}, \nu_n + \Omega_m)} \left[G^{(\mathbf{p}, \nu_n)} \right]^2 \varepsilon_{\mathbf{p}}^{\delta}
\end{aligned} \tag{A.138}$$

allows us to cancel most terms. The combined result is then

$$\begin{aligned}
\chi_2^{B, \alpha\beta}(\tilde{\mathbf{q}}, i\Omega_m) &= \frac{e^3}{\hbar^3 \beta} \sum_{\mathbf{p}, \nu_n} \varepsilon_{\mathbf{p}}^{\alpha} \varepsilon_{\mathbf{p}}^{\beta\gamma} A_{\tilde{\mathbf{q}}}^{\gamma} \varepsilon_{\mathbf{p}}^{\delta} \frac{\tilde{\mathbf{q}}^{\delta}}{2} \left[\left[G^{(\mathbf{p}, \nu_n + \Omega_m)} \right]^2 G^{(\mathbf{p}, \nu_n)} - G^{(\mathbf{p}, \nu_n + \Omega_m)} \left[G^{(\mathbf{p}, \nu_n)} \right]^2 \right] \\
&= -\frac{e^3}{\hbar^3 \beta} \sum_{\mathbf{p}, \nu_n} \varepsilon_{\mathbf{p}}^{\alpha} \varepsilon_{\mathbf{p}}^{\beta\gamma} A_{\tilde{\mathbf{q}}}^{\gamma} \varepsilon_{\mathbf{p}}^{\delta} \frac{\tilde{\mathbf{q}}^{\delta}}{2} \left[G^{(\mathbf{p}, \nu_n)} \right]^2 \left[G^{(\mathbf{p}, \nu_n + \Omega_m)} - G^{(\mathbf{p}, \nu_n - \Omega_m)} \right]
\end{aligned} \tag{A.139}$$

where we exploited a fermionic frequency shift of $i\nu_n \rightarrow i\nu_n - i\Omega_m$ in the first term.

χ_3 evaluation

$$\begin{aligned}
\chi_3^{B, \alpha\beta}(\tilde{\mathbf{q}}, i\Omega_m) &= \frac{e^3}{\hbar^3} \sum_{\mathbf{p}, \mathbf{q}, \mathbf{p}', \mathbf{p}''} \varepsilon_{\mathbf{p}-\mathbf{q}/2}^{\gamma} A_{\tilde{\mathbf{q}}}^{\gamma} \varepsilon_{\mathbf{p}'-\tilde{\mathbf{q}}/2}^{\alpha} \varepsilon_{\mathbf{p}''}^{\beta} \\
& \int_0^{\beta} d\tau e^{i\Omega_m \tau} \int_0^{\beta} d\tau' \underbrace{\left\langle T_{\tau} \hat{c}_{\mathbf{p}+\mathbf{q}}^{\dagger}(\tau') \hat{c}_{\mathbf{p}}(\tau') \hat{c}_{\mathbf{p}'-\tilde{\mathbf{q}}}^{\dagger}(\tau) \hat{c}_{\mathbf{p}'}(\tau) \hat{c}_{\mathbf{p}''}^{\dagger}(0) \hat{c}_{\mathbf{p}''}(0) \right\rangle}_{\substack{G^{\mathbf{p}''}(-\tau') G^{\mathbf{p}}(\tau'-\tau) G^{\mathbf{p}'}(\tau) \delta_{\mathbf{p}'', \mathbf{p}+\mathbf{q}} \delta_{\mathbf{p}', -\tilde{\mathbf{q}}} \delta_{\mathbf{p}', \mathbf{p}''} \\ + G^{\mathbf{p}''}(-\tau) G^{\mathbf{p}'}(\tau-\tau') G^{\mathbf{p}}(\tau') \delta_{\mathbf{p}', \mathbf{p}+\mathbf{q}} \delta_{\mathbf{p}'', \mathbf{p}'-\tilde{\mathbf{q}}} \delta_{\mathbf{p}, \mathbf{p}''}} \\
&= \frac{e^3}{\hbar^3} \sum_{\mathbf{p}} \int_0^{\beta} d\tau e^{i\Omega_m \tau} \int_0^{\beta} d\tau' \left[\varepsilon_{\mathbf{p}+\tilde{\mathbf{q}}/2}^{\gamma} A_{\tilde{\mathbf{q}}}^{\gamma} \varepsilon_{\mathbf{p}+\tilde{\mathbf{q}}/2}^{\alpha} \varepsilon_{\mathbf{p}+\tilde{\mathbf{q}}}^{\beta} G^{\mathbf{p}+\tilde{\mathbf{q}}}(-\tau') G^{\mathbf{p}}(\tau'-\tau) G^{\mathbf{p}+\tilde{\mathbf{q}}}(\tau) \right. \\
& \quad \left. + \varepsilon_{\mathbf{p}+\tilde{\mathbf{q}}/2}^{\gamma} A_{\tilde{\mathbf{q}}}^{\gamma} \varepsilon_{\mathbf{p}+\tilde{\mathbf{q}}/2}^{\alpha} \varepsilon_{\mathbf{p}}^{\beta} G^{\mathbf{p}}(-\tau) G^{\mathbf{p}+\tilde{\mathbf{q}}}(\tau-\tau') G^{\mathbf{p}}(\tau') \right] \\
&= \frac{e^3}{\hbar^3} \frac{1}{\beta} \sum_{\mathbf{p}, \nu_n} \left[\varepsilon_{\mathbf{p}+\tilde{\mathbf{q}}/2}^{\gamma} A_{\tilde{\mathbf{q}}}^{\gamma} \varepsilon_{\mathbf{p}+\tilde{\mathbf{q}}/2}^{\alpha} \varepsilon_{\mathbf{p}+\tilde{\mathbf{q}}}^{\beta} G^{(\mathbf{p}+\tilde{\mathbf{q}}, \nu_n)} G^{(\mathbf{p}, \nu_n)} G^{(\mathbf{p}+\tilde{\mathbf{q}}, \nu_n + \Omega_m)} \right. \\
& \quad \left. + \varepsilon_{\mathbf{p}+\tilde{\mathbf{q}}/2}^{\gamma} A_{\tilde{\mathbf{q}}}^{\gamma} \varepsilon_{\mathbf{p}+\tilde{\mathbf{q}}/2}^{\alpha} \varepsilon_{\mathbf{p}}^{\beta} G^{(\mathbf{p}, \nu_n)} G^{(\mathbf{p}+\tilde{\mathbf{q}}, \nu_n + \Omega_m)} G^{(\mathbf{p}, \nu_n + \Omega_m)} \right]
\end{aligned}$$

$$\begin{aligned}
&= \frac{e^3}{\hbar^3} \frac{1}{\beta} \sum_{\mathbf{p}, \nu_n} \left[\varepsilon_{\mathbf{p}}^\alpha \varepsilon_{\mathbf{p}+\tilde{\mathbf{q}}/2}^\beta \varepsilon_{\mathbf{p}}^\gamma A_{\tilde{\mathbf{q}}}^\gamma G^{(\mathbf{p}+\tilde{\mathbf{q}}/2, \nu_n)} G^{(\mathbf{p}-\tilde{\mathbf{q}}/2, \nu_n)} G^{(\mathbf{p}+\tilde{\mathbf{q}}/2, \nu_n+\Omega_m)} \right. \\
&\quad \left. + \varepsilon_{\mathbf{p}}^\alpha \varepsilon_{\mathbf{p}-\tilde{\mathbf{q}}/2}^\beta \varepsilon_{\mathbf{p}}^\gamma A_{\tilde{\mathbf{q}}}^\gamma G^{(\mathbf{p}-\tilde{\mathbf{q}}/2, \nu_n)} G^{(\mathbf{p}+\tilde{\mathbf{q}}/2, \nu_n)} G^{(\mathbf{p}-\tilde{\mathbf{q}}/2, \nu_n-\Omega_m)} \right] \quad (\text{A.140})
\end{aligned}$$

In the first line we performed the necessary Wick contractions to generate the physically relevant triangle diagrams (see Ref. [524] for their importance in nonlinear responses), in the second line we performed the momentum selection stemming from the delta-functions and in the third line we performed the Fourier transform. Finally, to generate the ‘‘symmetric’’ expression in the fourth line we shifted the (internal) momentum sum of both terms via $\mathbf{p} \rightarrow \mathbf{p} - \tilde{\mathbf{q}}/2$ and shifted the fermionic Matsubara frequencies of the second term via $\nu_n \rightarrow \nu_n - \Omega_m$.

We again expand all terms in $\tilde{\mathbf{q}}$ up to linear order in $\tilde{\mathbf{q}}$ via

$$\begin{aligned}
\varepsilon_{\mathbf{p}+\tilde{\mathbf{q}}/2}^\beta G^{(\mathbf{p}+\tilde{\mathbf{q}}/2, \nu_n)} G^{(\mathbf{p}-\tilde{\mathbf{q}}/2, \nu_n)} G^{(\mathbf{p}+\tilde{\mathbf{q}}/2, \nu_n+\Omega_m)} &\rightarrow \left[\varepsilon_{\mathbf{p}}^\beta + \varepsilon_{\mathbf{p}}^{\beta\delta} \frac{\tilde{\mathbf{q}}^\delta}{2} \right] \times \left[G^{(\mathbf{p}, \nu_n)} + \left[G^{(\mathbf{p}, \nu_n)} \right]^2 \varepsilon_{\mathbf{p}}^\delta \frac{\tilde{\mathbf{q}}^\delta}{2} \right] \\
&\quad \times \left[G^{(\mathbf{p}, \nu_n)} - \left[G^{(\mathbf{p}, \nu_n)} \right]^2 \varepsilon_{\mathbf{p}}^\delta \frac{\tilde{\mathbf{q}}^\delta}{2} \right] \\
&\quad \times \left[G^{(\mathbf{p}, \nu_n+\Omega_m)} + \left[G^{(\mathbf{p}, \nu_n+\Omega_m)} \right]^2 \varepsilon_{\mathbf{p}}^\delta \frac{\tilde{\mathbf{q}}^\delta}{2} \right]
\end{aligned}$$

and similarly for the second line where the sign of the transfer momentum $\tilde{\mathbf{q}}$ is reversed.

The zeroth order expansion of χ_3 in $\tilde{\mathbf{q}}$ vanishes as $\varepsilon_{\mathbf{p}}^\alpha \varepsilon_{\mathbf{p}}^{\beta\delta} \varepsilon_{\mathbf{p}}^\gamma \left[G^{(\mathbf{p}, \nu_n)} \right]^2 G^{(\mathbf{p}, \nu_n+\Omega_m)}$ is antisymmetric w.r.t. momentum reversal $\mathbf{p} \leftrightarrow -\mathbf{p}$. In the first order expansion in $\tilde{\mathbf{q}}$, the contributions of $\mp \left[G^{(\mathbf{p}, \nu_n)} \right]^2 \left[G^{(\mathbf{p}, \nu_n \pm \Omega_m)} \right]^2$ vanish due to their evenness w.r.t. Ω_m . The other terms then combine to

$$\chi_3^{B, \alpha\beta}(\tilde{\mathbf{q}}, i\Omega_m) = \frac{e^3}{\hbar^3} \frac{1}{\beta} \sum_{\mathbf{p}, \nu_n} \varepsilon_{\mathbf{p}}^\alpha \varepsilon_{\mathbf{p}}^{\beta\delta} \varepsilon_{\mathbf{p}}^\gamma A_{\tilde{\mathbf{q}}}^\gamma \frac{\tilde{\mathbf{q}}^\delta}{2} \left[G^{(\mathbf{p}, \nu_n)} \right]^2 \left[G^{(\mathbf{p}, \nu_n+\Omega_m)} - G^{(\mathbf{p}, \nu_n-\Omega_m)} \right]. \quad (\text{A.141})$$

χ evaluation

Finally, the total correlation function χ can now be summed resulting in

$$\begin{aligned}
\chi_{jEjE}^{B, \alpha\beta}(\tilde{\mathbf{q}}, i\Omega_m) &= \chi_1^{B, \alpha\beta}(\tilde{\mathbf{q}}, i\Omega_m) + \chi_2^{B, \alpha\beta}(\tilde{\mathbf{q}}, i\Omega_m) + \chi_3^{B, \alpha\beta}(\tilde{\mathbf{q}}, i\Omega_m) \\
&= -\frac{e^3}{\hbar^3} \frac{1}{\beta} \sum_{\mathbf{p}, \nu_n} \varepsilon_{\mathbf{p}}^\alpha \varepsilon_{\mathbf{p}}^{\beta\delta} \varepsilon_{\mathbf{p}}^\gamma A_{\tilde{\mathbf{q}}}^\gamma \frac{\tilde{\mathbf{q}}^\delta}{2} \left[G^{(\mathbf{p}, \nu_n)} \right]^2 \left[G^{(\mathbf{p}, \nu_n+\Omega_m)} - G^{(\mathbf{p}, \nu_n-\Omega_m)} \right] \\
&\quad + \frac{e^3}{\hbar^3} \frac{1}{\beta} \sum_{\mathbf{p}, \nu_n} \varepsilon_{\mathbf{p}}^\alpha \varepsilon_{\mathbf{p}}^{\beta\delta} \varepsilon_{\mathbf{p}}^\gamma A_{\tilde{\mathbf{q}}}^\gamma \frac{\tilde{\mathbf{q}}^\delta}{2} \left[G^{(\mathbf{p}, \nu_n)} \right]^2 \left[G^{(\mathbf{p}, \nu_n+\Omega_m)} - G^{(\mathbf{p}, \nu_n-\Omega_m)} \right]
\end{aligned}$$

$$\begin{aligned}
&= -\frac{1}{2} \frac{e^3}{\hbar^3} \sum_{\mathbf{p}} \varepsilon_{\mathbf{p}}^{\alpha} \left[\varepsilon_{\mathbf{p}}^{\beta\gamma} \varepsilon_{\mathbf{p}}^{\delta} - \varepsilon_{\mathbf{p}}^{\beta\delta} \varepsilon_{\mathbf{p}}^{\gamma} \right] \tilde{\mathbf{q}}^{\delta} A_{\tilde{\mathbf{q}}}^{\gamma} \left[\Pi^{\mathbf{P}}(i\Omega_m) - \Pi^{\mathbf{P}}(-i\Omega_m) \right] \\
&= -\frac{1}{2} \frac{e^3}{\hbar^3} \sum_{\mathbf{p}} \varepsilon_{\mathbf{p}}^{\alpha} \varepsilon_{\mathbf{p}}^{\beta\gamma} \varepsilon_{\mathbf{p}}^{\delta} \underbrace{\left[\tilde{\mathbf{q}}^{\delta} A_{\tilde{\mathbf{q}}}^{\gamma} - \tilde{\mathbf{q}}^{\gamma} A_{\tilde{\mathbf{q}}}^{\delta} \right]}_{-iB^j \varepsilon_{j\delta\gamma}} \left[\Pi^{\mathbf{P}}(i\Omega_m) - \Pi^{\mathbf{P}}(-i\Omega_m) \right] \\
&= \frac{i}{2} \frac{e^3}{\hbar^3} \sum_{\mathbf{p}} B^j \varepsilon_{j\delta\gamma} \varepsilon_{\mathbf{p}}^{\alpha} \varepsilon_{\mathbf{p}}^{\beta\gamma} \varepsilon_{\mathbf{p}}^{\delta} \left[\Pi^{\mathbf{P}}(i\Omega_m) - \Pi^{\mathbf{P}}(-i\Omega_m) \right] \tag{A.142}
\end{aligned}$$

where we introduced the abbreviation

$$\Pi^{\mathbf{P}}(i\Omega_m) = \frac{1}{\beta} \sum_{\nu_n} \left[G^{(\mathbf{p}, \nu_n)} \right]^2 G^{(\mathbf{p}, \nu_n + \Omega_m)}, \tag{A.143}$$

which is illustrated in Fig. A.5. In Eq. (A.142) we employ the Maxwell equation $B(\tilde{\mathbf{q}}) = i\tilde{\mathbf{q}} \times \mathbf{A}_{\tilde{\mathbf{q}}}$ in tensor notation. In order to calculate the magnetic correction to the Onsager coefficients, as defined in the main text

$$\mathcal{L}_{ab}^{\alpha\beta}(\mathbf{B}) = \mathcal{L}_{ab}^{\alpha\beta} + \mathcal{L}_{ab}^{B, \alpha\beta\gamma} B^{\gamma} + \mathcal{O}(\mathbf{B}^2), \tag{A.144}$$

we need to consider the dynamic limit

$$\mathcal{L}_{11}^{B, \alpha\beta j} = \lim_{\omega \rightarrow 0^+} \frac{1}{\omega} \left[\frac{\Im \chi_{jEjE}^{B, \alpha\beta}(\tilde{\mathbf{q}} = \mathbf{0}, i\Omega_m \rightarrow \omega + i0^+)}{B^j} \right], \tag{A.145}$$

where we remove the explicit contribution of the magnetic field B^j . The direction of the B-field however remains encoded in the correlation function via the optical elements, cf. Section 3.3.4.2,

$$M_{\mathbf{p}}^{B, \alpha\beta j} = \varepsilon_{j\delta\gamma} \varepsilon_{\mathbf{p}}^{\alpha} \varepsilon_{\mathbf{p}}^{\beta\gamma} \varepsilon_{\mathbf{p}}^{\delta} \tag{A.146}$$

For an applied current in $\beta = x$ direction with a static magnetic field in $j = z$ direction, the resulting response in $\alpha = x$ direction then corresponds to the transversal conductivity with coupling element

$$M_{\mathbf{p}}^{B, yxz} = \varepsilon_{\mathbf{p}}^y \varepsilon_{\mathbf{p}}^{xy} \varepsilon_{\mathbf{p}}^x - \varepsilon_{\mathbf{p}}^y \varepsilon_{\mathbf{p}}^{xx} \varepsilon_{\mathbf{p}}^y. \tag{A.147}$$

On the other hand, the correction to the response in the same longitudinal $\beta = x$ direction, corresponding to magneto resistance, the coupling elements correspond to

$$M_{\mathbf{p}}^{B, xxz} = \varepsilon_{\mathbf{p}}^x \varepsilon_{\mathbf{p}}^{xy} \varepsilon_{\mathbf{p}}^x - \varepsilon_{\mathbf{p}}^x \varepsilon_{\mathbf{p}}^{xx} \varepsilon_{\mathbf{p}}^y. \tag{A.148}$$

The antisymmetry of $M_{\mathbf{p}}^{B, xxz}$ with respect to an inversion of p_x implies that magnetic corrections to the conductivity are only captured for higher order B -terms, at least if time reversal symmetry is maintained.

A.3.2.3 Matsubara sum

To finalize the derivation, we convert the Matsubara sum of Eq. (A.143), into an integral over real frequency, see Section 3.3. We consider

$$\Pi^{\mathbf{P}}(i\Omega_m) - \Pi^{\mathbf{P}}(-i\Omega_m) = \frac{1}{\beta} \sum_{\nu_n} \left[G^{(\mathbf{p}, \nu_n)} \right]^2 G^{(\mathbf{p}, \nu_n + \Omega_m)} - \left[G^{(\mathbf{p}, \nu_n)} \right]^2 G^{(\mathbf{p}, \nu_n - \Omega_m)} \quad (\text{A.149})$$

as the starting point, where from here on we will drop all momentum subscripts for clarity's sake. Let us emphasize, that this quantity is evidently not properly defined for the static limit $i\Omega_m = 0$. By taking a full (anticlockwise) circular integral centered around $z = 0$ we restore the Matsubara sum

$$\Pi(i\Omega_m) = -\frac{1}{2\pi i} \oint dz f_{FD}(z) G^2(z) G(z + i\Omega_m) \stackrel{!}{=} \frac{1}{\beta} \sum_{\nu_n} G^2(i\nu_n) G(i\nu_n + i\Omega_m). \quad (\text{A.150})$$

We can now deform the integral in such a way that we may circumvent possible branch cuts of the Green's function located at $z = \varepsilon$ and $z = \varepsilon - i\Omega_m$. By doing this, we generate "horizontal cuts" in the complex plane, see Figure A.4, corresponding to real-axis integrals

$$\begin{aligned} \oint f_{FD}(z) G^2(z) G(z + i\Omega_m) = & \quad (\text{A.151}) \\ \int_{-\infty}^{\infty} d\varepsilon \left[f_{FD}(\varepsilon + i0^+) G^2(\varepsilon + i0^+) G(\varepsilon + i\Omega_m) - f_{FD}(\varepsilon - i0^+) G^2(\varepsilon - i0^+) G(\varepsilon + i\Omega_m) \right. \\ & \left. + f_{FD}(\varepsilon - i\Omega_m + i0^+) G^2(\varepsilon - i\Omega_m) G(\varepsilon + i0^+) - f_{FD}(\varepsilon - i\Omega_m - i0^+) G^2(\varepsilon - i\Omega_m) G(\varepsilon - i0^+) \right] \end{aligned}$$

resulting in

$$\begin{aligned} \Pi(i\Omega_m) = & -\frac{1}{2\pi i} \int_{-\infty}^{\infty} d\varepsilon f_{FD}(\varepsilon) \left[G(\varepsilon + i\Omega_m) \left(G_{\text{ret}}^2(\varepsilon) - G_{\text{adv}}^2(\varepsilon) \right) + G^2(\varepsilon - i\Omega_m) \left(G_{\text{ret}}(\varepsilon) - G_{\text{adv}}(\varepsilon) \right) \right] \\ = & \int_{-\infty}^{\infty} d\varepsilon f_{FD}(\varepsilon) \left[G(\varepsilon + i\Omega_m) 2A(\varepsilon) \Re G_{\text{ret}}(\varepsilon) + G^2(\varepsilon - i\Omega_m) A(\varepsilon) \right] \end{aligned} \quad (\text{A.152})$$

where we employed the connections of Eqs. (A.117). Now we can compute the difference and perform the analytic continuation

$$\begin{aligned} [\Pi(i\Omega_m) - \Pi(-i\Omega_m)]_{i\Omega_m \rightarrow \omega + i0^+} = & \int_{-\infty}^{\infty} d\varepsilon f_{FD}(\varepsilon) 2A(\varepsilon) \Re G_{\text{ret}}(\varepsilon) [G_{\text{ret}}(\varepsilon + \omega) - G_{\text{adv}}(\varepsilon - \omega)] \\ & + \int_{-\infty}^{\infty} d\varepsilon f_{FD}(\varepsilon) A(\varepsilon) [G_{\text{adv}}^2(\varepsilon - \omega) - G_{\text{ret}}^2(\varepsilon + \omega)]. \end{aligned} \quad (\text{A.153})$$

We only have to consider the real part of Eq. (A.153). To this end we now fully expand all Green's functions into their real and imaginary parts $G_{\text{ret}} = \Re G_{\text{ret}} + i\Im G_{\text{ret}}$, $G_{\text{adv}} = \Re G_{\text{ret}} - i\Im G_{\text{ret}}$ yielding

$$\begin{aligned} \Re [\Pi(i\Omega_m) - \Pi(-i\Omega_m)]_{i\Omega_m \rightarrow \omega + i0^+} = & \quad (A.154) \\ & - \int_{-\infty}^{\infty} d\varepsilon \Re G_{\text{ret}}(\varepsilon) \Re G_{\text{ret}}(\varepsilon + \omega) 2 [f_{FD}(\varepsilon + \omega) A(\varepsilon + \omega) - f_{FD}(\varepsilon) A(\varepsilon)] \\ & - \int_{-\infty}^{\infty} d\varepsilon f_{FD}(\varepsilon) A(\varepsilon) [(\Re G_{\text{ret}}(\varepsilon + \omega))^2 - (\Re G_{\text{ret}}(\varepsilon - \omega))^2] \\ & + \int_{-\infty}^{\infty} d\varepsilon f_{FD}(\varepsilon) A(\varepsilon) [(\Im G_{\text{ret}}(\varepsilon + \omega))^2 - (\Im G_{\text{ret}}(\varepsilon - \omega))^2] \end{aligned}$$

$$\begin{aligned} \lim_{\omega \rightarrow 0^+} \frac{\Re [\Pi(i\Omega_m) - \Pi(-i\Omega_m)]_{i\Omega_m \rightarrow \omega + i0^+}}{\omega} &= \int_{-\infty}^{\infty} d\varepsilon f_{FD}(\varepsilon) A(\varepsilon) 2 \frac{\partial ((\Im G_{\text{ret}}(\varepsilon))^2)}{\partial \varepsilon} \\ &\quad - \underbrace{\int_{-\infty}^{\infty} d\varepsilon (\Re G_{\text{ret}}(\varepsilon))^2 2 \frac{\partial (f_{FD}(\varepsilon) A(\varepsilon))}{\partial \varepsilon} - \int_{-\infty}^{\infty} d\varepsilon f_{FD}(\varepsilon) A(\varepsilon) 2 \frac{\partial ((\Re G_{\text{ret}}(\varepsilon))^2)}{\partial \varepsilon}}_{\equiv 0} \\ &= \int_{-\infty}^{\infty} d\varepsilon f_{FD}(\varepsilon) A(\varepsilon) 2 \frac{\partial (\pi^2 A^2(\varepsilon))}{\partial \varepsilon} = -2\pi^2 \int_{-\infty}^{\infty} d\varepsilon A^2(\varepsilon) \frac{\partial (f_{FD}(\varepsilon) A(\varepsilon))}{\partial \varepsilon} \\ &= -2\pi^2 \int_{-\infty}^{\infty} d\varepsilon \left[A^3(\varepsilon) \frac{\partial f_{FD}(\varepsilon)}{\partial \varepsilon} + f_{FD}(\varepsilon) A^2(\varepsilon) \frac{\partial A(\varepsilon)}{\partial \varepsilon} \right] = -\frac{4}{3} \pi^2 \int_{-\infty}^{\infty} d\varepsilon A^3(\varepsilon) \frac{\partial f_{FD}(\varepsilon)}{\partial \varepsilon} \quad (A.155) \end{aligned}$$

Combining all pre-factors, the (spin dependent) Onsager coefficient results in

$$\mathcal{L}_{11}^{B,\alpha\beta j} = \frac{2\pi^2 e^3}{3V \hbar^2} \sum_{\mathbf{p}} \epsilon_{j\delta\gamma} \epsilon_{\mathbf{p}}^{\alpha} \epsilon_{\mathbf{p}}^{\beta\gamma} \epsilon_{\mathbf{p}}^{\delta} \int_{-\infty}^{\infty} d\varepsilon \left(-\frac{\partial f_{FD}}{\partial \varepsilon} \right) A_{\mathbf{p}}^3(\varepsilon), \quad (A.156)$$

where one additional \hbar factor is added to account for the energy integration. In the main text the \hbar pre-factors are absorbed into the band derivatives which serve as Fermi velocities / curvatures. For a detailed dimensionality analysis of the Onsager coefficients, please refer to the Appendix of Ref. [11].

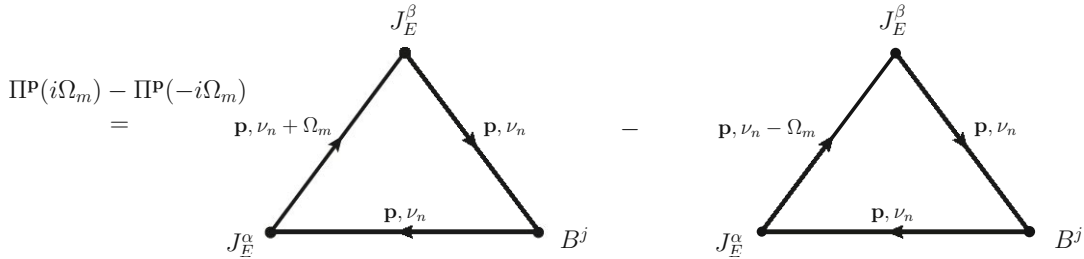


Figure A.5: Lowest order Feynman diagrams contributing to the Hall conductivity, see Eq. (A.142). Contrary to the electric field, the static, magnetic field does not induce a bosonic frequency transfer. The vertices signal the non-trivial coupling: $\epsilon_{j\delta\gamma} \epsilon_{\mathbf{p}}^{\alpha} \epsilon_{\mathbf{p}}^{\beta\gamma} \epsilon_{\mathbf{p}}^{\delta}$.

Bibliography

- [1] A. Galler, J. Kaufmann, P. Gunacker, M. Pickem, P. Thunström, J. M. Tomczak, and K. Held. “Towards ab initio calculations with the dynamical vertex approximation”. *Journal of the Physical Society of Japan* **87**(4), 041004, 2018. doi: [10.7566/JPSJ.87.041004](https://doi.org/10.7566/JPSJ.87.041004).
- [2] A. Galler, P. Thunström, J. Kaufmann, M. Pickem, J. M. Tomczak, and K. Held. “The AbinitioDFA Project v1.0: Non-local correlations beyond and susceptibilities within dynamical mean-field theory”. *Computer Physics Communications* **245**, 106847, 2019. doi: [10.1016/j.cpc.2019.07.012](https://doi.org/10.1016/j.cpc.2019.07.012).
- [3] P. Kappl, M. Wallerberger, J. Kaufmann, M. Pickem, and K. Held. “Statistical error estimates in dynamical mean-field theory and extensions thereof”. *Phys. Rev. B* **102**, 085124, Aug 2020. doi: [10.1103/PhysRevB.102.085124](https://doi.org/10.1103/PhysRevB.102.085124).
- [4] J. Kaufmann, C. Eckhardt, M. Pickem, M. Kitatani, A. Kauch, and K. Held. “Self-consistent ladder dynamical vertex approximation”. *Phys. Rev. B* **103**, 035120, Jan 2021. doi: [10.1103/PhysRevB.103.035120](https://doi.org/10.1103/PhysRevB.103.035120).
- [5] M. Pickem, J. Kaufmann, K. Held, and J. M. Tomczak. “Zoology of spin and orbital fluctuations in ultrathin oxide films”. *Phys. Rev. B* **104**, 024307, Jul 2021. doi: [10.1103/PhysRevB.104.024307](https://doi.org/10.1103/PhysRevB.104.024307).
- [6] P. Worm, C. Watzenböck, M. Pickem, A. Kauch, and K. Held. “Broadening and sharpening of the Drude peak through antiferromagnetic fluctuations”. *Phys. Rev. B* **104**, 115153, Sep 2021. doi: [10.1103/PhysRevB.104.115153](https://doi.org/10.1103/PhysRevB.104.115153).
- [7] M. Pickem, E. Maggio, and J. M. Tomczak. “Resistivity saturation in Kondo insulators”. *Communications Physics* **4**(1), 226, Oct 2021. doi: [10.1038/s42005-021-00723-z](https://doi.org/10.1038/s42005-021-00723-z).
- [8] J. Gabel, M. Pickem, P. Scheiderer, L. Dudy, B. Leikert, M. Fuchs, M. Stübinger, M. Schmitt, J. Küspert, G. Sangiovanni, J. M. Tomczak, K. Held, T.-L. Lee, R. Claessen, and M. Sing.

- “Toward functionalized ultrathin oxide films: The impact of surface apical oxygen”. *Advanced Electronic Materials* page 2101006, Dec 2021. doi: [10.1002/aelm.202101006](https://doi.org/10.1002/aelm.202101006).
- [9] M. Pickem, E. Maggio, and J. M. Tomczak. “Prototypical many-body signatures in transport properties of semiconductors”. *Phys. Rev. B* **105**, 085139, Feb 2022. doi: [10.1103/PhysRevB.105.085139](https://doi.org/10.1103/PhysRevB.105.085139).
- [10] M. Pickem, J. M. Tomczak, and K. Held. “Particle-hole asymmetric lifetimes promoted by nonlocal spin and orbital fluctuations in SrVO₃ monolayers”. *Phys. Rev. Research* **4**, 033253, Sep 2022. doi: [10.1103/PhysRevResearch.4.033253](https://doi.org/10.1103/PhysRevResearch.4.033253).
- [11] M. Pickem, E. Maggio, and J. M. Tomczak. “LinReTraCe: The linear response transport centre”. *SciPost Phys. Codebases* page 16, 2023. doi: [10.21468/SciPostPhysCodeb.16](https://doi.org/10.21468/SciPostPhysCodeb.16).
- [12] M. Pickem, E. Maggio, and J. M. Tomczak. “Codebase release 1.1 for LinReTraCe”. *SciPost Phys. Codebases* pages 16–r1.1, 2023. <https://github.com/LinReTraCe/LinReTraCe/>. doi: [10.21468/SciPostPhysCodeb.16-r1.1](https://doi.org/10.21468/SciPostPhysCodeb.16-r1.1).
- [13] C. R. Harris, K. J. Millman, S. J. van der Walt, R. Gommers, P. Virtanen, D. Cournapeau, E. Wieser, J. Taylor, S. Berg, N. J. Smith, R. Kern, M. Picus, S. Hoyer, M. H. van Kerkwijk, M. Brett, A. Haldane, J. F. del Río, M. Wiebe, P. Peterson, P. Gérard-Marchant, K. Sheppard, T. Reddy, W. Weckesser, H. Abbasi, C. Gohlke, and T. E. Oliphant. “Array programming with NumPy”. *Nature* **585**(7825), 357–362, Sep 2020. doi: [10.1038/s41586-020-2649-2](https://doi.org/10.1038/s41586-020-2649-2).
- [14] P. Virtanen, R. Gommers, T. E. Oliphant, M. Haberland, T. Reddy, D. Cournapeau, E. Burovski, P. Peterson, W. Weckesser, J. Bright, S. J. van der Walt, M. Brett, J. Wilson, K. J. Millman, N. Mayorov, A. R. J. Nelson, E. Jones, R. Kern, E. Larson, C. J. Carey, Í. Polat, Y. Feng, E. W. Moore, J. VanderPlas, D. Laxalde, J. Perktold, R. Cimrman, I. Henriksen, E. A. Quintero, C. R. Harris, A. M. Archibald, A. H. Ribeiro, F. Pedregosa, P. van Mulbregt, and SciPy 1.0 Contributors. “SciPy 1.0: Fundamental Algorithms for Scientific Computing in Python”. *Nature Methods* **17**, 261–272, 2020. doi: [10.1038/s41592-019-0686-2](https://doi.org/10.1038/s41592-019-0686-2).
- [15] J. D. Hunter. “Matplotlib: A 2D graphics environment”. *Computing in Science & Engineering* **9**(3), 90–95, 2007. doi: [10.1109/MCSE.2007.55](https://doi.org/10.1109/MCSE.2007.55).
- [16] M. Mark, M. Baurzhan, W. Tobias, W. Alexander, v. S. Bas, badshah400, Mo-Gu, T. G. Badger, J.-S. Zbigniew, kensington, and kylesower. “markumtmitchell/engauge-digitizer: Nonrelease (v12.2.1)”. *Zenodo* 2020. doi: [10.5281/zenodo.3941227](https://doi.org/10.5281/zenodo.3941227).

- [17] D. Binosi and L. Theußl. “JaxoDraw: A graphical user interface for drawing Feynman diagrams”. *Computer Physics Communications* **161**(1), 76–86, 2004. doi: [10.1016/j.cpc.2004.05.001](https://doi.org/10.1016/j.cpc.2004.05.001).
- [18] K. Momma and F. Izumi. “VESTA 3 for three-dimensional visualization of crystal, volumetric and morphology data”. *J. Appl. Crystallogr.* **44**, 1272–1276, 2011. doi: [10.1107/S0021889811038970](https://doi.org/10.1107/S0021889811038970).
- [19] M. Kawamura. “FermiSurfer: Fermi-surface viewer providing multiple representation schemes”. *Computer Physics Communications* **239**, 197–203, 2019. doi: [10.1016/j.cpc.2019.01.017](https://doi.org/10.1016/j.cpc.2019.01.017).
- [20] W. R. Inc. “Mathematica, Version 12.3”. Champaign, IL, 2024.
- [21] P. Blaha, K. Schwarz, G.-K.-H. Madsen, D. Kvasnicka, and J. Luitz. “WIEN2k, an augmented plane wave plus local orbitals program for calculating crystal properties”. *Vienna University of Technology, Austria* 2001. ISBN 3-9501031-1-2.
- [22] P. Blaha, K. Schwarz, F. Tran, R. Laskowski, G. K. H. Madsen, and L. D. Marks. “Wien2k: An APW+lo program for calculating the properties of solids”. *The Journal of Chemical Physics* **152**(7), 074101, 2020. doi: [10.1063/1.5143061](https://doi.org/10.1063/1.5143061).
- [23] J. P. Perdew, K. Burke, and M. Ernzerhof. “Generalized gradient approximation made simple”. *Phys. Rev. Lett.* **77**(18), 3865–3868, Oct 1996. doi: [10.1103/PhysRevLett.77.3865](https://doi.org/10.1103/PhysRevLett.77.3865).
- [24] G. Kresse and J. Hafner. “Ab initio molecular dynamics for liquid metals”. *Phys. Rev. B* **47**, 558–561, Jan 1993. doi: [10.1103/PhysRevB.47.558](https://doi.org/10.1103/PhysRevB.47.558).
- [25] G. Kresse and J. Hafner. “Ab initio molecular-dynamics simulation of the liquid-metal–amorphous-semiconductor transition in germanium”. *Phys. Rev. B* **49**, 14251–14269, May 1994. doi: [10.1103/PhysRevB.49.14251](https://doi.org/10.1103/PhysRevB.49.14251).
- [26] G. Kresse and J. Furthmüller. “Efficiency of ab-initio total energy calculations for metals and semiconductors using a plane-wave basis set”. *Comput. Mater. Sci.* **6**(1), 15 – 50, 1996. doi: [10.1016/0927-0256\(96\)00008-0](https://doi.org/10.1016/0927-0256(96)00008-0).
- [27] A. Kokalj. “XCrySDen—a new program for displaying crystalline structures and electron densities”. *Journal of Molecular Graphics and Modelling* **17**(3), 176–179, 1999. doi: [10.1016/S1093-3263\(99\)00028-5](https://doi.org/10.1016/S1093-3263(99)00028-5).
- [28] J. Kunes, R. Arita, P. Wissgott, A. Toschi, H. Ikeda, and K. Held. “Wien2wannier: From linearized augmented plane waves to maximally localized Wannier functions”. *Computer Physics Communications* **181**(11), 1888 – 1895, 2010. doi: [10.1016/j.cpc.2010.08.005](https://doi.org/10.1016/j.cpc.2010.08.005).

- [29] A. A. Mostofi, J. R. Yates, Y.-S. Lee, I. Souza, D. Vanderbilt, and N. Marzari. “wannier90: A tool for obtaining maximally-localised Wannier functions”. *Computer Physics Communications* **178**(9), 685 – 699, 2008. doi: [10.1016/j.cpc.2007.11.016](https://doi.org/10.1016/j.cpc.2007.11.016).
- [30] M. Wallerberger, A. Hausoel, P. Gunacker, A. Kowalski, N. Parragh, F. Goth, K. Held, and G. Sangiovanni. “w2dynamics: Local one- and two-particle quantities from dynamical mean field theory”. *Computer Physics Communications* **235**, 388 – 399, 2019. doi: [10.1016/j.cpc.2018.09.007](https://doi.org/10.1016/j.cpc.2018.09.007).
- [31] J. Kaufmann and K. Held. “ana_cont: Python package for analytic continuation”. *Computer Physics Communications* **282**, 108519, 2023. doi: [10.1016/j.cpc.2022.108519](https://doi.org/10.1016/j.cpc.2022.108519).
- [32] K. Haule, C.-H. Yee, and K. Kim. “Dynamical mean-field theory within the full-potential methods: Electronic structure of CeIrIn₅, CeCoIn₅, and CeRhIn₅”. *Phys. Rev. B* **81**(19), 195107, May 2010. doi: [10.1103/PhysRevB.81.195107](https://doi.org/10.1103/PhysRevB.81.195107).
- [33] A. Galler, P. Thunström, P. Gunacker, J. M. Tomczak, and K. Held. “Ab initio dynamical vertex approximation”. *Phys. Rev. B* **95**, 115107, Mar 2017. doi: [10.1103/PhysRevB.95.115107](https://doi.org/10.1103/PhysRevB.95.115107).
- [34] M. Born and R. Oppenheimer. “Zur Quantentheorie der Molekeln”. *Annalen der Physik* **389**(20), 457–484, 1927. doi: [10.1002/andp.19273892002](https://doi.org/10.1002/andp.19273892002).
- [35] P. Hohenberg and W. Kohn. “Inhomogeneous electron gas”. *Phys. Rev.* **136**(3B), B864–B871, Nov 1964. doi: [10.1103/PhysRev.136.B864](https://doi.org/10.1103/PhysRev.136.B864).
- [36] W. Kohn and L. J. Sham. “Self-consistent equations including exchange and correlation effects”. *Phys. Rev.* **140**(4A), A1133–A1138, Nov 1965. doi: [10.1103/PhysRev.140.A1133](https://doi.org/10.1103/PhysRev.140.A1133).
- [37] R. O. Jones and O. Gunnarsson. “The density functional formalism, its applications and prospects”. *Rev. Mod. Phys.* **61**(3), 689–746, Jul 1989. doi: [10.1103/RevModPhys.61.689](https://doi.org/10.1103/RevModPhys.61.689).
- [38] G. Kresse and J. Furthmüller. “Efficient iterative schemes for *ab initio* total-energy calculations using a plane-wave basis set”. *Phys. Rev. B* **54**, 11169–11186, Oct 1996. doi: [10.1103/PhysRevB.54.11169](https://doi.org/10.1103/PhysRevB.54.11169).
- [39] P. Giannozzi, S. Baroni, N. Bonini, M. Calandra, R. Car, C. Cavazzoni, D. Ceresoli, G. L. Chiarotti, M. Cococcioni, I. Dabo, A. Dal Corso, S. de Gironcoli, S. Fabris, G. Fratesi, R. Gebauer, U. Gerstmann, C. Gougoussis, A. Kokalj, M. Lazzeri, L. Martin-Samos, N. Marzari, F. Mauri, R. Mazzarello, S. Paolini, A. Pasquarello, L. Paulatto, C. Sbraccia,

- S. Scandolo, G. Scლაუzero, A. P. Seitsonen, A. Smogunov, P. Umari, and R. M. Wentzcovitch. “Quantum espresso: a modular and open-source software project for quantum simulations of materials”. *Journal of Physics: Condensed Matter* **21**(39), 395502, 2009. doi: [10.1088/0953-8984/21/39/395502](https://doi.org/10.1088/0953-8984/21/39/395502).
- [40] A. García, N. Papior, A. Akhtar, E. Artacho, V. Blum, E. Bosoni, P. Brandimarte, M. Brandbyge, J. I. Cerdá, F. Corsetti, R. Cuadrado, V. Dikan, J. Ferrer, J. Gale, P. García-Fernández, V. M. García-Suárez, S. García, G. Huhs, S. Illera, R. Korytár, P. Koval, I. Lebedeva, L. Lin, P. López-Tarifa, S. G. Mayo, S. Mohr, P. Ordejón, A. Postnikov, Y. Pouillon, M. Pruneda, R. Robles, D. Sánchez-Portal, J. M. Soler, R. Ullah, V. W.-z. Yu, and J. Junquera. “Siesta: Recent developments and applications”. *The Journal of Chemical Physics* **152**(20), 204108, 2020. doi: [10.1063/5.0005077](https://doi.org/10.1063/5.0005077).
- [41] K. Burke, J. P. Perdew, and Y. Wang. “Derivation of a generalized gradient approximation: The PW91 density functional”. *Springer US* pages 81–111, 1998. doi: [10.1007/978-1-4899-0316-7_7](https://doi.org/10.1007/978-1-4899-0316-7_7).
- [42] R. O. Jones. “Density functional theory: Its origins, rise to prominence, and future”. *Rev. Mod. Phys.* **87**, 897–923, Aug 2015. doi: [10.1103/RevModPhys.87.897](https://doi.org/10.1103/RevModPhys.87.897).
- [43] L. J. Sham and M. Schlüter. “Density-functional theory of the energy gap”. *Phys. Rev. Lett.* **51**, 1888–1891, Nov 1983. doi: [10.1103/PhysRevLett.51.1888](https://doi.org/10.1103/PhysRevLett.51.1888).
- [44] R. W. Godby, M. Schlüter, and L. J. Sham. “Accurate exchange-correlation potential for silicon and its discontinuity on addition of an electron”. *Phys. Rev. Lett.* **56**, 2415–2418, Jun 1986. doi: [10.1103/PhysRevLett.56.2415](https://doi.org/10.1103/PhysRevLett.56.2415).
- [45] A. Görling. “Exchange-correlation potentials with proper discontinuities for physically meaningful Kohn-Sham eigenvalues and band structures”. *Phys. Rev. B* **91**, 245120, Jun 2015. doi: [10.1103/PhysRevB.91.245120](https://doi.org/10.1103/PhysRevB.91.245120).
- [46] J. P. Perdew and M. Levy. “Physical content of the exact Kohn-Sham orbital energies: Band gaps and derivative discontinuities”. *Phys. Rev. Lett.* **51**, 1884–1887, Nov 1983. doi: [10.1103/PhysRevLett.51.1884](https://doi.org/10.1103/PhysRevLett.51.1884).
- [47] P. Mori-Sánchez and A. J. Cohen. “The derivative discontinuity of the exchange–correlation functional”. *Phys. Chem. Chem. Phys.* **16**(28), 14378–14387, 2014. doi: [10.1039/c4cp01170h](https://doi.org/10.1039/c4cp01170h).
- [48] F. Tran and P. Blaha. “Accurate band gaps of semiconductors and insulators with a semilocal exchange-correlation potential”. *Phys. Rev. Lett.* **102**, 226401, Jun 2009. doi: [10.1103/PhysRevLett.102.226401](https://doi.org/10.1103/PhysRevLett.102.226401).

- [49] M. Kuusma, J. Ojanen, J. Enkovaara, and T. T. Rantala. “Kohn-Sham potential with discontinuity for band gap materials”. *Phys. Rev. B* **82**, 115106, Sep 2010. doi: [10.1103/PhysRevB.82.115106](https://doi.org/10.1103/PhysRevB.82.115106).
- [50] F. Tran, S. Ehsan, and P. Blaha. “Assessment of the GLLB-SC potential for solid-state properties and attempts for improvement”. *Phys. Rev. Materials* **2**, 023802, Feb 2018. doi: [10.1103/PhysRevMaterials.2.023802](https://doi.org/10.1103/PhysRevMaterials.2.023802).
- [51] Wikimedia Commons. “Simple periodic table chart”. https://commons.wikimedia.org/wiki/File:Simple_Periodic_Table_Chart-en.svg, Dec 2017. Last visited: Feb 2024.
- [52] F. H. L. Essler, V. E. Korepin, and K. Schoutens. “Complete solution of the one-dimensional Hubbard model”. *Phys. Rev. Lett.* **67**, 3848–3851, Dec 1991. doi: [10.1103/PhysRevLett.67.3848](https://doi.org/10.1103/PhysRevLett.67.3848).
- [53] N. Blümer. *Mott-Hubbard Metal-Insulator Transition and Optical Conductivity in High Dimensions*. PhD thesis, Universität Augsburg, 1999.
- [54] J. Kuneš. “Efficient treatment of two-particle vertices in dynamical mean-field theory”. *Physical Review B* **83**(8), Feb 2011. doi: [10.1103/PhysRevB.83.085102](https://doi.org/10.1103/PhysRevB.83.085102).
- [55] V. I. Anisimov, J. Zaanen, and O. K. Andersen. “Band theory and Mott insulators: Hubbard U instead of Stoner I”. *Phys. Rev. B* **44**(3), 943–954, Jul 1991. doi: [10.1103/PhysRevB.44.943](https://doi.org/10.1103/PhysRevB.44.943).
- [56] A. I. Liechtenstein, V. I. Anisimov, and J. Zaanen. “Density-functional theory and strong interactions: Orbital ordering in Mott-Hubbard insulators”. *Phys. Rev. B* **52**, R5467–R5470, Aug 1995. doi: [10.1103/PhysRevB.52.R5467](https://doi.org/10.1103/PhysRevB.52.R5467).
- [57] S. Ryee and M. J. Han. “The effect of double counting, spin density, and Hund interaction in the different DFT+U functionals”. *Scientific Reports* **8**(1), 9559, 2018. doi: [10.1038/s41598-018-27731-4](https://doi.org/10.1038/s41598-018-27731-4).
- [58] P. Hansmann, A. Toschi, G. Sangiovanni, T. Saha-Dasgupta, S. Lupi, M. Marsi, and K. Held. “Mott–Hubbard transition in V_2O_3 revisited”. *physica status solidi (b)* **250**(7), 1251–1264, 2013. doi: [10.1002/pssb.201248476](https://doi.org/10.1002/pssb.201248476).
- [59] M. Imada, A. Fujimori, and Y. Tokura. “Metal-insulator transitions”. *Rev. Mod. Phys.* **70**(4), 1039–1263, Oct 1998. doi: [10.1103/RevModPhys.70.1039](https://doi.org/10.1103/RevModPhys.70.1039).
- [60] D. Grieger and F. Lechermann. “Effect of chromium doping on the correlated electronic structure of V_2O_3 ”. *Phys. Rev. B* **90**, 115115, Sep 2014. doi: [10.1103/PhysRevB.90.115115](https://doi.org/10.1103/PhysRevB.90.115115).

- [61] K. Burke and J. Kozłowski. “Lies my teacher told me about density functional theory: Seeing through them with the Hubbard dimer”. *arXiv* 2022. doi: [10.48550/arXiv.2108.11534](https://doi.org/10.48550/arXiv.2108.11534).
- [62] A. I. Poteryaev, J. M. Tomczak, S. Biermann, A. Georges, A. I. Lichtenstein, A. N. Rubtsov, T. Saha-Dasgupta, and O. K. Andersen. “Enhanced crystal-field splitting and orbital-selective coherence induced by strong correlations in V_2O_3 ”. *Phys. Rev. B* **76**(8) 085127, 2007. doi: [10.1103/PhysRevB.76.085127](https://doi.org/10.1103/PhysRevB.76.085127).
- [63] N. Marzari, A. A. Mostofi, J. R. Yates, I. Souza, and D. Vanderbilt. “Maximally localized Wannier functions: Theory and applications”. *Rev. Mod. Phys.* **84**, 1419–1475, Oct 2012. doi: [10.1103/RevModPhys.84.1419](https://doi.org/10.1103/RevModPhys.84.1419).
- [64] J. M. Tomczak. *Spectral and Optical Properties of Correlated Materials*. PhD thesis, École Polytechnique, Sep 2007.
- [65] F. Aryasetiawan, M. Imada, A. Georges, G. Kotliar, S. Biermann, and A. I. Lichtenstein. “Frequency-dependent local interactions and low-energy effective models from electronic structure calculations”. *Phys. Rev. B* **70**(19), 195104, Nov 2004. doi: [10.1103/PhysRevB.70.195104](https://doi.org/10.1103/PhysRevB.70.195104).
- [66] T. Miyake and F. Aryasetiawan. “Screened Coulomb interaction in the maximally localized Wannier basis”. *Phys. Rev. B* **77**(8) 085122, 2008. doi: [10.1103/PhysRevB.77.085122](https://doi.org/10.1103/PhysRevB.77.085122).
- [67] T. Miyake, F. Aryasetiawan, and M. Imada. “Ab initio procedure for constructing effective models of correlated materials with entangled band structure”. *Phys. Rev. B* **80**, 155134, (2009). doi: [10.1103/PhysRevB.80.155134](https://doi.org/10.1103/PhysRevB.80.155134).
- [68] V. I. Anisimov and O. Gunnarsson. “Density-functional calculation of effective Coulomb interactions in metals”. *Phys. Rev. B* **43**(10), 7570–7574, Apr 1991. doi: [10.1103/PhysRevB.43.7570](https://doi.org/10.1103/PhysRevB.43.7570).
- [69] M. Cococcioni and S. de Gironcoli. “Linear response approach to the calculation of the effective interaction parameters in the LDA+U method”. *Phys. Rev. B* **71**(3), 035105, Jan 2005. doi: [10.1103/PhysRevB.71.035105](https://doi.org/10.1103/PhysRevB.71.035105).
- [70] F. Nilsson, R. Sakuma, and F. Aryasetiawan. “Ab initio calculations of the Hubbard U for the early lanthanides using the constrained random-phase approximation”. *Phys. Rev. B* **88**, 125123, Sep 2013. doi: [10.1103/PhysRevB.88.125123](https://doi.org/10.1103/PhysRevB.88.125123).
- [71] L. Hedin. “New method for calculating the one-particle green’s function with application to the electron-gas problem”. *Phys. Rev.* **139**(3A), A796–A823, Aug 1965. doi: [10.1103/PhysRev.139.A796](https://doi.org/10.1103/PhysRev.139.A796).

- [72] S. Biermann, F. Aryasetiawan, and A. Georges. “First-principles approach to the electronic structure of strongly correlated systems: Combining the GW approximation and dynamical mean-field theory”. *Phys. Rev. Lett.* **90**(8), 086402, Feb 2003. doi: [10.1103/PhysRevLett.90.086402](https://doi.org/10.1103/PhysRevLett.90.086402).
- [73] S. Biermann. “Dynamical screening effects in correlated electron materials—a progress report on combined many-body perturbation and dynamical mean field theory: ‘GW + DMFT’”. *Journal of Physics: Condensed Matter* **26**(17), 173202, 2014. doi: [10.1088/0953-8984/26/17/173202](https://doi.org/10.1088/0953-8984/26/17/173202).
- [74] J. M. Tomczak, P. Liu, A. Toschi, G. Kresse, and K. Held. “Merging GW with DMFT and non-local correlations beyond”. *The European Physical Journal Special Topics* **226**(11), 2565–2590, Jul 2017. doi: [10.1140/epjst/e2017-70053-1](https://doi.org/10.1140/epjst/e2017-70053-1).
- [75] P. Werner and A. J. Millis. “Dynamical screening in correlated electron materials”. *Phys. Rev. Lett.* **104**, 146401, Apr 2010. doi: [10.1103/PhysRevLett.104.146401](https://doi.org/10.1103/PhysRevLett.104.146401).
- [76] O. Gunnarsson, O. K. Andersen, O. Jepsen, and J. Zaanen. “Density-functional calculation of the parameters in the Anderson model: Application to Mn in CdTe”. *Phys. Rev. B* **39**, 1708–1722, Jan 1989. doi: [10.1103/PhysRevB.39.1708](https://doi.org/10.1103/PhysRevB.39.1708).
- [77] L. Vaugier. *Electronic Structure of Correlated Materials From First Principles: Hubbard interaction and Hund’s exchange*. PhD thesis, École Polytechnique, Dec 2011.
- [78] F. Aryasetiawan, K. Karlsson, O. Jepsen, and U. Schönberger. “Calculations of Hubbard U from first-principles”. *Phys. Rev. B* **74**, 125106, Sep 2006. doi: [10.1103/PhysRevB.74.125106](https://doi.org/10.1103/PhysRevB.74.125106).
- [79] A. Sekiyama, H. Fujiwara, S. Imada, S. Suga, H. Eisaki, S. I. Uchida, K. Takegahara, H. Harima, Y. Saitoh, I. A. Nekrasov, G. Keller, D. E. Kondakov, A. V. Kozhevnikov, T. Pruschke, K. Held, D. Vollhardt, and V. I. Anisimov. “Mutual experimental and theoretical validation of bulk photoemission spectra of $\text{Sr}_{1-x}\text{Ca}_x\text{VO}_3$ ”. *Phys. Rev. Lett.* **93**, 156402, Oct 2004. doi: [10.1103/PhysRevLett.93.156402](https://doi.org/10.1103/PhysRevLett.93.156402).
- [80] J. A. Moyer, C. Eaton, and R. Engel-Herbert. “Highly conductive SrVO_3 as a bottom electrode for functional perovskite oxides”. *Advanced Materials* **25**(26), 3578–3582, 2013. doi: [10.1002/adma.201300900](https://doi.org/10.1002/adma.201300900).
- [81] L. Zhang, Y. Zhou, L. Guo, W. Zhao, A. Barnes, H.-T. Zhang, C. Eaton, Y. Zheng, M. Brahlek, H. F. Haneef, N. J. Podraza, M. H. W. Chan, V. Gopalan, K. M. Rabe, and R. Engel-Herbert. “Correlated metals as transparent conductors”. *Nat. Mater.* **15**(2), 204–210, Feb 2016. doi: [10.1038/nmat4493](https://doi.org/10.1038/nmat4493).

- [82] L. Si, J. Kaufmann, Z. Zhong, J. M. Tomczak, and K. Held. “Pitfalls and solutions for perovskite transparent conductors”. *Phys. Rev. B* **104**, L041112, Jul 2021. doi: [10.1103/PhysRevB.104.L041112](https://doi.org/10.1103/PhysRevB.104.L041112).
- [83] A. Haque, S. K. Mandal, A. Jeyaseelan, S. Vura, P. Nukala, and S. Raghavan. “Robust atmospherically stable hybrid SrVO₃/Graphene//SrTiO₃ template for fast and facile large-area transfer of complex oxides onto Si”. *arXiv* 2023. doi: [10.48550/arXiv.2307.03342](https://doi.org/10.48550/arXiv.2307.03342).
- [84] F. Macià, M. Mirjolet, and J. Fontcuberta. “Efficient spin pumping into metallic SrVO₃ epitaxial films”. *Journal of Magnetism and Magnetic Materials* **546**, 168871, 2022. doi: [10.1016/j.jmmm.2021.168871](https://doi.org/10.1016/j.jmmm.2021.168871).
- [85] K. Yoshimatsu, T. Okabe, H. Kumigashira, S. Okamoto, S. Aizaki, A. Fujimori, and M. Oshima. “Dimensional-crossover-driven metal-insulator transition in SrVO₃ ultrathin films”. *Phys. Rev. Lett.* **104**, 147601, Apr 2010. doi: [10.1103/PhysRevLett.104.147601](https://doi.org/10.1103/PhysRevLett.104.147601).
- [86] Z. Zhong, M. Wallerberger, J. M. Tomczak, C. Taranto, N. Parragh, A. Toschi, G. Sangiovanni, and K. Held. “Electronics with correlated oxides: SrVO₃/SrTiO₃ as a Mott transistor”. *Phys. Rev. Lett.* **114**, 246401, Jun 2015. doi: [10.1103/PhysRevLett.114.246401](https://doi.org/10.1103/PhysRevLett.114.246401).
- [87] E. Pavarini, A. Yamasaki, J. Nuss, and O. K. Andersen. “How chemistry controls electron localization in 3d¹ perovskites: a Wannier-function study”. *New Journal of Physics* **7**, 188, 2005. doi: [10.1088/1367-2630/7/1/188](https://doi.org/10.1088/1367-2630/7/1/188).
- [88] P. Hansmann, N. Parragh, A. Toschi, G. Sangiovanni, and K. Held. “Importance of d–p Coulomb interaction for high T_C cuprates and other oxides”. *New Journal of Physics* **16**(3), 033009, mar 2014. doi: [10.1088/1367-2630/16/3/033009](https://doi.org/10.1088/1367-2630/16/3/033009).
- [89] J. M. Tomczak, M. Casula, T. Miyake, F. Aryasetiawan, and S. Biermann. “Combined GW and dynamical mean-field theory: Dynamical screening effects in transition metal oxides”. *EPL (Europhysics Letters)* **100**(6), 67001, 2012. doi: [10.1209/0295-5075/100/67001](https://doi.org/10.1209/0295-5075/100/67001).
- [90] J. M. Tomczak, M. Casula, T. Miyake, and S. Biermann. “Asymmetry in band widening and quasiparticle lifetimes in SrVO₃: Competition between screened exchange and local correlations from combined GW and dynamical mean-field theory GW + DMFT”. *Phys. Rev. B* **90**, 165138, Oct 2014. doi: [10.1103/PhysRevB.90.165138](https://doi.org/10.1103/PhysRevB.90.165138).
- [91] M. Casula, A. Rubtsov, and S. Biermann. “Dynamical screening effects in correlated materials: Plasmon satellites and spectral weight transfers from a Green’s function

- ansatz to extended dynamical mean field theory”. *Phys. Rev. B* **85**, 035115, Jan 2012. doi: [10.1103/PhysRevB.85.035115](https://doi.org/10.1103/PhysRevB.85.035115).
- [92] L. Boehnke, F. Nilsson, F. Aryasetiawan, and P. Werner. “When strong correlations become weak: Consistent merging of GW and DMFT”. *Phys. Rev. B* **94**, 201106, Nov 2016. doi: [10.1103/PhysRevB.94.201106](https://doi.org/10.1103/PhysRevB.94.201106).
- [93] G. Rohringer, H. Hafermann, A. Toschi, A. A. Katanin, A. E. Antipov, M. I. Katsnelson, A. I. Lichtenstein, A. N. Rubtsov, and K. Held. “Diagrammatic routes to nonlocal correlations beyond dynamical mean field theory”. *Rev. Mod. Phys.* **90**, 025003, May 2018. doi: [10.1103/RevModPhys.90.025003](https://doi.org/10.1103/RevModPhys.90.025003).
- [94] A. Georges, G. Kotliar, W. Krauth, and M. J. Rozenberg. “Dynamical mean-field theory of strongly correlated fermion systems and the limit of infinite dimensions”. *Rev. Mod. Phys.* **68**, 13–125, Jan 1996. doi: [10.1103/RevModPhys.68.13](https://doi.org/10.1103/RevModPhys.68.13).
- [95] W. Metzner and D. Vollhardt. “Correlated Lattice Fermions in $d = \infty$ Dimensions”. *Phys. Rev. Lett.* **62**, 324–327, (1989). doi: [10.1103/PhysRevLett.62.324](https://doi.org/10.1103/PhysRevLett.62.324).
- [96] P. Gunacker, M. Wallerberger, E. Gull, A. Hausoel, G. Sangiovanni, and K. Held. “Continuous-time quantum Monte Carlo using worm sampling”. *Phys. Rev. B* **92**, 155102, (2015). doi: [10.1103/PhysRevB.92.155102](https://doi.org/10.1103/PhysRevB.92.155102).
- [97] E. Gull, A. J. Millis, A. I. Lichtenstein, A. N. Rubtsov, M. Troyer, and P. Werner. “Continuous-time Monte Carlo methods for quantum impurity models”. *Rev. Mod. Phys.* **83**, 349–404, May 2011. doi: [10.1103/RevModPhys.83.349](https://doi.org/10.1103/RevModPhys.83.349).
- [98] L. V. Pourovskii, B. Amadon, S. Biermann, and A. Georges. “Self-consistency over the charge density in dynamical mean-field theory: A linear muffin-tin implementation and some physical implications”. *Phys. Rev. B* **76**(23) 235101, 2007. doi: [10.1103/PhysRevB.76.235101](https://doi.org/10.1103/PhysRevB.76.235101).
- [99] S. Bhandary, E. Assmann, M. Aichhorn, and K. Held. “Charge self-consistency in density functional theory combined with dynamical mean field theory: k -space reoccupation and orbital order”. *Phys. Rev. B* **94**, 155131, Oct 2016. doi: [10.1103/PhysRevB.94.155131](https://doi.org/10.1103/PhysRevB.94.155131).
- [100] I. A. Nekrasov, G. Keller, D. E. Kondakov, A. V. Kozhevnikov, T. Pruschke, K. Held, D. Vollhardt, and V. I. Anisimov. “Explanation of the similarity of the experimental photoemission spectra of SrVO₃ and CaVO₃”. *arXiv* 2003. doi: [10.48550/arXiv.cond-mat/0211508](https://doi.org/10.48550/arXiv.cond-mat/0211508).

- [101] M. Jarrell and J. Gubernatis. “Bayesian inference and the analytic continuation of imaginary-time quantum Monte Carlo data”. *Physics Reports* **269**(3), 133 – 195, (1996). doi: [10.1016/0370-1573\(95\)00074-7](https://doi.org/10.1016/0370-1573(95)00074-7).
- [102] S. Gull. “Developments in maximum entropy data analysis”. *Springer Dordrecht* pages 53–71, 1989. ISBN 978-0-7923-0224-7.
- [103] T. Pillo, J. Hayoz, H. Berger, F. Lévy, L. Schlapbach, and P. Aebi. “Photoemission of bands above the Fermi level: The excitonic insulator phase transition in 1T-TiSe₂”. *Phys. Rev. B* **61**, 16213–16222, Jun 2000. doi: [10.1103/PhysRevB.61.16213](https://doi.org/10.1103/PhysRevB.61.16213).
- [104] F. Reinert and S. Hüfner. “Photoemission spectroscopy—from early days to recent applications”. *New Journal of Physics* **7**(1), 97, Apr 2005. doi: [10.1088/1367-2630/7/1/097](https://doi.org/10.1088/1367-2630/7/1/097).
- [105] S. Backes, T. C. Rödel, F. Fortuna, E. Frantzeskakis, P. Le Fère, F. Bertran, M. Kobayashi, R. Yukawa, T. Mitsuhashi, M. Kitamura, K. Horiba, H. Kumigashira, R. Saint-Martin, A. Fouchet, B. Berini, Y. Dumont, A. J. Kim, F. Lechermann, H. O. Jeschke, M. J. Rozenberg, R. Valentí, and A. F. Santander-Syro. “Hubbard band versus oxygen vacancy states in the correlated electron metal SrVO₃”. *Phys. Rev. B* **94**(24), 241110, December 2016. doi: [10.1103/PhysRevB.94.241110](https://doi.org/10.1103/PhysRevB.94.241110).
- [106] R. Eguchi, T. Kiss, S. Tsuda, T. Shimojima, T. Mizokami, T. Yokoya, A. Chainani, S. Shin, I. H. Inoue, T. Togashi, S. Watanabe, C. Q. Zhang, C. T. Chen, M. Arita, K. Shimada, H. Namatame, and M. Taniguchi. “Bulk- and surface-sensitive high-resolution photoemission study of two Mott-Hubbard systems: SrVO₃ and CaVO₃”. *Phys. Rev. Lett.* **96**, 076402, Feb 2006. doi: [10.1103/PhysRevLett.96.076402](https://doi.org/10.1103/PhysRevLett.96.076402).
- [107] V. Giannakopoulou, P. Odier, J. Bassat, and J. Loup. “SrVO₃ and Sr₂VO₄, electrical properties below and above room T”. *Solid State Communications* **93**(7), 579–583, 1995. doi: [10.1016/0038-1098\(94\)00834-Y](https://doi.org/10.1016/0038-1098(94)00834-Y).
- [108] I. H. Inoue, N. Shirakawa, I. Hase, O. Goto, H. Makino, and M. Ishikawa. “Specific heat of a single-crystalline perovskite,”. *Journal of Physics: Condensed Matter* **10**(49), 11541–11545, December 1998. doi: [10.1088/0953-8984/10/49/041](https://doi.org/10.1088/0953-8984/10/49/041).
- [109] K. Yoshimatsu, K. Horiba, H. Kumigashira, T. Yoshida, A. Fujimori, and M. Oshima. “Metallic quantum well states in artificial structures of strongly correlated oxide”. *Science* **333**(6040), 319–322, Jul 2011. doi: [10.1126/science.1205771](https://doi.org/10.1126/science.1205771).

- [110] R. Yukawa, M. Kobayashi, T. Kanda, D. Shiga, K. Yoshimatsu, S. Ishibashi, M. Minohara, M. Kitamura, K. Horiba, A. F. Santander-Syro, and H. Kumigashira. “Resonant tunneling driven metal-insulator transition in double quantum-well structures of strongly correlated oxide”. *Nature Communications* **12**(1), 7070, 2021. doi: [10.1038/s41467-021-27327-z](https://doi.org/10.1038/s41467-021-27327-z).
- [111] C. Wang, H. Zhang, K. Deepak, C. Chen, A. Fouchet, J. Duan, D. Hilliard, U. Kentsch, D. Chen, M. Zeng, X. Gao, Y.-J. Zeng, M. Helm, W. Prellier, and S. Zhou. “Tuning the metal-insulator transition in epitaxial SrVO₃ films by uniaxial strain”. *Phys. Rev. Materials* **3**, 115001, Nov 2019. doi: [10.1103/PhysRevMaterials.3.115001](https://doi.org/10.1103/PhysRevMaterials.3.115001).
- [112] G. Wang, Z. Wang, M. Meng, M. Saghayezhian, L. Chen, C. Chen, H. Guo, Y. Zhu, E. W. Plummer, and J. Zhang. “Role of disorder and correlations in the metal-insulator transition in ultra-thin SrVO₃ films”. *Phys. Rev. B* **100**, 155114, Oct 2019. doi: [10.1103/PhysRevB.100.155114](https://doi.org/10.1103/PhysRevB.100.155114).
- [113] M. J. Rozenberg. “Integer-filling metal-insulator transitions in the degenerate Hubbard model”. *Phys. Rev. B* **55**, R4855–R4858, Feb 1997. doi: [10.1103/PhysRevB.55.R4855](https://doi.org/10.1103/PhysRevB.55.R4855).
- [114] A. Fujimori, I. Hase, H. Namatame, Y. Fujishima, Y. Tokura, H. Eisaki, S. Uchida, K. Takegahara, and F. M. F. de Groot. “Evolution of the spectral function in Mott-Hubbard systems with d¹ configuration”. *Phys. Rev. Lett.* **69**, 1796–1799, Sep 1992. doi: [10.1103/PhysRevLett.69.1796](https://doi.org/10.1103/PhysRevLett.69.1796).
- [115] H. Makino, I. H. Inoue, M. J. Rozenberg, I. Hase, Y. Aiura, and S. Onari. “Bandwidth control in a perovskite-type 3d¹-correlated metal Ca_{1-x}Sr_xVO₃. II. Optical spectroscopy”. *Phys. Rev. B* **58**, 4384–4393, Aug 1998. doi: [10.1103/PhysRevB.58.4384](https://doi.org/10.1103/PhysRevB.58.4384).
- [116] Y. Okimoto, T. Katsufuji, Y. Okada, T. Arima, and Y. Tokura. “Optical spectra in (La,Y)TiO₃: Variation of Mott-Hubbard gap features with change of electron correlation and band filling”. *Phys. Rev. B* **51**, 9581–9588, Apr 1995. doi: [10.1103/PhysRevB.51.9581](https://doi.org/10.1103/PhysRevB.51.9581).
- [117] V. M. Goldschmidt. “Die Gesetze der Krystallochemie”. *Naturwissenschaften* **14**(21), 477–485, 1926. doi: [10.1007/BF01507527](https://doi.org/10.1007/BF01507527).
- [118] D. McNally, X. Lu, J. Pelliciani, S. Beck, M. Dantz, M. Naamneh, T. Shang, M. Medarde, C. Schneider, V. Strocov, E. Pomjakushina, C. Ederer, M. Radovic, and T. Schmitt. “Electronic localization in CaVO₃ films via bandwidth control”. *npj Quantum Materials* **4**, 12 2019. doi: [10.1038/s41535-019-0146-3](https://doi.org/10.1038/s41535-019-0146-3).
- [119] E. Pavarini, S. Biermann, A. Poteryaev, A. I. Lichtenstein, A. Georges, and O. K. Andersen. “Mott transition and suppression of orbital fluctuations in orthorhombic 3d¹ perovskites”. *Phys. Rev. Lett.* **92**, 176403, Apr 2004. doi: [10.1103/PhysRevLett.92.176403](https://doi.org/10.1103/PhysRevLett.92.176403).

- [120] M. J. Christensen. *Epitaxy, Thin films and Superlattices*. PhD thesis, Risø National Laboratory, Apr 1997.
- [121] N. A. Shepelin, Z. P. Tehrani, N. Ohannessian, C. W. Schneider, D. Pergolesi, and T. Lipfert. “A practical guide to pulsed laser deposition”. *Chem. Soc. Rev.* **52**, 2294–2321, 2023. doi: [10.1039/D2CS00938B](https://doi.org/10.1039/D2CS00938B).
- [122] A. J. Haider, T. Alawsi, M. J. Haider, B. A. Taha, and H. A. Marhoon. “A comprehensive review on pulsed laser deposition technique to effective nanostructure production: trends and challenges”. *Optical and Quantum Electronics* **54**(8), 488, 2022. doi: [10.1007/s11082-022-03786-6](https://doi.org/10.1007/s11082-022-03786-6).
- [123] M. A. Hafez, M. K. Zayed, and H. E. Elsayed-Ali. “Review: Geometric interpretation of reflection and transmission RHEED patterns”. *Micron* **159**, 103286, 2022. doi: [10.1016/j.micron.2022.103286](https://doi.org/10.1016/j.micron.2022.103286).
- [124] D. Toyota, I. Ohkubo, H. Kumigashira, M. Oshima, T. Ohnishi, M. Lippmaa, M. Takizawa, A. Fujimori, K. Ono, M. Kawasaki, and H. Koinuma. “Thickness-dependent electronic structure of ultrathin SrRuO₃ films studied by in situ photoemission spectroscopy”. *Appl. Phys. Lett.* **87**(16), 162508, 2005. doi: [10.1063/1.2108123](https://doi.org/10.1063/1.2108123).
- [125] M. Golalikhani, Q. Lei, R. U. Chandrasena, L. Kasaei, H. Park, J. Bai, P. Orgiani, J. Ciston, G. E. Sterbinsky, D. A. Arena, P. Shafer, E. Arenholz, B. A. Davidson, A. J. Millis, A. X. Gray, and X. X. Xi. “Nature of the metal-insulator transition in few-unit-cell-thick LaNiO₃ films”. *Nature Communications* **9**(1), 2206, 2018. doi: [10.1038/s41467-018-04546-5](https://doi.org/10.1038/s41467-018-04546-5).
- [126] S. K. Chaluvadi, V. Polewczyk, A. Y. Petrov, G. Vinai, L. Braglia, J. M. Diez, V. Pieron, P. Perna, L. Mechin, P. Torelli, and P. Orgiani. “Electronic properties of fully strained La_{1-x}Sr_xMnO₃ thin films grown by molecular beam epitaxy (0.15 < x < 0.45)”. *ACS Omega* **7**(17), 14571–14578, 05 2022. doi: [10.1021/acsomega.1c06529](https://doi.org/10.1021/acsomega.1c06529).
- [127] A. Biswas and Y. H. Jeong. “Growth and engineering of perovskite SrIrO₃ thin films”. *Current Applied Physics* **17**(5), 605–614, 2017. Oxide Heterostructure Research in Korea. doi: [10.1016/j.cap.2016.09.020](https://doi.org/10.1016/j.cap.2016.09.020).
- [128] W. Qiu, Z. Ma, D. Patel, L. Sang, C. Cai, M. Shahriar Al Hossain, Z. Cheng, X. Wang, and S. X. Dou. “The interface structure of FeSe thin film on CaF₂ substrate and its influence on the superconducting performance”. *ACS Applied Materials & Interfaces* **9**(42), 37446–37453, 10 2017. doi: [10.1021/acsami.7b11853](https://doi.org/10.1021/acsami.7b11853).

- [129] K. S. Takahashi, J. Iguchi, Y. Tokura, and M. Kawasaki. “Metal-insulator transitions in strained single quantum wells of $\text{Sr}_{1-x}\text{La}_x\text{VO}_3$ ”. *Phys. Rev. B* **109**, 035158, Jan 2024. doi: [10.1103/PhysRevB.109.035158](https://doi.org/10.1103/PhysRevB.109.035158).
- [130] H. Okuma, Y. Katayama, K. Otomo, and K. Ueno. “Transport properties around the metal-insulator transition for SrVO_3 ultrathin films fabricated by electrochemical etching”. *Phys. Rev. B* **105**, 045138, Jan 2022. doi: [10.1103/PhysRevB.105.045138](https://doi.org/10.1103/PhysRevB.105.045138).
- [131] P. Scheiderer. *Spectroscopy of Prototypical Thin Film Mott Materials*. PhD thesis, University Würzburg, 2019.
- [132] R. Scherwitzl, S. Gariglio, M. Gabay, P. Zubko, M. Gibert, and J.-M. Triscone. “Metal-insulator transition in ultrathin LaNiO_3 films”. *Phys. Rev. Lett.* **106**(24), 246403, 2011. doi: [10.1103/PhysRevLett.106.246403](https://doi.org/10.1103/PhysRevLett.106.246403).
- [133] A. Rastogi, M. Brahlek, J. M. Ok, Z. Liao, C. Sohn, S. Feldman, and H. N. Lee. “Metal-insulator transition in (111) SrRuO_3 ultrathin films”. *APL Materials* **7**(9), 091106, 2019. doi: [10.1063/1.5109374](https://doi.org/10.1063/1.5109374).
- [134] S. S. Majid, D. K. Shukla, F. Rahman, K. Gautam, R. J. Choudhary, V. G. Sathe, and D. M. Phase. “Stabilization of metallic phase in V_2O_3 thin film”. *Applied Physics Letters* **110**(17), 173101, 2017. doi: [10.1063/1.4982588](https://doi.org/10.1063/1.4982588).
- [135] J.-H. Ha, H.-W. Kim, Y.-S. Jo, S.-W. Kim, and J.-I. Hong. “Tunable metal-insulator transition of V_2O_3 thin films strained by controlled inclusion of crystallographic defect”. *Applied Materials Today* **22**, 100984, 2021. doi: [10.1016/j.apmt.2021.100984](https://doi.org/10.1016/j.apmt.2021.100984).
- [136] O. Ivashko, M. Horio, W. Wan, N. B. Christensen, D. E. McNally, E. Paris, Y. Tseng, N. E. Shaik, H. M. Rønnow, H. I. Wei, C. Adamo, C. Lichtensteiger, M. Gibert, M. R. Beasley, K. M. Shen, J. M. Tomczak, T. Schmitt, and J. Chang. “Strain-engineering Mott-insulating La_2CuO_4 ”. *Nature Communications* **10**(1), 786, 2019. doi: [10.1038/s41467-019-08664-6](https://doi.org/10.1038/s41467-019-08664-6).
- [137] S.-Q. Wu, S. Cheng, L. Lu, M. Liu, X.-W. Jin, S.-D. Cheng, and S.-B. Mi. “B-site ordering and strain-induced phase transition in double-perovskite $\text{La}_2\text{NiMnO}_6$ films”. *Scientific Reports* **8**(1), 2516, 2018. doi: [10.1038/s41598-018-20812-4](https://doi.org/10.1038/s41598-018-20812-4).
- [138] L. Shoham, M. Baskin, T. Tiwald, G. Ankonina, M.-G. Han, A. Zakharova, S. Caspi, S. Joseph, Y. Zhu, I. H. Inoue, C. Piamonteze, M. J. Rozenberg, and L. Kornblum. “Bandwidth control and symmetry breaking in a Mott-Hubbard correlated metal”. *Advanced Functional Materials* Jun 2023. doi: [10.1002/adfm.202302330](https://doi.org/10.1002/adfm.202302330).

- [139] K. Yoshimatsu, S. Miyazaki, N. Hasegawa, and H. Kumigashira. “Evidence of lattice deformation induced metal-insulator transition in Ti_2O_3 ”. *Phys. Rev. B* **106**, L081110, Aug 2022. doi: [10.1103/PhysRevB.106.L081110](https://doi.org/10.1103/PhysRevB.106.L081110).
- [140] H. Guo, S. Dong, P. D. Rack, J. D. Budai, C. Beekman, Z. Gai, W. Siemons, C. M. Gonzalez, R. Timilsina, A. T. Wong, A. Herklotz, P. C. Snijders, E. Dagotto, and T. Z. Ward. “Strain doping: Reversible single-axis control of a complex oxide lattice via helium implantation”. *Phys. Rev. Lett.* **114**, 256801, Jun 2015. doi: [10.1103/PhysRevLett.114.256801](https://doi.org/10.1103/PhysRevLett.114.256801).
- [141] Y. Ding, D. Haskel, Y.-C. Tseng, E. Kaneshita, M. van Veenendaal, J. F. Mitchell, S. V. Sinogeikin, V. Prakapenka, and H.-k. Mao. “Pressure-induced magnetic transition in manganite ($\text{La}_{0.75}\text{Ca}_{0.25}\text{MnO}_3$)”. *Phys. Rev. Lett.* **102**, 237201, Jun 2009. doi: [10.1103/PhysRevLett.102.237201](https://doi.org/10.1103/PhysRevLett.102.237201).
- [142] W. Eerenstein, M. Wiora, J. L. Prieto, J. F. Scott, and N. D. Mathur. “Giant sharp and persistent converse magnetoelectric effects in multiferroic epitaxial heterostructures”. *Nature Materials* **6**(5), 348–351, 2007. doi: [10.1038/nmat1886](https://doi.org/10.1038/nmat1886).
- [143] P. A. Lee and T. V. Ramakrishnan. “Disordered electronic systems”. *Rev. Mod. Phys.* **57**, 287–337, Apr 1985. doi: [10.1103/RevModPhys.57.287](https://doi.org/10.1103/RevModPhys.57.287).
- [144] A. Fouchet, M. Allain, B. Bérini, E. Popova, P.-E. Janolin, N. Guiblin, E. Chikoidze, J. Scola, D. Hrabovsky, Y. Dumont, and N. Keller. “Study of the electronic phase transition with low dimensionality in SrVO_3 thin films”. *Materials Science and Engineering: B* **212**, 7–13, 2016. doi: [10.1016/j.mseb.2016.07.009](https://doi.org/10.1016/j.mseb.2016.07.009).
- [145] M. Mirjolet, F. Rivadulla, P. Marsik, V. Borisov, R. Valentí, and J. Fontcuberta. “Electron–Phonon Coupling and Electron–Phonon Scattering in SrVO_3 ”. *Advanced Science* **8**(15), 2004207, 2021. doi: [10.1002/advs.202004207](https://doi.org/10.1002/advs.202004207).
- [146] J. Rammer. *Quantum Transport Theory*. CRC Press, May 2018. ISBN 978-0-42-950283-5.
- [147] C. Wang, C.-H. Chang, A. Huang, P.-C. Wang, P.-C. Wu, L. Yang, C. Xu, P. Pandey, M. Zeng, R. Böttger, H.-T. Jeng, Y.-J. Zeng, M. Helm, Y.-H. Chu, R. Ganesh, and S. Zhou. “Tunable disorder and localization in the rare-earth nickelates”. *Phys. Rev. Mater.* **3**, 053801, May 2019. doi: [10.1103/PhysRevMaterials.3.053801](https://doi.org/10.1103/PhysRevMaterials.3.053801).
- [148] J. M. Tomczak, T. Miyake, R. Sakuma, and F. Aryasetiawan. “Effective Coulomb interactions in solids under pressure”. *Phys. Rev. B* **79**(23) 235133, 2009. doi: [10.1103/PhysRevB.79.235133](https://doi.org/10.1103/PhysRevB.79.235133).

- [149] G. Keller, K. Held, V. Eyert, D. Vollhardt, and V. I. Anisimov. “Electronic structure of paramagnetic V_2O_3 : Strongly correlated metallic and Mott insulating phase”. *Phys. Rev. B* **70**, 205116, Nov 2004. doi: [10.1103/PhysRevB.70.205116](https://doi.org/10.1103/PhysRevB.70.205116).
- [150] K. Dymkowski and C. Ederer. “Strain-induced insulator-to-metal transition in $LaTiO_3$ within DFT + DMFT”. *Phys. Rev. B* **89**, 161109, Apr 2014. doi: [10.1103/PhysRevB.89.161109](https://doi.org/10.1103/PhysRevB.89.161109).
- [151] H. Yamaoka, M. Matsunami, R. Eguchi, Y. Ishida, N. Tsujii, Y. Takahashi, Y. Senba, H. Ohashi, and S. Shin. “Electronic structure of $FeSi_{1-x}Ge_x$ and $FeGa_3$ investigated by soft x-ray photoelectron spectroscopy complementary to x-ray emission spectroscopy”. *Phys. Rev. B* **78**, 045125, Jul 2008. doi: [10.1103/PhysRevB.78.045125](https://doi.org/10.1103/PhysRevB.78.045125).
- [152] G. Sordi, P. Sémon, K. Haule, and A.-M. S. Tremblay. “Pseudogap temperature as a wisdom line in doped mott insulators”. *Scientific reports* **2**, 547, 07 2012. doi: [10.1038/srep00547](https://doi.org/10.1038/srep00547).
- [153] M. Reitner, P. Chalupa, L. Del Re, D. Springer, S. Ciuchi, G. Sangiovanni, and A. Toschi. “Attractive effect of a strong electronic repulsion: The physics of vertex divergences”. *Phys. Rev. Lett.* **125**, 196403, Nov 2020. doi: [10.1103/PhysRevLett.125.196403](https://doi.org/10.1103/PhysRevLett.125.196403).
- [154] E. Pavarini. *Quantum Materials: Experiments and Theory*, volume 6 of *Modeling and Simulation*, chapter Orbital Ordering. Verlag des Forschungszentrum Jülich, 2016. ISBN 978-3-95806-159-0.
- [155] K. Haule and T. Birol. “Free energy from stationary implementation of the DFT + DMFT functional”. *Phys. Rev. Lett.* **115**, 256402, Dec 2015. doi: [10.1103/PhysRevLett.115.256402](https://doi.org/10.1103/PhysRevLett.115.256402).
- [156] J. del Valle, P. Salev, F. Tesler, N. M. Vargas, Y. Kalcheim, P. Wang, J. Trastoy, M.-H. Lee, G. Kassabian, J. G. Ramírez, M. J. Rozenberg, and I. K. Schuller. “Subthreshold firing in Mott nanodevices”. *Nature* **569**(7756), 388–392, May 2019. doi: [10.1038/s41586-019-1159-6](https://doi.org/10.1038/s41586-019-1159-6).
- [157] J. Li, D. Yin, Q. Li, R. Sun, S. Huang, and F. Meng. “Interfacial defects induced electronic property transformation at perovskite $SrVO_3/SrTiO_3$ and $LaCrO_3/SrTiO_3$ heterointerfaces”. *Phys. Chem. Chem. Phys.* **19**, 6945–6951, 2017. doi: [10.1039/C6CP07691B](https://doi.org/10.1039/C6CP07691B).
- [158] A. Baki, J. Stöver, T. Schulz, T. Markurt, H. Amari, C. Richter, J. Martin, K. Irmscher, M. Albrecht, and J. Schwarzkopf. “Influence of Sr deficiency on structural and electrical properties of $SrTiO_3$ thin films grown by metal–organic vapor phase epitaxy”. *Scientific Reports* **11**(1), 7497, 2021. doi: [10.1038/s41598-021-87007-2](https://doi.org/10.1038/s41598-021-87007-2).

- [159] A. Kalabukhov, R. Gunnarsson, J. Börjesson, E. Olsson, T. Claeson, and D. Winkler. “Effect of oxygen vacancies in the SrTiO₃ substrate on the electrical properties of the LaAlO₃ / SrTiO₃ interface”. *Phys. Rev. B* **75**, 121404, Mar 2007. doi: [10.1103/PhysRevB.75.121404](https://doi.org/10.1103/PhysRevB.75.121404).
- [160] S. Miyoshi, J.-O. Hong, K. Yashiro, A. Kaimai, Y. Nigara, K. Kawamura, T. Kawada, and J. Mizusaki. “Lattice expansion upon reduction of perovskite-type LaMnO₃ with oxygen-deficit nonstoichiometry”. *Solid State Ionics* **161**(3), 209–217, 2003. doi: [10.1016/S0167-2738\(03\)00281-9](https://doi.org/10.1016/S0167-2738(03)00281-9).
- [161] Y.-M. Kim, J. He, M. D. Biegalski, H. Ambaye, V. Lauter, H. M. Christen, S. T. Pantelides, S. J. Pennycook, S. V. Kalinin, and A. Y. Borisevich. “Probing oxygen vacancy concentration and homogeneity in solid-oxide fuel-cell cathode materials on the subunit-cell level”. *Nature Materials* **11**(10), 888–894, 2012. doi: [10.1038/nmat3393](https://doi.org/10.1038/nmat3393).
- [162] K. K. Ghose, Y. Liu, and T. J. Frankcombe. “High-temperature reduction thermochemistry of SrVO_{3-δ}”. *Journal of Physics: Energy* **6**(1), 015007, Nov 2023. doi: [10.1088/2515-7655/ad0b8a](https://doi.org/10.1088/2515-7655/ad0b8a).
- [163] S. Beck, G. Sclauzero, U. Chopra, and C. Ederer. “Metal-insulator transition in CaVO₃ thin films: Interplay between epitaxial strain, dimensional confinement, and surface effects”. *Phys. Rev. B* **97**, 075107, Feb 2018. doi: [10.1103/PhysRevB.97.075107](https://doi.org/10.1103/PhysRevB.97.075107).
- [164] Y. Okada, S.-Y. Shiao, T.-R. Chang, G. Chang, M. Kobayashi, R. Shimizu, H.-T. Jeng, S. Shiraki, H. Kumigashira, A. Bansil, H. Lin, and T. Hitosugi. “Quasiparticle interference on cubic perovskite oxide surfaces”. *Phys. Rev. Lett.* **119**, 086801, Aug 2017. doi: [10.1103/PhysRevLett.119.086801](https://doi.org/10.1103/PhysRevLett.119.086801).
- [165] G. Silversmit, D. Depla, H. Poelman, G. B. Marin, and R. De Gryse. “Determination of the V2p XPS binding energies for different vanadium oxidation states (V⁵⁺ to V⁰⁺)”. *J. Electron Spectrosc. Relat. Phenom.* **135**(2-3), 167–175, Apr 2004. doi: [10.1016/j.elspec.2004.03.004](https://doi.org/10.1016/j.elspec.2004.03.004).
- [166] M. Takizawa, M. Minohara, H. Kumigashira, D. Toyota, M. Oshima, H. Wadati, T. Yoshida, A. Fujimori, M. Lippmaa, M. Kawasaki, H. Koinuma, G. Sordi, and M. Rozenberg. “Coherent and incoherent *d* band dispersions in SrVO₃”. *Phys. Rev. B* **80**(23), 235104, December 2009. doi: [10.1103/PhysRevB.80.235104](https://doi.org/10.1103/PhysRevB.80.235104).
- [167] G. Koster, B. L. Kropman, G. J. H. M. Rijnders, D. H. A. Blank, and H. Rogalla. “Quasi-ideal strontium titanate crystal surfaces through formation of strontium hydroxide”. *Appl. Phys. Lett.* **73**(20), 2920–2922, Nov 1998. doi: [10.1063/1.122630](https://doi.org/10.1063/1.122630).

- [168] M. L. Knotek and P. J. Feibelman. “Ion desorption by core-hole Auger decay”. *Phys. Rev. Lett.* **40**(14), 964–967, 1978. doi: [10.1103/PhysRevLett.40.964](https://doi.org/10.1103/PhysRevLett.40.964).
- [169] J. Laverock, J. Kuyyalil, B. Chen, R. P. Singh, B. Karlin, J. C. Woicik, G. Balakrishnan, and K. E. Smith. “Enhanced electron correlations at the $\text{Sr}_x\text{Ca}_{1-x}\text{VO}_3$ surface”. *Phys. Rev. B* **91**(16), 165123, Apr 2015. doi: [10.1103/PhysRevB.91.165123](https://doi.org/10.1103/PhysRevB.91.165123).
- [170] R. Eguchi, M. Taguchi, M. Matsunami, K. Horiba, K. Yamamoto, A. Chainani, Y. Takata, M. Yabashi, D. Miwa, Y. Nishino, K. Tamasaku, T. Ishikawa, Y. Senba, H. Ohashi, I. Inoue, Y. Muraoka, Z. Hiroi, and S. Shin. “Electronic structure of configuration vanadium oxides studied by soft X-ray and hard X-ray photoemission spectroscopy”. *J. Electron Spectrosc. Relat. Phenom.* **156-158**, 421–425, May 2007. doi: [10.1016/j.elspec.2006.12.055](https://doi.org/10.1016/j.elspec.2006.12.055).
- [171] L. Dudy, M. Sing, P. Scheiderer, J. D. Denlinger, P. Schütz, J. Gabel, M. Buchwald, C. Schlueter, T.-L. Lee, and R. Claessen. “In situ control of separate electronic phases on SrTiO_3 surfaces by oxygen dosing”. *Adv. Mater.* **28**(34), 7443–7449, Sep 2016. doi: [10.1002/adma.201600046](https://doi.org/10.1002/adma.201600046).
- [172] H. Oka, Y. Okada, T. Hitosugi, and T. Fukumura. “Two distinct surface terminations of SrVO_3 (001) ultrathin films as an influential factor on metallicity”. *Applied Physics Letters* **113**(17), 171601, Oct 2018. doi: [10.1063/1.5051434](https://doi.org/10.1063/1.5051434).
- [173] R. Shimizu, K. Iwaya, T. Ohsawa, S. Shiraki, T. Hasegawa, T. Hashizume, and T. Hitosugi. “Effect of oxygen deficiency on SrTiO_3 (001) surface reconstructions”. *Applied Physics Letters* **100**(26), 263106, Jun 2012. doi: [10.1063/1.4730409](https://doi.org/10.1063/1.4730409).
- [174] A. Liebsch. “Surface versus bulk Coulomb correlations in photoemission spectra of SrVO_3 and CaVO_3 ”. *Phys. Rev. Lett.* **90**(9), 096401, Mar 2003. doi: [10.1103/PhysRevLett.90.096401](https://doi.org/10.1103/PhysRevLett.90.096401).
- [175] M. Takayanagi, T. Tsuchiya, W. Namiki, T. Higuchi, and K. Terabe. “Correlated metal SrVO_3 based all-solid-state redox transistors achieved by Li^+ or H^+ transport”. *Journal of the Physical Society of Japan* **87**(3), 034802, 2018. doi: [10.7566/JPSJ.87.034802](https://doi.org/10.7566/JPSJ.87.034802).
- [176] M. Pickem. *Dynamical vertex approximation for SrVO_3 : Effects of non-local interactions, temperature and dimensionality*. Master thesis, Technische Universität Wien, 2018.
- [177] W. Wu, M. S. Scheurer, M. Ferrero, and A. Georges. “Effect of van Hove singularities in the onset of pseudogap states in Mott insulators”. *Phys. Rev. Research* **2**, 033067, Jul 2020. doi: [10.1103/PhysRevResearch.2.033067](https://doi.org/10.1103/PhysRevResearch.2.033067).

- [178] B. Klebel-Knobloch, T. Schäfer, A. Toschi, and J. M. Tomczak. “Anisotropy of electronic correlations: On the applicability of local theories to layered materials”. *Phys. Rev. B* **103**, 045121, Jan 2021. doi: [10.1103/PhysRevB.103.045121](https://doi.org/10.1103/PhysRevB.103.045121).
- [179] O. Gunnarsson, E. Koch, and R. M. Martin. “Mott transition in degenerate Hubbard models: Application to doped fullerenes”. *Phys. Rev. B* **54**, R11026–R11029, Oct 1996. doi: [10.1103/PhysRevB.54.R11026](https://doi.org/10.1103/PhysRevB.54.R11026).
- [180] T. Ribic, E. Assmann, A. Tóth, and K. Held. “Cubic interaction parameters for t_{2g} Wannier orbitals”. *Phys. Rev. B* **90**, 165105, Oct 2014. doi: [10.1103/PhysRevB.90.165105](https://doi.org/10.1103/PhysRevB.90.165105).
- [181] M. Gu, S. A. Wolf, and J. Lu. “Two-Dimensional Mott Insulators in SrVO₃ Ultrathin Films”. *Advanced Materials Interfaces* **1**(7), 1300126, 2014. doi: [10.1002/admi.201300126](https://doi.org/10.1002/admi.201300126).
- [182] J. Wang, N. Gauquelin, M. Huijben, J. Verbeeck, G. Rijnders, and G. Koster. “Metal-insulator transition of SrVO₃ ultrathin films embedded in SrVO₃ / SrTiO₃ superlattices”. *Applied Physics Letters* **117**(13), 133105, 2020. doi: [10.1063/5.0020615](https://doi.org/10.1063/5.0020615).
- [183] M. Gu, J. Laverock, B. Chen, K. E. Smith, S. A. Wolf, and J. Lu. “Metal-insulator transition induced in CaVO₃ thin films”. *Journal of Applied Physics* **113**(13), 133704, 2013. doi: [10.1063/1.4798963](https://doi.org/10.1063/1.4798963).
- [184] K. Held and D. Vollhardt. “Microscopic conditions favoring itinerant ferromagnetism: Hund’s rule coupling and orbital degeneracy”. *The European Physical Journal B - Condensed Matter and Complex Systems* **5**(3), 473–478, Oct 1998. doi: [10.1007/s100510050468](https://doi.org/10.1007/s100510050468).
- [185] T. Momoi and K. Kubo. “Ferromagnetism in the Hubbard model with orbital degeneracy in infinite dimensions”. *Phys. Rev. B* **58**, R567–R570, Jul 1998. doi: [10.1103/PhysRevB.58.R567](https://doi.org/10.1103/PhysRevB.58.R567).
- [186] Y. Tokura and N. Nagaosa. “Orbital physics in transition-metal oxides”. *Science* **288**(5465), 462–468, 2000. doi: [10.1126/science.288.5465.462](https://doi.org/10.1126/science.288.5465.462).
- [187] D. Khomskii and K. Kugel. “Orbital and magnetic structure of two-dimensional ferromagnets with Jahn-Teller ions”. *Solid State Communications* **13**(7), 763 – 766, 1973. doi: [10.1016/0038-1098\(73\)90362-1](https://doi.org/10.1016/0038-1098(73)90362-1).
- [188] P. Fazekas. *Lecture Notes on Electron Correlation and Magnetism*, volume 5 of *Series in Modern Condensed Matter Physics*. World Scientific, 1999. ISBN 978-981-02-2474-5.
- [189] H. Falk and L. W. Bruch. “Susceptibility and fluctuation”. *Phys. Rev.* **180**, 442–444, Apr 1969. doi: [10.1103/PhysRev.180.442](https://doi.org/10.1103/PhysRev.180.442).

- [190] R. Kenna and B. Berche. “Fisher’s scaling relation above the upper critical dimension”. *Europhysics Letters* **105**(2), 26005, feb 2014. doi: [10.1209/0295-5075/105/26005](https://doi.org/10.1209/0295-5075/105/26005).
- [191] R. Kubo. “Statistical-mechanical theory of irreversible processes I.” *Journal of the Physical Society of Japan* **12**, 570, Jun 1957. doi: [10.1143/JPSJ.12.570](https://doi.org/10.1143/JPSJ.12.570).
- [192] R. Kubo, M. Yokota, and S. Nakajima. “Statistical-mechanical theory of irreversible processes. II. response to thermal disturbance”. *Journal of the Physical Society of Japan* **12**(11), 1203–1211, Nov 1957. doi: [10.1143/jpsj.12.1203](https://doi.org/10.1143/jpsj.12.1203).
- [193] G. Rohringer. *New routes towards a theoretical treatment of nonlocal electronic correlations*. PhD thesis, Technische Universität Wien, 2013.
- [194] P. Chalupa, P. Gunacker, T. Schäfer, K. Held, and A. Toschi. “Divergences of the irreducible vertex functions in correlated metallic systems: Insights from the Anderson impurity model”. *Phys. Rev. B* **97**, 245136, Jun 2018. doi: [10.1103/PhysRevB.97.245136](https://doi.org/10.1103/PhysRevB.97.245136).
- [195] D. Springer, P. Chalupa, S. Ciuchi, G. Sangiovanni, and A. Toschi. “Interplay between local response and vertex divergences in many-fermion systems with on-site attraction”. *Phys. Rev. B* **101**, 155148, Apr 2020. doi: [10.1103/PhysRevB.101.155148](https://doi.org/10.1103/PhysRevB.101.155148).
- [196] H. Hafermann, E. G. C. P. van Loon, M. I. Katsnelson, A. I. Lichtenstein, and O. Parcollet. “Collective charge excitations of strongly correlated electrons, vertex corrections, and gauge invariance”. *Phys. Rev. B* **90**, 235105, Dec 2014. doi: [10.1103/PhysRevB.90.235105](https://doi.org/10.1103/PhysRevB.90.235105).
- [197] P. Werner, A. Comanac, L. de’ Medici, M. Troyer, and A. J. Millis. “Continuous-time solver for quantum impurity models”. *Phys. Rev. Lett.* **97**, 076405, Aug 2006. doi: [10.1103/PhysRevLett.97.076405](https://doi.org/10.1103/PhysRevLett.97.076405).
- [198] L. Si, Z. Zhong, J. M. Tomczak, and K. Held. “Route to room-temperature ferromagnetic ultrathin SrRuO₃ films”. *Phys. Rev. B* **92**, 041108(R), Jul 2015. doi: [10.1103/PhysRevB.92.041108](https://doi.org/10.1103/PhysRevB.92.041108).
- [199] W. Brzezicki, A. M. Oleś, and M. Cuoco. “Spin-orbital order modified by orbital dilution in transition-metal oxides: From spin defects to frustrated spins polarizing host orbitals”. *Phys. Rev. X* **5**, 011037, Mar 2015. doi: [10.1103/PhysRevX.5.011037](https://doi.org/10.1103/PhysRevX.5.011037).
- [200] G. Khaliullin, P. Horsch, and A. M. Oleś. “Spin order due to orbital fluctuations: Cubic vanadates”. *Phys. Rev. Lett.* **86**, 3879–3882, Apr 2001. doi: [10.1103/PhysRevLett.86.3879](https://doi.org/10.1103/PhysRevLett.86.3879).

- [201] Y. Ren, A. A. Nugroho, A. A. Menovsky, J. Stremper, U. Rütt, F. Iga, T. Takabatake, and C. W. Kimball. “Orbital-ordering-induced phase transition in LaVO_3 and CeVO_3 ”. *Phys. Rev. B* **67**, 014107, Jan 2003. doi: [10.1103/PhysRevB.67.014107](https://doi.org/10.1103/PhysRevB.67.014107).
- [202] G. Khaliullin and S. Maekawa. “Orbital liquid in three-dimensional Mott insulator: LaTiO_3 ”. *Phys. Rev. Lett.* **85**, 3950–3953, Oct 2000. doi: [10.1103/PhysRevLett.85.3950](https://doi.org/10.1103/PhysRevLett.85.3950).
- [203] T. Schäfer, A. Toschi, and J. M. Tomczak. “Separability of dynamical and non-local correlations in three dimensions”. *Phys. Rev. B* **91**, 121107(R), Mar 2015. doi: [10.1103/PhysRevB.91.121107](https://doi.org/10.1103/PhysRevB.91.121107).
- [204] A. A. Katanin, A. Toschi, and K. Held. “Comparing pertinent effects of antiferromagnetic fluctuations in the two- and three-dimensional Hubbard model”. *Phys. Rev. B* **80**, 075104, Aug 2009. doi: [10.1103/PhysRevB.80.075104](https://doi.org/10.1103/PhysRevB.80.075104).
- [205] F. Krien, P. Worm, P. Chalupa-Gantner, A. Toschi, and K. Held. “Explaining the pseudogap through damping and antidamping on the fermi surface by imaginary spin scattering”. *Communications Physics* **5**(1), 336, 2022. doi: [10.1038/s42005-022-01117-5](https://doi.org/10.1038/s42005-022-01117-5).
- [206] O. Gunnarsson, T. Schäfer, J. P. F. LeBlanc, E. Gull, J. Merino, G. Sangiovanni, G. Rohringer, and A. Toschi. “Fluctuation diagnostics of the electron self-energy: Origin of the pseudogap physics”. *Phys. Rev. Lett.* **114**, 236402, Jun 2015. doi: [10.1103/PhysRevLett.114.236402](https://doi.org/10.1103/PhysRevLett.114.236402).
- [207] T. Schäfer and A. Toschi. “How to read between the lines of electronic spectra: the diagnostics of fluctuations in strongly correlated electron systems”. *Journal of Physics: Condensed Matter* **33**(21), 214001, April 2021. doi: [10.1088/1361-648x/abeb44](https://doi.org/10.1088/1361-648x/abeb44).
- [208] L. Del Re and G. Rohringer. “Fluctuations analysis of spin susceptibility: Néel ordering revisited in dynamical mean field theory”. *Phys. Rev. B* **104**, 235128, Dec 2021. doi: [10.1103/PhysRevB.104.235128](https://doi.org/10.1103/PhysRevB.104.235128).
- [209] G. Mahan and J. Sofo. “The best thermoelectric”. *PNAS* **93**(15), 7436–7439, 1996. doi: [10.1073/pnas.93.15.7436](https://doi.org/10.1073/pnas.93.15.7436).
- [210] K. Held, R. Arita, V. I. Anisimov, and K. Kuroki. “The LDA+DMFT route to identify good thermoelectrics”. In V. Zlatić and A. Hewson, editors, “Properties and Applications of Thermoelectric Materials”, NATO Science for Peace and Security Series B: Physics and Biophysics, page 141. Springer, 2009. ISBN 978-90-481-2892-1.

- [211] V. Zlatić and R. Monnier. *Modern Theory of Thermoelectricity*. Oxford University Press, 2014. ISBN 978-0-19-177443-0.
- [212] J. M. Tomczak. “Thermoelectricity in correlated narrow-gap semiconductors”. *J. Phys.: Condens. Matter (Topical Review)* **30**(18), 183001, 2018. doi: [10.1088/1361-648X/aab284](https://doi.org/10.1088/1361-648X/aab284).
- [213] K. Haule and G. Kotliar. “Thermoelectrics near the Mott localization—delocalization transition”. In V. Zlatić and A. C. Hewson, editors, “Properties and Applications of Thermoelectric Materials”, pages 119–131. Springer Netherlands, Dordrecht, 2009. ISBN 978-90-481-2892-1.
- [214] P. Sun, W. Xu, J. M. Tomczak, G. Kotliar, M. Søndergaard, B. B. Iversen, and F. Steglich. “Highly dispersive electron relaxation and colossal thermoelectricity in the correlated semiconductor FeSb₂”. *Phys. Rev. B* **88**, 245203, Dec 2013. doi: [10.1103/PhysRevB.88.245203](https://doi.org/10.1103/PhysRevB.88.245203).
- [215] A. Kauch, P. Pudleiner, K. Astleithner, P. Thunström, T. Ribic, and K. Held. “Generic optical excitations of correlated systems: π -tons”. *Phys. Rev. Lett.* **124**, 047401, Jan 2020. doi: [10.1103/PhysRevLett.124.047401](https://doi.org/10.1103/PhysRevLett.124.047401).
- [216] A. Toschi, A. A. Katanin, and K. Held. “Dynamical vertex approximation: A step beyond dynamical mean-field theory”. *Phys. Rev. B* **75**, 045118, Jan 2007. doi: [10.1103/PhysRevB.75.045118](https://doi.org/10.1103/PhysRevB.75.045118).
- [217] K. Held. *DMFT: From Infinite Dimensions to Real Materials*, volume 8 of *Modeling and Simulation*, chapter Quantum Criticality and Superconductivity in Diagrammatic Extensions of DMFT. Verlag des Forschungszentrum Jülich, 2018. ISBN 978-3-95806-313-6.
- [218] L. Del Re, M. Capone, and A. Toschi. “Dynamical vertex approximation for the attractive Hubbard model”. *Phys. Rev. B* **99**, 045137, Jan 2019. doi: [10.1103/PhysRevB.99.045137](https://doi.org/10.1103/PhysRevB.99.045137).
- [219] G. Li, A. Kauch, P. Pudleiner, and K. Held. “The victory project v1.0: An efficient parquet equations solver”. *Computer Physics Communications* **241**, 146–154, Aug 2019. doi: [10.1016/j.cpc.2019.03.008](https://doi.org/10.1016/j.cpc.2019.03.008).
- [220] N. D. Mermin and H. Wagner. “Absence of ferromagnetism or antiferromagnetism in one- or two-dimensional isotropic Heisenberg models”. *Phys. Rev. Lett.* **17**, 1133–1136, Nov 1966. doi: [10.1103/PhysRevLett.17.1133](https://doi.org/10.1103/PhysRevLett.17.1133).
- [221] P. C. Hohenberg. “Existence of long-range order in one and two dimensions”. *Phys. Rev.* **158**, 383–386, Jun 1967. doi: [10.1103/PhysRev.158.383](https://doi.org/10.1103/PhysRev.158.383).

- [222] S. Coleman. “There are no goldstone bosons in two dimensions”. *Communications in Mathematical Physics* **31**(4), 259–264, 1973. doi: [10.1007/BF01646487](https://doi.org/10.1007/BF01646487).
- [223] G. Rohringer and A. Toschi. “Impact of nonlocal correlations over different energy scales: A dynamical vertex approximation study”. *Phys. Rev. B* **94**, 125144, Sep 2016. doi: [10.1103/PhysRevB.94.125144](https://doi.org/10.1103/PhysRevB.94.125144).
- [224] T. Schäfer, F. Geles, D. Rost, G. Rohringer, E. Arrigoni, K. Held, N. Blümer, M. Aichhorn, and A. Toschi. “Fate of the false Mott-Hubbard transition in two dimensions”. *Phys. Rev. B* **91**, 125109, Mar 2015. doi: [10.1103/PhysRevB.91.125109](https://doi.org/10.1103/PhysRevB.91.125109).
- [225] T. Schäfer, A. A. Katanin, M. Kitatani, A. Toschi, and K. Held. “Quantum criticality in the two-dimensional periodic Anderson model”. *Phys. Rev. Lett.* **122**, 227201, Jun 2019. doi: [10.1103/PhysRevLett.122.227201](https://doi.org/10.1103/PhysRevLett.122.227201).
- [226] T. Schäfer. *Classical and quantum phase transitions in strongly correlated electron systems*. PhD thesis, Technische Universität Wien, 2016.
- [227] G. Palle and D. K. Sunko. “Physical limitations of the Hohenberg–Mermin–Wagner theorem”. *Journal of Physics A: Mathematical and Theoretical* **54**(31), 315001, jul 2021. doi: [10.1088/1751-8121/ac0a9d](https://doi.org/10.1088/1751-8121/ac0a9d).
- [228] G. Rohringer, A. Toschi, A. Katanin, and K. Held. “Critical properties of the half-filled Hubbard model in three dimensions”. *Phys. Rev. Lett.* **107**, 256402, Dec 2011. doi: [10.1103/PhysRevLett.107.256402](https://doi.org/10.1103/PhysRevLett.107.256402).
- [229] D. Hirschmeier, H. Hafermann, E. Gull, A. I. Lichtenstein, and A. E. Antipov. “Mechanisms of finite-temperature magnetism in the three-dimensional Hubbard model”. *Phys. Rev. B* **92**, 144409, Oct 2015. doi: [10.1103/PhysRevB.92.144409](https://doi.org/10.1103/PhysRevB.92.144409).
- [230] T. Schäfer, A. A. Katanin, K. Held, and A. Toschi. “Interplay of correlations and Kohn anomalies in three dimensions: Quantum criticality with a twist”. *Phys. Rev. Lett.* **119**, 046402, Jul 2017. doi: [10.1103/PhysRevLett.119.046402](https://doi.org/10.1103/PhysRevLett.119.046402).
- [231] J. Kaufmann. *Local and Nonlocal Correlations in Interacting Electron Systems*. PhD thesis, Technische Universität Wien, 2021.
- [232] K. F. Mak, M. Y. Sfeir, Y. Wu, C. H. Lui, J. A. Misewich, and T. F. Heinz. “Measurement of the optical conductivity of graphene”. *Phys. Rev. Lett.* **101**, 196405, Nov 2008. doi: [10.1103/PhysRevLett.101.196405](https://doi.org/10.1103/PhysRevLett.101.196405).

- [233] A. Boileau, A. Cheikh, A. Fouchet, A. David, R. Escobar-Galindo, C. Labbé, P. Marie, F. Gourbilleau, and U. Lüders. “Optical and electrical properties of the transparent conductor SrVO_3 without long-range crystalline order”. *Applied Physics Letters* **112**(2), Jan 2018. doi: [10.1063/1.5016245](https://doi.org/10.1063/1.5016245).
- [234] R. Peierls. “Zur Theorie des Diamagnetismus von Leitungselektronen”. *Z. Physik* **80**, 763, 1933. doi: [10.1007/BF01342591](https://doi.org/10.1007/BF01342591).
- [235] P. Drude. “Zur Elektronentheorie der Metalle”. *Annalen der Physik* **306**(3), 566–613, 1900. doi: [10.1002/andp.19003060312](https://doi.org/10.1002/andp.19003060312).
- [236] D. Geffroy, J. Kaufmann, A. Hariki, P. Gunacker, A. Hausoel, and J. Kuneš. “Collective modes in excitonic magnets: Dynamical mean-field study”. *Phys. Rev. Lett.* **122**, 127601, Mar 2019. doi: [10.1103/PhysRevLett.122.127601](https://doi.org/10.1103/PhysRevLett.122.127601).
- [237] D. Bergeron, V. Hankevych, B. Kyung, and A.-M. S. Tremblay. “Optical and dc conductivity of the two-dimensional Hubbard model in the pseudogap regime and across the antiferromagnetic quantum critical point including vertex corrections”. *Phys. Rev. B* **84**, 085128, Aug 2011. doi: [10.1103/PhysRevB.84.085128](https://doi.org/10.1103/PhysRevB.84.085128).
- [238] O. Simard, S. Takayoshi, and P. Werner. “Diagrammatic study of optical excitations in correlated systems”. *Phys. Rev. B* **103**, 104415, Mar 2021. doi: [10.1103/PhysRevB.103.104415](https://doi.org/10.1103/PhysRevB.103.104415).
- [239] P. Coleman. *Introduction to Many-Body Physics*. Cambridge University Press, 2015. ISBN 978-1-13-902091-6.
- [240] T. Schäfer, S. Ciuchi, M. Wallerberger, P. Thunström, O. Gunnarsson, G. Sangiovanni, G. Rohringer, and A. Toschi. “Nonperturbative landscape of the Mott-Hubbard transition: Multiple divergence lines around the critical endpoint”. *Phys. Rev. B* **94**, 235108, Dec 2016. doi: [10.1103/PhysRevB.94.235108](https://doi.org/10.1103/PhysRevB.94.235108).
- [241] T. Schäfer, N. Wentzell, F. Šimkovic, Y.-Y. He, C. Hille, M. Klett, C. J. Eckhardt, B. Arzhang, V. Harkov, F. m. c.-M. Le Régent, A. Kirsch, Y. Wang, A. J. Kim, E. Kozik, E. A. Stepanov, A. Kauch, S. Andergassen, P. Hansmann, D. Rohe, Y. M. Vilch, J. P. F. LeBlanc, S. Zhang, A.-M. S. Tremblay, M. Ferrero, O. Parcollet, and A. Georges. “Tracking the footprints of spin fluctuations: A MultiMethod, MultiMessenger study of the two-dimensional Hubbard model”. *Phys. Rev. X* **11**, 011058, Mar 2021. doi: [10.1103/PhysRevX.11.011058](https://doi.org/10.1103/PhysRevX.11.011058).
- [242] A. Kaminski, T. Kondo, T. Takeuchi, and G. Gu. “Pairing, pseudogap and fermi arcs in cuprates”. *Philosophical Magazine* **95**(5-6), 453–466, 2015. doi: [10.1080/14786435.2014.906758](https://doi.org/10.1080/14786435.2014.906758).

- [243] W. Wu, M. S. Scheurer, S. Chatterjee, S. Sachdev, A. Georges, and M. Ferrero. “Pseudogap and fermi-surface topology in the two-dimensional Hubbard model”. *Phys. Rev. X* **8**, 021048, May 2018. doi: [10.1103/PhysRevX.8.021048](https://doi.org/10.1103/PhysRevX.8.021048).
- [244] N. P. Armitage, P. Fournier, and R. L. Greene. “Progress and perspectives on electron-doped cuprates”. *Rev. Mod. Phys.* **82**, 2421–2487, Sep 2010. doi: [10.1103/RevModPhys.82.2421](https://doi.org/10.1103/RevModPhys.82.2421).
- [245] C. J. Eckhardt, C. Honerkamp, K. Held, and A. Kauch. “Truncated unity parquet solver”. *Phys. Rev. B* **101**, 155104, Apr 2020. doi: [10.1103/PhysRevB.101.155104](https://doi.org/10.1103/PhysRevB.101.155104).
- [246] J. Vučićević, J. Kokalj, R. Žitko, N. Wentzell, D. Tanasković, and J. Mravlje. “Conductivity in the square lattice Hubbard model at high temperatures: Importance of vertex corrections”. *Phys. Rev. Lett.* **123**, 036601, Jul 2019. doi: [10.1103/PhysRevLett.123.036601](https://doi.org/10.1103/PhysRevLett.123.036601).
- [247] M. Kitatani, T. Schäfer, H. Aoki, and K. Held. “Why the critical temperature of high- T_c cuprate superconductors is so low: The importance of the dynamical vertex structure”. *Phys. Rev. B* **99**, 041115, Jan 2019. doi: [10.1103/PhysRevB.99.041115](https://doi.org/10.1103/PhysRevB.99.041115).
- [248] M. Kitatani, L. Si, O. Janson, R. Arita, Z. Zhong, and K. Held. “Nickelate superconductors—a renaissance of the one-band Hubbard model”. *npj Quantum Materials* **5**(1), 59, Aug 2020. doi: [10.1038/s41535-020-00260-y](https://doi.org/10.1038/s41535-020-00260-y).
- [249] P. Worm, L. Si, M. Kitatani, R. Arita, J. M. Tomczak, and K. Held. “Correlations tune the electronic structure of pentalayer nickelates into the superconducting regime”. *Phys. Rev. Mater.* **6**, L091801, Sep 2022. doi: [10.1103/PhysRevMaterials.6.L091801](https://doi.org/10.1103/PhysRevMaterials.6.L091801).
- [250] P. S. Riseborough. “Heavy fermion semiconductors”. *Advances in Physics* **49**(3), 257–320, 2000. doi: [10.1080/000187300243345](https://doi.org/10.1080/000187300243345).
- [251] Y. Ōnuki and T. Komatsubara. “Heavy fermion state in CeCu₆”. *Journal of Magnetism and Magnetic Materials* **63–64**, 281–288, 1987. doi: [10.1016/0304-8853\(87\)90587-7](https://doi.org/10.1016/0304-8853(87)90587-7).
- [252] H. R. Ott, H. Rudigier, Z. Fisk, and J. L. Smith. “UBe₁₃: An unconventional actinide superconductor”. *Phys. Rev. Lett.* **50**, 1595–1598, May 1983. doi: [10.1103/PhysRevLett.50.1595](https://doi.org/10.1103/PhysRevLett.50.1595).
- [253] M. F. Hundley, P. C. Canfield, J. D. Thompson, Z. Fisk, and J. M. Lawrence. “Hybridization gap in Ce₃Bi₄Pt₃”. *Phys. Rev. B* **42**, 6842–6845, Oct 1990. doi: [10.1103/PhysRevB.42.6842](https://doi.org/10.1103/PhysRevB.42.6842).
- [254] O. Trovarelli, C. Geibel, S. Mederle, C. Langhammer, F. M. Grosche, P. Gegenwart, M. Lang, G. Sparn, and F. Steglich. “YbRh₂Si₂: Pronounced non-Fermi-liquid effects

- above a low-lying magnetic phase transition”. *Phys. Rev. Lett.* **85**, 626–629, Jul 2000. doi: [10.1103/PhysRevLett.85.626](https://doi.org/10.1103/PhysRevLett.85.626).
- [255] J. M. Lawrence, P. S. Riseborough, and R. D. Parks. “Valence fluctuation phenomena”. *Reports on Progress in Physics* **44**(1), 1, 1981. doi: [10.1088/0034-4885/44/1/001](https://doi.org/10.1088/0034-4885/44/1/001).
- [256] A. Menth, E. Buehler, and T. H. Geballe. “Magnetic and Semiconducting Properties of SmB_6 ”. *Phys. Rev. Lett.* **22**, 295–297, Feb 1969. doi: [10.1103/PhysRevLett.22.295](https://doi.org/10.1103/PhysRevLett.22.295).
- [257] P. Thunström and K. Held. “Topology of SmB_6 determined by dynamical mean field theory”. *Phys. Rev. B* **104**, 075131, Aug 2021. doi: [10.1103/PhysRevB.104.075131](https://doi.org/10.1103/PhysRevB.104.075131).
- [258] L. Fu and C. L. Kane. “Topological insulators with inversion symmetry”. *Phys. Rev. B* **76**, 045302, Jul 2007. doi: [10.1103/PhysRevB.76.045302](https://doi.org/10.1103/PhysRevB.76.045302).
- [259] M. Dzero, K. Sun, V. Galitski, and P. Coleman. “Topological Kondo insulators”. *Phys. Rev. Lett.* **104**, 106408, Mar 2010. doi: [10.1103/PhysRevLett.104.106408](https://doi.org/10.1103/PhysRevLett.104.106408).
- [260] M. P. Sarachik, E. Corenzwit, and L. D. Longinotti. “Resistivity of Mo-Nb and Mo-Re alloys containing 1% Fe”. *Phys. Rev.* **135**, A1041–A1045, Aug 1964. doi: [10.1103/PhysRev.135.A1041](https://doi.org/10.1103/PhysRev.135.A1041).
- [261] G. Van Den Berg. *Chapter IV Anomalies in Dilute Metallic Solutions of Transition Elements*, volume 4 of *Progress in Low Temperature Physics*, pages 194–264. Elsevier, 1964. ISBN 978-0-444-53310-4.
- [262] J. Kondo. “Resistance minimum in dilute magnetic alloys”. *Progress of Theoretical Physics* **32**(1), 37–49, Jul 1964. doi: [10.1143/ptp.32.37](https://doi.org/10.1143/ptp.32.37).
- [263] A. C. Hewson. *The Kondo Problem to Heavy Fermions*. Cambridge University Press, 1993. ISBN 978-0-52-136382-2.
- [264] A. H. Nevidomskyy. *Many-Body Physics: From Kondo to Hubbard*, volume 4 of *Modeling and Simulation*, chapter The Kondo Model and Poor Man’s Scaling. Verlag des Forschungszentrum Jülich, 2015. ISBN 978-3-95806-074-6.
- [265] A. A. Abrikosov. “Electron scattering on magnetic impurities in metals and anomalous resistivity effects”. *Physics Physique Fizika* **2**, 5–20, Sep 1965. doi: [10.1103/PhysicsPhysiqueFizika.2.5](https://doi.org/10.1103/PhysicsPhysiqueFizika.2.5).
- [266] K. G. Wilson. “The renormalization group: Critical phenomena and the Kondo problem”. *Rev. Mod. Phys.* **47**, 773–840, Oct 1975. doi: [10.1103/RevModPhys.47.773](https://doi.org/10.1103/RevModPhys.47.773).

- [267] P. Nozières. “A “fermi-liquid” description of the Kondo problem at low temperatures”. *Journal of Low Temperature Physics* **17**(1), 31–42, 1974. doi: [10.1007/BF00654541](https://doi.org/10.1007/BF00654541).
- [268] I. Affleck. “The Kondo screening cloud: what it is and how to observe it”. *arXiv* 2009. doi: [10.48550/arXiv.0911.2209](https://doi.org/10.48550/arXiv.0911.2209).
- [269] I. V. Borzenets, J. Shim, J. C. H. Chen, A. Ludwig, A. D. Wieck, S. Tarucha, H. S. Sim, and M. Yamamoto. “Observation of the Kondo screening cloud”. *Nature* **579**(7798), 210–213, 2020. doi: [10.1038/s41586-020-2058-6](https://doi.org/10.1038/s41586-020-2058-6).
- [270] A. F. Otte, M. Ternes, K. von Bergmann, S. Loth, H. Brune, C. P. Lutz, C. F. Hirjibehedin, and A. J. Heinrich. “The role of magnetic anisotropy in the Kondo effect”. *Nature Physics* **4**(11), 847–850, 2008. doi: [10.1038/nphys1072](https://doi.org/10.1038/nphys1072).
- [271] J. R. Schrieffer and P. A. Wolff. “Relation between the Anderson and Kondo Hamiltonians”. *Phys. Rev.* **149**, 491–492, Sep 1966. doi: [10.1103/PhysRev.149.491](https://doi.org/10.1103/PhysRev.149.491).
- [272] P. W. Anderson. “Localized magnetic states in metals”. *Phys. Rev.* **124**(1), 41–53, Oct 1961. doi: [10.1103/PhysRev.124.41](https://doi.org/10.1103/PhysRev.124.41).
- [273] P. Chalupa-Gantner. *The nonperturbative feats of local electronic correlation: The physics of irreducible vertex divergences*. PhD thesis, Technische Universität Wien, 2022.
- [274] H. R. Krishna-murthy, K. G. Wilson, and J. W. Wilkins. “Temperature-dependent susceptibility of the symmetric Anderson model: Connection to the Kondo model”. *Phys. Rev. Lett.* **35**, 1101–1104, Oct 1975. doi: [10.1103/PhysRevLett.35.1101](https://doi.org/10.1103/PhysRevLett.35.1101).
- [275] H. R. Krishna-murthy, J. W. Wilkins, and K. G. Wilson. “Renormalization-group approach to the Anderson model of dilute magnetic alloys. I. Static properties for the symmetric case”. *Phys. Rev. B* **21**, 1003–1043, Feb 1980. doi: [10.1103/PhysRevB.21.1003](https://doi.org/10.1103/PhysRevB.21.1003).
- [276] H. Suhl. “Dispersion theory of the Kondo effect”. *Phys. Rev.* **138**, A515–A523, Apr 1965. doi: [10.1103/PhysRev.138.A515](https://doi.org/10.1103/PhysRev.138.A515).
- [277] Y. Nagaoka. “Self-consistent treatment of Kondo’s effect in dilute alloys”. *Phys. Rev.* **138**, A1112–A1120, May 1965. doi: [10.1103/PhysRev.138.A1112](https://doi.org/10.1103/PhysRev.138.A1112).
- [278] H. Suhl. “Paramagnetic impurities in metals at finite temperatures”. *Physics Physique Fizika* **2**, 39–59, Sep 1965. doi: [10.1103/PhysicsPhysiqueFizika.2.39](https://doi.org/10.1103/PhysicsPhysiqueFizika.2.39).

- [279] M. Grobis, I. G. Rau, R. M. Potok, H. Shtrikman, and D. Goldhaber-Gordon. “Universal scaling in nonequilibrium transport through a single channel Kondo dot”. *Phys. Rev. Lett.* **100**, 246601, Jun 2008. doi: [10.1103/PhysRevLett.100.246601](https://doi.org/10.1103/PhysRevLett.100.246601).
- [280] G. R. Stewart. “Heavy-fermion systems”. *Rev. Mod. Phys.* **56**, 755–787, Oct 1984. doi: [10.1103/RevModPhys.56.755](https://doi.org/10.1103/RevModPhys.56.755).
- [281] M. A. Ruderman and C. Kittel. “Indirect exchange coupling of nuclear magnetic moments by conduction electrons”. *Phys. Rev.* **96**, 99–102, Oct 1954. doi: [10.1103/PhysRev.96.99](https://doi.org/10.1103/PhysRev.96.99).
- [282] T. Kasuya. “A theory of metallic ferro- and antiferromagnetism on Zener’s model”. *Progress of Theoretical Physics* **16**(1), 45–57, Jul 1956. doi: [10.1143/ptp.16.45](https://doi.org/10.1143/ptp.16.45).
- [283] K. Yosida. “Magnetic properties of Cu-Mn alloys”. *Phys. Rev.* **106**, 893–898, Jun 1957. doi: [10.1103/PhysRev.106.893](https://doi.org/10.1103/PhysRev.106.893).
- [284] K. Held, A. K. McMahan, and R. T. Scalettar. “Cerium volume collapse: Results from the merger of dynamical mean-field theory and local density approximation”. *Phys. Rev. Lett.* **87**(27), 276404, Dec 2001. doi: [10.1103/PhysRevLett.87.276404](https://doi.org/10.1103/PhysRevLett.87.276404).
- [285] V. Jaccarino, G. K. Wertheim, J. H. Wernick, L. R. Walker, and S. Arajs. “Paramagnetic excited state of FeSi”. *Phys. Rev.* **160**(3), 476–482, Aug 1967. doi: [10.1103/PhysRev.160.476](https://doi.org/10.1103/PhysRev.160.476).
- [286] H. Ikeda and K. Miyake. “A theory of anisotropic semiconductor of heavy fermions”. *Journal of the Physical Society of Japan* **65**(6), 1769–1781, 1996. doi: [10.1143/JPSJ.65.1769](https://doi.org/10.1143/JPSJ.65.1769).
- [287] Z. Fisk, J. Sarrao, J. Thompson, D. Mandrus, M. Hundley, A. Miglori, B. Bucher, Z. Schlesinger, G. Aeppli, E. Bucher, J. DiTusa, C. Oglesby, H.-R. Ott, P. Canfield, and S. Brown. “Kondo insulators”. *Physica B*: **206**, 798 – 803, 1995. doi: [10.1016/0921-4526\(94\)00588-M](https://doi.org/10.1016/0921-4526(94)00588-M).
- [288] A. Severing, J. D. Thompson, P. C. Canfield, Z. Fisk, and P. Riseborough. “Gap in the magnetic excitation spectrum of $\text{Ce}_3\text{Bi}_4\text{Pt}_3$ ”. *Phys. Rev. B* **44**, 6832–6837, Oct 1991. doi: [10.1103/PhysRevB.44.6832](https://doi.org/10.1103/PhysRevB.44.6832).
- [289] T. E. Mason, G. Aeppli, A. P. Ramirez, K. N. Clausen, C. Broholm, N. Stücheli, E. Bucher, and T. T. M. Palstra. “Spin gap and antiferromagnetic correlations in the Kondo insulator CeNiSn ”. *Phys. Rev. Lett.* **69**, 490–493, Jul 1992. doi: [10.1103/PhysRevLett.69.490](https://doi.org/10.1103/PhysRevLett.69.490).
- [290] E. M. Brüning, M. Brando, M. Baenitz, A. Bentiën, A. M. Strydom, R. E. Walstedt, and F. Steglich. “Low-temperature properties of CeRu_4Sn_6 from NMR and specific heat measure-

- ments: Heavy fermions emerging from a Kondo-insulating state”. *Phys. Rev. B* **82**, 125115, Sep 2010. doi: [10.1103/PhysRevB.82.125115](https://doi.org/10.1103/PhysRevB.82.125115).
- [291] S. Wolgast, Ç. Kurdak, K. Sun, J. W. Allen, D.-J. Kim, and Z. Fisk. “Low-temperature surface conduction in the Kondo insulator SmB₆”. *Phys. Rev. B* **88**, 180405, Nov 2013. doi: [10.1103/PhysRevB.88.180405](https://doi.org/10.1103/PhysRevB.88.180405).
- [292] M. Kasaya, F. Iga, M. Takigawa, and T. Kasuya. “Mixed valence properties of YbB₁₂”. *Journal of Magnetism and Magnetic Materials* **47-48**, 429–435, 1985. doi: [10.1016/0304-8853\(85\)90458-5](https://doi.org/10.1016/0304-8853(85)90458-5).
- [293] S. Seiro, L. Jiao, S. Kirchner, S. Hartmann, S. Friedemann, C. Krellner, C. Geibel, Q. Si, F. Steglich, and S. Wirth. “Evolution of the Kondo lattice and non-Fermi liquid excitations in a heavy-fermion metal”. *Nature Communications* **9**(1), 3324, 2018. doi: [10.1038/s41467-018-05801-5](https://doi.org/10.1038/s41467-018-05801-5).
- [294] J. L. G. Jimenez, C. Melnick, K. P. Koirala, R. Adler, F. Wang, M. Berrada, B. Chen, L. Wang, D. Walker, G. Kotliar, and W. Xie. “Tetragonal Kondo insulator EuCd₂Sb₂ discovered via high pressure high temperature synthesis”. *Advanced Functional Materials* **33**(36), 2303612, 2023/11/08 2023. doi: [10.1002/adfm.202303612](https://doi.org/10.1002/adfm.202303612).
- [295] S. Paschen, M. Baenitz, V. H. Tran, A. Rabis, F. Steglich, W. Carrillo-Cabrera, Y. Grin, A. M. Strydom, and P. d. V. du Plessis. “Towards strongly correlated semimetals: U₂Ru₂Sn and Eu₈Ga₁₆Ge₃₀”. *Journal of Physics and Chemistry of Solids* **63**(6), 1183–1188, 2002. doi: [10.1016/S0022-3697\(02\)00160-9](https://doi.org/10.1016/S0022-3697(02)00160-9).
- [296] M.-T. Suzuki and P. M. Oppeneer. “Dynamical mean-field theory of a correlated gap formation in plutonium monochalcogenides”. *Phys. Rev. B* **80**, 161103, Oct 2009. doi: [10.1103/PhysRevB.80.161103](https://doi.org/10.1103/PhysRevB.80.161103).
- [297] Z. Schlesinger, Z. Fisk, H.-T. Zhang, M. B. Maple, J. DiTusa, and G. Aeppli. “Unconventional charge gap formation in FeSi”. *Phys. Rev. Lett.* **71**(11), 1748–1751, Sep 1993. doi: [10.1103/PhysRevLett.71.1748](https://doi.org/10.1103/PhysRevLett.71.1748).
- [298] Y. S. Eo, K. Avers, J. A. Horn, H. Yoon, S. R. Saha, A. Suarez, M. S. Fuhrer, and J. Paglione. “Extraordinary bulk-insulating behavior in the strongly correlated materials FeSi and FeSb₂”. *Applied Physics Letters* **122**(23), Jun 2023. doi: [10.1063/5.0148249](https://doi.org/10.1063/5.0148249).

- [299] C. Petrovic, J. W. Kim, S. L. Bud'ko, A. I. Goldman, P. C. Canfield, W. Choe, and G. J. Miller. "Anisotropy and large magnetoresistance in the narrow-gap semiconductor FeSb₂". *Phys. Rev. B* **67**, 155205, Apr 2003. doi: [10.1103/PhysRevB.67.155205](https://doi.org/10.1103/PhysRevB.67.155205).
- [300] C. Petrovic, Y. Lee, T. Vogt, N. D. Lazarov, S. L. Bud'ko, and P. C. Canfield. "Kondo insulator description of spin state transition in FeSb₂". *Phys. Rev. B* **72**(4), 045103, Jul 2005. doi: [10.1103/PhysRevB.72.045103](https://doi.org/10.1103/PhysRevB.72.045103).
- [301] A. R. Pokharel, S. Y. Agustsson, V. V. Kabanov, F. Iga, T. Takabatake, H. Okamura, and J. Demsar. "Robust hybridization gap in the Kondo insulator YbB₁₂ probed by femtosecond optical spectroscopy". *Phys. Rev. B* **103**, 115134, Mar 2021. doi: [10.1103/PhysRevB.103.115134](https://doi.org/10.1103/PhysRevB.103.115134).
- [302] M. Jaime, R. Movshovich, G. R. Stewart, W. P. Beyermann, M. G. Berisso, M. F. Hundley, P. C. Canfield, and J. L. Sarrao. "Closing the spin gap in the Kondo insulator Ce₃Bi₄Pt₃ at high magnetic fields". *Nature* **405**(6783), 160–163, May 2000. doi: [10.1038/35012027](https://doi.org/10.1038/35012027).
- [303] Z. Xiang, L. Chen, K.-W. Chen, C. Tinsman, Y. Sato, T. Asaba, H. Lu, Y. Kasahara, M. Jaime, F. Balakirev, F. Iga, Y. Matsuda, J. Singleton, and L. Li. "Unusual high-field metal in a Kondo insulator". *Nature Physics* **17**(7), 788–793, 2021. doi: [10.1038/s41567-021-01216-0](https://doi.org/10.1038/s41567-021-01216-0).
- [304] P. Coleman. *Heavy Fermions: Electrons at the Edge of Magnetism*. John Wiley & Sons, Ltd, 2007. ISBN 978-0-47-002218-4.
- [305] J. M. Tomczak. "Isoelectronic tuning of heavy fermion systems: Proposal to synthesize Ce₃Sb₄Pd₃". *Phys. Rev. B* **101**, 035116, Jan 2020. doi: [10.1103/PhysRevB.101.035116](https://doi.org/10.1103/PhysRevB.101.035116).
- [306] T. Pietrus, H. v. Löhneysen, and P. Schlottmann. "Kondo-hole conduction in the La-doped Kondo insulator Ce₃Bi₄Pt₃". *Phys. Rev. B* **77**, 115134, Mar 2008. doi: [10.1103/PhysRevB.77.115134](https://doi.org/10.1103/PhysRevB.77.115134).
- [307] T. Kagayama, T. Ishii, and G. Oomi. "Effect of pressure on the electrical resistivity of the heavy fermion CeAl₃". *Journal of Alloys and Compounds* **207-208**, 263–266, 1994. doi: [10.1016/0925-8388\(94\)90217-8](https://doi.org/10.1016/0925-8388(94)90217-8).
- [308] M. Koeda, M. Hedo, Y. Uwatoko, T. Matsumoto, N. Takeda, and M. Ishikawa. "Effect of pressure on the electrical resistivity of CeCu₂Si₂". *Journal of Magnetism and Magnetic Materials* **272-276**, E175–E176, 2004. doi: [10.1016/j.jmmm.2003.11.103](https://doi.org/10.1016/j.jmmm.2003.11.103).
- [309] R. Movshovich, A. Lacerda, P. C. Canfield, J. D. Thompson, and Z. Fisk. "Fermi surface instability and symmetry breaking in heavy-fermion compound YbBiPt". *Phys. Rev. Lett.* **73**, 492–495, Jul 1994. doi: [10.1103/PhysRevLett.73.492](https://doi.org/10.1103/PhysRevLett.73.492).

- [310] A. Abdelwahab and E. Jeckelmann. “Correlations and confinement of excitations in an asymmetric Hubbard ladder”. *The European Physical Journal B* **91**(9), 207, 2018. doi: [10.1140/epjb/e2018-90360-9](https://doi.org/10.1140/epjb/e2018-90360-9).
- [311] K. Capelle, G. Vignale, and C. A. Ullrich. “Spin gaps and spin-flip energies in density-functional theory”. *Physical Review B* **81**(12), Mar 2010. doi: [10.1103/physrevb.81.125114](https://doi.org/10.1103/physrevb.81.125114).
- [312] H. J. Silverstein, A. E. Smith, C. Mauws, D. L. Abernathy, H. Zhou, Z. Dun, J. van Lierop, and C. R. Wiebe. “Direct measurement of the spin gap in a quasi-one-dimensional clinopyroxene: NaTiSi₂O₆”. *Physical Review B* **90**(14), Oct 2014. doi: [10.1103/physrevb.90.140402](https://doi.org/10.1103/physrevb.90.140402).
- [313] D. Adroja, K. Mcewen, J.-G. Park, A. Hillier, N. Tateda, P. Riseborough, and T. Takabatake. “Inelastic neutron scattering study of spin gap formation in heavy fermion compounds”. *Journal of Optoelectronics and Advanced Materials* **10**, 1564–1582, 07 2008.
- [314] P. J. Baker, S. J. Blundell, F. L. Pratt, T. Lancaster, M. L. Brooks, W. Hayes, M. Isobe, Y. Ueda, M. Hoinkis, M. Sing, M. Klemm, S. Horn, and R. Claessen. “Muon-spin relaxation measurements on the dimerized spin-1/2 chains NaTiSi₂O₆ and TiOCl”. *Phys. Rev. B* **75**, 094404, Mar 2007. doi: [10.1103/PhysRevB.75.094404](https://doi.org/10.1103/PhysRevB.75.094404).
- [315] E. Ehrenfreund and L. S. Smith. “Nuclear-spin-lattice relaxation process in spin-Peierls systems”. *Phys. Rev. B* **16**, 1870–1874, Sep 1977. doi: [10.1103/PhysRevB.16.1870](https://doi.org/10.1103/PhysRevB.16.1870).
- [316] K. Sturm. “Dynamic structure factor: An introduction”. *Zeitschrift für Naturforschung A* **48**(1-2), 233–242, 1993. doi: [10.1515/zna-1993-1-244](https://doi.org/10.1515/zna-1993-1-244).
- [317] R. G. Pereira, J. Sirker, J.-S. Caux, R. Hagemans, J. M. Maillet, S. R. White, and I. Affleck. “Dynamical spin structure factor for the anisotropic spin-1/2 Heisenberg chain”. *Phys. Rev. Lett.* **96**, 257202, Jun 2006. doi: [10.1103/PhysRevLett.96.257202](https://doi.org/10.1103/PhysRevLett.96.257202).
- [318] J. Kaufmann, K. Steiner, R. T. Scalettar, K. Held, and O. Janson. “How correlations change the magnetic structure factor of the kagome Hubbard model”. *Phys. Rev. B* **104**, 165127, Oct 2021. doi: [10.1103/PhysRevB.104.165127](https://doi.org/10.1103/PhysRevB.104.165127).
- [319] M. Sentef, J. Kuneš, P. Werner, and A. P. Kampf. “Correlations in a band insulator”. *Phys. Rev. B* **80**, 155116, Oct 2009. doi: [10.1103/PhysRevB.80.155116](https://doi.org/10.1103/PhysRevB.80.155116).
- [320] J. M. Tomczak, K. Haule, and G. Kotliar. “Signatures of electronic correlations in iron silicide”. *PNAS* **109**(9), 3243–3246, 2012. doi: [10.1073/pnas.1118371109](https://doi.org/10.1073/pnas.1118371109).

- [321] G. M. Abramova, A. Hanzawa, T. Kagayama, Y. Mita, E. V. Eremin, G. M. Zeer, S. M. Zharkov, and S. G. Ovchinnikov. “Pressure-induced metallization of the Mott insulator $\text{Fe}_x\text{Mn}_{1-x}\text{S}$ system”. *Journal of Magnetism and Magnetic Materials* **465**, 775–779, 2018. doi: [10.1016/j.jmmm.2018.05.056](https://doi.org/10.1016/j.jmmm.2018.05.056).
- [322] J. Kuneš, J., D. M. Korotin, M. A. Korotin, V. I. Anisimov, and P. Werner. “Pressure-driven metal-insulator transition in hematite from dynamical mean-field theory”. *Phys. Rev. Lett.* **102**, 146402, Apr 2009. doi: [10.1103/PhysRevLett.102.146402](https://doi.org/10.1103/PhysRevLett.102.146402).
- [323] D. J. Campbell, Z. E. Brubaker, C. Roncaioli, P. Saraf, Y. Xiao, P. Chow, C. Kenney-Benson, D. Popov, R. J. Zieve, J. R. Jeffries, and J. Paglione. “Pressure-driven valence increase and metallization in the Kondo insulator $\text{Ce}_3\text{Bi}_4\text{Pt}_3$ ”. *Phys. Rev. B* **100**, 235133, Dec 2019. doi: [10.1103/PhysRevB.100.235133](https://doi.org/10.1103/PhysRevB.100.235133).
- [324] M. Jarrell. “Symmetric periodic Anderson model in infinite dimensions”. *Phys. Rev. B* **51**, 7429–7440, Mar 1995. doi: [10.1103/PhysRevB.51.7429](https://doi.org/10.1103/PhysRevB.51.7429).
- [325] K. Friedrich. *Conserving dynamical mean-field approaches to strongly correlated systems*. PhD thesis, Universität Hamburg, 2018.
- [326] H. Tsunetsugu, M. Sigrist, and K. Ueda. “The ground-state phase diagram of the one-dimensional Kondo lattice model”. *Rev. Mod. Phys.* **69**, 809–864, Jul 1997. doi: [10.1103/RevModPhys.69.809](https://doi.org/10.1103/RevModPhys.69.809).
- [327] T. Mitsui, S. Sakai, S. Li, T. Ueno, T. Watanuki, Y. Kobayashi, R. Masuda, M. Seto, and H. Akai. “Magnetic Friedel oscillation at the $\text{Fe}(001)$ surface: Direct observation by atomic-layer-resolved synchrotron radiation ^{57}Fe Mössbauer spectroscopy”. *Phys. Rev. Lett.* **125**, 236806, Dec 2020. doi: [10.1103/PhysRevLett.125.236806](https://doi.org/10.1103/PhysRevLett.125.236806).
- [328] S. Doniach. “The Kondo lattice and weak antiferromagnetism”. *Physica B+C* **91**, 231 – 234, 1977. doi: [10.1016/0378-4363\(77\)90190-5](https://doi.org/10.1016/0378-4363(77)90190-5).
- [329] P. Coleman and A. J. Schofield. “Quantum criticality”. *Nature* **433**(7023), 226–229, 2005. doi: [10.1038/nature03279](https://doi.org/10.1038/nature03279).
- [330] T. Schäfer. *Classical and quantum phase transitions in strongly correlated electron systems*. PhD thesis, Technische Universität Wien, 2016.
- [331] J. M. Tomczak, K. Haule, T. Miyake, A. Georges, and G. Kotliar. “Thermopower of correlated semiconductors: Application to FeAs_2 and FeSb_2 ”. *Phys. Rev. B* **82**(8), 085104, Aug 2010. doi: [10.1103/PhysRevB.82.085104](https://doi.org/10.1103/PhysRevB.82.085104).

- [332] S. Wirth and F. Steglich. “Exploring heavy fermions from macroscopic to microscopic length scales”. *Nat. Rev. Materials* **1**, 16051, Aug 2016. doi: [10.1038/natrevmats.2016.51](https://doi.org/10.1038/natrevmats.2016.51).
- [333] J. C. Cooley, M. C. Aronson, and P. C. Canfield. “High pressures and the Kondo gap in $\text{Ce}_3\text{Bi}_4\text{Pt}_3$ ”. *Phys. Rev. B* **55**, 7533–7538, Mar 1997. doi: [10.1103/PhysRevB.55.7533](https://doi.org/10.1103/PhysRevB.55.7533).
- [334] N. Wakeham, P. F. S. Rosa, Y. Q. Wang, M. Kang, Z. Fisk, F. Ronning, and J. D. Thompson. “Low-temperature conducting state in two candidate topological Kondo insulators: SmB_6 and $\text{Ce}_3\text{Bi}_4\text{Pt}_3$ ”. *Phys. Rev. B* **94**, 035127, Jul 2016. doi: [10.1103/PhysRevB.94.035127](https://doi.org/10.1103/PhysRevB.94.035127).
- [335] P. S. Riseborough. “Collapse of the coherence gap in Kondo semiconductors”. *Phys. Rev. B* **68**, 235213, Dec 2003. doi: [10.1103/PhysRevB.68.235213](https://doi.org/10.1103/PhysRevB.68.235213).
- [336] Y. Takeda, M. Arita, H. Sato, K. Shimada, H. Namatame, M. Taniguchi, K. Katoh, F. Iga, and T. Takabatake. “Temperature-dependent high-resolution photoemission study of the Kondo insulator $\text{Ce}_3\text{Bi}_4\text{Pt}_3$ ”. *J Electron Spectrosc* **101–103**, 721 – 724, 1999. doi: [10.1016/S0368-2048\(98\)00406-X](https://doi.org/10.1016/S0368-2048(98)00406-X).
- [337] B. Bucher, Z. Schlesinger, P. C. Canfield, and Z. Fisk. “Kondo coupling induced charge gap in $\text{Ce}_3\text{Bi}_4\text{Pt}_3$ ”. *Phys. Rev. Lett.* **72**, 522–525, Jan 1994. doi: [10.1103/PhysRevLett.72.522](https://doi.org/10.1103/PhysRevLett.72.522).
- [338] G. Boebinger, A. Passner, P. Canfield, and Z. Fisk. “Studies of the Kondo insulator $\text{Ce}_3\text{Bi}_4\text{Pt}_3$ in 61T pulsed magnetic fields”. *Physica B*: **211**(1), 227 – 229, 1995. doi: [10.1016/0921-4526\(94\)00992-5](https://doi.org/10.1016/0921-4526(94)00992-5).
- [339] J. M. Tomczak. “Realistic many-body theory of Kondo insulators: Renormalizations and fluctuations in $\text{Ce}_3\text{Bi}_4\text{Pt}_3$ ”. *arXiv* 2019. doi: [10.48550/arXiv.1904.01346](https://doi.org/10.48550/arXiv.1904.01346).
- [340] P.-Y. Chang, O. Erten, and P. Coleman. “Möbius Kondo insulators”. *Nature Physics* **13**(8), 794–798, 2017. doi: [10.1038/nphys4092](https://doi.org/10.1038/nphys4092).
- [341] S. K. Kushwaha, M. K. Chan, J. Park, S. M. Thomas, E. D. Bauer, J. D. Thompson, F. Ronning, P. F. S. Rosa, and N. Harrison. “Magnetic field-tuned Fermi liquid in a Kondo insulator”. *Nature Communications* **10**(1), 5487, 2019. doi: [10.1038/s41467-019-13421-w](https://doi.org/10.1038/s41467-019-13421-w).
- [342] F. R. de Boer, J. Klaasse, J. Aarts, C. D. Bredl, W. Lieke, U. Rauchschwalbe, F. Steglich, R. Felten, U. Umhofer, and G. Weber. “Magnetization and specific heat of CeAl_3 ”. *Journal of Magnetism and Magnetic Materials* **47-48**, 60–62, 1985. doi: [10.1016/0304-8853\(85\)90357-9](https://doi.org/10.1016/0304-8853(85)90357-9).

- [343] W. T. Fuhrman, J. C. Leiner, J. W. Freeland, M. van Veenendaal, S. M. Koohpayeh, W. A. Phelan, T. M. McQueen, and C. Broholm. “Magnetic dichroism in the Kondo insulator SmB_6 ”. *Phys. Rev. B* **99**, 020401, Jan 2019. doi: [10.1103/PhysRevB.99.020401](https://doi.org/10.1103/PhysRevB.99.020401).
- [344] K. Katoh and T. Takabatake. “Crystal growth and semiconducting properties of $\text{Ce}_3\text{Bi}_4\text{Pt}_3$ ”. *Journal of Alloys and Compounds* **268**(1–2), 22 – 24, 1998. doi: [10.1016/S0925-8388\(97\)00583-5](https://doi.org/10.1016/S0925-8388(97)00583-5).
- [345] C. Cao, G.-X. Zhi, and J.-X. Zhu. “From trivial Kondo insulator $\text{Ce}_3\text{Pt}_3\text{Bi}_4$ to topological nodal-line semimetal $\text{Ce}_3\text{Pd}_3\text{Bi}_4$ ”. *Phys. Rev. Lett.* **124**, 166403, Apr 2020. doi: [10.1103/PhysRevLett.124.166403](https://doi.org/10.1103/PhysRevLett.124.166403).
- [346] F. Lechermann. *DMFT: From Infinite Dimensions to Real Materials*, volume 8 of *Modeling and Simulation*, chapter Charge Self-Consistency in Correlated Electronic Structure. Verlag des Forschungszentrum Jülich, 2018. ISBN 978-3-95806-313-6.
- [347] The Materials Project. “Materials Data on $\text{Ce}_3\text{Bi}_4\text{Pt}_3$ by Materials Project”, 2020. <https://next-gen.materialsproject.org/materials/mp-1105392> Last visited: Feb 2024.
- [348] K. Takegahara, H. Harima, Y. Kaneta, and A. Yanase. “Electronic band structures of $\text{Ce}_3\text{Pt}_3\text{Sb}_4$ and $\text{Ce}_3\text{Pt}_3\text{Bi}_4$ ”. *Journal of the Physical Society of Japan* **62**(6), 2103–2111, Jun 1993. doi: [10.1143/jpsj.62.2103](https://doi.org/10.1143/jpsj.62.2103).
- [349] M. O. Ajeesh, S. K. Kushwaha, S. M. Thomas, J. D. Thompson, M. K. Chan, N. Harrison, J. M. Tomczak, and P. F. S. Rosa. “Localized f -electron magnetism in the semimetal $\text{Ce}_3\text{Bi}_4\text{Au}_3$ ”. *Phys. Rev. B* **108**, 245125, Dec 2023. doi: [10.1103/PhysRevB.108.245125](https://doi.org/10.1103/PhysRevB.108.245125).
- [350] M. Hundley, A. Lacerda, P. Canfield, J. Thompson, and Z. Fisk. “Magnetoresistance of the Kondo insulator $\text{Ce}_3\text{Bi}_4\text{Pt}_3$ ”. *Physica B: Condensed Matter* **186–188**, 425–427, May 1993. doi: [10.1016/0921-4526\(93\)90593-u](https://doi.org/10.1016/0921-4526(93)90593-u).
- [351] S. Gabáni, E. Bauer, S. Berger, K. Flachbart, Y. Paderno, C. Paul, V. Pavlík, and N. Shitsevalova. “Pressure-induced fermi-liquid behavior in the Kondo insulator SmB_6 : Possible transition through a quantum critical point”. *Phys. Rev. B* **67**, 172406, May 2003. doi: [10.1103/PhysRevB.67.172406](https://doi.org/10.1103/PhysRevB.67.172406).
- [352] Y. Zhou, Q. Wu, P. F. Rosa, R. Yu, J. Guo, W. Yi, S. Zhang, Z. Wang, H. Wang, S. Cai, K. Yang, A. Li, Z. Jiang, S. Zhang, X. Wei, Y. Huang, P. Sun, Y. feng Yang, Z. Fisk, Q. Si, Z. Zhao, and L. Sun. “Quantum phase transition and destruction of Kondo effect in pressurized SmB_6 ”. *Science Bulletin* **62**(21), 1439 – 1444, 2017. doi: [10.1016/j.scib.2017.10.008](https://doi.org/10.1016/j.scib.2017.10.008).

- [353] Y. Uwatoko, T. Ishii, G. Oomi, H. Takahashi, N. Mōri, J. D. Thompson, J. L. Shero, D. Madru, and Z. Fisk. “Pressure collapse of Kondo gap in Kondo compound CeRhSb”. *Journal of the Physical Society of Japan* **65**(1), 27–29, 1996. doi: [10.1143/JPSJ.65.27](https://doi.org/10.1143/JPSJ.65.27).
- [354] G. R. Hearne, P. Musyimi, S. Bhattacharjee, M. K. Forthaus, and M. M. Abd-Elmeguid. “Unusual pressure-induced metallic state in the correlated narrow band-gap semiconductor FeSi”. *Phys. Rev. B* **100**, 155118, Oct 2019. doi: [10.1103/PhysRevB.100.155118](https://doi.org/10.1103/PhysRevB.100.155118).
- [355] I. Jarrige, H. Yamaoka, J.-P. Rueff, J.-F. Lin, M. Taguchi, N. Hiraoka, H. Ishii, K. D. Tsuei, K. Imura, T. Matsumura, A. Ochiai, H. S. Suzuki, and A. Kotani. “Unified understanding of the valence transition in the rare-earth monochalcogenides under pressure”. *Phys. Rev. B* **87**, 115107, Mar 2013. doi: [10.1103/PhysRevB.87.115107](https://doi.org/10.1103/PhysRevB.87.115107).
- [356] G. H. Kwei, J. M. Lawrence, and P. C. Canfield. “Temperature dependence of the 4f occupation of Ce₃Bi₄Pt₃”. *Phys. Rev. B* **49**, 14708–14710, May 1994. doi: [10.1103/PhysRevB.49.14708](https://doi.org/10.1103/PhysRevB.49.14708).
- [357] G. H. Kwei, J. M. Lawrence, P. C. Canfield, W. P. Beyermann, J. D. Thompson, Z. Fisk, A. C. Lawson, and J. A. Goldstone. “Thermal expansion of Ce₃Bi₄Pt₃ at ambient and high pressures”. *Phys. Rev. B* **46**, 8067–8072, Oct 1992. doi: [10.1103/PhysRevB.46.8067](https://doi.org/10.1103/PhysRevB.46.8067).
- [358] G. D. Mahan. *Many-particle Physics*. Plenum Press, 1990. ISBN 978-0-306-46338-9.
- [359] I. Paul and G. Kotliar. “Thermal transport for many-body tight-binding models”. *Phys. Rev. B* **67**(11), 115131, Mar 2003. doi: [10.1103/PhysRevB.67.115131](https://doi.org/10.1103/PhysRevB.67.115131).
- [360] C. Ambrosch-Draxl and J. O. Sofo. “Linear optical properties of solids within the full-potential linearized augmented planewave method”. *Computer Physics Communications* **175**(1), 1 – 14, 2006. doi: [10.1016/j.cpc.2006.03.005](https://doi.org/10.1016/j.cpc.2006.03.005).
- [361] S. Sen, N. S. Vidhyadhiraja, E. Miranda, V. Dobrosavljević, and W. Ku. “Fragility of the Kondo insulating gap against disorder: Relevance to recent puzzles in topological Kondo insulators”. *Phys. Rev. Research* **2**, 033370, Sep 2020. doi: [10.1103/PhysRevResearch.2.033370](https://doi.org/10.1103/PhysRevResearch.2.033370).
- [362] J. M. Tomczak and S. Biermann. “Optical properties of correlated materials: Generalized Peierls approach and its application to VO₂”. *Phys. Rev. B* **80**(8) 085117, 2009. doi: [10.1103/PhysRevB.80.085117](https://doi.org/10.1103/PhysRevB.80.085117).
- [363] S. Poncé, W. Li, S. Reichardt, and F. Giustino. “First-principles calculations of charge carrier mobility and conductivity in bulk semiconductors and two-dimensional materials”. *Reports on Progress in Physics* **83**(3), 036501, Feb 2020. doi: [10.1088/1361-6633/ab6a43](https://doi.org/10.1088/1361-6633/ab6a43).

- [364] S. Cai, J. Guo, V. A. Sidorov, Y. Zhou, H. Wang, G. Lin, X. Li, Y. Li, K. Yang, A. Li, Q. Wu, J. Hu, S. K. Kushwaha, R. J. Cava, and L. Sun. “Independence of topological surface state and bulk conductance in three-dimensional topological insulators”. *npj Quantum Materials* **3**(1), 62, Nov 2018. doi: [10.1038/s41535-018-0134-z](https://doi.org/10.1038/s41535-018-0134-z).
- [365] A. Valli and J. M. Tomczak. “Resistance saturation in semi-conducting polyacetylene molecular wires”. *Journal of Computational Electronics* **22**(5), 1363–1376, Oct 2023. doi: [10.1007/s10825-023-02043-7](https://doi.org/10.1007/s10825-023-02043-7).
- [366] Y. S. Eo, A. Rakoski, J. Lucien, D. Mihaliiov, C. Kurdak, P. F. S. Rosa, and Z. Fisk. “Transport gap in SmB_6 protected against disorder”. *Proceedings of the National Academy of Sciences* **116**(26), 12638–12641, 2019. doi: [10.1073/pnas.1901245116](https://doi.org/10.1073/pnas.1901245116).
- [367] C. D. W. Jones, K. A. Regan, and F. J. DiSalvo. “Thermoelectric properties of the doped Kondo insulator: $\text{Nd}_x\text{Ce}_{3-x}\text{Pt}_3\text{Sb}_4$ ”. *Phys. Rev. B* **58**, 16057–16063, Dec 1998. doi: [10.1103/PhysRevB.58.16057](https://doi.org/10.1103/PhysRevB.58.16057).
- [368] S. Dzsaber, L. Prochaska, A. Sidorenko, G. Eguchi, R. Svagera, M. Waas, A. Prokofiev, Q. Si, and S. Paschen. “Kondo insulator to semimetal transformation tuned by spin-orbit coupling”. *Phys. Rev. Lett.* **118**, 246601, Jun 2017. doi: [10.1103/PhysRevLett.118.246601](https://doi.org/10.1103/PhysRevLett.118.246601).
- [369] Y. Muro, K. Yutani, J. Kajino, T. Onimaru, and T. Takabatake. “Anisotropic c-f hybridization in the Kondo semiconductor $\text{CeFe}_2\text{Al}_{10}$ ”. *Journal of the Korean Physical Society* **63**(3), 508–511, Aug 2013. doi: [10.3938/jkps.63.508](https://doi.org/10.3938/jkps.63.508).
- [370] I. Das and E. V. Sampathkumaran. “Electrical-resistance anomalies in a Ce-Ru-Sn phase”. *Phys. Rev. B* **46**, 4250–4252, Aug 1992. doi: [10.1103/PhysRevB.46.4250](https://doi.org/10.1103/PhysRevB.46.4250).
- [371] A. Strydom, Z. Guo, S. Paschen, R. Viennois, and F. Steglich. “Electronic properties of semiconducting CeRu_4Sn_6 ”. *Physica B: Condensed Matter* **359-361**, 293 – 295, 2005. Proceedings of the International Conference on Strongly Correlated Electron Systems. doi: [10.1016/j.physb.2005.01.111](https://doi.org/10.1016/j.physb.2005.01.111).
- [372] J. Zhang, S. Zhang, Z. Chen, M. Lv, H. Zhao, Y. feng Yang, G. Chen, and P. Sun. “Pressure effect in the Kondo semimetal CeRu_4Sn_6 with nontrivial topology”. *Chinese Physics B* **27**(9), 097103, Sep 2018. doi: [10.1088/1674-1056/27/9/097103](https://doi.org/10.1088/1674-1056/27/9/097103).
- [373] D. J. Kim, S. Thomas, T. Grant, J. Botimer, Z. Fisk, and J. Xia. “Surface Hall effect and nonlocal transport in SmB_6 : Evidence for surface conduction”. *Scientific Reports* **3**(1), 3150, Nov 2013. doi: [10.1038/srep03150](https://doi.org/10.1038/srep03150).

- [374] P. Syers, D. Kim, M. S. Fuhrer, and J. Paglione. “Tuning bulk and surface conduction in the proposed topological Kondo insulator SmB_6 ”. *Phys. Rev. Lett.* **114**, 096601, Mar 2015. doi: [10.1103/PhysRevLett.114.096601](https://doi.org/10.1103/PhysRevLett.114.096601).
- [375] Y. Sato, Z. Xiang, Y. Kasahara, T. Taniguchi, S. Kasahara, L. Chen, T. Asaba, C. Tinsman, H. Murayama, O. Tanaka, Y. Mizukami, T. Shibauchi, F. Iga, J. Singleton, L. Li, and Y. Matsuda. “Unconventional thermal metallic state of charge-neutral fermions in an insulator”. *Nature Physics* **15**(9), 954–959, Sep 2019. doi: [10.1038/s41567-019-0552-2](https://doi.org/10.1038/s41567-019-0552-2).
- [376] P. Canfield, A. Lacerda, J. Thompson, G. Sparn, W. Beyermann, M. Hundley, and Z. Fisk. “Doping and pressure study of $\text{U}_3\text{Sb}_4\text{Pt}_3$ ”. *Journal of Alloys and Compounds* **181**(1), 77 – 81, 1992. Proceedings of the 19th Rare Earth Research Conference. doi: [10.1016/0925-8388\(92\)90300-X](https://doi.org/10.1016/0925-8388(92)90300-X).
- [377] Y. Xu, C. Yue, H. Weng, and X. Dai. “Heavy Weyl fermion state in CeRu_4Sn_6 ”. *Phys. Rev. X* **7**, 011027, Mar 2017. doi: [10.1103/PhysRevX.7.011027](https://doi.org/10.1103/PhysRevX.7.011027).
- [378] K. Sengupta, K. K. Iyer, R. Ranganathan, and E. V. Sampathkumaran. “Unusual pressure response of electronic transport properties of a Kondo insulator CeRu_4Sn_6 ”. *Journal of Physics: Conference Series* **377**, 012029, jul 2012. doi: [10.1088/1742-6596/377/1/012029](https://doi.org/10.1088/1742-6596/377/1/012029).
- [379] N. Harrison. “Highly asymmetric nodal semimetal in bulk SmB_6 ”. *Phys. Rev. Lett.* **121**, 026602, Jul 2018. doi: [10.1103/PhysRevLett.121.026602](https://doi.org/10.1103/PhysRevLett.121.026602).
- [380] H. Shen and L. Fu. “Quantum oscillation from in-gap states and a non-Hermitian Landau level problem”. *Phys. Rev. Lett.* **121**, 026403, Jul 2018. doi: [10.1103/PhysRevLett.121.026403](https://doi.org/10.1103/PhysRevLett.121.026403).
- [381] G. Li, Z. Xiang, F. Yu, T. Asaba, B. Lawson, P. Cai, C. Tinsman, A. Berkley, S. Wolgast, Y. S. Eo, D.-J. Kim, C. Kurdak, J. W. Allen, K. Sun, X. H. Chen, Y. Y. Wang, Z. Fisk, and L. Li. “Two-dimensional Fermi surfaces in Kondo insulator SmB_6 ”. *Science* **346**(6214), 1208–1212, 2014. doi: [10.1126/science.1250366](https://doi.org/10.1126/science.1250366).
- [382] B. S. Tan, Y.-T. Hsu, B. Zeng, M. C. Hatnean, N. Harrison, Z. Zhu, M. Hartstein, M. Kiourlapou, A. Srivastava, M. D. Johannes, T. P. Murphy, J.-H. Park, L. Balicas, G. G. Lonzarich, G. Balakrishnan, and S. E. Sebastian. “Unconventional Fermi surface in an insulating state”. *Science* **349**(6245), 287–290, 2015. doi: [10.1126/science.aaa7974](https://doi.org/10.1126/science.aaa7974).
- [383] K. Behnia. *Fundamentals of Thermoelectricity*. Oxford University Press, 2015. ISBN 978-0-19-969766-3.

- [384] P. Voruganti, A. Golubentsev, and S. John. “Conductivity and Hall effect in the two-dimensional Hubbard model”. *Phys. Rev. B* **45**, 13945–13961, Jun 1992. doi: [10.1103/PhysRevB.45.13945](https://doi.org/10.1103/PhysRevB.45.13945).
- [385] H. Kohno and K. Yamada. “A General Expression for Hall Coefficient Based on Fermi Liquid Theory”. *Progress of Theoretical Physics* **80**(4), 623–643, 10 1988. doi: [10.1143/PTP.80.623](https://doi.org/10.1143/PTP.80.623).
- [386] W. Xu. *Transport and magnetic properties of correlated electron systems*. PhD thesis, Rutgers University, 2014.
- [387] S. Shtrikman and H. Thomas. “Remarks on linear magneto-resistance and magneto-heat-conductivity”. *Solid State Communications* **3**(7), 147–150, 1965. doi: [10.1016/0038-1098\(65\)90178-X](https://doi.org/10.1016/0038-1098(65)90178-X).
- [388] N. Nagaosa, J. Sinova, S. Onoda, A. H. MacDonald, and N. P. Ong. “Anomalous Hall effect”. *Rev. Mod. Phys.* **82**, 1539–1592, May 2010. doi: [10.1103/RevModPhys.82.1539](https://doi.org/10.1103/RevModPhys.82.1539).
- [389] P. Streda. “Theory of quantised Hall conductivity in two dimensions”. *Journal of Physics C: Solid State Physics* **15**(22), L717–L721, aug 1982. doi: [10.1088/0022-3719/15/22/005](https://doi.org/10.1088/0022-3719/15/22/005).
- [390] J. Mitscherling and W. Metzner. “Longitudinal conductivity and Hall coefficient in two-dimensional metals with spiral magnetic order”. *Phys. Rev. B* **98**, 195126, Nov 2018. doi: [10.1103/PhysRevB.98.195126](https://doi.org/10.1103/PhysRevB.98.195126).
- [391] J. Mitscherling. “Longitudinal and anomalous Hall conductivity of a general two-band model”. *Phys. Rev. B* **102**, 165151, Oct 2020. doi: [10.1103/PhysRevB.102.165151](https://doi.org/10.1103/PhysRevB.102.165151).
- [392] K. Behnia. “The Nernst effect and the boundaries of the Fermi liquid picture”. *Journal of Physics: Condensed Matter* **21**(11), 113101, 2009. doi: [10.1088/0953-8984/21/11/113101](https://doi.org/10.1088/0953-8984/21/11/113101).
- [393] W. Thomson. “Ix.—On the dynamical theory of heat. Part V. Thermo-electric currents”. *Transactions of the Royal Society of Edinburgh* **21**(1), 123–171, 1857. doi: [10.1017/s0080456800032014](https://doi.org/10.1017/s0080456800032014).
- [394] K. Behnia and H. Aubin. “Nernst effect in metals and superconductors: a review of concepts and experiments”. *Reports on Progress in Physics* **79**(4), 046502, 2016. doi: [10.1088/0034-4885/79/4/046502](https://doi.org/10.1088/0034-4885/79/4/046502).
- [395] E. Taylor and C. Kallin. “Intrinsic hall effect in a multiband chiral superconductor in the absence of an external magnetic field”. *Phys. Rev. Lett.* **108**, 157001, Apr 2012. doi: [10.1103/PhysRevLett.108.157001](https://doi.org/10.1103/PhysRevLett.108.157001).

- [396] I. Paul. *Thermal and charge transport in correlated electron systems*. PhD thesis, Rutgers University, 2003.
- [397] H. Kontani. *Transport Phenomena in Strongly Correlated Fermi Liquids*. Springer Berlin, Heidelberg, 2013. ISBN 978-3-642-35364-2.
- [398] H. Kontani. “General formula for the thermoelectric transport phenomena based on Fermi liquid theory: Thermoelectric power, Nernst coefficient, and thermal conductivity”. *Phys. Rev. B* **67**, 014408, Jan 2003. doi: [10.1103/PhysRevB.67.014408](https://doi.org/10.1103/PhysRevB.67.014408).
- [399] R. Nourafkan and A.-M. S. Tremblay. “Hall and Faraday effects in interacting multiband systems with arbitrary band topology and spin-orbit coupling”. *Phys. Rev. B* **98**, 165130, Oct 2018. doi: [10.1103/PhysRevB.98.165130](https://doi.org/10.1103/PhysRevB.98.165130).
- [400] A. A. Markov, G. Rohringer, and A. N. Rubtsov. “Robustness of the topological quantization of the Hall conductivity for correlated lattice electrons at finite temperatures”. *Phys. Rev. B* **100**, 115102, Sep 2019. doi: [10.1103/PhysRevB.100.115102](https://doi.org/10.1103/PhysRevB.100.115102).
- [401] A. Khurana. “Electrical conductivity in the infinite-dimensional Hubbard model”. *Phys. Rev. Lett.* **64**(16), 1990, Apr 1990. doi: [10.1103/PhysRevLett.64.1990](https://doi.org/10.1103/PhysRevLett.64.1990).
- [402] N. Wagner, S. Ciuchi, A. Toschi, B. Trauzettel, and G. Sangiovanni. “Resistivity exponents in 3d Dirac semimetals from electron-electron interaction”. *Phys. Rev. Lett.* **126**, 206601, May 2021. doi: [10.1103/PhysRevLett.126.206601](https://doi.org/10.1103/PhysRevLett.126.206601).
- [403] K. Miyake and A. Tsuruta. “Compact representation for specific heat of interacting fermion systems in terms of fully renormalized matsubara green function”. *Journal of the Physical Society of Japan* **84**(9), 094708, 2024/03/12 2015. doi: [10.7566/JPSJ.84.094708](https://doi.org/10.7566/JPSJ.84.094708).
- [404] Y. L. Luke. “Chapter II the Gamma function and related functions”. In “The Special Functions and Their Approximations”, volume 53 of *Mathematics in Science and Engineering*, pages 8–37. Elsevier, 1969. ISBN 978-0-12-459901-7.
- [405] A. J. Millis. “Optical Conductivity and Correlated Electron Physics”. In “Strong Interactions in Low Dimensions”, volume 25, page 195ff. *Physics and Chemistry of Materials with Low-Dimensional Structures*, 2004. ISBN 978-1-4020-1798-8.
- [406] G. K. Madsen and D. J. Singh. “BoltzTraP. A code for calculating band-structure dependent quantities”. *Computer Physics Communications* **175**(1), 67 – 71, 2006. doi: [10.1016/j.cpc.2006.03.007](https://doi.org/10.1016/j.cpc.2006.03.007).

- [407] G. K. Madsen, J. Carrete, and M. J. Verstraete. “BoltzTraP2, a program for interpolating band structures and calculating semi-classical transport coefficients”. *Computer Physics Communications* **231**, 140–145, 2018. doi: [10.1016/j.cpc.2018.05.010](https://doi.org/10.1016/j.cpc.2018.05.010).
- [408] G. Pizzi, D. Volja, B. Kozinsky, M. Fornari, and N. Marzari. “BoltzWann: A code for the evaluation of thermoelectric and electronic transport properties with a maximally-localized Wannier functions basis”. *Computer Physics Communications* **185**(1), 422 – 429, 2014. doi: [10.1016/j.cpc.2013.09.015](https://doi.org/10.1016/j.cpc.2013.09.015).
- [409] S. Ponc e, E. Margine, C. Verdi, and F. Giustino. “Epw: Electron–phonon coupling, transport and superconducting properties using maximally localized Wannier functions”. *Computer Physics Communications* **209**, 116 – 133, 2016. doi: [10.1016/j.cpc.2016.07.028](https://doi.org/10.1016/j.cpc.2016.07.028).
- [410] J.-J. Zhou, J. Park, I.-T. Lu, I. Maliyov, X. Tong, and M. Bernardi. “Perturbo: A software package for ab initio electron–phonon interactions, charge transport and ultrafast dynamics”. *Computer Physics Communications* **264**, 107970, 2021. doi: [10.1016/j.cpc.2021.107970](https://doi.org/10.1016/j.cpc.2021.107970).
- [411] X. Li, Z. Zhang, J. Xi, D. J. Singh, Y. Sheng, J. Yang, and W. Zhang. “TransOpt. A code to solve electrical transport properties of semiconductors in constant electron–phonon coupling approximation”. *Computational Materials Science* **186**, 110074, 2021. doi: [10.1016/j.commatsci.2020.110074](https://doi.org/10.1016/j.commatsci.2020.110074).
- [412] N. H. Protik, C. Li, M. Pruneda, D. Broido, and P. Ordej n. “The elphbolt ab initio solver for the coupled electron-phonon Boltzmann transport equations”. *npj Computational Materials* **8**(1), 28, 2022. doi: [10.1038/s41524-022-00710-0](https://doi.org/10.1038/s41524-022-00710-0).
- [413] M. Zebarjadi, S. E. Rezaei, M. S. Akhanda, and K. Esfarjani. “Nernst coefficient within relaxation time approximation”. *Phys. Rev. B* **103**, 144404, Apr 2021. doi: [10.1103/PhysRevB.103.144404](https://doi.org/10.1103/PhysRevB.103.144404).
- [414] V. S. Oudovenko and G. Kotliar. “Thermoelectric properties of the degenerate Hubbard model”. *Phys. Rev. B* **65**(7), 075102, Jan 2002. doi: [10.1103/PhysRevB.65.075102](https://doi.org/10.1103/PhysRevB.65.075102).
- [415] K. Haule and G. Kotliar. *Properties and Applications of Thermoelectric Materials, Proceedings of the NATO Advanced Research Workshop on Properties and Application of Thermoelectric Materials, Hvar, Croatia, 21-26 September 2008*, chapter Thermoelectrics Near the Mott Localization–Delocalization Transition, pages 119–131. NATO Science for Peace and Security Series B: Physics and Biophysics. Springer Netherlands, 2009. ISBN 978-90-481-2890-7.

- [416] K. Behnia, D. Jaccard, and J. Flouquet. “On the thermoelectricity of correlated electrons in the zero-temperature limit”. *Journal of Physics: Condensed Matter* **16**(28), 5187, 2004. doi: [10.1088/0953-8984/16/28/037](https://doi.org/10.1088/0953-8984/16/28/037).
- [417] A. Bentien, S. Johnsen, G. K. H. Madsen, B. B. Iversen, and F. Steglich. “Colossal Seebeck coefficient in strongly correlated semiconductor FeSb₂”. *EPL (Europhysics Letters)* **80**(1), 17008 (5pp), 2007. doi: [10.1209/0295-5075/80/17008](https://doi.org/10.1209/0295-5075/80/17008).
- [418] A. Chikina, J.-Z. Ma, W. H. Brito, S. Choi, P. Sémon, A. Kutepov, Q. Du, J. Jandke, H. Liu, N. C. Plumb, M. Shi, C. Petrovic, M. Radovic, and G. Kotliar. “Correlated electronic structure of colossal thermopower FeSb₂: An ARPES and ab initio study”. *Phys. Rev. Research* **2**, 023190, May 2020. doi: [10.1103/PhysRevResearch.2.023190](https://doi.org/10.1103/PhysRevResearch.2.023190).
- [419] M. Pokharel, H. Zhao, K. Lukas, Z. Ren, C. Opeil, and B. Mihaila. “Phonon drag effect in nanocomposite FeSb₂”. *MRS Communications* **3**, 31–36, 3 2013. doi: [10.1557/mrc.2013.7](https://doi.org/10.1557/mrc.2013.7).
- [420] H. Takahashi, R. Okazaki, S. Ishiwata, H. Taniguchi, A. Okutani, M. Hagiwara, and I. Terasaki. “Colossal Seebeck effect enhanced by quasi-ballistic phonons dragging massive electrons in FeSb₂”. *Nature Communications* **7**, 12732 EP –, Sep 2016. doi: [10.1038/ncomms12732](https://doi.org/10.1038/ncomms12732).
- [421] M. Battiato, J. M. Tomczak, Z. Zhong, and K. Held. “Unified picture for the colossal thermopower compound FeSb₂”. *Phys. Rev. Lett.* **114**, 236603, Jun 2015. doi: [10.1103/PhysRevLett.114.236603](https://doi.org/10.1103/PhysRevLett.114.236603).
- [422] H. Matsuura, H. Maebashi, M. Ogata, and H. Fukuyama. “Effect of phonon drag on Seebeck coefficient based on linear response theory: Application to FeSb₂”. *Journal of the Physical Society of Japan* **88**(7), 074601, 2019. doi: [10.7566/JPSJ.88.074601](https://doi.org/10.7566/JPSJ.88.074601).
- [423] R. Masuki, T. Nomoto, and R. Arita. “Origin of anomalous temperature dependence of the Nernst effect in narrow-gap semiconductors”. *Phys. Rev. B* **103**, L041202, Jan 2021. doi: [10.1103/PhysRevB.103.L041202](https://doi.org/10.1103/PhysRevB.103.L041202).
- [424] P. Sun, N. Oeschler, S. Johnsen, B. B. Iversen, and F. Steglich. “Narrow band gap and enhanced thermoelectricity in FeSb₂”. *Dalton Transactions* **39**(4), 1012–1019, 2010. doi: [10.1039/b918909b](https://doi.org/10.1039/b918909b).
- [425] M. Wagner-Reetz, D. Kasinathan, W. Schnelle, R. Cardoso-Gil, H. Rosner, Y. Grin, and P. Gille. “Phonon-drag effect in FeGa₃”. *Phys. Rev. B* **90**, 195206, Nov 2014. doi: [10.1103/PhysRevB.90.195206](https://doi.org/10.1103/PhysRevB.90.195206).

- [426] H. Takahashi, R. Okazaki, I. Terasaki, and Y. Yasui. “Origin of the energy gap in the narrow-gap semiconductor FeSb₂ revealed by high-pressure magnetotransport measurements”. *Phys. Rev. B* **88**, 165205, Oct 2013. doi: [10.1103/PhysRevB.88.165205](https://doi.org/10.1103/PhysRevB.88.165205).
- [427] Q. Du and C. Petrovic. “Optimal carrier concentration for FeSb₂ colossal thermopower”. *Applied Physics Letters* **118**(23), 233901, 2021. doi: [10.1063/5.0048165](https://doi.org/10.1063/5.0048165).
- [428] Q. Du, L. Wu, H. Cao, C.-J. Kang, C. Nelson, G. L. Pascut, T. Besara, T. Siegrist, K. Haule, G. Kotliar, I. Zaliznyak, Y. Zhu, and C. Petrovic. “Vacancy defect control of colossal thermopower in FeSb₂”. *npj Quantum Materials* **6**(1), 13, Feb 2021. doi: [10.1038/s41535-020-00308-z](https://doi.org/10.1038/s41535-020-00308-z).
- [429] A. Bentiën, G. K. H. Madsen, S. Johnsen, and B. B. Iversen. “Experimental and theoretical investigations of strongly correlated FeSb_{2-x}Sn_x”. *Phys. Rev. B* **74**(20) 205105, 2006. doi: [10.1103/PhysRevB.74.205105](https://doi.org/10.1103/PhysRevB.74.205105).
- [430] A. V. Sanchela, A. D. Thakur, and C. Tomy. “Enhancement in thermoelectric properties of FeSb₂ by Sb site deficiency”. *Journal of Materiomics* **1**(3), 205 – 212, 2015. doi: [10.1016/j.jmat.2015.04.005](https://doi.org/10.1016/j.jmat.2015.04.005).
- [431] P. Sun, N. Oeschler, S. Johnsen, B. B. Iversen, and F. Steglich. “Huge thermoelectric power factor: FeSb₂ versus FeAs₂ and RuSb₂”. *Applied Physics Express* **2**(9), 091102, 2009. doi: [10.1143/APEX.2.091102](https://doi.org/10.1143/APEX.2.091102).
- [432] P. Sun, N. Oeschler, S. Johnsen, B. B. Iversen, and F. Steglich. “Thermoelectric properties of the narrow-gap semiconductors FeSb₂ and RuSb₂ : A comparative study”. *Journal of Physics: Conference Series* **150**(1), 012049, 2009. doi: [10.1088/1742-6596/150/1/012049](https://doi.org/10.1088/1742-6596/150/1/012049).
- [433] M. K. Fuccillo, Q. D. Gibson, M. N. Ali, L. M. Schoop, and R. J. Cava. “Correlated evolution of colossal thermoelectric effect and Kondo insulating behavior”. *APL Materials* **1**(6) 062102, 2013. doi: [10.1063/1.4833055](https://doi.org/10.1063/1.4833055).
- [434] B. C. Sales, A. F. May, M. A. McGuire, M. B. Stone, D. J. Singh, and D. Mandrus. “Transport, thermal, and magnetic properties of the narrow-gap semiconductor CrSb₂”. *Phys. Rev. B* **86**, 235136, Dec 2012. doi: [10.1103/PhysRevB.86.235136](https://doi.org/10.1103/PhysRevB.86.235136).
- [435] R. Wolfe, J. H. Wernick, and S. E. Haszko. “Thermoelectric properties of FeSi”. *Physics Letters* **19**(6), 449 – 450, 1965. doi: [0031-9163\(65\)90094-6](https://doi.org/10.1016/0031-9163(65)90094-6).

- [436] B. C. Sales, O. Delaire, M. A. McGuire, and A. F. May. “Thermoelectric properties of Co-, Ir-, and Os-doped FeSi alloys: Evidence for strong electron-phonon coupling”. *Phys. Rev. B* **83**(12), 125209, Mar 2011. doi: [10.1103/PhysRevB.83.125209](https://doi.org/10.1103/PhysRevB.83.125209).
- [437] H. Hohl, A. Ramirez, C. Goldmann, G. Ernst, and E. Bucher. “Transport properties of RuSi, RuGe, OsSi, and quasi-binary alloys of these compounds”. *Journal of Alloys and Compounds* **278**(1-2), 39 – 43, 1998. doi: [10.1016/S0925-8388\(98\)00584-2](https://doi.org/10.1016/S0925-8388(98)00584-2).
- [438] B. Buschinger, C. Geibel, J. Diehl, M. Weiden, W. Guth, A. Wildbrett, S. Horn, and F. Steglich. “Preparation and low temperature properties of FeSi-type RuSi”. *Journal of Alloys and Compounds* **256**(1), 57 – 60, 1997. doi: [10.1016/S0925-8388\(96\)03021-6](https://doi.org/10.1016/S0925-8388(96)03021-6).
- [439] J. M. Tomczak, K. Haule, and G. Kotliar. “Thermopower of the correlated narrow gap semiconductor FeSi and comparison to RuSi”. In V. Zlatić and A. Hewson, editors, “New Materials for Thermoelectric Applications: Theory and Experiment”, NATO Science for Peace and Security Series B: Physics and Biophysics, pages 45–57. Springer Netherlands, 2013. ISBN 978-94-007-4984-9.
- [440] Y. Nishino, M. Kato, S. Asano, K. Soda, M. Hayasaki, and U. Mizutani. “Semiconductorlike behavior of electrical resistivity in Heusler-type Fe₂VAl compound”. *Phys. Rev. Lett.* **79**, 1909–1912, Sep 1997. doi: [10.1103/PhysRevLett.79.1909](https://doi.org/10.1103/PhysRevLett.79.1909).
- [441] M. Kato, Y. Nishino, U. Mizutani, and S. Asano. “Electronic, magnetic and transport properties of (Fe_{1-x}V_x)₃Al alloys”. *Journal of Physics: Condensed Matter* **12**(8), 1769, 2000. doi: [10.1088/0953-8984/12/8/318](https://doi.org/10.1088/0953-8984/12/8/318).
- [442] T. Naka, A. M. Nikitin, Y. Pan, A. de Visser, T. Nakane, F. Ishikawa, Y. Yamada, M. Imai, and A. Matsushita. “Composition induced metal–insulator quantum phase transition in the Heusler type Fe₂VAl”. *Journal of Physics: Condensed Matter* **28**(28), 285601, 2016. doi: [10.1088/0953-8984/28/28/285601](https://doi.org/10.1088/0953-8984/28/28/285601).
- [443] T. Nakama, Y. Takaesu, K. Yagasaki, T. Naka, A. Matsushita, K. Fukuda, and Y. Yamada. “Transport properties of Heusler compounds Fe_{3-x}V_xAl”. *Journal of the Physical Society of Japan* **74**(5), 1378–1381, 2005. doi: [10.1143/JPSJ.74.1378](https://doi.org/10.1143/JPSJ.74.1378).
- [444] B. Hinterleitner, I. Knapp, M. Poner, Y. Shi, H. Müller, G. Eguchi, C. Eisenmenger-Sittner, M. Stöger-Pollach, Y. Kakefuda, N. Kawamoto, Q. Guo, T. Baba, T. Mori, S. Ullah, X.-Q. Chen, and E. Bauer. “Thermoelectric performance of a metastable thin-film Heusler alloy”. *Nature* **576**(7785), 85–90, Dec 2019. doi: [10.1038/s41586-019-1751-9](https://doi.org/10.1038/s41586-019-1751-9).

- [445] M. S. Likhhanov and A. V. Shevelkov. “Intermetallic compounds with non-metallic properties”. *Russian Chemical Bulletin* **69**(12), 2231–2255, Dec 2020. doi: [10.1007/s11172-020-3047-5](https://doi.org/10.1007/s11172-020-3047-5).
- [446] Y. Hadano, S. Narazu, M. A. Avila, T. Onimaru, and T. Takabatake. “Thermoelectric and magnetic properties of a narrow-gap semiconductor FeGa₃”. *Journal of the Physical Society of Japan* **78**(1), 013702, 2009. doi: [10.1143/JPSJ.78.013702](https://doi.org/10.1143/JPSJ.78.013702).
- [447] M. B. Gamza, J. M. Tomczak, C. Brown, A. Puri, G. Kotliar, and M. C. Aronson. “Electronic correlations in FeGa₃ and the effect of hole doping on its magnetic properties”. *Phys. Rev. B* **89**, 195102, May 2014. doi: [10.1103/PhysRevB.89.195102](https://doi.org/10.1103/PhysRevB.89.195102).
- [448] J. M. Ziman. *Principles of the theory of solids*. University Press, Cambridge, 1972. ISBN 978-1-13-964407-5.
- [449] H. Goldsmid and J. Sharp. “Estimation of the thermal band gap of a semiconductor from Seebeck measurements”. *Journal of Electronic Materials* **28**, 869–872, 1999. doi: [10.1007/s11664-999-0211-y](https://doi.org/10.1007/s11664-999-0211-y).
- [450] C. Fu, M. Yao, X. Chen, L. Z. Maulana, X. Li, J. Yang, K. Imasato, F. Zhu, G. Li, G. Auffermann, U. Burkhardt, W. Schnelle, J. Zhou, T. Zhu, X. Zhao, M. Shi, M. Dressel, A. V. Pronin, G. J. Snyder, and C. Felser. “Revealing the intrinsic electronic structure of 3d half-Heusler thermoelectric materials by angle-resolved photoemission spectroscopy”. *Advanced Science* **7**(1), 1902409, 2020. doi: [10.1002/advs.201902409](https://doi.org/10.1002/advs.201902409).
- [451] A. L. Kutepov and A. Ruth. “Electronic structure and thermoelectric properties of CoAsSb with post-DFT approaches”. *Applied Physics A* **126**(2), 137, Jan 2020. doi: [10.1007/s00339-020-3304-3](https://doi.org/10.1007/s00339-020-3304-3).
- [452] F. Garmroudi, A. Riss, M. Parzer, N. Reumann, H. Müller, E. Bauer, S. Khmelevskiy, R. Podloucky, T. Mori, K. Tobita, Y. Katsura, and K. Kimura. “Boosting the thermoelectric performance of Fe₂VAl-type Heusler compounds by band engineering”. *Phys. Rev. B* **103**, 085202, Feb 2021. doi: [10.1103/PhysRevB.103.085202](https://doi.org/10.1103/PhysRevB.103.085202).
- [453] T. Deng, J. Recatala-Gomez, M. Ohnishi, D. V. M. Repaka, P. Kumar, A. Suwardi, A. Abutaha, I. Nandhakumar, K. Biswas, M. B. Sullivan, G. Wu, J. Shiomi, S.-W. Yang, and K. Hippalgaonkar. “Electronic transport descriptors for the rapid screening of thermoelectric materials”. *Mater. Horiz.* **8**, 2463–2474, 2021. doi: [10.1039/D1MH00751C](https://doi.org/10.1039/D1MH00751C).

- [454] Z. M. Gibbs, H.-S. Kim, H. Wang, and G. J. Snyder. “Band gap estimation from temperature dependent Seebeck measurement—deviations from the $2e|S_{max}|T_{max}$ relation”. *Applied Physics Letters* **106**(2), 022112, 2015. doi: [10.1063/1.4905922](https://doi.org/10.1063/1.4905922).
- [455] M. Cutler and N. F. Mott. “Observation of Anderson localization in an electron gas”. *Phys. Rev.* **181**, 1336–1340, May 1969. doi: [10.1103/PhysRev.181.1336](https://doi.org/10.1103/PhysRev.181.1336).
- [456] M. Jonson and G. D. Mahan. “Mott’s formula for the thermopower and the Wiedemann-Franz law”. *Phys. Rev. B* **21**, 4223–4229, May 1980. doi: [10.1103/PhysRevB.21.4223](https://doi.org/10.1103/PhysRevB.21.4223).
- [457] Y. Wang, Z. A. Xu, T. Kakeshita, S. Uchida, S. Ono, Y. Ando, and N. P. Ong. “Onset of the vortexlike Nernst signal above T_c in $\text{La}_{2-x}\text{Sr}_x\text{CuO}_4$ and $\text{Bi}_2\text{Sr}_{2-y}\text{La}_y\text{CuO}_6$ ”. *Phys. Rev. B* **64**, 224519, Nov 2001. doi: [10.1103/PhysRevB.64.224519](https://doi.org/10.1103/PhysRevB.64.224519).
- [458] V. Oganesyan and I. Ussishkin. “Nernst effect, quasiparticles, and d -density waves in cuprates”. *Phys. Rev. B* **70**, 054503, Aug 2004. doi: [10.1103/PhysRevB.70.054503](https://doi.org/10.1103/PhysRevB.70.054503).
- [459] E. H. Sondheimer and A. H. Wilson. “The theory of the galvanomagnetic and thermomagnetic effects in metals”. *Proceedings of the Royal Society of London. Series A. Mathematical and Physical Sciences* **193**(1035), 484–512, 1948. doi: [10.1098/rspa.1948.0058](https://doi.org/10.1098/rspa.1948.0058).
- [460] P. Sun, B. Wei, J. Zhang, J. M. Tomczak, A. M. Strydom, M. Søndergaard, B. B. Iversen, and F. Steglich. “Large Seebeck effect by charge-mobility engineering”. *Nat Commun* **6**, 7475, Jun 2015. doi: [10.1038/ncomms8475](https://doi.org/10.1038/ncomms8475).
- [461] W.-R. Lee, A. M. Finkel’stein, K. Michaeli, and G. Schwiete. “Role of electron-electron collisions for charge and heat transport at intermediate temperatures”. *Phys. Rev. Research* **2**, 013148, Feb 2020. doi: [10.1103/PhysRevResearch.2.013148](https://doi.org/10.1103/PhysRevResearch.2.013148).
- [462] A. Lavasani, D. Bulmash, and S. Das Sarma. “Wiedemann-Franz law and Fermi liquids”. *Phys. Rev. B* **99**, 085104, Feb 2019. doi: [10.1103/PhysRevB.99.085104](https://doi.org/10.1103/PhysRevB.99.085104).
- [463] I. Opahle, G. K. H. Madsen, and R. Drautz. “High throughput density functional investigations of the stability, electronic structure and thermoelectric properties of binary silicides”. *Phys. Chem. Chem. Phys.* **14**, 16197–16202, 2012. doi: [10.1039/C2CP41826F](https://doi.org/10.1039/C2CP41826F).
- [464] S. Wang, Z. Wang, W. Setyawan, N. Mingo, and S. Curtarolo. “Assessing the thermoelectric properties of sintered compounds via high-throughput ab initio calculations”. *Phys. Rev. X* **1**, 021012, Nov 2011. doi: [10.1103/PhysRevX.1.021012](https://doi.org/10.1103/PhysRevX.1.021012).

- [465] W. Chen, J.-H. Pohls, G. Hautier, D. Broberg, S. Bajaj, U. Aydemir, Z. M. Gibbs, H. Zhu, M. Asta, G. J. Snyder, B. Meredig, M. A. White, K. Persson, and A. Jain. “Understanding thermoelectric properties from high-throughput calculations: trends, insights, and comparisons with experiment”. *J. Mater. Chem. C* **4**, 4414–4426, 2016. doi: [10.1039/C5TC04339E](https://doi.org/10.1039/C5TC04339E).
- [466] T. Katase, X. He, T. Tadano, J. M. Tomczak, T. Onozato, K. Ide, B. Feng, T. Tohei, H. Hiramatsu, H. Ohta, Y. Ikuhara, H. Hosono, and T. Kamiya. “Breaking of thermopower–conductivity trade-off in LaTiO₃ film around Mott insulator to metal transition”. *Advanced Science* **8**(23), 2102097, 2021. doi: [10.1002/advs.202102097](https://doi.org/10.1002/advs.202102097).
- [467] S. Bocelli, F. Marabelli, R. Spolenak, and E. Bauer. “Evolution of the optical response from a very narrow gap semiconductor to a metallic material in (Fe_xMn_{1-x})Si”. *MRS Online Proceedings Library* **402**, 361–366, 1996. doi: [10.1557/PROC-402-361](https://doi.org/10.1557/PROC-402-361).
- [468] A. Perucchi, L. Degiorgi, R. Hu, C. Petrovic, and V. F. Mitrovic. “Optical investigation of the metal-insulator transition in FeSb₂”. *The European Physical Journal B* **54**(2), 175–183, 2006. doi: [10.1140/epjb/e2006-00433-1](https://doi.org/10.1140/epjb/e2006-00433-1).
- [469] C. C. Homes, Q. Du, C. Petrovic, W. H. Brito, S. Choi, and G. Kotliar. “Unusual electronic and vibrational properties in the colossal thermopower material FeSb₂”. *Scientific Reports* **8**(1), 11692, 2018. doi: [10.1038/s41598-018-29909-2](https://doi.org/10.1038/s41598-018-29909-2).
- [470] T. Jarlborg. “Temperature-dependent electronic structure: from heavy fermion behaviour to phase stability”. *Reports on Progress in Physics* **60**(11), 1305, 1997. doi: [10.1088/0034-4885/60/11/003](https://doi.org/10.1088/0034-4885/60/11/003).
- [471] O. Delaire, K. Marty, M. B. Stone, P. R. C. Kent, M. S. Lucas, D. L. Abernathy, D. Mandrus, and B. C. Sales. “Phonon softening and metallization of a narrow-gap semiconductor by thermal disorder”. *PNAS* **108**(12), 4725–4730, 2011. doi: [10.1073/pnas.1014869108](https://doi.org/10.1073/pnas.1014869108).
- [472] R. Hu, V. F. Mitrović, and C. Petrovic. “Anisotropy in the magnetic and transport properties of Fe_{1-x}Co_xSb₂”. *Phys. Rev. B* **74**(19), 195130, Nov 2006. doi: [10.1103/PhysRevB.74.195130](https://doi.org/10.1103/PhysRevB.74.195130).
- [473] T. Deguchi, K. Matsubayashi, Y. Uwatoko, T. Koyama, T. Kohara, H. Nakamura, Y. Mitsui, and K. Koyama. “Magnetic measurements of narrow-gap semiconductor FeSb₂ under high pressure”. *Materials Transactions* **61**(8), 1476–1479, 2020. doi: [10.2320/matertrans.MT-MN2019015](https://doi.org/10.2320/matertrans.MT-MN2019015).
- [474] K.-J. Xu, S.-D. Chen, Y. He, J. He, S. Tang, C. Jia, E. Yue Ma, S.-K. Mo, D. Lu, M. Hashimoto, T. P. Devereaux, and Z.-X. Shen. “Metallic surface states in a correlated d-electron topological

- Kondo insulator candidate FeSb_2 ". *Proceedings of the National Academy of Sciences* **117**(27), 15409–15413, 2020. doi: [10.1073/pnas.2002361117](https://doi.org/10.1073/pnas.2002361117).
- [475] C. Herring. "Theory of the thermoelectric power of semiconductors". *Phys. Rev.* **96**(5), 1163–1187, Dec 1954. doi: [10.1103/PhysRev.96.1163](https://doi.org/10.1103/PhysRev.96.1163).
- [476] J. Zhou, B. Liao, B. Qiu, S. Huberman, K. Esfarjani, M. S. Dresselhaus, and G. Chen. "Ab initio optimization of phonon drag effect for lower-temperature thermoelectric energy conversion". *Proceedings of the National Academy of Sciences* **112**(48), 14777–14782, 2015. doi: [10.1073/pnas.1512328112](https://doi.org/10.1073/pnas.1512328112).
- [477] M. Kimura, X. He, T. Katase, T. Tadano, J. M. Tomczak, M. Minohara, R. Aso, H. Yoshida, K. Ide, S. Ueda, H. Hiramatsu, H. Kumigashira, H. Hosono, and T. Kamiya. "Large phonon drag thermopower boosted by massive electrons and phonon leaking in $\text{LaAlO}_3/\text{LaNiO}_3/\text{LaAlO}_3$ heterostructure". *Nano Letters* **21**(21), 9240–9246, 11 2021. doi: [10.1021/acs.nanolett.1c03143](https://doi.org/10.1021/acs.nanolett.1c03143).
- [478] Q. Du, X. Tong, Y. Liu, and C. Petrovic. "Suppression of thermal conductivity and electronic correlations in $\text{Fe}_{1-x}\text{Ru}_x\text{Sb}_2$ ($0 \leq x \leq 1$)". *Applied Physics Letters* **118**(17), 171904, 2021. doi: [10.1063/5.0046779](https://doi.org/10.1063/5.0046779).
- [479] W. Kohn. "Nobel lecture: Electronic structure of matter-wave functions and density functionals". *Rev. Mod. Phys.* **71**(5), 1253–1266, Oct 1999. doi: [10.1103/RevModPhys.71.1253](https://doi.org/10.1103/RevModPhys.71.1253).
- [480] F. Aryasetiawan and O. Gunnarsson. "The GW method". *Reports on Progress in Physics* **61**(3), 237–312, 1998. doi: [10.1088/0034-4885/61/3/002](https://doi.org/10.1088/0034-4885/61/3/002).
- [481] G. Onida, L. Reining, and A. Rubio. "Electronic excitations: density-functional versus many-body Green's-function approaches". *Rev. Mod. Phys.* **74**(2), 601–659, Jun 2002. doi: [10.1103/RevModPhys.74.601](https://doi.org/10.1103/RevModPhys.74.601).
- [482] K. Held. "Electronic structure calculations using dynamical mean field theory". *Advances in Physics* **56**(6), 829–926, 2007. doi: [10.1080/00018730701619647](https://doi.org/10.1080/00018730701619647).
- [483] W. Li, J. Carrete, N. A. Katcho, and N. Mingo. "Shengbte: A solver of the Boltzmann transport equation for phonons". *Computer Physics Communications* **185**(6), 1747–1758, 2014. doi: [10.1016/j.cpc.2014.02.015](https://doi.org/10.1016/j.cpc.2014.02.015).
- [484] J. Carrete, B. Vermeersch, A. Katre, A. van Roekeghem, T. Wang, G. K. Madsen, and N. Mingo. "almaBTE : A solver of the space-time dependent Boltzmann transport equation

- for phonons in structured materials”. *Computer Physics Communications* **220**, 351–362, 2017. doi: [10.1016/j.cpc.2017.06.023](https://doi.org/10.1016/j.cpc.2017.06.023).
- [485] Y. Nomura and R. Arita. “Ab initio downfolding for electron-phonon-coupled systems: Constrained density-functional perturbation theory”. *Phys. Rev. B* **92**, 245108, Dec 2015. doi: [10.1103/PhysRevB.92.245108](https://doi.org/10.1103/PhysRevB.92.245108).
- [486] S. Poncé, F. Macheda, E. R. Margine, N. Marzari, N. Bonini, and F. Giustino. “First-principles predictions of Hall and drift mobilities in semiconductors”. *Phys. Rev. Research* **3**, 043022, Oct 2021. doi: [10.1103/PhysRevResearch.3.043022](https://doi.org/10.1103/PhysRevResearch.3.043022).
- [487] S. Bhattacharya and G. K. H. Madsen. “High-throughput exploration of alloying as design strategy for thermoelectrics”. *Phys. Rev. B* **92**, 085205, Aug 2015. doi: [10.1103/PhysRevB.92.085205](https://doi.org/10.1103/PhysRevB.92.085205).
- [488] A. van Roekeghem, J. Carrete, C. Oses, S. Curtarolo, and N. Mingo. “High-throughput computation of thermal conductivity of high-temperature solid phases: The case of oxide and fluoride perovskites”. *Phys. Rev. X* **6**, 041061, Dec 2016. doi: [10.1103/PhysRevX.6.041061](https://doi.org/10.1103/PhysRevX.6.041061).
- [489] F. Ricci, W. Chen, U. Aydemir, G. J. Snyder, G.-M. Rignanese, A. Jain, and G. Hautier. “An ab initio electronic transport database for inorganic materials”. *Sci Data* **4**, 170085, Jul 2017. doi: [10.1038/sdata.2017.85](https://doi.org/10.1038/sdata.2017.85).
- [490] P. Gorai, V. Stevanovic, and E. S. Toberer. “Computationally guided discovery of thermoelectric materials”. *Nat Rev Mater* **2**, 17053, Aug 2017. doi: [10.1038/natrevmats.2017.53](https://doi.org/10.1038/natrevmats.2017.53).
- [491] R. Li, X. Li, L. Xi, J. Yang, D. J. Singh, and W. Zhang. “High-throughput screening for advanced thermoelectric materials: Diamond-like ABX₂ compounds”. *ACS Applied Materials & Interfaces* **11**(28), 24859–24866, 2019. doi: [10.1021/acsami.9b01196](https://doi.org/10.1021/acsami.9b01196).
- [492] X. Deng, J. Mravlje, R. Žitko, M. Ferrero, G. Kotliar, and A. Georges. “How bad metals turn good: Spectroscopic signatures of resilient quasiparticles”. *Phys. Rev. Lett.* **110**, 086401, Feb 2013. doi: [10.1103/PhysRevLett.110.086401](https://doi.org/10.1103/PhysRevLett.110.086401).
- [493] W. Xu, K. Haule, and G. Kotliar. “Hidden Fermi liquid, scattering rate saturation, and Nernst effect: A dynamical mean-field theory perspective”. *Phys. Rev. Lett.* **111**, 036401, Jul 2013. doi: [10.1103/PhysRevLett.111.036401](https://doi.org/10.1103/PhysRevLett.111.036401).
- [494] J. Mravlje and A. Georges. “Thermopower and entropy: Lessons from Sr₂RuO₄”. *Phys. Rev. Lett.* **117**, 036401, Jul 2016. doi: [10.1103/PhysRevLett.117.036401](https://doi.org/10.1103/PhysRevLett.117.036401).

- [495] J. M. Tomczak, L. V. Pourovskii, L. Vaugier, A. Georges, and S. Biermann. “Rare-earth vs. heavy metal pigments and their colors from first principles”. *PNAS* **110**(3), 904–907, 2013. doi: [10.1073/pnas.1215066110](https://doi.org/10.1073/pnas.1215066110).
- [496] E. Assmann, P. Wissgott, J. Kuneš, A. Toschi, P. Blaha, and K. Held. “woptic: Optical conductivity with Wannier functions and adaptive k-mesh refinement”. *Computer Physics Communications* **202**, 1 – 11, 2016. doi: [10.1016/j.cpc.2015.12.010](https://doi.org/10.1016/j.cpc.2015.12.010).
- [497] M. Aichhorn, L. Pourovskii, P. Seth, V. Vildosola, M. Zingl, O. E. Peil, X. Deng, J. Mravlje, G. J. Kraberger, C. Martins, M. Ferrero, and O. Parcollet. “TRIQS/DFTTools: A TRIQS application for ab initio calculations of correlated materials”. *Computer Physics Communications* **204**, 200–208, 2016. doi: [10.1016/j.cpc.2016.03.014](https://doi.org/10.1016/j.cpc.2016.03.014).
- [498] L. Boehnke and F. Lechermann. “Getting back to Na_xCoO_2 : Spectral and thermoelectric properties”. *physica status solidi (a)* **211**(6), 1267–1272, 2014. doi: [10.1002/pssa.201300197](https://doi.org/10.1002/pssa.201300197).
- [499] L. Calderín, V. Karasiev, and S. Trickey. “Kubo-Greenwood electrical conductivity formulation and implementation for projector augmented wave datasets”. *Computer Physics Communications* **221**, 118–142, 2017. doi: [10.1016/j.cpc.2017.08.008](https://doi.org/10.1016/j.cpc.2017.08.008).
- [500] A. Sihi and S. K. Pandey. “TRACK: A python code for calculating the transport properties of correlated electron systems using Kubo formalism”. *arXiv* 2021. doi: [10.48550/arXiv.2110.07243](https://doi.org/10.48550/arXiv.2110.07243).
- [501] G. L. W. Hart, J. J. Jorgensen, W. S. Morgan, and R. W. Forcade. “A robust algorithm for k-point grid generation and symmetry reduction”. *Journal of Physics Communications* **3**(6), 065009, Jun 2019. doi: [10.1088/2399-6528/ab2937](https://doi.org/10.1088/2399-6528/ab2937).
- [502] CERN. “CERN program library”. discontinued in 2003; available under GNU GPL; <https://cernlib.web.cern.ch/cernlib/> Last visited: Feb 2024.
- [503] K. Kölbig. “Programs for computing the logarithm of the gamma function, and the digamma function, for complex argument”. *Computer Physics Communications* **4**(2), 221 – 226, 1972. doi: [10.1016/0010-4655\(72\)90012-4](https://doi.org/10.1016/0010-4655(72)90012-4).
- [504] G. Madsen, A. Bentien, S. Johnsen, and B. Iversen. “Electronic structure in FeSb_2 , FeAs_2 and FeSi ”. In “25th International Conference on Thermoelectrics, ICT ’06.”, pages 579–581. 2006.
- [505] G. J. Snyder and E. S. Toberer. “Complex thermoelectric materials”. *Nat Mater* **7**(2), 105–114, Feb 2008. doi: [10.1038/nmat2090](https://doi.org/10.1038/nmat2090).

- [506] Q. Du, D. Guzman, S. Choi, and C. Petrovic. “Crystal size effects on giant thermopower in CrSb₂”. *Phys. Rev. B* **101**, 035125, Jan 2020. doi: [10.1103/PhysRevB.101.035125](https://doi.org/10.1103/PhysRevB.101.035125).
- [507] J. P. Heremans, V. Jovovic, E. S. Toberer, A. Saramat, K. Kurosaki, A. Charoenthanakdee, S. Yamanaka, and G. J. Snyder. “Enhancement of thermoelectric efficiency in PbTe by distortion of the electronic density of states”. *Science* **321**(5888), 554–557, 2008. doi: [10.1126/science.1159725](https://doi.org/10.1126/science.1159725).
- [508] Y. Matsushita, H. Bluhm, T. H. Geballe, and I. R. Fisher. “Evidence for charge Kondo effect in superconducting Tl-doped PbTe”. *Phys. Rev. Lett.* **94**, 157002, Apr 2005. doi: [10.1103/PhysRevLett.94.157002](https://doi.org/10.1103/PhysRevLett.94.157002).
- [509] H. Matsuura, H. Mukuda, and K. Miyake. “Valence skipping phenomena, charge Kondo effect, and superconductivity”. *AAPPS Bulletin* **32**(1), 30, 2022. doi: [10.1007/s43673-022-00056-1](https://doi.org/10.1007/s43673-022-00056-1).
- [510] H. Matsuura and K. Miyake. “Theory of charge Kondo effect on pair hopping mechanism”. *Journal of the Physical Society of Japan* **81**(11), 113705, Nov 2012. doi: [10.1143/jpsj.81.113705](https://doi.org/10.1143/jpsj.81.113705).
- [511] S. Sekiguchi, T. Shiraishi, K. Miura, C. Kawashima, K. Yoshimatsu, A. Ohtomo, H. Kamioka, and H. Takahashi. “High-pressure study of superconductivity in Ti₄O₇ film”. *Journal of the Physical Society of Japan* **88**(3), 035001, Mar 2019. doi: [10.7566/jpsj.88.035001](https://doi.org/10.7566/jpsj.88.035001).
- [512] M. Ogata and H. Fukuyama. “Range of validity of Sommerfeld–Bethe relation associated with Seebeck coefficient and phonon drag contribution”. *Journal of the Physical Society of Japan* **88**(7), 074703, Jul 2019. doi: [10.7566/jpsj.88.074703](https://doi.org/10.7566/jpsj.88.074703).
- [513] D. Miura and A. Sakuma. “Microscopic theory of magnon-drag thermoelectric transport in ferromagnetic metals”. *Journal of the Physical Society of Japan* **81**(11), 113602, 2024/02/20 2012. doi: [10.1143/JPSJ.81.113602](https://doi.org/10.1143/JPSJ.81.113602).
- [514] D. Vanderbilt. *Berry Phases in Electronic Structure Theory: Electric Polarization, Orbital Magnetization and Topological Insulators*. Cambridge University Press, Oct 2018. ISBN 978-1-10-715765-1.
- [515] L. Del Re and A. Toschi. “Dynamical vertex approximation for many-electron systems with spontaneously broken SU(2) symmetry”. *Phys. Rev. B* **104**, 085120, Aug 2021. doi: [10.1103/PhysRevB.104.085120](https://doi.org/10.1103/PhysRevB.104.085120).
- [516] D. G. Cantrell and P. N. Butcher. “A calculation of the phonon-drag contribution to the thermopower of quasi-2D electrons coupled to 3D phonons. I. General theory”. *Journal of Physics C: Solid State Physics* **20**(13), 1985, 1987. doi: [10.1088/0022-3719/20/13/014](https://doi.org/10.1088/0022-3719/20/13/014).

- [517] J. D. Wasscher and C. Haas. “Contribution of magnon-drag to the thermoelectric power of antiferromagnetic Mn Te”. *Physics Letters* **8**(5), 302–304, 1964. doi: [10.1016/S0031-9163\(64\)80006-8](https://doi.org/10.1016/S0031-9163(64)80006-8).
- [518] R. Niu and W. K. Zhu. “Materials and possible mechanisms of extremely large magnetoresistance: a review”. *Journal of Physics: Condensed Matter* **34**(11), 113001, 2022. doi: [10.1088/1361-648X/ac3b24](https://doi.org/10.1088/1361-648X/ac3b24).
- [519] I. Floss, C. Lemell, G. Wachter, V. Smejkal, S. A. Sato, X.-M. Tong, K. Yabana, and J. Burgdörfer. “Ab initio multiscale simulation of high-order harmonic generation in solids”. *Phys. Rev. A* **97**, 011401, Jan 2018. doi: [10.1103/PhysRevA.97.011401](https://doi.org/10.1103/PhysRevA.97.011401).
- [520] V. N.-S. Bong and B. T. Wong. “The effect of phonon anisotropic scattering on the thermal conductivity of silicon thin films at 300K and 400K”. *Journal of Physics and Chemistry of Solids* **88**, 41–46, 2016. doi: [10.1016/j.jpcs.2015.09.010](https://doi.org/10.1016/j.jpcs.2015.09.010).
- [521] T. Matsubara. “A new approach to quantum-statistical mechanics”. *Progress of Theoretical Physics* **14**(4), 351–378, (1955). doi: [10.1143/PTP.14.351](https://doi.org/10.1143/PTP.14.351).
- [522] A. Abrikosov, L. Gorkov, and I. Dzyaloshinski. *Methods of quantum field theory in statistical physics*. Dover, 1975. ISBN 978-0-48-663228-5.
- [523] A. M. Zagoskin. *Quantum theory of many-body systems: techniques and applications*. Springer, 1998. ISBN 978-0-38-798384-4.
- [524] P. Kappl, F. Krien, C. Watzenböck, and K. Held. “Nonlinear responses and three-particle correlators in correlated electron systems exemplified by the Anderson impurity model”. *Phys. Rev. B* **107**, 205108, May 2023. doi: [10.1103/PhysRevB.107.205108](https://doi.org/10.1103/PhysRevB.107.205108).

Acknowledgments

This thesis would not have been possible without the contributions and support of a lot of people. First and foremost I would like to thank my supervisor Jan Tomczak. Without his unrelenting support, encouragement, patience, and expertise the present doctoral thesis would have never been completed. Never bothered by my persistent, ongoing barrage of questions, he was able to guide me through scientific complexities and resolve my consistent confusions on a daily basis. By allowing me to follow my scientific interests, many of the here presented topics were made possible.

A special thanks goes towards Karsten Held for providing me with the opportunity to work and prove myself in his research group: Starting from introductory projects, to my master thesis and finally to the present doctoral thesis. I will forever be grateful for the support I received over the years. I would also like to thank Anna Kauch for always having an open ear for my questions, and for the interesting discussions that often times went beyond physics.

Next I want to acknowledge the immensely welcoming, friendly, and comradely environment the office space at the TU Wien has provided to me, the importance of which became painfully clear during the COVID-19 pandemic. Among the many faces that have come and gone during my stay, I would like to specifically emphasize Patrick Chalupa-Gantner and Severino Adler. By always encouraging one another I truly believe that we motivated and pushed ourselves to achieve our goals. I truly relish the time we shared, and will forever cherish the great memories. I would also like to highlight Josef Kaufmann who was a delight to work with during the development of the AbinitioDFA project.

Lastly a list of people that helped me throughout my studies and require explicit mentioning (in no specific order): Juan Fernández Afonso, Daniel Springer, Anna Galler, Alessandro Toschi, Judith Gabel, Patrick Gunacker, Emanuele Maggio, Andriy Smolyanyuk, and Markus Wallerberger.

Ohne die unerbittliche Unterstützung meiner Eltern wäre weder mein Studium noch der Abschluss dieser Dissertation möglich gewesen: Ihr habt das nahezu Unmögliche geschafft Exzellenz zu fördern, ohne unangemessenen Druck auszuüben. Nur durch euch ist es mir möglich gewesen, dorthin zu kommen wo ich heute stehe. Im gleichen Sinne muss die Bereicherung durch meine Schwester Andrea hervorgehoben werden: Deine Unterstützung bedeutet die Welt für mich. An meine Nichte Katharina, falls du diesen Text jemals lesen wirst: Ich hoffe, du findest Erfüllung in deinem Leben und erreichst alles, was du dir vornimmst. Bleib der Neugierde treu, denn sie ist der Schlüssel um die Welt zu entdecken. Eine weitere riesige Danksagung steht Simon Rommer zu: Durch deine konsistente Unterstützung und Fähigkeit, mich an den Boden der Realität zurückzuführen, hast du indirekt mehr zu dieser Arbeit beigetragen, als du dir jemals vorstellen kannst.

MIMÉ BRIXHT,

<TTPÉ ZHFRZ,

↑FII HMFM HIXH.

XZ <MMtNI I+TQ tM MIZT, QFM PFRRIQR.

FtHfTtT PftTÉ FQR SQR.

Curriculum vitae

Personal information

name: Matthias Pickem
date of birth: 8 March 1992
nationality: Austria
email: matthias.pickem@gmail.com

Education

2018- Doctoral Programme in Natural Sciences, TU Wien
Institute of Solid State Physics — Computational Materials Science
2016-2018 Master's Programme Technical Physics, TU Wien
2011-2016 Bachelor's Programme Technical Physics, TU Wien
2006-2011 HTBLA Eisenstadt
2002-2006 BG/BRG Neusiedl am See

Academic employment and teaching

2018-2021 Project assistant — funding through
ERC: AbinitioDFA, FWF: VeCoCo, FWF: LinReTraCe, FWF: Eco3P
2017 Student assistant — funding through ERC: AbinitioDFA
2016-2017 Tutor Quantum Theory 1, Numerical Methods and Simulation

Conferences and workshops

2020-2021 COVID-19 pandemic
2019 Summer school Cargèse: Emergent Phenomena in Correlated Quantum Matter
2019 DPG Regensburg (Talk)
2018 SFB ViCoM Workshop Krumbach
2018 Autumn school Jülich: DMFT: From Infinite Dimensions to Real Materials
2018 Summer school Vienna: Bandstructure meets Quantum Field Theory (Lecture)